Proceedings of the 7th International Digital Human Modeling Symposium

Aug. 29-31, 2022

University of Iowa
Iowa City, Iowa 52242, USA

Karim Malek, PhD, University of Iowa, USA, Chair
Gunther Paul, PhD, James Cook University, Australia, Co-Chair

Hosted by Iowa Technology Institute, University of Iowa
Endorsed by the International Ergonomics Association

In Collaboration with the International Ergonomics Association
Technical Committee on Digital Human Modeling and Simulation

University of Iowa, 2022

ISBN: 978-0-9840378-4-1

Contents

Conference Synopsis

Organizing Committee

Scientific Committee

Session 1: DHM in Production Planning

Improving ergonomic value of product interface materials using numerical digital human models

Gregor Harih and Vasja Plesec
Paper 1 • 9 pages

Digital production planning and human simulation of manual and hybrid work processes using the ema Software Suite

Michael Spitzhirn, Sascha Ullman, Sebastian Bauer and Lars Fritzsche
Paper 2 • 13 pages

Using time-based musculoskeletal risk assessment methods to assess worker well-being in optimizations in a welding station design

Aitor Iriondo Pascual, Elia Mora, Dan Högberg, Lars Hanson, Mikael Lebram and Dan Lämkull
Paper 3 • 13 pages

Design concept evaluation in digital human modeling tools

Lars Hanson, Dan Högberg, Anna Brolin, Erik Brolin, Mikael Lebram, Aitor Iriondo Pascual, Andreas Lind and Niclas Delfs
Paper 4 • 9 pages

The effects of sex and handedness on lumbar kinetics during asymmetric lifting tasks: A pilot study

Jazmin Cruz, Ivan Aguilar and James Yang
Paper 5 • 10 pages

Session 2: DHM in Automotive

On the progress of knowledge-based motion simulation techniques in ergonomic vehicle design

Hans-Joachim Wirsching and Norman Hofmann
Paper 6 • 11 pages

Influence of different pedestrian behavior models on the performance assessment of autonomous emergency braking (AEB) systems via virtual simulation

Lucas Fonseca Alexandre de Oliveira, Martin Meywerk, Lars Schories, Maria Meier, Ramakrishna Nanjundaiah, Paulthi Victor, Francesco Foglino, Mark Carroll and Arunaachalam Muralidharan
Paper 7 • 10 pages

Takeover performance according to the level of disengagement during automated driving

Evan Gallouin, Xuguang Wang, Philippe Beillas and Thierry Bellet
Paper 8 • 9 pages

Quantifying vision obstruction of Formula One (F1) halo concept variants

Sriram Srinivasan and H. Onan Demirel
Paper 9 • 9 pages

The use of DHM to quantify a measure of direct vision performance in trucks

Steve Summerskill, Russell Marshall, Abby Paterson and Anthony Eland
Paper 10 • 9 pages

Session 3: Body Shape and Anthropometry

Overview of software and file exchange formats in 3D and 4D body shape scanning

Sofia Scataglini and Steven Truijen
Paper 11 • 9 pages

A methodology to obtain anthropometric measurements from 4D scans

Jordi Uriel, Ana Ruescas, Sofia Iranzo, Alfredo Ballester, Eduardo Parrilla, Alfredo Remón and Sandra Alemany
Paper 12 • 13 pages

Development of body shape data based digital human models for ergonomics simulations

Erik Brolin, Niclas Delfs, Martin Rebas, Tobias Karlsson, Lars Hanson and Dan Högberg
Paper 13 • 9 pages

Digitizing human scalp shape through 3D scanning

Peng Li, Asbed Tashjian and Matthew Hurley
Paper 14 • 3 pages

Session 4: DHM in Biomechanics (Part 1)

Assessing effects of environmental factors on physical workload during motor-manual timber harvesting using motion capturing data and biomechanical modeling

Oliver Brunner, Christopher Brandl and Verena Nitsch
Paper 15 • 11 pages

Simulation of abdominal belt effects on IAP and spinal compressive force with musculoskeletal human model

Zhenkai Zhao, Leiming Gao, Benjamin Simpson, James Campbell and Neil Mansfield
Paper 16 • 9 pages

Effects of sex and weighted vest load arrangements on lower biomechanics and jump height during countermovement jump

Juan Baus, John R. Harry and James Yang
Paper 17 • 8 pages

Joint velocity dependence of fatigue in isokinetic tasks

Ritwik Rakshit, Shuvrodeb Barman, Yujiang Xiang and James Yang
Paper 18 • 10 pages

Multi-modal event standardization platform of biometric-derived human performance models in university students

Joseph Alemany, Meghan Garvey, Kristin Gowers, Robyn Highfill-McRoy, Patrick Walsh and Arlington Wilson
Short Presentation 19 • 2 pages

Session 5: Hand Modeling

Wrist model for the whole human hand

Esteban Peña-Pitarch
Paper 20 • 8 pages

User-guided grasp planning for digital hand

Yi Li, Niclas Delfs and Johan S. Carlson
Paper 21 • 11 pages

Session 6: Exoskeletons

Modeling and simulation of a powered exoskeleton system to aid human-robot collaborative lifting

Asif Arefeen and Yujiang Xiang
Paper 22 • 11 pages

Prediction of walking kinematics and muscle activities under idealized lower limb exoskeleton assistances

Neethan Ratnakumar, Vinay Devulapalli, Niranjan Deepak and Xianlian Zhou
Paper 23 • 9 pages

Experimental assessment of effectiveness of arm-supporting exoskeleton for overhead work

Parisa Torkinejad Ziarati, Ting Xia, Simon Kudernatsch and Donald Peterson
Paper 24 • 10 pages

Session 7: DHM in Biomechanics (Part 2)

Definition of spinal joint coordination laws for repositioning a digital human model based on MRI observations in four different postures

Shabahang Shayegan and Xuguang Wang
Paper 25 • 3 pages

Forward and Backward Reaching Inverse Kinematics (FABRIK) solver for DHM: A pilot study

Maurice Lamb, Seunghun Lee, Erik Billing, Dan Högberg and James Yang
Paper 26 • 11 pages

Balance stability characteristics of human walking with preferred, fast, and slow speeds

William Peng and Joo H. Kim
Paper 27 • 3 pages

Session 8: DHM Using Finite Element Modeling

Evaluation of personalized human body buttock-thigh finite element models in terms of soft tissue deformation for seat comfort assessment

Goutham Sridhar, Leo Savonnet, Yoann Lafon and Xuguang Wang
Paper 28 • 4 pages

Developing a full-body finite element model and its preliminary validation for seating comfort

Shenghui Liu, Philippe Beillas, Li Ding and Xuguang Wang
Paper 29 • 14 pages

Moving deforming mesh modeling of human organ systems

Hamidreza Mortazavy Beni, Hamed Mortazavi, Gunther Paul and Mohammad Saidul Islam
Paper 30 • 11 pages

Understanding buttock deformation in a seated posture

Russell Marshall, Michael Harry and Michael Fray
Paper 31 • 10 pages

Optimization of nucleus pulposus removal rate in the intervertebral disc during artificial nucleus replacement using lumbar finite element model simulation

Yeeun Kang, Jaemin Kim and Junghwa Hong
Paper 32 • 3 pages

Automatic generation of partially homogenized FEM human body models based on 3D body scan data

Yordan Kyosev, Tino Kühn and Ann-Malin Schmidt
Short Presentation 33 • 2 pages

Session 9: DHM in Packaging

Simulation of hip joint location for occupant packaging design

Estela Perez Luque, Erik Brolin, Maurice Lamb and Dan Högberg
Paper 34 • 12 pages

Using Santos Pro™ trade-off analysis to inform the rear chassis design of a novel electric scooter

Steven Fischer, Justin Davidson and Sanjay Veerasammy
Abstract 35 • 1 page

Identifying the best objective function weightings to predict comfortable motorcycle riding postures

Justin Davidson and Steven Fischer
Abstract 36 • 2 pages

Analysis of the influence of non-driving-related activities on seat parameters and sitting posters

Manuel Kipp
Short Presentation 37 • 3 pages

Session 10: Virtual Reality and Digital Twin

Evaluation of upper body postural assessment of forklift driving using a single depth camera

Veeresh Elango, Simona Petravic and Lars Hanson
Paper 38 • 12 pages

Improving the efficiency of virtual-reality-based ergonomics assessments with digital human models in multi-agent collaborative virtual environments

Francisco Garcia Rivera, Maurice Lamb and Melanie Waddell
Paper 39 • 11 pages

Reinforcement learning with digital human models of varying visual characteristics

Nitesh Bhatia, Ciara M. Pike-Burke, Eduardo M. Normando and Omar K. Matar
Paper 40 • 16 pages

Human digital twin with applications

Zhiqing Cheng
Paper 41 • 10 pages

Modeling ability to perform common soldier tasks based on the Army Combat Fitness Test dead lift

Laura A. Frey-Law, Rajan Bhatt, Russell Schneider, Guillermo Laguna Mosqueda, Marco Tena Salais, Landon Evans and Karim Abdel-Malek
Paper 42 • 15 pages

Identifying benefits of using an instruction language for virtual simulation of manual assembly and logistics

Peter Mårdberg, Johan S. Carlson and Dan Högberg
Short Presentation 43 • 2 pages

Session 11: DHM Modeling Methods

Improved modeling approach for the usage of mixed linear effects models in empirical digital human models

Martin Fleischer
Paper 44 • 9 pages

Multi-factorial modeling of comfort in an aircraft cabin considering thermal, noise, and vibration metrics

Neil Mansfield, Geetika Aggarwal, Frederique Vanheusden and Steve Faulkner
Paper 45 • 10 pages

The study of endolymph flow and hair cell control analysis simulation model through electromagnetic fields

Hyeyeong Song, Soonmoon Jung and Junghwa Hong
Paper 46 • 3 pages

Methods for including human variability in system performance models

Randall J. Hodkin Jr. and Michael E. Miller
Paper 47 • 9 pages

Santos the virtual soldier predicts human behavior

Karim Abdel-Malek, Rajan Bhatt, Chris Murphy and Marco Tena Salais
Paper 48 • 12 pages

ME-BVH: Memory Efficient Bounding Volume Hierarchies

Evan Shellshear, Yi Li and Johan S. Carlson
Paper 49 • 13 pages

Developing a response surface methodology to determine the best objective function weightings for predicting probable postures

Justin Davidson, Joshua Cashaback and Steven Fischer
Abstract 50 • 2 pages

Conference Synopsis

The International Digital Human Modeling Symposium provides an international forum for researchers and practitioners to report their latest innovations, summarize the state of the art in the field, and exchange ideas, results, and visions in all fields of digital human modeling research and applications.

Organizing Committee

Karim Malek, Chair – *University of Iowa Technology Institute, USA*
Gunther Paul, Co-Chair – *James Cook University*, *Australia*
Gregor Harih – *University of Maribor*, *Slovenia*
Melanie Laverman – *University of Iowa Technology Institute, USA*
Brian Morelli – *University of Iowa Technology Institute, USA*
Sofia Scataglini – *University of Antwerp*, *Belgium*
James Yang – *Texas Tech University, USA*

Scientific Committee

Karim Malek, Chair – *University of Iowa Technology Institute, USA*
Gunther Paul, Co-Chair – *James Cook University*, *Australia*
Alexander Siefert – *Simuserv, Germany*
Andre Rueckert – *ESI Software Germany GmbH*, *Germany*
Andrew Merryweather – *University of Utah, USA*
Bruce Bradtmiller – *Anthrotech*, *USA*
Dan Högberg – *University of Skövde, Sweden*
Dan Lämkull – *Volvo Cars*, *Sweden*
Dominik Bonin – *BAUA Dortmund, Germany*
Erik Billing – *University of Skövde*, *Sweden*
Giuseppe Andreoni – *POLIMI*, *Italy*
Gregor Harih – *University of Maribor*, *Slovenia*
Isabel Sacco – *Universidade de São Paulo, Brazil*
James Yang – *Texas Tech University*, *USA*
Josip Stjepandic – *PROSTEP AG*, *Germany*
Julie Charland – *3DS - Dassault Systemes*, *Canada*
Lars Hanson – *University of Skövde, Sweden*
Mac Reynolds – *ERL Haslett, USA*
Maurice Lamb – *University of Skövde*, *Sweden*
Michael Spitzhirn – *imk automotive, Germany*
Mitsunori Tada – *AIST - National Institute of Advanced Industrial Science and Technology*, *Japan*
Neil Mansfield – *Nottingham Trent University*, *UK*

Onan Demirel – *Oregon State University, USA*
Pauline Maurice – *Université de Lorraine, France*
Pierre-Olivier Lemieux – *3DS - Dassault Systemes*, *Canada*
Rajan Bhatt – *University of Iowa, USA*
Ravindra Goonetilleke – *HKUST, Hong Kong*
Riender Happee – *TU Delft*, *Netherlands*
Rush Green – *Boeing*, *USA*
Russell Marshall – *Loughborough University*, *UK*
Sandra Alemany – *IBV Valencia, Spain*
Sofia Scataglini – *University of Antwerp*, *Belgium*
Steve Summerskill – *Loughborough University*, *UK*
Xuguang Wang – *IFSTTAR - Institut Français des Sciences et Technologies des Transports, de l'Aménagement et des Réseaux*, *France*
Yan Luximon – *Hong Kong Polytechnic University, Hong Kong*

Improving ergonomic value of product interface materials using numerical digital human models

Gregor Harih and Vasja Plesec
University of Maribor, Slovenia

Abstract

Digital human models are usually constructed to study the human anatomical or topological features and its variance and to optimize the size and shape of various products and tasks. Therefore, most of the researchers focussed on developing accurate three-dimensional digital human models based on surface mesh using various methods and techniques. However, such models do not allow biomechanical and ergonomic analyses of product interface materials that are in direct contact with the user. Based on manual testing using various materials and analysing the subjective response of users, researchers have shown that product interface material has an important impact on the overall product safety, comfort and even performance. Basic ergonomic and biomechanical guidelines regarding the material choice were provided based on the findings, however detailed material choice and even material parameter determination has not been studied, evaluated, and discussed due to the complex biomechanical systems and lack of appropriate digital human models.

To overcome these limitations, numerical methods, especially the finite element method has been already used in the past by several authors. Finite element method allows calculating of various results in terms of internal stresses and contact pressure, deformations, and displacements, however it requires accurate development of numerical digital human models that accurately represent the anatomical, topological, material properties and boundary conditions.

In this paper we present theoretical background and provide methodology for successful development of numerical digital human models that can be used for biomechanical analyses and product material ergonomic improvement. This is presented with a case study of the development of a numerical digital human finger model for ergonomic improvement of the biomechanical response of a product handle deformable interface material. Based on the developed numerical model, a novel deformable interface material is analysed that reduces the resulting contact pressure during grasping and provides more uniform pressure distribution while still providing sufficient stability.

Keywords: finite element method, numerical model, biomechanics, product ergonomics, material properties.

Introduction

Digital human models are usually constructed to study the human anatomical or topological features and its variance and to optimize the size and shape of various products and tasks (Duffy, 2016). Therefore, most of the researchers focused on developing accurate three-dimensional digital human models based on surface mesh using various methods and techniques. However, such models do not allow biomechanical and ergonomic analyses of product interface materials that are in direct contact with the user (Harih, Borovinšek, Ren, & Dolšak, 2015). Based on manual testing using various materials and analyzing the subjective response of users, researchers have shown that product interface material has an important impact on the overall product safety, comfort and even performance (Wongsriruksa, Howes, Conreen, & Miodownik, 2012). Basic ergonomic and biomechanical guidelines regarding the material choice were provided based on the findings, however detailed material choice and even material parameter determination has not been studied, evaluated, and discussed due to the complex biomechanical systems and lack of appropriate digital human models.

Previous research has shown that soft tissue (skin, subcutaneous tissue, muscle, fascia, etc.) exhibits non-linear mechanical behaviour with low stiffness at small strains with a sudden increase of stiffness with higher strains. Therefore, also the resulting contact pressure when in contact with various products, equipment, etc results in high contact pressures, which leads to sudden increase in discomfort and pain (Hokari, Pramudita, Ito, Noda, & Tanabe, 2019).

Distinctive mechanical behaviour of soft tissue suggests the interface materials should be deformable to be able to reduce the resulting contact pressure and provide more uniform pressure distribution (Harih & Tada, 2015). Hence, companies tend to use foam materials in the areas of the products which are in direct contact with the user and result in high contact pressures. However authors did not optimize material properties of the interface foam material to improve ergonomics, which usually results in decreased ergonomic value with lower subjective comfort (Cupar, Kaljun, Dolšak, & Harih, 2020). Research has shown that foam rubber interface material provide more uniform contact pressure distribution, however it can also lead to excessive deformation of the foam resulting in the loss of control and stability feeling when grasping the product (Fellows & Freivalds, 1991).

Measurements of contact pressure at the contact regions are mostly impossible with existing measurement systems due to complex organic geometry of the anatomical parts that are in direct contact with the product. Hence, improvement of interface materials using conventional quantitative methods is not possible. Therefore, several researchers already developed numerical digital human models based on finite element method (FEM) for biomechanical and ergonomic analyses. Previous research has shown that FEM provides extensive results (stresses, deformations, displacements, contact pressure, etc), which can be used for quantitative biomechanical and ergonomic analyses and optimization (Tony & Alphin, 2019). Authors have shown that such technique require accurate development of numerical digital human models that accurately represent the anatomical, topological, material properties and boundary conditions to obtain results that are accurate.

Hence, in this paper we present theoretical background and provide methodology for successful development of numerical digital human models that can be used for biomechanical analyses and product material ergonomic improvement. Additionally, a case study of the development of a numerical digital human finger model and numerical analysis and ergonomic improvement of a product handle with deformable material is studied.

Methods

Finite element method software Ansys was used to develop the numerical model and simulate the mechanical behavior of the biomechanical system.

Numerical model – geometry determination

Obtaining accurate geometrical information of the studied part is crucial for obtaining accurate results. Hence, most of the researchers utilize medical imaging for the determination of the accurate geometry since it allows to obtain geometrical information of internal anatomical structures as well. However, specific geometry based on imaged subject results also in specific geometry of the subject, which can differ from the average size and shape of the studied anatomical part of the target population. When developing numerical models, simplifications need to be chosen carefully to describe the studied biomechanical system accurately enough and maintain numerical stability.

In the case study of the numerical digital human finger model development, the geometry of the finger has been obtained by medical imaging (CT) and later with reverse engineering technology. Average sized human finger has been considered according to anthropometric measurements. The handle interface material has been modelled as a half cylinder resembling a product handle as seen in Figure 1.

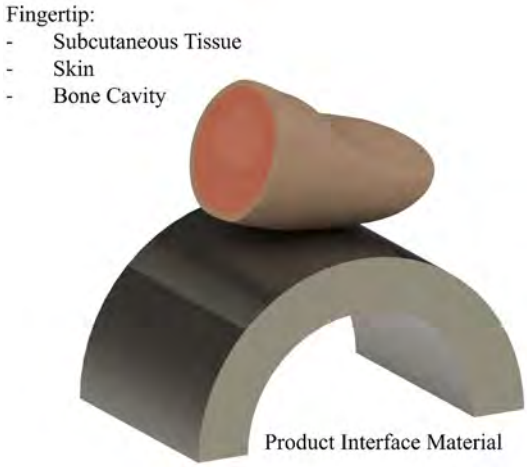

Figure 1. Geometry of the finger with product interface material.

Numerical model – material properties

Biological soft tissue shows highly non-linear mechanical behavior; therefore, it is crucial to include this behavior in the numerical simulations with appropriate numerical models to obtain accurate results. Simplifications by utilizing linear material models have shown to oversimplify the mechanical behavior and can be only used for simplified biomechanical analyses. Hyper-elastic material models should be used to include the actual mechanical behavior of the given soft tissue structure.

Therefore, in our case soft tissue was numerically modelled with Ogden hyper-elastic material model, which has been validated by us in previous research (Harih & Tada, 2019). We considered homogenous material and isotropic material behavior due to limited experimental data and to provide improved numerical stability. Bone was considered rigid since it is it is magnitudes stiffer than soft tissue and is not an anatomical part of interest in terms of results.

For the evaluation and comparison of the interface materials we considered two common materials that can be found with products, namely steel and rubber. Additionally for the biomechanical analysis and ergonomic evaluation we performed also numerical simulation using cellular meta-material that has already shown improved comfort with subjective testing (Cupar et al., 2020). Material properties of the numerical digital human finger model and interface materials are presented in Table 1.

Table 1. Material properties

Material	**Material model**	**Parameters**
Subcutaneous tissue	Ogden 3rd order	MU1 = -0,04895 MPa A1 = 5,511 MU2 = 0,00989 MPa A2 = 6,571 MU3 = 0,03964 A3 = 5,262 D1 = -4,2267 MPa^{-1} D2 = 20,92 MPa^{-1} D3 = 5,2194 MPa^{-1}
Skin	Ogden 3rd order	MU1 = -0,07594 MPa A1 = 4,941 MU2 = 0,01138 MPa A2 = 6,425 MU3 = 0,06572 A3 = 4,712 D1 = -2,7245 MPa^{-1} D2 = 18,181 MPa^{-1} D3 = 3,1482 MPa^{-1}
Steel	Linear-elastic	2100000 MPa $\nu = 0,3$
Rubber	Linear-elastic	E = 33,7 MPa $\nu = 0,49$
Cellular meta-material	Segmentially linear	$\sigma_1 = 0,23$ MPa $\varepsilon_1 = 0,1$ $\sigma_2 = 0,28$ MPa $\varepsilon_2 = 0,4$ $\sigma_3 = 0,65$ MPa $\varepsilon_3 = 0,53$ $\nu = 0,4$

Numerical model –boundary conditions

Boundary conditions need to reflect the actual biomechanical behavior in terms of movement and external loading on the structure. Loading scenarios on a distinctive studied biomechanical structure can be complex, therefore appropriate simplifications need to be undertaken to obtain numerically stable model. Biomechanical movement presents additional challenge since biomechanical movement is usually complex and stochastic. Hence, motion capture systems should be used to obtain actual movement data for the given study.

In our case study of the numerical digital finger model, grasping has been simplified with a normal force of 35N on the distal phalange bone. Finger phalange bone was fixed in all directions, except the direction of the vertical force as seen in Figure 2. The value represents a typical power grasp scenario, where the object is firmly grasped for transferring of high loads and moments and to increase stability. All interface materials have been numerically tested and results can be observed in following section.

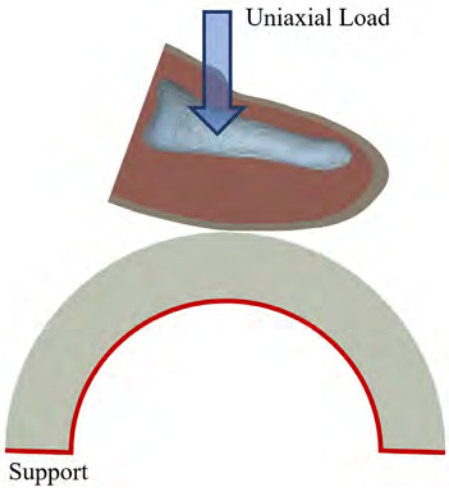

Figure 2. Boundary conditions of simplified grasping scenario.

Results

The developed numerical digital human model has been extensively validated in the past and results show comparable contact pressure, deformation, and displacements (Harih, Tada, & Dolšak, 2016). Therefore, the result is a numerically stable and feasible numerical digital human model that provides accurate biomechanical behavior and provides results in terms of stresses, strains, deformations, displacements, contact pressure, etc.

As presented, obtained results can be used to perform biomechanical analyses and product interface material ergonomic evaluation and improvement. Hence, results of contact pressure distribution for studied interface materials are provided in Figure 3 and maximum contact pressure for each interface material is provided in Figure 4. Additionally, stability is analyzed with results of displacement of finger and product interface material in lateral cross-section in Figure 5.

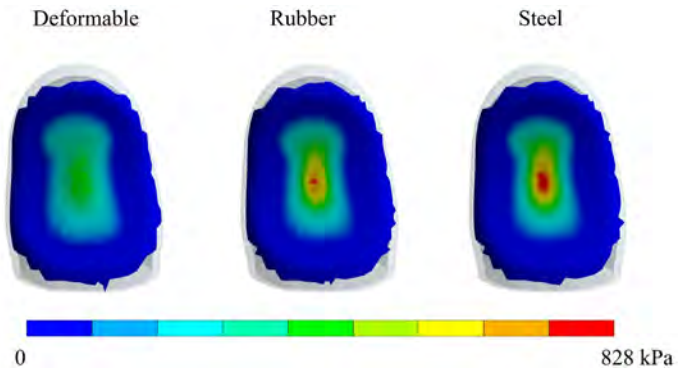

Figure 3. Contact pressure distribution for each infertface material.

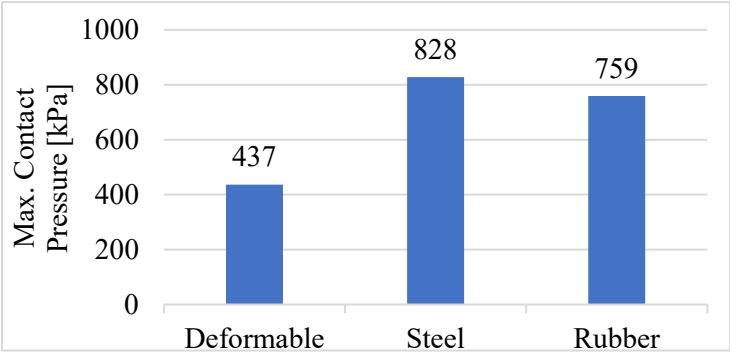

Figure 4. Maximum contact pressures for each interface material.

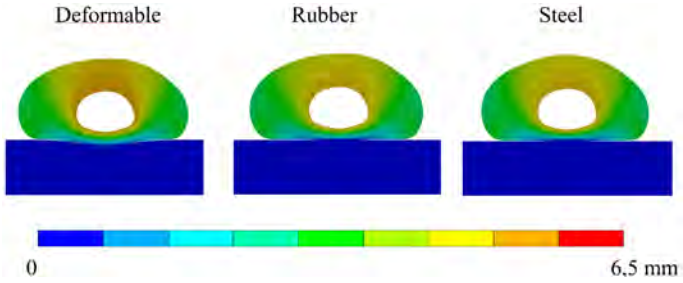

Figure 5. Displacement of finger and product interface material in lateral cross-section.

Discussion and Conclusions

When developing numerical digital human models, through validation of the model is needed for the later use of the model in terms of biomechanical analyses and ergonomic evaluations. Research has shown that validation of biomechanical systems is usually very complex and demanding due to simplifications that need to be incorporated into the numerical models. These simplifications usually need to be included due to limitations defining actual model geometry, material determination and definition and boundary

conditions. This also influences the numerical stability and feasibility; hence an appropriate compromise needs to be set to obtain usable results with good numerical stability. Hence most of the numerical digital human models are best suited for relative comparison in terms of biomechanics and ergonomics.

Human grasping of various products usually requires high grasping forces, therefore also the resulting loads on the hand are high, which can lead to musculo-skeletal disorders. Most of the researchers focused on defining correct sizes and shapes of the product for the best fit with the user, however they rarely investigated the materials that are in direct contact. Development of digital human models in last years had increased substantially, however they are limited to geometrical data and statistical shape models that can be used for size and shape optimization. Product material choice and determination is usually defined based on product manufacturing requirements and limitations and also ergonomic recommendations. This leaves possibility for further ergonomic improvement as presented in this study.

Results have shown that steel is magnitudes stiffer than soft-tissue and hence all deformation can be attributed to the finger. This is also reflected in the results where numerical simulations with steel interface material produce the highest contact pressure and concentrated distribution. Rubber interface material can be found on many products, where manufacturers try to provide better human-product interaction. While stability is increased due to higher friction of the rubber, contact pressure is reduced just slightly as shown by results. Contact pressure distribution is similar to steel and hence rubber interface materials cannot be effectively used for contact pressure reduction and uniform contact pressure distribution. On the other hand, the proposed deformable interface material reduces the maximum contact pressure substantially (48%). Additionally, deformable interface material provides more uniform contact pressure distribution when compared to steel and rubber. When comparing the vertical displacement, all three biomechanical systems show similar results, hence stability of the product is maintained even with the deformable interface material.

We have shown that FEM can be successfully used for obtaining results in terms of stresses, contact pressure, displacements that can be used for ergonomic evaluation. In our case study we focused on novel deformable meta-material, that allows minimization of contact pressure with maintaining stability. This is achieved with inverse mechanical behavior to soft tissue, where the proposed deformable material stays quasi-stiff at low stresses and starts to deform when critical stress (contact pressure) is achieved to provide higher contact area and distribute contact pressure more uniformly. This behavior of the biomechanical system has been also confirmed by the results. Based on previous extensive subjective comfort rating measurement and evaluation we have shown that proposed deformable material provides increased comfort compared to quasi-stiff materials such has rubber, while providing same stability.

Using the FEM, the quantitative results that affect the comfort rating values have been evaluated in this study and have shown that they correspond well to results from subjective comfort rating evaluation. Hence, appropriately validated numerical digital human models can be successfully used for ergonomic analyses and evaluations, especially in the area of biomechanical behavior.

Acknowledgments

The authors acknowledge the financial support from the Slovenian Research Agency (Research Core Funding No. P2-0063 and Z2-8185).

References

Cupar, A., Kaljun, J., Dolšak, B., & Harih, G. (2020). *Design of 3D Printed Cellular Meta-materials for Improved Tool-Handle Ergonomics*. Paper presented at the Advances in Intelligent Systems and Computing, AHFE 2020.

Duffy, V. G. (2016). *Handbook of digital human modeling: research for applied ergonomics and human factors engineering*: CRC press.

Fellows, G. L., & Freivalds, A. (1991). Ergonomics evaluation of a foam rubber grip for tool handles. *Applied Ergonomics, 22*(4), 225-230. doi:10.1016/0003-6870(91)90225-7

Harih, G., Borovinšek, M., Ren, Z., & Dolšak, B. (2015). Optimal product's hand-handle interface parameter identification. *International Journal of Simulation Modelling, 14*(3), 404-415.

Harih, G., & Tada, M. (2015). Finite element evaluation of the effect of fingertip geometry on contact pressure during flat contact. *International Journal for Numerical Methods in Biomedical Engineering, 31*(6), 1-13. doi:10.1002/cnm.2712

Harih, G., & Tada, M. (2019). Development of a feasible finite element digital human hand model. In S. Scataglini & G. Paul (Eds.), *DHM and Posturography* (pp. 273-286): Academic Press.

Harih, G., Tada, M., & Dolšak, B. (2016). Justification for a 2D versus 3D fingertip finite element model during static contact simulations. *Computer Methods in Biomechanics and Biomedical Engineering, 19*(13), 1409-1417.

Hokari, K., Pramudita, J. A., Ito, M., Noda, S., & Tanabe, Y. (2019). The relationships of gripping comfort to contact pressure and hand posture during gripping. *International Journal of Industrial Ergonomics, 70*, 84-91.

Tony, B. J. A., & Alphin, M. S. (2019). Finite element analysis to assess the biomechanical behavior of a finger model gripping handles with different diameters. *Biomedical Human Kinetics, 11*(1), 69-79.

Wongsriruksa, S., Howes, P., Conreen, M., & Miodownik, M. (2012). The use of physical property data to predict the touch perception of materials. *Materials & Design, 42*(0), 238-244. doi:10.1016/j.matdes.2012.05.054

Digital production planning and human simulation of manual and hybrid work processes using the ema Software Suite

Michael Spitzhirn[1], Sascha Ullmann, Sebastian Bauer, Lars Fritzsche

imk Industrial Intelligence GmbH, Chemnitz, Germany

Abstract

For planning and designing production and work systems, a holistic approach is necessary that considers both levels of factory planning and workplace design. Currently, separate digital tools are mostly used for the design of factories and the detailed planning of work systems. That leads to workers being considered inadequately or too late in the planning process of production. The consequence can be a time-consuming and costly replanning to solve problems in existing production and work processes. Using the example of an assembly of washing machines, an iterative approach is presented for a combined digital planning on factory and workplace level. A holistic design of the assembly line is carried out using the ema Software Suite, consisting of the ema Plant Designer (emaPD) and ema Work Designer (emaWD). In the case study, emaPD is used to optimize production elements such as operating resources, layout, and logistics by considering the material flow, throughput times, and production costs. These results are applied for detailed planning and design at the workstation level with emaWD, which uses an algorithmic approach for self-initiated motion generation based on objective task descriptions. The generated simulations are examined and optimized based on production time estimation (MTM-UAS) and ergonomic risk assessments (EAWS, NIOSH, reach and vision analysis) as well as workers' abilities (age, anthropometry). As a result, an efficient factory with an optimized material flow could be planned while minimizing the manufacturing costs and throughput times while complying with the space specifications and ergonomics. The takeover of ergonomically unfavorable processes by robots as hybrid workstations enables, among other things, an improvement in ergonomics. The digital planning approach of combined factory (emaPD) and workplace design (emaWD) also enable early, coordinated, efficient planning of economical and ergonomic production.

Keywords: Ergonomics 4.0, Industry 4.0, Digital Factory, Digital Human Modeling (DHM), human-robot-interaction

[1] Corresponding author. Email: michael.spitzhirn@imk-ic.com

1. Challenges of design of economical and ergonomic factory and work systems

Increasing cost pressure from competition, labor and material costs, greater variety and shorter product life and market launch cycles require that production and work systems must be planned and reconfigured faster and more frequently (Spath et al. 2017, Bracht et al. 2018). When planning and designing production and work systems, in addition to costs, times, quality, time-to-market and flexibility, the ergonomic design for the user group as well as the skill-based deployment of the workforce must be considered (Schenk et al., 2014; Schlick et al., 2018). Different departments are usually involved in planning the factory / production respectively work system design. At the factory planning level, the focus is on the production program, the dimensioning, as well as the structuring and design of the factory and production systems. Work planning deal with the design of the workplaces and processes e.g., design of the workplace heights or the design of the human-machine / robot interaction according to economic and ergonomic criteria. Early, coordinated, and efficient planning of factory design as well as production and individual workplaces is important, but is often not done sufficiently (Bracht et al., 2018).

Many companies use digital design and simulation tools for their factory as well as work planning processes (Wiendahl et al. 2015, Bracht et al. 2018, Burggräf et al. 2021) The available software provides more and more functionalities such as Integrated Factory Modelling (IFM) model which offers the advantage of being able to access more detailed information than a pure 3D visualization (Burggräf et al. 2021). However, digital tools are mostly used separately for designing factories / logistics and for detailed planning of work systems (Bracht et al., 2018, Gunther, 2021). These software systems differ, amongst others, in functional scope as well as in the software handling. A common data basis is not available and must be achieved through data conversions. This is a time-consuming process and can lead to errors. Companies invest a lot of money for the software operation and must have design and simulation experts for the different applications who are expensive too. Not all software systems offer the appropriate interfaces to one another, so that factory and workplace planning often must be carried out separately. That can lead to that worker are considered inadequate or too late in the planning process of production. The consequence can be a time-consuming and costly replanning to solve problems in existing production and work processes.

For planning and designing production and work systems, a holistic approach is necessary that considers both the level of factory planning and workplace design to improve the quality of results and to reduce the effort. In the following, an iterative approach to continuous digital planning between the factory and workplace levels using the EMA Software Suite is presented.

2. Digital factory & work planning for economic and ergonomic production design

A procedure for iterative, combined factory and work planning using the software system 'EMA Software Suite' is described on the example of a washing machine production and assembly project. The aim is to redesign the assembly line and optimization the production line. It also should be checked whether the planned production program can be realized with the existing machines and assembly and how an improvement in the economic efficiency of the overall production could be realized next to good ergonomic condition for the worker on the single workplaces.

Based on the production program and range, the target quantities, the planning period and requirements for the quality and quantity of the production are to be defined. The product must also be analyzed, since the single components determine the manufacturing methods, the handling technology, etc. and the product structure the assembly sequence too. Product changes such as simplifying or merging functional units can also affect the technical, economic as well as ergonomic conditions (e.g. weight, forces, grasping) of the production (Schenk et al., 2014; Bracht et., 2018).

The washing machine consists of 86 components including a washing machine frame, washing machine drum, drain pump, various cables, hoses, and screws (see Fig. 1). The parts vary in shape, dimensions, and weight. The total weight is 82.95 kg and the individual weights vary from a few grams to more than 10 kg. The washing machine is produced in three color variants (white, blue, orange).

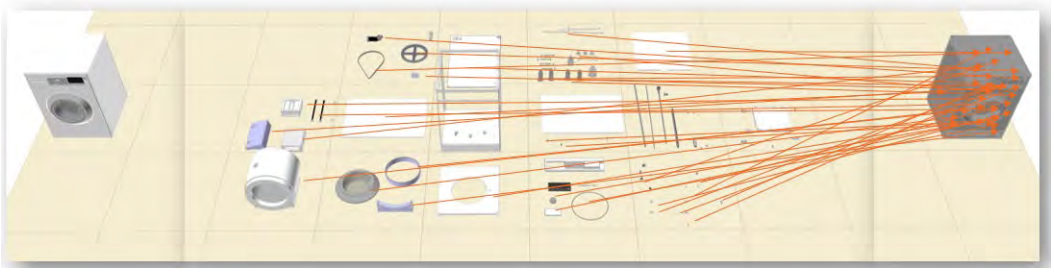

Figure 1. assembled washing machine (left) and individual parts of the washing machine (right)

Figure 2 illustrates the goals and functions of the EMA Software Suite with its two software systems EMA Plant Designer (emaPD, left side) and EMA Work Designers (emaWD, right side). The systems emaPD and emaWD can be used independently or together in one interface. In emaPD the planning of production and assembly takes place at the factory level (macro level) and in emaWD the exact 3D visualization and designing of production lines up to the workplace level are done according to economical, time and ergonomics criteria. The current planning statuses can be exchanged directly and

synchronously via the bidirectional interface between emaPD and emaWD to update and refine the planning data.

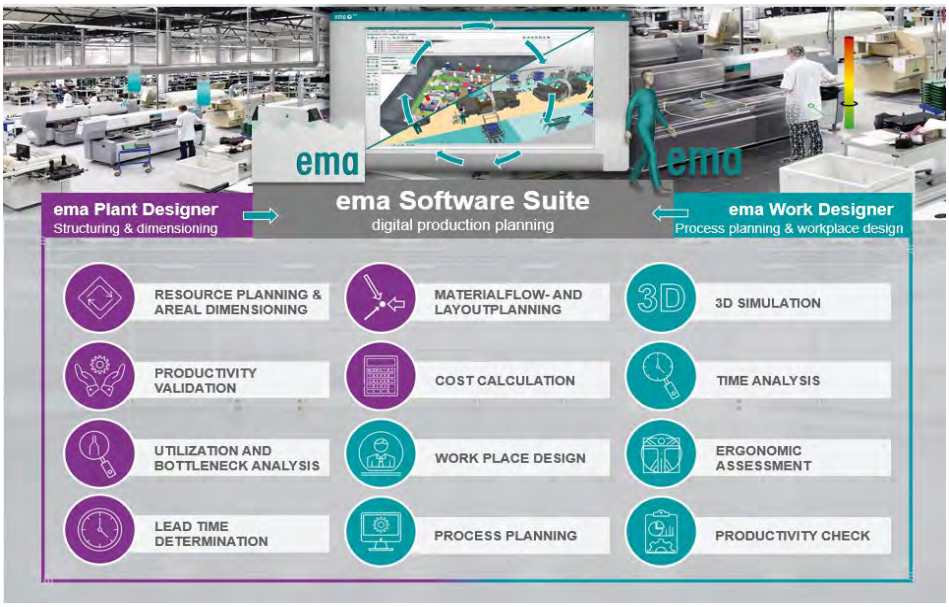

Figure 2. goals and functions of EMA Software Suite with emaPD (left) and emaWD (right).

On the basis of mathematical-analytical calculation methods (e.g. queuing theory (Manitz 2008)), computer-aided modeling, analysis and optimization of production with regard to throughput times, space requirements and manufacturing costs are carried out in the emaPD. Product data (planned quantities, parts list, lot sizes), process data (work plans, container data) and resource data (availability, costs, areas, shift models), which can be transferred via intersection, serve as inputs. As first step it is to be determined whether the production program (target: 80,000 washing machines per year) can be realized under the existing conditions (e.g. number, types of machines). Possible bottlenecks, space requirements or the critical path of production can be identified so that measures for improvement (e.g. adding more machines, buffer spaces) can be derived. Furthermore, a decision must be made about the proportion of in-house production and external procurement, as well as the equipment (machines) to be used and the work processes to be defined. Alternative machines and work plans can be created for the factory / production and variants can be calculated for the overall production plan considering output quantity, costs, utilization, space requirements and throughput times. Possible problems for workers in space, ergonomics aspects as well as a specification of the time requirements can be determined by transferring the results of emaPD to the emaWD. The interaction between the human using a digital human model with various characteristics and the workplace can be analyzed in emaWD and can be adapted according to ergonomic and economic requirements.

By calculating the overall equipment effectiveness (OEE) in the emaPD, the productivity and any losses of the machines can be determined. Set-up and processing times, scrap and rework rates, resource time, availability, planned downtimes can be defined and optimized by suitable measures. In emaWD, the production and assembly times can be specified at the work process level using the standard time method such as MTM-UAS (Bokranz & Landau, 2012). Another important point concerns the analysis of the costs of production and investment. The material and manufacturing costs can be calculated in emaPD considering the cost of material storage, the machines (hourly rates or fixed/variable costs), purchased and raw parts. In combination with emaWD, investment costs can be included for the resources, which in turn affect the costs of production.

At the overall production level in the emaPD, the total utilization of the machines and the available space in the factory must be included. Based on the entries, various scenarios can be set up and evaluated and compared according to KPIs such as required space, production volume and costs. For the dimensioning of the areas, among other things, operation areas are defined in the emaPD. A precise design of the layout (exact arrangement of machine, workplaces) and the creation of path maps can be specified in emaWD and can be returned to the emaPD. This allows the optimization of material flow based on transport intensity and effort. In addition, physical strain on humans could be also included in the planning process. For the creation and design of the layout in 3D, standard machines and workplaces can be defined in emaPD (left) and automatically imported into emaWD (right).

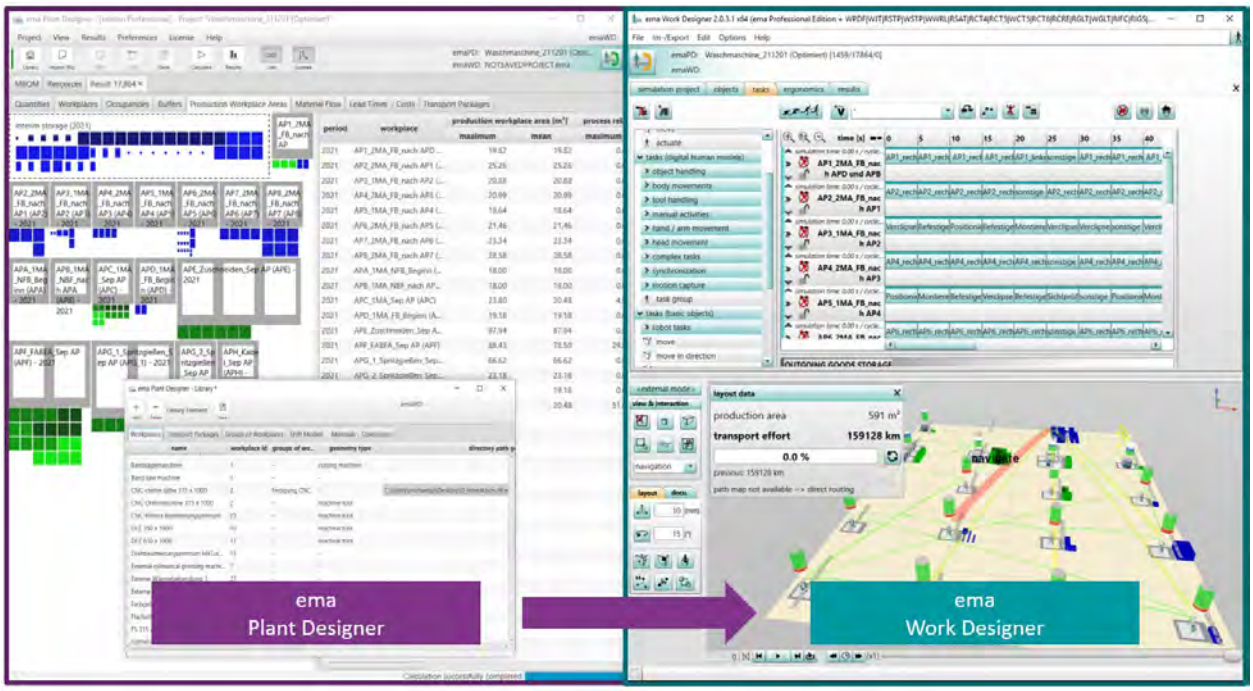

Figure 2. Transfer of washing machine production from emaPD (left) to ema WD (right).

In emaWD, the workstations can be supplemented with additional external objects via command CAD-formats such as *step, *jt, *dae, *obj, *wrl, *CATProduct and many more. Parameterizable objects such tables, tools, robots can also be used from the built in ema object library to expand or rebuilt the factory and the single workplaces.

The detailed planning and design of the workplaces is carried out in emaWD using anthropometric human models from small women (F05) to large men (M95) with different abilities (age-dependent flexibility, forces) for the design of economical, ergonomic, and ability-based work processes (Ullmann & Fritzsche, 2021). The human model configurator (cp. fig. 3) allows the user to add manikins in the 3D-environment. Digital human models in emaWD can be varied in the anthropometry related to different populations (e.g. German, Chinese, Mexican), different body dimensions (e.g. body height: 5th, 50th, 95th percentiles), gender and age groups (20, 40, 60 years), which based on anthropometry database and standards such as DIN 33402-2: 2020 for German population. The selection of an age-related average or restricted range of motion can also be selected (Spitzhirn 2017). Furthermore, the age group have an impact to the maximum forces in the ergonomic assessment (Ullmann & Fritzsche, 2017).

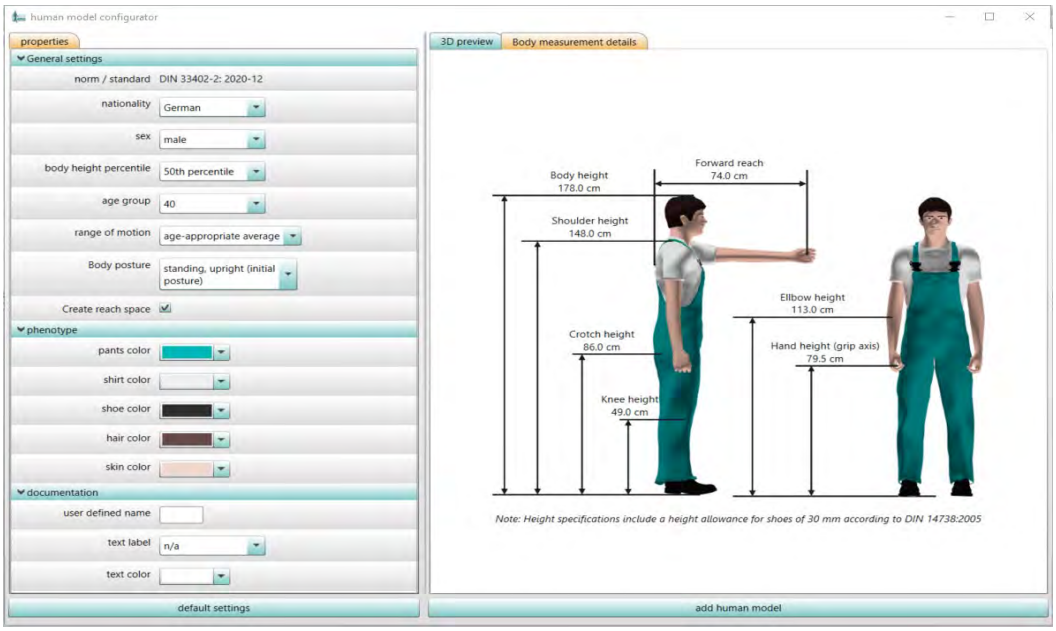

Figure 3. Human model configurator with 3D-Preview in emaWD.

The planning of manual and partially automated processes as well as human-robot interactions is possible using the process simulation in emaWD. To specify the work processes, the path and movement execution of the digital human model is automatically generated on the basis of a parameterized activity description (ema task library) with specification of basic work conditions (e.g. objects to be handled, target positions).

The user can use a lot of different and well know analysis methods such as standard execution time according to MTM-UAS (Bokranz & Landau, 2012), walking distances, proportion of value-adding activities as well as ergonomic analyzes of feasibility (reachability, visual analysis) and ergonomics and health risk assessment according to EAWS (Ergonomic Assessment Worksheet, Schaub et al., 2012) and NIOSH lifting index (Waters et al. 1994) in the emaWD to identify economic and ergonomic problems (Fritzsche et al., 2019b, Spitzhirn et al. 2022). Improvements can be made by changing the environment (e.g. table height), by transferring unfavorable activities from humans to the robot or by shifting work content between workstations. Different human-robot task distributions can be evaluated according to ergonomics and time, so that the best variant can be determined.

The changes can be examined via the bidirectional intersection for their effects at the factory level in the emaPD and thus an iterative optimization process can be carried out. The final concept is documented in the EMA software suite using reports, images, videos and the simulation of the production scenario.

3. Results of digital iterative production planning using digital factory and work planning

A production of 80,000 washing machines in three color variants (white: 55k, blue: 15k, orange: 10k) is planned. Fig. 4 shows example results for washing machine production.

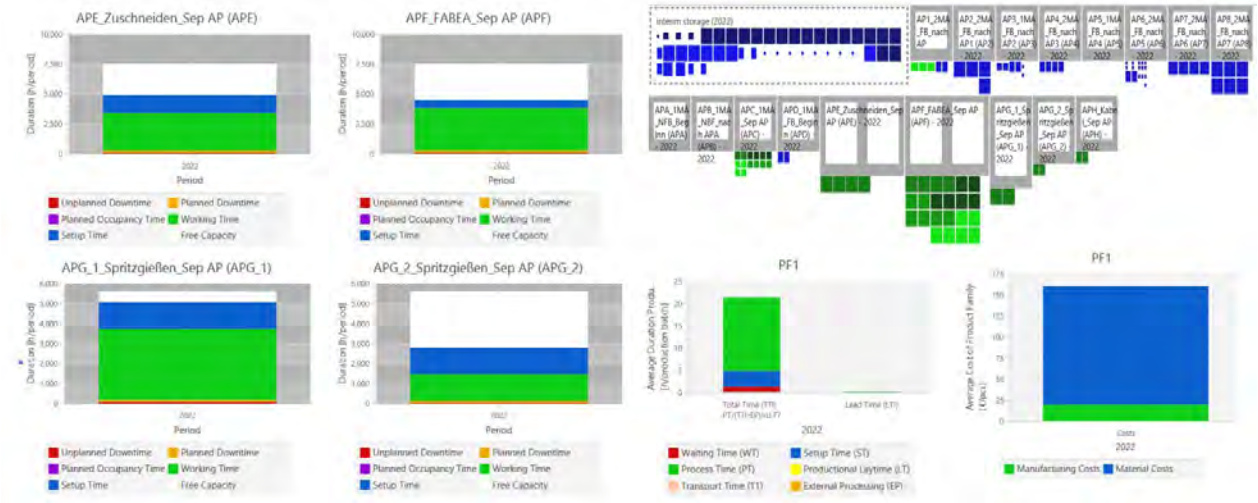

Figure 4. example results for washing machine production using emaPD.

Taking into account the availability of the machines as well as delivery costs, times and availability, 23 parts are manufactured in-house and 63 parts are purchased. The calculation of the current situation resulted in a deficit of 7,587 units. By increasing the number of cutting machines from 2 to 3, adjusting and harmonizing batch sizes and optimizing execution times (reducing waiting times, shifting orders to

other machines), it was possible to achieve the production volume in production. In the assembly line, consisting of 8 linked workstations with a total of 14 employees, the blocking times at APB was decreased from 348 hours to 180 hours and at AP1 from 133 hours to 60 hours as well as the idle times on AP1 from 86h to 0h by integrating buffer areas between APB & AP1 (5 buffer areas), AP1 & AP2 (8 buffer areas). The production area is 530.06 m² with production costs of €159.98. The utilization of individual workstations differs from 98.6% for the assembly line to 48.6% for the injection molding machine type A.

The production and assembly line were transferred from emaPD to emaWD. In emaWD the material flow, including the route network, was rearranged (see Fig. 5, left) and the assembly was simulated in emaWD (see Fig. 5, right). New objects such as conveyor belts, shelves, and boxes as well as necessary input variables (weights, forces, placement accuracy) for ergonomics and time evaluations were added.

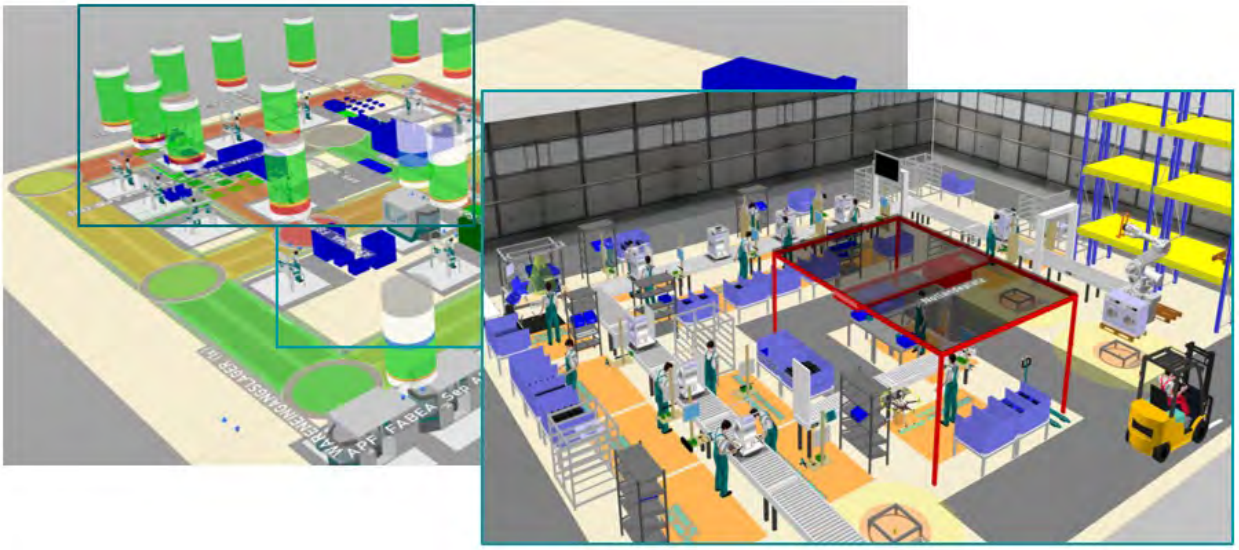

Figure 5. Layout optimization of production (left); simulation of the washing machine assembly (right)

The analysis of the current assembly stations using an average 50th percentile male digital human model (M50-AK40: age group: 40 years, 50th percentile body height: 178 cm according to DIN 14738:2005, age appropriate avenge range of motion and force) showed that there are 4 red workplaces, 7 yellow workplaces and 3 green workplaces according to EAWS (red > 50 points, yellow >25 points, green ≤ 25 points). The red and yellow workplaces mean an increased risk of getting musculoskeletal disorders. In addition, an age-appropriate work evaluation was done by adding different human models - small old women (F05-AK60: age group: 60 years; 5th percentile body height 60: 154 cm, age appropriate reduce range of motion), an tall young man (M95-AK20: age group: 20 years 95th percentile body height: 194 cm, age group: age appropriate avenge range of motion and force) and a tall old man (M95-AK60: age

group: 60 years 95th percentile body height: 183,5 cm, age group: age appropriate reduce range of motion and force) to the simulation.

The feasibility test showed that the middle-sized man (M50-AK40) and the tall sized man young (M95-AK20) and tall sized old man (M95-AK60) can carry out all activities. However, the small woman (F05-AK60) cannot reach all locations that are needed for the activities on the washing machine assembly line. Figure 6 shows an excerpt of the activities that cannot be carried out by the woman F05 (age group:60). For example, the woman F05-AK60 cannot push the washing machine drum into the frame (workplace 1R). This also affects workplace 1L, as workers 1R and 1L work together to fasten the drum.

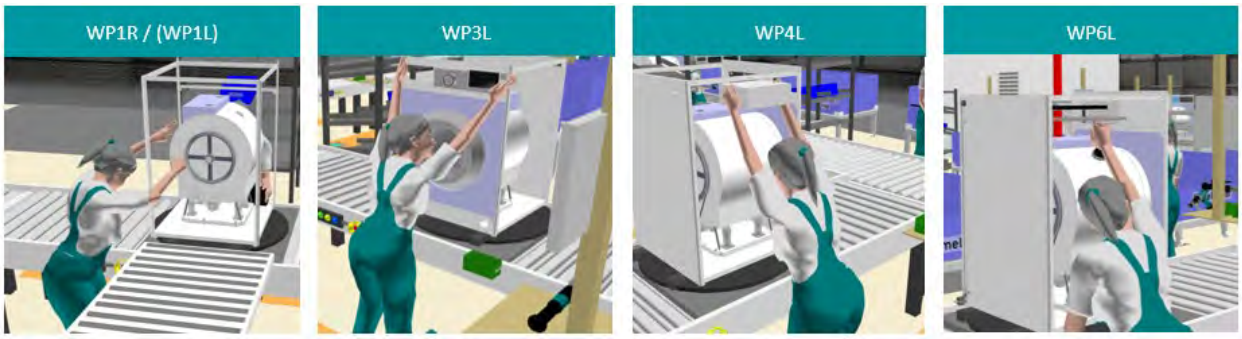

Figure 6. Non-executable activities (woman F05, age group: 60 years) by using emaWD feasibility check

The different characteristics of the people (different anthropometry, mobility, maximum strength) also affect the workload assessment and biomechanical risk score according to EAWS. Tab. 1 shows that the physical strain according to EAWS at workplaces 1R, 2R and 4L is higher for the small woman F05-AK60 than for the men M50-AK40 and M95 AK60. In addition, the feasibility as shown in Figure 6 and table 1 is limited or not feasible for workplace 1R and 4L due to the smaller body size and body reach as well as the age-related reduction of flexibility (Spitzhirn 2017).

Table 1. Excerpt of ergonomic results based on feasibility test and EAWS for workplaces 1R, 2R,4L

	Workplace 1R			**Workplace 2R**			**Workplace 4L**		
	M50-AK40	**F05-AK60**	**M95-AK60**	**M50-AK40**	**F05-AK60**	**M95-AK60**	**M50-AK40**	**F05-AK60**	**M95-AK60**
Feasibility	yes	no	yes	yes	yes	yes	yes	no	yes
= EAWS Points [1]	61,5	(70,0) [2]	68,5	52,5	56,5	52,5	59	(63) [2]	37
+ Body posture points	*6*	*(5,5)*	*7,5*	*2*	*2*	*2*	*24*	*(28)*	*2*
+ Force points	*50*	*(59)*	*56*	*34*	*34*	*34*	*33*	*(33)*	*33*
+ Load handling points	-	*(-)*	-	*16,5*	*20,5*	*16,5*	-	*(-)*	-
+ Extra points	*5,5*	*(5,5)*	*5,5*	-	-	-	*2*	*(2)*	*2*

[1]cutline: EAWS (high health risk > 50 points, possible health risk >25 points, low health risk ≤ 25 points)
[2] no executability according to emaWD feasibility check; theoretical points in case of reachability

To improve the ergonomic and economic conditions, the following measures were simulated in emaWD and evaluated using EAWS and MTM-UAS. A Fanuc CR35ia robot, which can carry out a maximum weight of 35 kg (weight of washing drum = 30,7kg), is integrated at workplace 1R (handling the washing drum (EAWS: 61,5 to 23 points), an UR10e robot on workplace 2R (taking over the rear wall EAWS:;52,5 to 32 points) and a pedestal on workplace 4L (EAWS: from 59 to 31,5 points) as well as on workplace 5L (EAWS: from 40,5 to 40,0 points). A relocation of work content (relay assembly from workplace 3L (EAWS: 55,5 to 42 points) to workplace 7R) was also done to improve the ergonomic conditions and make a line balancing. During the redesign, the cycle time according to MTM-UAS could also reduce from 70 s to 60 s and the workstations were rebalanced by shifting tasks from one workplace to another. Figure 7 shows the results of the optimization process for the four red workplaces 1R, 2R, 3L, 4L compared to the initial state according to EAWS.

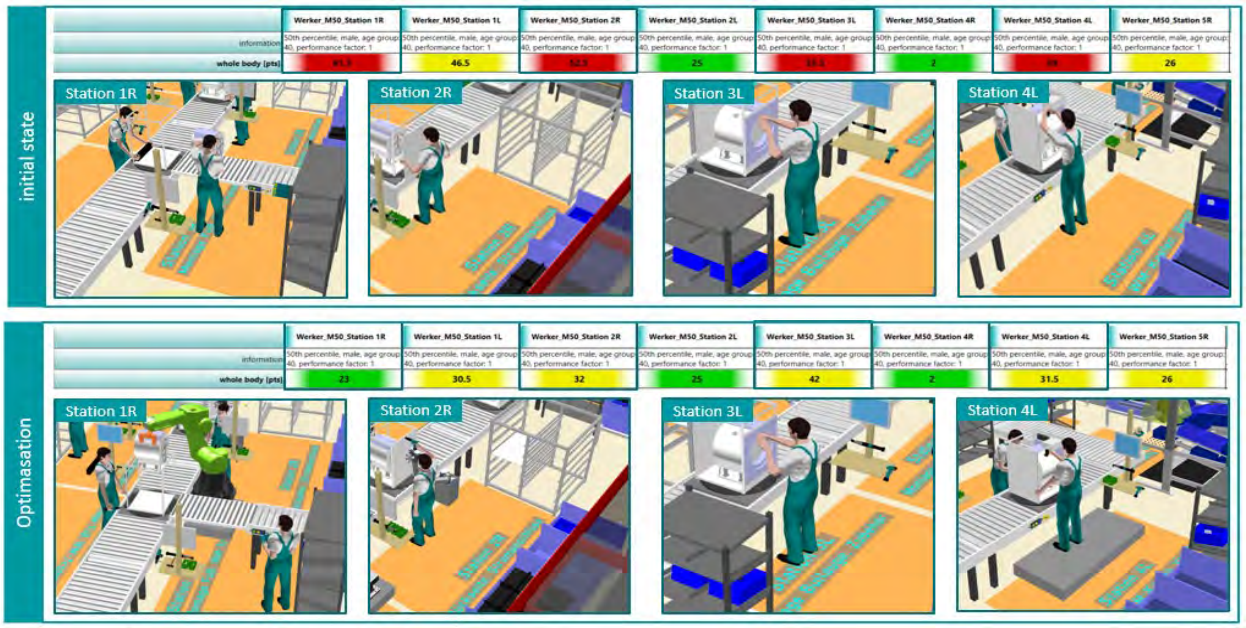

Figure 7. Comparison of ergonomics accord. EAWS in initial state (top) to optimized state (below)

The results of the optimization process in emaWD were transferred back to the emaPD. Due to the line balancing and the other improvements the number of buffer space could reduce signifyingly. Only one buffer space between station APB and AP1 still remains. The idle and blocking times on the assembly line could be reduced to less than 50 h and the manufacturing costs by almost 10 % while at the same time increasing the possible output.

Discussion and conclusion

The combined digital factory and work planning presented made it possible to achieve significant improvements of washing machine production in terms of economic efficiency and ergonomics. Various

methods are available in emaPD for an extensive factory planning. By using the emaPD the defined quantities of washing machines are obtained and the space requirements, production costs are reduced significantly as well as material flows are optimized. Compared to a simulation, the mathematical modeling in emaPD offers significant time savings in model creation (-90%) and computing time (-99%), while at the same time there is a high level of agreement in the accuracy of the forecast (approx. 3% deviation according to Bolch et al., 2006). This makes it possible to carry out different variations of the planning in a reasonable amount of time. To calculate the variants, various data such as parts lists are required, which are either entered manually or can be integrated from other systems via an interface, which can significantly reduce the time required.

As other component of the ema Software Suite, the emaWD ensure that the workplaces and processes, are economical, safe, and human-oriented designed. Aspects such as feasibility (visibility or reachability analyses), health risk (e.g. according to NISOH, EAWS) are considered in detail. By integrating different human models (M50-AK40, F05-AK60, M95-AK20, M95-AK60) with the respective characteristics (body height, force, range of motion, appearance related to age, nationality) an age-appropriate work design can be carried out (Spitzhirn et al., 2022). It is important that a representative range of characteristics (anthropometry, mobility, strength) are mapped to ensure broad use by later users. The analysis shows that non-compliance could result in that worker such as F05-AK60 cannot execute all work tasks. This can be avoided by using the feasibility check in emaWD. A further advantage of the combined factory and work planning approach is the detailed simulation and the visualization of the process in emaWD. That ensure, that no necessary process is forgotten by the user. In addition, necessary places can be planned for example for optimization measures such as pedestal (no use for tall men such as M95-AK20 or M95-AK60), manipulators, robots, or seating to prevent expensive corrections in the field. This can save significant time and money. The employees are thus more at the center of the planning. In addition to economic advantages (e.g. avoiding unfavorable and time-consuming movements, reducing the reject rate, increasing motivation), good ergonomic design can achieve greater flexibility and longer employability of employees (Fritzsche et al., 2019a).

The ema software suite supports a new economic and human oriented approach in the field of factory and work planning, and has the potential to improve the cooperation of both disciplines significantly. The direct interaction between emaPD and emaWD enables planning to be detailed and accelerated. This means that extensive data is available for planning that do not have to be obtained from other systems first. A good usability, bidirectional interfaces between emaPD and emaWD as well as integrated methods support an interactive, joint, efficient creation, calculation, analysis and improvement process of the factory and production. An extensive library as well as standard workstations and machines reduce the

time for construction of the environment. Furthermore, the assembly times (e.g. MTM-UAS) based on emaWD simulation can be used to specify the planning data in the emaPD. The extensive evaluations (time, ergonomic, material flow etc.) in combination with a graphic user interface including dynamic simulation provide the basis for the discussion and evaluation of various measures with different stakeholders (e.g. planners, works council, production). This increases acceptance and can help improve the planning results. In the example, the manufacturing costs and unplanned downtimes could be significantly reduced, and the ergonomic conditions improved, for example by integrating robots into hybrid workstations. Furthermore, the use of the system should not be viewed in isolation from other software systems in the respective company. For that purpose, ema Software Suite offers extensive interfaces to other systems (import and export of CAD data and movements, process data), which can be used for example for further investigations or visualizations with virtual reality applications.

References

Bolch, G., Greiner, S., de Meer H., Trivedi, K.S. (2006). *Queueing Networks and Markov Chains: Modeling and Performance Evaluation with Computer Science Applications*. Wiley-Interscience; 2. Auflage.

Bracht,U., Geckler, D., Wenzel, S. (2018). *Digitale Fabrik – Methoden und Praxisbeispiele.*·Springer Berlin Heidelberg.

Burggräf, P., Dannapfel, M., Hahn, V. et al. Uncovering the human evaluation of changeability for automated factory layout planning: an expert survey. Prod. Eng. Res. Devel. 15, 285–298 (2021). https://doi.org/10.1007/s11740-020-01015-1

Dombrowski U., Ruping, A. (2018). *Herausforderungen der Digitalen Fabrik im Kon-text von Industrie 4.0.* In: ZWF 113 (12), 845–849. DOI: 10.3139/104.112030.

Fritzsche, L., Hölzel, C. & Spitzhirn, M. (2019a). *Weiterentwicklung der Kosten-Nutzen-Bewertung für Ergonomiemaßnahmen anhand von Praxisbeispielen der Automobilindustrie*. *Proceedings of 65. Frühjahrskongress Gesellschaft für Arbeitswissenschaften*, Beitrag A.7.2. Dortmund: GfA-Press.1-6

Fritzsche, L., Ullmann, S., Bauer, S. & Sylaja, V. J. (2019b). *Task-based digital human simulation with Editor for Manual Work Activities – Industrial applications in product design and production planning*. In G. Paul & S. Scataglini (Eds.), DHM and Posturography. London, UK: Elsevier. 569-575.

Gunter, E. P. (2011). Digital Human Modeling in Design. In: Salvendy G. & Karwowski W. (ed.), *Handbook of Human Factors*. John Wiley & Sons, Inc., Hoboken, New Jersey. 704-735.

Manitz, M. (2008). *Queueing-model based analysis of assembly lines with finite buffers and general service times*. Computers & Operations Research 35, 2520 – 2536.

Schenk M., Wirth, S., Müller, E. (2014). *Fabrikplanung und Fabrikbetrieb. Methoden für die wandlungsfähige, vernetzte und ressourceneffiziente Fabrik*. Berlin, Heidelberg: Vieweg

Schaub, K.G., Mühlstedt, J., Illmann, B., Bauer, S., Fritzsche, L., Wagner, T., Bullinger-Hoffmann, A.C., Bruder, R. (2012). Ergonomic assessment of automotive assembly tasks with digital human modelling and the 'ergonomics assessment worksheet' (EAWS). Int. J. Human Factors Modelling and Simulation, Vol. 3, Nos. 3/4, 398-426.

Schlick, C., Bruder, R., Luczak, H. (2018). *Arbeitswissenschaft.* Heidelberg: Springer-Verlag.

Spath, D., Westkämper, E., Bullinger, H.J., Warnecke, H.J. (2017). *Neue Entwicklungen in der Unternehmensorganisation*. Berlin, Heidelberg: Vieweg (VDI-Buch Serie).

Spitzhirn, M. (2017). *Integration altersbedingter Veränderung der Beweglichkeit zur altersgerechten Arbeitsprozessgestaltung in digitalen Menschmodellen*. In: Frühjahrskongress 2017, Brugg und Zürich: Soziotechnische Gestaltung des digitalen Wandels – kreativ, innovativ, sinnhaft. Gesellschaft für Arbeitswissenschaft e.V., Dortmund (Hrsg.), A.1., 1-6

Spitzhirn, M., Ullmann, S., Fritzsche L. (2022). *Human-centered design of industrial work tasks with ema software – Considering individual abilities and age-related changes in digital production planning*. In: Z. Arb. Wiss. Vol. 76. Issue 4, Dec. 2022 (accepted).

Horton, D., & Wohl, R. R. (1956). Mass communication and para-social interaction: Observations on intimacy at a distance. Psychiatry, 19(3), 215–229. https://doi.org/10.1080/00-332747.1956.11023049

Ullmann, S., Fritzsche, L. (2021). *Einsatz digitaler Menschmodelle zur fähigkeitsgerechten Arbeitsgestaltung: Beispiele aus der Praxis*. Arbeitsmedizin, Sozialmedizin, Umweltmedizin, Zeitschrift für medizinische Prävention: 10/2021, 594-597.

Ullmann, S. & Fritzsche, L. (2017). *Ergonomic Work Design for Older and Performance-restricted Workers using Digital Human Models*. In: Bundesanstalt für Arbeitsschutz und Arbeitsmedizin (Hrsg.), Proceedings of the 5th International Digital Human Modeling Symposium. Dortmund/Berlin/Dresden: Bundesanstalt für Arbeitsschutz und Arbeitsmedizin.

Waters, T. R., Putz-Anderson, V., & Garg, A. (1994). *Applications manual for the revised NIOSH lifting equation*. Cincinnati: U.S. Department of Health and Human Services.

Wiendahl, H-P., Reichardt, J., Nyhuis, P. (2015) Handbook factory planning and design, 25 edn. Springer Berlin Heidelberg, Berlin, Heidelberg

Using Time-Based Musculoskeletal Risk Assessment Methods to Assess Worker Well-Being in Optimizations in a Welding Station Design

Aitor Iriondo Pascual[1], Elia Mora[1], Dan Högberg[1], Lars Hanson[1,2], Mikael Lebram[1] and Dan Lämkull[3]

[1] University of Skövde, School of Engineering Science. University of Skövde, Virtual Engineering Research Environment.; aitor.iriondo.pascual@his.se, dan.hogberg@his.se, mikael.lebram@his.se.

[2] Scania CV, Södertälje, Sweden.; lars.hanson@scania.com

[3] Advanced Manufacturing Engineering, Volvo Car Corporation, Göteborg, Sweden.; dan.lamkull@volvocars.com

Abstract

Simulation using virtual models is used widely in industries because it enables efficient creation, testing, and optimization of the design of products and production systems in virtual worlds. Simulation is also used in the design of workstations to assess worker well-being by using digital human modelling (DHM) tools. DHM tools typically include musculoskeletal risk assessment methods, such as RULA, REBA, OWAS, and NIOSH Lifting Equation, that can be used to study, analyse, and evaluate the risk of work-related musculoskeletal disorders of different design solutions in a proactive manner. However, most musculoskeletal risk assessment methods implemented in DHM tools are in essence made to assess static instances only. Also, the methods are typically made to support manual observations of the work rather than by algorithms in a software. This means that, when simulating full work sequences to evaluate manikins' well-being, using these methods becomes problematic in terms of the legitimacy of the evaluation results. In addition to that, to consider objectives in optimizations they should be measurable with real numbers, which most of musculoskeletal risk assessment methods cannot provide when simulating full work sequences.

In this study, we implemented the musculoskeletal risk assessment method OWAS in a digital tool connected to the DHM tool IPS IMMA. We applied the Lundqvist index on top of the OWAS whole body risk category score. This gave us an integer of the time-based ergonomic load for a specific simulation sequence, enabling us to qualitatively compare different design solutions. Using this approach, we performed an optimization in a welding gun workstation to improve the design of the workstation. The results show that using time-based musculoskeletal risk assessment methods as objective functions in

optimizations in DHM tools can provide valuable decision support in finding solutions for workstation designs that consider worker well-being.

Keywords: Ergonomics, Simulation, Time-based, Evaluation, Optimization

Introduction

Simulation using virtual models is used widely in industries because it enables efficient creation, testing, and optimization of the design of products and production systems in virtual worlds (Fisher et al., 2011; Kuhn, 2006; Oppelt & Urbas, 2014). Simulation is also used in the design of workstations to assess worker well-being by using digital human modelling (DHM) tools. One development of DHM tools in recent years is that many DHM tools, such as Siemens Jack (Raschke & Cort, 2019), IPS IMMA (Hanson et al., 2019) and Santos (Abdel-Malek et al., 2019), now can predict and represent human motions, enabling simulations of full motion sequences.

DHM tools typically include musculoskeletal risk assessment methods, such as RULA (Rapid Upper Limb Assessment) (McAtamney & Nigel Corlett, 1993), REBA (Rapid Entire Body Assessment) (Hignett & McAtamney, 2000), OWAS (Ovako Working Posture Assessment System) (Karhu et al., 1977), and NIOSH (National Institute for Occupational Safety and Health) Lifting Equation (Waters et al., 1993), that can be used to study, analyse, and evaluate the risk of work-related musculoskeletal disorders (WMSDs) of different design solutions in a proactive manner. However, most musculoskeletal risk assessment methods implemented in DHM tools are in essence made to assess static instances only (Berlin & Kajaks, 2010). Also, the methods are typically made to support manual observations of the work rather than by algorithms in a software. This means that, when simulating full work sequences to evaluate manikins' well-being, using these methods becomes problematic in terms of the legitimacy of the evaluation results. In addition to that, to consider objectives in optimizations the results of the musculoskeletal risk assessment methods should be measurable with real numbers, which most of them cannot provide for complete motions.

This paper investigates how to implement a time-based musculoskeletal risk assessment method in DHM based simulations of motion sequences, and how outcomes from the method can be used within objective functions in optimizations. In order to test and illustrate, the approach is implemented in a use case from industry, representing a manual welding workstation.

Methods

A case study was used to test and illustrate time-based musculoskeletal risk assessment methods in optimizations. The case study and the modelling in a DHM tool, representation of anthropometric diversity, ergonomics assessments by OWAS Lundqvist index, and the optimization definitions, are described in the following subsections.

Case study and modelling in IPS IMMA

The case study represents a manual welding task within manufacturing at Volvo Cars in a factory located in China. This task involves the use of a welding gun to weld two parts together. Since the gun is supported by a lifting device, workers are not affected by the weight of the gun. Inertia effects from moving the guns are not considered in this study. The DHM tool IPS IMMA (Hanson et al., 2019) was used to model the workstation and the welding task performed by the workers (Figure 1).

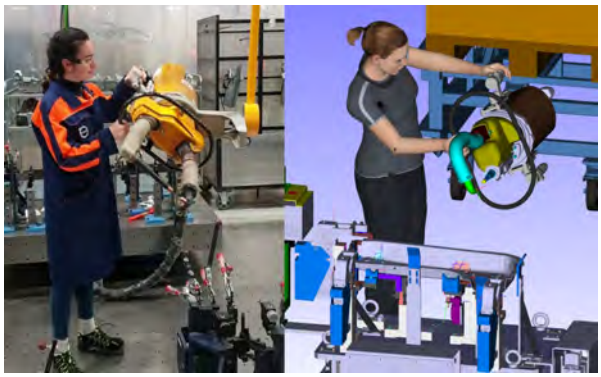

Figure 1. Real workstation (left) and corresponding model of the workstation in IPS IMMA (right)

The welding gun can be grasped in different positions, and the welding can be performed in different angles if the welding gun is kept perpendicular to the welding spot (Figure 2). The geometry of the workstation can cause collisions with the welding gun and limits the possible angles of welding (Figure 3).

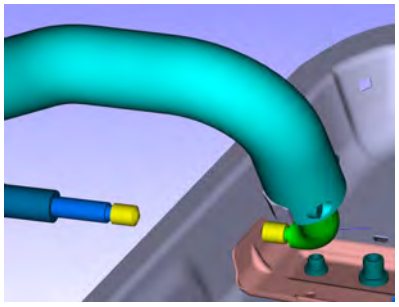

Figure 2. Perpendicular welding position of the welding gun

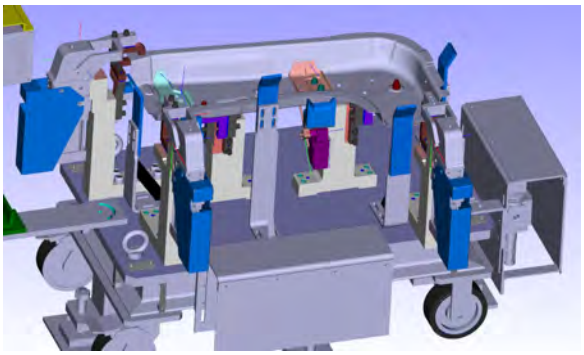

Figure 3. Geometry of the welding workstation

The welding gun motion is planned with a path planning algorithm in IPS IMMA (Hanson et al., 2019) to enter to the welding position in a valid path without considering the manikin well-being. This motion requires the manikin rotating and placing the welding gun (Figure 4).

Figure 4. Welding motion modelled in IPS IMMA

Representation of anthropometric diversity

The factory of the use case is located in China. A manikin family was created to represent the anthropometric variation in stature and elbow height, which were considered two key anthropometric measures of this workstation. The CAESAR database on Asian population (SAE International, 2022) was used to obtain anthropometric data of 176 individuals (83 male and 93 female). This data was used to create two confidence ellipsoids, one for males and one for females, both with a confidence interval of 95% (Brolin et al., 2012). Using the method described in Högberg et al. (2011), considering axial and centre cases of both ellipsoids, a family of 10 manikins (Table 1) was created in IPS IMMA (Figure 5).

Table 1. Anthropometric measures of the manikins

Nº Case	Gender	Stature	Elbow Height

		(mm)	(%-ile)	(mm)	(%-ile)
Case 0 (Median)	Female	1571.16	50.00	964.27	50.00
Case 1	Female	1711.24	99.19	1064.66	99.19
Case 2	Female	1431.09	0.81	863.88	0.81
Case 3	Female	1598.02	67.76	945.02	32.24
Case 4	Female	1544.31	32.24	983.51	67.76
Case 5 (Median)	Male	1698.93	50.00	1040.37	50.00
Case 6	Male	1875.53	99.22	1164.28	99.22
Case 7	Male	1522.33	0.78	916.47	0.78
Case 8	Male	1727.50	65.21	1020.33	34.79
Case 9	Male	1670.35	34.79	1060.42	65.21

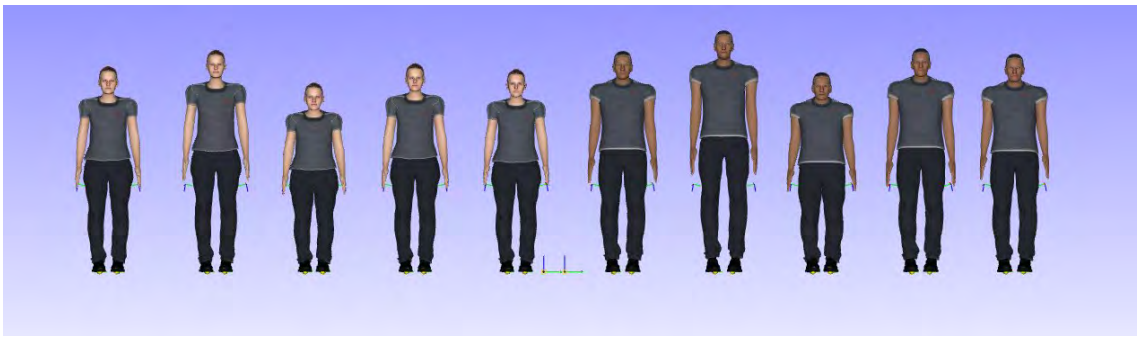

Figure 5. Cases 0 to 9 modelled in IPS IMMA

Ergonomics assessments by OWAS Lundqvist index

Ovako Working posture Analysing System (OWAS) is an musculoskeletal risk assessment method used to classify working postures of the *Back*, *Arms*, *Legs*, and *Use of force* (Karhu et al., 1977; Louhevaara et al., 1992). OWAS is based on the classification of 84 basic work postures, covering common and easily identifiable work postures. The *Use of force* category is classified into three levels, meaning that there are 252 possible combinations in total, each resulting in a unique OWAS code consisting of four digits. Each OWAS code results in one of four possible action categories, representing the risk level for WMSDs: 1 (*green, no corrective measures*), 2 (*yellow, corrective measures in the near future*), 3 (*orange, corrective measures as soon as possible*), and, 4 (*red, corrective measures immediately*) (Karhu et al., 1977; Louhevaara et al., 1992). The OWAS method provides the assessment of postural load over time, but only on sublevel, i.e. on the specific back, arms and legs postures separately (Karhu et al., 1977; Louhevaara et al., 1992). In order to make OWAS a time-based musculoskeletal risk assessment method able to indicate ergonomic load on an aggregated level, i.e. considering both working postures of the back, arms, legs, and use of force, in an integrated manner, the OWAS method can be complemented with the Lundqvist index (Lundqvist, 1988; Pinzke, 2016). This is a cumulative load index that helps to assess the workload over

time. The index is represented by a number from 100 (meaning that 100% worktime is in action category 1) up to 400 (meaning that 100% worktime is in action category 4). Hence, higher values of the Lundqvist index represent a higher risk of developing WMSDs. The Lundqvist index method provides no action levels however. Still the method can be used to qualitatively assess different design solutions from the perspective of risks for WMSDs, as well as in objective functions in optimization.

Optimization definition

The optimization variable defined for this case is the welding angle. The welding angle has been defined without considering collision with the workstation. This allows to explore solutions that could be more beneficial for the well-being of the manikins but would be in collision with the actual design of the workstation.

When the angle is changed, the simulation is run again for the entire manikin family, and the OWAS Lundqvist index values are sent to the optimization algorithm for it to define the welding angle for the next iteration. There are ten manikins, which provide ten OWAS Lundqvist index values that form the ten optimization objectives to minimize for the use case, which makes the optimization problem a multi-objective optimization. The optimization algorithm NSGA-II (Deb et al., 2002) was used for this use case due to its efficiency in multi-objective optimizations and has been run for 100 iterations.

Results

After performing the optimization, the results were analysed and interpreted to obtain more insights of how the time-based method behaved in the optimization, as well as of the workstation design itself.

Optimization results

For every iteration the welding gun angle was changed by the optimization algorithm, making the 10 manikins perform the welding in different postures. In order to perform the welding in different postures, the entire motion of the welding gun changed by using the input of the optimization algorithm implemented in the optimization platform (Iriondo Pascual et al., 2022) and the path planning algorithm of the DHM tool (Figure 6).

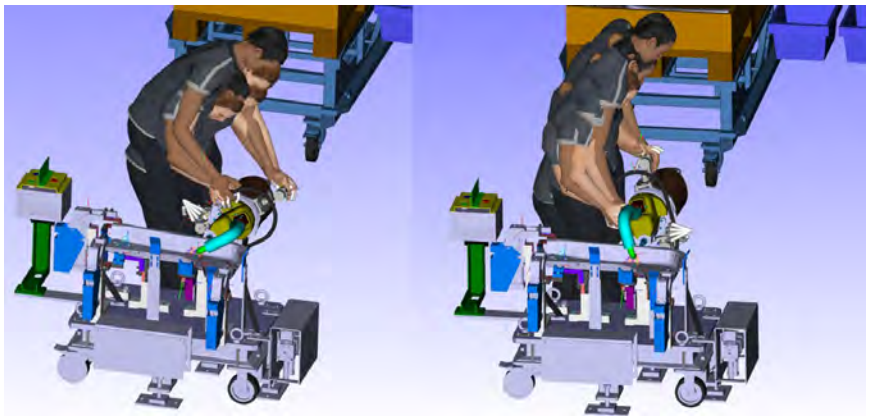

Figure 6. Different positioning of the welding gun provided by the optimization platform

After finishing all the iterations, the results of the OWAS Lundqvist index for every manikin and welding gun positioning were analysed. The results show that some manikins obtained higher values of OWAS Lundqvist index than others (Figure 7).

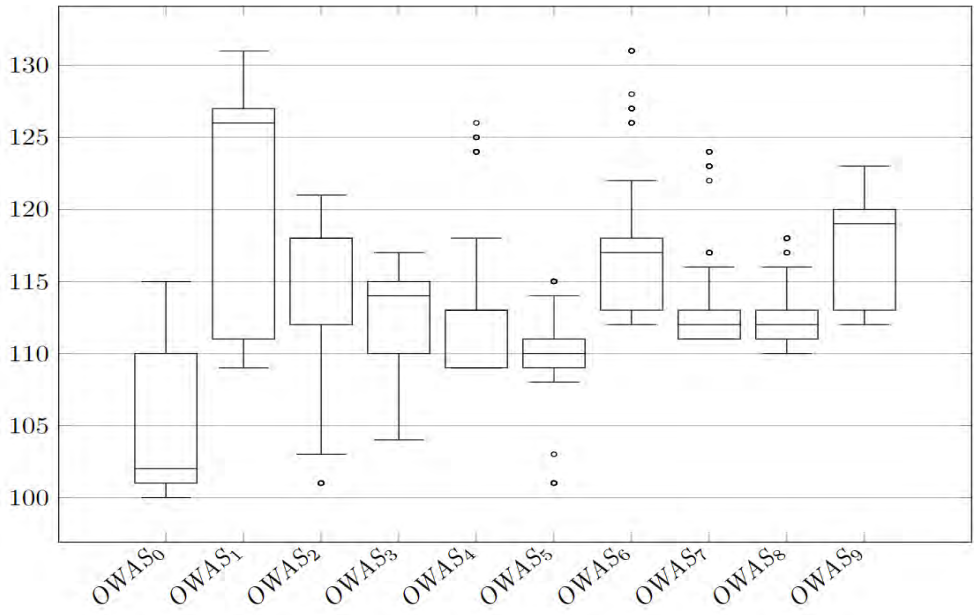

Figure 7. OWAS Lundqvist index result for each manikin

The results also showed low correlation between the optimization variable, i.e. the welding gun angle, and the objectives, i.e. OWAS Lundqvist index. For example, for manikin 0, the results show that there are two main clusters in the OWAS Lundqvist index values, and that the lowest values in both clusters were for a welding gun angle between 50-80° and 160-170° (Figure 8).

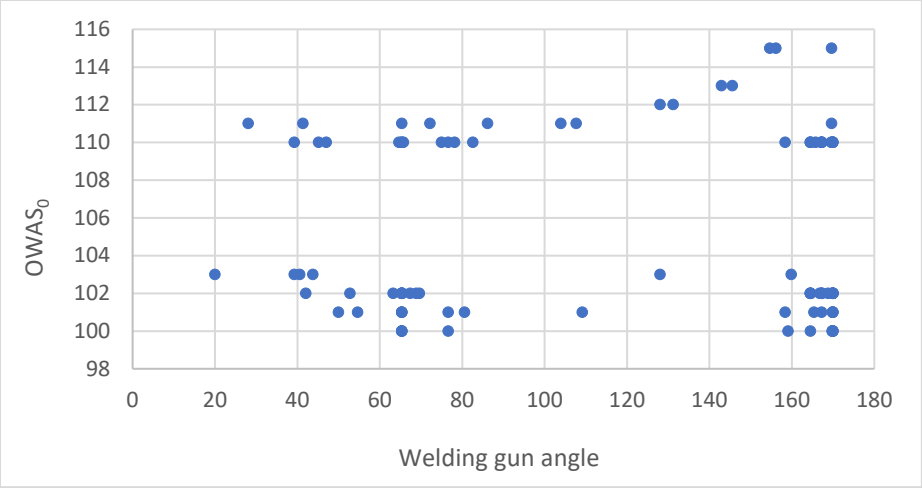

Figure 8. OWAS Lundqvist index results for manikin 0 depending on the welding gun angle

For some manikins (e.g. manikins 1, 2 and 3) the results for the welding gun angles are directly related, and the positioning of the gun provide either higher or lower OWAS Lundqvist index values equally for them (Figure 9).

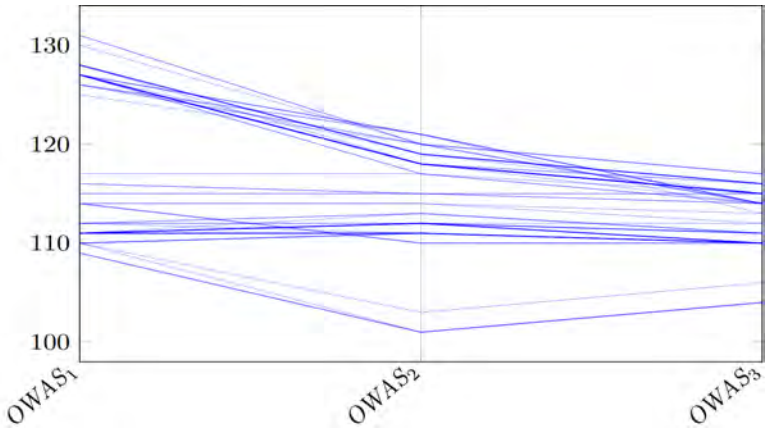

Figure 9. Direct relationship of OWAS Lundqvist indexes of manikins 1, 2 and 3

However, in some cases (e.g. manikins 0 and 1) the welding gun angles that can be positive for one manikin can be negative for the other manikin (Figure 10).

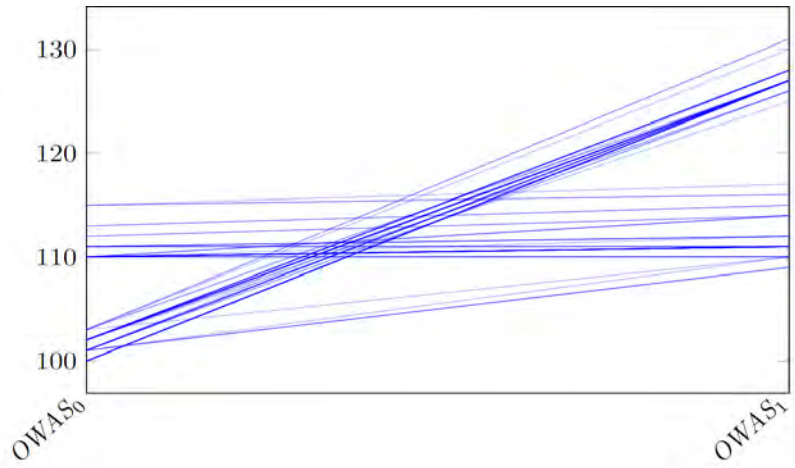

Figure 10. Inverse relationship of OWAS Lundqvist indexes of manikins 0 and 1

Interpretation of results

The results show that some manikins got higher OWAS Lundqvist index values. If we relate the values (Figure 7) to the anthropometric measures of the manikins (Table 1) the results show higher values for the manikins with a higher stature, especially for the female manikin 1 and for the male manikin 6. These manikins correspond to the higher axial cases in both stature and elbow height for female and male populations. These results (Figure 7) show that even in the best positioning they can have worse postures than lower stature manikins.

When analysing manikins individually, two clusters are found in all the cases. For example, in Figure 8 the clusters for manikin 0 are over the OWAS Lundqvist index scores 110 and under 104. When analysing the resulting simulations it can be seen that the cluster with the highest values was created by simulations where manikins could not obtain a proper positioning to hold the welding gun, e.g., simulations where manikins stopped grasping the welding gun.

Some welding positions that gave low OWAS Lundqvist index values had collision with the geometry of the workstation. Hence, they could not be achieved with the actual design of the workstation (Figure 11). However, as it might be possible to resolve the collisions by redesign of the workstation, we set up the optimization to include also solutions with collision, since that can be valuable information to the designer.

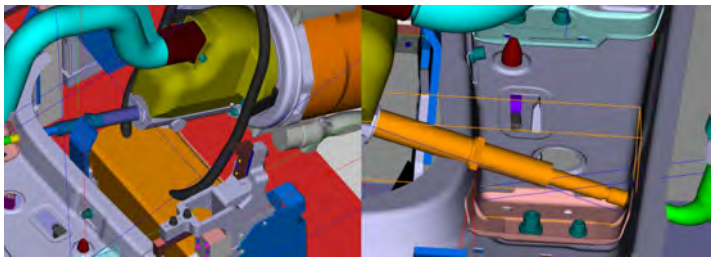

Figure 11. Positioning of the welding gun in collision with the workstation geometry

Discussion and Conclusions

Designing a workstation considering workers' well-being in DHM tools requires using musculoskeletal risk assessment methods that can assess the risk of workers developing WMSDs. Using time-based musculoskeletal risk assessment methods, like the one provided by combining OWAS with Lundqvist index, in DHM tools allows users to analyse complete motions of manikins in simulations instead of single postures. The analysis allows finding out if performing the motions enhances the risk of developing WMSDs. With common single posture ergonomics evaluation methods, such as RULA (McAtamney & Nigel Corlett, 1993) and REBA (Hignett & McAtamney, 2000), there is a possibility to choose the wrong postures to assess, and therefore, underestimate the risk of performing certain operations. With time-based ergonomics evaluation methods all the postures in the motion are evaluated, leading to a lower risk of evaluating the wrong postures, as well as considering the aggregated load. However, using time-based ergonomics evaluation methods requires the motions of the manikins to be representative of how real humans perform work tasks.

The musculoskeletal risk assessment method OWAS Lundqvist index has been found to be appropriate to use together with optimization algorithms. OWAS Lundqvist index provides a single integer per manikin as an optimization objective, which allows using the integers as objective functions in optimization algorithms. In this case, ten manikins were used to represent the anthropometric diversity at the workstation, i.e. resulting in a ten objective optimization problem, and a single optimization variable, i.e. the welding angle. The results show a relation between the anthropometric measures of the manikins and the OWAS Lundqvist index values, obtaining the highest risk scores in the manikins with highest stature and elbow height values. In addition to that, the optimal welding positions for different manikins are different, meaning that there is a risk of designing a workstation that would hinder individuals in the population to perform the work with an appropriate work posture, and therefore increase their risk of developing WMSDs, should the designer only consider one or a few manikins. In this study some beneficial welding positions were found in collision, therefore, modifying the design of the workstation to

allow these positions could enable workers to perform the welding task with lower risk to develop WMSDs.

In conclusion, implementing time-based musculoskeletal risk assessment methods in optimizations in DHM tools allows users to perform optimizations of workstation designs where full work sequences are simulated. The optimizations could be performed for any design parameter, e.g., layout, tool positioning, and task order, and use time-based musculoskeletal risk assessment methods to assess the worker well-being. In addition to that, anthropometric diversity can be included to assess the level of inclusion of the workplace, and by that supporting a sustainable work life for all members of the workforce, basically by assisting designers to find better workstation design solutions. This study has been limited to one time-based musculoskeletal risk assessment methods, i.e., OWAS Lundqvist index, however, other time-based musculoskeletal risk assessment methods should be studied to find the most appropriate ones for the task assessed. Also, this study did not consider productivity metrics, but future work will include system performance metrics such as cycle time, spaghetti diagram, and value adding time, added to the optimization. Optimising both human well-being and system performance is in-line with the definition and purpose of ergonomics

Acknowledgments

This work has been supported by ITEA3 in the project MOSIM, the Knowledge Foundation and the associated INFINIT research environment at the University of Skövde, within the Virtual Factories with Knowledge-Driven Optimization (VF-KDO) research profile and the Synergy Virtual Ergonomics (SVE) project, and by the participating organizations. Their support is gratefully acknowledged.

References

Abdel-Malek, K., Arora, J., Bhatt, R., Farrell, K., Murphy, C., & Kregel, K. (2019). Chapter 6 - Santos: An integrated human modeling and simulation platform. In S. Scataglini & G. Paul (Eds.), *DHM and Posturography* (pp. 63–77). Academic Press. https://doi.org/10.1016/B978-0-12-816713-7.00006-4

Berlin, C., & Kajaks, T. (2010). Time-related ergonomics evaluation for DHMs: A literature review. *International Journal of Human Factors Modelling and Simulation*, *1*(4), 356–379. https://doi.org/10.1504/IJHFMS.2010.040271

Brolin, E., Högberg, D., & Hanson, L. (2012). Description of boundary case methodology for anthropometric diversity consideration. *International Journal of Human Factors Modelling and Simulation*, *3*(2), 204–223. https://doi.org/10.1504/IJHFMS.2012.051097

Deb, K., Pratap, A., Agarwal, S., & Meyarivan, T. (2002). A fast and elitist multiobjective genetic algorithm: NSGA-II. *IEEE Transactions on Evolutionary Computation*, *6*(2), 182–197. https://doi.org/10.1109/4235.996017

Fisher, D. L., Rizzo, M., Caird, J., & Lee, J. D. (2011). *Handbook of Driving Simulation for Engineering, Medicine, and Psychology*. CRC Press.

Hanson, L., Högberg, D., Carlson, J. S., Delfs, N., Brolin, E., Mårdberg, P., Spensieri, D., Björkenstam, S., Nyström, J., & Ore, F. (2019). Chapter 11—Industrial Path Solutions – Intelligently Moving Manikins. In S. Scataglini & G. Paul (Eds.), *DHM and Posturography* (pp. 115–124). Academic Press. https://doi.org/10.1016/B978-0-12-816713-7.00011-8

Hignett, S., & McAtamney, L. (2000). Rapid entire body assessment (REBA). *Applied Ergonomics*, *31*(2), 201–205.

Högberg, D., Bertilsson, E., & Hanson, L. (2011). *A basic step towards increased accommodation level accuracy when using DHM tools*. 1–6. http://urn.kb.se/resolve?urn=urn:nbn:se:his:diva-5736

Iriondo Pascual, A., Lind, A., H&#246, Gberg, D., Syberfeldt, A., & Hanson, L. (2022). Enabling Concurrent Multi-Objective Optimization of Worker Well-Being and Productivity in DHM Tools. *SPS2022*, 404–414. https://doi.org/10.3233/ATDE220159

Karhu, O., Kansi, P., & Kuorinka, I. (1977). Correcting working postures in industry: A practical method for analysis. *Applied Ergonomics*, *8*(4), 199–201. https://doi.org/10.1016/0003-6870(77)90164-8

Kuhn, W. (2006). Digital Factory—Simulation Enhancing the Product and Production Engineering Process. *Proceedings of the 2006 Winter Simulation Conference*, 1899–1906. https://doi.org/10.1109/WSC.2006.322972

Louhevaara, V., Suurnäkki, T., Hinkkanen, S., & Helminen, P. (1992). *OWAS: A method for the evaluation of postural load during work* (6a ed.). Helsinki: Institute of Occupational Health. Centre for Occupational Safety. https://www.worldcat.org/title/owas-a-method-for-the-evaluation-of-postural-load-during-work/oclc/928946461

Lundqvist, P. (1988). *Psychosocial Factors in the Working Environment of Young Swedish Farmers with Milk Production. Working Environment in Farm Buildings. Diss. Rapport 58. Lund: LBT*, 187–222.

McAtamney, L., & Nigel Corlett, E. (1993). RULA: A survey method for the investigation of work-related upper limb disorders. *Applied Ergonomics*, *24*(2), 91–99. https://doi.org/10.1016/0003-6870(93)90080-S

Oppelt, M., & Urbas, L. (2014). Integrated virtual commissioning an essential activity in the automation engineering process: From virtual commissioning to simulation supported engineering. *IECON 2014 - 40th Annual Conference of the IEEE Industrial Electronics Society*, 2564–2570. https://doi.org/10.1109/IECON.2014.7048867

Pinzke, S. (2016). Comparison of Working Conditions and Prevalence of Musculoskeletal Symptoms among Dairy Farmers in Southern Sweden over a 25-Year Period. *Frontiers in Public Health*, *4*, 1–12. https://doi.org/10.3389/fpubh.2016.00098

Raschke, U., & Cort, C. (2019). Chapter 3—Siemens Jack. In S. Scataglini & G. Paul (Eds.), *DHM and Posturography* (pp. 35–48). Academic Press. https://doi.org/10.1016/B978-0-12-816713-7.00003-9

SAE International. (2022). *Digitally Defining the Human Body, CAESAR*. SAE International. https://www.sae.org/standardsdev/tsb/cooperative/caesar.htm

Waters, T. R., Putz-Anderson, V., Garg, A., & Fine, L. J. (1993). Revised NIOSH equation for the design and evaluation of manual lifting tasks. *Ergonomics*, *36*(7), 749–776. https://doi.org/10.1080/00140139308967940

Design Concept Evaluation in Digital Human Modelling Tools

Lars Hanson[a,b], Dan Högberg[b], Anna Brolin[b], Erik Brolin[b], Mikael Lebram[c] Aitor Iriondo Pascual[b], Andreas Lind[a,b], Niclas Delfs [d]

[a]*Global Industrial Development, Scania CV AB, Sweden*
[b]*School of Engineering Science, University of Skövde, Sweden*
[c]*School of Informatics, University of Skövde, Sweden*
[d]*Fraunhofer-Chalmers Centre, Gothenburg, Sweden*

Abstract

In the design process of products and production systems, the activity to systematically evaluate initial alternative design concepts is an important step. The digital human modelling (DHM) tools include several different types of assessment methods in order to evaluate product and production systems. Despite this, and the fact that a DHM tool in essence is a computer supported design and analysis tool, none of the DHM tools provide the functionality to, in a systematic way, use the results generated in the DHM tool to compare design concepts between each other. The aim of this paper is to illustrate how a systematic concept evaluation method is integrated in a DHM tool, and to exemplify how it can be used to systematically assess design alternatives. Pugh´s method was integrated into the IPS software with LUA scripting to systematically compare design concepts. Four workstation layout concepts were generated by four engineers. The four concepts were systematically evaluated with 2 methods focus on human well-being, 2 methods focus on system performance and cost. The result is very promising. The demonstrator illustrates that it is possible to perform a systematic concept evaluation based on both human well-being, overall system performance, and other parameters, where some of the data is automatically provided by the DHM tool and other manual. The demonstrator can also be used to evaluate only one design concept, where it provides the software user and the decision maker with an objective and visible overview of the success of the design proposal from the perspective of several evaluation methods

Keywords: IPS IMMA, ergonomics, simulation, design, evaluation

Introduction

Simulation and automation are elements in the Industry 4.0 transformation that affect manufacturing industries' production systems and way of working (Rosin et al., 2019). Industry 5.0 has been introduced, reinforcing the human-centric perspective onto Industry 4.0 (Nahavandi, 2019). Digital human modelling (DHM) tools is a human-centric category of simulation software that facilitates proactive consideration of ergonomics in computer-generated environments, hence requiring no physical prototypes (Scataglini &

Paul, 2019). DHM tools can for example be used at the early stages of the design process to create, visualize, assess, optimize, and verify workplace designs. In the design process of products and production systems, the activity to systematically evaluate initial alternative design solutions, often referred to as concepts, is an important step since the choice of concept has a strong impact on the subsequent steps of the design process. Several different methods for performing systematic concept assessments are available, e.g. Pugh's method for controlled convergence (Pugh, 1981), weighted concept scoring (Ulrich et al., 2020), analytical hierarchy process (Saaty, 1980), and the ELECTRE methods (Roy, 1991). Honkala et al. (2007) compare different concept selection methods, where they suggest that comparisons of concept alternatives should start with more simple methods, e.g. Pugh's method or weighted scoring methods, and if there is a reason to question the result from the more simple methods, the use of more detailed methods can be justified. Several DHM tools exist, e.g. EMA (Fritzsche et al., 2011), IPS IMMA (Högberg et al., 2016), Ramsis (Seidl, 1997), Santos (Yang et al., 2005), and Siemens Jack (Badler et al., 1993). DHM tools include several different types of assessment methods in order to evaluate the human-system interaction represented in the scenario modelled in the DHM tool, e.g. in regards to reach, vision, and risks for musculoskeletal disorders (MSDs). Despite this, and the fact that a DHM tool in essence is a computer supported design and analysis tool, none of the DHM tools provide the functionality to, in a systematic way, use the results generated in the DHM tool to compare design concepts between each other. The purpose of such a systematic comparison is to identify those design solutions that are superior compared to other design alternatives. Hence it is a convergent activity in the design process. The aim of this paper is to illustrate how a systematic concept evaluation method is integrated in a DHM tool, and to exemplify how it can be used to systematically assess design alternatives.

Methods

The DHM tool IPS IMMA was used as a software platform to demonstrate the integration. Pugh´s method was interpreted and then integrated into the software with LUA scripting to systematically compare design concepts. A graphical interface for comparing concepts was created. In order to test and illustrate the functionality of the demonstrator, four engineers were recruited as test subjects. The four engineers were familiar with DHM tools in general, and IPS IMMA in specific, and had overall knowledge about the work task represented in the test case, i.e. a pedal car assembly work. The task of the test subjects was to design a workstation layout for pedal car assembly. Four parts were to be mounted at the pedal car assembly in the station: a mud guard, a wheel, a bracket for the seat, and the seat itself. The four parts and the pedal car assembly were available with CAD models in an IPS IMMA scene. The given sequence and tasks only included manual efforts from an assembly operator and there are therefore no need for hand

hold tools or other resources to mount the parts on the pedal car assembly. To simplify the test, anthropometric diversity was not considered, and therefore just one manikin was used, representing a Swedish 50th percentile male in stature.. The workstation area was not allowed to exceed 8 m2, i.e. the workstation the test subjects designed should fit inside a box in the scene. The test subjects were free to add any fixtures, logistic racks, primitives, etc. to make the workstation complete and functional before giving the manikin tasks. The subjects were creating one layout concept and were informed that four evaluation methods should be used to assess the design concepts:

1. Lundqvist OWAS index (the lower the better) (Lundqvist, 1988)

2. Arvidsson's action levels for preventing MSDs (Arvidsson et al., 2021)

3. Length of spaghetti diagram (total walking distance) (Kanaganayagam et al., 2015)

4. Percentage of time performing value adding tasks (Womack & Jones, 2003)

The design concepts were also evaluated from an "engineering cost perspective", represented by the time the test subjects spent on designing the workstation layout. The cost was measured in minutes. The clock for measuring the minutes started when the test subject received the written instruction. The subjects had accepted to participate in the test, and they were notified in advance that they would receive an email with instructions and access to software files on a specific day and time. The cost clock for a certain test subject was stopped when the IPS IMMA scene was sent back by email, i.e. representing the test subject's proposed design of the workstation layout. Three of the four subjects fulfilled the task and replied with an IPS IMMA file of the suggested workstation layout (example in Figure 1).

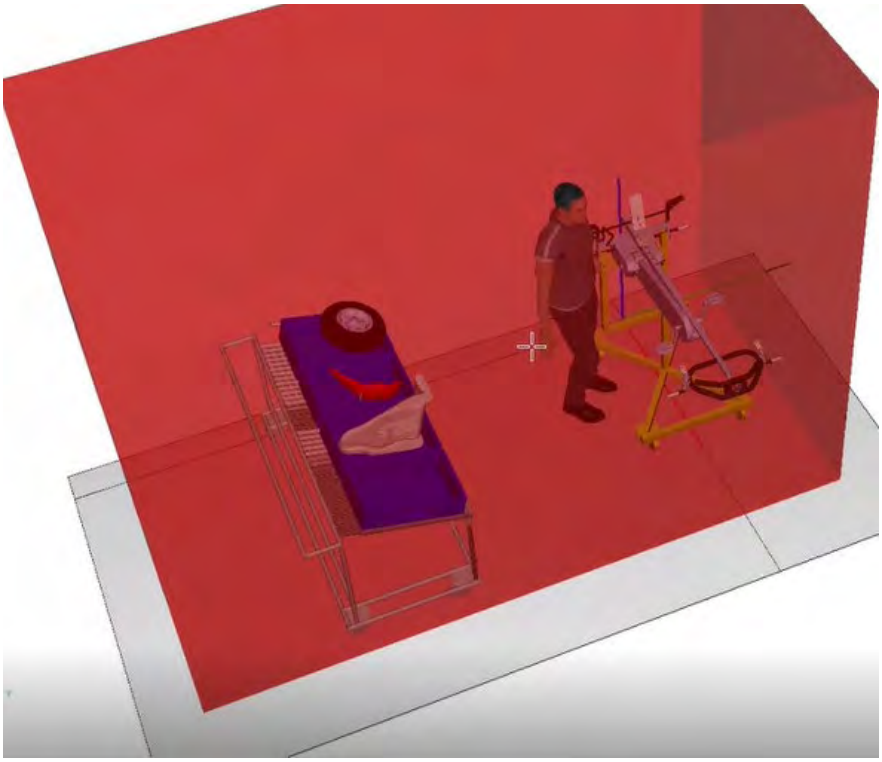

Figure 1. Example of one test subject's proposed design of the workstation layout.

Results

The result demonstrates an integrated solution where design concepts can be compared in a systematic way. The solution provides a demonstrator that provides objective design decision support, based on data automatically generated in the DHM software. When needed, data can also be manually added, as done for the "engineering cost" in this case. The demonstrator (Figure 2) includes two major steps: (1) to build up the Pugh matrix, and (2) to use the matrix for the design concept comparisons. The Pugh matrix build up phase is carried out using two major selectors: the concept alternatives selector (building the matrix horizontally), and the criterion selector (building the matrix vertically). In the first selector the design concepts, as described in unique IPS IMMA files, that are to be included in the design concept evaluation are selected. In accordance with Pugh's method for controlled convergence, one of the concepts selected will form the datum, i.e. the reference concept that all other concepts will be compared with. The second selector is the criterion selector, where the user selects the parameters to be considered in the concept evaluation. As ergonomics, per definition, regards the optimization of both human well-being and overall system performance (Wilson, 2000), the demonstrator enables adding criteria that are based on data on both human well-being and overall system performance. Here, the following two criteria were used to assess human well-being: Lundqvist OWAS index (Lundqvist, 1988) and one of the suggested action

levels for preventing MSDs by Arvidsson et al. (2021), namely the right arm angular velocity. For the assessment of system performance, the following two criteria were used: length of spaghetti diagram (Kanaganayagam et al., 2015) and percentage of time spent on performing value adding tasks (Womack & Jones, 2003). The data for these four criteria came from the IPS IMMA simulation of the pedal car assembly tasks, performed by the manikin in the proposed workstation layout. Hence, objective data was retrieved automatically per design concept, based on the data provided by the DHM simulations of each concept. In the matrix it is highlighted in red if any criteria are outside the recommendation for the criteria, e.g. if an exposure exceeds the recommended action level. It is also possible for the user to add own criteria, as well as values that do not origin from the DHM simulation itself. In this case, cost based on time spend to carry out the design task was added as a criteria, and the time value per design concept was added manually. This step ends the first step to build up the Pugh matrix.

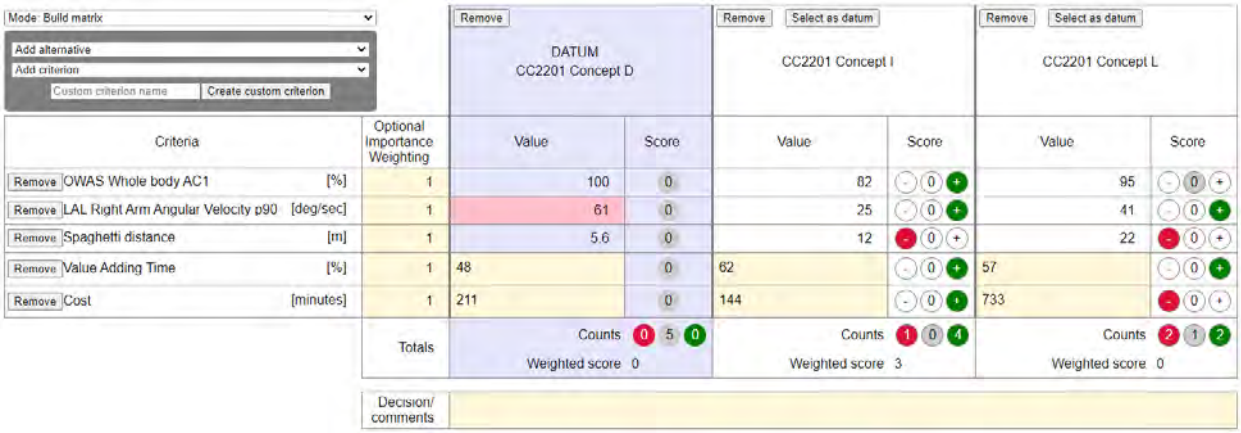

Figure 2. The Pugh concept evaluation matrix demonstrator in IPS IMMA.

The second step is the assessment step, which consist of comparing design concepts and making decisions on how to progress in the design process. In the demonstrator there is an option for the user to add weighting factors per criterion, if one or several criterions are more important than others. In accordance with Pugh's method for controlled convergence, the demonstrator provides the functionality for the user, or for a multi-disciplinary team when the concept evaluation is performed as a group activity, to rate concepts with consideration to each criterion, using the scale: worse than reference concept (-), equal to reference concept (0), or better than reference concept (+). In the summary section of Pugh's method, the numbers of -, 0 and + for each concept are automatically calculated, as well as the weighted sum of the scores. This to ease the user or the team to make decisions of how to progress in the design process, e.g.

to select a concept or several concepts to develop further, or possibly to iterate the design process in order to find even better design solutions or combine design concepts.

Discussion

The demonstrator illustrates that it is possible to perform a systematic concept evaluation based on both human well-being, overall system performance, and other parameters, where at least some of the data is automatically provided by the DHM tool. The result is very promising. A key feature of the presented approach, which is believed to be a large strength, is that the concept evaluation can be performed with support of objective data automatically generated from the simulation in the DHM tool. Thus, the potential of the DHM tool to provide objective data based on simulations of human-system interactions is used to find better design solutions. To use simulation tools to a high extent is one of the focus areas in Industry 4.0 (Nahavandi, 2019). Another focus area in Industry 4.0 is automation. The demonstrator is semi-automatic, which we believe is advantageous for concept evaluation activities, in order to facilitate transparency, dialogue in the design team, and to facilitate consideration of aspects that cannot be provided by the DHM simulation. Still, the criteria values are automatically filled in for the concepts, and quantities and sums are automatically calculated. The possibility to manually add criteria makes it possible for the user to customize the matrix. While such customized matrices most likely have been made before using tools such as spreadsheets, the demonstrator provides the functionality to make evaluations of multiple design concepts in a structured way in the DHM tool. The ability to perform the evaluation in the DHM tool will increase the efficiency as the user do not have to copy and paste information from one software to another. There is also less risk to make human errors, if information is kept within one software, or automatically transferred between different software, and do not have to be entered in another software. The ability to easily, quickly and objectively assess and compare different design concepts directly in the DHM tool is also believed to encourage the DHM tool user to find even better design solutions, hence assisting the design work being carried out in ‘small loops‘ as discussed in Högberg (2009) as a way to enhance design process performance.

The demonstrator also facilitates method triangulation. There are several evaluation methods that have been developed to evaluate human well-being and system performance. Each of them has a unique set of advantages and disadvantages and using them in appropriate combinations is essential to get a representative evaluation that covers several relevant perspectives. The demonstrator can therefore also be used to evaluate only one design concept, where it provides the software user and the decision maker with an objective and visible overview of the success of the design proposal from the perspective of several evaluation methods. The objective and visual presentation will support the decision maker to compare the

results of each evaluation method, and hence assist to make a well-founded decision. In summary, the demonstrator acts as a design decision support tool, utilizing the capability of the DHM tool to provide objective data, but also enables the user to enter additional data, and the design team to discuss and agree on decisions. The demonstrator that supports that data are transparent to the stakeholders, e.g. engineers, managers and ergonomists, and that arguments and conclusions regarding DHM simulations can be documented, stored and traced, which is in line with the guide and documentation system to support DHM tool usage proposed by Hanson et al. (2005). Even if the presented demonstrator is promising, more integration and usability work needs to be carried out based on user feedback.

Acknowledgments

This research was carried out within the VF-KDO profile (Virtual Factories with Knowledge-Driven Optimization) and the Synergy project Virtual Ergonomics, both funded by the Knowledge Foundation in Sweden, as well as the VINNOVA-funded project VIVA – the Virtual Vehicle Assembler.

References

Arvidsson, I., Dahlqvist, C., Enquist, H., & Nordander, C. (2021). Action Levels for the Prevention of Work-Related Musculoskeletal Disorders in the Neck and Upper Extremities: A Proposal. Annals of Work Exposures and Health, 65(7), 741-747.

Badler, N.I., Phillips, C.B., & Webber, B.L. (1993). Simulating humans: Computer graphics animation and control. New York, USA, Oxford University Press.

Fritzsche, L., Jendrusch, R., Leidholdt, W., Bauer, S., Jäckel, T., & Pirger, A. (2011). Introducing ema (Editor for Manual Work Activities) – A New Tool for Enhancing Accuracy and Efficiency of Human Simulations in Digital Production Planning. Proceedings of International Conference on Digital Human Modeling, Orlando, USA, 272-281.

Hanson, L., Blomé, M., Dukic, T., & Högberg, D. (2006). Guide and documentation system to support digital human modeling applications. International Journal of Industrial Ergonomics, 36(1), 17-24.
Högberg, D. (2009). Digital human modelling for user-centred vehicle design and anthropometric analysis. International Journal of Vehicle Design, 51(3/4), 306-323.

Högberg, D., Hanson, L., Bohlin, R., & Carlson, J.S. (2016). Creating and shaping the DHM tool IMMA for ergonomic product and production design. International Journal of the Digital Human, 1(2), 132-152.

Honkala, S., Hämäläinen, M., & Salonen, M. (2007). Comparison of four existing concept selection methods. Proceedings of International Conference on Engineering Design, Paris, France, 1-11.
Kanaganayagam, K., Muthuswamy, S., & Damoran, P. (2015). Lean methodologies to improve assembly line efficiency: An industrial application. International Journal of Industrial and Systems Engineering, 20(1), 104-116.

Lundqvist, P. (1988). Psychosocial factors in the working environment of young Swedish farmers with milk production. Working environment in farm buildings. Diss. Rapport 58, Lund, Sweden, Swedish University of Agricultural Sciences, Department of Farm Buildings.

Nahavandi, S. (2019). Industry 5.0—A Human-Centric Solution. Sustainability, 11(16), 4371.

Pugh, S. (1981). Concept Selection: A Method That Works. Proceedings of the 1981 International Conference on Engineering Design, Rome, Italy, 497-506.

7th International Digital Human Modeling Symposium (DHM 2022) Rosin, F., Forget, P., Lamouri, S., & Pellerin, R. (2019). Impacts of Industry 4.0 technologies on Lean principles. International Journal of Production Research, 58(6), 1644-1661.

Roy, B. (1991). The Outranking Approach and the Foundation of ELECTRE Methods. Theory and Decision, 31, 49-73.

Saaty, T.L. (1980). The Analytical Hierarchy Process. McGraw-Hill, New York, USA.

Scataglini, S., & Paul, G. (Eds.). (2019). DHM and Posturography. Academic Press.

Seidl, A. (1997). RAMSIS, a new CAD tool for ergonomic analysis of vehicles developed for the German automotive industry. Automotive concurrent/simultaneous engineering, SAE Special Publications, 1233, 51-57.

Ulrich, K.T., Eppinger, S.D., & Yang, M.C. (2020). Product Design and Development (7th ed.). McGraw-Hill, New York, USA.

Wilson, J.R. (2000) Fundamentals of ergonomics in theory and practice, Applied Ergonomics, V31 (6), 557-567,

Womack, J.P., & Jones, D. (2003). Lean thinking. Banish waste and create wealth in your corporation. Free Press, New York, USA.

Yang, J., Marler, T., Kim, H., Farrell, K., Mathai, A., Beck, S., Abdel-Malek, K., Arora, J., & Nebel, K. (2005). Santos ™: A New Generation of Virtual Humans. SAE Technical Paper No 2005-01-1407, Warrendale, USA.

The Effects of Sex and Handedness on Lumbar Kinetics During Asymmetric Lifting Tasks: A Pilot Study

Jazmin Cruz, Ivan Aguilar, and James Yang*

Human-Centric Design Research Lab, Department of Mechanical Engineering, Texas Tech University, Lubbock, TX 79409, USA, *Corresponding author: james.yang@ttu.edu

Abstract

Manual material handling such as box lifting is a very common task that is used in the industrial and medical fields. It is widely accepted that manual lifting can potentially lead to low back injury. Asymmetric lifting, which involves twisting of the trunk, shifts trunk muscle activation and can increase the lower back loading on the spine thus further increasing the likelihood of injury. Other researchers have explored asymmetric lifting but have not considered the effects of handedness. Sex has also been considered as a factor related to low back injury, but majority of research work include only male subjects in literature. This work aims to examine the effects of sex, handedness, box load, and box origin on the maximum lumbar flexion/extension L5-S1 joint moments generated during two-handed box lifting so that safer lifting recommendations can be made for those tasks. Eight participants (sex: 4 women, 4 men; age: 28.62 ± 4.53 years; height: 170.00 ± 7.45 cm; body mass: 72.36 ± 8.97 kg; handedness: 4 left-dominant, 4 right-dominant) performed two-handed box lifts with five different box origins (two left lifts, one sagittally symmetric lift, and two right lifts) and three different box weights (1.20 kg, 5.74 kg, 10.27 kg). Motion data was collected using a motion capture system and force plates. There were no clear trends for the effect of sex, but our results suggest that individuals should lift from their dominant-hand side when performing asymmetric two-handed lifting tasks. Future work which will incorporate the use multiscale modeling (musculoskeletal modeling and finite element modeling) to perform a deeper analysis of spine biomechanics during these lifts at the muscle and tissue levels, respectively.

Keywords: Manual Material Handling; Lumber Spine; Low Back Pain; Asymmetric Lifting.

Introduction

Low back pain is a common symptom experienced by all age groups. It is the leading cause of disability across the globe and accounts for more lost workdays than any other occupational musculoskeletal condition (Hartvigsen et al., 2018). In addition to physical cost of low back pain, the USA spends more than $100 billion on low back pain management (Katz et al., 2006). A better understanding of low back pain is needed so that prevention may be possible.

It is believed that manual material handling may have some direct relationship with low back pain as it is the most common musculoskeletal disorder experienced by workers performing heavy physical work and lifting tasks (Marras, 2000). For example, it has been shown that individuals triggered an episode of low back pain shortly after performing awkwardly positioned manual tasks, heavy load manual tasks, or a combination of the two (Steffens et al., 2015). This connection has prompted further exploration of the causality of low back pain by other researchers who have looked at factors such as foot placement (Delise et al., 1996), box weight (Potvin et al., 2021; Song & Qu, 2014; Weston et al., 2020), and more.

Differences in lifting biomechanics between the sexes have been identified with regards to coordination (Lindbeck & Kjellberg, 2001) and lumbar spinal loading (Firouzabadi et al., 2021). Furthermore, the peak risk of low back pain for men and women occurs at different ages such as 40 and 60 years old, respectively (Marras, 2000). Over the years, researchers have taken sex into account but majority of these works include only male participants (Beaucage-Gauvreau et al., 2019; Delise et al., 1996; Ghofrani et al., 2021). It is critically important to include women in low back pain research studies as low back pain is more common in women than in men (Hartvigsen et al., 2018).

In addition to sex, handedness has yet to be thoroughly explored in lifting research. One study identified that spine compression and lateral shear increased at double the rate during asymmetric lifts beginning from the left side than the same lift from the right side (Marras & Davis, 1998). Intuition leads us to believe that humans naturally favor one side over the other, but little research has considered handedness during lifting (Butler et al., 2009; Weston et al., 2020).

The objective of this work is to examine the effects of sex, handedness, box load, and box origin on the maximum lumbar flexion/extension L5-S1 joint moments generated during box lifting as producing a higher low back joint moment is known to indicate low back pain risk (Hoozemans et al., 2008; Kingma et al., 2010). We hypothesize that women will experience higher maximum lumbar joint moment across all loading conditions. Additionally, we expect that individuals will experience higher maximum lumbar joint moment when lifting from their dominant side.

Methods

OpenSim Lifting Model

The previously validated lifting full-body (LFB) OpenSim model was used in this work (Beaucage-Gauvreau et al., 2019). It contains 30 rigid body segments, 29 degrees-of-freedom, and 238 musculotendon actuators as shown in Figure 1. The model treats the trunk and head as a rigid body, but contains spherical joints at the T12/L1, L1/L2, L2/L3, L4/L5, and L5/S1 intervertebral joints within the spine.

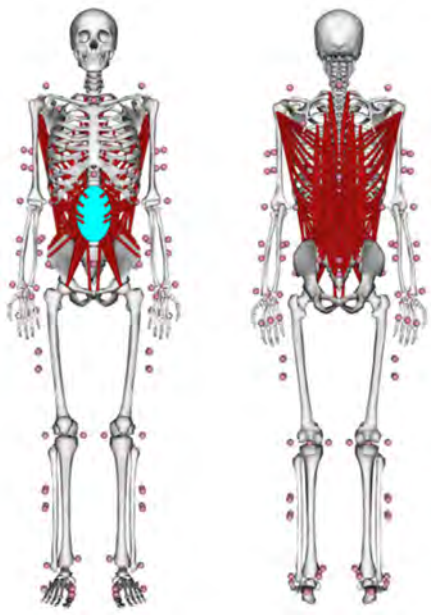

Figure 1: Lifting full-body (LFB) OpenSim Model

Lifting Protocol

The lifting protocol consisted of five box origins as shown in Figure 2. The milk crate was lifted with three loading conditions: unloaded (1.20 kg), 10 lbs (5.74 kg), and 20 lbs (10.27 kg). Each trial began in T-Pose and ended the lift with the milk crate at hip level while facing forward. Participants performed 30 lifts that included two repetitions of all box origins under all loading conditions in a randomized order. Subjects were allowed to lift in whatever way felt most natural to them but were instructed to keep one foot on each force plate throughout each trial. Figure 3 shows a subject mid-lift where they are turning to their right-hand side to pick up the box from the P5 box origin.

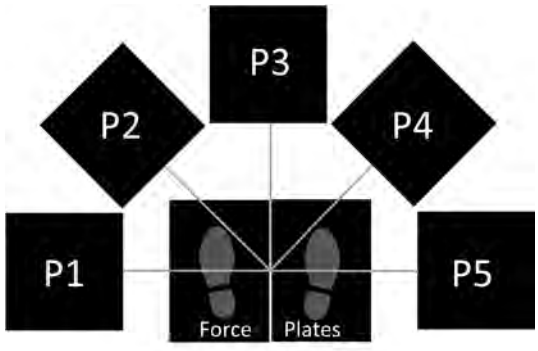

Figure 2: Box Origins

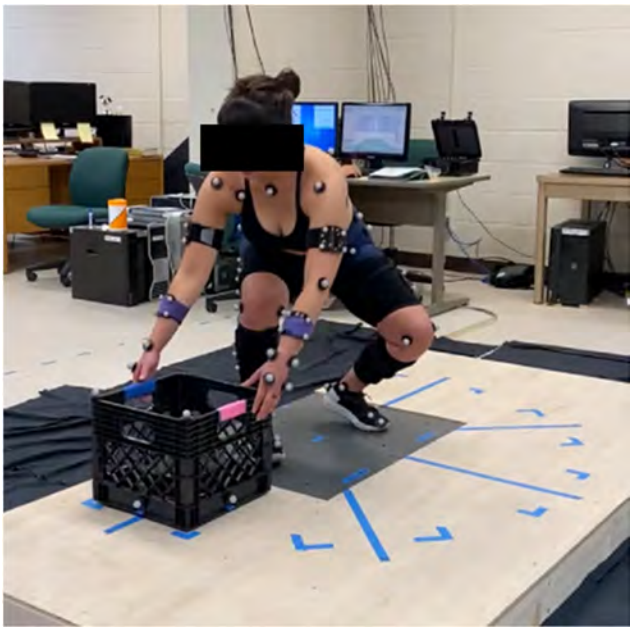

Figure 3: Subject Lifting Box from P5

Experimental Data Collection and Processing

Eight subjects participated in this study (sex: 4 women, 4 men; age: 28.62 ± 4.53 years; height: 170.00 ± 7.45 cm; body mass: 72.36 ± 8.97 kg; handedness: 4 left-dominant, 4 right-dominant). This study was approved by the Institutional Review Board of Texas Tech University (IRB2017-406) and participants signed informed consent forms. Participants had reflective markers and marker clusters placed throughout the whole body as shown on the LFB OpenSim model and Figure 3. Motion data was collected using an 8-camera motion analysis system (Motion Analysis Corp., Santa Rosa, California, USA) and two force plates (Bertec Corporation, Columbus, OH, USA) at 100 Hz and 2000 Hz, respectively. Kinematic and kinetic data were filtered using a Butterworth filter with a cutoff frequency of 6 Hz.

OpenSim Simulation Workflow

This study closely follows the workflow methodology described in a recent publication (Akhavanfar et al., 2022). First the LFB model is scaled to match each participant by using their static T-Pose motion file. Inverse kinematics is performed using the motion files of the tasks with the newly scaled model. Lastly, inverse dynamics is performed using the inverse kinematic results and filtered force plate data. The box load was applied as a downwards external force to the mid-point between the second and fifth metacarpal bones, i.e., half of the box load was applied to each hand. Maximum joint moments at the L5-S1 intervertebral level were extracted for flexion/extension for all lifting scenarios and were normalized by participant mass.

Results

The results for the overall group, left-handed/right-handed groups, and male/female groups can be seen in Figures 4, 5, and 6. Tabular versions of these groups can be seen in Tables 1, 2, and 3.

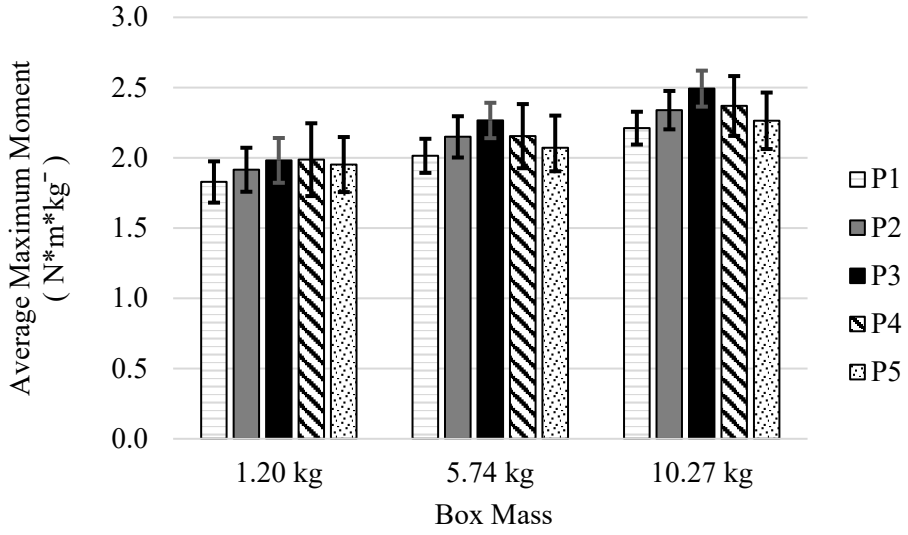

Figure 4: Average Maximum Flexion/Extension Moment at L5-S1

Table 1. Average Maximum Flexion/Extension Moment at L5-S1 Tabular Results (Average ± 1 SD in N*m*kg⁻)

	1.20 kg	5.74 kg	10.27 kg
P1	1.83 ± 0.15	2.01 ± 0.12	2.21 ± 0.12
P2	1.92 ± 0.16	2.15 ± 0.15	2.34 ± 0.14
P3	1.98 ± 0.16	2.27 ± 0.13	2.49 ± 0.13
P4	1.99 ± 0.26	2.15 ± 0.23	2.37 ± 0.21
P5	1.95 ± 0.20	2.07 ± 0.17	2.26 ± 0.20

Table 2. Left-Handed and Right-Handed Average Maximum Flexion/Extension Moment at L5-S1 Tabular Results (Average ± 1 SD in N*m*kg⁻)

	Left-Handed			Right-Handed		
	1.20 kg	5.74 kg	10.27 kg	1.20 kg	5.74 kg	10.27 kg
P1	1.82 ± 0.16	2.05 ± 0.12	2.15 ± 0.09	1.84 ± 0.15	1.98 ± 0.12	2.28 ± 0.11
P2	1.95 ± 0.17	2.16 ± 0.13	2.36 ± 0.15	1.88 ± 0.14	2.14 ± 0.17	2.32 ± 0.13
P3	2.01 ± 0.15	2.34 ± 0.05	2.48 ± 0.17	1.95 ± 0.17	2.19 ± 0.13	2.51 ± 0.08
P4	2.08 ± 0.22	2.33 ± 0.13	2.44 ± 0.15	1.89 ± 0.27	1.98 ± 0.16	2.30 ± 0.26
P5	2.05 ± 0.17	2.15 ± 0.20	2.30 ± 0.23	1.85 ± 0.17	2.00 ± 0.09	2.23 ± 0.17

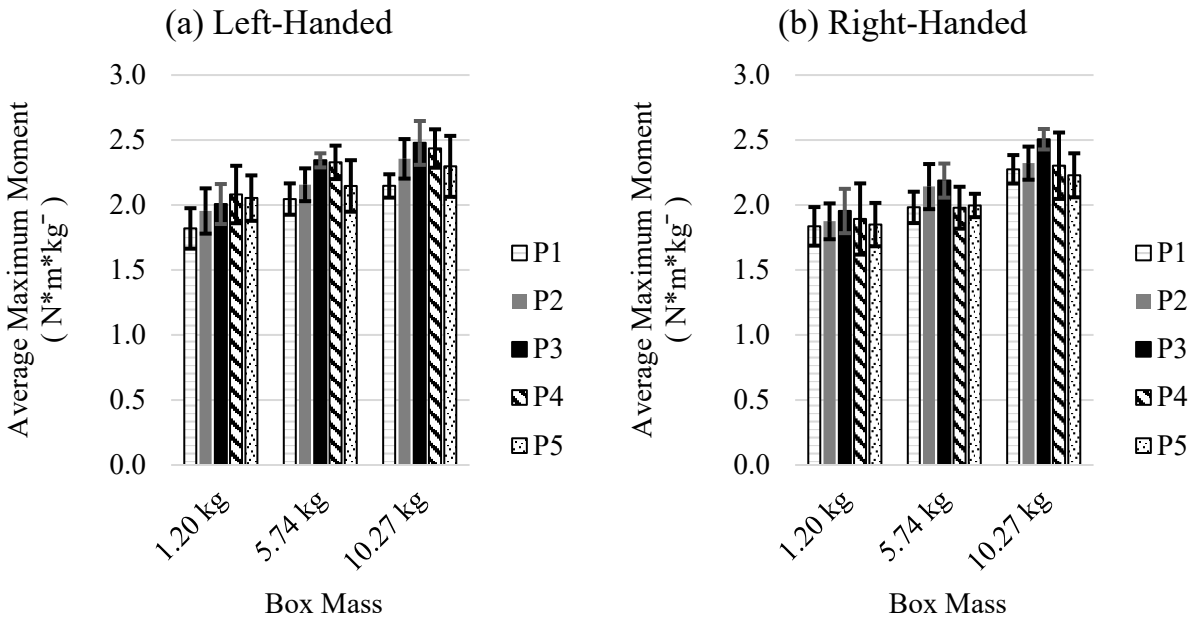

Figure 5: Average Maximum Flexion/Extension Moment at L5-S1 for (a) Left-Handed and (b) Right-Handed Groups

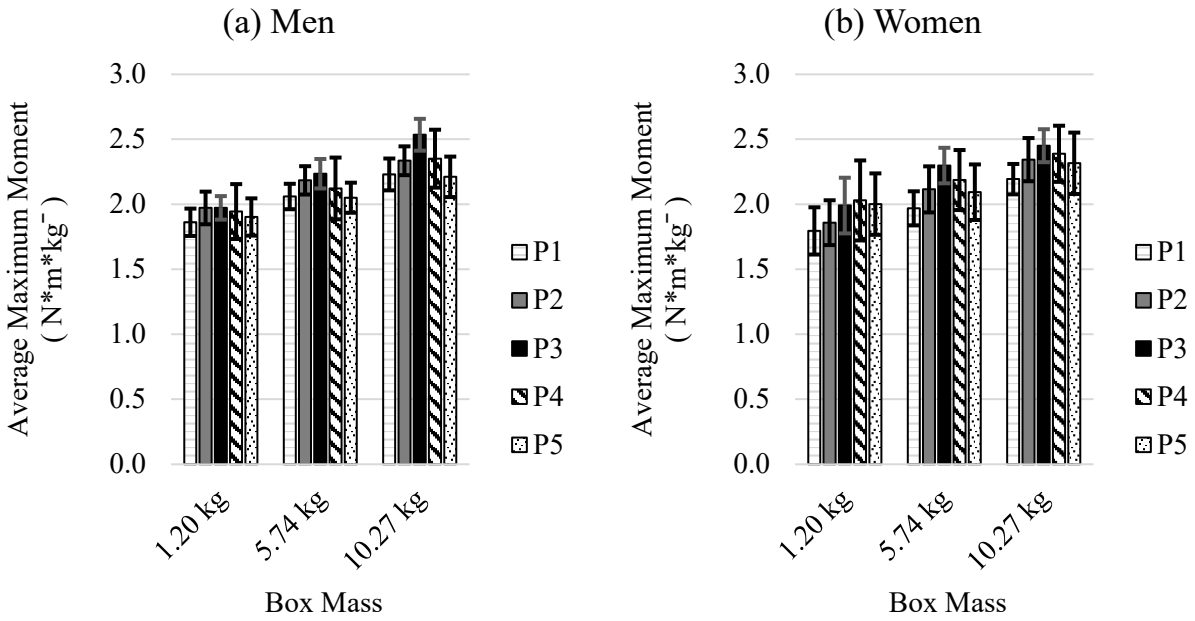

Figure 6: Average Maximum Flexion/Extension Moment at L5-S1 for (a) Male and (b) Female Groups

Table 3. Male and Female Average Maximum Flexion/Extension Moment at L5-S1 Tabular Results (Average ± 1 SD in N*m*kg⁻)

	Male			Female		
	1.20 kg	5.74 kg	10.27 kg	1.20 kg	5.74 kg	10.27 kg
P1	1.86 ± 0.11	2.06 ± 0.10	2.23 ± 0.12	1.80 ± 0.18	1.97 ± 0.13	2.19 ± 0.12
P2	1.97 ± 0.13	2.18 ± 0.11	2.34 ± 0.11	1.86 ± 0.17	2.11 ± 0.18	2.34 ± 0.17
P3	1.97 ± 0.09	2.23 ± 0.11	2.53 ± 0.12	1.99 ± 0.21	2.30 ± 0.14	2.45 ± 0.13
P4	1.94 ± 0.21	2.12 ± 0.24	2.35 ± 0.22	2.03 ± 0.31	2.19 ± 0.23	2.39 ± 0.22
P5	1.90 ± 0.14	2.05 ± 0.12	2.21 ± 0.16	2.00 ± 0.24	2.09 ± 0.21	2.32 ± 0.24

Discussion and Conclusions

Box Mass

The effect of box mass on lumbar moment across each lifting scenario can be seen in

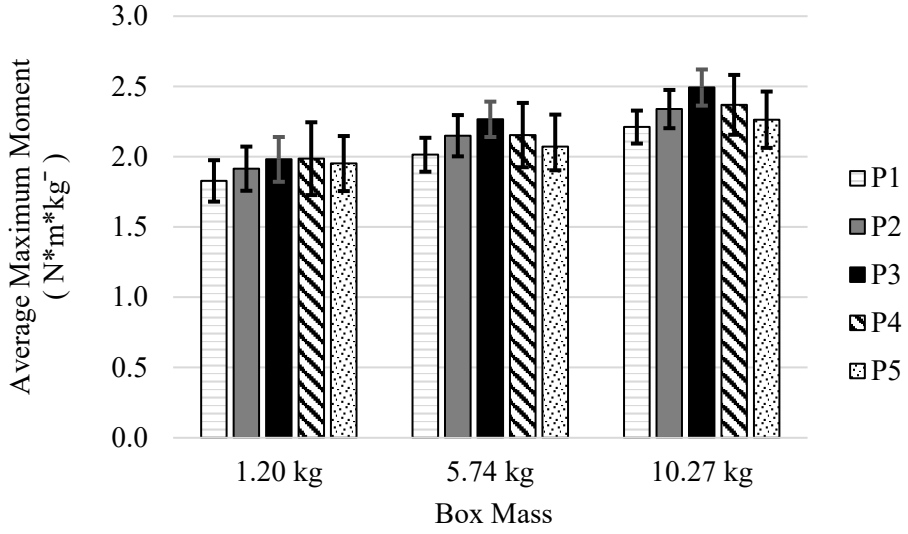

Figure 4. In general, the lumbar moment increases as the box mass increases, which is consistent with what has been found in the literature (Song & Qu, 2014).

Box Origin

The box origin of the lift had an influence on the lumbar moment. Figure 4 shows that the greatest flexion moment occurred when lifting from P3, while the lower flexion moments occurred when lifting from P1 and P5. This is an interesting result as it was expected that asymmetric lifts should be the most dangerous. This work did not take lateral bending or rotational moments into account, which have been known to increase during heavy asymmetric lifting tasks (Kim & Zhang, 2017). It is possible that the combination

of increased lateral bending and rotational moment could result in higher risk of low back pain and should be explored in future work to assess low back pain risk.

Handedness

Our original hypothesis was that individuals will experience higher maximum lumbar joint moment when lifting from their dominant side, however, Figure 5 shows the opposite trend. Across all mass conditions, left-handed individuals experienced higher lumbar moments during right side lifts than they did during the reflected left side lifts, i.e. P1 vs P5 and P2 vs P4. Similarly, right-handed individuals experienced higher lumbar moments during left side lifts than right sided lifts, except for the 1.20 kg condition. This finding suggests that individuals should lift from their dominant-hand side if they want to reduce their lumbar flexion moment and, in turn, reduce their risk for low back pain.

Sex

We expected women to experience higher lumbar moments than their male counterparts. However, as shown in Figure 6, there does not appear to be any large differences in moments between the sexes. This suggests that men and women can be treated equally when lifting under the conditions tested in this work.

Limitations

This study is not without limitations. First, only eight participants were analyzed which prevented a robust statistical analysis to be performed. This small sample size provides preliminary trends, but a thorough statistical analysis with a larger sample set would further support the current conclusions. Our future work includes the data processing of 12 additional subjects. With a larger data set, an analysis of variance (ANOVA) can be calculated to identify the statistical significance of sex, handedness, box mass, and box origin on the average maximum flexion/extension moment. Second, the study only explored the flexion/extension moment and has not yet investigated the lateral bending or rotational moments at the L5-S1 level. Future work will include these moments.

Conclusions

This work aimed to assess the effects of sex, handedness, box mass, and box origin on the maximum lumbar flexion/extension joint moments during two-handed lifting tasks. There were no clear trends for the effect of sex, but our results suggest that individuals should lift from their dominant-hand side when performing asymmetric two-handed lifting tasks. This preliminary work serves as a starting point in identifying how sex and handedness affect underlying biomechanics of lifting. A better understanding of these tasks can lead to safer lifting recommendations to individuals that work in manual material handling occupations. Besides including a larger sample set, future work will incorporate the use of

musculoskeletal modeling and finite element modeling to perform a deeper analysis of spine biomechanics during these lifts at the muscle and tissue levels, respectively.

Acknowledgments

We would like to thank Brandon Cruz and Juan Baus for their help with data collection for this work.

This work was partially funded by National Science Foundation CBET #2014278.

References

1. Akhavanfar, M., Uchida, T. K., Clouthier, A. L., & Graham, R. B. (2022). Sharing the load: modeling loads in OpenSim to simulate two-handed lifting. *Multibody System Dynamics*, 213–234. https://doi.org/10.1007/s11044-021-09808-7
2. Beaucage-Gauvreau, E., Robertson, W. S. P., Brandon, S. C. E., Fraser, R., Freeman, B. J. C., Graham, R. B., Thewlis, D., & Jones, C. F. (2019). Validation of an OpenSim full-body model with detailed lumbar spine for estimating lower lumbar spine loads during symmetric and asymmetric lifting tasks. *Computer Methods in Biomechanics and Biomedical Engineering*, *22*(5), 451–464. https://doi.org/10.1080/10255842.2018.1564819
3. Butler, H. L., Hubley-Kozey, C. L., & Kozey, J. W. (2009). Activation amplitude patterns do not change for back muscles but are altered for abdominal muscles between dominant and non-dominant hands during one-handed lifts. *European Journal of Applied Physiology*, *106*(1), 95–104. https://doi.org/10.1007/S00421-009-0994-9
4. Delise, A., Gagnon, M., & Desjardins, P. (1996). Load Acceleration and Footstep Strategies in Asymmetrical Lifting and Lowering. *International Journal of Occupational Safety and Ergonomics*, *2*(3), 185–195. https://doi.org/10.1080/10803548.1996.11076347
5. Firouzabadi, A., Arjmand, N., Pan, F., Zander, T., & Schmidt, H. (2021). Sex-Dependent Estimation of Spinal Loads During Static Manual Material Handling Activities—Combined in vivo and in silico Analyses. *Frontiers in Bioengineering and Biotechnology*, *9*, 1030. https://doi.org/10.3389/fbioe.2021.750862
6. Ghofrani, M., Soleimanifar, M., & Talebian, S. (2021). Control of trunk muscles activity while manual material handling symmetrically and asymmetrically, Based on Motor control strategy. *Pakistan Journal of Medical and Health Sciences*, *15*(6), 1736–1740. https://doi.org/10.53350/pjmhs211561736
7. Hartvigsen, J., Hancock, M. J., Kongsted, A., Louw, Q., Ferreira, M. L., Genevay, S., Hoy, D., Karppinen, J., Pransky, G., Sieper, J., Smeets, R. J., Underwood, M., Buchbinder, R., Cherkin, D., Foster, N. E., Maher, C. G., van Tulder, M., Anema, J. R., Chou, R., … Woolf, A. (2018). What low back pain is and why we need to pay attention. In *The Lancet* (Vol. 391, Issue 10137, pp. 2356–2367). https://doi.org/10.1016/S0140-6736(18)30480-X
8. Hoozemans, M. J. M., Kingma, I., de Vries, W., & van Dieën, J. (2008). Effect of lifting height and load mass on low back loading. *Ergonomics*, *51*(7), 1053–1063. https://doi.org/10.1080/00140130801958642
9. Katz, J. N., Disorders, L. D., Pain, L., & Factors, S. (2006). Lumbar disc disorders and low-back pain: socioeconomic factors and consequences. *The Journal of Bone and Joint Surgery. American Volume*, *88 Suppl 2*, 21–24. https://doi.org/10.2106/JBJS.E.01273
10. Kim, H. K., & Zhang, Y. (2017). Estimation of lumbar spinal loading and trunk muscle forces during asymmetric lifting tasks: application of whole-body musculoskeletal modelling in OpenSim. *Ergonomics*, *60*(4), 563–576. https://doi.org/10.1080/00140139.2016.1191679
11. Kingma, I., Faber, G. S., & van Dieën, J. H. (2010). How to lift a box that is too large to fit between the knees. *Ergonomics*, *53*(10), 1228–1238. https://doi.org/10.1080/00140139.2010.512983

12. Lindbeck, L., & Kjellberg, K. (2001). Gender differences in lifting technique. *Ergonomics*, *44*(2), 202–214. https://doi.org/10.1080/00140130120142
13. Marras, W. S. (2000). Occupational low back disorder causation and control. *Ergonomics*, *43*(7), 880–902. https://doi.org/10.1080/001401300409080
14. Marras, W. S., & Davis, K. G. (1998). Spine loading during asymmetric lifting using one versus two hands. *Ergonomics*, *41*(6), 817–834. https://doi.org/10.1080/001401398186667
15. Potvin, J. R., Ciriello, V. M., Snook, S. H., Maynard, W. S., & Brogmus, G. E. (2021). The Liberty Mutual manual materials handling (LM-MMH) equations. *Ergonomics*, *0*(0), 1–17. https://doi.org/10.1080/00140139.2021.1891297
16. Song, J., & Qu, X. (2014). Effects of age and its interaction with task parameters on lifting biomechanics. *Ergonomics*, *57*(5), 653–668. https://doi.org/10.1080/00140139.2014.897376
17. Steffens, D., Ferreira, M. L., Latimer, J., Ferreira, P. H., Koes, B. W., Blyth, F., Li, Q., & Maher, C. G. (2015). What triggers an episode of acute low back pain? A case-crossover study. *Arthritis Care and Research*, *67*(3), 403–410. https://doi.org/10.1002/ACR.22533/ABSTRACT
18. Weston, E. B., Aurand, A. M., Dufour, J. S., Knapik, G. G., & Marras, W. S. (2020). One versus two-handed lifting and lowering: lumbar spine loads and recommended one-handed limits protecting the lower back. *Ergonomics*, *63*(4), 505–521. https://doi.org/10.1080/00140139.2020.1727023

On the progress of knowledge-based motion simulation techniques in ergonomic vehicle design

Hans-Joachim Wirsching[1] and Norman Hofmann[2]

[1] *Human Solutions, Germany*

[2] *Institute for Mechatronics, Germany*

Abstract

Applying DHMs in ergonomic design of vehicle interiors has been established for many years. Most use cases focus on various aspects of static driving configurations. But several dynamical occupant tasks must be evaluated for new vehicle concepts in addition. Because of the task complexity these tests are still performed in physical mock-ups. Over the past years new DHM technologies have supported evaluating dynamic ergonomics of interior designs in digital mock-ups more efficient. Nevertheless, there are still simulation aspects to be improved for proper industrial applications. This paper presents the recent development progress on knowledge-based motion simulation techniques using motion capture data and DHM prediction methods. The focus was put on a large variability of motions in the database, more user control on the simulated motions and functions for collision avoidance. Based on adjustable mock-ups, a range of ingress and egress motions into a truck and a passenger car were systematically measured taking various positions of vehicle components like steps, doors, pillars and roofs into account. These motion takes were reconstructed and annotated by DHMs and stored in a database. A new simulation tool was developed which use the database to predict motions in virtual environments. The GUI provides a range of motion components subjected to various motion data and simulation methods. These components can be combined to create a cumulative motion. In addition, the intersection frames of consecutive components can be controlled by user-defined postures or tasks. Smooth transitions are supported by specific truncating and sewing up consecutive motions. In addition, the tool got new functions to consider collision avoidance during simulation. First, characteristic parameters (door angle) are extracted from the environment and used to find corresponding collision-free motions in the database. Second, specific geometric constraints avoid collisions at key frames. Applying both functions supports qualitative motion strategy changes and quantitative body positions to cope with collision situations. The tool development is accompanied by user evaluations with respect to usability and prediction capabilities. These identified open issues to be solved and pushed the tool further forward to a productive level.

Keywords: Motion measurement and analysis, Knowledge-based motion simulation, Motion control, Collision avoidance

Introduction

DHM applications in ergonomic vehicle design have a long history. Nowadays industrial engineers use DHM systems to optimize the interior ergonomics focusing on static aspects of driver and passenger configurations like comfort, vision, reachability and roominess (Raschke 2019, Wirsching 2019). But several design questions require the analysis of dynamic aspects like ingress / egress motions which currently are not provided by these tools in a sufficient matter and hence require still expensive physical tests in mock-ups.

A necessary technology for this would be a task-specific simulation of human motions in vehicle environments. While the digitalization and analysis of real motions have reached a sufficient application level (Hermsdorf et al., 2019), the simulation of complex motions is still under research. Cherednichenko (2008) proposed a functional model for predicting ingress motions into a car. Model approaches like this require an extensive investigation and understanding of real motions to catch characteristics which can be represented by a simulation model. These models can hardly be used in a generic way and their complexity increases with the number of parameters to be considered.

A more pragmatic approach for simulating motions is the direct use of captured motions in a database which showed promising results with respect to usability and functionality (Wirsching et al. 2013, 2016). This approach does not require to understand drivers of motions, but just a standardized description how the motion looks like with respect to the environment. It provides a generic procedure which can be applied to all kind of motions, especially highly constrained motions. Just the size of the database determines the simulation quality.

Nevertheless, this approach suffered from several shortcomings like restricted data pools, inflexible user control and insufficient collision handling. This paper focusses on these shortcomings and describes the next evolution step for this technology applied in a car and a truck ingress use case.

Methods

Overview

The methods utilize a simulation framework which simulates task-specific motions by extracting a best fitting motion from a database and adapting this motion to the given environment. The system

architecture and motion digitization & simulation process is similar to Wirsching et al. (2016), but enhanced in the following aspects to overcome the identified shortcomings:

- The experiments are setup to provide a large variability of annotated motions in different car and truck ingress concept variants.
- The motion simulation environment allows flexible input and more control on the simulated motions, especially the concatenation of motions.
- The simulation engine has several functions to handle collisions in qualitative and quantitative aspects.

These enhancements are described in the following sections.

Experiments

Real movements are necessary for realistic movements in the virtual world. Therefore, motion studies were realized on a real mock-up for a truck and for a car. The mock-ups were designed in such a way that certain geometric parameters could be varied. In the case of the truck, the height, width, and angle of the steps can be varied as can the door opening. The experiments for truck ingress have already been explained in Dorynek et al. (2021). In the case of the car, the variations concerned the height of the sill and the roof. Figure 1 shows a photo of the car mockup.

An optical motion capture system made by ART is used for high-quality digitization of human movement. Nineteen targets are applied to the human body to record the motion trajectories of the segments. Further targets are also applied to parts of the mock-up to record these. In case of the truck these are the mock-up itself, the door, seat and steering wheel and in case of the car these are the seat backrest, seat surface, steering wheel, roof and sill. Figure 1 shows the visualization of the recorded targets and the colored point clouds for seat, steering wheel, roof and sill.

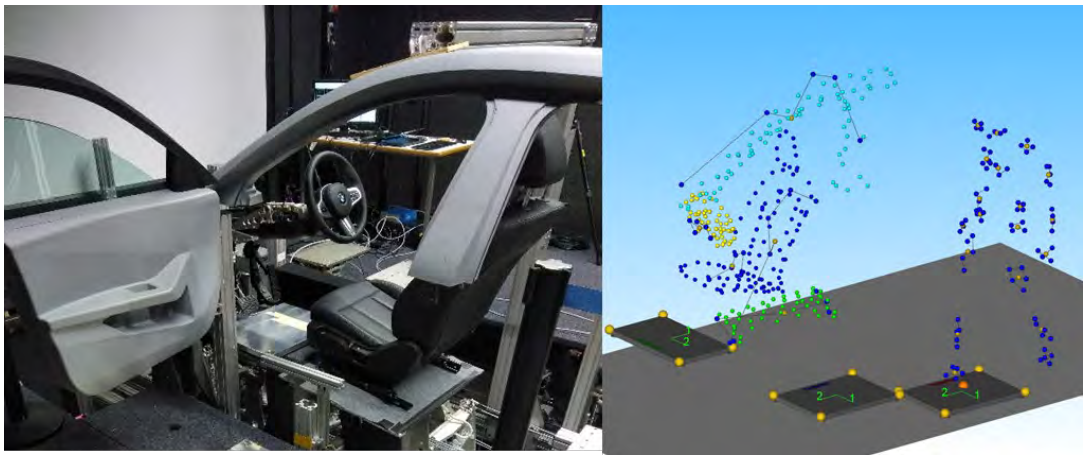

Figure 1: Car mockup and visualization of the recorded targets

The truck ingress study included 29 subjects with 9 to 12 mockup variations. The car ingress study contained 10 subjects with 9 variations of the mockup. Each subject completed 10 trials per variation. After completion of the measurements, the database contains ingress and egress movements into a truck (approximately 3000) and a car (approximately 900).

Data processing

The simulation model consists of the two components human and environment. The methodical description and application of the Dynamicus model can be found in (Hermsdorf 2019). Dynamicus is a biomechanical human model which uses the methods of multi-body dynamics. It consists of 43 bodies that describe the kinematic structure of the human body. The bodies are connected by joints where the movement possibilities can be configured. The spine represents all vertebral bodies and is controlled by a movement pattern. The individualization of the human being is represented in Dynamicus via the parameterization of anthropometry. The model of the environment is based on the construction data. The motion of the human and the environment is based on the captured marker trajectories. This information is transferred to the human model Dynamicus. The inverse kinematics methodology is used for this purpose. For the analysis of the interactions, geometric equivalent bodies are used, which, analyze the contact between the model bodies. The following Figure 2 shows the model of the human and the environment (colored point clouds) as well as the functional model (red planes and boxes).

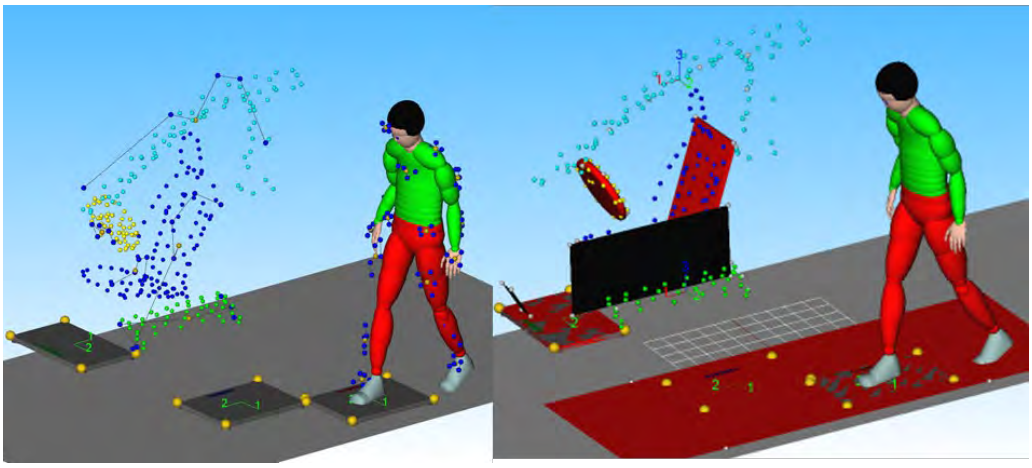

Figure 2: DHM Dynamicus, environment and the functional model

The interaction between the reconstructed motion of the DHM and the functional model of the mock-up can be detected and analyzed. The functional model contains in case of the car the ground outside, cabin floor, sill, roof, seat backrest, seat surface, pedals, and steering wheel. In the case of the truck the functional model contains of the ground outside, cabin floor, steps, handrails, steering wheel, seat backrest, seat surface and the door. But there is also a functional model for the human model, and this includes contact elements in hands, feet, head, and pelvis. By linking the results of the interaction analysis with the biomechanical parameters of the movement, it is possible to describe an annotation of events. An example is shown in the following Figure 3.

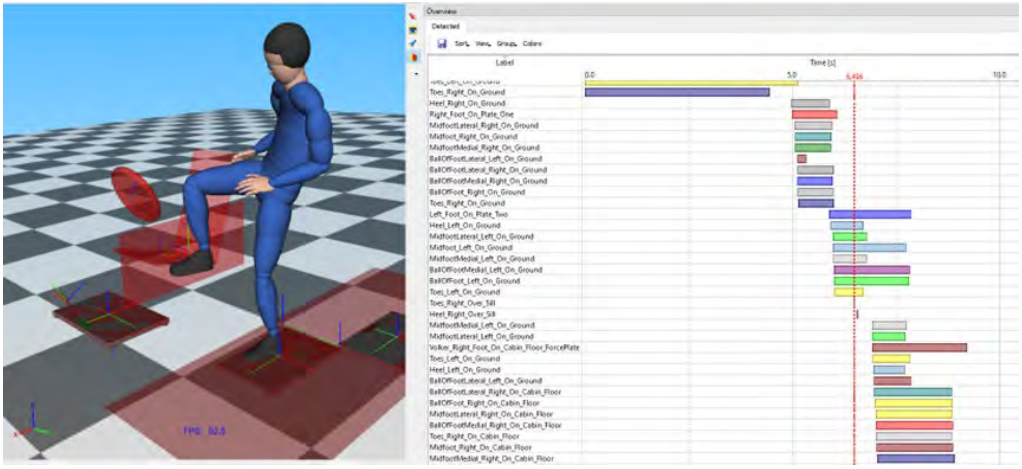

Figure 3:Annotation of events along the motion

Simulation framework

While the framework in Wirsching et al. (2016) focusses on one motion for one manikin, the current framework allows the concatenation of various motion components (e.g. car & truck ingress. walking) from a library and the application to manikin samples. Each motion component runs an individual simulation engine (e.g. database or animation techniques) and requires corresponding input parameter like geometry and strategies. The connection between consecutive motion components is controlled by connectors which define the transition postures. In the connector mode “free” this posture is calculated from the motion component, in mode “posture” the posture is given by the user and in mode “restrictions” the posture is calculated from restrictions given by the user. The final motion sequence is calculated in an iterative process by successively predicting transition postures and motions in-between.

This procedure guarantees continuous transitions between consecutive motion components. But this leads into a non-smooth total motion in many cases because motion-capture-based motion components start or end in static standing postures in general. A possible solution is to intelligently truncate the motions before concatenating them. The implementation of this procedure is shown for the concatenation of a walk and a truck ingress motion (Figure 4). The ingress motion is simulated starting at the key frame when the manikin grasps both handrails and lifts the left foot from the ground (Figure 4, top row, image with star). The original segment from the start standing posture is automatically truncated. The walk motion is simulated until the key frame when the manikin lifts the left foot from the ground, but requiring to adopt the start posture from the ingress motion (Figure 4, bottom row, image with star). The original segment to the end standing posture is automatically truncated.

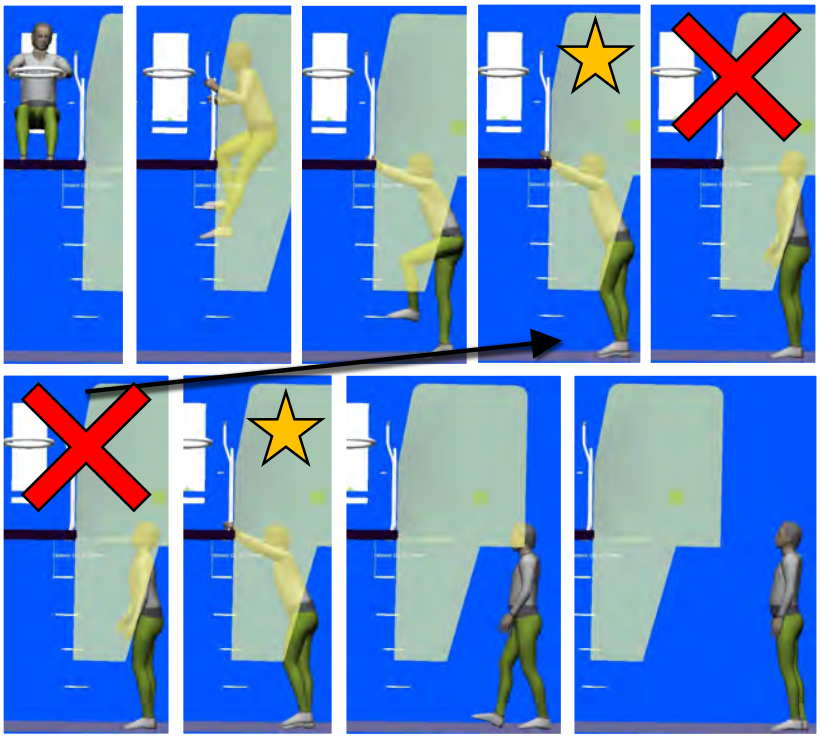

Figure 4 Concatenation of walk (bottom) and ingress (top) motion

Collision avoidance simulation

The collision avoidance is done on two levels. First collision relevant parameters are extracted from the environment (e.g. door opening angle) and a best fitting motion to that parameter is extracted from the database.

Since the best fitting motion may show a qualitative motion strategy change for the collision but does not guarantee to quantitatively fulfill all collision requirements, this motion is additional adapted in a second step on key frame level. A key frame defines a frame of the motion when the interaction of the occupant with the environment changes, for example when a foot is placed on the first step. Specific collision avoiding restrictions are added to these tasks from which the relevant key frame postures are calculated.

This method is illustrated for the truck ingress use case (Figure 5) in the following. For the specific step height and door opening angle in the environment the best fitting motion is extracted from the database containing motion patterns for step heights 280mm - 400mm and opening angles 30° - 95°. From this motion, the prediction of the key frame postures while the manikin grasps the handrails takes collision avoiding restrictions between the door surface and the shoulder, elbow, hip and knee into account.

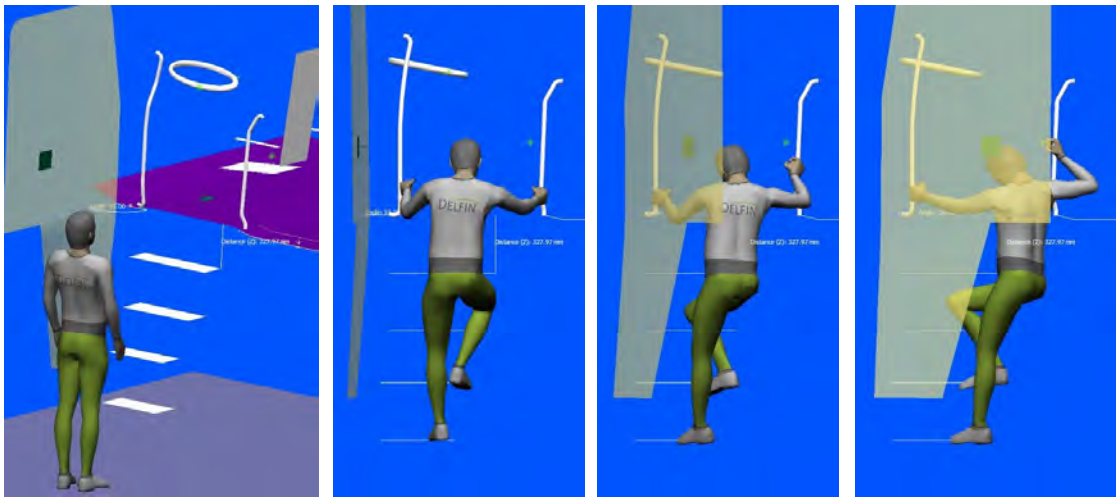

Figure 5 Collision avoidance of cabin door during truck ingress (door angle 95, 60, 30) (left to right)

Another application of this method is illustrated for the car ingress use case (Figure 6) in the following. For the specific roof and sill height the best fitting motion is extracted from the database containing motions (with different patterns) for roof heights 1237mm - 1558mm and sill heights 315mm – 450mm. From this motion, the prediction of the key frame postures while the manikin feet are above the sill and the head is below the roof takes collision avoiding restrictions between the sill and the foot and between the roof and the head into account. This leads to an evasive movement starting before and ending after the phase when the collision originally occurs.

Figure 6 Collision avoidance of during car ingress (r. foot to sill, head to roof, l. foot to sill) (left to right)

Results

The results can be separated in a structured motion data pool and a DHM simulation tool making use of that pool. The motion data is transferred from the DHM Dynamicus to the DHM RAMSIS following the principal process in Wirsching et al. (2016).

The simulation framework and the collision functions are integrated into a tool based on the DHM RAMSIS. The GUI supports the user specification of concatenated motions (Figure 7).

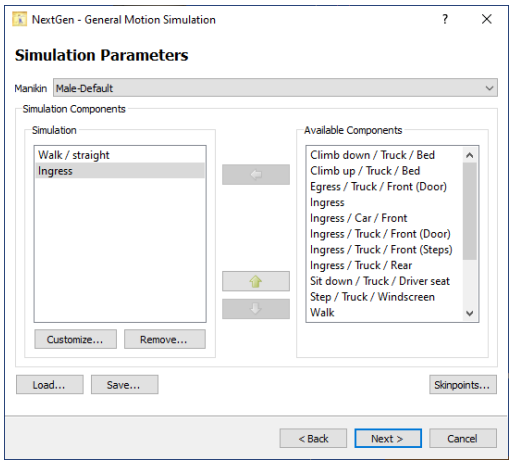

Figure 7 GUI for definition of concatenated motions

From the (right) list of available motion components the user can assembly the desired motion in the left list. The necessary parameters for each motion component and the connectors are defined by the user through specific masks (Figure 8).

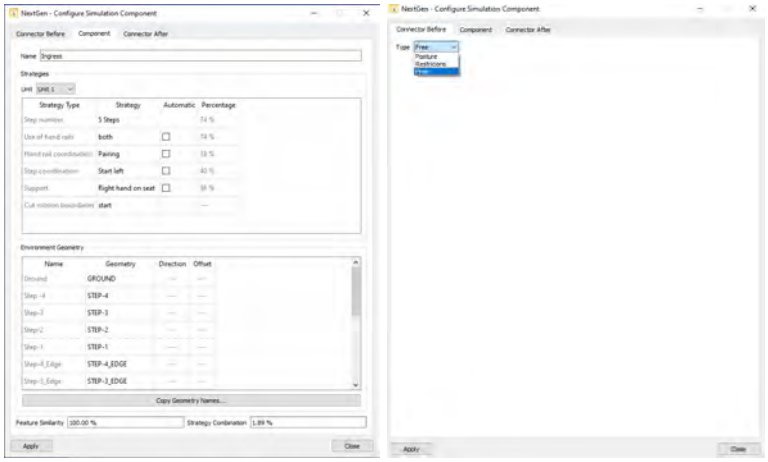

Figure 8 Motion component (left) and connector (right) definition

The motion component parameters depend on the available motion data of the specific component (Figure 8 left). First the user specifies the available strategies for the motion. The GUI supports here by displaying the percentages of the strategies and providing the option to automatically determine the most probable strategy. Second the user has to define geometrical objects which are required by the motion component simulation engine. The percentage of the selected strategy with respect to the entire database as well as feature similarity is displayed at the bottom of the mask. The latter measures the similarity between the best fitting motion and the to-be simulated motion with respect to features like stature and vehicle parameters.

The connector parameters depend on the user selection “Free”, “Posture” or “Restrictions”. In the latter two selections the user additionally specifies which posture or restriction set should be used for the connector posture. Selecting “restrictions” enables the user to run the entire motion component definition (Figure 8) on different sized manikins.

Discussion and Conclusions

The presented motion simulation approach shows promising results and resolved the following formerly shortcomings:

The motion measurement procedure has been applied to truck and car ingress applications considering several vehicle variations which increases the prediction capabilities of the entire system. Nevertheless, especially in the car use case the number of measured subjects should be increased in the future.

The user control of the simulation is now more flexible. Motions can be concatenated and the transition postures can be defined. The method to smoothly join motions is promising but requires a lot of manual modeling work in advance to define the segments to be truncated. This procedure should be done automatically in the future.

The collision handling is now more powerful than in formerly versions. It still focuses on discrete key frames which is suitable for many applications. But the collision control of the entire motion should be investigated in a next step.

The user evaluation of the tools is still in progress. A big user benefit of the tool has been perceived, but it is currently open how it finally can be used in the daily productive engineering work. This is closely related to the possibility of assessing motions with respect to various ergonomic criteria. This function would be very important for engineers to compare different design variants.

Most simulated truck and car ingress motions are smooth and plausible, but the planned quantitative evaluation of the motion simulation quality will bring more confidence in the tools.

Acknowledgments

This study was conducted in the context of the project DELFIN funded by the Federal Ministry of Education and Research of the Federal Republic of Germany.

References

Cherednichenko, A. (2008). Funktionales Modell der Einstiegsbewegung in einen PKW. Zugl.: München, Techn. Univ., Diss., 2007. Utz Herbert: Ergonomie. München.

Dorynek, M., Zhang, H., Hofmann, N., Bengler, K. (2021). New Approaches to Movement Evaluation Using Accurate Truck Ingress Data. In book: Digital Human Modeling and Applications in Health, Safety, Ergonomics and Risk Management. Human Body, Motion and Behavior (pp.110-121), DOI:10.1007/978-3-030-77817-0_10

Hermsdorf, H., Hofmann, N., Keil, A. (2019). alaska/Dynamicus – human movements in interplay with the environment, Editor(s): Sofia Scataglini, Gunther Paul, DHM and Posturography, Academic Press, 2019, G.,978-0-12-816713-7, Elsevier

Raschke, U., Cort, C. (2019). Siemens Jack. Editor(s): Sofia Scataglini, Gunther Paul, DHM and Posturography, Academic Press, 2019, Chapter 3, Pages 35-48, ISBN 9780128167137. https://doi.org/10.1016/B978-0-12-816713-7.00003-9.

Wirsching, H.-J., Bichler, R. (2013). Integrating motion capture data into knowledge-based ingress motion simulation tool. Digital Human Modeling Symposium, Ann Arbor, USA.

Wirsching, H.-J., Enderlein, V., Stechow, R. (2016). On the application of a knowledge-based motion simulation tool to ergonomic truck cabin design. 7th International Conference, DHM 2016, Toronto, ON, Canada, July 17-22, 2016 : proceedings

Wirsching, H.-J. (2019). Human Solutions RAMSIS. Editor(s): Sofia Scataglini, Gunther Paul, DHM and Posturography, Academic Press, 2019, Chapter 4, Pages 49-55, ISBN 9780128167137. https://doi.org/10.1016/B978-0-12-816713-7.00004-0.

Influence of different pedestrian behavior models on the performance assessment of autonomous emergency braking (AEB) Systems via virtual simulation

Lucas Fonseca Alexandre de Oliveira [1], Martin Meywerk [2], Lars Schories [1], Maria Meier [3], Ramakrishna Nanjundaiah [3], Victor Paulthi [3], Francesco Foglino [3], Mark Carroll [3] and Arunaachalam Muralidharan [3]

[1] *ZF Friedrichshafen AG, Germany*

[2] *Helmut Schmidt University, Germany*

[3] *Phantasma Labs GmbH, Germany*

Abstract

Pedestrian safety is a central topic in the automotive industry because of the high number of deaths in car-to-pedestrian accidents. Different systems have been developed to protect pedestrians and other vulnerable road users. So-called Active Safety Systems are used to avoid possible collisions with the VRU or to mitigate injury severity by reducing the collision speed in case the collision can't longer be prevented. The autonomous emergency braking system (AEB) is one of these systems and aims to intervene in conflict situations by stopping the car, Haus et al. (2019). The performance assessment of the AEB System can be done via virtual simulation. One crucial aspect is the modeling of pedestrian behavior. Current studies use a simple pedestrian behavior model, sometimes called a trajectory-based model, in which the pedestrian moves with constant speed on a given path and without any interaction with the environment. This study investigates how the AEB Performance in virtual environments is influenced by using a more realistic pedestrian behavior model based on reinforcement learning approach, a particular Machine Learning branch perfectly suited for modeling decision-making processes. For that, a generic AEB-System, the trajectory-based pedestrian model, and the reinforcement learning model were implemented in CARLA Simulator. A scenario catalog was created by varying some parameters and used to evaluate the front collisions with and without the AEB system. The study indicates that due to some pedestrian reactions of the reinforcement learning model, like unexpected stopping in front of the car, the performance of the AEB-System is reduced.

Keywords: Pedestrian Crossing behavior, efficiency assessment, active safety, simulation

Introduction

Vulnerable Road Users (VRU) are non or poor-protected road users like pedestrians or users or passengers of non-motorized or powered two-wheelers e.g., cyclists or motorcyclists. They accounted for 51,4% of all total road fatalities in the European Union in 2021 (Decae, 2022). An Autonomous emergency braking (AEB) system, an active safety system used to avoid imminent collisions, can help to reduce this higher number of fatalities. Its performance assessment can be done via virtual simulation, but one current limitation is the pedestrian representation, which only walks a pre-defined path with constant velocity without interacting with the environment. This model is called in trajectory-based model in this study.

The aim of this paper was to investigate if a pedestrian behavior model with visual perception and interaction with the environment and other agents, changes the performance of the AEB-System in a virtual simulation. For that, a behavior model based on a reinforcement learning algorithm was developed by Phantasma Labs GmbH (https://www.phantasma.global/) and compared with the current trajectory-based model. In Methods, the simulation platform used in this study is presented together with the vehicle model and the two pedestrian models. In the same section, the generic model of the AEB system, the road network, and the parameterization of the simulation for the generation of different scenarios are presented. Finally, the results are presented and discussed for both pedestrian models.

Methods

Pedestrian Models

Modeling pedestrian behavior and movement are very complex, especially considering the decision-making process. Papadimitriou et al. (2009) highlight the relevance of two aspects of pedestrian behavior to be modeled. One of them is the route choice, which regards the decision process about the optimal path between the current location and destination. The other one is the crossing behavior regarding the decision of when and where to cross the road. They conclude that most pedestrian behavior models treat route choice and crossing behavior separately. Teknomo et al. (2016) reviewed different approaches to modeling pedestrian movement on a microscopic level, where the pedestrian is treated individually. In general, pedestrian movement between a start point and destination uses repulsive effects between the pedestrians and other obstacles and in most cases is not validated or calibrated on real pedestrian movement data. The pedestrian models available in most vehicle dynamic simulation tools, the trajectory-based models, don't model the route choice or the crossing behavior either. Both aspects are defined before the simulation and

implemented manually by giving the pedestrian a pre-defined trajectory. The pedestrian in most cases is also devoid of visual perception and internal representation in such a way that the interactions with the infrastructure (avoiding obstacles) and with other road users, like vehicles and other pedestrians, is not present. Similar models are used in current studies by Lindman et al. (2010), Schanchner et al. (2020), and Hamdane et al. (2015).

Considering that car-to-pedestrian accidents occur in most cases in urban areas (Adminaité-Fodor et al., 2020) on the road or very close to it and involve mostly just one pedestrian, the microscopic approach is the most suitable for this study, Wakim et al. (2004). The pedestrian should also be able to choose different routes between start point and destination, exhibit an unsafe crossing behavior, have visual perception, and interact with road infrastructure and other agents. No model was found in the literature that achieves all the requirements above. For this paper, a new model was developed based on a reinforcement learning (RL) method, once this machine learning approach is perfectly suited for modeling decision-making process and therefore can directly be employed for the design of pedestrian behavior models. RL is a branch of machine learning that faces a real problem from the perspective of a learning agent interacting with its environment to achieve a goal. This requires that the agent is capable to perceive the state of the environment and to take actions to affect the state. By this category of learning algorithms, the agent always collects new data points by directly interacting with the provided environment and later uses them for training. In this study, the model will be called reinforcement learning behavior model (RL model) and it was developed for the specific traffic scenario analyzed in this paper. The learning agent is the pedestrian that interacts with the environment (road infrastructure and vehicles) to achieve the goal, a specific position on the other side of the road. During the development of the model, attention was paid to the maximum possible pedestrian-car interactions (this also covers the visual perception, internal interpretation, and decision making) and plausible, human-like, and diverse trajectories.

In this study, the trajectory-based model and the RL model were used. By the trajectory-based model approach, the pedestrian is spawned at the start position at the beginning of the simulation and crosses the road following a pre-defined path perpendicular to the vehicle's direction with a constant speed until it reaches the other side of the road. The pedestrian does not interact with the environment and other agents. This approach reflects the pedestrian dummy used in the Euro NCAP test protocol (Euro NCAP, 2019). The RL model, unlike the previous model, perceives its environment and interacts with other agents. The model moves towards in order to reach a defined destination. Unlike the previous model, the RL model developed for this study is not capable of being parameterized, so the speed cannot be set, and the starting point and destination cannot be changed.

Simulation Environment and Road Network

CARLA, Car Learning to Act, (Dosovistikiy et al., 2017) is an open-source simulator for urban driving. CARLA was built in a server-client architecture. The server runs the simulation, rendering the scene and the client, a python API, defines the scenario and establishes the interaction between the agent and the server. The simulation run in a synchronous mode with a constant time step of $\Delta t = 0.04$ s (25 Hz). The road network was designed based on the definition from the Euro NCAP test protocol. In addition to this definition, a parking area was added with two parking vehicles. In Figure 1 the road in CARLA can be seen.

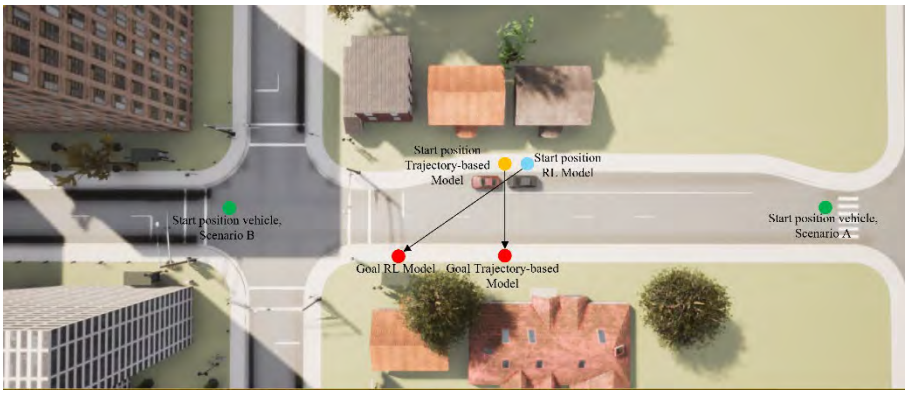

Figure 1 - A representation of the road. The blue mark indicates the initial position of the RL model and the orange mark of the trajectory-based model. The red is the destination of the pedestrian. The green mark is the start position of the vehicle. The road has 2 driving lanes and a parking lane with widths of 3.5 m. The arrows indicate the direction of movement of the pedestrian. The OpenDRIVE format was used to define the road network.

AEB System and vehicle model

Against other simulation platforms, CARLA does not provide a pre-implemented AEB system. A generic AEB system was implemented based on the definition given by the harmonization group Prospective Effectiveness Assessment for Road Safety (P.E.A.R.S.), Page et al. (2015). The systems consist of an ideal sensor, a decision algorithm, and a control algorithm.

This study assumed an ideal sensor for pedestrian detection. An algorithm was implemented in the client that, based on the current position of the vehicle, calculates the field of view of the sensor as an arc of a circle using the maximum range and azimuth angle, see Figure 2 (a). At each timestep, the algorithm checks if the pedestrian is inside of the field of view using the current pedestrian position. In a positive case, the pedestrian is considered to have been detected by the sensor and a signal is sent to the decision algorithm.

The decision algorithm defines the intervention strategy of the AEB. It is based on the time-to-collision (TTC) and on the detection of the pedestrian. This calculation holds if the vector of relative velocity, $\vec{v}_{rel} := \vec{v}_{car} - \vec{v}_{ped}$ is in the same direction as the relative position $\vec{r}_{rel} = \vec{r}_{ped} - \vec{r}_{car}$. Equation 1 hold:

$$\vec{v}_{rel}\, TTC = \quad \vec{r}_{rel} \tag{1}$$

Once the pedestrian is inside of the field of view and the TTC gets equal to or smaller than 1.0 s, the vehicle starts the braking process. The control algorithm calculates the vehicle speed at each time step. By normal driving, the vehicle drives at a constant speed. Once the AEB is activated the new car velocity based on the current deceleration is calculated and applied to the vehicle. The deceleration profile is defined by an actuator delay, a build-up time, and a maximal deceleration. The deceleration increase over time is modeled to be linear until the maximum value. The deceleration profile can be seen in Figure 2 (b). Two settings for the AEB system were evaluated in this study (cf. Table1), one based on P.E.A.R.S. and the other based on the setting applied in Schachner et al. (2020).

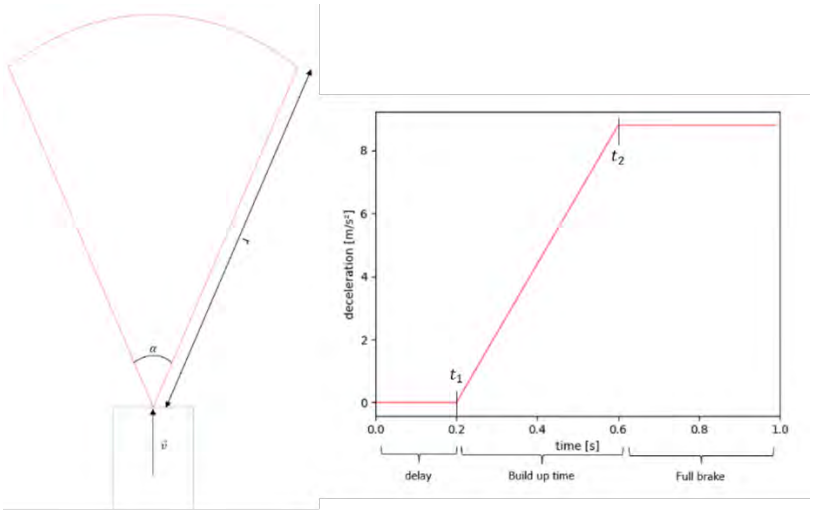

Figure 2 - (a) - Field of View of the ideal perception systems. It is parametrized through azimuth angle α and maximum range r. At each time step is checked based on the current position of the pedestrian and the vehicle if the pedestrian is in the sensor's Field-of-View. (b)The deceleration profile for settings 1. It is divided into three steps. It is divided into three steps: actuator delay, build up time (deceleration increases linearly with the time), and the full brake (maximum deceleration is achieved and stays constant until the vehicle stands still).

Table 1: AEB parameter settings

Parameters	*Maximum deceleration*	*Build-up time*	*Actuator delay*	*Braking gradient*	*Maximum range*	*Azimuth angle*
Settings 1	8,8 $\frac{m}{s^2}$	0,4 s	0,2 s	24,525 $\frac{m}{s^3}$	60 m	60 °
Settings 2	7,0 $\frac{m}{s^2}$	0,35 s	0,25 s	20 $\frac{m}{s^3}$	60 m	60 °

Scenario Generation

One approach to generate scenarios in order to assess the performance of the AEB system is to reproduce conflict scenarios based on accident data, Jeppsson et al. (2018), Gruber et al. (2019), Li et al. (2021). In this case, the pedestrian follows a given trajectory. Schachner et al. (2020) propose a different approach

generating a scenario catalog of critical car-pedestrian conflict situations by varying the following parameters: vehicle speed, pedestrian speed, and pedestrian waiting time. The trajectory for vehicle and pedestrian was previously defined. A similar approach was implemented in this study with some adaptations considering some constraints of the RL behavior model. The base scenario was inspired by the Euro NCAP test cases Car-Pedestrian Nearside (CPNA) and Car-Pedestrian Farside (CPFA). Two conflict situations were simulated. In conflict situation A the vehicle drives forward on a straight road, and the pedestrian was crossing the road coming from the vehicle's nearside. This conflict scenario was simulated with both pedestrian models. In conflict situation B the vehicle drives forward on a straight road, and the pedestrian was crossing the road coming from the vehicle's farside. This conflict scenario was simulated only with the RL model. The parameters used to generate scenarios with the trajectory-based model and RL model can be found in Table 2. For the RL model, no pedestrian waiting time is possible since setting this as a tunable parameter is not possible, as well as the constant pedestrian speed. Instead, the waiting time was applied to the vehicle. The car waiting time was extended to 8 s, to generate more interaction between pedestrian and higher vehicle speeds.

Table 2: Parameters to generate different conflict scenarios for trajectory-based pedestrian model and RL model.

Parameter	*Value*	*Step size*
Trajectory-based pedestrian model		
Vehicle speed [km/h]	10 – 60	2,5 km/h
Pedestrian speed [km/h]	1 - 12	1 km/h
Pedestrian waiting time [s]	0.1 – 3.6	0.5 s
Reinforcement Learning behavior model		
Vehicle speed [km/h]	10 – 60	2,5 km/h
vehicle waiting time [s]	0 – 8	0.2 s

Results

The performance of the AEB was evaluated by comparing the number of frontal collisions between the baseline simulations (vehicle without an AEB system) and the simulations with the AEB system in conflict situations A and B. The results discussed here are referent to the AEB system with settings 1. Tables 3 and 4 show all results including the AEB system with settings 2.

Table 3: Results trajectory-based pedestrian model

	Baseline	*AEB System, setting 1*	*AEB System, setting 2*
Number of scenarios	2016	2016	2016
front collisions	201	123	162
Percentage of front collisions	10 %	6,1%	8,0%
Collision reduction due the AEB system	-	38,8%	19,4%

As expected, the results with a lower maximal deceleration and higher actuator delay led to lower performance. In 2016 baseline simulations with the trajectory-based model, 201 ended in front collisions. This number was reduced to 123 with the AEB system, a reduction from 38,8%. This result agrees with the

literature, Lindman et al. (2010), Handame et al. (2015), Gruber et al. (2019), Schachner et al. (2020) that goes from 20% up to 50%. With the RL model, a total of 862 baseline scenarios were generated resulting in 182 frontal collisions, generating 10% more collisions concerning the total, than in the trajectory-based pedestrian model. This higher number of collisions is due to the unsafe behavior of the pedestrian. The pedestrian's trajectories make the pedestrian stay more time on the road in the same lane as the vehicle, see figure 3 (a). The average pedestrian speed over time is shown in Figure 3 (b).

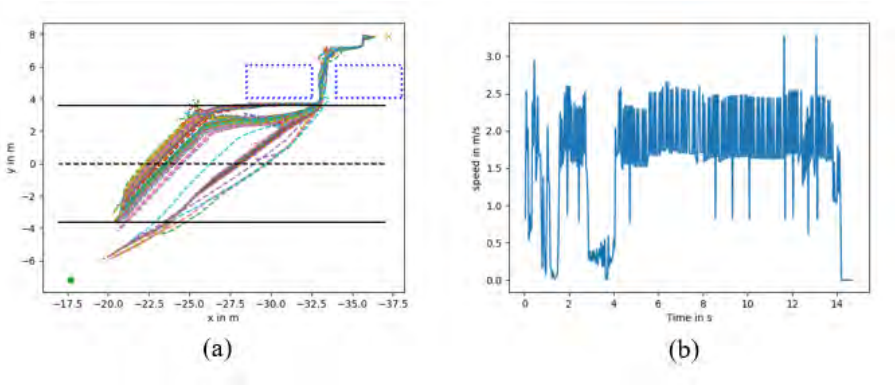

Figure 3 - (a) Pedestrian path over all simulations scenario A; (b) Pedestrian average speed

The AEB system reduced the number of front collisions to 108, a reduction from 40,6% similar to the results of the trajectory-based model. Unfortunately, in most cases of conflict situation A, the pedestrian crosses the road with his back to the approaching vehicle. Once the field of view of the pedestrian has an opening angle of 180°, he was not able to see the car and then did not react to it. To force this situation, the conflict situation B was simulated, where the vehicle was in the field of view of the pedestrian. In this situation, there were 191 front collisions in the baseline simulations and 138 with the AEB, a reduction from 27,7%.

Table 4: Results reinforcement learning behavior model

	Baseline, Scenario A	*Baseline, Scenario B*	*AEB System, Scenario A, setting 1*	*AEB System, Scenario B, setting 1*	*AEB System, Scenario A, setting 2*	*AEB System, Scenario B, setting 2*
Number of simulations	861	861	861	861	861	861
front collisions	182	191	108	138	140	149
Percentage of front collisions	21,1%	22,2%	12,5%	16%	16,2%	17,3%
Collision reduction due the AEB system	-	-	40,6%	27,7%	23,1%	21,9%

Discussion and Conclusions

All behavior shown were considered human-like, once he didn’t walk into stationary objects, moves with an average speed not too fast or too slow, and didn’t shake, walk laterally or backward. It was observed that the RL behavior model shows a higher variability in the trajectories when the car is in the field of view

of the pedestrian. The pedestrian's most common reactions to the approaching vehicle were "waiting/looking around"," slowing down", "moving forward" and "standing still". The "standing still" behavior together with the fact that the pedestrian walks in the opposite direction of the car in conflict situation B was one of main the causes of frontal collisions. The reinforcement learning behavior model showed to be useful to evaluate a generic AEB system by generating more collision and different corner cases due to the different trajectories and their interactions with the vehicle. These interactions have decreased the performance of the AEB system. It needs to be considered that the model was not trained for conflict situation B and the performance of the behavior could not be guaranteed in this situation. Further development of the model in this direction should be considered for future works. Another enhancement to the current study would be to include more pedestrians crossing the road, getting conflict scenarios closer to real-world situations. The vehicle model also needs to be improved with a better vehicle dynamic model.

Acknowledgments

The pedestrian behavior model developed using reinforcement learning approach were acquired from Phantasma Labs Gmbh in a proof-of-concept for ZF Friedrichshafen AG.

References

Adminaité-Fodor,D., & Jost, G., (2020). HOW SAFE IS WALKING AND CYCLING IN EUROPE?, PIN Flash Report 38, January 2020 – European Transport Safety Council. https://etsc.eu/wp-content/uploads/PIN-Flash-38_FINAL.pdf

Decae, R. (2022). Annual statistical report on road safety in the EU, 2021. European Road Safety Observatory. Brussels, European Commission, Directorate General for Transport. https://road-safety.transport.ec.europa.eu/statistics-and-analysis/data-and-analysis/annual-statistical-report_en

Dosovistikiy, A., Ros, G., Codevilla, F., Lopez, A., Koltun, V. (2017). CARLA: An Open Urban Driving Simulator. Proceedings of the 1st Annual Conference on Robot Learning. PMLR Vol. 78 of Proceedings of Machine Learning research, pp 1-16. https://doi.org/10.48550/arXiv.1711.03938

Euro NCAP, 2019, Test Protocol – AEB VRU Systems (Online). https://cdn.euroncap.com/media/62795/euro-ncap-aeb-vru-test-protocol-v304.pdf (Acessed 09 june 2022).

Gruber, M., Kolk, H., Tomasch, E., Feist, F., Klug, C., Schneider, A., Roth, F., Labenski, V., Shanmugam, K., Lindman, M., & Fredriksson, A. (2019). The effect of p-aeb system parameters on the effectiveness for real world pedestrian accidents. The 26th International Technical Conference and exhibition on the

Enhanced Safety of Vehicles (ESV), Pages 1-16. https://graz.pure.elsevier.com/en/publications/the-effect-of-p-aeb-system-parameters-on-the-effectiveness-for-re

Hamdane, H., Serre, T., Masson, C., & Anderson, R. (2015). Issues and challenges for pedestrian active safety systems based on real world accidents. Accident Analysis & Prevention, Volume 82, 53-60. https://doi.org/10.1016/j.aap.2015.05.014

Jeppsson, H., Östling, M., & Lubbe, N. (2018). Real life safety benefits of increasing brake deceleration in car-to-pedestrian accidents: Simulation of Vacuum Emergency Braking. Accident Analysis & Prevention, Volume 111, 311-320, https://doi.org/10.1016/j.aap.2017.12.001

Lindman, M., Oedblom, A., Bergvall, E., Eidehall, A., Svanberg, B., & Lukaszewicz, T. (2010). Benefit estimation model for pedestrian auto brake functionality. 4th International Conference on ESAR, (77). http://worldcat.org/issn/09439307

Page, Y., Fahrenkrog, F., Fiorentino, A., Gwehenberger, Helmer, T., Lindman, M., op den Camp, Lex van Rooij, O., Punch, S., Fränzle, M., Sander, U., & Wimmer, P. (2015). A comprehensive and harmonized method for assessing the effectiveness of advanced driver assistance systems by virtual simulation: the p.e.a.r.s. initiative. The 24th ESV Conference Proceedings, 1-12. https://graz.pure.elsevier.com/de/publications/a-comprehensive-and-harmonized-method-for-assessing-the-effective

Papadimitriou, E., Yannis, G., & Golias J. (2009). A critical assessment of pedestrian behaviour models. Transportation Research Part F 12, 242-255, https://doi.org/10.1016/j.trf.2008.12.004

Rasouli, A., Kotsureba, I., K. Tsotsos, J.K., 2018. Understanding pedestrian behavior in complex Traffic Scenes. IEEE Transactions on Intelligent Vehicles, volume 3, Issue:1, pages 61-70, http://dx.doi.org/10.1109/TIV.2017.2788193

Schachner, M., Sinz, W., Thomson,R., & Klug, C. (2020). Development and evaluation of potential accident scenarios involving pedestrian and AEB-equipped vehicles to demonstrate the efficiency of an enhanced open-source simulation framework. Accident Analysis and Prevention, 148. https://doi.org/10.1016/j.aap.2020.105831

Haus, S.H., Sherony, R., & Gabler, H.C. (2019) Estimated benefit of automated emergency braking systems for vehicle-pedestrian crashes in the United States. Traffic Injury Prevention. 2019, 20(sup1), 171-176. DOI: 10.1080/15389588.2019.1602729

Teknomo, K., Takeyama, Y., & Inamura, H. (2016). Review on Microscopic Pedestrian Model. Proceedings Japan Society of Civil Engineering Conference. https://doi.org/10.48550/arXiv.1609.01808

Wakim, C.F., Capperon, S., & Oksman, J. (2004). A Markovian model of pedestrian behavior. IEEE International Conference on Systems, Man and Cybernetics, 4, 4028-4033 vol. 4. https://doi.org/10.1109/ICSMC.2004.1400974

Takeover performance according to the level of disengagement during automated driving

Evan Gallouin, Xuguang Wang, Philippe Beillas, and Thierry Bellet
Université Gustave Eiffel, France

Abstract

Taking over the manual control of a car after Automated Driving (AD) is a key issue for future road safety. However, performance to resume this manual control may be dependant of the driver's level of engagement in driving during AD. Indeed, according to the level of automation (from L2 to L3 of the SAE), drivers will be in charge of monitoring the driving situation, or will be allowed to perform non-driving related tasks (NDRT) and thus, to be fully disengaged of the driving task. In this context, the present study aims to investigate the influence of the driver's level of engagement/disengagement during AD on takeover performance using a driving simulator. Four levels of engagement/disengagement were studied: (C1) being engaged in driving situation monitoring without TakeOver Request (TOR) to resume the manual control, (C2) being engaged in driving situation monitoring with a TOR to resume the manual control, (C3) being disengaged of the driving monitoring by performing a cognitively demanding secondary task with a TOR to resume the manual control, and (C4) being disengaged of the driving monitoring in a relaxed position situation with eyes closed and with a TOR to resume the manual control. Forty participants were performed sixteen critical takeover scenarios involving different critical takeover situations. Drivers reaction times and collision risks were measured to assess their takeover performances and to investigate the safety of automation levels 2 and 3. Driving situation monitoring with a TOR (C2) induce shortest reaction times and a lower number of collisions. For the relaxed posture (C4), drivers took longer time to react than the other three conditions. Driving situation monitoring without TOR (C1), had the highest number of collisions. This suggests that the engagement in driving is not always effective and efficient without TOR. Moreover, being in a relaxed position during automated driving decreases takeover performance.

Keywords: Takeover Performance; Automated Driving; Driving Supervision; Reaction Time; Collision

Introduction

Until today, car drivers have to be fully engaged in driving. Driving seems simple and intuitive, but this task is in reality complex and cognitively demanding for the driver. In the future, thanks to technical advances in automation, drivers may become less and less engaged in driving. Depending on the degree of automation (SAE, 2021), drivers will have to monitor the driving situation (level 2, partial automation) or will have the possibility to be engaged (level 3, conditional automation) in Non-Driving Related Tasks (NDRT). Drivers may be less vigilant than in manual driving because they will no longer need to control the vehicle constantly. Meanwhile, they may be engaged in a more or less cognitively demanding NDRT. The meta-analysis by De Winter et al. (2014) indeed shows that drivers' situational awareness (SA) is deteriorated with a Highly Automated Driving (HAD) or with Adaptative Cruise Control (ACC). Furthermore, in the study by Dingus et al. (2016), observation of real-world driving revealed that crash risk increased significantly when drivers' eyes were off the road for only two seconds. For the Level 3 of automated driving, occupants will be able to take their eyes off the road not for a few seconds, but for several minutes before they have to resume manual control of the vehicle.

Takeover Performance

In addition to having to monitor the driving or to perform NDRTs, takeover activities are new. Due to unexpected situations, such as accidents or road constructions, the automation system can request to resume the manual control of the vehicle in unplanned emergency TakeOver Requests (TOR). For this purpose, takeover performance has been studied in recent years (Gold et al., 2018; Yang et al., 2018; Lin et al., 2020). Most frequently characterized by the time and quality of takeover, the analysis of takeover performance in critical situations is important and necessary for safety (Gold et al., 2013). Its performance varies depending on many factors, such as the time available to takeover, the type of alarm or the engagement in the NDRT (Zhang et al., 2019).

Takeover Request

At level 2 of automation, the system manages the lateral and longitudinal control of the vehicle while the driver has to be engaged in driving situation monitoring. The driver must supervise the AD and be able to resume manual control at any time without being asked to intervene, because the system is not always able to detect its malfunctions or its limits. At level 3 of automation, drivers will be able to perform NDRTs and thus will no longer be required to be engaged in driving supervision. This implies that the AD systems must be able to detect all relevant limits and reliably return control to the driver by using a warning.

It could therefore be argued that supervising the road constantly, as opposed to being disengaged from driving monitoring, increases takeover performance because drivers have their eyes on the road and can detect failures more quickly.

Out-of-the-Loop

On the one hand, research suggests that drivers may neglect their monitoring task (Banks et al., 2018) and do not always respect safety requirements. Indeed, Boos et al. (2020) showed that drivers who were well aware of their responsibility to supervise the road tended to neglect their supervision task, in part because they were too confident in their system. On the other hand, when drivers performed NRDT while the system was in AD, they were considered as not being in the driving control loop. Endsley et al. (1995) then discussed the out-of-the-loop performance problem, leaving "*operators of automated systems handicapped in their ability to take over manual operations in the event of automation failure*", partly due to decreased Situation Awareness (SA). Unlike L2 of automation, drivers will be disengaged from driving situation monitoring for L3. When they have to take the control of the vehicle, they must collect information about the environment and the situational risks in order to make an adequate decision and response to avoid an accident, which requires time.

Non-Driving Related Tasks

Furthermore, many studies focused on NDRTs as a factor that influences takeover performance including time and quality (Bueno et al., 2016; Gold et al., 2016). In particular, engagement in NDRTs has a significant effect on the quality of takeover (Lee et al., 2021; Zeeb et al., 2016), especially if the driver is engaged in the NDRT when a TOR is issued. Yang et al. (2019) also showed that a relaxed posture could have a negative effect on takeover performance.

Objectives and Research Questions

Using a driving simulator, the purpose of this study is to examine the effects of the level of engagement in driving situation monitoring on takeover performances as well as the effects of engagement in NDRT. Two research questions were formulated: (1) When engaged in driving monitoring, does TOR improve takeover performances? And (2) when engaged in NDRT, does the state of vigilance affect takeover performances?

Methods

Participants and Experimental Setup

Forty volunteers (20 males and 20 females) between 20 and 43 years old (M=26.9, SD=5.1) participated to this study. Their body varied between 158 and 190 cm in height (M=174 cm, SD=8.1 cm) and between 47 and 108 kg in weight (M=70.85 kg, SD=14.5 kg). The local ethics committee approved the experimental protocol. Informed consent was obtained prior to experiment for all participants.

This study was conducted using a static driving simulator composed of a steering wheel, three pedals, a control panel and five screens in a semicircle and three mirrors are integrated. The vehicle automation was simulated by the V-HCD software environment (Bellet et al. 2019). All data from the driving simulator, including vehicle control commands and environmental information such as collisions, lane positions and vehicle speeds, were recorded under the RTMaps software environment.

Scenarios and Experimental Conditions

16 scenarios were designed, taking place on a two or three lane highway at a cruising speed of 90 km/h for a duration of 2 to 4.20 minutes and all end with a critical situation that must be controlled manually by the vehicle occupant. For each scenario, the participant could either brake or change lane to avoid the collision. The times available (Time Budget - TB) to takeover control and to avoid accident were short in order to simulate an emergency situation (mean TB=4.2 s). Pre-tests were carried out to ensure that the TB was short enough provide a challenging task in terms of manual control resuming, but not too short to allow the participants to avoid the crash in case of a prompt and efficient reaction.

In order to investigate the influence of the driver's level of engagement/disengagement during AD on takeover performance, four test conditions were studied (Figure 1):

- Condition 1 (C1): Being engaged in the driving situation monitoring to decide to resume the manual control without any TOR, implying a cognitively demanding task of supervision.
- Condition 2 (C2): Being engaged in driving situation monitoring but supported by a TOR when a takeover is required, implying a supervision that is less demanding from the cognitive aspect.
- Condition 3 (C3): Being disengaged from the task of monitoring by performing a cognitively demanding NDRT, implying a state of hyper-vigilance.
- Condition 4 (C4): Being disengaged from the task of supervision in a relaxed position with eyes closed, implying a state of hypo-vigilance.

For C3 and C4, participants experienced automated driving with 2 NDRTs. These two NDRTs were selected to induce two opposite states of vigilance in the driver. First, the objective was to induce a state of hyper-vigilance (C3) thanks to a game on a touch pad. The touch pad was placed on the dashboard in the right of the steering wheel. Participants were asked to, as fast as possible, select the verbs (1 to 3) in the infinitive form among 5 words in French on the pad in a given time. The difficulty level increased with less and less time given for selecting right verbs as the game progressed. This task required a high level of engagement in gaming. Participants had no time to observe the road environment before TOR, thus were disengaged from the task of road supervision.

C4 corresponded to a state of hypo-vigilance (C4) where the participants were in a relaxed position with their eyes closed. The seat was tilted back 40° for all participants and they were instructed not to open their eyes until the TOR was present.

A same traffic scenario cannot be used to test more than two conditions. Sixteen traffic scenarios were all different in order for participants to avoid learning effect. They were grouped into 4 blocks of 4 scenarios. Combining 4 test conditions and 4 blocks of scenarios forms 16 combinations, allowing a group of 4 participants to test 4 conditions. Therefore, each block of 4 scenarios was played once for each test condition, while each participant performed 16 trials (4 conditions x 4 scenarios).

Figure 1. Overview of the 4 tests conditions

Procedure

Before starting the experiment, participants were informed about the study and filled in a demographic questionnaire. The driving simulator and its operation were then presented to them. A phase of training with the simulator was first performed in manual driving. Then, before each test condition, participants

performed two additional short trainings in order to be prepared and to understand how each condition works. Finally, they performed 4 scenarios by condition. The experiment lasted about 3 hours (including 2 breaks) for each participant.

Takeover performance measures

In this study, TakeOver Time (TOT) was used to measure takeover performance. It was determined by the interval from the TOR to the first action performed by the participant on the steering wheel, the pedals (brake or accelerator) or one of the turn signals which will deactivate the AD mode. To measure takeover quality, the number of collisions was considered.

Results

A total of 640 takeover situations (40 participants x 16 takeovers) were performed. Among these 640 scenarios, 10 were not correctly registered due to technical issues. Data was analysed therefore presented from 630 observations. Regarding the first action to takeover control, 96.5% (608) of reaction concerned the brake pedal use, 1.3% (8) the activation of a turn signal, 1.1% (7) depressing accelerator pedal and 1.1% (7) the rotating of the steering wheel. Three different ways of takeovers were observed: 58.1% (366) of situations were controlled by staying on the same lane, 28.7% (181) of the situations were achieved by changing lanes to the left, and 13.2% (83) by changing lanes to the right.

TakeOver Time

Due to the short TB available in this experiment, the mean TOTs obtained were also very short (from 1.01 s for C2 to 1.41 s for C4). A repeated measures Analyse of Variance (ANOVA) was conducted on TOTs for the four test conditions (C1 to C4), showed in Figure 2. A post-hoc Bonferroni test showed that participants took significantly shorter time in C2 to takeover control than the three others conditions ($p<0.001$).

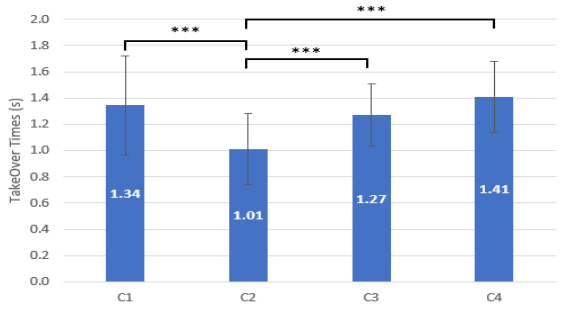

Figure 2. Mean TOTS in all situations

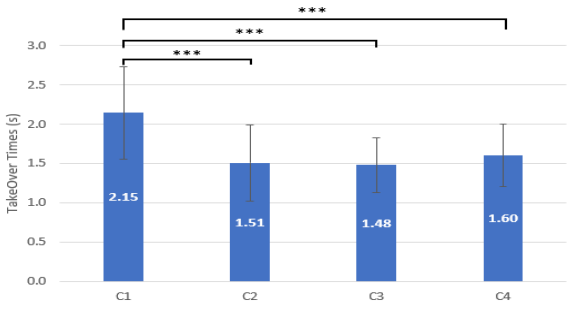

Figure 3. Mean TOTs when collisions

Accidents Analysis

Among the 630 situations, 139 accidents occurred. The mean TOTs when a collision occurred were different from the mean TOTS in all situation. A repeated measures Analyse of Variance (ANOVA) was conducted on TOTs, showed in Figure 3. A post-hoc Bonferroni test showed that participant took significantly longer time in C1 to takeover control when a collision occurred than the three others conditions ($p<0.001$). In addition, the highest number of accidents was observed in C1 (48 collisions) and C4 (40 collisions), followed by C3 with 27 collisions and C2 with the smallest number of collisions (24).

Discussion and Conclusions

The main objective of this study was to investigate the influence of the driver's level of engagement/disengagement during AD (partial and conditional automation) on takeover performance using a driving simulator. We were interested in takeover time and in the collisions as a quality of the takeover performance. Our results suggest that the TakeOver Request is very important in partial automation. Without TOR, drivers take longer to react and have more accidents, which could indeed confirm that drivers neglect their supervisory task (Boos et al., 2020) and perform worse in reacting to critical situations. It appears here that the TOR positively affects takeover performance.

When participants were engaged in NDRT, we found no significant differences in TOT between hyper and hypo-vigilant state. In contrast, the number of accidents was higher in case of takeover from a hypo-vigilant state (40) compared to a hyper-vigilant state (27). This could be explained by the postural difference, since according to Fitts's law (Fitts, 1954), the longer the distance between the hands and the steering wheel, the longer the takeover task from a reclined posture. On the other hand, the fact that drivers have to be cognitively engaged in the NDRT prevents them from being in a hypo-vigilant state and thus from being in a state that is more favourable to taking control of the driving. It could therefore be accepted that the state of vigilance has an impact on the quality of accident takeover.

Finally, when drivers are required to supervise driving without being alerted to a possible system failure, the results show that they took about the same amount of time to regain control of the system as when they were engaged in cognitively engaging NDRTs. In contrast, they had more accidents in the first case (48 vs 27). Results thus show the limits of human drivers' abilities to monitor L2 systems that might fail. A large amount of additional data has been collected and remain to be analysed in the near future, as the time of the eyes on the road, takeover quality, visual strategies, motor behaviours of drivers, etc.

References

Banks, V. A., Eriksson, A., O'Donoghue, J., & Stanton, N. A. (2018). Is partially automated driving a bad idea? Observations from an on-road study. Applied ergonomics, 68, 138-145.

Boos, A., Feldhütter, A., Schwiebacher, J., & Bengler, K. (2020, September). Mode Errors and Intentional Violations in Visual Monitoring of Level 2 Driving Automation. In *2020 IEEE 23rd International Conference on Intelligent Transportation Systems (ITSC)* (pp. 1-7). IEEE.

Bellet, T., Deniel, J., Bornard, J. C., & Richard, B. (2019). Driver modeling and simulation to support the virtual human centered design of future driving aids. In Proceeding of the INCOSE International Conference on Human-Systems Integration (HSI2019), Biarritz, France (pp. 11-13).

Bueno, M., Dogan, E., Selem, F. H., Monacelli, E., Boverie, S., & Guillaume, A. (2016, November). How different mental workload levels affect the take-over control after automated driving. In 2016 IEEE 19th International Conference on Intelligent Transportation Systems (ITSC) (pp. 2040-2045). IEEE.

De Winter, J. C., Happee, R., Martens, M. H., & Stanton, N. A. (2014). Effects of adaptive cruise control and highly automated driving on workload and situation awareness: A review of the empirical evidence. Transportation research part F: traffic psychology and behaviour, 27, 196-217.

Dingus, T. A., Guo, F., Lee, S., Antin, J. F., Perez, M., Buchanan-King, M., & Hankey, J. (2016). Driver crash risk factors and prevalence evaluation using naturalistic driving data. Proceedings of the National Academy of Sciences, 113(10), 2636-2641.

Dogan, E., Honnêt, V., Masfrand, S., & Guillaume, A. (2019). Effects of non-driving-related tasks on takeover performance in different takeover situations in conditionally automated driving. Transportation research part F: traffic psychology and behaviour, 62, 494-504.

Endsley, M. R., Kiris, E. O. (1995). The out-of-the-loop performance problem and level of control in automation. Human Factors: The Journal of the Human Factors and Ergonomics Society, 37, 381–394.doi:10.1518/001872095779064555

Fitts, P. M. (1954). The information capacity of the human motor system in controlling the amplitude of movement. Journal of experimental psychology, 47(6), 381.

Gold, C., Happee, R., & Bengler, K. (2018). Modeling take-over performance in level 3 conditionally automated vehicles. Accident Analysis & Prevention, 116, 3-13.

Gold, C., Körber, M., Lechner, D., & Bengler, K. (2016). Taking over control from highly automated vehicles in complex traffic situations: the role of traffic density. Human factors, 58(4), 642-652.

Gold, C., Damböck, D., Lorenz, L., & Bengler, K. (2013, September). "Take over!" How long does it take to get the driver back into the loop?. In Proceedings of the human factors and ergonomics society annual meeting (Vol. 57, No. 1, pp. 1938-1942). Sage CA: Los Angeles, CA: Sage Publications.

Lee, S. C., Yoon, S. H., & Ji, Y. G. (2021). Effects of non-driving-related task attributes on takeover quality in automated vehicles. International Journal of Human–Computer Interaction, 37(3), 211-219.

Lin, Q., Li, S., Ma, X., & Lu, G. (2020). Understanding take-over performance of high crash risk drivers during conditionally automated driving. Accident Analysis & Prevention, 143, 105543.

SAE (2021). Taxonomy and Definitions for Terms Related to Driving Automation Systems for On-Road Motor Vehicles - SAE International. (s. d.).

Yang, Y., Gerlicher, M., & Bengler, K. (2018, September). How does relaxing posture influence take-over performance in an automated vehicle?. In Proceedings of the Human Factors and Ergonomics Society Annual Meeting (Vol. 62, No. 1, pp. 696-700). Sage CA: Los Angeles, CA: SAGE Publications.

Zeeb, K., Buchner, A., & Schrauf, M. (2016). Is take-over time all that matters? The impact of visual-cognitive load on driver take-over quality after conditionally automated driving. Accident analysis & prevention, 92, 230-239.

Zhang, B., de Winter, J., Varotto, S., Happee, R., & Martens, M. (2019). Determinants of take-over time from automated driving: A meta-analysis of 129 studies. Transportation research part F: traffic psychology and behaviour, 64, 285-307.

Quantifying Vision Obstruction of Formula One (F1) Halo Concept Variants

Sriram Srinivasan, H. Onan Demirel[1]
Oregon State University, School of Mechanical, Industrial and Manufacturing Engineering
Corvallis, Oregon, United States

Abstract

This paper presents an early-design methodology to quantify vision obstruction caused by halo-type cockpit safety equipment introduced into Formula One (F1) racing in 2018. The *halo* is a curved bar that surrounds the driver's head over the cockpit opening and offers additional protection to drivers. However, the halo's introduction has raised concerns over vision obstruction-related issues due to its vertical and horizontal bars (pillar-like elements) sitting in front of the cockpit. This study assesses vision obstructions by exploring the driver's forward field of view (FoV) based on the coverage zone analysis. This research utilizes digital manikins inserted in a digital F1 racecar mockup to assess the effects of halo concept variants on vision obstruction. The preliminary results showed that the vision obstruction was not only affected by the halo geometry and size but also the orientation of the F1 car in different racetrack segments. The methodology discussed in this study is critical for other early-stage product design and development challenges, where designers demand "quick-and-dirty" ergonomics evaluation of vision obstruction before building time-consuming and costly physical mockups.

Keywords: Preliminary Design, Human-Centered Design, Digital Human Modeling, Formula One, Vision Obstruction

1. Introduction

Past incidents in Formula One (F1) racing have resulted in severe injuries and deaths due to a lack of a cockpit closure. Advanced helmets have only provided limited protection to minimize the threat of rollover crashes and high-speed projectiles hitting the driver's head. Current F1 race cars have recently incorporated the *halo* safety device to mitigate the adverse effects of open cockpit racing to protect the driver's head. The halo is a curved bar attached to the F1 car at multiple points. It offers additional protection by surrounding the driver's head over the cockpit opening (Fig. 1). The generic halo safety device is made of titanium, weighs around 6 to 10 kgs, and is designed and manufactured by the Federation Internationale de l'Automobile (FIA). Although the halo device has brought an additional layer of improved safety to drivers, its introduction was unorthodox as it went against the aspect of the open cockpit racing style by creating a canopy-like

[1] Corresponding Author, Email: onan.demirel@oregonstate.edu

cockpit enclosure. In addition, the halo design has received controversial reviews among F1 drivers and critics due to its potential to obstruct drivers' forward field of view (FoV) [1].

Mental and physical fatigue effects on a driver are known to be strenuous while operating an F1 car. The added visual fatigue due to maintaining an intensely focused driving for the entire race duration impacts the driver's overall performance. Hence, providing the driver with an unobstructed field of view (FoV) is crucial for safety and performance. The halo design introduces a narrower and more articulated vision through a semi-confined space, which can tax visual performance. Some critiques have also expressed concerns that the vertical bars included in the halo design may have compounding effects along with the sudden acceleration and deceleration throughout the race [2,3].

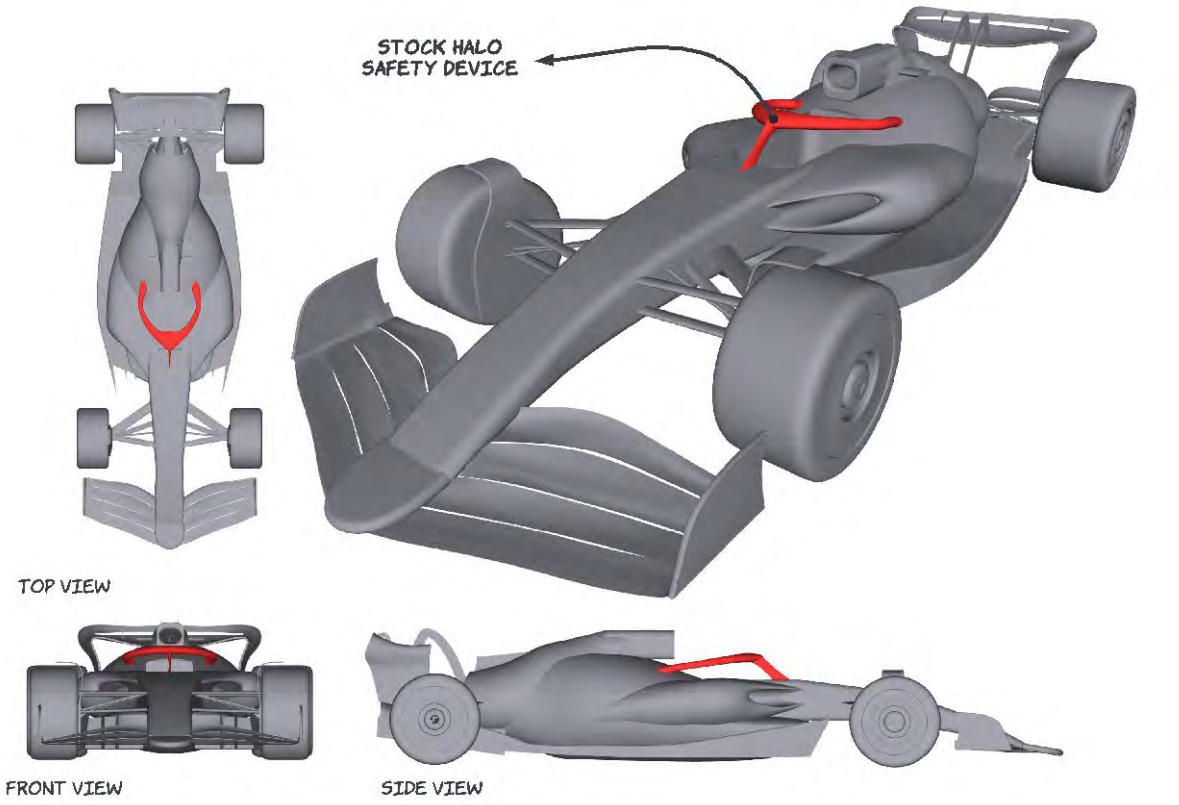

Figure 1. Generic 2022 F1 racecar model with the stock halo (in red) located over the cockpit opening.

The development F1 racing car reveals that cost often restricts the battle to meet performance requirements. The financial burden of prototyping and manufacturing costly bespoke physical prototypes is excruciating even for F1 teams. When designing for human factors engineering (HFE), the vehicle development process requires expensive mockups where any rework or retrofitting to correct ergonomics errors adds to the overall time and cost. Thus, early in design, the lack of proactive ergonomics impacts the final product's quality in terms of safety and usability, whether it's an F1 or a road-going car [5–7]. This study proposes a computational design approach that integrates DHM with visualization techniques to facilitate a "quick-and-dirty" vision obstruction assessment for concept halo variants.

2. Methods

Since having adequate visibility is critical for the safety and performance of operating an F1 car, we propose a preliminary design method to evaluate halo concept variants in terms of their performance in reducing drivers' forward vision obstruction zones. This research proposes a proactive ergonomics approach for early design concept evaluation of halo variants by integrating CAD, DHM, and VR (Fig. 2). The following subsections elaborate more on the model and simulation development.

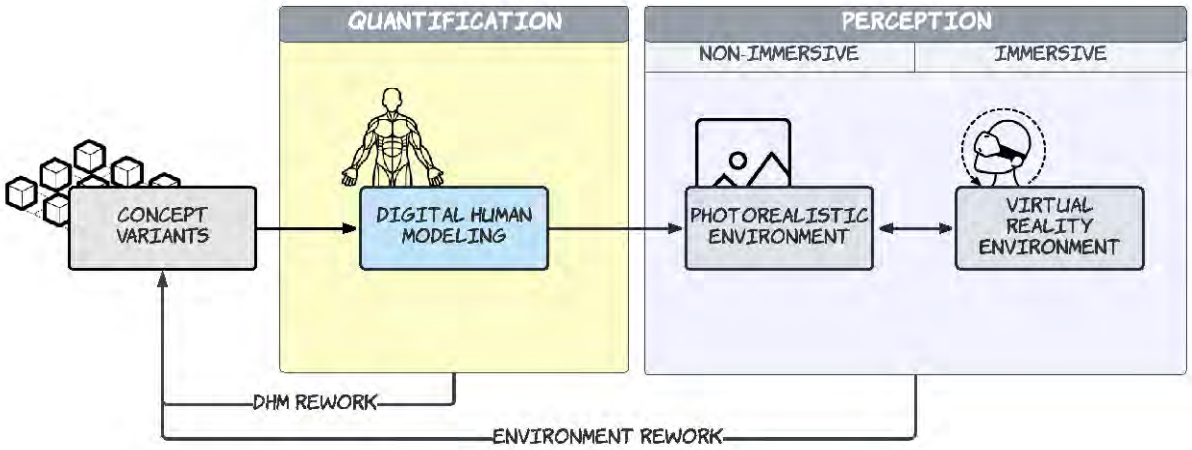

Figure 2. The methodology proposed in this paper provides opportunities to inject proactive ergonomics early in design. It links human modeling with photorealistic and virtual reality techniques.

2.1 Development of CAD Models:

A generic F1 2022 car model was created based on guidelines proposed by Formula One Group (FOM), which provides insight into the basic form and the development of body designs that are mandatory rules for teams. We used these guidelines to replicate a 1:1 scale CAD model to accommodate different halo concept designs (Fig. 3). Each halo model was created, modified, and adjusted to meet design requirements. Along with the vehicle and halo models, we modeled two different racing scenarios (based on racetrack segments) to illustrate cases where the opponent vehicle is blocked in the driver's vision by the halo. CAD models of the racetrack segments were created by considering the track width, length, and elevation changes. It is important to note that representing elevation changes in the CAD racetrack models was essential since a portion of this study focused on creating photorealistic and virtual reality environments to represent the racing scene with high fidelity (Fig. 4).

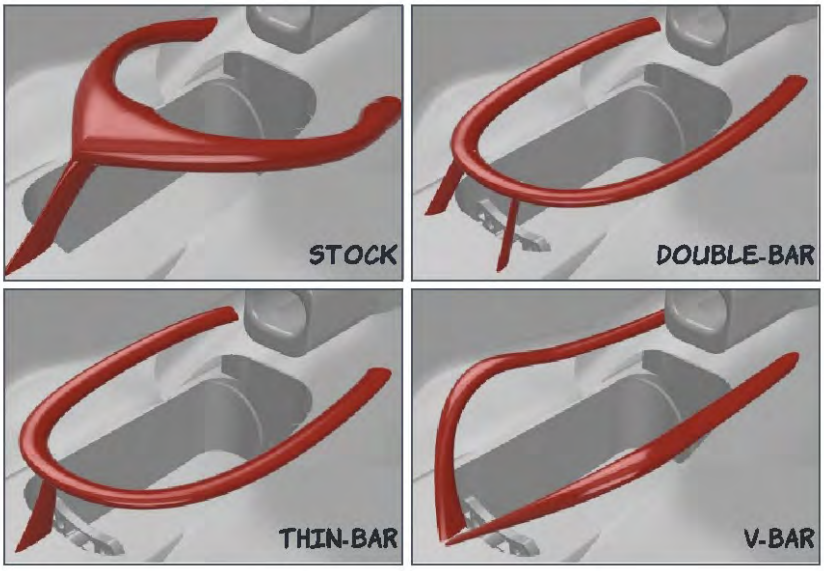

Figure 3. Concept halo design variants implemented on a generic 2022 F1 racecar model.

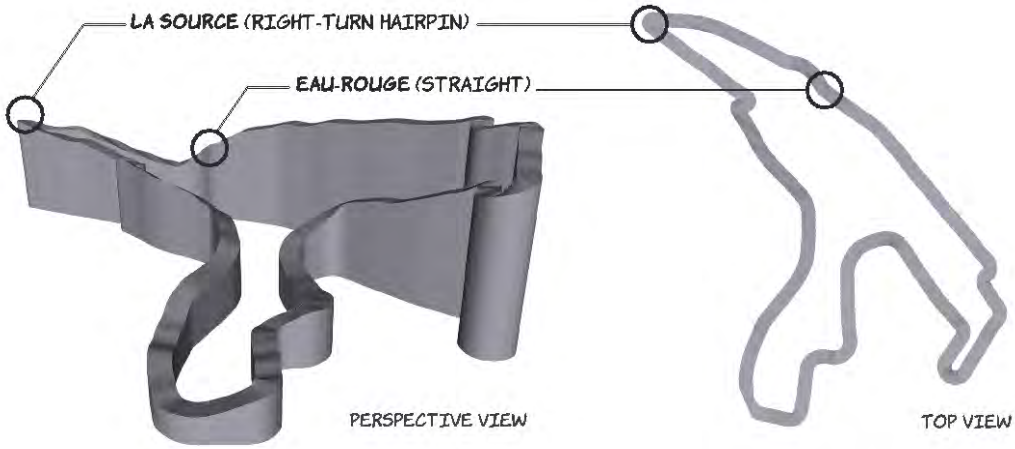

Figure 4. A simplified 3D CAD model of the Circuit de Spa-Francorchamps racetrack (La Source and Eau-Rouge segments) used in this study includes realistic elevation changes and track camber.

2.2 Digital Human Modeling Simulation Setup:

Prior research shows that incorporating HFE design principles in the early-stage design process can positively impact user interaction and the overall quality of products [8,9]. Applying proactive ergonomics with the aid of digital manikins enables engineers to discover potential design errors that can be identified and fixed before the physical prototyping process starts [10,11]. Further, in this study, we hypothesize that DHM-based design that combines high-fidelity models of the products and their use environments can help increase the success of injecting proactive ergonomics during early-stage design.

In this research, we created a computational representation of the racing environment, including the vehicles, racetrack, driver manikins, and environment objects, illustrating a simulation environment comparable to the real-life scenario. The integrated design framework proposed in this research intends to push the boundaries of traditional DHM what-if scenarios and extend the fidelity of early design

assessments. This study uses a 3D model of the Belgium Circuit de Spa-Francorchamps racetrack, including realistic elevation changes and track camber (Fig. 4). We selected two segments from the racetrack: (1) the Eau-Rouge straight and (2) the La Source right-turn hairpin. These segments represent scenes of the racetrack where drivers are involved in overtaking maneuvers that require heavy vision concentration.

A 50th percentile male from the Anthropometric Survey of US Army Personnel (ANSUR) manikin database representing an F1 driver was seated inside the generic 2022 F1 cockpit. The manikin's head/neck joint (atlanto occipital) was adjusted based on a vision target (coverage plane) representing another F1 car ahead (Fig. 5). The posture represents typical scenarios of high-speed maneuvering of corners and the effect of cornering on the driver's posture. Meanwhile, another F1 car is situated on the track where it has stopped directly ahead by the distance covered in one second. For example, the F1 car is expected to enter the corner at 300 km/h and exit at 180 km/h. In the event of a mishap at this corner, the driver's reaction time demands less than one second. If this sub-second reaction time is missed, the driver will directly collide with the vehicle placed roughly 80 meters ahead immediately.

In this DHM study, the vision obstruction due to the presence of the halo design was measured using the *coverage zone* analysis in Siemens Jack software. The ray-casting-based vision analysis toolkit within Siemens Jack software was used for exploring vision obstructed by the pillar elements of the halo design (Fig. 6). While designing the DHM approach is superior in quantifying vision obstruction based on rough CAD and environment models, it lacks mimicking actual racing conditions. The absence of high-fidelity information regarding the use environment causes perception-related data only partially represented in DHM platforms. To overcome these issues, DHM models were imported into high-fidelity visualization (photorealistic and virtual reality) software to improve early design capabilities.

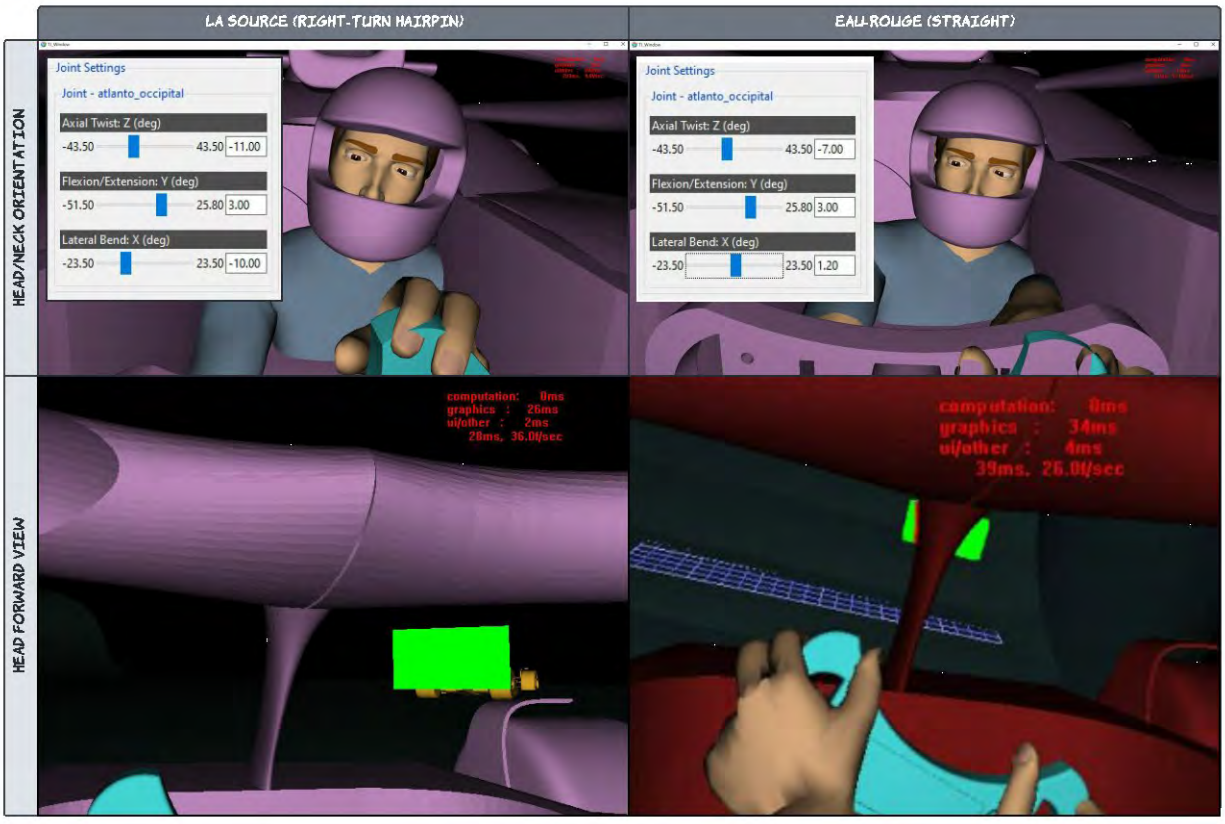

Figure 5. Head forward view of the driver with the stock halo used in *coverage zone* analysis.

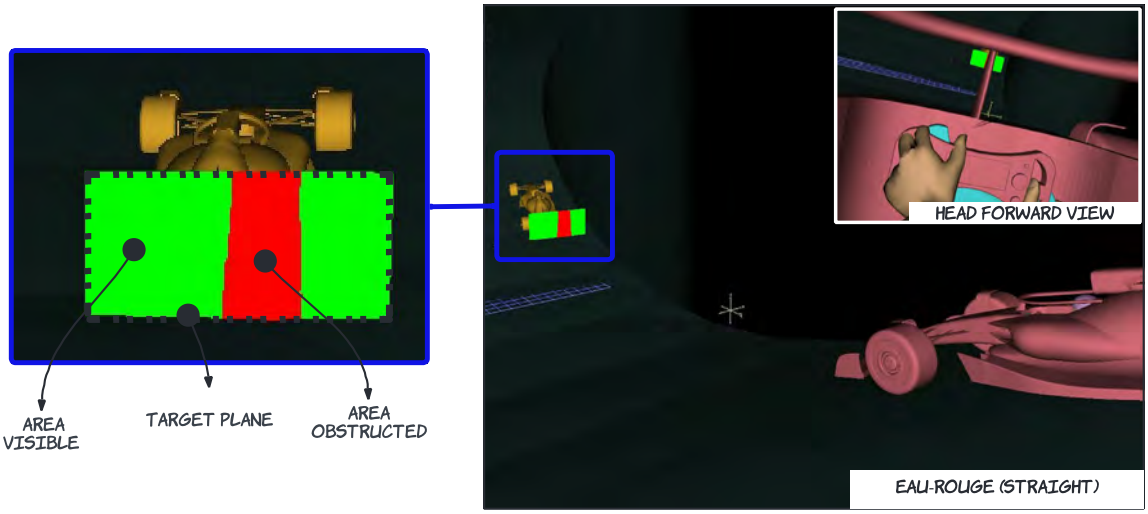

Figure 6. The image illustrates the *coverage zone* analysis performed in the 2022 F1 model with the thin-bar halo design. The area of the target plane (represented with dash lines) shaded in green represents the rays blocked by the vertical bar.

2.3 Photorealistic and Virtual Reality Environment Setup

Our current paper only focuses on the design and analysis efforts up to the photorealistic and virtual environment study. Our photorealistic (Fig. 7) and virtual reality (Fig. 8) studies are currently under development and will enable us to investigate the perception/cognitive aspects of the halo vision obstruction.

Figure 7. Photorealistic models and screenshots of the Spa racetrack from the VR environment.

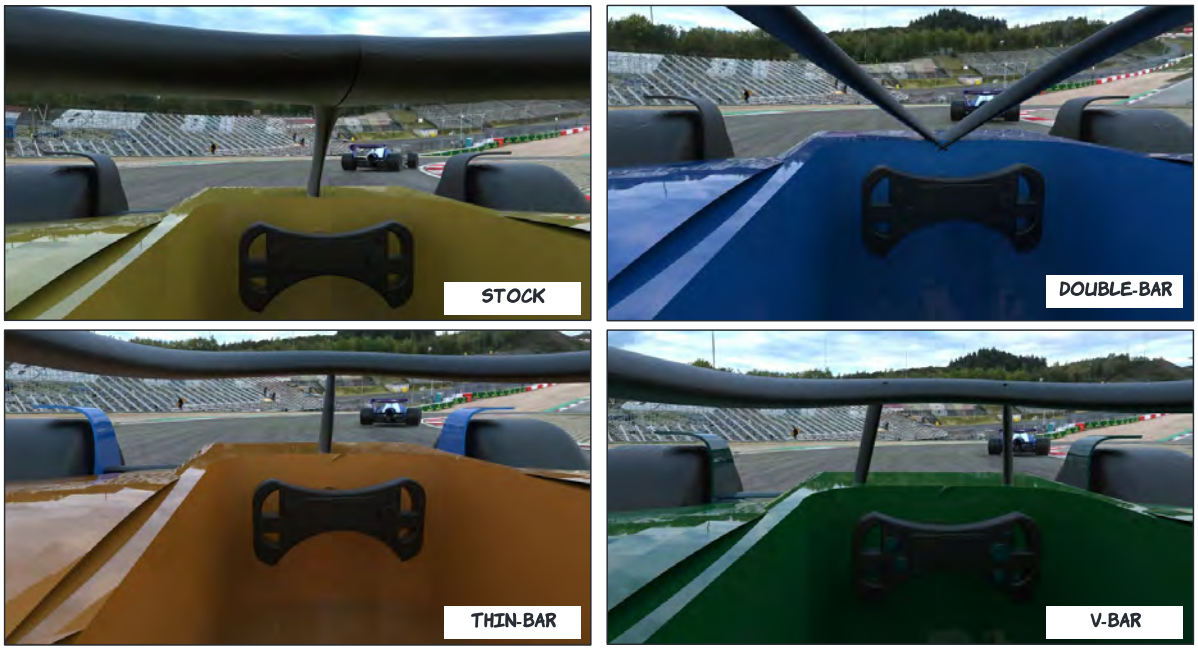

Figure 8. VR mockups of halo concept variants from the driver's point of view along with the high-fidelity visualization of the track segments.

3. Results

In this case study, we used *coverage zone* analysis to compare four halo concepts (illustrated in Fig. 3) in two track segments (La Source and Eau-Rouge) to measure percent visibility. The initial DHM assessments showed that the double-bar (100%) and v-bar (100%) halo models provided better visibility of the opponent vehicle when in the trough of Eau-Rouge on the Spa circuit. In contrast, stock and thin-bar designs only resulted in lower percent visibility, 32% and 75.4%, respectively. Likewise, the single wide central pillar design found in the stock (100%) and thin-bar (100%) halo variant models provide better visibility of the opponent vehicle during the La Source right-turn hairpin of the Spa circuit. In contrast, double-bar and v-bar designs yielded 84.6% and 55.4% visibility. These results indicate that the percent visibility of the forward field of view (FoV) vehicle varies based on the shape and size of halo designs and the track segment. Thus, no single design provides high visibility in both conditions. Different halo concept designs work differently based on track conditions and racing scenarios.

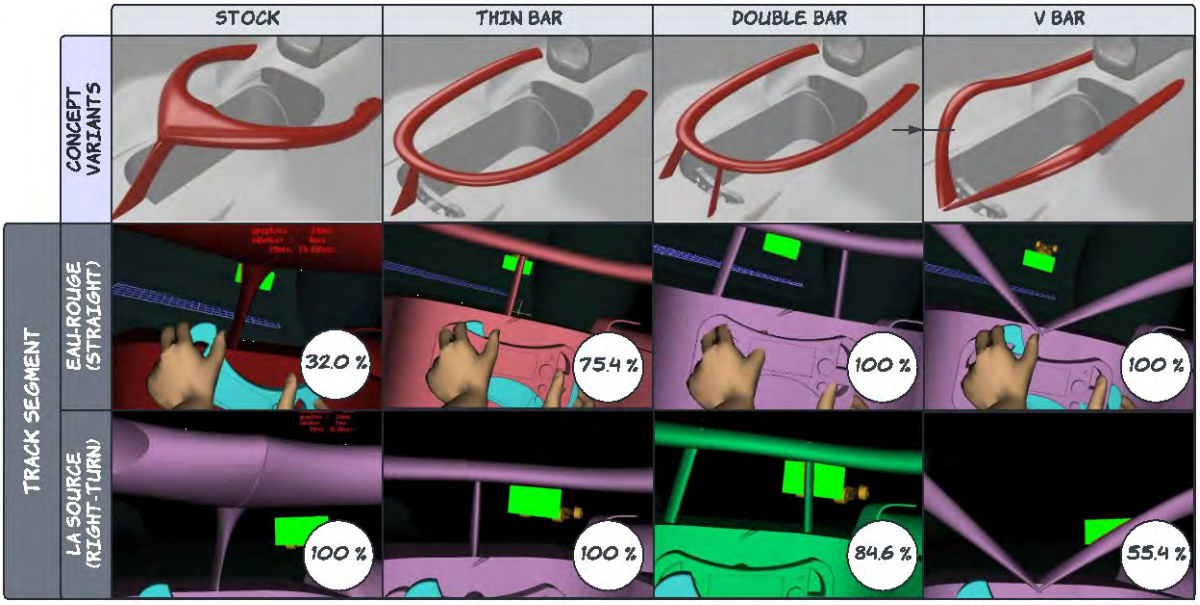

Figure 9. Visibility assessments (provided inside the callout bubbles) based on coverage zone outcomes indicate percent visibility in each scenario per halo concept variant.

4. Discussion and Conclusions:

While DHM simulation results are considered favorably for early design purposes, the simulation outcomes obtained in this study provide a limited understanding of vision obstructions caused by halo concept variants in F1 racing. The ray-casting approach used in *coverage zone* analysis utilizes static images on a 2D target plane, which lacks fidelity. There is a need to consider the effects of halo structure on human vision beyond investigating motion in 2D. Also, further development in DHM vision analysis should include factors such as perspective and depth of field.

There is also a need to replicate the dynamic nature of the simulation environment in DHM and VR studies to increase the fidelity further. Overall, integrating DHM and VR early in design allows the creation of a design feedback loop that minimizes the necessity of physical prototype testing and evaluation. Experiments for fit and feel using the VR setup would allow for a more robust design evaluation method by keeping humans (drivers) in the loop, which we plan to explore in our future studies.

Even with the introduction of dynamic driving simulation and advanced VR techniques, it remains challenging for any driver to identify and detect objects hidden behind the halo zone. Further research is needed to investigate halo variants that further minimize the obstruction zones. Models that use topology optimization and generative design techniques can help designers develop see-through zones (cut-out sections) on halo structure, which enables improved forward FoV.

References

[1] Jennings, A. (2018). Percent Area Visual Obscuration of F1 Racecar Canopies. : Oregon State University.

[2] Land, M. F., & Tatler, B. W. (2001). Steering with the head: The visual strategy of a racing driver. Current Biology, 11(15), 1215-1220.

[3] Gürbüz, H., & Buyruk, S. (2019). Improvement of safe stopping distance and accident risk coefficient based on active driver sight field on real road conditions. IET Intelligent Transport Systems, 13(12), 1843-1850.

[4] "Accident Panel | Federation Internationale de l'Automobile." https://www.fia.com/news/accident-panel (accessed Jun. 05, 2022).

[5] Chang, K. H. (2014). *Product design modeling using CAD/CAE: the computer-aided engineering design series*. Academic Press.

[6] Ullman, D. G. (2010). The mechanical design process. Boston: McGraw-Hill Higher Education.

[7] Demirel, H.O & Duffy, V. G. (2016). Building quality into design process through digital human modelling. Int. J Digital Human, 1(2), 153.

[8] Zare, M., Croq, M., Hossein-Arabi, F., Brunet, R., & Roquelaure, Y. (2016). Does ergonomics improve product quality and reduce costs? A review article. Human Factors and Ergonomics in Manufacturing & Service Industries, 26(2), 205-223.

[9] Kim, S., Seol, H., Ikuma, L. H., & Nussbaum, M. A. (2008). Knowledge and opinions of designers of industrialized wall panels regarding incorporating ergonomics in design. International Journal of Industrial Ergonomics, 38(2), 150-157.

[10] Demirel, H. O., & Duffy, V. G. (2009). Impact of force feedback on computer aided ergonomic analyses. In International Conference on Digital Human Modeling (pp. 608-613). Springer, Berlin, Heidelberg.

[11] Dul, J., & Neumann, W. P. (2009). Ergonomics contributions to company strategies. Applied ergonomics, 40(4), 745-752.

[12] Ahmed, S., Irshad, L., Gawand, M. S., & Demirel, H. O. (2021). Integrating human factors early in the design process using digital human modelling and surrogate modelling. *Journal of Engineering Design*, *32*(4), 165-186.

The use of DHM to quantify a measure of direct vision performance in trucks

Stephen Summerskill[1], Russell Marshall[1], Abby Paterson[1], Anthony Eland[1]

[1] School of Design and the Creative Arts, Loughborough Universty, Ashby Road, Loughborough, Leicershire, United Kingdom, LE11 3TU

Corresponding author: s.j.summerskill2@lboro.ac.uk

Abstract

Accidents between vulnerable road users and trucks have been linked to the inability of drivers to directly see the areas in close proximity to the front and sides of the vehicle cab. The lack of direct vision is mitigated through the use of mirrors. The coverage requirements of mirrors are standardized in a UNECE standard. Direct Vision for trucks is not currently standardized in any way. Research by the authors identified key requirements for a Direct Vision Standard (DVS) which was subsequently designed. The method used to quantify direct vison measures the volume of space that is visible, of an assessment volume around the vehicle cab, from a driver's eye point. The result is a volumetric score in m^3. This standard is now being applied in London, England, and a UNECE version is in development. This paper describes how DHM was used to provide a measure of real-world performance which correlates to a high level with the volumetric score, and an automated version of this process that is being used in the UNECE version.

Keywords: Blind spot, collision, regulation, safety.

Introduction

This paper reports the development of methods for quantifying direct vision from heavy good vehicles. Whilst there has been general improvement in road safety the UK, there has been an increase in collisions between Vulnerable Road Users (VRUs) and Heavy Goods Vehicles (HGV, category N3, with a gross weight in access of 12 tonnes.). Research has identified that the number of accidents occurring is disproportionate to the number of HGVs on the road and identified specific scenarios in which accidents are most likely to occur (Talbot 2014, Cook 2011, Summerskill 2019a). In Europe over 4000 VRUs are killed or seriously injured in collisions with HGVs each year. The size and location of blind spots in direct vision of the HGV driver caused by the height and structure of the vehicle has been the focus of multiple research projects and papers. The height of the HGV driver’s eye point above the ground plane can be in excess of 3m for European vehicle designs. Therefore, direct vision is not possible for large areas in close proximity to the cab. Figure 1 shows a typical long haul design which can obscure the direct

vision of the a large number of cyclists from a single eye point. The inset image shows the view from the driver's eye point that was derived from the methods reported in Reed (2005).

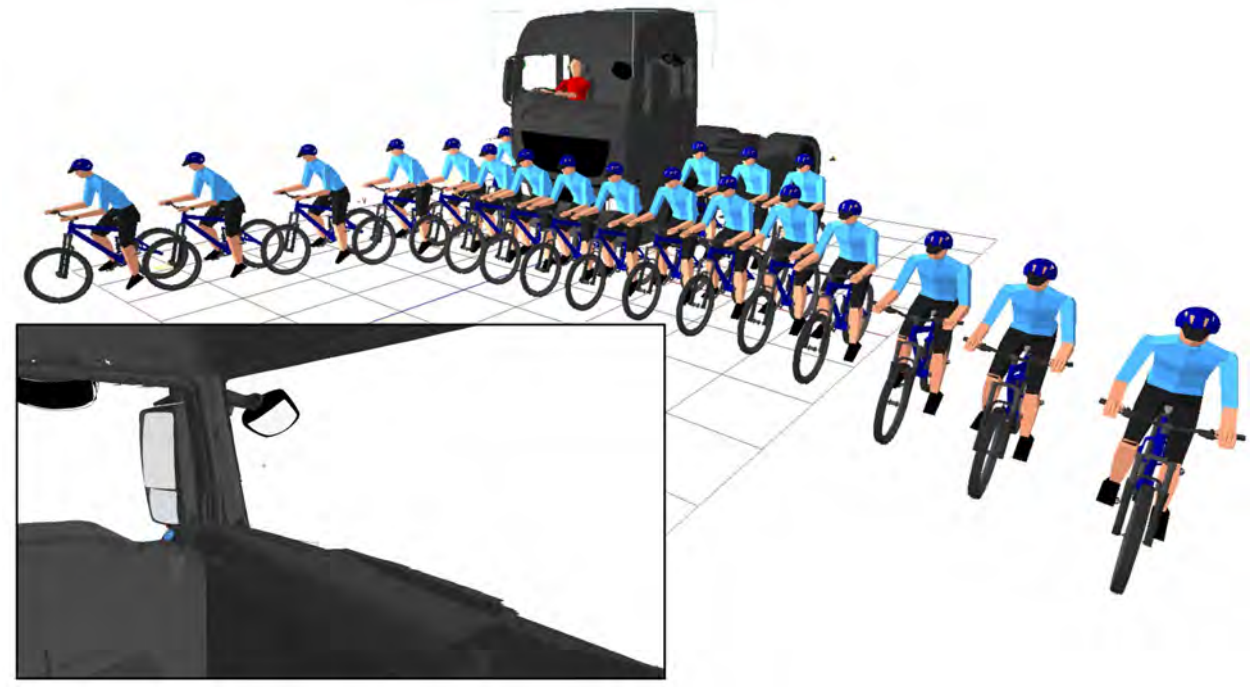

Figure 1. From the defined eye point, none of the cyclists can be seen using direct vision.

In Summerskill (2015a) a blind spot was reported which existed between the volume of space visible to a driver through windows (direct vision) and the volume of space visible through mirrors (indirect vision). The identification of this blind spot led to the revision of UNECE regulation 46 which improved the coverage of the Class V mirror (UNECE, 2015). Further work has been reported in Summerskill (2015b) to examine and measure blind spot locations for all sides of 19 European HGV cab designs. The findings of this work indicated there were multiple factors in the design and use of HGV cabs that potentially contribute to the size and location of blind spots for HGV drivers. These included the height of the driver's eye point above the ground, the position of the driver in relation to the front and sides of the cab and height of the windscreen and lateral window bottom edges with respect to the driver's eye point.

This is mitigated for by the use of six standardized mirrors which must meet the coverage specification of UNECE regulation 46 (UNECE, 2015). The use of six mirrors and multiple windows produces a minimum of nine 'viewports' that must be scanned to enable situational awareness of the areas in close proximity to the vehicle cab in urban environments. Mole (2017) examined this situation in a simulator study and determined that when comparing the use of direct vision and indirect vision to identify VRU's, indirect vision use increased the reaction time of HGV drivers by 0.7 seconds. This, combined with the

findings of Summerskill (2015a) led to the definition of a requirement for a direct vision standard by the authors. The aim of the direct vision standard was to determine a minimum direct vision requirement for HGVs to be used in urban environments, and therefore foster safer cab designs which refine direct vision capabilities in future vehicles. This direct vision standard uses DHM and CAD methods to accurately measure the direct vision performance of a cab design. This is achieved by placing an assessment volume around the vehicle determining the volume of the assessment volume that can be direct seen from a predefined set of eye points (Summerskill, 2019a and 2019b). Figure 2 shows the keys stages of this process. The test produces a volume of visible space that can be split into the views provided by the windscreen and lateral windows. The result is presented in m3. However, it is clear that it is difficult to determine what a minimum requirement is for the volume is in isolation as a value of 12.4m^3 is a difficult measure to relate to real world accident scenarios. This paper presents the method that was used to quantify the volumetric scores that were produced for the 56 vehicle variants that were included in the sample. The method described in Summerskill (2019a) has now been adopted in a direct vision standard which applies to all vehicles entering London. A minimum direct vision requirement of 10.04m^3 has been defined.

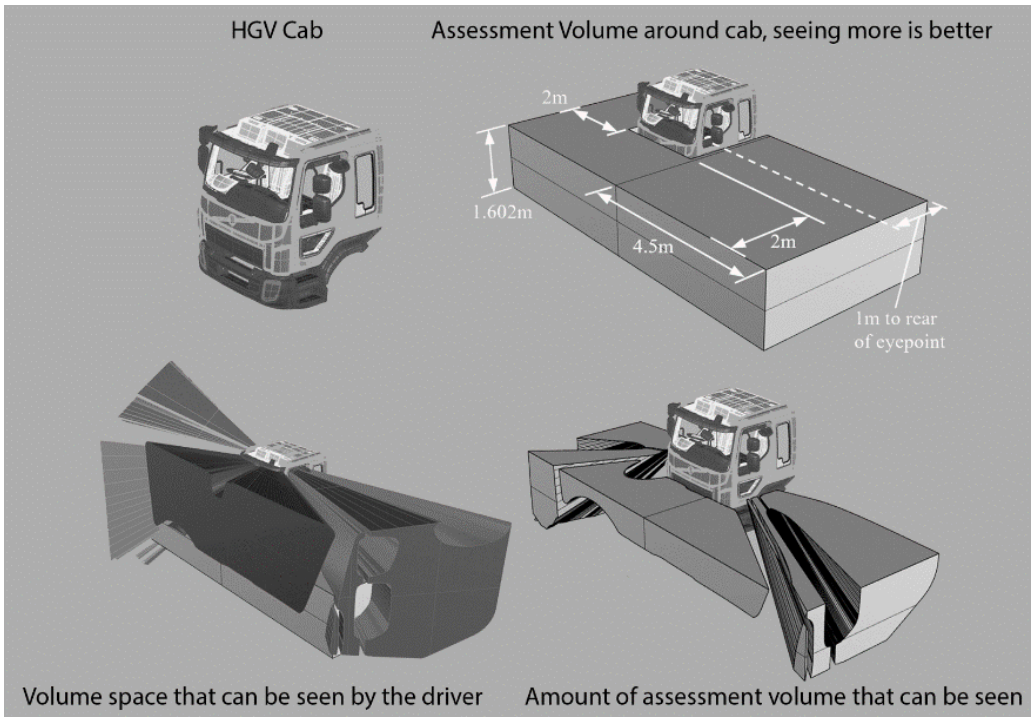

Figure 2. The key stages of the process used to measure the direct vision performance of HGVs

Methods

The following section describes the methodology used to explore the issue of quantifying the volumetric scoring system.

Sample of vehicles

The project that defined the DVS was funded by Transport for London (TfL), the organization that runs the public transport and road network in the UK capital. TfL built a working group which included all major European HGV manufacturers. The specification of European vehicles in terms of engine size and suspension type can lead to a wide variability in the driver height above the ground plane. One example vehicle that was analyzed in the project had a cab mounting height range of over 800mm. This issue needed to be accounted for in the definition of the sample. In order to address this each manufacturer was asked to provide CAD data for the cab designs, and data on the absolute maximum and minimum height at which the cab can mounted based upon component specification. Therefore two variants were tested for each of 28 different designs, leading to a sample of 56 vehicles. This covered over 98% of the vehicle cab designs sold in the UK.

Accident scenarios considered

A review of accident data in the UK was performed to determine which are the most common accident scenarios. This resulted in the identification of two scenarios which accounted for 90% of accidents in the UK. These were, a vehicle pulling away from a crossing point and hitting a pedestrian that was not seen, and cyclists colliding with HGVs which are turning left, with the cyclist on the passenger side of the vehicle. The detail on the accident statistics analysis can be seen in Summerskill (2019a).

The definition of the driver eye points to be used for the projection of volumes and viewing VRU locations

The definition of the eye points used in the DHM simulations has been detailed in Summerskill (2019b). It involved the definition of a common H-point envelope by combining data from all vehicle designs, determining a common achievable H-point. An offset was then produced from the H-point to the front eye point using an average of Dutch, British, German, Italian and French 50^{th0}%ile Drivers with 90:10 male female ration. The left and right eye points were then determined by a rotation based upon UNECE regulation 125.

Design of the assessment volume

The concept of defining a volume of space around the vehicle and determining how much of that volume can be seen was defined in the proposal for the project work. The actual size and shape of the assessment

volume was determined as part of the project. A number of alternatives were considered in the design of the standard (See Appendix B in Summerskill, 2019a). The end result shown in Figure 2. The rationale for the final assessment volume is that direct vision should, where ever possible, allow the volume of space that is currently visible through indirect vision (mirrors) to be directly visible to drivers. Hence, the assessment volume in plan view covers the same area as the mirror coverage zones defined by UNECE regulation 46. That is, 2m to the front of the vehicle, and 4.5m to the passenger side of the vehicle. Whilst accidents to the driver side of the vehicle account for 10% of accidents between VRUs and HGVs, and direct vision is generally good in the area due to the proximity of the driver the driver's window. With no other evidence found for the definition of a specific value, the area to the driver's side matched the distance from the front, 2m. The height of the assessment volume was defined by the shoulder height of the 99th%ile Dutch Male (the tallest population in the world).

Methods for quantifying the minimum volume requirement for urban environments

The research performed in Cook (2011) and Summerskill (2015a) used DHM simulations of VRUs, and determined the distance from the sides and front of the cab at which those VRUs could be hidden from the driver's view. This was a model that was followed in the work to quantify what a particular volumetric score means in terms of a real-world accident scenario. The hypothesis was that the distance at which VRUs can be visible from the side and front of the truck could correlate with the volumetric score for each cab design assessed. However, some modification to the method were required. In this case it was important to determine the distance at which a VRU could be seen, whereas the previous methods measured to the point at which they just invisible. A review of the literature was performed to try and determine how much of a VRU should be visible to allow recognition, but none was found. Therefore, an approach was taken which linked to the data gathered in surveys of pedestrians by TfL. This highlighted that making eye contact with a driver was seen as important by pedestrians as it gave some assurance that their presence had been noted. The solution was determined to be that the driver should be able to see the head and shoulders of the VRU simulation. The size of the VRU simulation was a great source of debate. The accident data showed that collisions with children were rare, and that elderly people were more likely to be involved in the pedestrian scenario. This led to an adult population being selected. The smallest population in Europe is the Italian Females (Peebles, 1998). Italian females with a stature of 5th%ile weere selected for the VRU simulation as this allowed over 95% of the adult European population to be visible to the driver for a vehicle that passes the minimum requirement. A rig of VRU simulations was created in the DHM system which were arranged around the vehicle in a predetermined manner as shown in Figure 3. The was based upon the position of VRU simulations in Summerskill (2015a). The two VRUs closest to rear of the cab shown in Figure 3 were located in the X axis by an offset of one body width from the

forward eye point. The ten lateral VRU simulations were then moved in the Y axis until their head and shoulders were visible from the predefined eye points. The front three VRUs were located in the center of the HGV cab and at the lateral extents of the cab, and were again moved in the X axis until their head and shoulders were visible from the predefined eye point. The aim was to determine the quality of the correlation between VRU distance and volume. Nine VRU simulations were initially considered, but this was increased to thirteen as this improved the quality of the correlation between VRU distance and volumetric score.

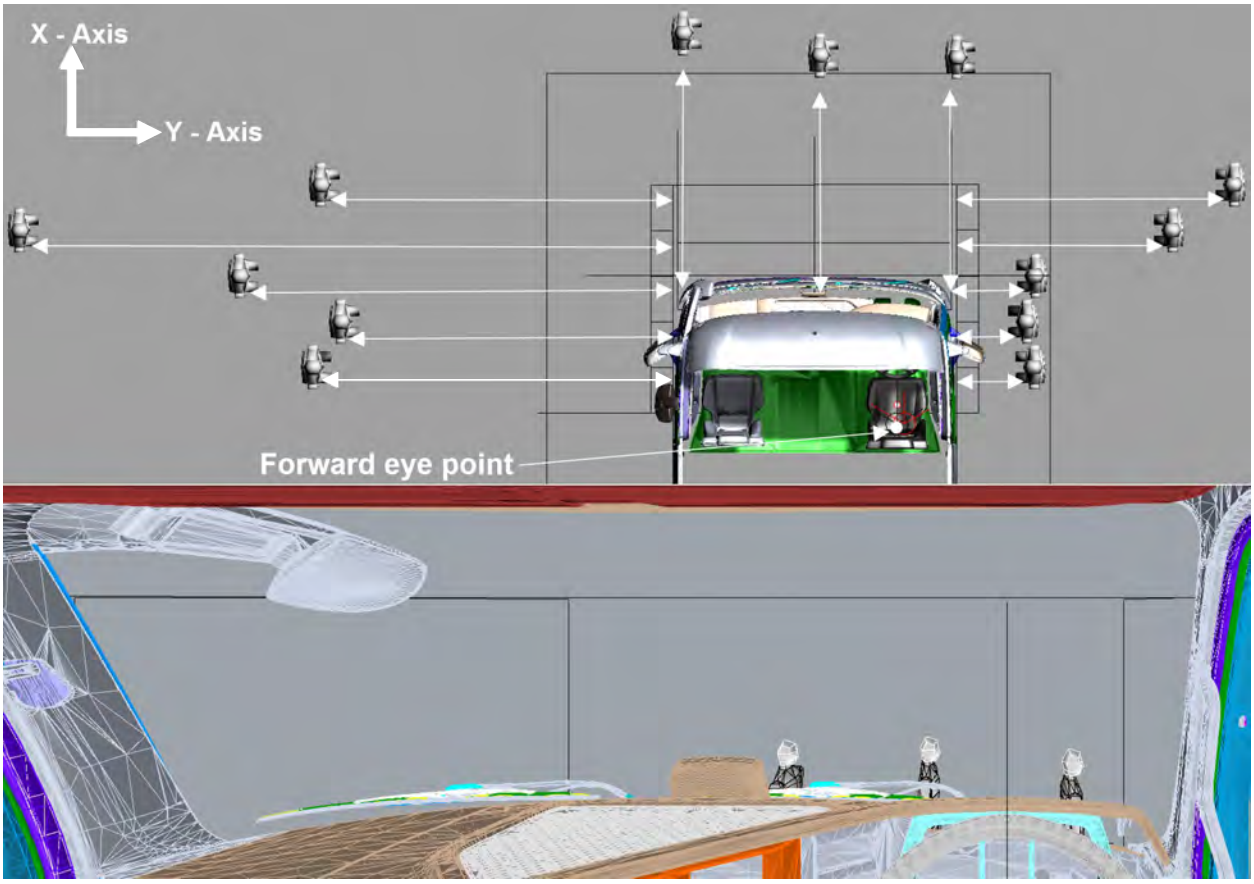

Figure 3. The arrangement of the VRU simulations and the view from the eye point used to determine the VRU location where the head and shoulders were visible

Results

Figure 4 shows the results of the volumetric and VRU distance scoring of each of the design variants included in the sample. The correlation between these measures is 0.97 using Pearson's test, where a value of 1 is a perfect correlation. Values above 0.5 are considered to be strong. As discussed, other versions of the assessment volume were tested, including a much larger assessment volume, and a version

that was weighted by area in terms of accident risk (see Appendix B, Summerskill, 2019a). However, the result shown in Figure 2 provided the best differentiation between the vehicle designs and was considered the superior method due to the design of the assessment volume.

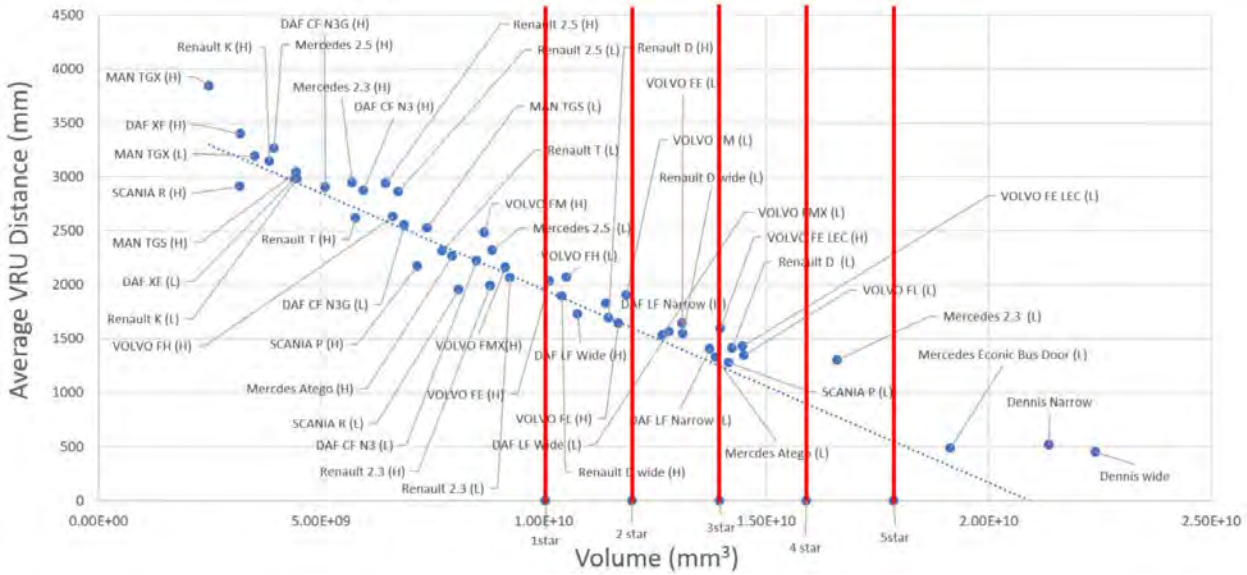

Figure 4. Graph showing the correlation between VRU distance and volumetric score for each cab design

With a good correlation achieved the method was seen as sufficient for defining the minimum volumetric requirement by consideration of the acceptable distance at which VRUs can be seen from the side and front of the HGV. The TfL working group was involved in the decision of how to define the minimum requirements for direct vision. The rationale was that should not be a situation in which a VRU can be located around the vehicle, and not be seen in either direct or indirect vision. Figure 5 shows such a situation.

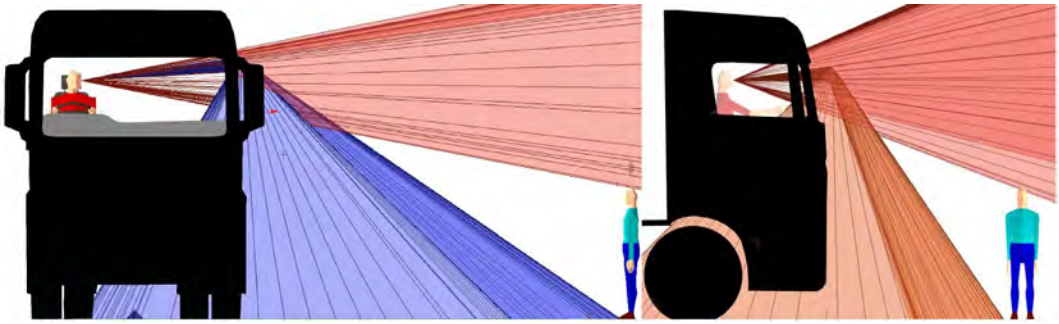

Figure 5. A situation in which the VRU simulation cannot be seen by the driver in either direct vision though windows or indirect vision through mirrors

This equates to a maximum average VRU distance of 2m to the front of the cab, 4.5m to the passenger side and 0.6m to the driver's side. A Vehicle was identified which had VRUs distances at these values or better. The volumetric performance of this vehicle defined the minimum volumetric requirement for the direct vision standard, with a total visible volume of 10.4m^3

Discussion and Conclusions

The methodology that has been defined to quantify volumetric performance with a test that shows the real-world implications has been successful. There is a high correlation between the two methods of measuring direct vision. The CAD based approach allows the effect of design changes on direct vision to be quantified in an accurate manner and the VRU distance measure provides context for what a volume score means. As can be seen in Figure 4, the majority of the vehicles in the sample are unable to meet the minimum requirement 10.4m^3. This means that VRUs can be obscured from direct vision at a distance beyond the mirror cover zone, creating a blind spot. The original announcement of the Direct Vision Standard by the London Mayor included a policy of banning HGV designs which did not meet the minimum direct vision requirement. However, the poor performance of the fleet was unexpected and an impact assessment of banning such a large proportion of the vehicle fleet showed that the economic impact would be too severe. Therefore, TfL defined a system of safety measures which would need to be fitted to any vehicle not meeting the minimum requirement. Interest in the DVS increased from cities in Europe and the USA where HGV-VRU accidents were also increasing. The research team supported TfL's lobbying efforts of the European Parliament, which added to the calls for a DVS for all HGVs. This policy was adopted by the EU in 2019 (EU, 2019), and subsequently the research team has been supporting the development of a UNECE standard for all HGVs in Europe. The UNECE DVS adopts the methodology defined by the authors in its entirety, with modifications that increase the minimum direct vision requirements and specific minimum to each side of the vehicle. This new standard will finally be adopted in November of 2022. The minimum requirements for direct vision will be applied to all vehicles from 2026, and all vehicles by 2029. A substantial proportion of the European cab designs will need to be redesigned. An impact assessment funded by the European Commission (EC, 2015) states that the DVS should save 550 lives per year in Europe by reducing the size of HGV blind spots.

Acknowledgments

The research discussed in the paper has been funded by the UK Department for Transport, Transport for London, and the Road Safety Trust.

References

Cook, S., Summerskill, S., Marshall. R., ... et al., 2011. The development of improvements to drivers' direct and indirect vision from vehicles - phase 2. Report for Department for Transport DfT TTS Project Ref: S0906 / V8. Loughborough: Loughborough University and MIRA Ltd. https://hdl.handle.net/2134/8873

Talbot, R., Reed, S., Barnes, J., Thomas, P., Christie, N. (2014) Pedal Cyclist Fatalities in London: Analysis of Police Collision Files (2007-2011). Research Report. Transport Safety Research Centre, Loughborough University, Centre for Transport Studies, University College London. URL: https://dspace.lboro.ac.uk/2134/16487 (2014).

EC (2015) Benefit and feasibility of a range of new technologies and unregulated measures in the field of vehicle occupant safety and protection of vulnerable road users. Publications office of the European Union. https://op.europa.eu/en/publication-detail/-/publication/47beb77e-b33e-44c8-b5ed-505acd6e76c0/

EU (2019). Regulation (EU) 2019/2144 of the European Parliament and of the Council. Official Journal of the European Union. Article 9 section 5.

Reed, M.P. (2005). Development of a New Eyellipse and Seating Accommodation Model for Trucks and Buses. Technical Report UMTRI-2005-30. University of Michigan Transportation Research Institute, Ann Arbor, Michigan.

Peebles, L. and Norris, B. 1998 Adultdata. The handbook of adult anthropometric and strength measurements - Data for design safety. (London: Department of Trade and Industry), DTI publication 2917/3k/6/98/NP URN 98/736.

Summerskill, S. ... et al, (2015a). The use of volumetric projections in Digital Human Modelling software for the identification of large goods vehicle blind spots. Applied Ergonomics, 53, pt. A, pp.267-280. DOI: 10.1016/j.apergo.2015.10.013

Summerskill, S. Marshall, R; Paterson, A; Reed, S (2015b): Understanding direct and indirect driver vision in heavy goods vehicles. Report. https://hdl.handle.net/2134/21028

Summerskill, S. ... et al, (2019a). The definition, production and validation of the direct vision standard (DVS) for HGVS. Final Report for TfL review. Version 1.1. London: Transport for London. Report https://hdl.handle.net/2134/36622

Summerskill S, Marshall R, Paterson A, Eland A (2019b). The Development of a Direct Vision Standard for Trucks in London Using a Volumetric Approach. International Conference on Applied Human Factors and Ergonomics, Washington D.C., DC, USA, 24 Jul 2019-28 Jul 2019. Advances in Intelligent Systems and Computing. 964: 440-452. 06 Jun 2019

UNECE (2015). UNECE Regulation 46. Uniform Provisions for Devices for Indirect Vision and of Motor. Vehicles with Regard to the Installation of these Devices. UN ECE Vehicle Regulations.

Mole, C.D., Wilkie, R.M.G., (2017). Looking forward to safer HGVs: The impact of mirrors on driver reaction times. Accident Analysis and Prevention 107, 173–185. doi:10.1016/j.aap.2017.07.027

Overview of software and file exchange formats in 3D and 4D body shape scanning

Sofia Scataglini and Steven Truijen
University of Antwerp, Belgium

Abstract

3D body scanning is well known in various application areas such as medicine, automotive, sports, clothing, product design and gaming. These models have some limitations in that they are unable to capture dynamic poses that can provide more information about real-time tasks and interactions with a real-life object, machine or environment. As a result, in the literature, to provide a more realistic movement of static shape models, researchers provided an idea of attribute kinematic capturing or "skeletal animation" as Biovision Hierarchy (BVH) file using a wearable inertial mocap system applied to a 3D statistical shape model, obtaining a "moving statistical shape" using exchange format in open source software like Blender. But in this case, the attribution was not a perfect attribution of the real-time capturing of a dynamic 3D body shape in real-time Nowadays, 4D body scanning can perform 4D measurements in real-time of dynamic body shape without using any wearable inertial mocap system that can occlude the scanning surface and represent a comfortable solution without influencing the performance of the user. In addition, 3D and 4D can be used in open and closed source software using specific file exchange formats for modeling and animation or interaction and integration with other devices, e.g., synchronization with pressure mat and force platform. In particular, open-source software represents a more intuitive, fast and inexpensive platform for performing animation, modeling, and file exchange formats in a multidisciplinary approach. Based on the previous assumptions, in this study, we will provide an overview of open and closed source software along with file exchange formats in 3D and 4D body scanning, looking at the advantages and disadvantages of their use in different fields of applications. Future research will focus on studying the interoperability of data interchange formats utilizing 4D scanning technology, with an emphasis on developing and validating a methodology using a universal skeleton capable of representing and rigging a real population capture.

Keywords: body scanning, dynamic anthropometry, file exchange formats, DHM

Introduction

Digital anthropometry appears with the first 3D body scan device, arise in 1987 with the Loughborough Anthropometric Shadow Scanner (LASS), as an advanced solution to digitally measuring three dimensional body shape, substituting traditional anthropometry based on the identification of anatomical points

(landmarks) by palpation, which requires calipers or tape to take measurements (Brooke-Wavellet, Jones, West, 1994). Bartol et al. (2022) recently reviewed the body measurements using 3D scanning, focusing on describing the 3D scanning technologies, the body measurements, and their extraction and classification. While Heymsfield et al. (2018) presented a critical review of digital anthropometry, describing the techniques and the field of applications. However, from these reviews emerged the software used and the problematic issues related to the compatibility and interoperability of exchange data formats between software and a standard procedure of introducing or exporting them starting from survey databases. Indeed, the emergence of 3D body scanning technology around 2000 created the need to examine population variability between countries. The first survey appeared in 2000, entitled "CAESAR database", covering the USA (Cyberware) and part of Europe (NL and Italy, Vitus pro). This was followed by a survey from UK (Size UK, 2001-02, TC2), Japan (2004-10, Voxelan LPW-2000 Hamano engineering), France (2003-04, Vitus smart), Korea (Size Korea 2003-04, 2010, Cyberware and Hamamatsu), Romania (2007-09, Vitus Smart), Thailand (2007-2008, TC2), Spain (2007-2014, Vitus smart), Germany (2007-09, Vitus smart), India (2009-2010, Vitus smart), Brazil (2012, TC2), Belgium (Smart Fit, 2013, SYMCAD II TC2), Italy (2012-2013, Vitus pro), Portugal (2014, TC2), China (2018, Vitus smart), (Alemany, Ballester, Parilla, 2019). The databases use different body scanners and, consequently, different output data formats that are decided by the proprietary body scanning companies, limiting the interoperability. It appears that each body scanner tool is using a different data format such as: PLY, OBJ, WRL and STL, see Table 1.

Table 1. 3D body scanners (S), their light sources system (LS), and their data exchange formats (D).

S	Cyberware	Vitus Pro and Smart	TC^2	Hamamatsu Body Line	SYMCAD II TC^2	Voxelan LPW-2000 Hamano Engineering
LS	Laser	Laser	White light	Infrared light	White light	Laser
D	PLY	OBJ, STL	OBJ, STL	PLY	OBJ, STL, PLY	PLY

Consequently, it is necessary to study the interoperability of the data formats, especially when we are using the 3 dimensional body shape (DHM) file for importing and exporting in open and closed software programs (DHM tools) for successive elaboration. But in 2004, digital anthropometry was evolving with the evolution of the 3D scanning techniques (Werghi, 2007; Fan, Yu, & Hunter, 2004) that were able to map digitally the

3D geometry of the body surface in 4D scanning techniques (Liberadzki, Adamczyk, Witkowski, & Sitnik, 2018) where the geometry was evolving in time, adding a 4th dimension: time (Nowak & Sitnik, 2020). In 2004, 3dMD introduced the dynamic 4D system that captures the body in 1.5 milliseconds with dense markerless surface tracking (400 plus points), (John Tzou, Artner, Pona, Hold, Placheta, Kropatsch, Frey, 2014). While, in 2019, the Biomechanical Institute of Valencia introduced the 4D scanning device, Move4D, that delivers noise and artefact-free watertight dense mesh (99k triface) per frame (up to 180fps) with a spatial resolution of 1mm. One sequence's 3D models can be provided with point-to-point correspondence (50K landmarks) and rigged (23-joint skeleton), according to Parilla et al. (2019). 4D scanning technology with respect to optoelectronic systems is able to capture the movement without using any markers attached to the body, providing free natural movement with no contact, especially during COVID time. This possibility ensures maintaining distance and the deployment of less operators in the lab. In addition, the 4D scanning device can be synchronized with other biometrical signals without interfering with other optical sets, permitting the synchronization of 4D scanning technology with for example force plate signal for measuring postural control or gait, as it is possible in traditional standard optoelectronic motion capture systems. The processing software used in this technology is based on deep learning and a data-driven body model that includes shape, position, and soft-tissue deformation. The system exports PLY, OBJ, and FBX files, but not yet a BVH file. Furthermore, studying 3D body shape, soft tissue deformation, and texture in motion using high-resolution photogrammetric cameras opens up a new pathway into human-system and environmental interaction for personalization and customization in a variety of fields of application, including medicine, sport, clothing, automotive, and product design. In this scanning evolution, we are passing from using 3D scanning for animating DHM during different activities (functional measures) to capturing measurements during movement (dynamic measures), (Gupta, 2014). In both situations, we are reproducing a movement that requires additional data formats such as FBX files as in the case of the MOVE 4D device to track the vertices along the motion frames or rigging as association of the skeleton (bones) animation of an OBJ file using motions described in a BVH file that comes from an external device as an inertial mocap wearable system integrated into open source software (Scataglini, Danckaers, Haelterman, Huysmans, & Sijbers, J., 2018). According to the previous assumptions, the authors present an overview of exchange data formats in 3D and 4D scanning, considering open and closed software for DHM simulations.

Methods and Results

Data formats

Data formats can contain geometry, or texture and material information, a scene, rigging for animation, and encoding for animation. In this review we are selecting data formats that are used in 3D and 4D body scanners, such as OBJ, PLY, STL, FBX, and BVH (McHenry & Bajcsy, 2008). The OBJ (Wavefront Object) is an open file format that contains the geometry, specifically, the vertex position, the UV positions of each texture coordinate vertex, vertex normals, and the faces that make up each polygon, expressed as a list of vertices and texture vertices. By default, vertices are kept in counter-clockwise order, making explicit specification of face normals unnecessary. Although OBJ coordinates lack units, OBJ files can include scale information in a human-readable comment line. While the Polygon file format (PLY), also known as Stanford Triangle Format, contains three-dimensional data from the scanner that is described as a group of polygons. However, the PLY format can be used to specify color, the specification's core element list does not include capabilities for describing material properties, shading, or the usage of images to define surface appearance. The STL file is a file format known as "standard triangle language or standard tessellation language" that is used more for 4D prototyping, 3D printing, and computer-aided design (CAD). The STL represents the surface of objects as a mesh composed completely of triangles, which is only sufficient for elementary geometry. A higher model resolution necessitates a bigger number of triangles, increasing the file size nearly tenfold. While OBJ contains several polygons in a single file and allows for exact surface encoding. Instead of facet forms, surfaces can instead be specified by Non-Uniform Rational Basis Splines (NURBS) patches, resulting in a considerably smoother and more realistic depiction. Nevertheless, this comes at the expense of bigger file sizes. OBJ, on the other hand, comprises several polygons in a single file and enables precise surface encoding. Surfaces can be described by NURBS patches rather than facet forms, resulting in a much smoother and more realistic representation. This, however, comes at the expense of larger file sizes. While its FBX (Filmbox) format comprises geometry, animation, and scenes. Although the FBX file format is proprietary, the format definition is available in the FBX Extensions SDK, which includes header files for FBX readers and writers (Peters, Wischniewski, Paul, 2019). Regarding the motion data, Biovision Hierarchical Data (BVH file) developed by motion capturing company Biovision contains two parts: one that describes the hierarchy and initial pose of a skeleton and a second part with motion data. In this case, the skeleton that is used for rigging and animation comes from devices such as wearable inertial mocap systems that have the number of joints that are configured by the company itself. It means that it can differ from company to company in the number of joints of a skeleton of a wearable mocap system, affecting not only the quality of the rigging and animation but also the compatibility, (Paul & Scataglini, 2019).

Open and closed source software for animating the 3D shapes of digital humans

In this section, we are collecting all the software open source (OA) and not open source (N-OA) with relative data formats that are used for elaborating body shape data for different purposes in different fields of application.

Table 2. Open (OA) and closed source software (N-OA), their website and exchange data format (D)

Name	**Website**	**(OA) and (N-OA)**	**D**
3ds Max	https://www.autodesk.be/	N-OA	STL, OBJ
Blender	https://www.blender.org/	OA	FBX, OBJ, PLY, STL
Cinema 4D	https://www.maxon.net/en/cinema-4d	N-OA	FBX, OBJ, STL
Clara.io	https://clara.io/	OA	OBJ, PLY, STL, BVH
Daz Studio	https://www.daz3d.com/daz_studio	OA	OBJ, FBX
IClone7	https://www.reallusion.com/iclone/	N-OA	BVH, FBX, OBJ
Maya	https://www.autodesk.fr/products/maya/	N-OA	OBJ, STL
Unity	https://store.unity.com/	N-OA	FBX, OBJ

Importing different data format and 4D scanning in Clara.io

In order to test the interoperability of the data formats coming from 4D scanning, an FBX file representing a subject that is walking was imported into Clara.io open software. The file shows only the rigged 23 joints skeleton but not the body mesh. Therefore, to understand the interoperability of BVH file, we decided to import the BVH file of wearable motion capturing system as Yost Labs (17 joints skeleton) and Xsens (22 joints skeleton) into Clara.io, see Figure

1. All the skeletons can be used for rigging and animation of body shape, but one of them comes from a 4D scanner (MOVE 4D, IBV, Valencia). As a result, we can see that a universal skeleton that is used for motion capturing does not exist.

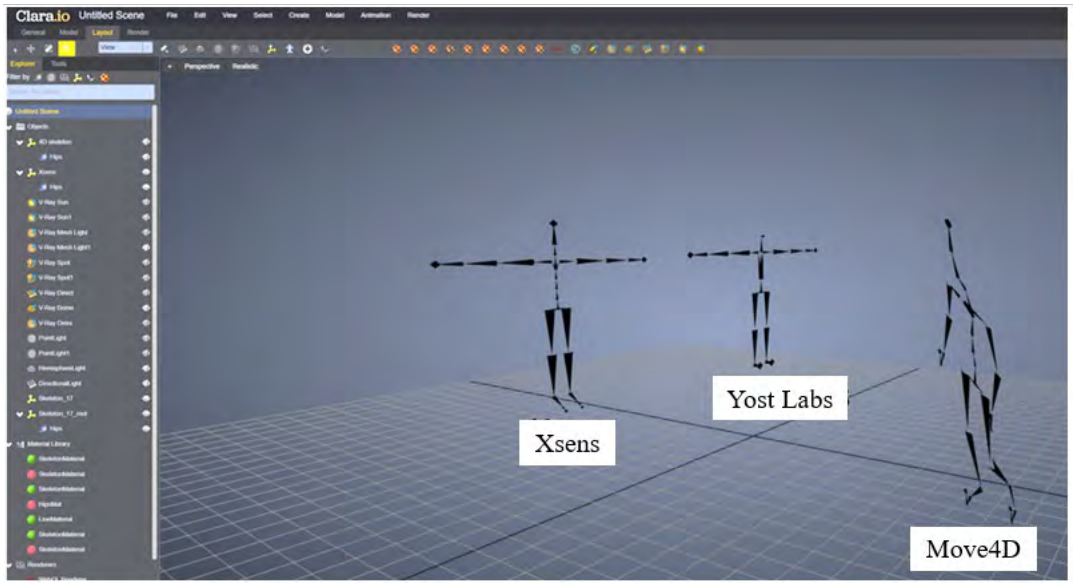

Figure 1. Importing of two BVH files coming from Xsens and Yost Labs wearable mocap systems and a FBX file from 4D scanning for Move4D in Clara.io.

Discussion and Conclusions

In marker-based movement analysis, markers are positioned on the body for the estimation of the joint positions and, consequently, the movement. In 4D scanning, without using any markers, we can identify the vertex of the homologous mesh (Karoui, M.F., Kuebler, T. (2019) that represents the same position as a marker-based movement analysis system to identify and calculate the joint positions (Faisal, Majumder, Mondal, Cowan, Naseh, & Deen, 2019). If we compute the structure of the skeleton using the kinematic approach with the vertex of the homologous anatomical points, the joints that we obtain are different from the joints that are used in the rigging. As a consequence, we have two skeletons that have the same structure of bones and joints but the position is different. The animation obtained with the traditional optoelectronic system respects the animation obtained using the inertial measurement system, which is different. The two models are obtained in different ways: one is based on the markers positioned on the body to identify the structure, while the other is based on the inertial sensors positioned in different locations to animate the mesh. Accordingly, it is necessary to have a universal skeleton (Wu & Cavanagh, 1995) that can be used internally for the rigging and externally from the vertices of the 3D mesh that communicate in a data format

such as the BVH file. Therefore, in DHM, one of the problems that we are encountering with the introduction of the 4D scanning technologies is not only related to data formats but also to skeleton formats. In inertial wearable measurement systems such as Xsens, the positions of anatomical landmarks are not measured directly as in optical mocap systems (Roetenberg, Luinge & Slycke, 2009), but calculated using the measured segment kinematics in combination with the anatomical model (Mavor, Ross, Clouthier, Karakolis, & Graham, 2020). Sfalcin et al., 2019 compared an optical system with two inertial full mocap measurement systems (Xsens and Perception Neuron) using Jack ™ found errors in joint kinematics. The Xsens system reduced this error. However, the authors suggest using optoelectronic traditional systems for their accuracy respecting the inertial measurement units, especially when the animation is used for ergonomics assessments. Indeed, if we are animating a static file, for example, in Blender, we are losing the potential of the scanner that is capturing the external 3D shape in each frame of the movement. If we are comparing the same frame animated with the rigging in Blender with a 4D scan, then we can see that the surface of the body is different. The solution should be to use exchange data that can combine the rigging animation that is more "artistic" with a real scan using 3D in a real way. Scataglini et al. (2019) animated a static mesh from the CAESAR database in Blender using a BVH file obtained from the inertial measurement mocap system Xsens without using an optoelectronic system. However, no comparison in accuracy of the animation using the rigging from Xsens and optoelectronic systems was studied, representing a limitation. As a result, future research will focus on studying the interoperability of data interchange formats utilizing 4D scanning technology, with an emphasis on developing and validating a methodology using a universal skeleton capable of representing and rigging a real population capture.

References

Alemany, S., Uriel, J., Ballester, A., & Parrilla, E. (2019). Three-dimensional body shape modeling and posturography. DHM and Posturography, 441–457. doi:10.1016/b978-0-12-816713-7.00032-5.

Bartol, K., Bojanić, D., Petković, T., Peharec, S., & Pribanić, T. (2022). Linear Regression vs. Deep Learning: A Simple Yet Effective Baseline for Human Body Measurement. Sensors (Basel, Switzerland), 22(5), 1885. https://doi.org/10.3390/s22051885

Brooke-Wavell, K., Jones, P. R., & West, G. M. (1994). Reliability and repeatability of 3-D body scanner (LASS) measurements compared to anthropometry. Annals of human biology, 21(6), 571–577. https://doi.org/10.1080/03014469400003572

Roetenberg, D., Luinge, H., & Slycke, P. (2009). Xsens MVN: Full 6DOF human motion tracking using miniature inertial sensors. Xsens Motion Technologies BV, Tech. Rep, 1, 1-7.

Faisal, A. I., Majumder, S., Mondal, T., Cowan, D., Naseh, S., & Deen, M. J. (2019). Monitoring Methods of Human Body Joints: State-of-the-Art and Research Challenges. Sensors, 19(11), 2629. MDPI AG. Retrieved from http://dx.doi.org/10.3390/s19112629

Fan, J., Yu, W., & Hunter, L. (2004). Clothing appearance and fit: Science and technology. Woodhead Publishing.

Gupta, D. (2014) 'Anthropometry and the design and production of apparel: an overview', in Gupta, D. and Zakaria, N. (eds) Anthropometry, Apparel Sizing and Design. Woodhead Publishing Series in Textiles, pp. 34–66. doi:10.1533/9780857096890.1.34.

Heymsfield, S. B., Bourgeois, B., Ng, B. K., Sommer, M. J., Li, X., & Shepherd, J. A. (2018). Digital anthropometry: a critical review. European journal of clinical nutrition, 72(5), 680–687. https://doi.org/10.1038/s41430-018-0145-7.

Karoui, M.F., Kuebler, T. (2019). Homologous Mesh Extraction via Monocular Systems. In: Duffy, V. (eds) Digital Human Modeling and Applications in Health, Safety, Ergonomics and Risk Management. Human Body and Motion. HCII 2019. Lecture Notes in Computer Science, vol 11581. Springer, Cham. https://doi-org.libproxy.viko.lt/10.1007/978-3-030-22216-1_14

Liberadzki, P., Adamczyk, M., Witkowski, M., & Sitnik, R. (2018). Structured-Light-Based System for Shape Measurement of the Human Body in Motion. Sensors, 18(9), 2827. MDPI AG. Retrieved from http://dx.doi.org/10.3390/s18092827

McHenry, K., & Bajcsy, P. (2008). An overview of 3d data content, file formats and viewers. National Center for Supercomputing Applications, 1205, 22.

Mavor, M. P., Ross, G. B., Clouthier, A. L., Karakolis, T., & Graham, R. B. (2020). Validation of an IMU Suit for Military-Based Tasks. Sensors (Basel, Switzerland), 20(15), 4280.https://doi.org/10.3390/s20154280

Nowak, M., & Sitnik, R. (2020). High-Detail Animation of Human Body Shape and Pose From High-Resolution 4D Scans Using Iterative Closest Point and Shape Maps. Applied Sciences, 10(21), 7535. doi:10.3390/app10217535.

Nowak, M., & Sitnik, R. (2020). High-Detail Animation of Human Body Shape and Pose From High-Resolution 4D Scans Using Iterative Closest Point and Shape Maps. Applied Sciences, 10(21), 7535. MDPI AG. Retrieved from http://dx.doi.org/10.3390/app10217535

Parilla E., Ballester A., Parra F., Ruescas A.V., Uriel J., Garrido D., Alemany S., MOVE 4D: Accurate High-Speed 3D Body Models in Motion", in Proc. of 3DBODY.TECH 2019 - 10th Int. Conf. and Exh. on 3D Body Scanning and Processing Technologies, Lugano, Switzerland, 22-23 Oct. 2019, pp. 30-32, doi:10.15221/19.030.

Paul, G., & Scataglini, S. (2019). Open-source software to create a kinematic model in digital human modeling. DHM and Posturography, 201–213. doi:10.1016/b978-0-12-816713-7.00017-9.

Peters, M., Wischniewski, S., & Paul, G. (2019). DHM data exchange protocols. DHM and Posturography, 663–670. doi:10.1016/b978-0-12-816713-7.00051-9.

Scataglini, S., Danckaers, F., Haelterman, R., Huysmans, T., & Sijbers, J. (2018). Moving Statistical Body Shape Models Using Blender. Proceedings of the 20th Congress of the International Ergonomics Association (IEA 2018), 28–38. doi:10.1007/978-3-319-96077-7_4.

Scataglini, S., Danckaers, F., Haelterman, R., Huysmans, T., Sijbers, J., & Andreoni, G. (2018). Using 3D Statistical Shape Models for Designing Smart Clothing. Proceedings of the 20th Congress of the International Ergonomics Association (IEA 2018), 18–27. doi:10.1007/978-3-319-96077-7_3.

Sfalcin, B., Ji, X., Gouw, A. de, Potvin, J., & Cort, J. (2019). Optical and inertial motion capture joint angle comparison using Jack™. Proceedings of the Human Factors and Ergonomics Society Annual Meeting, 63(1), 1137–1141. doi:10.1177/1071181319631153.

Wu, G., & Cavanagh, P. R. (1995). ISB recommendations for standardization in the reporting of kinematic data. Journal of biomechanics, 28(10), 1257-1262.

Werghi, N. (2007). Segmentation and Modeling of Full Human Body Shape From 3-D Scan Data: A Survey. IEEE Transactions on Systems, Man and Cybernetics, Part C (Applications and Reviews), 37(6), 1122–1136. doi:10.1109/tsmcc.2007.905808.

Tzou, C. H., Artner, N. M., Pona, I., Hold, A., Placheta, E., Kropatsch, W. G., & Frey, M. (2014). Comparison of three-dimensional surface-imaging systems. Journal of Plastic, Reconstructive & Aesthetic Surgery: JPRAS, 67(4), 489-497.

A methodology to obtain anthropometric measurements from 4D scans

Jordi Uriel, Ana Ruescas, Sofia Iranzo, Alfredo Ballester, Eduardo Parrilla, Alfredo Remón, and Sandra Alemany
Instituto de Biomecánica de Valencia, Spain

Abstract

Anthropometric data can be measured manually, through traditional methods, or obtained from a 3D body scan. In both cases, anthropometric dimensions are measured in a static posture (e.g. standing, sitting) however, people interact with products and environments in movement. Anthropometry applied to the ergonomic design of spaces (e.g. workplace, cockpits) includes measurements of reaches and considers dynamic anthropometry, that is the functional ranges of movements of the limbs. In the case of wearables, products that are worn in contact to the body (e.g. clothing, protective gear), the variability of the shape and dimensions during the moment is crucial information to achieve a good fitting, comfort and performance.

The appearance of new 4D body scanning technology enables the generation of digital human models in movement which reproduce the actual body shape in motion. Anthropometry in movement is a new category of body metrics that can be obtained from a sequence of scans. In this paper, the variability of eight anthropometric dimensions (neck to waist length, back length, arm length, thigh girth, crotch length, arm girth, waist girth and hip girth) is analyzed in different movements. For this purpose, ten subjects, with a variety of morphotypes, have been measured performing different movements using a 4D scanning system. The methodology to process the sequence of body scans is described to obtain automatically anatomical references of the anthropometric measurements along the movement. The results presented show the evolution of the eight anthropometric dimensions during the movement for the different subjects and movements. The mean ranges of variation are also reported and can reach values between 2-14 cm that will be relevant information for wearable design. Anthropometric dimensions in movement is a new body metric that require further research to establish new protocols, better anthropometric definitions and the creation of new datasets.

Keywords: Anthropometry, 4D body scanning, dynamic anthropometry, body scanning in motion

Introduction

One of the main applications that drives advances in anthropometry and body shape modeling is the industry of wearables, understood as a product that is worn in direct contact with the body (e.g. personal protective equipment, clothing, exoskeletons). For those fields, there is a demand of advanced technics of body measurement, such as new protocols and advanced scanners, with the aim of ensuring an appropriate fit and comfort and to optimize product performance. The use of traditional manual techniques, have been widely used to obtain heights, widths, lengths or circumferences through the definition of anatomical points in static postures described in several standards (*ISO 7250-1:2017*, 2017; ISO 8559, 1989). Also, the appearance of conventional 3D body scanners permitted new ways of capturing the shape of the body (Daanen & Ter Haar, 2013). However, the common use of this technology consisted basically of measurement extractors, and the potential was not exploited to their maximum (Ballester et al., 2014; Robinette, 2012). Several authors study new body measurements in extreme postures with the objective of achieving better fit and performance of protective and sports clothing (Braganca et al., 2016; Klepser et al., 2020b; Masaaki Mochimaru, 2010). Scanning in cycling postures for the study of aerodynamics (Garimella et al., 2019) or, scanning in driving postures as part of the design of car interiors (Reed et al., 2014).

In the field of ergonomics, there are numerous software with specific packages for ergonomic applications which uses anthropometry. The data are re-scaled according to stature or weight to build body models of different populations and morphotypes (Rajesh & Srinath, 2016; Bubb, 2019). With respect of the design of wearable products, the variability of shapes and dimensions of the body in the interaction with the devices, is an essential input to consider. However, the interaction of device-body in movement has not been solved, further study from a dynamic perspective is required.

Klepser et al., (2020a) defined the “functional measurements”, they analysed body measurements with respect to the body using a 3D body scanner. They found points of improvement in the reproducibility of the landmarks and in the limitations of the scanners. However, all the studies on the dynamic measurements have used 3D scans to capture static postures in extreme positions. The evolution of the dynamic measurements over time while the motions are performed has not yet been studied.

New 4D scanning technology is able to capture the human body surface in motion. Thus, more realistic and complex anthropometric data can be collected allowing its application in a CAD environment for simulating human-product interactions. These 4D systems provide an enormous amount of data that must be processed automatically before being applied in ergonomics.

In the present work, a 4D scanner was used to capture a sample of people performing a series of motions. Post-processing based on homologous meshes, enables the computation of body measurements over time.

The aim of this study is to create new anthropometric definitions for eight body measurements that can be computed from 3D body scans in movement. The new anthropometric definitions should consider that anatomical references (e.g. planes, axis, landmarks) vary during the movement. The new measurements have been analyzed in a limited preliminary study with subjects.

Methods

Five females with mean heights of 163±7cm, mean weights of 60±11kg, and a distribution of Body Mass Indexes (BMI) between 17 (underweight) and 27 (overweight) kg/m^2 to cover a variety morphotypes and five males with mean heights of 173±9cm, mean weights of 75±15kg, and BMI between 17 (underweight) and 33 (obesity) kg/m^2participated in the study.

Subjects were scanned in movement using MOVE4D. This scanner is composed of modules composed by a pair of IR cameras for capturing shape and an RGB camera for capturing texture. The scanning volume is of 3x2x3m with a total of 16 modules arranged in two rows. The total resolution is under 1mm with accuracies in the order of 0.1mm. An automatic template-fitting processing was applied to obtain homologous sequences of meshes with a common topology of 50 thousand vertices (Parrilla et al., 2019). The mesh is obtained from an A-Pose template and has point-to-point correspondence along the sequence of frames and across different subjects (Ballester et al., 2018)

Each subject was scanned performing four movements at the specified frequency rates: running (60 fps), vertical jump (60 fps), trunk flexion touching feet (30 fps), and a squat (30 fps). For all these sequences of movements we have obtained eight measurements. They are the distance through the back from neck to waist, the arm length from the acromion to the wrist, the thigh girth at 25%, 50% and 75% distance from the knee to the hip respectively, the total crotch length which goes from the back waist to the front waist passing through the crotch, the arm girth, the waist girth and the hip girth. So far, measurements are taken in a static A-Pose with little postural variation across subjects (Ballester et al., 2014; Trieb et al., 2013). And are defined using the ISO 7250-1 (*ISO 7250-1:2017*, 2017; ISO 8559, 1989)and ISO 8559 (ISO 8559, 1989) standards. This makes it possible to use planes with a normal in one of the reference axes. For example, the waist girth in a static pose is obtained by slicing the body mesh with a plane at waist point with a plane perpendicular to the y axis. This procedure is not possible in dynamic poses where the waist isn't aligned with the y axis. For example, the torso could be abducted to one side or tilted front or back, and using a plane perpendicular to the y axis would give undesirable results. Table 1 includes the strategies used for the definition of the selected measurements and Figure 1 shows the measurements over the A-Pose of two users together with the points used for the calculi. In general, lengths obtained over the

body surface can adopt the same definition for the standard A-pose and during the movement while girths should be redefined considering axis relative to the body segment.

Neck to waist length and total crotch length use the sagittal line of the human model to compute the respective measurements. This method of computing the measurements is inherently compatible with dynamic measurements because the sagittal line is well defined in any pose. Arm length measurement is computed by adding the measurement of two segments, one from the acromion to the elbow and another one from the elbow to the wrist. Each segment is computed by measuring the distance of the intersection of a plane and the human model surface from landmark to landmark. The orientation of these planes are obtained from the cross product of the vector joining the landmarks and the mean of the points' normals in the geodesic path between the landmarks. The definition of thigh girth and arm girth uses the orientation of the corresponding bone to create a perpendicular plane. Waist girth is computed in two segments that go from the left waist landmark to the right waist landmark, one segment goes through the front and the other one through the back. The orientation of the segment is computed as the plane that passes through left and right waist landmarks and a front landmark for the front segment, and similarly for the back segment. Finally, the hip girth is divided 5 segments. One for the back, and 4 segments for the front of the hip. This subdivision in the front of the hip is done so that when the legs reach the height of the hip, such as in a squat, the measurement doesn't go through the legs. All the above-mentioned measurements are computed using convex hull, except neck to waist and total crotch length.

Table 1. Definition of the anthropometric measurements.

Neck to waist length	Length of the sagittal semantic line from the neck to the waist.
Back length	Sum of sections from right acromion to seventh cervical vertebrae and from seventh cervical vertebrae to left acromion. The orientation of this segments is computed using the normals of the geodesic paths.
Arm length	Sum of section from acromion to elbow and from elbow to wrist. Orientation of the segments is computed with geodesic path point normals.
Thigh girth (25%, 50%, 75%)	Perimeter of the leg obtained at the corresponding percentage between the hip and knee joints with the orientation of the bone.
Total crotch length	Length of the sagittal semantic line from waist back to waist front passing through the crotch
Arm girth	Perimeter of the arm obtained in the midpoint of the acromion and the elbow with the orientation of the bone that goes from the shoulder to the elbow

Waist girth	Static definition: Perimeter at the height of the waist with horizontal orientation Dynamic definition: Sum of front and back section that go from left waist to right waist. The orientation of the front section is computed using the left and right waist points and a homologous point representing the front waist. The back section is analogous except it uses a homologous point representing the back waist.
Hip girth	Static definition: Perimeter at the height of the hip with horizontal orientation. Dynamic definition: Hip girth divided into segments, one for the back and 4 for the front. Orientation of the segments is computed with geodesic path point normals.

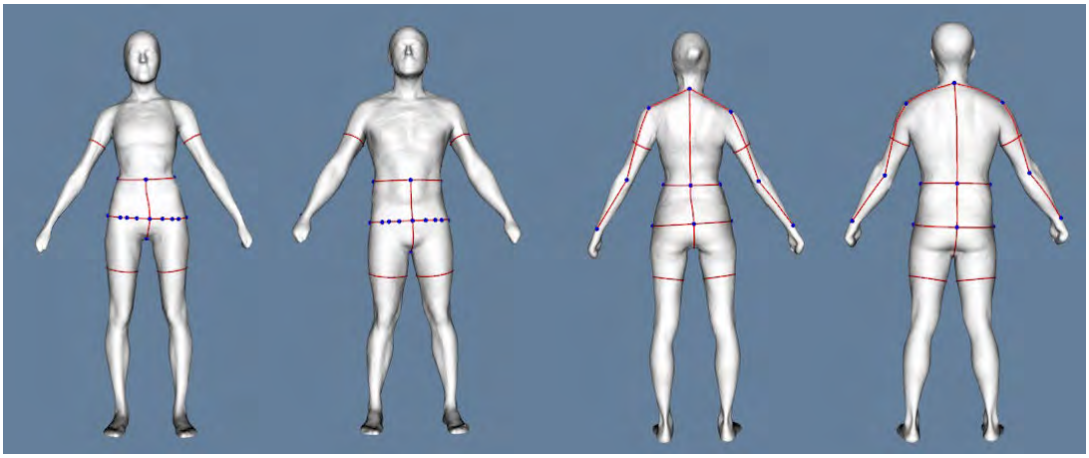

Figure 1. Surface without texture of the homologous meshes obtained with post-processing algorithms of two participants in A-Pose, front view on the left, back view on the right. Over the surface, blue points marking the points used in the definition of the 10 measurements, which appear in red.

Results

The evolution of each anthropometric measurement along the movement has been calculated in order to check if similar patterns can be observed among subjects. The patterns described by the measurements are in line of the movement. In order to illustrate this result, Figure 1 plots the measurements' evolution along the movements (frames) of a specific participant and selected motion.

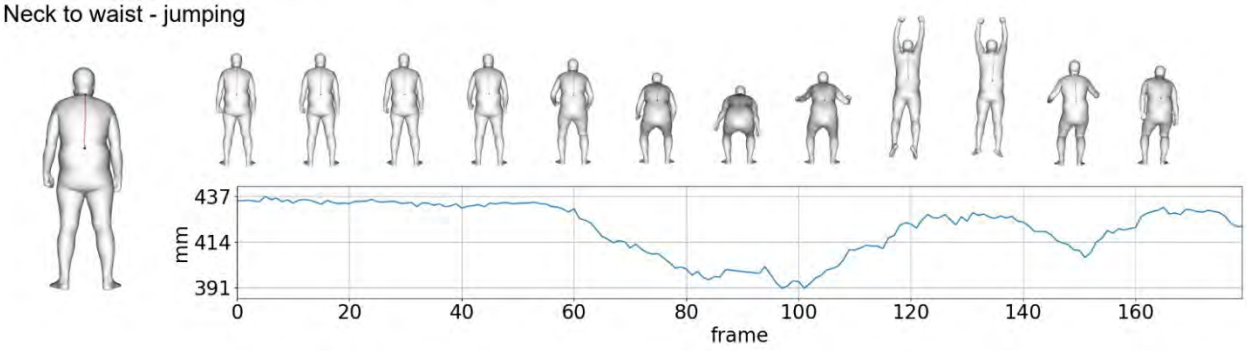

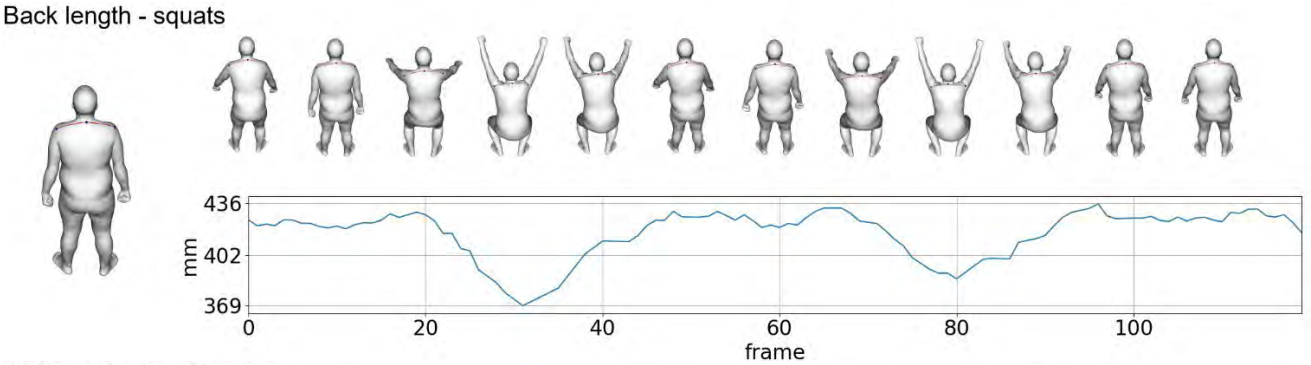
Back length - squats
436
402
369
mm
0
20
40
60
80
100
frame

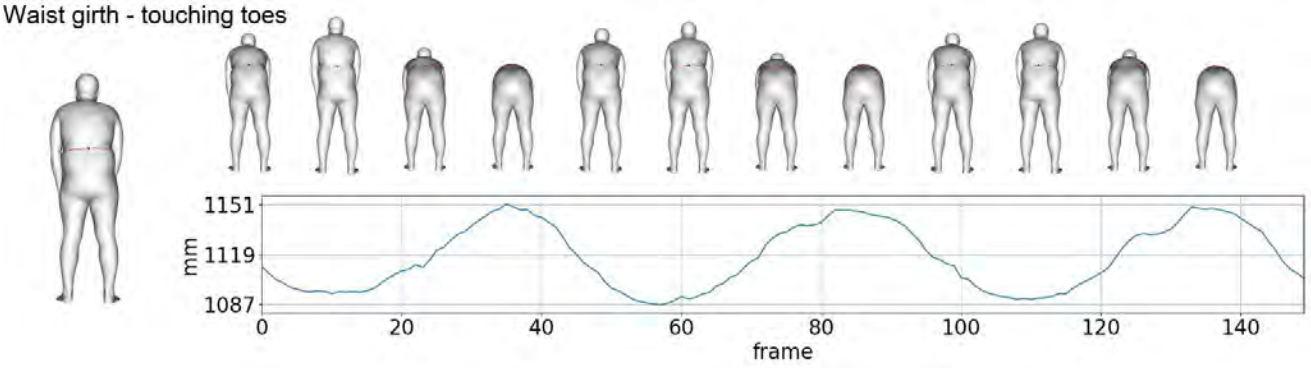
Waist girth - touching toes
1151
1119
1087
mm
0
20
40
60
80
100
120
140
frame

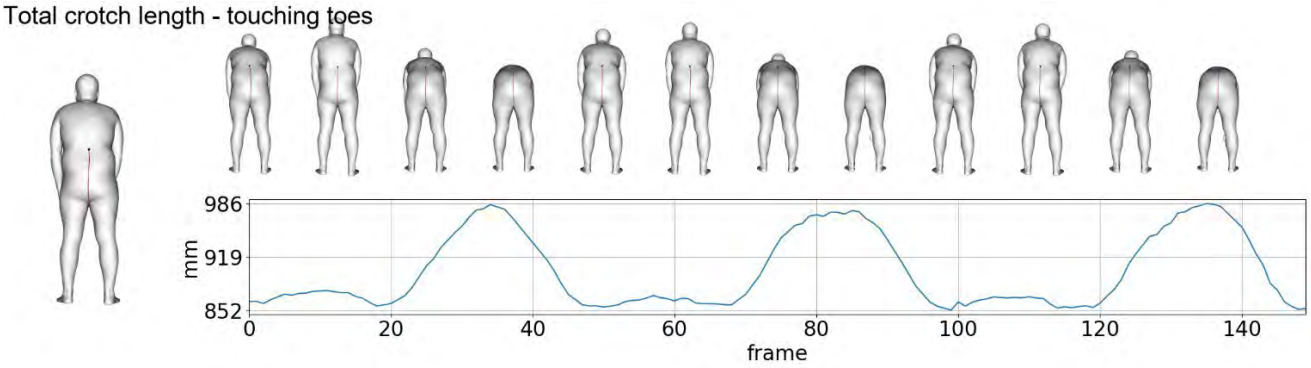
Total crotch length - touching toes
986
919
852
mm
0
20
40
60
80
100
120
140
frame

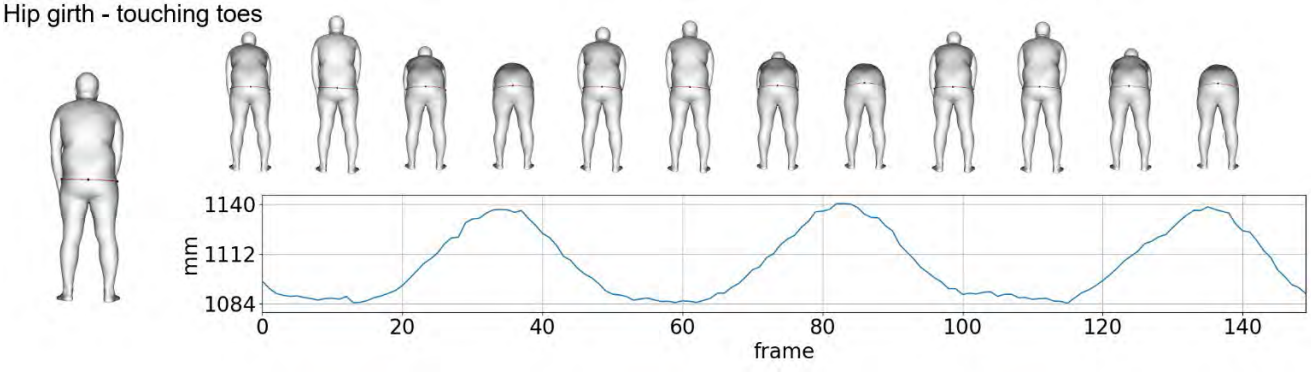
Hip girth - touching toes
1140
1112
1084
mm
0
20
40
60
80
100
120
140
frame

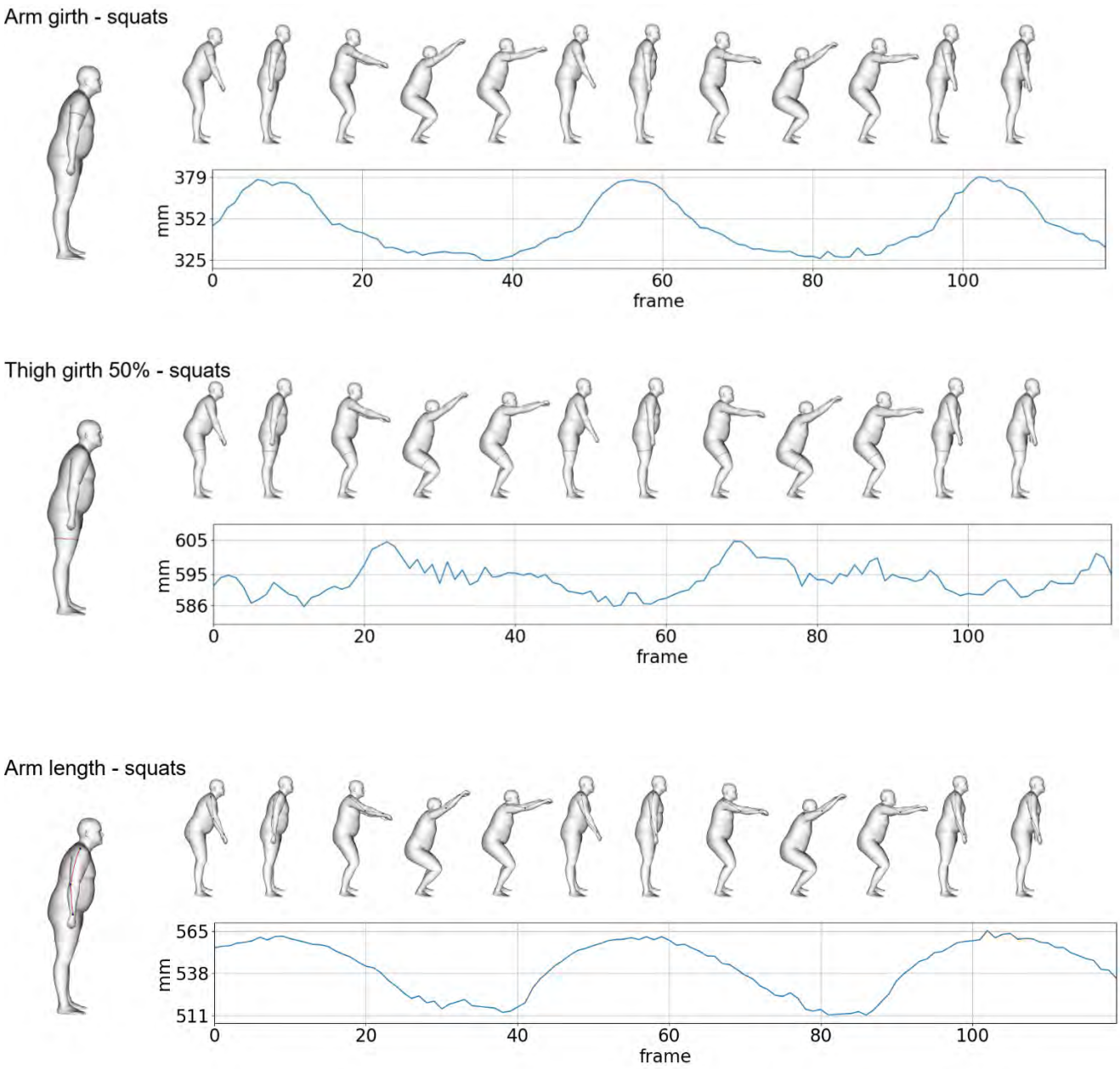

Figure 2. Plots of the measurements evolutions along the movements (frames) for one measurement and motion.

For quantifying the magnitude of the variation of each measurement throughout a motion, the range (maximum minus minimum value of length) was calculated. As an example, looking at last plot in Figure 1, the arm length of a given user varies from 511mm to 565mm while performing squats. So, the measurement's range is 54 mm, which expresses the total variation. These ranges were calculated for all motions and the mean and standard deviation of all users were obtained. In Figure 2 the plots of the four motions (running (a),jumping (b), squats (c), and touching toes (d)) mean ranges are shown.

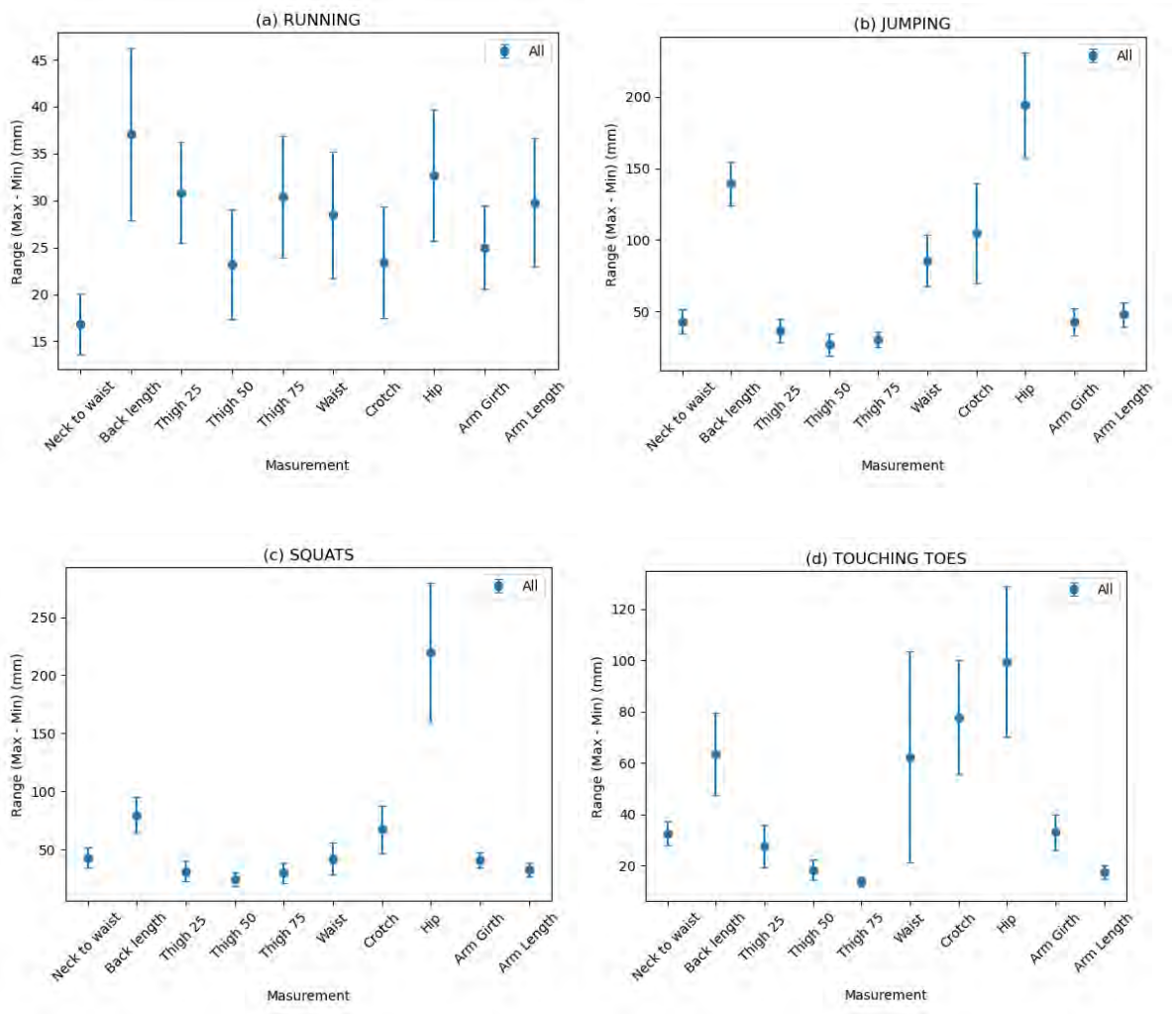

Figure 3. Mean range and standard deviations by motion: running (a), jumping (b), squats (c), and touching toes (d).

In Table 2, the mean values of ranges and their standard deviation for each motion included in Figure 2 are listed.

Table 2. Measurements mean values of ranges (maximum minus minimum) and their standard deviation by motion.

	RUNNING	JUMPING	SQUAT	TOUCHING TOES
	Mean ± St. Dev (mm)	Mean ± St. Dev (mm)	Mean ± St. Dev (mm)	Mean ± St. Dev (mm)
Neck to waist	16.8 ± 3.2	42.8 ± 8.4	42.6 ± 8.7	32.5 ± 4.5
Back length	37.1 ± 9.2	139.4 ± 15.2	79.6 ± 15.4	63.4 ± 16.1
Thigh 25	30.8 ± 5.4	36.5 ± 7.9	31.1 ± 8.7	27.5 ± 8.3
Thigh 50	23.2 ± 5.8	26.7 ± 7.7	24.2 ± 5.8	18.3 ± 4.1
Thigh 75	30.4 ± 6.5	30.5 ± 5.6	29.6 ± 8.8	13.7 ± 1.8
Waist	28.5 ± 6.7	85.4 ± 17.9	41.9 ± 13.7	62.4 ± 41.2
Crotch	23.4 ± 6.0	104.8 ± 35.0	67.2 ± 20.1	77.7 ± 22.3
Hip	32.7 ± 7.0	194.5 ± 36.7	219.7 ± 60.0	99.5 ± 29.5
Arm Girth	25.0 ± 4.4	42.6 ± 9.4	41.0 ± 6.5	33.0 ± 6.9
Arm Length	29.8 ± 6.8	48.0 ± 8.5	32.4 ± 5.7	17.5 ± 2.6

Discussion and Conclusions

When observing the graphs in Figure 1 it is appreciated that in the cyclic motions, such as squat, running, and touching toes, it is clearly observable the cyclic variation in the length of the measurement. The graphs are useful to visually get an idea of the pattern and the magnitude of contraction and expansion of each measurement. In the plot neck to waist, and thigh girth in Figure 1, it can be seen that the values fluctuate from one frame to the next. This is due to the current processing methodology based on template-fitting which is calculated frame by frame. In future work, these issues will be solved by introducing a new condition that considers the neighbour frames.

The results of mean ranges (Figure 2 and Table 2) express clear variations among the four movements due to the deformation produced on each body part. The values obtained of arm and thigh girths ranges are consistent with the expected variations, and show small dispersion among users. The three thigh girths, 25, 50, and 75 ranges vary among 2 to 4 cm depending on the motion performed. In the case of the arm girth and length, the values of ranges are similar to the low extremities. The measurement of neck to waist was one of the measurements obtained without relevant discrepancies, depending on the motion. For example, when running, the ranges were smaller, being around 2 cm, while in jumping this measurement reaches a highest range around 4 cm. In the case of back length, the differences are considerably higher, conditionally to the back motion in the different exercises, vary from 4 cm when running, where no great changes are found, to 14 cm in the case of jumping.

Besides, measurements related to the trunk, such as waist girth, hip girth, and crotch length presented some noteworthy limitations. The calculation of these measurements relies on the obtaining of certain contours that depend on the rotation axes of the spinal cord, which have many degrees of freedom and change during motion. Also, some of the motions interfere in the contours, as for example, the leg raising or opening may introduce errors in the calculation of the hip girth. In conclusion, the definition of both

measurements should be reconsidered. The crotch measurement also shows high ranges, from 2 cm in the case of running, to around 10 cm in the case of jumping, but no relevant problems were observed.

To compare the differences obtained with the data available in literature, only the study done by Klepser et al., (2020a) can approach the type of measurements calculated in this work. From the differences obtained the authors only "neck to hip" distance could be analogue to the present "neck to waist". The results, for one specific subject, shows up to 14 cm of maximum range compared to 3.25 ± 0.45 cm obtained in the present study. This discrepancy can be caused but the fact that author's measurement includes the low back part, and also, on the lack of a standard definition of the measurements in dynamic postures. Further investigation in the characterization of the deformation of the back vertical dimension is required.

Anthropometry has evolved from manual to digital measurements. Current standards based their definition of body measurements on anatomical landmarks, typically identified by palpation. The implementation of these anthropometric definitions in digital calculations from 3D body scans requires an interpretation of software developers that ends in lack of compatibility among studies. The new possibilities of computing anthropometry variation in movement capture with 4D body scanners requires additional specifications for the anthropometric definitions. Some studies are already been carried out, to investigate the validity of moving from surface markers to 4D scans (Ruescas Nicolau et al., 2022).

References related to relative axis and planes as for instance, those used in kinetic models may be a good contribution. Also, definitions that consider the possible interferences among body parts. In this context, it is relevant to advance in standardization of anthropometric definitions with a more digital perspective. Besides, measurements like the hip girth show a to high ranges and dispersion, by reason of artifacts in certain points of the movement. The occlusion of some parts of the body and the interference between parts, makes it inviable to work with a definition that was valid for static conditions. Such outcomes of the present study highlight the need of defining measurements relying on their application.

Finally, this work is presented as a first exploration in the measurement of the human body dimensions dynamically. Despite of the still existing limitations, the present methodologies open a new range of possibilities. With deeper investigation to better shaping the dynamic measurement definitions, the 4D capturing and post-processing based on homologous meshes offers new valuable data and opens a new range of possibilities in the design of wearables.

Acknowledgments

This research has been funded by IBERUS project: (CER-20211003), CERVERA Network financed by the Ministry of Science and Innovation through the Centre for Industrial Technological Development (CDTI), charged to the General State Budgets 2021 and the Recovery, Transformation and Resilience Plan. Research Activity (IMAMCA/2022/7) supported by Instituto Valenciano de Competitividad Empresarial (IVACE) and Valencian Regional Government (GVA) funding.

The authors gratefully acknowledge the computer resources at Artemisa, funded by the European Union ERDF and Comunitat Valenciana as well as the technical support provided by the Instituto de Física Corpuscular, IFIC (CSIC-UV).

References

Ballester, A., Parrilla, E., Uriel, J., Pierola, A., Alemany, S., Nacher, B., Gonzalez, J., & Gonzalez, J. C. (2014). 3D-based resources fostering the analysis, use, and exploitation of available body anthropometric data. *5th international conference on 3D body scanning technologies*.

Ballester, A., Pierola, A., Parrilla, E., Uriel, J., Ruescas, A. V., Perez, C., Dura, J. V., & Alemany, S. (2018). 3D Human Models from 1D, 2D and 3D Inputs: Reliability and Compatibility of Body Measurements. *Proceedings of 3DBODY.TECH 2018 - 9th International Conference and Exhibition on 3D Body Scanning and Processing Technologies, Lugano, Switzerland, 16-17 Oct. 2018*, 132-141. https://doi.org/10.15221/18.132

Braganca, S., Arezes, P., Carvalho, M., & Ashdown, S. (2016, junio). *Implications of dynamic working postures in garments' comfort*. https://pure.solent.ac.uk/en/publications/implications-of-dynamic-working-postures-in-garments-comfort

Bubb, H. (2019). Why do we need digital human models? En *DHM and Posturography* (pp. 7-32). Elsevier.

Daanen, H. A. M., & Ter Haar, F. B. (2013). 3D whole body scanners revisited. *Displays*, *34*(4), 270-275. https://doi.org/10.1016/j.displa.2013.08.011

Garimella, R., Beyers, K., Huysmans, T., & Verwulgen, S. (2019). Rigging and Re-posing a Human Model from Standing to Cycling Configuration. *International Conference on Applied Human Factors and Ergonomics*, 525-532.

ISO 7250-1:2017—Basic human body measurements for technological design -- Part 1: Body measurement definitions and landmarks, (2017). https://www.iso.org/standard/65246.html

ISO 8559:1989 Garment construction and anthropometric surveys—Body dimensions, ISO, 8559 (1989).

Klepser, A., Morlock, S., Loercher, C., & Schenk, A. (2020a). Functional measurements and mobility restriction (from 3D to 4D scanning). En *Anthropometry, Apparel Sizing and Design* (pp. 169-199). Elsevier. https://doi.org/10.1016/B978-0-08-102604-5.00007-X

Klepser, A., Morlock, S., Loercher, C., & Schenk, A. (2020b). 7—Functional measurements and mobility restriction (from 3D to 4D scanning). En N. Zakaria & D. Gupta (Eds.), *Anthropometry, Apparel Sizing and Design (Second Edition)* (pp. 169-199). Woodhead Publishing. https://doi.org/10.1016/B978-0-08-102604-5.00007-X

Masaaki Mochimaru, S.-I. P. (2010). Sports Garment Design. *Advances in Applied Digital Human Modeling*, *207*.

Parrilla, E., Ballester, A., Parra, P., Ruescas, A., Uriel, J., Garrido, D., & Alemany, S. (2019). MOVE 4D: Accurate High-Speed 3D Body Models in Motion. *Proc. of 3DBODY.TECH 2019*, 30-32. https://doi.org/doi:10.15221/19.030

Rajesh, R., & Srinath, R. (2016). Review of recent developments in ergonomic design and digital human models. *Ind Eng Manage*, *5*(186), 2169-0316.

Reed, M. P., Raschke, U., Tirumali, R., & Parkinson, M. B. (2014). Developing and implementing parametric human body shape models in ergonomics software. *Proceedings of the 3rd international digital human modeling conference, Tokyo*.

Robinette, K. M. (2012). Anthropometry for product design. *Handbook of human factors and ergonomics*, *4*, 330-346.

Ruescas Nicolau, A. V., De Rosario, H., Della-Vedova, F. B., Bernabé, E. P., Juan, M.-C., & López-Pascual, J. (2022). Accuracy of a 3D Temporal Scanning System for Gait Analysis: Comparative With a Marker-based Photogrammetry System. *Gait & Posture*. https://doi.org/10.1016/j.gaitpost.2022.07.001

Trieb, R., Ballester, A., Kartsounis, G., Alemany, S., Uriel, J., Hansen, G., Fourlic, F., SANGUINETTI, M., & VANGENABITH, M. (2013). EUROFIT—integration, homogenisation and extension of the scope of large 3D anthropometric data pools for product development. *4th International Conference and Exhibition on 3D Body Scanning Technologies, Long Beach, CA, USA*, 19-20.

Development of body shape data based digital human models for ergonomics simulations

Erik Brolin[1], Niclas Delfs[2], Martin Rebas[2], Tobias Karlsson[2], Lars Hanson[1] and Dan Högberg[1]

[1] *University of Skövde, School of Engineering Science, 541 28 Skövde, Sweden*

[2] *Fraunhofer-Chalmers Centre, Geometry and Motion Planning, 412 58 Gothenburg, Sweden*

Abstract

This paper presents the development of body shape data based digital human models, i.e. manikins, for ergonomics simulations. In Digital human modelling (DHM) tools it is important that the generated manikin models are accurate and representative for different body sizes and shapes as well as being able to scale and move during motion simulations. The developed DHM models described in this paper are based on body scan data from the CAESAR anthropometric survey. The described development process consists of six steps and includes alignment of body scans, fitting of template mesh through homologous body modelling, statistical prediction of body shape, joint centre prediction, adjustment of posture to T-pose and finally generation of relation between predicted mesh and manikin mesh. The implemented method can be used to create any type of manikin size that directly can be used in a simulation. To evaluate the results a comparison was done of original body scans and statistically predicted meshes generated in an intermediary step as well as the resulting DHM manikins. The accuracy of the statistically predicted meshes are relatively good even though differences can be seen, mostly related to postural differences and differences around smaller areas with distinct shapes. The biggest differences between the final manikin models and the original scans can be found in the shoulder and abdominal area, in addition to the significantly different initial posture that the manikin models have. To further improve and evaluate the generated manikin models additional body scan data sets that includes more diverse postures would be useful. DHM tool functionality could also be improved to enable evaluation of the accuracy of the generated manikin models, possibly resulting in DHM tools more compliant with standard documents. At the same time standard documents might need to be updated in some aspects to include more three-dimensional accuracy analysis.

Keywords: Anthropometry, 3D body scanning, body shape, statistical body model, joint centre.

Introduction

Digital human modelling (DHM) tools are useful when evaluating human-machine interaction and enables consideration of anthropometric diversity by creating human models, so called manikins, of different sizes and proportions. This functionality is a central feature when using DHM tools for product and production development to ensure that the design fits the intended proportion of the targeted population, from a physical perspective (Duffy, 2009; Scataglini & Paul, 2019). Therefore, it is important that these generated manikin models are accurate and representative for different body sizes and shapes, for both women and men, as well different age groups. To be compliant with standard documents functionality should exist in DHM tools that enables manikin measurement and data documentation (ISO, 2005; ISO, 2007). Since the first big body scanning based anthropometric survey CAESAR (Robinette et al., 2002) numerous additional surveys have been conducted around the world. Three-dimensional body scan data makes it possible to accurately recreate body shapes using statistical models with input data of more one-dimensional anthropometric data, e.g. stature, body weight and sitting height (Allen et al., 2003). Additional mathematical models exist that describes how joint centres are related to anthropometric landmarks in a three-dimensional space (Reed et al., 1999; Murphy et al., 2011; Hara et al., 2016). Using statistical body shape models in combination with joint centre equations makes it possible to generate manikin models with realistic and accurate body shapes as well as a biomechanical skeleton (Reed et al., 2014). This paper presents the development and implementation of body shape data based digital human models for ergonomics simulations in a demonstrator version of the Swedish DHM tool IPS IMMA (Intelligently Moving Manikins) (Högberg et al., 2016). The current version of the IPS IMMA manikin´s mesh model only scales in the length directions of each body part and not enough regarding circumference and depth measurements and therefore needs to be updated and improved.

Methods

The body shape data based digital human models described in this paper are based on body scan data from the CAESAR anthropometric survey. Specifically, the North American data set is used and the motivation behind this choice is that this data set has a large sample size and diversity considering the range of measurement values for the anthropometric one-dimensional data. The described development process includes 6 steps:

1. Rotate and translate landmark data as well as body scan point cloud
2. Homologous body modelling to fit body scan point cloud with template mesh
3. Statistical prediction of landmarks and mesh
4. Joint centre prediction based on landmarks and mesh
5. Adjust posture to T-pose

6. Align statistical mesh with clothed manikin mesh and calculate relation between meshes

In first step using data of landmark pairs, found on both sides of the mid sagittal plane, a suitable rotation angle around the vertical axes could be calculated. Based on landmarks known to be found on the mid sagittal plane, together with the known height of the measuring platform for each subject, a translation distance in three-dimensional space could be calculated. Through a MATLAB (The Math Works Inc., 2021) script these rotation angles and translation distances were used to align all body scan point clouds (1118 women and 1254 men) in a similar position and orientation (Figure 1).

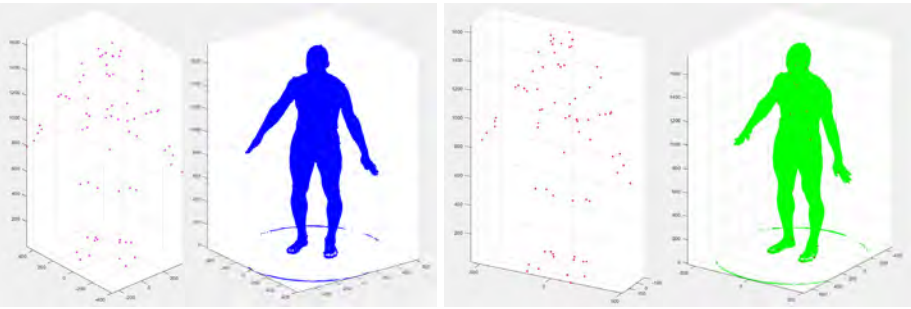

Figure 1. Landmarks and point cloud rotated and translated

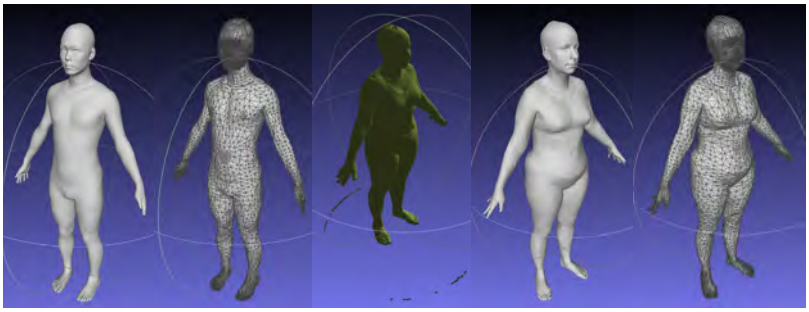

Figure 2. Template mesh (left) fitted to (right) body scan point cloud (middle)

In the second step, after the alignment had been done, a template mesh was fitted to all body scan point clouds using the software mHBM (Markerless Homologous Body Modelling) (Yamazaki et al., 2013) (Figure 2). Fitting of the template mesh was successful for most subjects but the sample size used in the statistical analysis was reduced to 849 women and 838 men. In the third step, the fitted template mesh and landmark data were used to generate statistical prediction of both landmark points and mesh vertices coordinates. The statistical prediction was done in a two-step procedure where 73 landmarks were first predicted based on 44 anthropometric measurements, including age. Principal component regression was used where the number of principal components used in the regression was 32 for the male data and 34 for the female data. The coordinates of the landmarks were adjusted to make pairs symmetrical and mid

points aligned to the mid sagittal plane. Then all mesh vertices were predicted based on the predicted landmark coordinates as well as age, stature and weight. The number of principal components used in the second regression was 116 for the male data and 120 for the female data. In the fourth step, based on the statistically predicted landmarks points and mesh vertices internal joint centre locations could be estimated using methods found in literature (Reed et al., 1999; Murphy et al., 2011; Hara et al., 2016). In the fifth step, the posture of the statistically predicted mesh, including landmarks and joint centre locations, was adjusted into a T-pose to be able to align it to the clothed IPS-IMMA manikin mesh (Figure 3). The T-pose adjustment was done by rotating landmark and mesh vertices around the glenohumeral, acromioclavicular, and sternoclavicular joints using estimation of how the movements in these joints contributes to a final T-pose (Inman et al., 1944). In the sixth step, the two meshes were aligned in Blender (Blender Online Community, 2018) (Figure 3) where a relationship was established where the ten closest mesh vertices of the statistical mesh were used to predict the position of each mesh vertex on the clothed IPS-IMMA mesh. Step 3-5 were initially realized through MATLAB (The Math Works Inc., 2021) scripts but then translated and implemented into the IPS-IMMA software using C++ (ISO/IEC (2014).

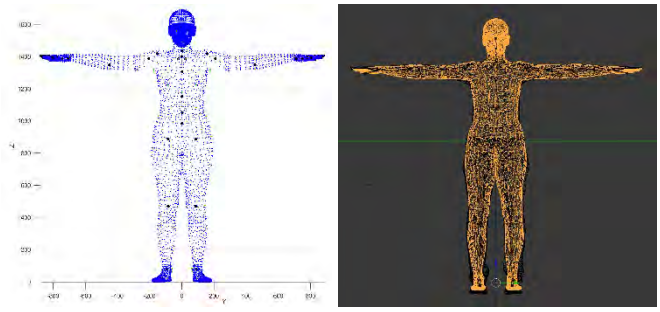

Figure 3. Template mesh adjusted to T-pose and aligned with IPS-IMMA manikin mesh in Blender.

Results

By using the functionality of predicting one-dimensional anthropometric data in IPS-IMMA, the implemented method can be used to create any type of manikin size that directly can be used in a simulation, Figure 4.

Figure 4. Body scan based IPS-IMMA manikins used in a simulation.

Table 1: Measurement from six subjects used for evaluation of generated models

Description	**F1 (S)**	**F2 (M)**	**F3 (L)**	**M1 (S)**	**M2 (M)**	**M3 (L)**
Sex	Female	Female	Female	Male	Male	Male
Age (years)	30	30	34	34	32	47
Body mass (kg)	50	68	89	68	85	123
Stature (mm)	1530	1634	1774	1641	1771	1901
Crotch height (mm)	701	766	824	709	806	828
Sitting height (mm)	810	858	915	885	926	953
Biacromial breadth (mm)	352	375	388	433	413	446
Bideltoid breadth (mm)	384	432	472	482	480	560
Hip breadth, sitting (mm)	375	397	425	350	380	444
Hand length (mm)	174	186	203	187	207	221
Foot length (mm)	232	244	260	240	265	282
Foot breadth (mm)	87	99	106	97	106	113
Head length (mm)	186	191	191	195	205	215
Head breadth (mm)	136	149	147	156	160	156
Face length (mm)	105	113	117	116	124	141
Buttock-knee length (mm)	551	567	627	570	613	691

To evaluate the validity of the generated digital human models based on standard documents it would be necessary to posture the manikins in predefined postures and provide coordinates of the landmarks (ISO, 2007). This is not possible in the current version of IPS-IMMA and therefore a comparison was done of the original body scan and the resulting IPS-IMMA manikin of six subjects (3 women and 3 men) with different body sizes, Table 1. In addition, the statistically predicted mesh generated in an intermediary step is also used in the comparison, Table 2. Since the IPS-IMMA manikin is dressed the comparison between the final manikins and the original body scans is done visually. The statistically predicted

intermediary meshes are evaluated with heatmap colours based on the distance differences between the predicted mesh and the original body scans of the selected test subjects.

Discussion and Conclusions

The results show that the method presented in this paper is able to produce manikin models with different body shapes that can be used in ergonomics simulations. The accuracy of the statistically predicted meshes are relatively good even though differences can be seen. These differences are mostly related to postural differences as the statistically predicted meshes have an average posture based on all included body scans and are centred and symmetrical on both sides of the mid-sagittal plane. Differences can also be seen regarding smaller areas with distinct shapes, i.e. muscles in the torso. Since the meshes are predicted with statistical regression, which predicts the most likely (average) body shape based on the input data, it is difficult to recreate finer details of a person's body shape. The final manikin models show a relatively good similarity with the original scans but there are some areas that needs to be improved. Biggest differences between the final manikin models and the original scans can be found in the shoulder and abdominal area. The manikin models also have an initial neutral posture that significantly differs from the postures in the original scans.

Table 2. Comparison of the original body scans, statistically predicted meshes and IPS-IMMA manikins

Subject	F1 (S)	F2 (M)	F3 (L)	M1 (S)	M2 (M)	M3 (L)
Original body scans	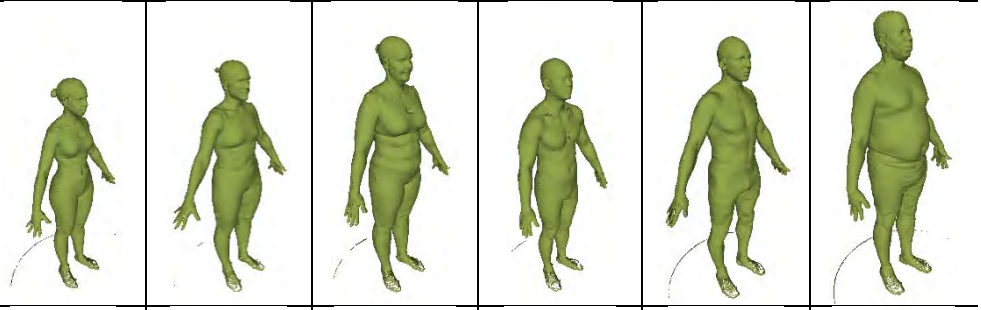					
Statistically predicted meshes*	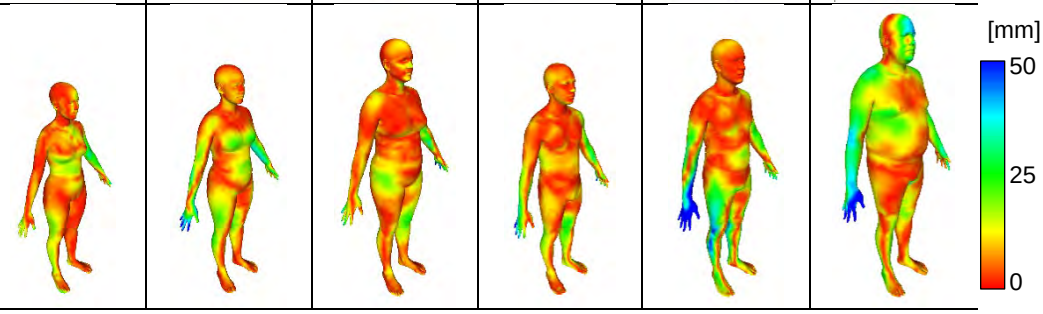					

* The colours on the statistically predicted meshes indicates distance differences with the original body scans according to the scale on the right.

A conclusion is that improvement potential exists, both related to the generation of the manikin models as well as functionality for evaluating the accuracy of the models. The CAESAR data set that the presented method is based on is a relatively old body scan survey and only provides data in one standing posture and two seated postures. Additional data sets that includes more diverse postures would be useful for improving and evaluating the manikin models, e.g. body scan data sets with seated posture to show and evaluate how soft tissue deforms when seated (Park, 2021). In addition, improved and usable tool functionality needs to be developed for evaluating the accuracy of generated manikin models, compared to measurements of real people that manikins are modelled after. This would make DHM tools more compliant with standard documents, i.e. *ISO 15536-2 – Ergonomics – Computer manikins and body templates – Part 2: Verification of functions and validation of dimensions for computer manikin systems* (ISO, 2007). To realise such functionality, it would be necessary to have an undressed manikin as the base mesh and include the predicted posture of the manikin when generating it in the DHM tool. As stated in Reed et al. (2014) the question what should be considered as an acceptably accuracy is still not answered as standard documents only provide guidance of how the accuracy should calculated and documented based on one-dimensional anthropometric measurements (ISO, 2007). It could be argued that such accuracy analysis also should include distance analysis of three-dimensional data from body scan point clouds and fitted template meshes compared to the body shape of manikin meshes, which indicates that the standard documents might need to be updated and improved in some aspects. The body shape data based digital human models will be continually developed and are intended to be fully implemented in the DHM tool IPS IMMA to be able to better represent the diversity of humans for the design of products and work environments.

Acknowledgments

This work has been made possible with support from the Knowledge Foundation and the associated INFINIT research environment at the University of Skived (projects: Synergy Virtual Ergonomics and ADOPTIVE), and with support from Vinnova in the VIVA project, and SAFER - Vehicle and Traffic

Safety Centre at Chalmers, Sweden, and by the participating organizations. This support is gratefully acknowledged.

References

Allen, B., Curless, B., & Popovic, Z. (2003). The space of human body shapes: reconstruction and parameterization from range scans. Proceedings of the 2003 International Conference on Computer Graphics and Interactive Techniques (SIGGRAPH). San Diego, CA.

Blender Online Community (2018). Blender - a 3D modelling and rendering package. Stichting Blender Foundation, Amsterdam. Retrieved from http://www.blender.org

Duffy, V.G. (2009). Handbook of Digital Human Modeling, Boca Raton, CRC Press.

Hara, R., McGinley, J., Briggs, C., Baker, R., & Sangeux, M. (2016). Predicting the location of the hip joint centres, impact of age group and sex. Scientific reports, 6(1), 1-9.

Högberg, D., Hanson, L., Bohlin, R., & Carlson, J.S. (2016). Creating and shaping the DHM tool IMMA for ergonomic product and production design. *International Journal of the Digital Human, 1*(2), 132-152.

Inman, V. T., Saunders, J. D. M., & Abbott, L. C. (1944). Observations on the function of the shoulder joint. JBJS, 26(1), 1-30.

ISO (2005). Ergonomics – Computer manikins and body templates – Part 1: General requirements (ISO 15536-1:2005). Geneva, Switzerland: International Organization for Standardization (ISO).

ISO (2007). Ergonomics – Computer manikins and body templates – Part 2: Verification of functions and validation of dimensions for computer manikin systems (ISO 15536-2:2007). Geneva, Switzerland: International Organization for Standardization (ISO).

ISO/IEC (2014). Programming languages — C++ (ISO/IEC 14882:2020). Geneva, Switzerland: International Organization for Standardization (ISO).

The Math Works, Inc. (2021). *MATLAB* (Version 2021b) [Computer software]. https://www.mathworks.com/

Murphy, A. J., Bull, A. M. J., & McGregor, A. H. (2011). Predicting the lumbosacral joint centre location from palpable anatomical landmarks. Proceedings of the Institution of Mechanical Engineers, Part H: Journal of Engineering in Medicine, 225(11), 1078-1083.

Park, B-K D., Jones, M.LH., Ebert, S.M., & Reed, M.P. (2021). A parametric modeling of adult body shape in a supported seated posture including effects of age. Ergonomics, 65:6, 795-803.

Reed, M.P., Raschke, U., Tirumali, R., & Parkinson, M.B. (2014). Developing and implementing parametric human body shape models in ergonomics software. In Proceedings of the 3rd international Digital Human Modeling symposium, Tokyo, May, 2014.

Robinette, K.M., Blackwell, S., Daanen, H., Boehmer, M., Fleming, S., Brill, T., Hoeferlin, D. & Burnsides, D. (2002). Civilian American and European surface anthropometry resource (CAESAR), final report: Air Force Research laboratory, Wright-Patterson AFB, OH, and Society of Automotive Engineers International, Warrendale, PA.

Scataglini, S., Paul, G. (eds.). (2019). DHM and Posturography. Academic Press.

Yamazaki, S., Kouchi, M., & Mochimaru, M. (2013). Markerless landmark localization on body shape scans by non-rigid model fitting. In Proceedings of the 2nd Digital Human Modeling symposium, Ann Arbor, USA, June 2013.

Digitizing human scalp shape through 3D scanning

Peng Li, Asbed Tashjian, and Matthew Hurley
US Army DEVCOM SC, United States

Abstract

This short paper presents a novel approach to digitize scalp shape with a combination of a scalp probing rig and 3D head scanning.

Keywords: Scalp shape, head shape modeling, 3D head scanning, head under hair

Introduction

Acquiring true scalp shape under hair, especially for females and other individuals with substantial hair, has been a challenging task for anthropologists, digital human modelers and product designers. It is not always a viable option to recruit bald headed subjects or require subjects shave their head. The most feasible way to capture scalp shape under the hair is through physical probing or digitizing. Using mechanical probes to obtain scalp shape under hair can be traced back to US Army's Personal Armor System for Ground Troops (PASGT) helmet project which used a physical probing device to read distance from the device's spherical surface to the scalp surface. Recently the US Air Force has collected female's scalp shape using a FARO Arm digitizer.

A probing process that uses physical probes or a digitizer typically requires a subject to sit still for a considerable time, which is difficult and uncomfortable and became a greater challenge under Covid safety restrictions. To improve the efficiency and acceptability, we developed a scalp probing rig with 54 adjustable probes that can be worn and fit by the subjects. After fitting all probes so they lightly touch the subject's scalp, a 3D head scanner was used to capture the image of the scalp probing rig in place. The final merged 3D image was imported to an in-house developed program to detect probes and calculate the coordinates of the probe tips. A scatter point set of the probe tips is then fed to a scalp shape reconstruction program (Morpheus-InfoSciTex) to recover the true scalp shape. This paper describes the design of the scalp shape rig, 3D scan processing methods to detect the probes' coordinates.

Methods

The scalp rig is a helmet-like shell that has 54 threaded holes to host probes. Each probe has a fixed length and consists of a cylinder section and a screw section. The end tip of the screw section is a ball shape that will contact to skin surface of the scalp. Figure 1 a) is the CAD rendering of the scalp rig assembly on a head model. The rig was 3D printed to make its weight light. When a test participant wears the scalp probe rig, each probe will be screwed to touch his/her scalp skin and the cylinder section of a probe is visible on the outside of the helmet shell. From a complete 3D image of the scalp probe rig, the coordinates of the tip point of the probes are derived from the coordinates of the end face of the cylinder section and the long axis of the probe, that is by adding an offset of the probe length to the end point of the cylinder shape in the direction defined by the probe's axis.

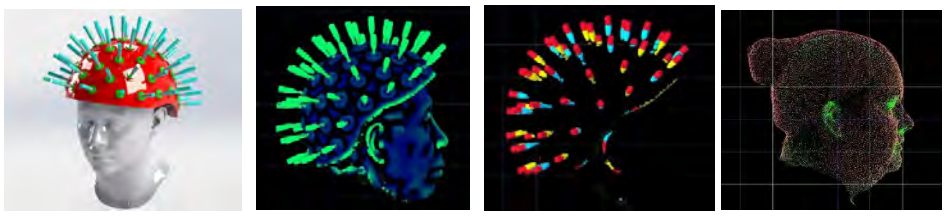

a) b) c) d)

Figure 1. The scalp rig and probe detection method: a) the scalp rig; b) mean curvature of the rig; c) detected candidate probe regions; d) reconstructed female scalp shape superimposed with head scan.

The detection of the probes is based on mean curvature of the 3D scan of the scalp rig. The probe shape has a high curvature compared to other parts of the scalp rig (figure 1b), which supports a mean curvature based segmentation algorithm. After the segmentation we applied the principal component decomposition to each candidate probe region to obtain their three principal axes. Three dimensional points of each region were projected to a plane defined by the centroid of the region and a normal vector of the shortest axis from three principal axes. In this way we can compute the standard deviation of the data from a fitted line as an estimator of the diameter of the candidate probes. Figure 1c shows detected candidate probes, where the end points of each probe region were computed. From derived probe coordinates on scalp surface a surface reconstruction program was used to generate the scalp shape. Figure 1d shows a superimposed a head scan with hair (red) to the reconstructed scalp surface (green).

Discussion and Conclusions

An evaluation of this rig has been conducted on a headform where scans with and without the scalp rig were taken. The mean distance between the computed probe tip points to the headform surface is -0.3073 mm (SD = 0.4886 mm). The accuracy of the detected scalp shape on human head may be affected by a

few factors such as the contact pressure of each probe to skin surface and individual's sensitivity to the probe pressure. The device has been used to collect female head shape under hair from local population.

Assessing Effects of Environmental Factors on Physical Workload during Motor-manual Timber Harvesting using Motion Capturing Data and Biomechanical Modeling

Oliver Brunner, Christopher Brandl, and Verena Nitsch
RWTH Aachen University, Germany

Abstract

Forestry workers are at significant risk to suffer from work-related musculoskeletal disorders (WMSD). Challenging environmental factors of the forest can have a significant impact on physical workload of motor-manual timber harvesting, which is already considered highly physical work. Conventional observation methods of risk assessment may underestimate specific environmental factors that influence forestry work. In order to determine whether such factors can increase the risk of WMSD and should therefore be integrated into standard risk assessment methods, a field study was conducted with N=10 forestry workers. The effects of environmental factors on physical workload were analyzed using motion capturing, force measures and biomechanical parameters for the activity of manually pulling a steel cable from a skidder winch over a distance of 20 meters in the forest. Type of execution, ground condition and soil slope as environmental factors were varied to investigate their effects on biomechanical parameters. Compressive force and shear force on the L5/S1 disc were calculated using a biomechanical approach. The results indicated that mean compressive and mean shear forces differed significantly depending on the environmental factors type of execution and soil slope. No significant influence of the factor ground condition was found. The combination of all environmental factors showed a significant interaction effect on mean compressive and shear forces. The average maximum values of compressive force did not exceed recommended load limits. However, the average maximum values of shear force exceeded recommended load limits repeatedly by more than 30%, which clearly indicates a health risk. The findings of this biomechanical approach were compared to an assessment with the Key Indicator Method for pushing and pulling, which is a conventional observational method for risk assessment. The comparison indicated that this conventional method might systematically underestimate the influence of some environmental factors in the forest and thus may also underestimate a potential health risk.

Keywords: biomechanics, compressive force, shear force, ergonomics, pulling, motor-manual timber harvesting

Introduction

Manual forestry work is a physically demanding job. Work-related musculoskeletal disorders (WMSD) and occupational accidents occur more frequently compared to other occupations (Federal Ministry of Food and Agriculture, 2017.) Back injuries or even herniated discs are the most commonly reported WMSD (Hoy et al., 2010). The health risk of manual forestry work is difficult to assess with conventional observation methods such as the Rapid Upper Limb Assessment (McAtamney & Corlett 1993) or the Ovako Working Posture Analysis System (Karhu et al., 1977). For these assessments, mainly the body posture and the load to be handled have to be analyzed (David, 2005). A general risk value is then determined to decide which, if any, measures need to be taken. While the Key Indicator Method, another conventional risk assessment method, additionally considers some environmental factors (Klussmann et al., 2010), these do not cover some of the specific conditions that are found in forestry work.

Environmental factors in the forest change dynamically even within a working day. They are much more complex and demanding than in the manufacturing industry, where conventional observation methods are widely applied. Some work operations, such as felling, may be sufficiently assessed using these methods, since the most influencing factors for an assessment of a potential health risk during lifting and holding tasks are the body posture and the load to be handled. Even though further analysis of hand-arm vibration may be required. The Key Indicator Method for pushing and pulling might be sufficient to analyze tasks related to motor-manual wood harvesting such as skidding since it considers some environmental factors in the assessment. However, the method is mainly focused on pushing and pulling of carriages or barrows and therefore not optimal for assessing skidding with the challenging environmental factors in the forest affecting this work activity.

There are very few studies that investigate physical workload during skidding. For example, Berendt et al. (2020) showed that metabolic strain is frequently high during this activity. Further investigations on whether this physical workload also causes back injuries or WMSD have, to the best of our knowledge, not yet been reported. Characteristic biomechanical parameters such as compressive force (CF) and shear force (SF) on the intervertebral discs can be used to analyze physical load on the back. These values, compared with recommended load limits, can provide an indication of health risk. Therefore, analysis of CF and SF may provide an indication of the causes of frequently occurring back injuries in manual forestry work.

The Key Indicator Method for pushing and pulling analyzes the environmental factors body posture, ground condition and soil slope. Berendt et al. (2020) identified an influence of soil slope on the metabolic strain during skidding. Laursen & Schibye (2002) could prove a correlation of CF and SF with ground condition in a study where containers were pulled on different ground surfaces. Both these studies indicate an

influence of the task execution on the physical workload. Therefore the environmental factors to be investigated were derived as ground condition, soil slope and type of execution, which mainly changes the body posture during the task.

Based on the reasoning outlined above, a study was designed to investigate a potential risk for WMSD during skidding. The following research questions were derived:

1. Are biomechanical parameters suitable for identifying a potential health risk during skidding?
2. Which environmental variables contribute towards increased WMSD risk during skidding?

Methods

Motion capturing, force measures and biomechanical parameters analyze effects of environmental factors on physical workload for the activity of manually pulling a steel cable from a skidder winch over a distance of 20 meters in the forest. Based on literature, a biomechanical approach calculates CF and SF on the L5/S1 intervertebral disc using motion capture data from a full-body IMU-system and the pulling force from a DTS force sensor.

Biomechanical Approach

The calculation of the biomechanical parameters CF and SF for this field study is based on Jäger's theory (Jäger & Luttmann, 1992; Jäger et al., 2001). The average and maximum CF and SF on the L5/S1 intervertebral disc are calculated. This intervertebral disc is considered, because the highest load is assumed to impact there as others indicate in their studies (Glitsch et al., 2004; Bütting et al., 2017). Input factors are the body weight of the subjects, the tensile force to be applied, force direction, body posture and body acceleration. For this evaluation a MATLAB tool was developed. First, raw data are transferred and processed in the form of a frequency adjustment. This is necessary because the force sensor measures with a much higher frequency than the IMU-sensors. Furthermore, necessary intermediate calculations for e.g. acceleration forces, moments or the angle and position of the disc L5/S1 but also dynamic factors for the considered work action, such as cable angle, are performed before the CF and SF can be calculated.

Study design

This study was designed to investigate whether different environmental factors affect measurably physical work load during skidding as indicated by biomechanical parameters and whether the risk indicated by these parameters is comparable to that determined by a standard risk assessment method, specifically the Key Indicator Method for pulling and pushing. Three environmental factors represent the independent

variables of this experiment and are summarized in Table 1. Figure 1 visualize the real conditions of the independent variables ground condition of this field experiment. The dependent variables were average compressive (CFmean) and shear forces (SFmean) on the L5/S1 disc. Each subject performed the work task eight times, i.e., in all combinations of the factor levels of the independent variables. The following hypotheses were formulated to analyze the influence of environmental factors on the physical workload of skidding:

- H01: Type of execution significantly affects the average CF and average SF on the L5/S1 disc.
- H02: Ground condition significantly affect the average CF and average SF on the L5/S1 disc.
- H03: Soil slope significantly affects the average CF and average SF on the L5/S1 disc.

The average maximum values of CF and SF are compared to recommended load limits to determine if a health risk can be identified (Gallagher & Marras, 2012; Jäger 2018). These findings are compared to risk assessment of the Key Indicator Method pushing and pulling.

Table 1: Independent variables and their factor levels for the conducted study

Independent variables	**Factor levels**
Type of execution	behind the back (A)
	over the shoulder (B)
Ground condition	without obstacles (C)
	with obstacles (D)
Soil slope	< 2% (1)
	> 4% (2)

Figure 1: Experimental conditions of the field study, left (without obstacles, < 2% soil slope), right (with obstacles < 2% soil slope)

Participants

The field study included 10 male professional foresters who were familiar with the work task. Exclusion criteria for participation in the study were having diagnosed back injuries. The mean age of participants was M=32.6 (SD=14.7). Their age ranged from 17 – 53 years.

Experimental setup

The study took place in the Arnsberg forest. Here, selected areas with different soil slope requirements offered a constant slope above 4% and a constant slope below 2%. For one of the lanes in each area, the ground was cleared as much as possible and on the other lanes the ground remained as it is. Each lane was measured to exactly 20 meters and marked with a start and finish line. The skidder was placed 1.5 meters in front of the start line to perform the respective measurements.

The measurement system consisted of a full body IMU-system with 14 myoMotion Reasearch Pro sensors and a DTS force sensor for data acquisition with MR3 myoResearch 3.14.76 software for control and synchronization. The skidder used was a Fendt Xylon 522 with a Pflanzelt fixed cable winche type 0308 and a PYTHON 6 R+F rope with 12 mm diameter.

Statistical Analysis

A MANOVA with repeated measures was calculated using SPSS version 28.0 software. Furthermore, descriptive statistics of maximum values for SF and CF were calculated and compared with recommended load limits from the literature. The results of the MANOVA were followed up with post-hoc ANOVA.

Results

The statistical assumptions for performing a MANOVA with repeated measures were tested and met (Field, 2013). Table 2 shows the results of the MANOVA. Statistically significant differences are shown in the combined dependent variables depending on type of execution, soil slope and the interaction of execution, ground conditions and soil slope. The univariate post-hoc analyses provide detailed information on the effects of the tested independent variables on the average SF and CF as Table 3 indicates. Post-hoc univariate ANOVA were conducted for every dependent variable. Results show statistically significant differences between the two factor levels of type of execution on CFmean and between the two factor levels of type of execution on SFmean. A statistically significant difference between the two factor levels of soil slope on CFmean was also indicated, but not on SFmean. Results yielded that there was a statistically significant difference between the combinations of type of execution,

ground condition and soil slope on CFmean, as well as on SFmean on CFmean. Thus, the results demonstrated that there was sufficient evidence to accept the hypothesis H01 and H03. Hypothesis H02 had to be rejected.

Table 2: Results of multivariate tests of the conducted analysis

Variable	Wilks Lambda	F	Sig.	Partial Eta Squared
Type of execution	.174	18.989	<.001	.826
Ground condition	.834	.796	.484	.166
Soil slope	.375	6.669	.020	.625
Type of execution * Ground condition	.742	1.392	.303	.258
Type of execution * Soil slope	.750	1.334	.316	.250
Ground condition * Soil slope	.819	.886	.449	.181
Type of execution * Ground condition * Soil slope	.470	4.515	.049	.530

Table 3: Risk scores of the conducted study according to the Key Indicator Method pushing and pulling

Environmental factors	**Key indicator risk score**
Type of execution (A) * Ground condition (D) * Soil slope (1)	42.5
Type of execution (A) * Ground condition (C) * Soil slope (1)	47.5
Type of execution (B) * Ground condition (D) * Soil slope (1)	50
Type of execution (B) * Ground condition (C) * Soil slope (1)	55
Type of execution (A) * Ground condition (D) * Soil slope (2)	55
Type of execution (A) * Ground condition (C) * Soil slope (2)	60
Type of execution (B) * Ground condition (D) * Soil slope (2)	62.5
Type of execution (B) * Ground condition (C) * Soil slope (2)	67.5

The average maximum value of the CF is 2628.44 N, the age- and gender-specific recommended load limit according to Jäger is 3100 N for 50-year-old men (Jäger, 2018). The average maximum value of SF is 922.51 N, according to Gallagher exceeding 700 N, is considered a potential health risk for repetitive shear loading (Gallagher & Marras, 2012). The absolute maximum values are 4050.69 N for CF and 1311.80 N for SF.

The results of the assessment of the same activities using the Key Indicator Method are shown in Table 4. A daily work duration of 20 minutes was assumed for the evaluation. The evaluation of the type of execution is for A = 5 and for B = 8 points, ground condition factor level C = 3 points as well as D = 1 point. Soil slope is rated as 1 = 0 points and 2 = 5 points. All other factors were evaluated with 11 points in sum and kept constant. The risk intervals are subdivided from low (< 20 points) to slightly increased (20 - 50 points) and substantially increased (50 - 100 points) to high (> 100 points).

Table 4: Results of univariate tests of the conducted analysis

Variable	Measure	F	Sig.	Partial Eta Squared
Type of execution	CFmean	41.235	<.001	0.821
	SFmean	24.407	<.001	0.731
Ground condition	CFmean	1.791	0.214	0.166
	SFmean	0.906	0.366	0.091
Soil slope	CFmean	12.664	0.006	0.585
	SFmean	3.903	0.08	0.302
Type of execution * Ground condition	CFmean	0.99	0.346	0.099
	SFmean	3.098	0.112	0.256
Type of execution * Soil slope	CFmean	2.907	0.122	0.244
	SFmean	2.853	0.125	0.241
Ground condition * Soil slope	CFmean	0.528	0.486	0.055
	SFmean	1.936	0.198	0.177
Type of execution * Ground condition * Soil slope	CFmean	6.163	0.035	0.406
	SFmean	10.112	0.011	0.529

Discussion and Conclusions

This field study illustrates that environmental factors impact physical workload during skidding using the biomechanical parameters of CF and SF. A significant influence of the type of execution and soil slope was identified. On the other hand, no influence of the ground condition was found, which is in contrast to the findings of Laursen & Schibye (2002), who could prove a correlation with the ground condition in a study in which waste containers had to be pushed and pulled over different soil surfaces. The combination of type of execution, ground condition, and soil slope also showed a significant effect on mean CF and SF. Hypotheses H01 and H03 were therefore confirmed.

The univariate analysis of execution types reveals significant differences for both, the mean CF and the mean SF. Type of execution mainly affects the body posture, which is not specified in work instructions and is in part strongly dependent on individual behavior. Posture has a high significance in the ergonomic evaluation of work activities. The soil slope shows significant differences in the univariate tests only for the CF. The presence of a slope therefore affects the vertical forces more than the horizontal forces in the body; Berendt et al. (2020) also mention this. Combining type of execution, ground condition and soil slope shows significant differences for CF and SF. Argubi-Wollesen et al. (2017) concludes in a literature review investigating pushing and pulling activities, that with challenging environmental factors, physical workload increases as well. Assumingly, biomechanical parameters increase in the same way. Compared to the recommended load limits the average maximum SF values indicate a potential health risk from the actions of the field study conducted. Average maximum CF values do not exceed recommended load limits, although some individual values did.

The analysis with conventional observational methods also shows an immense influence of the body posture on physical load. However, difference in physical load estimated via the Key Indicator Method are predominantly based on differences in factor levels of soil slope. Thus, the Key Indicator Method suggests similar relationships to those found in the presented field study. That being said, the Key Indicator Method is not adequately adapted to the environmental factors in the forest. The selection of objects to pull or push is almost exclusively limited to barrows and carriages. Correspondingly, the evaluation of ground condition also focuses on objects with rolls and friction resistance. Overall, the evaluation of the Key Indicator Method shows that the work situation is assessed with an increased risk at most and is partially assessed with an acceptable risk. The analysis of the average maximum SF showed that recommended load limits are exceeded repetitively by more than 30%. Although an assessment using the Key Indicator Method gives a good indication, a potential health risks could be underestimated with this method. Thus, this study indicates that biomechanical parameters can be used to identify potential

health risks in forestry work and to analyze them more accurately than with conventional observation methods. It also indicates that the Key Indicator Method might need to be adapted in order to account for more varied environmental conditions such as those found in forestry work.

Limitations occurring in this field study include the small sample size with 10 participants, resulting in reduced statistical power and less chances on finding existing correlations at a statistically significant level. The individual behavior of the subjects might also have had an influence on the measurement results. This is particularly evident in the analysis of the maximum values. The absolute maximum value of the CF is about 70% higher than the mean maximum value of the CF. With an increased number of participants, this difference might also reduce. Therefore, the mean maximum values had to be compared with recommended load limits. Finally, the significant 3-way interaction effect on CF and SF mean values indicate more complex effects that cannot be interpreted on the basis of this study and therefore need to be investigated in further research.

High physical workload, many occupational accidents and WMSD characterize manual forestry work. This paper presents a procedure for analyzing forest work using biomechanical parameters. The results indicate potential health risks in skidding, as the type of execution and soil slope were observed to have a significant influence on biomechanical parameters. The introduced applied biomechanical approach can identify these risks more accurately compared to traditional observational methods. These results contribute to a better identification of the physical workload in forestry and thus, in the long run, to the promotion of health at the workplace. In the future, further studies on different forest-specific conditions and with a larger number of participants should be carried out in order to gain further insights into health-related risks of forestry work.

Acknowledgments

This field study was conducted as part of the project KWH4.0 and funded by the European Regional Development Fund (ANBest-EFRE) within the funding program "Investments in Growth and Employment" (reference number EFRE-0200459).

References

1. Argubi-Wollesen, A., Wollesen, B., Leitner, M., & Mattes, K. (2017). Human body mechanics of pushing and pulling: analyzing the factors of task-related strain on the musculoskeletal system. Safety and Health at Work, 8(1), 11-18. https://doi.org/10.1016/j.shaw.2016.07.003

2. Berendt, F., Hoffmann, S., Jaeger, D., Prettin, S., & Schweier, J. (2020). Application of spiroergometry to determine work metabolism related strain in the course of cable work with a mini forestry crawler. International Journal of Forest Engineering, 31, 114 - 125. https://doi.org/10.1080/14942119.2020.1735198

3. Brütting, M., Hermanns, I., Nienhaus, A., & Ellegast, R. (2017). Muskel-Skelett-Belastungen beim Schieben und Ziehen von Krankenbetten und Rollstühlen. Zentralblatt für Arbeitsmedizin, Arbeitsschutz und Ergonomie, 67(2), 64-77. DOI:10.1007/s40664-016-0150-4

4. David, G. C. (2005). Ergonomic methods for assessing exposure to risk factors for work-related musculoskeletal disorders. Occupational Medicine, 55(3), 190-199. https://doi.org/10.1093/occmed/kqi082

5. Federal Ministry of Food and Agriculture (2017). Waldbericht der Bundesregierung 2017. Bonn.

6. Field, A. (2013). Discovering statistics using IBM SPSS statistics (4th Edition). Sage.

7. Gallagher, S., & Marras, W. S. (2012). Tolerance of the lumbar spine to shear: a review and recommended exposure limits. Clinical Biomechanics (Bristol, Avon), 27(10), 973–978. https://doi.org/10.1016/j.clinbiomech.2012.08.009

8. Glitsch, U., Ottersbach, H., Ellegast, R., Schaub, K. et al., "Musculo-Skeletal Loads on Flight Attendants when Pushing and Pulling Trolleys aboard Aircraft," SAE Technical Paper 2004-01-2131, 2004, https://doi.org/10.4271/2004-01-2131.

9. Hoy, D., March, L., Brooks, P., Blyth, F., Woolf, A., Bain, C., Williams, G., Smith, E., Vos, T., Barendregt, J., Murray, C., Burstein, R., & Buchbinder, R. (2014). The global burden of low back pain: estimates from the Global Burden of Disease 2010 study. Annals of the Rheumatic Diseases, 73(6), 968–974. https://doi.org/10.1136/annrheumdis-2013-204428

10. Jäger, M., & Luttmann, A. (1992). The load on the lumbar spine during asymmetrical bi-manual materials handling. Ergonomics, 35(7-8), 783–805. https://doi.org/10.1080/00140139208967363

11. Jäger, M., Luttmann, A., Göllner, R., & Laurig, W. (2001). "The Dortmunder"-Biomechanical Model for Quantification and Assessment of the Load on the Lumbar Spine. SAE transactions, 2163-2171. https://doi.org/10.4271/2001-01-2085

12. Jäger, M. (2018). Extended compilation of autopsy-material measurements on lumbar ultimate compressive strength for deriving reference values in ergonomic work design: The Revised Dortmund Recommendations. EXCLI journal, 17, 362. https://dx.doi.org/10.17179%2Fexcli2018-1206

13. Karhu, O., Kansi, P., & Kuorinka, I. (1977). Correcting working postures in industry: A practical method for analysis. Applied Ergonomics, 8(4), 199-201. https://doi.org/10.1016/0003-6870(77)90164-8

14. Klussmann, A., Steinberg, U., Liebers, F. et al. The Key Indicator Method for Manual Handling Operations (KIM-MHO) - evaluation of a new method for the assessment of working conditions within a cross-sectional study. BMC Musculoskelet Disord 11, 272 (2010). https://doi.org/10.1186/1471-2474-11-272

15. Laursen, B., & Schibye, B. (2002). The effect of different surfaces on biomechanical loading of shoulder and lumbar spine during pushing and pulling of two-wheeled containers. Applied Ergonomics, 33(2), 167-174. https://doi.org/10.1016/S0003-6870(01)00054-0

16. McAtamney, L., & Corlett, E. N. (1993). RULA: a survey method for the investigation of work-related upper limb disorders. Applied Ergonomics, 24(2), 91-99. https://doi.org/10.1016/0003-6870(93)90080-S

Simulation of abdominal belt effects on IAP and spinal compressive force with musculoskeletal human model

Zhenkai Zhao[1#], Leiming Gao[1#], Benjamin Simpson[1], James Campbell[2], Neil J. Mansfield[1#]

1. Department of Engineering, Nottingham Trent University, Clifton Lane, Nottingham NG11 8NS, UK.

2. BMT, 1 Park Road, Teddington, London, TW11 0AP

#Corresponidng author: Neil J. Mansfield, neil.mansfield@ntu.ac.uk; Zhenkai Zhao, zhenkai.zhao@ntu.ac.uk; Leiming Gao leiming.gao@ntu.ac.uk

Abstract

Repeated High-G shocks and whole-body vibration (WBV) can increase the risk of fatigue and injuries in the lumbar region of the spine for crew and passengers on High-speed craft (HSC). Existing reviews have suggested the beneficial effects of abdominal belts regarding lumbar torso stabilization and spinal unloading. The paper provides a novel 3-D seated human model with a virtual belt to simulate the belt effects for occupants on HSC. The model is built with AnyBody, a commercial software for musculoskeletal simulation based on the inverse dynamics method. The belt behaves like an additional force exerted in the lumbar region, and the force magnitude has been optimized to avoid discomfort during long journeys. The belt effects have been studied with different levels of wave shock, anthropometries, and belt design parameters such as belt width and position. Wave shocks exerted on seat surface are considered to include both vertical and off-vertical (horizontal) acceleration and expressed with a half-sine pulse. The belt effects are evaluated with intra-abdominal pressure (IAP), transversus muscle activities, and spinal compressive force. The results have shown a combined increase of IAP (137% maximum) and a decrease of spinal compressive force at the L4/L5 joint (15.5% maximum) once the belt is applied under various circumstances. Transverse abdominis activity is also reduced with belt application. The belt performs best when it covers the entire lumbar region. Reduction of belt width might lead to increased muscle activity for the muscle that isn't covered by the belt, inducing over-recruited muscle. For the same belt width, belt position variations are irrelevant to the belt performance. It has been validated that the abdominal belt can significantly assist abdominal muscles and maintain a solid core during intense WBV generated in different sea states, reducing fatigue and the risk of injury to the lumbar. Therefore, the model can be a preliminary guide for designing the abdominal belt.

Keywords: Abdominal belt, whole-body vibration, high-G shock, intra-abdominal pressure, spinal compressive forces, muscle activity, high-speed craft.

Introduction

Repeated shocks and whole-body vibration always lead to detrimental effects on crew and passengers on high-speed craft (HSC) (Halswell, Wilson, Taunton, & Austen, 2016). Low back musculoskeletal injury is one of the most commonly seen symptoms for occupants with apparent muscle pains in the lumbar region (Bartleson, 2001; Bridger, 1999). Existing methods used to mitigate the symptom include limitations of the vehicle speed and improving the seat design for better vibration absorption (Cripps, Cain, Phillips, Rees, & Richards, 2003; Garme, Burstrom, & Kuttenkeuler, 2011; Myers et al., 2012; Townsend, Coe, Wilson, & Shenoi, 2012). However, these methodologies can increase the complexity and cost of the craft potentially. Therefore, protections on occupants with an abdominal belt was considered.

The abdominal belt was firstly considered as a support for athletes such as heavy weight lifters. The effect of the belt can be evaluated with intra-abdominal pressure (IAP), which is a parameter supposed to aid in reducing spinal disc compressive force (Grillner S Fau - Nilsson, Nilsson J Fau - Thorstensson, & Thorstensson). Harman *et al* did experiments on dead-lifting behaviour with and without a belt and compared the measured IAP (Harman, Rosenstein, Frykman, & Nigro, 1989). Significant increment of IAP was found after the belt was applied to stabilize the lumbar region. Similar conclusions were made, such as increasing intradiscal pressure (Miyamoto, Iinuma, Maeda, Wada, & Shimizu, 1996) and reduced spinal compressive force (Woldstad & R. Sherman, 1998). Although there existed controversial results that the belt did not contribute to the reduction of spinal compressive force (Ivancic, Cholewicki, & Radebold, 2002), no apparent findings showed that wearing a belt can either decrease IAP or increase the compressive force.

IAP and muscle forces are normally measured with transducers on human skin, and electromyography, which can cause potential injuries to the participants. It is also difficult to perform experiments with subjects exposed to extreme shock, such as those experienced on HSC. Therefore, the musculoskeletal model was created to simulate the muscle effects and body reactions to external shocks as an inexpensive and efficient method. De Zee *et al* built a lumbar model that can estimate the maximum extension moment in an upright position (de Zee, Hansen, Wong, Rasmussen, & Simonsen, 2007). An optimized model was later built by adding new elements to the model and was capable of estimating the muscle and tendon forces (Christophy, Faruk Senan, Lotz, & O'Reilly, 2012). Further studies have included the IAP effects, and the musculoskeletal model was coupled with Finite-element (FE) method (Liu, Khalaf, Adeeb, & El-Rich,

2019; Liu, Khalaf, Naserkhaki, & El-Rich, 2018). The results implied that the inclusion of IAP reduced global muscle forces, the disc loads and intradiscal pressure.

Based on the previous research, this paper has introduced a musculoskeletal model with virtual belts to simulate the belt effects for passengers on HSC with AnyBody Modelling System, a software for the development and analysis of the musculoskeletal system. Concerned parameters such as IAP, muscle activity, and spinal compressive force have been studied. In general, the abdominal belt can positively contribute to the stabilization of the core muscle in the lumbar region.

Methods

The seated human model was developed using AnyBody and depicted in **Figure 1A**. The chair was simplified as rigid to focus on the response of rigid components of the model during the force transmission. The real vibration was represented by vertical and off-vertical acceleration with different magnitudes. The signals were produced with a digital model (Olausson and Garme model) in MATLAB, as shown in **Figure 1B**. The half-sine pulse was fitted to a sine function (shown with **Equation 1**) and used as input in AnyBody to mimic the external vibration effects. In the equation, A represents the magnitude of the acceleration, and α is the shock wave amplitude.

$$A = \alpha \sin(\omega t + \varphi) \tag{1}$$

In the model, the lumbar region contained vertebra and transversus muscle. Five vertebra segments were included ranging from L1 to L5. As depicted in **Figure 1C**, the transversus muscle was connected to the vertebra, and the virtual belt will cover this region. The abdominal volume was idealized as a cylinder. In AnyBody, any force applied on the abdominal muscle can generate abdominal pressure. Therefore, the stretchy belt works like a virtual muscle with similar properties to the transversus muscle, but can provide a uniform inward force to help stabilize the lumbar region and generate IAP.

A B C

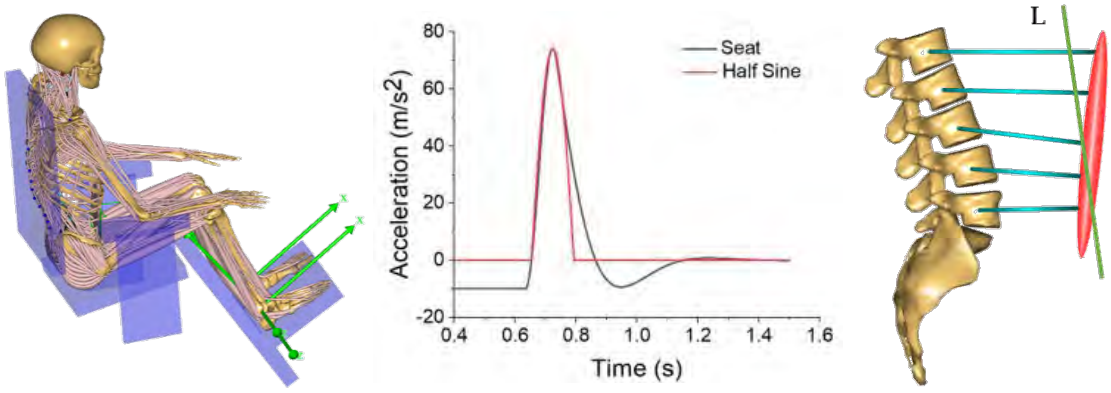

Figure 1. (A) A 3-D view of a seated human model in AnyBody software. (B) Half-sine pulse for simulation and the shock pulse on the seat surface. (C) Lumbar region structure with vertebra and transversus muscle.

In general, the numerical model was evaluated with shocks under different sea states ranging from 3g to 10g. Besides, occupants with different anthropometric dimensions were studied as well as different belt widths. Finally, both vertical and off-vertical accelerations with different amplitudes were simulated.

Results

Three main parameters were used to evaluate the effect of the abdominal belts, and results were obtained from the human MSK model. The first parameter is IAP, which is closely related to the stabilization of the lumbar region against external loading. The second one is the transversus muscle activity (TrA), which is calculated by dividing the actual muscle strength under vertical acceleration by the maximum muscle strength of the transvers abdominal muscle group. The maximum muscle strength is an inherent property of the muscle, and the value is constant. Therefore, muscle activity can represent muscle recruitment. The third is the spinal compressive force which is represented by a reaction force between adjacent vertebrae L4 and L5.

The three main results were initially shown in **Figure 2**, based on a seated human model experiencing 10g pure vertical acceleration with and without a belt. There was a significant increase in IAP (120%) after the belt was applied. Both the transversus muscle activity and L4/L5 compressive force were decreased with the virtual belt, indicating a positive effect of the belt application. These findings are consistent with the previous results that the back belt can enhance IAP and reduce measured back muscle electromyography (Kingma et al., 2020).

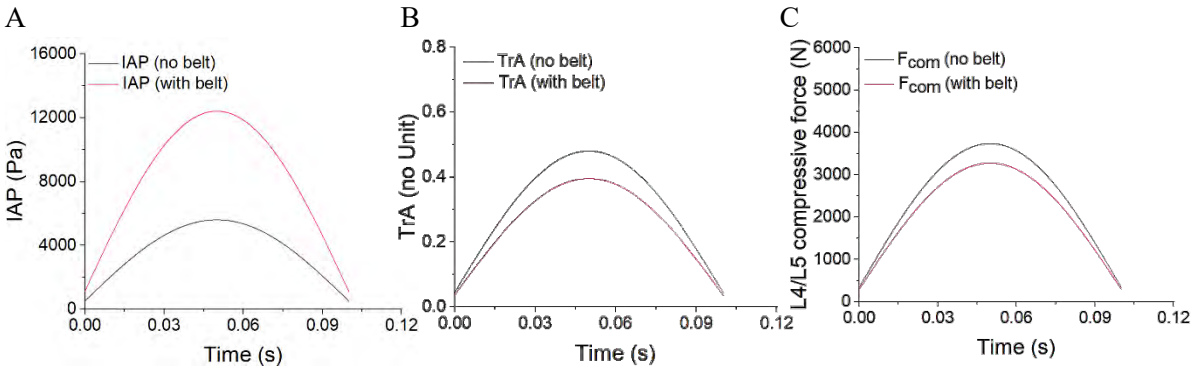

Figure 2. Belt effects on seated human model. (A) IAP value comparison. (B) Transversus muscle activity comparison. (C) Comparison of compressive force at L4/L5 joint.

The belt effects under different sea states were tested with data from previous literature (Riley, Haupt, Ganey, & Coats, 2018). A total of six levels of vertical acceleration were selected, ranging from 3g to 10g. in **Figure 3**, the maximum values of IAP, TrA, and L4/L5 compressive forces were evaluated under different vertical accelerations. As expected, the belt had an overall beneficial effect on all sea states. Similar results were found for people with different anthropometric dimensions. As displayed in **Table 1**, there was a significant reduction of compressive forces at L4/L5 joint after the belt was applied for 5%, 50%, and 95% anthropometric dimensions.

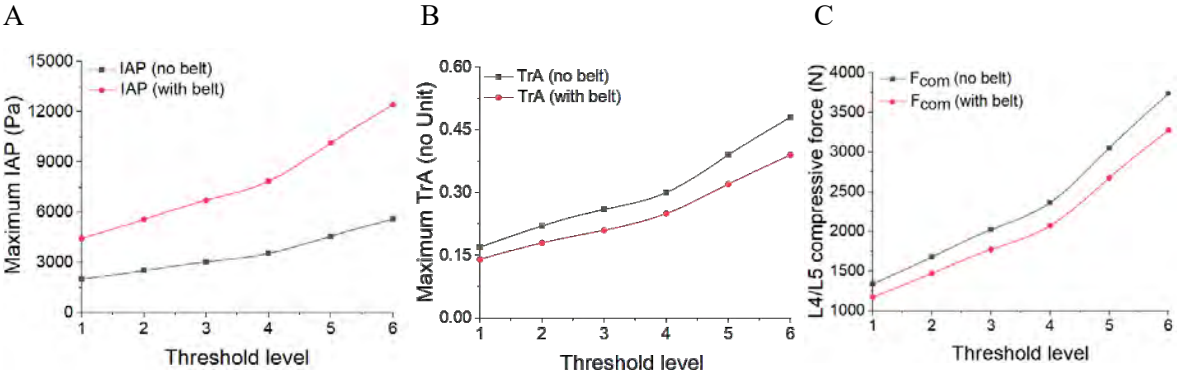

Figure 3. Belt influences under different vertical accelerations. (A) Maximum IAP comparison. (B) Maximum transversus muscle activity comparison. (C) Maximum compressive force at L4/L5 joint comparison.

Table 1. Belt effects for a human model with different anthropometric dimensions

	5th percentile	50th percentile	95th percentile
Body weight/height	69kg/169.3mm	81kg/178.1mm	96kg/189.8mm
IAP	+114%	+121%	+107%
TrA	-21.5%	-17.7%	-14.7
L4.L5 force	-12%	-12.3%	-10.3%

Values in the table are the differences before and after the belt was applied expressed in percentage; '+' indicates increased value, and '-' indicates reduced value.

The belt width effects were also studied. There are five vertebrae segments in the lumbar region; the belt width levels were represented by the number of segments covered by the abdominal belt. **Figure 4** shows that a level 5 belt width had the best belt performance, i.e., a belt that covers the entire lumbar region.

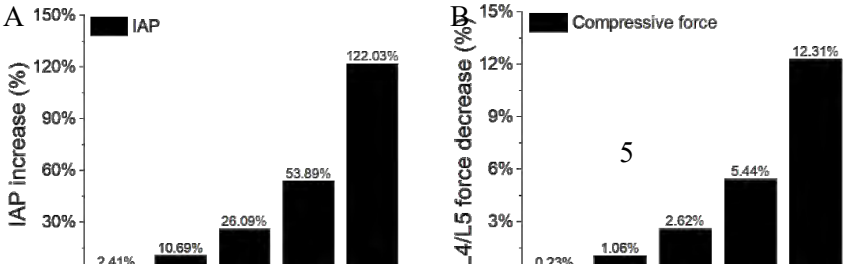

Figure 4. Belt width levels influence on (A) IAP increase. (B) L4/L5 compressive force decrease.

When the off-vertical acceleration was included, there was a significant increase in the spinal compressive force, indicating larger pressure on the human spine compared to pure vertical acceleration. To test the effects of off-vertical acceleration, six cases were tested and compared with vertical-only conditions (shown in **Table 2**). Composite values for the total acceleration for all cases were kept the same at 10g. Belt effects were shown in **Figure 5**; compared to pure vertical acceleration, the belt had a larger effect in both increase of IAP and the reduction of compressive force. However, large lateral acceleration can lead to the transverse abdominis activity value higher than 1, inducing a significant drop in the belt effects expressed with red dots in the figure.

Table 2. Parameters used for off-vertical acceleration.

Case	V (vertical)	L1(Lateral 1)	L2	L3	L4	L5	L6
Vertical acceleration (g)	10	9.98	9.95	9.88	9.8	9.54	8.66
Lateral acceleration (g)	0	0.5	1	1.5	2	3	5

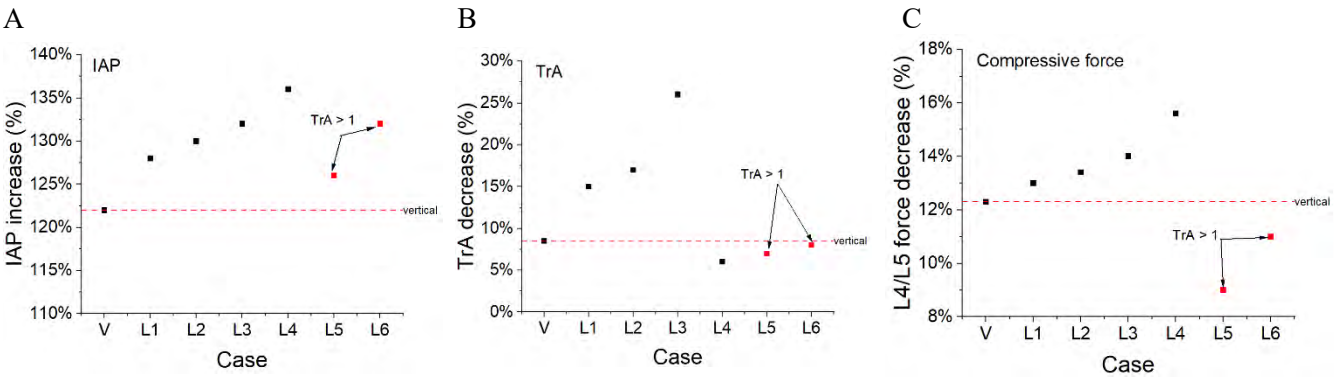

Figure 5. Belt effects on off-vertical acceleration. (A) IAP increment. (B) Transverse abdominis activity decrease. (C) L4/L5 compressive force decrease.

Discussion and Conclusions

For all of the shock conditions tested, the abdominal belt reduced the spinal loading in the lumbar region. This decrease in loading was due to the load being partially supported by the IAP. In no case did the belt make the response to the shock more severe in the lumbar region, thereby indicating a protective effect.

When the belt covers the entire lumbar region, all the transversus abdominis have the same muscle activity. However, a reduction of belt width might lead to increased muscle activity for the muscle that was not covered by the belt, and the increment value is inversely proportional to the number of muscles not covered by the belt. When the belt covered four vertebra segments, the activity of the unconstrained muscle increased by 60%, which can be over-recruited. This finding supports the result that the abdominal belt performed best when it covered the entire lumbar region.

With large values of lateral acceleration, the transverse abdominis activity can be higher 1, indicating that the muscle is not capable of responding to the shock, suggesting a limited value for shock exposure. Beyond the threshold of 1, the modelling indicates non-linear responses and the accuracy of the model is not guaranteed. Lateral acceleration also led to a potential threat to the human model with much higher spinal compressive forces; better belt effects compared to vertical-only acceleration implies that the belt can provide multi-axis support.

AnyBody is a modelling tool that is capable of simulating musculoskeletal loading and therefore allows for the analyses reported here. However, it has a limitation, such that it does not simulate the dynamic motion of segments and associated geometric non-linearities. Non-linearities of apparent mass and transmissibility under WBV reflected by changes in resonance frequency can be studied with experimental measurements and numerical simulation (Coe, Xing, Shenoi, & Taunton, 2009; Mansfield & Griffin, 2000; Shabana, Gantoi, & Brown, 2011). Besides, the belt model was limited to simulating only stretchy belts that provided a constant inward force, rather than a body reacting to the presence of a non-stretch belt around the abdomen. The belt is also an idealized cylinder, with no variation in width or rigid design elements that may be present in a physical product. In order to model these, a different approach would be needed, potentially building more complex models combining active elements and finite element analysis (FEA).

In this paper, a novel biomechanical model was built with AnyBody software to study potential belt protection for seated humans on HSC. The impact of the belt was evaluated by IAP, muscle activities and spinal compressive forces. The results have shown a combined increase of IAP (137% maximum) and a decrease of spinal compressive force at the L4/L5 joint (15.5% maximum) once the belt is applied under various circumstances, including vertical and off-vertical acceleration. To achieve the best belt performance, the belt should cover the full range of the lumbar region, which is also comfortable for a

human being. This study can provide a preliminary guide to the design of an abdominal belt to protect occupants on the HSC.

Acknowledgements

The technical aspects of this study were conducted independently and exclusively by Nottingham Trent University with industry liaison provided by BMT Defence and Security UK Ltd. The work was funded by the UK Ministry of Defence (MOD) Defence and Security Accelerator (DASA).

References

Bartleson, J. D. (2001). Low Back Pain. (1092-8480 (Print)).

Bridger, R. S. (1999). Musculoskeletal Pain in Fisheries Protection Squadron Seaboat User. *Technical Report.*

Christophy, M., Faruk Senan, N. A., Lotz, J. C., & O'Reilly, O. M. (2012). A musculoskeletal model for the lumbar spine. *Biomech Model Mechanobiol, 11*(1-2), 19-34. doi:10.1007/s10237-011-0290-6

Coe, T. E., Xing, J. T., Shenoi, R. A., & Taunton, D. (2009). A simplified 3-D human body–seat interaction model and its applications to the vibration isolation design of high-speed marine craft. *Ocean Engineering, 36*(9-10), 732-746. doi:10.1016/j.oceaneng.2009.04.007

Cripps, R., Cain, C., Phillips, H., Rees, S., & Richards, D. (2003). Development of a new crew seat for all weather life boats.

de Zee, M., Hansen, L., Wong, C., Rasmussen, J., & Simonsen, E. B. (2007). A generic detailed rigid-body lumbar spine model. *J Biomech, 40*(6), 1219-1227. doi:10.1016/j.jbiomech.2006.05.030

Garme, K., Burstrom, L., & Kuttenkeuler, J. (2011). Measures of vibration exposure for a high-speed craft crew. *Proceedings of the Institution of Mechanical Engineers, Part M: Journal of Engineering for the Maritime Environment, 225*, 338-349. doi:10.1177/1475090211418747

Grillner S Fau - Nilsson, J., Nilsson J Fau - Thorstensson, A., & Thorstensson, A. Intra-abdominal pressure changes during natural movements in man. (0001-6772 (Print)).

Halswell, P. K., Wilson, P. A., Taunton, D. J., & Austen, S. (2016). An experimental investigation into the whole body vibration generated during the hydroelastic slamming of a high speed craft.

Harman, E. A., Rosenstein, R. M., Frykman, P. N., & Nigro, G. A. (1989). Effects of a belt on intra-abdominal pressure during weight lifting.

Ivancic, P. C., Cholewicki, J., & Radebold, A. (2002). Effects of the abdominal belt on muscle-generated spinal stability and L4/L5 joint compression force. *Ergonomics, 45*(7), 501-513. doi:10.1080/00140130210136035

Kingma, I., Faber Gs Fau - Suwarganda, E. K., Suwarganda Ek Fau - Bruijnen, T. B. M., Bruijnen Tb Fau - Peters, R. J. A., Peters Rj Fau - van Dieën, J. H., & van Dieën, J. H. (2020). Effect of a stiff lifting belt on spine compression during lifting. (1528-1159 (Electronic)).

Liu, T., Khalaf, K., Adeeb, S., & El-Rich, M. (2019). Numerical Investigation of Intra-abdominal Pressure Effects on Spinal Loads and Load-Sharing in Forward Flexion. *Front Bioeng Biotechnol, 7*, 428. doi:10.3389/fbioe.2019.00428

Liu, T., Khalaf, K., Naserkhaki, S., & El-Rich, M. (2018). Load-sharing in the lumbosacral spine in neutral standing & flexed postures - A combined finite element and inverse static study. *J Biomech, 70*, 43-50. doi:10.1016/j.jbiomech.2017.10.033

Mansfield, N. J., & Griffin, M. J. (2000). Non-linearities in apparent mass and transmissibility during exposure to whole-body vertical vibration. *Journal of Biomechanics, 33*.

Miyamoto, K., Iinuma, N., Maeda, M., Wada, E., & Shimizu, K. (1996). Effects of abdominal belts on intra-abdominal pressure, intramuscular pressure in the erector spinae muscles and myoelectrical activities of trunk muscles.

Myers, S. D., Dobbins Td Fau - King, S., King S Fau - Hall, B., Hall B Fau - Holmes, S. R., Holmes Sr Fau - Gunston, T., Gunston T Fau - Dyson, R., & Dyson, R. (2012). Effectiveness of suspension seats in maintaining performance following military high-speed boat transits. (0018-7208 (Print)).

Riley, M. R., Haupt, K. D., Ganey, D. H. C. N., & Coats, D. T. W. (2018). *Laboratory Test Requirements for Marine Shock Isolation Seats*. Retrieved from

Shabana, A. A., Gantoi, F. M., & Brown, M. A. (2011). Integration of finite element and multibody system algorithms for the analysis of human body motion. *Procedia IUTAM, 2*, 233-240. doi:10.1016/j.piutam.2011.04.022

Townsend, N. C., Coe, T. E., Wilson, P. A., & Shenoi, R. A. (2012). High speed marine craft motion mitigation using flexible hull design. *Ocean Engineering, 42*, 126-134. doi:10.1016/j.oceaneng.2012.01.007

Woldstad, J. C., & R. Sherman, B. (1998). The effects of a back belt on posture, strength, and spinal compressive force during static lift exertions. *International Journal of Industrial Ergonomics, 22*(6), 409-416. doi:https://doi.org/10.1016/S0169-8141(97)00012-7

Effects of sex and weighted vest load arrangements on lower biomechanics and jump height during countermovement jump

Juan Baus[1], John R. Harry[2], and James Yang[1]*
[1]Human-Centric Design Research Lab, Department of Mechanical Engineering
Texas Tech University, Lubbock, TX 79409, *Corresponding Author: james.yang@ttu.edu
[2]Human Performance & Biomechanics Lab, Department of Kinesiology and Sport Management, Texas Tech University, Lubbock, TX 79409

Abstract

Weighted vest (WV) use has been explored as a modifier of jumping and landing performance in athletes, but it is unclear whether performance is modified with different WV loading arrangements. The purposes of this study were to a) examine the effects of different external load arrangements on vertical jump height and lower-extremity biomechanics during a countermovement jump and b) understand the effects on men versus women. A scaled musculoskeletal gait model in OpenSim was used with sagittal plane inverse kinematics procedures for 24 participants (75.71 ± 18.88 Kg; 1.71 ± 0.09 m) equally divided between men and women performing jump-landing in four weighted vest loading conditions (back-loaded, front-loaded, split-loaded, unloaded). Mixed-model factorial analyses of variance (α=0.05) and effect sizes (ES) were used to identify and quantify differences between sexes and loading conditions. Regardless of loading conditions, men showed greater jump height ($p<0.001$, ES=2.22) and greater hip ($p<0.001$, ES=1.59), and knee ($p=0.026$, ES=0.90) moments. No significant difference in the hip ($p=0.478$, ES=0.30) or knee ($p=0.580$, ES=0.23) angular displacement was observed between men and women. Without considering sex, the unloaded condition showed greater jump height ($p<0.001$, ES=0.4), hip displacement ($p=0.006$, ES=0.34), and hip ($p=0.019$, ES=0.36), and knee ($p=0.004$, ES=0.48) moments when compared to the back-loaded condition. Jump height ($p=0.04$, ES=0.1) and hip moments ($p=0.028$, ES=0.36) were also greater for the split-loaded compared to the back-loaded condition. Both the unloaded and split-loaded conditions showed greater jump height ($p<0.001$, ES=0.4; $p<0.001$, ES=0.3) and hip moments ($p<0.001$, ES=0.55; $p=0.003$, ES=0.35) compared with the front-loaded condition. A significantly greater magnitude of the hip displacement was detected for the split loaded condition compared to the front-loaded condition ($p<0.001$, ES=0.19). These results indicate that different external loading arrangements significantly affect the biomechanical performance output and differences in the load accommodation strategies between men and women during the period between the weighting and propulsion phases of jumping.

Keywords: Countermovement jump, biomechanics, weighted vest, jump height

Introduction

Countermovement jump is a common practice in professional sports that, at the same time, is used to evaluate jumping performance and joint biomechanics. The countermovement jump consists of the subject standing, followed by a downward movement and a rapid upward movement to cause take-off [1]. Jumping performance studies seek opportunities to improve jumping techniques. At the same time, they analyze joint kinetics and kinematics to identify biomechanical performance of postural adjustment and center of mass shifting to maintain balance [2]. Jumping performance is closely related to the jumping technique that can be improved through different strategies [3]–[6]. It is essential to mention that an increased jump height will also increase the landing height, which requires a greater mechanical demand during the landing phase on the hip, knee, and ankle joints[7].

A weighted vest is one of many possible practices to add an external load to improve jumping performance in training. It is recommended to use an extra 10-15% body weight (BW) as the external load for training practices to enhance vertical jump height [8]–[10]. A warming-up protocol with a 2%

BW weighted vest effectively enhanced jumping performance [11]. Typically, the load on the weighted vest is positioned such that it is symmetrically arranged over the trunk. Asymmetrically loading the weighted vest can also cause different biomechanical demands during jumping and landing [12]. Modified hip, knee, and ankle responses have been observed for symmetrical loading, causing different energy absorption during the landing phase [13]. External loading studies are commonly done for the landing phase because during this period, the jumper experiences the peak ground reaction forces, so the injury risk is increased [14], [15].

In contrast, this study focuses on the jumping's weighting, unweighting, breaking, and flying phases that define the jumping performance [16]. The purpose of this study is to investigate the knee and hip kinetics and kinematics for different load arrangements of weighted vests. We hypothesize that the jump height will be greater in magnitude in men than women and for the unloaded case compared to the other loading conditions. Also, it is expected to observe lower hip and knee moment and angular displacement for women and the unloaded condition. The novelty of this study is that four different loading arrangements (back-loaded, front-loaded, split-loaded, and unloaded) are tested for hip and knee kinetic sand kinematics comparison using OpenSim software [17], [18]. We expect to find significant differences when comparing the unloaded condition with any other loading conditions. Also, we hope to see significant differences when comparing the split-loaded condition against the front-loaded and back-loaded conditions.

Methods

Participants

Twenty-four recreationally active adults (26.13 ± 3.33 years) were recruited for this study and among them there were 12 males (88.75 ± 16.36 Kg; 1.77 ± 0.07 m) and 12 females (62.67 ± 10.32 Kg; 1.65 ± 0.06 m). The recruit criterion was that they did not have a recent history (≤ 1 year) of significant injuries in the lower extremities. Institutional Review Board approved the experimental protocol at the site of data collection.

Experimental Protocol

Data collection was conducted in a single laboratory session that started with collecting demographic and anthropometrics of each participant (gender, age, mass, height). Participants were provided with appropriate-sized athletic shoes (Vazee Pace v2; New Balance Athletics, Inc., Boston, MA) as a control method for potential footwear effects. After the protocol was explained, the participants went through a standardized warm-up protocol that required five-minute walking or jogging on a treadmill at a self-selected pace and five vertical jump landings (VJL) separated by 30 seconds. Posteriorly, the participants performed eight maximum effort countermovement jumps in four experimental conditions. The conditions were defined as zero added mass (Unloaded), 10% body mass added symmetrically over the trunk (Split-loaded), 10% body mass added over the anterior aspect of the trunk (Front-loaded), and 10% body mass added over the posterior aspect of the trunk (Back-loaded) by wearing a weighted vest (Mir Vest, Inc., San Jose, CA, USA). The loading conditions were presented to the participants in a counterbalanced order.

The participants were instructed to start the trial by positioning each foot on a force platform and later perform the jump using a self-selected countermovement depth and preferred arm swing strategy. It was required to be considered a fair trial for the participant to land with each foot in contact with a force platform and return to a motionless standing position. A trial was discarded if the jump appeared to be submaximal effort, the participant could not land with each foot in an individual force platform, or the participant could not return to the motionless standing position.

Three-dimensional kinematic data were obtained using a 10-camera motion capture system (Vicon Motion Systems, Ltd., Oxford, UK; 200 Hz) that tracked reflective spherical markers (14mm). The markers were positioned in the following locations: acromion process, iliac crest, anterior superior iliac spine, posterior superior iliac spine, medial and lateral aspects at the knee, and the medial and lateral malleoli. Individual markers were also placed on the C7 vertebrae, the sternoclavicular notch, and the sacrum. Also, three-marker cluster sets adhered bilaterally over the calcaneus. Four-marker cluster sets adhered bilaterally to the lateral aspect of the thigh and shank to complete the set. Simultaneously, a dual force platform system (Kistler Instruments, Corp., Amherst, NY; 1000 Hz) was used to obtain three-dimensional ground reaction force (GRF) data.

Data Processing

Subject-specific musculoskeletal models were scaled using OpenSim [17], [18] software from a gait model that has no upper extremities (Gait 2354) [19]–[22]. The scaling process required adjusting the generic model with the height and weight of each participant and inputting estimated values of the inertial properties. Once the model was scaled to a specific participant, an inverse kinematic (IK) analysis was done by reducing the error between the position of the physical markers data obtained with motion capture with the virtual markers on the model [23]. The obtained results provide the joint kinematics necessary to perform the inverse dynamics (ID) process to give the internal joint moments.

After the results from ID were smoothed with a Butterworth filter with a cut-off frequency of 6Hz, the results were exported to MATLAB® to divide the jumping motion into propulsion and flying phases based on the ground reaction force data. The propulsion phase was defined from the onset movement to the take-off instant. The flying phase was defined from take-off to ground contact [16]. The maximum joint displacement and moment were taken from the right limb since asymmetries in the sagittal plane are unlikely to happen [24]–[26]. Taking advantage of the OpenSim analysis tool, the body center of mass position was calculated to obtain the maximum jump height during the flying phase as the difference between the highest position of the center of mass position during the flying phase and at the beginning motionless standing position.

Statistical Analysis

The mean and standard deviation (SD) of kinetic and kinematic values were calculated for each participant's trial for each loading condition. IBM SPSS software (v28; IBM Corp., Armonk, NY) was used to run a mixed-model factorial ANOVA (α=0.05), with sex as the between factor and loading condition as the within factor. In the case of a significant interaction, independent sample t-test and paired sample t-test were used to assess sex differences between loading conditions and loading conditions differences between sex, respectively. When no significant interaction was detected, Sidak adjustment was used to compare the main effects. The data normality was assessed using the Shapiro-Wilk test. Cohen's d effect sizes (ES) were calculated to normalize the magnitude of the mean differences and identify the presence of a meaningful effect [27]. Sawilowsky's scale was selected to interpret the values of the effects size. The scale is defined as follow: very small: ES<0.2, small: 0.2≤ES<0.5, medium: 0.5≤ES<0.8, large: 0.8≤ES<1.2, very large: 1.2≤ES<2.0, and huge: ES≥2.0 [28].

Results

The data presented the flexion and flexion moment in thi section is defined as positive for both the knee and hip joints. Hip and knee moments were normalized with respect to system weight (subject and weighted vest mass). No significant interactions were detected for the maximum jump height (p=0.579), hip (p=0.499) and knee (p=0.269) moment, or hip (p=0.541) or knee (p=0.851) angular displacement. Accordingly, main effects were obtained for the differences between sexes with pooled load conditions and load conditions with pooled sex data.

Sex effects

Statistical analysis results for the sex data are listed in Table 1. A huge sex difference was detected for greater maximum jump height ($p<0.001$, ES=2.22) for men compared to women. A very large difference was detected for the hip moment ($p<0.001$, ES=1.59), with a greater magnitude for men than women. For the knee moment, a large difference was detected ($p=0.026$, ES=0.90) with greater magnitude in the case of men compared to women. No significant differences were detected for hip ($p=0.478$, ES=0.30) and knee ($p=0.580$, ES=0.23) angular displacement.

Table 1:Differences between Men and Women

Variables	Men		Women			
	Mean	SD	Mean	SD	p	ES
Jump Height*	0.49	0.08	0.34	0.06	<0.001	2.22
Hip Displacement	91.30	19.66	86.34	13.89	0.478	0.30
Hip Moment*	2.09	0.40	1.51	0.36	<0.001	1.59
Knee Displacement	107.21	12.75	104.82	8.73	0.580	0.23
Knee Moment*	1.69	0.22	1.52	0.17	0.026	0.90

Note: Units of measurement for jump height (m), hip and knee displacement (°), hip and knee moment ($N\ m\ Kg^{-1}$); Mean: average across participants; SD: ± one standard deviation; p=statistical probability; ES = Cohen's d effect size; * significant difference between men and women ($p<0.05$).

Load condition effects

Results for load condition data are presented in Table 2. For the jump height, small load condition differences were detected with greater jump height for the unloaded condition when compared to the back-loaded condition ($p<0.001$, ES=0.4), the front-loaded condition ($p<0.001$, ES=0.4), and split-loaded condition ($p<0.001$, ES=0.3). Also, a very small difference was detected for a more significant jump height when comparing the back-loaded and split-loaded conditions ($p=0.04$, ES=0.1). Small significant differences were seen for the hip moment with a smaller magnitude for the back-loaded condition when compared to the split-loaded condition ($p=0.028$, ES=0.36) and with the unloaded condition ($p=0.019$, ES=0.36). For the knee moment, a small significant difference was detected with greater magnitude for the unloaded condition compared to the back-loaded condition ($p=0.004$, ES=0.48). Small significant differences were seen for the hip angular displacement with greater magnitude for the unloaded condition when compared to the back-loaded ($p=0.006$, ES=0.34) and split-loaded ($p=0.003$, ES=0.35) conditions. A medium significant difference was detected with greater hip angular displacement for the unloaded condition than the front-loaded condition ($p<0.001$, ES=0.55). A greater magnitude of hip angular displacement for the split-loaded condition than the front-loaded condition showed a very small significant difference ($p<0.001$, ES=0.19).

Table 2: Differences between Loading Conditions

Variables	Back-loaded		Front-loaded		Split-loaded		Unloaded		
	Mean	SD	Mean	SD	Mean	SD	Mean	SD	p
Jump Height †‡§¶	0.40	0.10	0.40	0.10	0.41	0.10	0.44	0.11	<0.001
Hip Displacement †§¶#	88.36	16.69	84.92	17.23	88.14	17.67	93.85	16.71	<0.001
Hip Moment †‡	1.70	0.48	1.78	0.50	1.87	0.50	1.86	0.44	<0.001
Knee Displacement	105.44	9.91	105.46	9.90	106.88	11.99	106.27	12.34	0.498
Knee Moment †	1.55	0.23	1.60	0.19	1.60	0.18	1.66	0.25	0.015

Note: Units of measurement for jump height (m), hip and knee displacement (°), hip and knee moment ($N\ m\ Kg^{-1}$); Mean: average across participants; SD: ± one standard deviation; p=statistical probability; † significant difference between unloaded and back-loaded conditions ($p<0.05$), ‡ significant difference

between back-loaded and split-loaded conditions ($p<0.05$), § significant difference between front-loaded and unloaded conditions ($p<0.05$), ¶ significant difference between split-loaded and unloaded conditions ($p<0.05$), # significant difference between front-loaded and split-loaded conditions ($p<0.05$).

Discussion

This study aimed to investigate if using different loading arrangements as a weighted vest during the first phases of countermovement jump will alter the jump height and biomechanics of the hip and knee joints in male and female subjects. From the first hypothesis, for pooled loading conditions (Table 1), a higher jumping height was observed for men than women, which is consistent with results previously reported in the literature [29]. When looking at Table 2, the unloaded condition showed the highest jump height since it has a lesser mechanical demand than other loading conditions, so there is less mass to overcome. The significant differences in the jump height and hip moment between the back-loaded and the split-loaded conditions suggest that the load arrangement does influence the performance output with a more substantial jump height with less hip involvement. Previous studies have investigated the progressive use of loading strategies over different periods, showing improvements in jump height [30], [31]. Our study did not focus on warm-up or training protocols to obtain better jumping performance results in the long term, so a future study could implement the different load and different loading arrangements, as proposed in this paper, to investigate the improvement in jump height [32], [33].

By looking at Table 1, there is a significant difference between male and female subjects for both knee and hip moments. Considering that men are typically stronger from a gross perspective, they can sustain much higher stretch loads [34]; it is shown that they also generate more relative torque during jumping. These results are consistent with previous studies reporting that higher jumps are directly related to more significant knee and hip moments [35]. Muscle strength and power output have been considered predictors of jumping performance [30]. Still, we are looking at a situation where joint moments could be viewed as another critical factor in this prediction. In the case of joint angular displacement, a significant difference was found only for the hip joint, comparing different loading conditions (Table 2). Previous studies have reported trunk position adaptations with the added external load during landing [13] and differences in the hip work between men and women with different energy storage or concentric mechanical output [36]. Our results suggest that there might be similar adaptations during the unweighting, breaking, and propulsion phases of jumping. Even when the results followed our hypothesis, the small differences in jump height and hip moment need further investigation to find their meaningfulness in this context.

The differences in kinetic and kinematic factors could be considered an accommodation strategy [37] that differs between men and women and across loading conditions in response to a change in an external stressor in the form of additional external weight to the body. It is essential to mention that, even when similar jump height could be achieved for different jumpers, its downward phase movement strategy during the countermovement jump could be different. During the unweighting and breaking phases of jumping, the joints' kinetic and kinematics qualities may differ from one subject to another, so differences in joints' moment and angular displacement are expected [38]. Also, short-term and long-term responses are different because neuromuscular and metabolic adaptations have been observed for external loading conditions [39]. Finally, it is worth mentioning that all results were kinetic and kinematic results were obtained using OpenSim. A future study could test the reliability of these results when comparing with other software with the same capabilities in simulation and predicting biomechanical parameters.

Conclusion

This study showed adjustment in the knee and hip moments for the back-loading condition as a strategy to achieve greater jump height during the flying phase of the countermovement jump. Because of symmetrical and asymmetrical loading, there was a significant difference in the jump height and the hip moment when comparing the back-loaded and the split-loaded conditions. The same behavior was

observed for the hip angular displacement in comparing front-loaded and split-loaded conditions. In contrast, independent of the symmetry or asymmetry of the additional load, significant differences were detected for jump height and hip displacement for the front-loaded versus unloaded and the split-loaded versus unloaded cases. When comparing sex, large, very large, and huge effects sizes were detected for knee moment, hip moment, and jump height, respectively, suggesting that differences are meaningful. Different loading arrangements may be implemented in various warm-up protocols or training programs depending on the implementation of and desired results in terms of performance.

Acknowledgments

This work was supported by Distinguished Graduate Student Fellowship, Graduate School, Texas Tech University.

References

[1] B. Van Hooren and J. Zolotarjova, "The Difference between Countermovement and Squat Jump Performances: A Review of Underlying Mechanisms with Practical Applications," *J. Strength Cond. Res.*, vol. 31, no. 7, pp. 2011–2020, 2017, doi: 10.1519/JSC.0000000000001913.

[2] A. Le Pellec and B. Maton, "Initiation of a vertical jump: the human body's upward propulsion depends on control of forward equilibrium," 2002. [Online]. Available: www.elsevier.com/locate/neulet.

[3] H. M. Ericksen, A. C. Thomas, P. A. Gribble, S. C. Doebel, and B. G. Pietrosimone, "Immediate effects of real-time feedback on jump-landing kinematics," *J. Orthop. Sports Phys. Ther.*, vol. 45, no. 2, pp. 112–118, Feb. 2015, doi: 10.2519/jospt.2015.4997.

[4] H. M. Ericksen, A. C. Thomas, P. A. Gribble, C. Armstrong, M. Rice, and B. Pietrosimone, "Jump-landing biomechanics following a 4-week real-time feedback intervention and retention," *Clin. Biomech.*, vol. 32, pp. 85–91, Feb. 2016, doi: 10.1016/j.clinbiomech.2016.01.005.

[5] K. R. Ford *et al.*, "Use of an Overhead Goal Alters Vertical Jump Performance and Biomechanics," 2005.

[6] K. R. Ford, A. D. Nguyen, E. J. Hegedus, and J. B. Taylor, "Vertical jump biomechanics altered with virtual overhead goal," *J. Appl. Biomech.*, vol. 33, no. 2, pp. 153–159, Apr. 2017, doi: 10.1123/jab.2016-0179.

[7] H. Te Peng, T. W. Kernozek, and C. Y. Song, "Quadricep and hamstring activation during drop jumps with changes in drop height," *Phys. Ther. Sport*, vol. 12, no. 3, pp. 127–132, Aug. 2011, doi: 10.1016/j.ptsp.2010.10.001.

[8] A. G. Thompsen, T. Kackley, M. A. Palumbo, and A. D. Faigenbaum, "Acute Effects of Different Warm-Up Protocols with and without a Weighted Vest on Jumping Performance in Athletic Women," *J. Strength Cond. Res.*, vol. 21, no. 1, pp. 52–56, Feb. 2007, doi: 10.1519/00124278-200702000-00010.

[9] R. Khlifa *et al.*, "Effects of a Plyometric Training Program With and Without Added Load on Jumping Ability in Basketball Players," *J. Strength Cond. Res.*, vol. 24, no. 11, pp. 2955–2961, Nov. 2010, doi: 10.1519/JSC.0b013e3181e37fbe.

[10] J. D. Simpson *et al.*, "Effects of Weighted Vest Loading During Daily Living Activities on Countermovement Jump and Sprint Performance," *Int. J. Sports Physiol. Perform.*, vol. 15, no. 3, pp. 309–318, Mar. 2020, doi: 10.1123/ijspp.2019-0318.

[11] A. D. Faigenbaum, J. E. McFarland, J. A. Schwerdtman, N. A. Ratamess, J. Kang, and J. R. Hoffman, "Dynamic warm-up protocols, with and without a weighted vest, and fitness performance in high school female athletes.," *J. Athl. Train.*, vol. 41, no. 4, pp. 357–63, 2006, [Online]. Available: http://www.ncbi.nlm.nih.gov/pubmed/17273458.

[12] F. Vaverka *et al.*, "The Influence of an Additional Load on Time and Force Changes in the Ground Reaction Force During the Countermovement Vertical Jump," *J. Hum. Kinet.*, vol. 38, pp. 191–200, Sep. 2013, doi: 10.2478/hukin-2013-0059.

[13] A. Kulas, P. Zalewski, T. Hortobagyi, and P. DeVita, "Effects of added trunk load and corresponding trunk position adaptations on lower extremity biomechanics during drop-landings," *J. Biomech.*, vol. 41, no. 1, pp. 180–185, Jan. 2008, doi: 10.1016/j.jbiomech.2007.06.027.
[14] K. N. S. K. Syamimi, M. S. Salim, and N. Omar, "A biomechanical analysis of the knee during jump landing," *30th Annu. Conf. Biomech. Sport.*, no. 39, pp. 265–268, 2012.
[15] C. H. Yeow, P. V. S. Lee, and J. C. H. Goh, "An investigation of lower extremity energy dissipation strategies during single-leg and double-leg landing based on sagittal and frontal plane biomechanics," *Hum. Mov. Sci.*, vol. 30, no. 3, pp. 624–635, Jun. 2011, doi: 10.1016/j.humov.2010.11.010.
[16] J. J. McMahon, T. J. Suchomel, J. P. Lake, and P. Comfort, "Understanding the Key Phases of the Countermovement Jump Force-Time Curve," *Strength Cond. J.*, vol. 40, no. 4, pp. 96–106, Aug. 2018, doi: 10.1519/SSC.0000000000000375.
[17] A. Seth *et al.*, "OpenSim: Simulating musculoskeletal dynamics and neuromuscular control to study human and animal movement," *PLOS Comput. Biol.*, vol. 14, no. 7, p. e1006223, Jul. 2018, doi: 10.1371/journal.pcbi.1006223.
[18] S. L. Delp *et al.*, "OpenSim: Open-Source Software to Create and Analyze Dynamic Simulations of Movement," *IEEE Trans. Biomed. Eng.*, vol. 54, no. 11, pp. 1940–1950, Nov. 2007, doi: 10.1109/TBME.2007.901024.
[19] F. C. Anderson and M. G. Pandy, "A Dynamic Optimization Solution for Vertical Jumping in Three Dimensions," *Comput. Methods Biomech. Biomed. Engin.*, vol. 2, no. 3, pp. 201–231, Jan. 1999, doi: 10.1080/10255849908907988.
[20] F. C. Anderson and M. G. Pandy, "Dynamic Optimization of Human Walking," *J. Biomech. Eng.*, vol. 123, no. 5, pp. 381–390, Oct. 2001, doi: 10.1115/1.1392310.
[21] S. L. Delp, J. P. Loan, M. G. Hoy, F. E. Zajac, E. L. Topp, and J. M. Rosen, "An interactive graphics-based model of the lower extremity to study orthopaedic surgical procedures," *IEEE Trans. Biomed. Eng.*, vol. 37, no. 8, pp. 757–767, 1990, doi: 10.1109/10.102791.
[22] G. T. Yamaguchi and F. E. Zajac, "A planar model of the knee joint to characterize the knee extensor mechanism," *J. Biomech.*, vol. 22, no. 1, pp. 1–10, Jan. 1989, doi: 10.1016/0021-9290(89)90179-6.
[23] R. Ueno *et al.*, "Quadriceps force and anterior tibial force occur obviously later than vertical ground reaction force: a simulation study," *BMC Musculoskelet. Disord.*, vol. 18, no. 1, p. 467, Dec. 2017, doi: 10.1186/s12891-017-1832-6.
[24] J. R. Harry, C. R. James, and J. S. Dufek, "Weighted vest effects on impact forces and joint work during vertical jump landings in men and women," *Hum. Mov. Sci.*, vol. 63, pp. 156–163, Feb. 2019, doi: 10.1016/j.humov.2018.12.001.
[25] J. R. Harry, J. Freedman Silvernail, J. A. Mercer, and J. S. Dufek, "Bilateral Comparison of Vertical Jump Landings and Step-off Landings From Equal Heights," *J. Strength Cond. Res.*, vol. 32, no. 7, pp. 1937–1947, Jul. 2018, doi: 10.1519/JSC.0000000000002093.
[26] J. R. Harry, J. Freedman Silvernail, J. A. Mercer, and J. S. Dufek, "Comparison of pre-contact joint kinematics and vertical impulse between vertical jump landings and step-off landings from equal heights," *Hum. Mov. Sci.*, vol. 56, pp. 88–97, Dec. 2017, doi: 10.1016/j.humov.2017.10.022.
[27] G. M. Sullivan and R. Feinn, "Using Effect Size—or Why the P Value Is Not Enough," *J. Grad. Med. Educ.*, vol. 4, no. 3, pp. 279–282, Sep. 2012, doi: 10.4300/JGME-D-12-00156.1.
[28] S. S. Sawilowsky, "New Effect Size Rules of Thumb," *J. Mod. Appl. Stat. Methods*, vol. 8, no. 2, pp. 597–599, Nov. 2009, doi: 10.22237/jmasm/1257035100.
[29] C. E. Quatman, K. R. Ford, G. D. Myer, and T. E. Hewett, "Maturation leads to gender differences in landing force and vertical jump performance: A longitudinal study," *Am. J. Sports Med.*, vol. 34, no. 5, pp. 806–813, 2006, doi: 10.1177/0363546505281916.
[30] S. Markovic, D. M. Mirkov, O. M. Knezevic, and S. Jaric, "Jump training with different loads: effects on jumping performance and power output," *Eur. J. Appl. Physiol.*, vol. 113, no. 10, pp. 2511–2521, Oct. 2013, doi: 10.1007/s00421-013-2688-6.

[31] W. A. Sands, R. C. Poole, H. R. Ford, R. D. Cervantez, R. C. Irvin, and J. A. Major, "Hypergravity Training: Women's Track and Field," *J. Strength Cond. Res.*, vol. 10, no. 1, 1996, [Online]. Available: https://journals.lww.com/nsca-jscr/Fulltext/1996/02000/Hypergravity_Training__Women_s_Track_and_Field.6.aspx.

[32] C. Chattong, L. E. Brown, J. W. Coburn, and G. J. Noffal, "Effect of a Dynamic Loaded Warm-Up on Vertical Jump Performance," *J. Strength Cond. Res.*, vol. 24, no. 7, pp. 1751–1754, Jul. 2010, doi: 10.1519/JSC.0b013e3181ddf665.

[33] G. M. Duthie, W. B. Young, and D. A. Aitken, "The acute effects of heavy loads on jump squat performance: an evaluation of the complex and contrast methods of power development.," *J. strength Cond. Res.*, vol. 16, no. 4, pp. 530–8, Nov. 2002, [Online]. Available: http://www.ncbi.nlm.nih.gov/pubmed/12423181.

[34] P. V Komi and C. Bosco, "Utilization of stored elastic energy in leg extensor muscles by men and women.," *Med. Sci. Sports*, vol. 10, no. 4, pp. 261–5, 1978, [Online]. Available: http://www.ncbi.nlm.nih.gov/pubmed/750844.

[35] A. Vanezis and A. Lees, "A biomechanical analysis of good and poor performers of the vertical jump," *Ergonomics*, vol. 48, no. 11–14, pp. 1594–1603, Sep. 2005, doi: 10.1080/00140130500101262.

[36] J. R. Harry, L. A. Barker, and M. R. Paquette, "Sex and acute weighted vest differences in force production and joint work during countermovement vertical jumping," *J. Sports Sci.*, vol. 37, no. 12, pp. 1318–1326, 2019, doi: 10.1080/02640414.2018.1557825.

[37] C. R. James, L. T. Atkins, J. S. Dufek, and B. T. Bates, "An exploration of load accommodation strategies during walking with extremity-carried weights," *Hum. Mov. Sci.*, vol. 35, pp. 17–29, Jun. 2014, doi: 10.1016/j.humov.2014.03.012.

[38] J. Rauch, E. Leidersdorf, T. Reeves, L. Borkan, M. Elliott, and C. Ugrinowitsch, "Different Movement Strategies in the Countermovement Jump Amongst a Large Cohort of NBA Players," *Int. J. Environ. Res. Public Health*, vol. 17, no. 17, p. 6394, Sep. 2020, doi: 10.3390/ijerph17176394.

[39] C. Bosco *et al.*, "The influence of extra load on the mechanical behavior of skeletal muscle," *Eur. J. Appl. Physiol. Occup. Physiol.*, vol. 53, no. 2, pp. 149–154, Oct. 1984, doi: 10.1007/BF00422578.

Joint velocity dependence of fatigue in isokinetic leg extension tasks

Ritwik Rakshit[1], Shuvrodeb Barman[2], Yujiang Xiang[2], and James Yang[1]*

[1]Human-Centric Design Research Lab, Department of Mechanical Engineering, Texas Tech University, Lubbock, TX 79409, USA, *Corresponding Author: james.yang@ttu.edu
[2]School of Mechanical and Aerospace Engineering, Oklahoma State University, Stillwater, OK 74078, USA

Abstract

The ability to predict the decline in muscle strength over the course of an activity (fatigue) can be a crucial aid to task design, injury prevention and rehabilitation efforts. Current models of muscle fatigue have been hitherto validated only for isometric contractions, but most real-world tasks are dynamic in nature involving continuously varying joint velocities. It has previously been proposed that a three-compartment-controller model with enhanced recovery (3CCr) might be used to predict fatigue for such tasks by using it in conjunction with joint- and direction-specific torque-velocity-angle (TVA) surfaces. This allows for the calculation of a time-varying target load parameter that can be used by the 3CCr model, but it increases model complexity considerably and has not been validated by experimental data. The predictions using the 3CCr methods are contrasted against experimental data collected from 10 male participants in a series of isokinetic leg extension tests, covering velocities ranging from 30 to 150 degrees/s. A much lower degree of fatigue is observed for moderate velocities (90 degrees/s) compared to that for lower or higher velocities. The need for a velocity parameter in the 3CCr model is indicated, but further testing with larger sample sizes and more joints is needed before a reliable parameter can be estimated.

Keywords: muscle fatigue, velocity, isokinetic, leg extensors

Introduction

Muscle fatigue is a temporary, exercise-induced decline in muscle strength. It is an inevitable consequence of even the most basic human activities such as lifting weights, running, walking, cycling, driving an automobile, and sitting. Being able to estimate the extent of fatigue can provide crucial input in the fields of ergonomics and task design, where often the goal is to design the task to never require more than the participant's strength at any given time. Its importance is especially amplified in situations where small changes in strength can produce disproportionate outcomes, such as in a dead man's switch or vigilance device. Directly measuring strength, however, is not always feasible—it may be invasive, and always requires specialized equipment, a controlled environment, and, at minimum, task interruption.

Musculoskeletal models can bridge this gap by providing estimates of muscle force or joint torque during the performance of a simulated task using only a computer and no human involvement. At present, however, no musculoskeletal models exist that can account for skeletal muscle fatigue, and the predictions for all such models are therefore only valid for scenarios in which the digital human is unfatigued. Additionally, since high loads cause strength to decline much faster than smaller ones, even these predictions may not be accurate for high-load cases. This underscores the need for musculoskeletal models to incorporate fatigue calculations in their analyses.

Estimations of the extent of fatigue can be made using muscle fatigue models (MFM), which may be either empirical or theoretical. Empirical models provide estimates of strength as a function of time, usually for sustained isometric tasks. They are simple curve fits to experimental data and are easy to implement due to their mathematical simplicity but are limited to the specific cases that the experimental data tested. Theoretical models, on the other hand, are more mathematically complex, but allow for more task parameters than just task intensity and therefore allow the modeling of a wider variety of activities. The 3-compartment controller model (3CC) (Xia & Frey-Law, 2008)—a theoretical MFM—allows the modelling of any task by matching the measured torque output to a reference torque-velocity-angle (TVA) surface to obtain a normalized task intensity, and then using this as the model input. The model was validated for sustained isometric contractions (SIC) (Frey-Law, Looft, et al., 2012), and subsequently adapted for use with intermittent isometric contractions (IIC) by the introduction of an enhanced recovery parameter *r* in the 3-compartment controller model with enhanced recovery (3CCr) model (Looft et al., 2018). The model has not been validated for any tasks where the joint velocities are non-zero.

In this work, we assess the 3CCr MFM's performance in predicting fatigue for a set of isokinetic contractions, and propose the introduction of a velocity parameter to improve prediction accuracy.

Methods

Experiment

Participants

10 male participants—19-32 years of age, with a body-mass index (BMI) between 18.5 and 29.9, and with no history of musculoskeletal or neural disorders or injuries—contributed to the data in this study. All participants gave their informed consent and came in on 6 days, with a minimum of 48 hours separating two consecutive experimental sessions. The first session was used to familiarize the participant

with the experimental protocol and train them to follow the commands. Data from this session was not used for any analysis. On each of the remaining 5 days, an identical protocol was followed.

Protocol

A Biodex System 4 isokinetic dynamometer (Biodex Inc, Shirley, NY, USA) was used for all measurement. The participant was securely strapped into the seat of the dynamometer with the shank of their dominant leg attached to the dynamometer arm. The range of motion (ROM) of the knee was restricted to between 90 and 15 degrees of flexion. The protocol consisted of 5 sets of maximal voluntary isometric contractions (MVIC) interspersed by 4 sets of isokinetic contractions.

The MVICs were measured at 6 joint angles—90, 75, 60, 45, 30, and 15 degrees—in both the extension and flexion directions. This was implemented as 3 seconds of MVIC in the extension direction followed by 2 seconds of rest, and then 3 seconds of MVIC in the flexion direction followed by 2 seconds of rest, before repeating this process for the next joint angle. The entire set of isometric measurements lasted 90 seconds, after which the next phase of the protocol began.

During the isokinetic phase, the participant flexed and extended their leg around the knee joint at a predetermined velocity for a period of 60 seconds. The same velocity was used for both flexion and extension, and the same ROM (90-15 degrees) was used here as for the isometric phase. The participant was instructed to exert maximum effort throughout. The velocity was monitored throughout, and the participant was verbally encouraged to increase their effort if they failed to maintain the velocity for more than one cycle. At the end of the 60 seconds, the participant was instructed to stop, at which point the next isometric phase began.

Only one velocity was used for all 4 isokinetic phases tested on any particular day. This velocity was chosen from 30, 60, 90, 120 or 150 degrees per second, and all participants performed the experiment at all 5 velocities over 5 days. However, the order in which they tested at each velocity was randomized to ensure that experience of a prior velocity did not influence performance in a subsequent session for the group as a whole.

Simulation

The 3CCr model and the experimental protocol were recreated in MATLAB (*MATLAB*, 2021). The 5 isometric measurement phases were modelled as IICs with target load (TL)=1. Since extension MVICs were performed for 3 of every 15 seconds devoted to each joint angle, the duty cycle (DC) was set at 3/15=0.2, and cycle time (CT) was set at 15 s. Since the participants were instructed to exert maximum

effort at all times during the isokinetic phase, TL was set at 1. Because the knee extensors were used during the extension phase which made up half of the extension-flexion cycle, DC was set at 0.5. The isokinetic CT (CT_{isok}) was calculated based on the isokinetic velocity (v_{isok}) and ROM as:

$$CT_{isok} = \frac{2 \times ROM}{v_{isok}} \quad (1)$$

The parameters used to define the two phases of the experimental protocol as IICs are listed in Table 1.

Table 1. Task parameters for the experimental protocol.

Parameter	**Isometric phase**	**Isokinetic phase**
TL	1	1
DC	0.2	0.5
CT	15 s	$\frac{2 \times ROM}{v_{isok}}$

The ode23 solver was used to solve the 3CCr control equations (Looft et al., 2018) over the entire domain. The parameters used to define the fatigue and recovery properties of the knee extensors were drawn from (Rakshit et al., 2021) and are shown in Table 2.

Table 2. Functional-muscle-group- and sex-specific parameters for the knee extensors (male).

Parameter	**Value**
F	0.01420
R	0.00153
r	12.27

Experimental data processing

The isometric measurements from the experiments were stored as absolute values within a MATLAB data structure. The maximum isometric strength recorded for a particular participant on a particular day for any angle, and at any isometric measurement (ISOM) iteration, was used to linearly scale all the other MVICs down so that all MVICs were expressed as unitless quantities between 0 and 1. This ensured that

each participant had at least one reading of strength = 1 at each session. The normalized strength at each ISOM iteration and at each joint angle was averaged across all participants to yield 5 strength-versus-angle (TA) curves—one for each ISOM iteration. The scaled V=0 slice of the TVA surface for the leg extensors from (Frey-Law, Laake, et al., 2012) which best fit the experimental TA curve at each iteration was chosen as the final TA curve. Only 4 of the 6 torque values (corresponding to the 6 joint angles at which strength was measured) in the experiment were used for scaling. The 4 points whose use resulted in the lowest residual error were chosen programmatically for scaling to reduce imperfections in data which might result from a participant absent-mindedly exerting a submaximal force. It was assumed that this would occur at most twice at any ISOM iteration.

Results

Simulation

Since all phases of the protocol are modelled as IICs, the unmodified 3CCr MFM can be used to predict the progress of fatigue. The normalized residual capacity (RC), which is the sum of the fractions of the active motor units (M_A) and the resting motor units (M_R), is depicted in Figure 1 for $v_{isok} = 30°/s$.

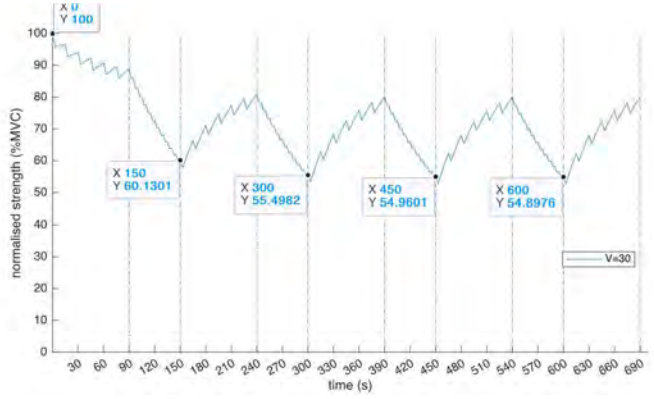

Figure 1. Normalized residual strength prediction from unmodified 3CCr.

While any experimental measurements would reflect only the active compartment size, the sum of active and resting compartment sizes is shown here for clarity. During MVICs, M_R=0 and M_A≠0. During periods of rest, M_R ≠0 and M_A=0. The 6 dips in RC between 0-90s (and 150-240s, 300-390s, 450-540s, and 600-690s) represent the 6 3-second MVICs at each ISOM iteration. The climb following each dip represents the 12-second recovery period before the next MVIC. It may be noted that the dips represent M_A, while the climbs represent M_R.

It is observed that M_A decreases during the first ISOM iteration (ISOM1), and rises during all subsequent ISOM iterations (ISOM2-ISOM5). M_A always decreases during each isokinetic iteration (ISOK1-ISOK4).

The same predictions are also generated for $v_{isok} = 90°/s$ and depicted in Figure 2.

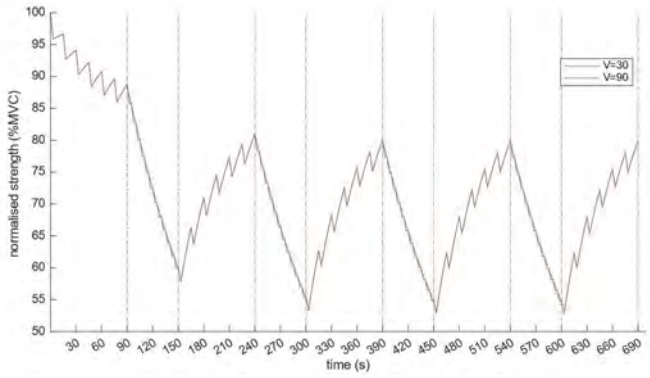

Figure 2. Normalized residual strength prediction using the unmodified 3CCr for two isokinetic velocities.

The two plots are observed to almost overlap, with no discernible difference in the ISOM phases. Even in the ISOK phases, the M_R and M_A values for the two velocities track each other almost exactly, as can be seen in Figure 3.

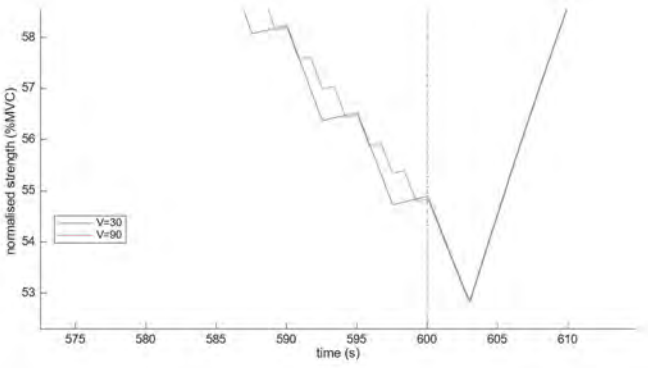

Figure 3. A zoomed-in version of the normalized residual strength for two isokinetic velocities around t=600 s.

Using $v_{isok} = 30°/s$ but two distinct values of the isokinetic target load ($TL_{isok} \in \{1, 0.7\}$), two plots are obtained in Figure 4.

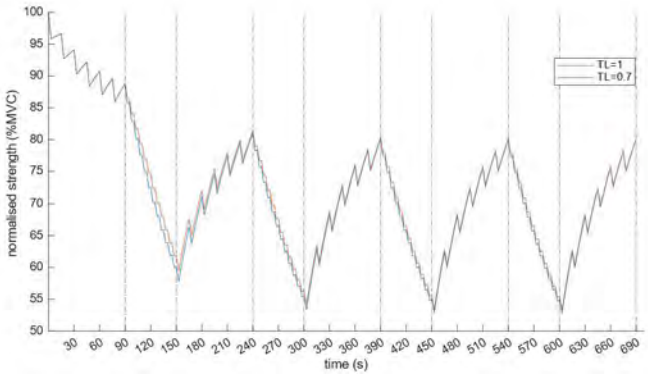

Figure 4. Effect of changing isokinetic target load on the unmodified 3CCr MFM.

There is a small difference (<2% MVC) in the RC between $TL_{isok} = 1$ and $TL_{isok} = 0.7$ by the end of ISOK1. However, as the experiment progresses, even this subtle difference diminishes.

Experiment

The averaged normalized strengths measured at 5 stages is plotted for each of the 5 isokinetic velocities in Figure 5 (a). Each curve is scaled up so that it begins at exactly 100% strength. Each plot is then fit to an exponential curve of the form $y = ae^{bx}$ with a weight vector of [10, 1, 1, 1, 1] to force the fits to assign greater importance to the initial unfatigued torque value. The resulting fits are shown in Figure 5 (b), with the goodness of fit data tabulated in Table 3.

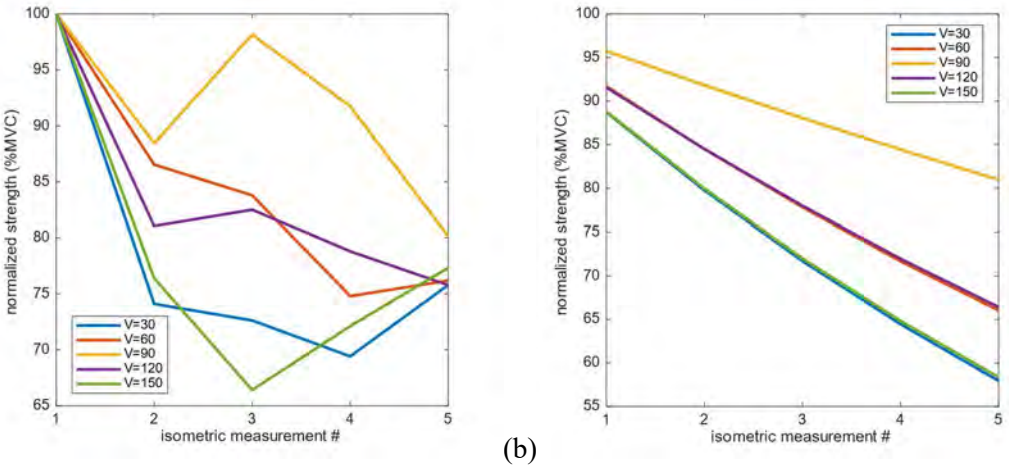

Figure 5. (a) Scaled variation in fatigue rate with velocity, and (b) exponential fits to variation in fatigue rate data.

Table 3. Goodness of fit data for exponential curve fits to fatigue rate variation.

Velocity	**a**	**b**	**R-square**	**RMSE**
30	0.9869	-0.1065	0.803	0.1176
60	0.9956	-0.0821	0.951	0.0441
90	0.9985	-0.0419	0.736	0.0647
120	0.9921	-0.0803	0.889	0.0672
150	0.9862	-0.1049	0.761	0.1307

From both the scaled and the fit experimental data it is apparent that the rate of fatigue varies with velocity. Faster fatigue is indicated for the extreme velocities (30 and 150 degrees/second), with the rate of fatigue decreasing until it reaches a minimum at a velocity of 90 degrees/second.

Discussion and Conclusions

The present 3CCr model makes almost identical predictions regardless of contraction velocity, as indicated by Figure 2. Yet, limited experimental data shows that the rate of fatigue is indeed affected by velocity. A high rate of fatigue is observed for both extremely low and extremely high velocities, and the fatigue rate is observed to decrease until it reaches its minimum value at a tested velocity of 90 degrees/second. The exponential fits, however, tend to diverge with increasing number of iterations (Figure 5 (b)), whereas the original data initially diverges and then converges (Figure 5(a)). This may indicate that some other function may be better suited to represent the variation in fatigue rates. Additionally, a larger sample size may also help increase model integrity.

The performance of the MVICs themselves causes a certain amount of fatigue or recovery. Within the first isometric test, strength is predicted to decline by about 6%. This occurs because all of the constituent motor units (MU) are initially in the resting state, and after they are recruited into the active state they pass on into the fatigued state. Once a significant fraction of MUs are in the fatigued state, the recovery process dominates in order to move a sufficient fraction of MUs to the resting and subsequently active states to fulfill the target load requirement. This is why RC is observed to rise after it has been sufficiently depleted during the first isokinetic phase. Since every isokinetic phase depletes RC by roughly the same amount, the recovery process dominates every subsequent isometric phase due to the low DC. The current data processing pipeline maps all strengths from an isometric measurement phase to the V=0 slice of an experimentally determined TVA peak strength surface. While only the first strength in each phase

(measured at 90 degrees of joint flexion and then scaled) is used to estimate the RC, it may be more robust to compare the strengths at every angle while accounting for fatigue and recovery to obtain an indicative strength after every isokinetic phase.

The protocol currently allows breaks to test isometric strength. A more faithful depiction of the decline in strength with isokinetic activity might be observed if the breaks were less frequent, but pilot experiments revealed that subjects were far less likely to be able to continue maximal effort isokinetic contractions beyond 1 minute. The rest periods allow a measurement of isometric strength and allow the participant to recover so that they may continue with the protocol. A certain unestimated amount of central fatigue was also observed to contribute since most participants reported being unable to continue beyond the 5^{th} isometric measurement, despite the torque readings being not much lower than those at the 4^{th} measurement.

Another source of uncertainty lies in the contribution of the leg extensors during leg flexion. For the purposes of the simulation this contribution has been assumed to be 0. However, antagonistic muscles do serve to stabilize the joint during contractions, so a certain TL might need to be assumed to make the prediction more closely resemble reality.

In conclusion, initial results show that while the 3CCr model is capable of modelling isokinetic tasks as IICs, it likely requires modification to account for the variation in fatigue rates due to different velocities. Fatigue rate decreases with increasing velocity, and then increases again as velocity is increased further. A comfortable mediocre velocity of 90 degrees/second is found to provide the lowest fatigue rate of all the velocities tested. Further testing with a larger number of participants of more joints—elbow, shoulder, hip—for both flexion and extension—should reveal whether the same conclusions hold, and what kind of modifications might be needed to accommodate the effect of varying velocity on the rate of fatigue in the 3CCr model.

Acknowledgments

The authors wish to thank Yvonne Cebe for her invaluable assistance and input during all phases of experimental data collection. This work was partially supported by National Science Foundation (Award CBET # 1703093 and 1849279; 2014278 and 2014281).

References

Frey-Law, L. A., Laake, A., Avin, K. G., Heitsman, J., Marler, T., & Abdel-Malek, K. (2012). Knee and

Elbow 3D Strength Surfaces: Peak Torque-Angle-Velocity Relationships. *Journal of Applied Biomechanics*, *28*(6), 726–737. https://doi.org/10.1123/jab.28.6.726

Frey-Law, L. A., Looft, J. M., & Heitsman, J. (2012). A three-compartment muscle fatigue model accurately predicts joint-specific maximum endurance times for sustained isometric tasks. *Journal of Biomechanics*, *45*(10), 1803–1808. https://doi.org/10.1016/j.jbiomech.2012.04.018

Looft, J. M., Herkert, N., & Frey-Law, L. A. (2018). Modification of a three-compartment muscle fatigue model to predict peak torque decline during intermittent tasks. *Journal of Biomechanics*, *77*, 16–25. https://doi.org/10.1016/j.jbiomech.2018.06.005

MATLAB (9.10.0.1851785 (R2021a) Update 6). (2021). The Mathworks, Inc.

Rakshit, R., Xiang, Y., & Yang, J. (2021). Functional muscle group- and sex-specific parameters for a three-compartment controller muscle fatigue model applied to isometric contractions. *Journal of Biomechanics*, *127*(August), 110695. https://doi.org/10.1016/j.jbiomech.2021.110695

Xia, T., & Frey-Law, L. A. (2008). A theoretical approach for modeling peripheral muscle fatigue and recovery. *Journal of Biomechanics*, *41*(14), 3046–3052. https://doi.org/10.1016/j.jbiomech.2008.07.013

Multi-modal Event Standardization Platform of Biometric-Derived Human Performance Models in University Students

Joseph Alemany, Meghan Garvey, Kristin Gowers, Robyn Highfill-McRoy, Patrick Walsh, and Arlington Wilson

Leidos Inc., United States

Capturing biometric-based data from wearable sensors on the physical activities of Service Members while completing military missions in theater would greatly advance Digital Human Performance modeling efforts. However, there are several logistic, regulatory, and scientific challenges that must be overcome before it will be possible to develop and deploy solutions for collecting and integrating such data. Likewise, additional challenges remain when using this data to create predictive models of Human Performance that adhere to the data standards that are put in place to protect operational security. This research explores whether currently deployed data-collection products used by the Armed Services could integrate commercial-off-the-shelf wearable products into their architecture given the cybersecurity and networking limitations required to meet DoD specifications.

This study sought to leverage stand-alone clone of a Leidos-owned, pre-existing platform that is already being utilized in deployed settings by DoD Service Members. The product is a modular, open-source approach for tactical applications that ensures timely collection, processing, and delivery of mission critical information from the tactical edge to relevant stakeholders in a rapidly consumable form. At this time, the data captured during testing sessions is not saved and the project has yet to acquire permissions necessary to store information to a secure server that meets Defense Health Agency standards. However, despite these limitations, this Leidos-owned platform can be easily modified to serve as the technological infrastructure for our efforts, can operate on the limited bandwidth conditions experienced in theater, and has met the regulatory and cyber-security guidelines necessary to interact with the Android Tactical Assault Kit (ATAK).

This modified platform would be used to extract data from college students enrolled at university in the continental United States. These study participants are previously Active Duty Service Members and have agreed to return to duty and have extended their current contract after graduation. In this study, they will participate in an experimentally-controlled, physically challenging task designed to monitor the adaptive changes in physiology after engaging in repeated levels of exercise. The University partners working with our Leidos team have conducted and analyzed pilot data on participants engaged in activities based on the DoD Personnel Fitness Test. For this new effort, the participants will be outfitted with three

wearable products (a ring, watch, and patch) to collect a variety of physiological data, including heart rate variability, activity level, sleep patterns, and sweat output. The intent of this study is to capture lessons learned, and the shortcomings from, extracting data from wearable biometric sensor on this simple, but easy to implement, approach, as well as, identify insights on how a more customized data-integration product destined for down-range deployment should be built in the future.

At the same time, quality assurance testing and technical landscape reviews are being conducted by Leidos that will both assess (via field testing and literature reviews) which wearable products will perform best under different DoD specific use cases(e.g., a ring-based wearable might be good for capturing physiology measure while running, but may negatively affect grip positioning on a marksmanship test) or procedures that might be of interest to the different Branches of the Armed Forces.

Initial results suggest that the largest impediment to future, wide-spread adoption by the DoD of using commercial vendor created wearable sensors for Digital Human Modeling will be the un-willingness of said vendors to 1) release their rights to the raw data created from their device, and 2) provide detailed descriptions of the proprietary algorithms used to provide metrics of a user's data. Ultimately, the DoD cannot acquire and be the sole customer to a wearables company, meaning that wearables vendors must instead tailor their product and offerings as broad a client base as possible to remain commercially viable; under these conditions, it is not possible for commercial vendors to remain competitive and to satisfy DoD acquisition/ruggedization standards (e.g., manufacturing their products without Bluetooth hardware). As the technologies used by these vendors continues to mature and the price of the sub-components used to make these products decreases, it will one day be possible for federal entities to manufacture wearable devices that meet all the necessary standards required to outfit the entire Force; but not disrupt the private sector market. Until that day arrives, research in this arena will need to identify and produce solutions to problems with integrating wearables into currently deployed, data-collecting offerings so that the advantages of wearable sensors afforded to Digital Human Modeling and Force Readiness measures can be deployed to the Warfighter in a timely and efficient manner.

Wrist model for the whole human hand

Esteban Peña-Pitarch
EPSEM - UPC, Spain

Abstract

A hand with 25 degrees of freedom (DOF) was proposed with forward and inverse kinematics for all fingers, with a realistic virtual simulation. However, the wrist is not in the model. Today, several authors have proposed in the literature that the wrist has a relative movement between the two rows of bones with eight bones. Some authors discuss a comparison of four joint coordinate systems previously described in the literature. Others propose a helical movement of wrist bones in distal movements.

Objective: A new design the hand model of 25 DOF adding a movement of two rows and eight bones of the wrist.

Methods: Once we locate a new coordinates system in the end of the radius close to the scaphoid, we apply Denavit-Hartenberg for all joints. Forward and inverse kinematics are applied. We include ten ligaments to apply restrictions in the wrist movement, which affects fingertip position.

Results: A new model of a virtual human hand with more accuracy is presented and validated with a Cyberglove™ and Leap Motion.

Conclusions: This new model that includes wrist movement yields a more accurate virtual human hand. New DOFs are added to the 25-DOF hand model.

Keywords: virtual human hand, wrist, 29 DOF.

Introduction

Author's hand with 25 Degree of Freedom (DOF) was proposed in Peña_Pitarch et al. (2019). With the forward and inverse kinematic for all the fingers, they proposed a realistic virtual simulation. However, the wrist not was included in the model. Today, several authors proposed in the literature that the wrist has a relative movement between the two rows of bones with eight bones. Padmore et al. (2020) discuss a comparison of four joint coordinates systems previously described in the literature. Garcia-Elias et al. (2017) proposed a helical movement of wrist bones in distal movements. During thumb oppositional motion, internal rotation of the first metacarpal occurred, with the palmar base rotating primarily with

respect to dorsal base. This is one of conclusions achieved by Kawanishi et al. (2017), and it follows that first metacarpal flexes and pronates with the dorsal base as the center. However, Akhbari et al. (2019) do not consider in their work a significant factor as the pisiform, which plays a minimal role in wrist kinematics.

When comparing healthy with osteoarthritic subjects, the minimal joint space was slightly higher during the neutral, adduction, extension and lateral key pinch configurations than during the abduction, flexion, power grasp and jar twist configurations is analyzed in D'Agostino et al. (2017).

Kapanji (1996) and Tubiana (1981) have detail description of taxonomy for the hand. Neu et al. (2001) studied the movement between different bones of the wrist, i.e. the movement of the radio-capitate joint during wrist flexion–extension and radio-ulnar deviation. Sonenbluma et al. (2004) considered the motion of the scaphotrapezio–trapezoidal (STT) joint.

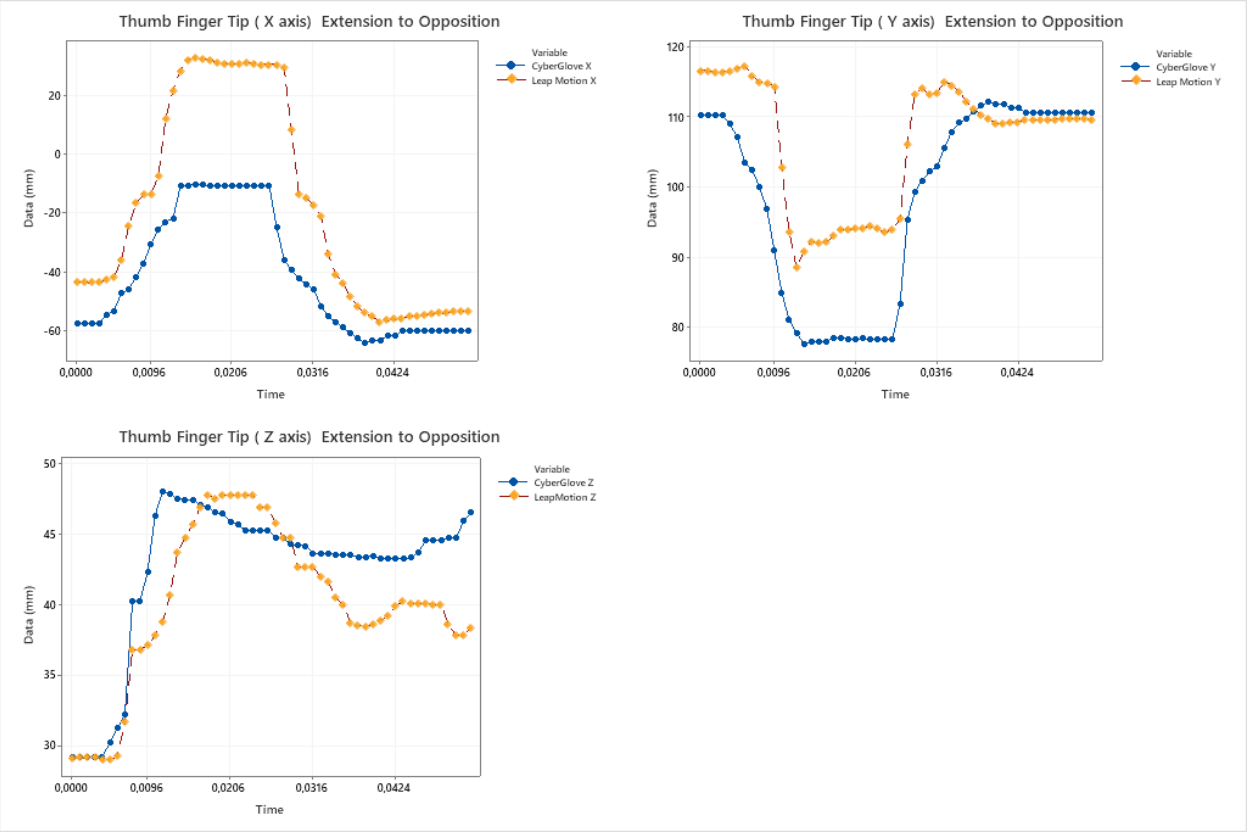

Figure 1. For the X axis (left) we observed a big difference between the capture with Cyberglobe and Leap Motion. Similar for the Y axis (right) and Z axis below.

Figure 1 shows a big difference in the thumb fingertip, orange line (more realistic) is captured with the system of Leap Motion. Axis system of Leap Motion is shown in Figure 4. The blue line is captured by

Cyberglobe™ with eighteen sensors and adapted to model of 25 DOF. Based in this difference the need to remodeled the thumb based in the wrist movement is presented below.

From the aforementioned research, it is possible to conclude that the virtual human hand with 25 DOF will improve adding 4 DOF in the thumb chain.

Paper is organized as follow, in section 2 methods is exposed. In section 3 we show the results. In section 4 the discussion and conclusions are finally shown.

Methods

All of joints in the hand are revolute and if we use a generalized coordinate q_i that represents one degree of freedom, then the generalized coordinate vector can be represented by $\boldsymbol{q} = [q_1, \ldots, q_{29}]$. However, the movements of fingers have some natural constraints (e.g. the middle finger cannot flex over 60 degrees).

Figure 2 shows a model proposed with 29 DOF.

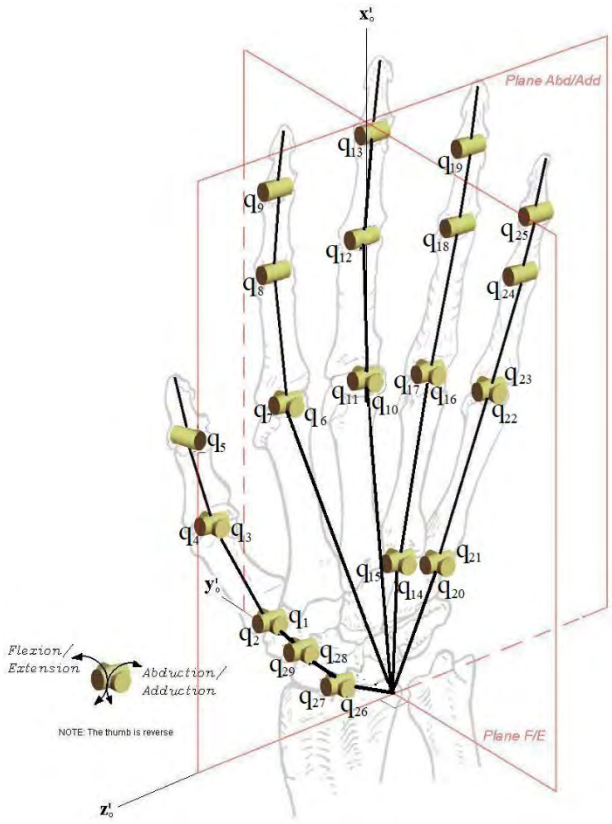

Figure 2. Dorsal view right hand model.

We validate the mathematical model doing experiments with healthy and poststroke patients, with the validate table Action Research Arm Test (ARAT), using Cyberglobl[TM], shown in Figure 3, and Leap Motion, shows in Figure 4.

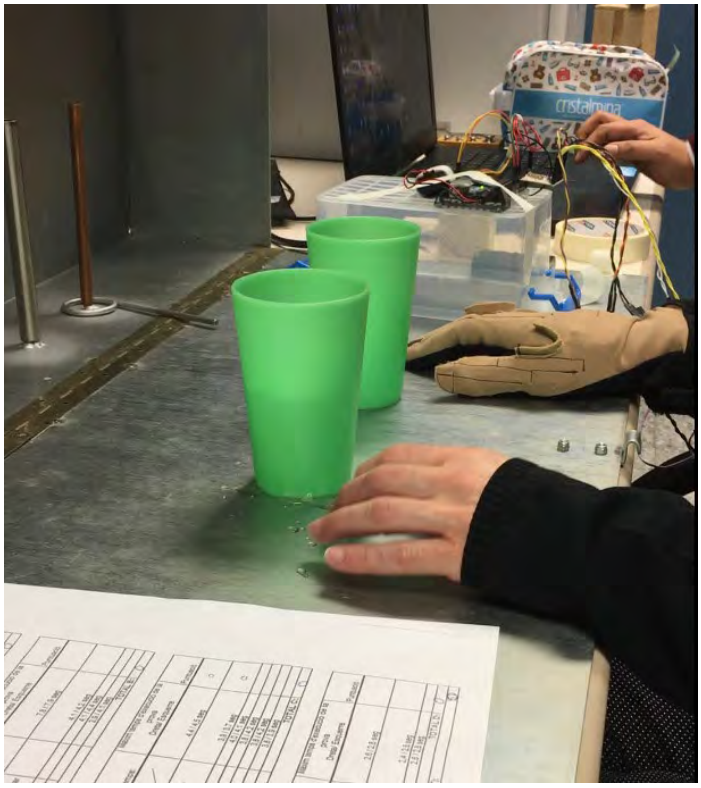

Figure 3. One moment of ARAT test experiments.

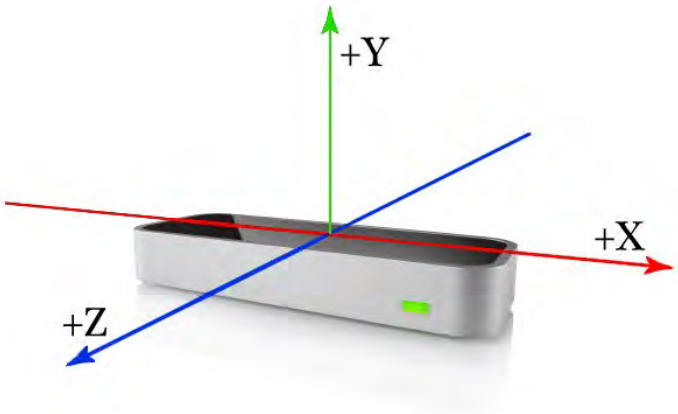

Figure 4. Axis system used in Leap Motion

Results

The algorithm has been implemented in a virtual hand environment. Table 1 presents neutral position of one hand.

Neutral gesture of the hand				
Thumb	Index	Middle	Ring	Little
q_1=0	q_6=0	q_{10}=0	q_{14}=0	q_{20}=0
q_2=0	q_7=30	q_{11}=30	q_{15}=2	q_{21}=5
q_3=30	q_8=30	q_{12}=30	q_{16}=0	q_{22}=0
q_4=0	q_9=10	q_{13}=10	q_{17}=30	q_{23}=30
q_5=30			q_{18}=30	q_{24}=30
q_{26}=0			q_{19}=10	q_{25}=10
q_{27}=0				
q_{28}=0				
q_{29}=0				

Table 1. Angles for the neutral position of hand (in degrees).

By the forward kinematics we can obtain the position vectors of fingertips (millimeter) corresponding to the neutral gesture of the hand shown in Table 2.

Neutral gesture of the hand					
Position	Thumb	Index	Middle	Ring	Little
x	-109.9	3.14	16.28	36.34	55.37
y	79.3	158.25	159.71	145.73	118.74
z	-15.8	-69.5	-77.44	-79.3	-68.14

Table 2. Fingertip positions corresponding to the neutral gesture (with respect to the global coordinates).

Discussion and Conclusions

Figure 5 shows the palm arch. The hand arches in two parts of the palm, that means, the two bones trapezium and scaphoid wrist bones move relative between them and the thumb metacarpal bone have movement with respect to the trapezium (Kawanishi et al., 2017). Scaphoid bone moves between the trapezium and the radius. Global coordinates system is located in the radius shown in Figure 2. The other bones located in the wrist, trapezoid, capitate and lunate don't have movement between them and the hamate, pisiform and triquetum have relative movement between then. However, these movements are not significant for the position of the fingertip.

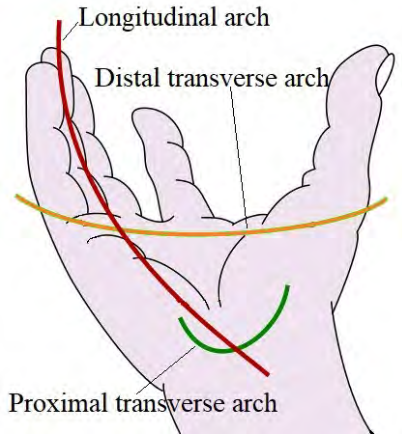

Fig. 5. Palm arch.

The action of the ligaments of the wrist are not trivial. The ligaments contribute to stabilize the bone. As a future work is interesting to study the influence of each ligament, observing which ligament is working when there is some movement of the hand, like opposing thumb to finger, palmar abduction, or retroposition.

Figure 6. Left, apparel to measure the ligament displacement. Right, jig designed by physicians of Univertitat Autonoma de Barcelona (UAB).

Figure 6 shows the testing used to investigate ligament synergies in the loaded wrist, described in Garcia-Elias et al., (2017), and adapted system shown in the right.

As a conclusion, new hand model with 29 DOF is developed to simulate more realistic movements of the fingers, specially the thumb. Thumb is adjusted to permit movements of the palm arcs in different sections of the hand. Mathematical model is validated with Cyberglove™ and Leap Motion. Proposed new studies are in process, like a proposed apparel to measure the displacements induced isometrically loading the wrist or by axially distracting the metacarpal bone away from the radius.

Acknowledgments

This work was partially supported for Spanish government by the project PID2020-114819GB-I00.

References

Peña-Pitarch, E., Al Omar, Anas, Alcelay Larrión, Jose Ignacio, Vives Costa, Jordi. (2019). Virtual human hand: grasps and fingertip deformation. *Advances in Additive Manufacturing, Modeling Systems and 3D Prototyping: proceedings of the AHFE 2019 International Conference on Additive Manufacturing, Modeling Systems and 3D Prototyping*, July 24-28, 2019, Washington D.C., USA. Berlín: Springer, 484-492.

Padmore, C., Langohr, G.D., Suh, N., Johnson. (2020). The effect of coordinate system selection on wrist kinematics. *Journal of Biomechanics*, Elsevier, 109, 1-7.

Garcia-Elias, M., Puig de la Bellacasa, I., Shouten, C. (2017). Carpal Ligaments. Afunctional Classification. *Hand Clin.*, 33, 511-520.

Kawanishi, Y., Oka, K., Tanaka, H. Okada, K., Sugamoto, K. Murase, T. (2017). In vivo 3-Dimensional Kinematics of the thumb Carpometacarpal Joint During Thumb Opposition. *Journal of Hand Surgery*, 43, 1-7.

Akhbari, B., Moore, D.C., Laidlaw, D.H., Weiss, A-P.C., Akelman, E., Wolfe,S.W., Crisco,J.J. (2019). Predicting Carpal Bone Kinematics Using an Expanded Digital Database of Wrist Carpal Bone Anatomy and Kinematics. *J.Orthop.Res.,* 37(12), 2661-2670.

D'Agostino, P., Dourthe, B., Kerkhof, F., Van Lenthe, G.H., Stock,ans, F., Vereecke, E.E. (2017). In vivo biomechanical behavior of the trapeziometacarpal joint in healthy and osteoarthritic subjects. *Clinical Biomechanics*, 49, 119-127.

Kapandji, I.A. (1996). Fisiologia articular. Miembro superior. *Medica Panamericana*, Madrid, 5 Edición.

Tubiana, R. (1981). The hand. Volume I. *W.B. Saunders company*. 2 edition.

Neu, C.P., J.J. Crisco & S.W. Wolfe. (2001). In vivo kinematic behavior of the radio-capitate joint during wrist flexion–extension and radio-ulnar deviation. *Journal of Biomechanics*, 34, 1429-1438.

Sonenbluma, S.E., Crisco, J.J., Kangb, L., Akelman, E. (2004). In vivo motion of the scaphtrapzio trapezoidal (STT) joint. *Journal of Biomechanics*, 37, 645-652.

Denavit, J., Hartenberg, R.S. (1955). A Kinematic Notation for Lower-pair Mechanisms Based on Matrices. *Journal of Applied Mechanics*, ASME, 22, 215-221

Elatta, M.A., Elgaind, S.M., Talat, E., Alqaseer, A.M., Basheer, H.M. (2019). Scapho-Capitate Ratio for Estimation of Scaphoid Length. *The Journal of Hand Surgery (Asian-Pacific Volume)* 14(2), 1-6

User-Guided Grasp Planning for Digital Hand

Yi Li, Niclas Delfs, and Johan S. Carlson
The Geometry and Motion Planning Department
Fraunhofer Chalmers Centre
SE-412 88 Gothenburg, Sweden
E-mail address of the corresponding author: yi.li@fcc.chalmers.se

Abstract

In order to assemble a part (of e.g., an engine), a human hand must obtain complete control of its motion through application of forces and toques at multiple contact points. Today, it is often time-consuming to synthesize a good hand grasp of a part using Digital Human Modeling (DHM) tools because these tools require detailed manual inputs from a user such as manually placing a digital hand around a feasible grasp location and then closing the fingers around the part. In a previous paper, we presented two different methods (i.e., Pointwise Shortest Distance and Environment Clearance) to color part surfaces by taking environmental distance constraints into account so that a user such as an assembly simulation expert can easily identify feasible grasp locations. Due to the robustness of the implementation, even triangle meshes with common geometric flaws such as cracks and gaps can be handled. In this paper, we leverage on this feasibility analysis and present a user-guided grasp planning approach that significantly speeds up the grasp modeling process. First, the user selects a predefined grip type and then sets an approach direction for the hand. To synthesize many grasps, we randomly sample the hand's rotation around the approach direction. Next, the hand is moved towards the part until the hand's Grasp Center Point (GCP) reaches the geometry of the part or a collision between the hand and the part is detected. If a collision was detected, we move the hand backwards until there is no collision between the hand and the part anymore. Finally, we close the hand's fingers around the part to synthesize a grasp. In this way, we can quickly synthesize a multitude of grasps and let the user choose among the ones with the best grasp qualities, where each grasp quality is computed using the corresponding 6D grasp wrench hull. We believe that this user-guided grasp planning approach can significantly enhance DHM tools such as Intelligently Moving Manikins (IMMA) when it comes to user usability.

Keywords: Assembly Simulation, Digital Human Model, Ergonomics, Grasping, Visualization.

Introduction

Before fabricating a physical prototype, a DHM tool such as IMMA (Högberg, Hanson, Bohlin, & Carlson, 2016) in the Industrial Path Solutions (IPS) platform can be used to evaluate both human-product interactions and human-production system interactions. To assemble a part such as the Central Electronic Module (CEM) box shown in Figure 1, a feasible grasp location for a manikin must be identified prior to the grasping of the part by a manikin hand.

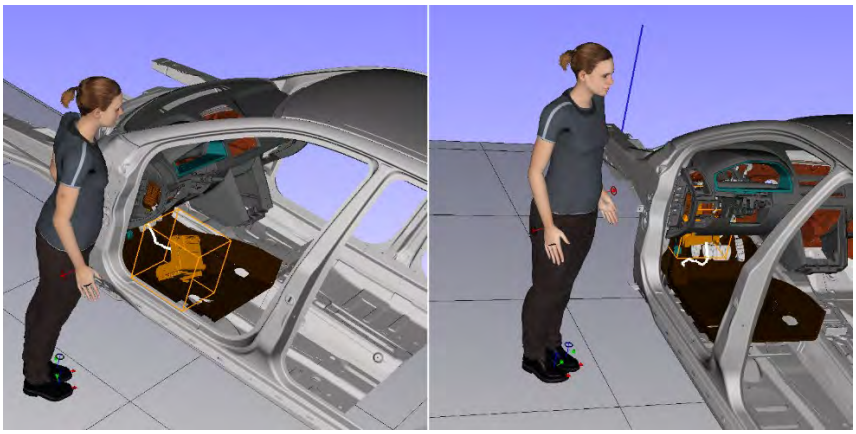

Figure 1. To assemble the Central Electronic Module (CEM) box, the manikin must grasp it and then move from its start pose (i.e., the combination of position and orientation) shown in the left subfigure to its goal pose shown in the right subfigure while following the path shown in white.

In the field of robotics, many researchers assume that the part to be grasped is alone (Li, Saut, Pettré, Sahbani, & Multon, 2015) (i.e., the grasp planner does not need to take into account any other objects) and the manipulator is disembodied (i.e., the kinematics of the robot is not taken into account). Consequently, most DHM tools still rely on teleoperation or hand scripted grasps. As the first step towards autonomous grasp planning in IPS IMMA, we presented two methods called *Pointwise Shortest Distance* and *Environment Clearance* in (Li, Kressin, Vajedi, & Carlson, 2017) to visualize part surfaces so that best collision-free grasp locations can be easily identified. Pointwise Shortest Distance is designed so that surfaces of a part can be colored as fast as possible (i.e., at a low computational cost), because the color at each vertex is simply determined by the shortest distance between it and the environment (i.e., the obstacle objects). On the contrary, Environment Clearance (Berenson, Diankov, Nishiwaki, Kagami, & Kuffner, 2017) is much more computationally expensive because it relies on the clearance along the normal vector at each vertex to handle parts with complex shapes. In (Li, Kressin, Vajedi, & Carlson, 2017) and in this paper, both the part to be assembled (or disassembled) and the environment are represented by triangle meshes. Since many triangle meshes are not always consistently oriented (i.e., the

normal vectors sometimes point in the "wrong" directions), our GPU-based algorithm called *Visual Shell* is applied in (Li, Kressin, Vajedi, & Carlson, 2017) to flip inconsistently oriented normal vectors. The upside of Environment Clearance is that it is much better at isolating/highlighting potential grasp locations than Pointwise Shortest Distance. In Figure 2, both methods are applied to color the surfaces of the tunnel console, which is the part that has to be disassembled. As shown in the left subfigure, several surface patches on the left side of the tunnel console are colored in red using Pointwise Shortest Distance, because triangle vertices on these patches are located very close to either the gear stick or the handbrake, even though these patches can be easily accessed by a manikin hand. However, these surface patches are rendered in blue in the right subfigure where Environment Clearance is used instead.

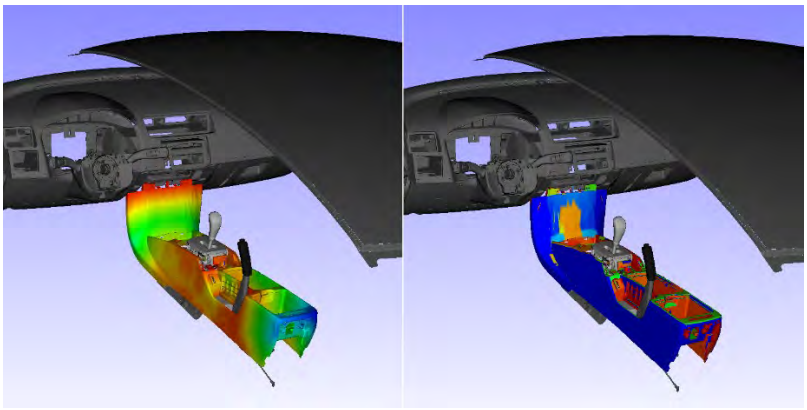

Figure 2. The tunnel console is colored using Pointwise Shortest Distance in the left subfigure, whereas Environment Clearance is used to color the surfaces of the tunnel console in the right subfigure.

After determining feasible grasp locations for a manikin in (Li, Kressin, Vajedi, & Carlson, 2017), an IMMA user still has to manually place the hand at a grasp location and then close the fingers to grasp the part. This procedure not only is time-consuming, but also does not evaluate newly synthesized grasp (i.e., computing the corresponding grasp quality). In this paper, the grasp modeling procedure is significantly easier because the user only needs to define a single approach direction that the hand has to follow during the synthesis process. In this way, many grasps can be quickly synthesized, and the user only needs to select one of these grasps that have *closure* (i.e., these grasps can be maintained for every possible disturbance load) at the end. There are two types of grasp closure: *form closure* and *force closure*. We are only concerned with force closure in this paper because a force closure grasp (also called a precision grasp) is able to balance any disturbance by applying forces with friction at contact points and hence requires fewer contact points than are required for a form closure grasp (also called power grasp or enveloping grasp).

Methods

In this section, we present a user-guided grasp planning approach that significantly speeds up the grasp modeling process after giving a short description about how we model and evaluate a grasp from a mathematical perspective.

IMMA Hand Modeling

The configuration of an IMMA hand is high-dimensional (with 19 bones, 19 joints, and 32 degrees of freedom (DOF)). It is modeled by Rectangular Swept Spheres (RSSs) (Larsen, Gottschalk, Lin, & Manocha, 2000) (see Figure 3) when contacts between the hand and the part are queried. Furthermore, IMMA comes with 9 predefined grip types (i.e., Chuck Grip, Closed Hand, Cylindrical Power Grip, Diagonal Power Grip, Lateral Pinch, Parallel Extension, Prismatic 4F Pinch, Spherical Grip, and Tip Pinch as shown in Figure 4). For each grip type, IMMA also defines the corresponding two sets of joint angles describing the open hand configuration and the closed hand configuration, respectively. A hand can be opened/closed by simply interpolating the joint angles between these two configurations as shown in Figure 3.

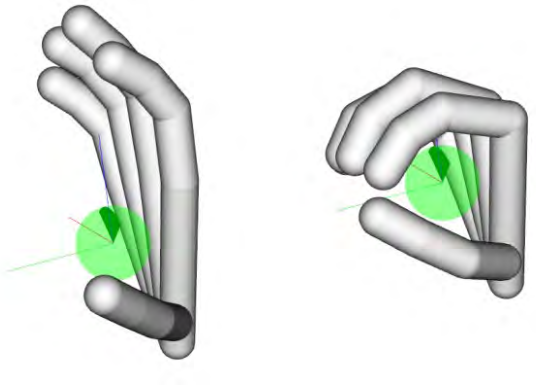

Figure 3. Spherical grip's open hand configuration and closed hand configuration, respectively.

Grasp Modeling and Grasp Evaluation

An IMMA manikin obtains complete control of the part's motion by grasping it through application of forces and torques at multiple contacts between the hand and the part. Because the configuration of a manikin hand is high-dimensional and the geometry of the part restricts the space of feasible contacts, it is a challenging task to synthesize a stable grasp. To simplify the task of grasping a part, point-on-plane contact models are used in this paper in grasp analysis because neither point-on-point contact nor point-

on-line contact is stable. Additionally, possible contact points for most objects are seldom sharp edges or points.

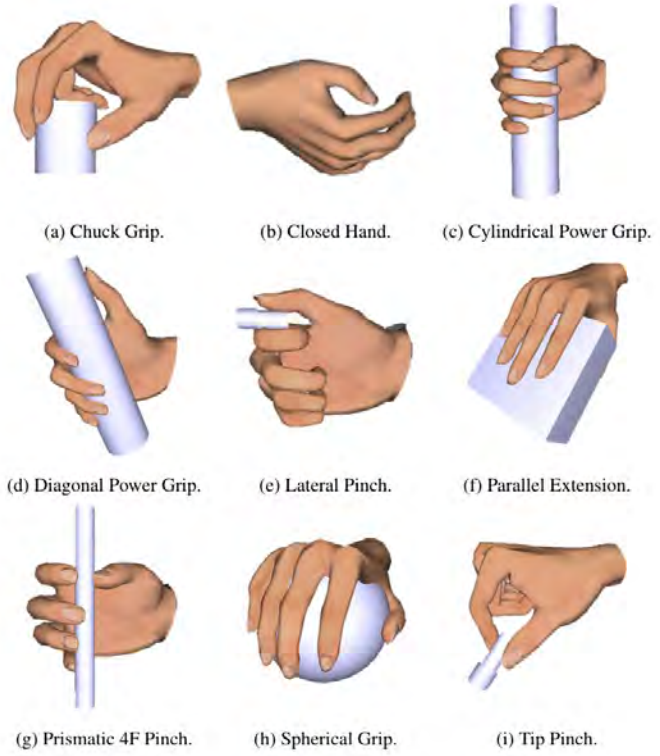

Figure 4. Predefined grip types in IMMA.

Assume that after the hand is closed around the part, there are k contact points. If we assume that these contact points are not frictionless, then the forces that don't lead to slipping (i.e., the admissible forces) can be defined by a *friction cone* (as shown in the left subfigure in Figure 5):

$$\mathcal{F} = \{\boldsymbol{f} \mid \|\boldsymbol{f}_{tangent}\| \leq \mu \|\boldsymbol{f}_{\perp}\|, \quad f_z \geq 0\},$$

where μ is the coefficient of static friction associated with the surface, $\boldsymbol{f} = \boldsymbol{f}_{\perp} + \boldsymbol{f}_{tangent}$ is the total force acting on the part at a contact point, $\boldsymbol{f}_{\perp} = [0, 0, f_z]$, $\boldsymbol{f}_{tangent} = [f_x, f_y, 0]$, and the positive z-direction points in the direction of the part's surface normal at the contact point and into the part. It is very convenient from a computational standpoint to *inner* approximate the true friction cone with a pyramid. In the right subfigure in Figure 5, the pyramidal inner-approximation of the friction cone is defined by 8 vectors (i.e., $\boldsymbol{f}_1, \cdots, \boldsymbol{f}_8$).

Given a grasp defined by k contact points and the corresponding k linearized friction cones $\mathcal{F}_i$ defined by m bounded forces $\{\boldsymbol{f}_{i,1}, \boldsymbol{f}_{i,2}, \cdots, \boldsymbol{f}_{i,m}\}$, the *grasp wrench space* $\mathcal{W}$ is the set of all possible wrenches that

can be applied to the part by the grasp and it can be used to evaluate the grasp. A wrench vector $\boldsymbol{w}_{i,j}$ is a stacked vector of a force $\boldsymbol{f}_{i,j} \in \mathbb{R}^3$ and torque $\boldsymbol{\tau}_{i,j} \in \mathbb{R}^3$ applied at the torque origin, often the object's center of mass:

$$\boldsymbol{w}_{i,j} = \begin{bmatrix} \boldsymbol{f}_{i,j} \\ \boldsymbol{\tau}_{i,j} \end{bmatrix} \in \mathbb{R}^6,$$

where indexes i and j represent the i-th contact point of the grasp and the j-th bounded force of linearized friction cone $\mathcal{F}_i$, respectively.

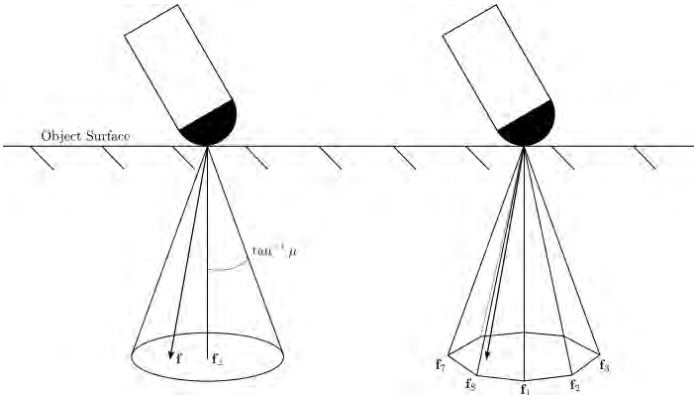

Figure 5. A friction cone and the corresponding pyramidal inner-approximation.

It can be rewritten as:

$$\boldsymbol{w}_{i,j} = \begin{bmatrix} \boldsymbol{f}_{i,j} \\ \lambda(\boldsymbol{d}_i \times \boldsymbol{f}_{i,j}) \end{bmatrix},$$

where $\lambda \in \mathbb{R}$ is the torque multiplier and vector $\boldsymbol{d}_i$ defines the position of contact point i with respect to the torque origin. Regarding the constant λ, it is arbitrary. However, a value of $\lambda = 1$ is common if the forces $\boldsymbol{f}_{i,j}$ are dimensional. In (Pollard, 1994), a value of $\lambda = \frac{1}{r}$ is used to ensure that the quality of a grasp is independent of object scale, where r is the maximum radius from the torque origin.

The *grasp wrench space* $\mathcal{W}$ is then defined as.

$$\mathcal{W} = \{\boldsymbol{w} \mid \boldsymbol{w} = \sum_{i=1}^{k}\sum_{j=1}^{m} \alpha_{i,j}\boldsymbol{w}_{i,j}, \quad \boldsymbol{w}_{i,j} = \begin{bmatrix} \boldsymbol{f}_{i,j} \\ \lambda(\boldsymbol{d}_i \times \boldsymbol{f}_{i,j}) \end{bmatrix}, \quad \sum_{j=1}^{m} \alpha_{i,j} \leq 1, \quad \alpha_{i,j} \geq 0\}$$

Unfortunately, the grasp wrench space $\mathcal{W}$ is cumbersome to compute in practice. Instead, the *grasp wrench hull* $\widetilde{\mathcal{W}}$ is used to characterize a grasp because it can be efficiently computed (with for example

the Qhull program (Barber, Dobkin, & Huhdanpaa, 1996) and more importantly the property $\tilde{\mathcal{W}} \subseteq \mathcal{W}$ holds by definition. The wrench hull $\tilde{\mathcal{W}}$ is defined as.

$$\tilde{\mathcal{W}} = \{\boldsymbol{w} \mid \boldsymbol{w} = \sum_{i=1}^{k}\sum_{j=1}^{m} \alpha_{i,j}\boldsymbol{w}_{i,j}, \quad \boldsymbol{w}_{i,j} = \begin{bmatrix} \boldsymbol{f}_{i,j} \\ \lambda(\boldsymbol{d}_i \times \boldsymbol{f}_{i,j}) \end{bmatrix}, \quad \sum_{i=1}^{k}\sum_{j=1}^{m} \alpha_{i,j} = 1, \quad \alpha_{i,j} \geq 0\}$$

Two grasp quality metrics can be defined based on the definition of the grasp wrench hull $\tilde{\mathcal{W}}$: *epsilon measure* and *volume measure* (Li & Sastry, 1988) (Miller & Allen, 1999). The epsilon measure is simply the radius of the largest 6D ball inside $\tilde{\mathcal{W}}$. A grasp is in force closure if and only if the radius is greater than zero (i.e., the origin is contained in the interior of $\tilde{\mathcal{W}}$). The epsilon measure is a worst-case metric because the radius represents the magnitude of the *smallest* external wrench that can push the grasp to its limits. Given a 3D object, at least three contacts are required for a grasp to be in force closure under a point contact with friction model. The volume measure is defined as the volume of $\tilde{\mathcal{W}}$ and it is an average case metric. Given two grasps with the same epsilon measure, the volume measure can be used to differentiate between them. Unfortunately, the volume measure does not reflect the stability of a grasp (i.e., it's not guaranteed to be in force closure even if it has a larger volume measure than a stable grasp). Another difference between the epsilon measure and the volume measure is that the volume measure is invariant to the choice of torque origin, whereas the epsilon measure is not.

Grasp Planning

In this subsection, we describe our user-guided grasp planner that is able to synthesize and then evaluate a multitude of grasps quickly using the two grasp quality metrics from the previous subsection and then presents the stable grasps to the IMMA user.

Firstly, the IMMA user selects a suitable grip type among the ones listed in Figure 4 and then defines the approach direction that the hand must follow during the synthesis process by selecting a point on the surface of the part. Assume that we want to grasp the top of the cylinder in the left subfigure in Figure 6, then we can select a single point on the top base of the cylinder to define the approach direction. In the left subfigure in Figure 6, the resulting approach direction visualized as a red arrow that points in the opposite direction of the surface normal vector at the selected point. The approach direction can also be modified by rotating the arrow's tip around the selected point.

Secondly, grasps are automatically synthesized by letting the hand assume the open hand configuration in the neighborhood of the part and then approach the part following the approach direction such that the hand is aligned so that the unit length vector halfway between the y and z axes in the local coordinate

system for the hand's Grasp Center Point (GCP) points in the approach direction. In Figure 3, the GCP coordinate system's x, y, and z axes are represented by red, green, and blue, whereas the origin of the coordinate system is enclosed inside a green sphere. To synthesize a multitude of grasps, we randomly sample the hand's rotation around the approach direction. The hand is moved towards the part until a collision between them is detected or the GCP is reached by the geometry of the part. In case of collision, the hand is moved away from the part until the collision is resolved (Vahrenkamp, et al., 2013). Next, the hand's fingers are closed one-by-one around the geometry of the part by interpolating the joint angles from the selected grip type's open hand configuration to its closed hand configuration. The resulting contact points between the fingers and the part are then used to compute both the epsilon measure and the volume measure. N.B.: A grasp is in force closure when its epsilon measure is greater than zero. In this way, many grasps can be quickly synthesized and the IMMA user only needs to select one of the stable grasps (e.g., the one in the right subfigure in Figure 6) at the end.

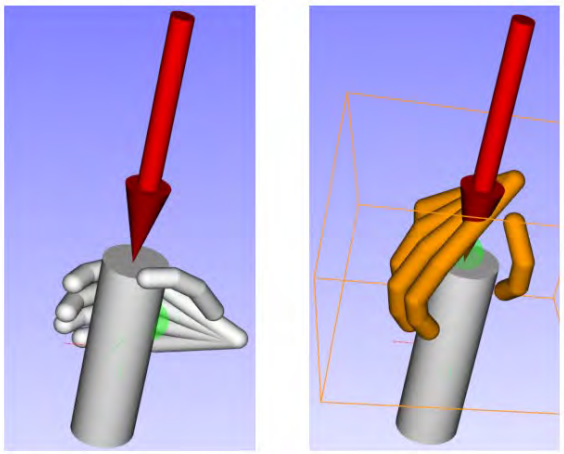

(a) Approach direction. (b) A stable grasp.

Figure 6. Use grasp approach direction to synthesize stable grasps.

Results

In this section, we present examples of grasp synthesis for a couple of objects using our user-guide grasp planner for the IMMA digital hands.

In the left subfigure in Figure 7, the Pointwise Shortest Distance method (Li, Kressin, Vajedi, & Carlson, 2017) is used to color the surface of the CEM box, where the red patches are the areas that are too close to the obstacles when the box is moved from the start pose to the goal pose. Instead, we select a point on a green patch during the assembly simulation to obtain an approach direction that points perpendicularly into the green patch as shown in the right subfigure in Figure 7. Next, we select grip type *Spherical Grip*

and run the grasp planner for 60 seconds. The most stable grasp (i.e., the one with the greatest positive epsilon measure) among the resulting grasps is also shown in the right subfigure.

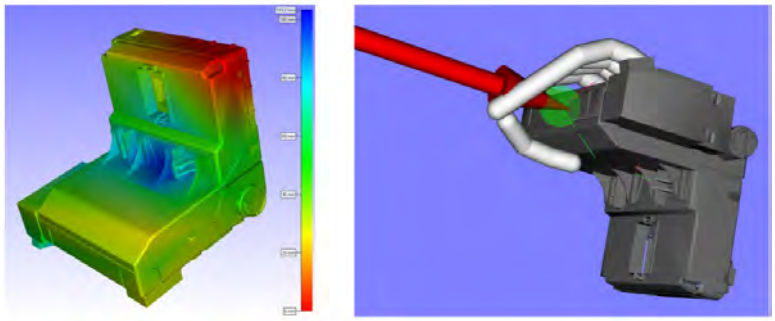

Figure 7. CEM box colored using the pointwise shortest distance method and a stable grasp.

In Figure 2, both Pointwise Shortest Distance and Environment Clearance are applied to color the surfaces of the tunnel console, where surface patches that can be easily accessed by a manikin hand are correctly rendered in blue by the Environment Clearance method as shown in the right subfigure. We select a point on a sloping edge of the tunnel console and then manually rotate the approach direction slightly so that its approximately points perpendicularly to the ground (assuming that the tunnel console is placed with its bottom on a table) as shown in Figure 8. Next, we select grip type *Cylindrical Power Grip* and run the grasp planner for 60 seconds. The most stable grasp (i.e., the one with the greatest positive epsilon measure) among the resulting grasps is also shown in the figure.

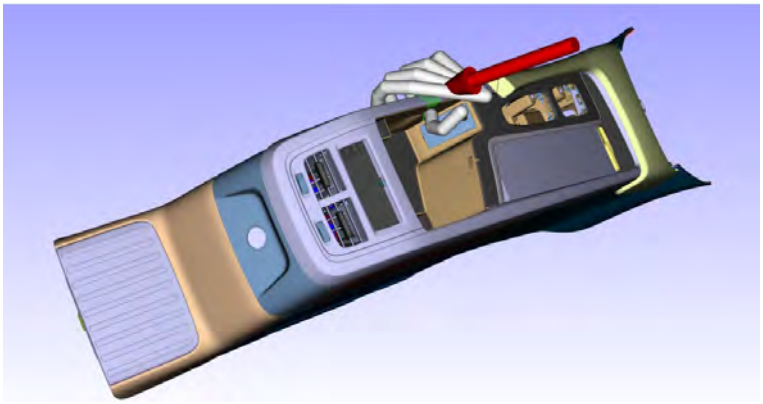

Figure 8. Volvo XC90 tunnel console and a stable grasp.

For a large object that requires at least two hands, it is not possible to find a stable grasp using a single hand. However, our user-guided grasp planner can still be used to synthesize good-looking grasps, where the resulting grasps can be sorted by the volume measure that does not reflect the stability of a grasp.

Discussion and Conclusions

We have demonstrated that our user-guided grasp planner is able to quickly synthesize a huge number of grasps for a given part so that an IMMA user can simply choose one among the grasps with the best grasp qualities instead of the previous time-consuming process of manual synthesizing a grasp by placing the hand at a suitable spot close to the part and then closing the fingers around it. Consequently, we believe that this user-guided grasp planning approach can significantly enhance IMMA's usability for assembly simulation experts. Future work will include adding support for a second hand to handle larger objects. We would also like to include a task-oriented grasp quality metric since both the epsilon measure and the volume measure are task-independent.

Acknowledgments

This work is part of the Sustainable Production Initiative and the Production Area of Advance at the Chalmers University of Technology. We would like to acknowledge the generosity of Volvo Cars in providing the models that were used for the experiments in this work.

References

Barber, C. B., Dobkin, D. P., & Huhdanpaa, H. T. (1996). ACM Trans. on Mathematical Software. *The quickhull algorithm for convex hulls*, 469-483.

Berenson, D., Diankov, R., Nishiwaki, K., Kagami, S., & Kuffner, J. (2017). Grasp planning in complex scenes. *Proceedings of the 7th IEEE-RAS International Conference on Humanoid Robots (Humanoids 2017)*, (pp. 42-48).

Högberg, D., Hanson, L., Bohlin, R., & Carlson, J. S. (2016). Creating and shaping the DHM tool IMMA for ergonomic product and production design. *International Journal of the Digital Human, 1*(2), 132-152.

Larsen, E., Gottschalk, S., Lin, M. C., & Manocha, D. (2000). Fast distance queries with rectangular swept sphere volumes. *Proceedings of 2000 IEEE International Conference on Robotics and Automation*, (pp. 3719-3726).

Li, Y., Kressin, J., Vajedi, S., & Carlson, J. S. (2017). Visualization of part surfaces for identifying feasible assembly grasp locations. *Proceedings of the 5th International Digital Human Modeling Symposium (DHM 2017).*

Li, Y., Saut, J. P., Pettré, J., Sahbani, A., & Multon, F. (2015). Fast Grasp Planning Using Cord Geometry. *IEEE Transactions on Robotics*, 1393-1403.

Li, Z., & Sastry, S. S. (1988). Task-oriented optimal grasping by multifingered robot hands. *IEEE Journal on Robotics and Automation*, 32-44.

Miller, A. T., & Allen, P. K. (1999). Examples of 3D grasp quality computations. *Proceedings of the 1999 IEEE International Conference on Robotics and Automation*, (pp. 1240-1246).

Pollard, N. S. (1994). *Parallel Methods for Synthesizing Whole-Hand Grasps from Generalized Prototypes.* Massachusetts Institute of Technology.

Vahrenkamp, N., Krohnert, M., Ulbrich, S., Asfour, T., Metta, G., Dillmann, R., & Sandini, G. (2013). Simox: A Robotics Toolbox for Simulation, Motion and Grasp Planning. In *Intelligent Autonomous Systems 12: Volume 1 Proceedings of the 12th International Conference IAS-12* (pp. 585-594). Springer.

Modeling and Simulation of a Powered Exoskeleton System to Aid Human-Robot Collaborative Lifting

Asif Arefeen and Yujiang Xiang*
School of Mechanical and Aerospace Engineering
Oklahoma State University, Stillwater, OK 74078, USA
*Corresponding Author: yujiang.xiang@okstate.edu

Abstract

Exoskeletons are remarkable technologies that improve human strength, reduce fatigue, and restore users' abilities. In this study, a novel physics-based optimization formulation is proposed to find the optimal control of a powered elbow exoskeleton to aid the human-robot collaborative lifting task. The three-dimensional (3D) human arm model has 13 degrees of freedom (DOFs), and the 3D robot arm (Sawyer robot arm) model has 10 DOFs. The inverse dynamics optimization is utilized to find the optimal lifting motion and the optimal exoskeleton assistive torque. The 3D human arm and robot arm are modeled in Denavit-Hartenberg (DH) representation. The electromechanical dynamics of the DC motor of the exoskeleton are considered in the dynamic human-robot collaborative lifting optimization. In addition, the 3D box is modeled as a floating-base rigid body with 6 global DOFs. The human-box and robot-box interactions are characterized as a collection of grasping forces. The joint torque squares of human arm and robot arm are minimized subjected to physics- and task-based constraints. The design variables include (1) control points of cubic B-splines of joint angle profiles of the human arm, robotic arm, and box; (2) control points of cubic B-splines of motor current for the exoskeleton; and (3) the discretized grasping forces during lifting. The constraints include joint angle limits for human arm and robot arm, joint torque limits for human arm, robot arm and exoskeleton, human-robot grasping positions, box balance condition, initial and final box locations, and bounds on design variables. A numerical example of lifting a 10 kg box is simulated. The nonlinear collaborative lifting optimization problem is solved using a sequential quadratic programming (SQP) method in SNOPT, and the optimal solutions are found in 136.11 seconds. The simulation reports the grasping force profiles, human arm's joint angles, and the powered elbow exoskeleton's torque profiles. The results reveal that the proposed optimization formulation can find the exoskeleton's optimal control and lifting strategy for the human-robot collaborative lifting task.

Keywords: Motion planning, optimal control, human-robot interaction, powered exoskeleton, and inverse dynamics optimization.

Introduction

Collaboration between humans and robots is a research topic with a wide range of applications and a major economic impact. Human-robot collaboration can considerably speed up production processes, improve manufacturing efficiency, and reduce structural costs. On the other hand, wearable devices such as exoskeletons have a wide range of applications in clinical neurorehabilitation settings and industrial settings for construction and manufacturing. These wearable technologies can improve a person's strength, minimize workplace fatigue, and restore a person's limited range of motion caused by diseases. In addition, the exoskeleton can prevent human injuries and increase human endurance during human-robot collaborative tasks. Therefore, human-robot collaborative lifting motion prediction with a powered exoskeleton is a state-of-the-art technology that has not been studied yet. Moreover, designing and simulating an optimal powered exoskeleton system is necessary to assist human-robot object lifting tasks.

Last few years, several optimization-based modeling methods have been used to simulate exoskeleton-wearer interaction (Agarwal et al., 2013; Bai & Rasmussen, 2011; Zhou et al., 2015). There have been a few studies on developing robotic exoskeletons to assist humans in lifting tasks. During manual lifting, a semi-squat lifting model was used to determine the hip joint output torque and power for the active hip exoskeleton to aid lifting motion (Wei et al., 2020). In Manns et al., (2017), a 2-DOF passive back exoskeleton was developed to aid the lifting motion. The spring parameters of the exoskeleton were optimized using an SQP-based direct multiple shooting method. In Zhang & Huang (2018), a compact series-elastic actuated 4-DOF powered hip exoskeleton was designed to alleviate lumbar compression by reducing muscular activities around the lumbar spine for both symmetric and asymmetric liftings. Xiang and Arefeen (2020) developed a human-human collaborative lifting motion prediction considering human-box grasping forces. In addition, an optimization-based human-robot collaborative lifting motion prediction has been developed in previous research (Arefeen et al., 2022a, 2022b; Arefeen & Xiang, 2021).

This work extends our previous collaborative lifting prediction for the 3D and 2D skeleton models (Arefeen et al., 2022b; Arefeen & Xiang, 2021; Xiang & Arefeen, 2020) to human-robot collaborative lifting with an elbow exoskeleton. This study proposes a novel physics-based optimization formulation to find the optimal control of a powered elbow exoskeleton to aid the human-robot collaborative lifting task. An inverse dynamics optimization formulation was used to optimize the lifting motion and exoskeleton control. An SQP algorithm in SNOPT (Gill et al., 2005) is used to solve the human-robot lifting problem. The simulation reports the human grasping force profiles, the human arm’s joint angles, and the powered elbow exoskeleton’s torque profiles.

Methods

This section discusses the 3D human arm model augmented by an active elbow exoskeleton and robot arm model. In addition, the floating-based 3D rigid box model is also discussed.

Human-exoskeleton and robot arm model

This work considers a 3D human skeletal arm model equipped with an active 1-DOF elbow exoskeleton, a 10-DOF robot arm model, and a rigid box, as shown in Figure 1. The human skeletal arm model has 13 DOFs. The box has 6 global DOFs, including three translations and three rotations. The human elbow joint is augmented by an active 1-DOF exoskeleton. The robotic formulation of the DH method is used to construct the human arm, robot and the box models. In addition, there are two grasping forces ($\mathbf{f}_{c1}$ and $\mathbf{f}_{c2}$) acting on the two bottom edges of the box. In this study, the human anthropometric data are obtained using GEBOD™ software (Cheng et al., 1994). The DH parameters for the human arm, robot arm, and box model are available in the literature (Arefeen & Xiang, 2021).

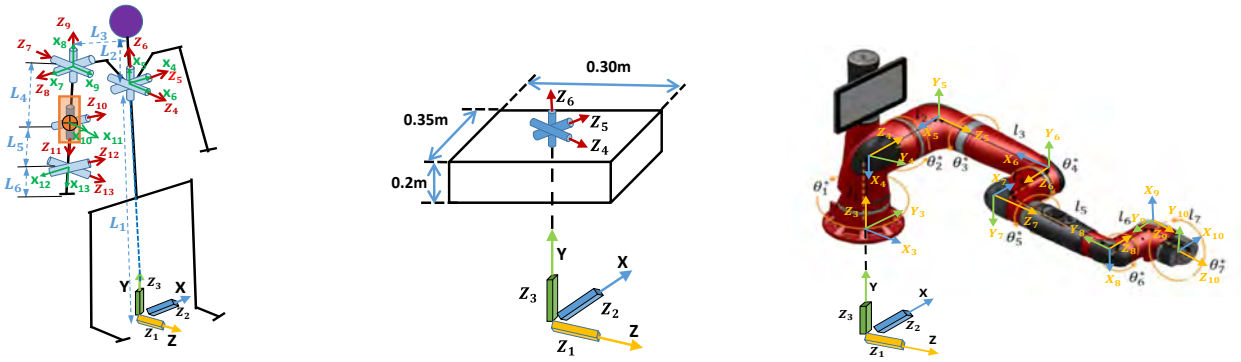

(a) (b) (c)

Figure 1. (a) The 3D human arm model (global DOFs: $z_1, z_2, z_3, z_4, z_5, z_6$) with an elbow exoskeleton (orange), (b) 3D box model (global DOFs: $z_1, z_2, z_3, z_4, z_5, z_6$), and (c) Sawyer robot arm (global DOFs: z_1, z_2, z_3).

Equation of motion (EOM)

The electromechanical dynamics of DC motors of the exoskeleton are modeled in the optimization-based dynamic human lifting motion prediction. The dynamics equations can be expressed as follow (Nguyen et al., 2020):

$$L\frac{dI}{dt} = V - K\frac{d\theta}{dt} - RI \tag{1}$$

$$T_{motor} = KI \tag{2}$$

$$T_l = T_{motor} - J_m \frac{d^2\theta}{dt^2} - b\frac{d\theta}{dt} \tag{3}$$

where *V*, *I*, *L*, and *R* are the voltage input, current, inductance, and resistance. The mechanical terms J_m, b, *K,* and θ are the rotor moment of inertia, coefficient of viscous friction of the motor, motor torque constant, and rotor angle. T_{motor} is the motor output torque and T_l is the load torque of the exoskeleton. The gearbox ratios (GB_r) are chosen so that the exoskeleton can provide the required torque output. Here, the exoskeleton includes the motor and the gearbox. So, the output torque (τ_e) of the exoskeleton can be expressed as follows:

$$\tau_e = GB_r \times T_l \tag{4}$$

The human-exoskeleton model is analyzed using recursive kinematics and Lagrangian dynamics (Xiang & Arefeen, 2020). Forward kinematics and backward dynamics are the two aspects of the process. The EOM of the human-exoskeleton systems and sensitivity analysis are formed using a recursive Lagrangian dynamics formulation. The dynamics can be expressed as follows:

$$\tau_{h_i} + \tau_{e_i} = \mathrm{tr}\left(\frac{\partial \mathbf{A}_i}{\partial q_i}\mathbf{D}_i\right) - \mathbf{g}^{\mathrm{T}}\frac{\partial \mathbf{A}_i}{\partial q_i}\mathbf{E}_i - \mathbf{f}_k^{\mathrm{T}}\frac{\partial \mathbf{A}_i}{\partial q_i}\mathbf{F}_i - \mathbf{G}_i^{\mathrm{T}}\mathbf{A}_{i-1}\mathbf{z}_0 \tag{5}$$

where τ_{h_i} is the actual human torque at the i^{th} joint and τ_{e_i} is the exoskeleton output torque for the i^{th} joint. $\mathbf{A}_i$ is the global position transformation matrices (4×4) for the i^{th} joint. $tr(\cdot)$ is the trace of a matrix $\mathbf{A}_i$, $\mathbf{C}_i$ are global position and acceleration transformation matrices, $\mathbf{I}_i$ is the inertia matrix for link *i*, $\mathbf{D}_i$ is the recursive inertia and Coriolis matrix, $\mathbf{E}_i$ is the recursive vector for gravity torque calculation, $\mathbf{F}_i$ is the recursive vector for external force-torque calculation, $\mathbf{G}_i$ is the recursive vector for external moment torque calculation, $\mathbf{g}$ is the gravity vector, m_i is the mass of link *i*, $\mathbf{r}_i$ is the COM of link *i* in the i^{th} local frame, $\mathbf{f}_k = [f_{kx} \quad f_{ky} \quad f_{kz} \quad 0]^{\mathrm{T}}$ is the external force applied on link *k*, $\mathbf{r}_k$ is the position of the external force in the k^{th} local frame, $\mathbf{h}_k = [h_x \quad h_y \quad h_z \quad 0]^{\mathrm{T}}$ is the external moment applied on link *k*, $\mathbf{z}_0 = [0 \quad 0 \quad 1 \quad 0]^{\mathrm{T}}$ is for a revolute joint, $\mathbf{z}_0 = [0 \quad 0 \quad 0 \quad 0]^{\mathrm{T}}$ is for a prismatic joint, finally, δ_{ik} is Kronecker delta, and the starting conditions are $\mathbf{D}_{n+1} = [\mathbf{0}]$ and $\mathbf{E}_{n+1} = \mathbf{F}_{n+1} = \mathbf{G}_{n+1} = [\mathbf{0}]$. The detailed formulas and sensitivity with respect to state variables are referred to Xiang & Arefeen (2020) and Xiang et al. (2009). Moreover, this study treats the grasping external forces of human-box and robot-box as unknowns (design variables) in the optimization formulation. As a result, the joint torques are a function of both state variables and varying grasping forces. To use gradient-based optimization, the sensitivity of joint

torque with respect to external force needs to be determined that was explained in detail in the literature (Arefeen et al., 2022a, 2022b).

Optimization formulation

The human-robot collaborative lifting is predicted by solving a nonlinear programming (NLP) problem. Here the box initial and final positions, the feet and robot base positions, and the box dimension and weight are given.

Design variables

The design variables (**x**) are cubic joint angle B-spline control points $\mathbf{P}_{human}$, $\mathbf{P}_{robot,}$ and $\mathbf{P}_{box}$ for the human, robot, and box. The motor current *I* profiles are also discretized using cubic B-splines so that the exoskeleton current control points $\mathbf{P}_{current}$ are also design variables. Furthermore, the grasping forces ($\mathbf{f}_1^c$ and $\mathbf{f}_2^c$) between human and box, and robot and box, are treated as additional design variables. As a result, the optimization design variables for the collaborative lifting are $\mathbf{x} = [\mathbf{P}_{human}^{\mathrm{T}} \quad \mathbf{P}_{robot}^{\mathrm{T}} \quad \mathbf{P}_{box}^{\mathrm{T}} \quad \mathbf{P}_{current}^{\mathrm{T}} \quad \mathbf{f}_{c1}^{\mathrm{T}} \quad \mathbf{f}_{c2}^{\mathrm{T}}]^{\mathrm{T}}$.

Objective function

The dynamics effort (Xiang & Arefeen, 2020) is used as the objective function for the collaborative lifting motion, which is defined as the sum of joint torques squared for human and robot (Arefeen & Xiang, 2020, 2021; Xiang & Arefeen, 2020; Xiang et al., 2009).

$$J(\mathbf{x}) = w_1 \sum_{i=6}^{n\_human} \int_0^T \{\tau_{i(human)}^2(\mathbf{P}_{human}, \mathbf{f}_1^c)\}dt + w_2 \sum_{i=3}^{n\_robot} \int_0^T \{\tau_{i(robot)}^2(\mathbf{P}_{robot}, \mathbf{f}_2^c)\}dt \quad (6)$$

where $n\_human = 13$, $n\_robot = 10$. The total time duration *T* is a specified input parameter, w_1 and w_2 are weighting coefficients for human and robot performance measure, respectively.

Constraints

The time-dependent constraints include joint angle limits, joint torque limits, human feet and robot base contacting position, box forward position, box range of motion, box grasping location, box global EOM, and exoskeleton torque limit. Time independent constraints include initial and final box locations, static conditions at the beginning and end of the motion. At each time discretization point, time-dependent constraints are sequentially determined during the optimization process. The time-independent constraints, however, are determined at a specific time point.

(a) Joint angle limits

$$\mathbf{q}_h^L \leq \mathbf{q}_h(\mathbf{x}, t) \leq \mathbf{q}_h^U \quad (7)$$
$$\mathbf{q}_r^L \leq \mathbf{q}_r(\mathbf{x}, t) \leq \mathbf{q}_r^U$$

where the superscript *L* and *U* denote the lower and upper bound of the limits, respectively. $\mathbf{q}_h$ and $\mathbf{q}_r$ are the joint angles for the human and robot arm.

(b) Joint torque limits

$$\boldsymbol{\tau}_h^L \leq \boldsymbol{\tau}_h(\mathbf{x}, t) \leq \boldsymbol{\tau}_h^U \quad (8)$$
$$\boldsymbol{\tau}_r^L \leq \boldsymbol{\tau}_r(\mathbf{x}, t) \leq \boldsymbol{\tau}_r^U$$

where $\boldsymbol{\tau}_h^L$ and $\boldsymbol{\tau}_h^U$ are human lower and upper joint torque limits, and $\boldsymbol{\tau}_r^L$ and $\boldsymbol{\tau}_r^U$ are robot lower and upper limits, respectively.

(c) Human feet and robot base contacting position

$$p_{h\_feet}(t) = p_{h\_feet}^s \quad (9)$$
$$p_{r\_base}(t) = p_{r\_base}^s$$

where $p_{h\_feet}^s$ and $p_{r\_base}^s$ are the specified feet and robot base contact position on the level ground.

(d) Box forward position

$$Z_{h\_wrist}(t) - Z_{h\_pelvis}(t) \geq 0 \quad (10)$$

where Z_{h_wrist} and Z_{h_pelvis} are the global Z coordinates of wrist and pelvis points of human.

(e) Box range of motion

$$\mathbf{q}_b^L \leq \mathbf{q}_b(t) \leq \mathbf{q}_b^U \quad (11)$$

where $\mathbf{q}_b^L$ is the lower box joint angle limits and $\mathbf{q}_b^U$ is the upper limits.

(f) Box grasping location

$$p_{h_{wrist}}(t) - p_b^L(t) = 0 \quad (12)$$
$$p_{r_{end\_effector}}(t) - p_b^R(t) = 0$$

where $p_{h_{wrist}}$ and $p_{r_{end\_effector}}$ are the wrist and end-effector (EE) positions of human and robot arm, respectively. p_b^L and p_b^R are the left and right edge positions of the box.

(g) Box global EOM

$$\left|\tau_i^b\right| \leq \varepsilon, \qquad i = 1,2,3,4,5,6 \tag{13}$$

where $\boldsymbol{\tau}_b$ is the global joint force and torque values of the box, $\varepsilon = 1$ N.

(h) Exoskeleton torque limits

$$\boldsymbol{\tau}_e^L \leq \boldsymbol{\tau}_e(\mathbf{x}, t) \leq \boldsymbol{\tau}_e^U \tag{14}$$

where $\boldsymbol{\tau}_e^L$ is lower torque limit, and $\boldsymbol{\tau}_e^U$ is the upper limit for the exoskeleton.

(i) Initial and final box (hand) positions

$$p_{h\_hand}(t) = p_{h\_hand}^S(t); \qquad t = 0, T \tag{15}$$
$$p_{r\_EE}(t) = p_{r\_EE}^S(t)$$

where, $p_{h\_hand}^S$ and $p_{r\_EE}^S$ are the specified hand and end-effector (EE) positions at initial and final times.

(j) Initial and final static conditions

$$\ddot{\mathbf{q}}_h(t) = \mathbf{0}; \qquad t = 0, T \tag{16}$$
$$\ddot{\mathbf{q}}_r(t) = \mathbf{0}$$
$$\ddot{\mathbf{q}}_b(t) = \mathbf{0}$$

where $\ddot{\mathbf{q}}$ is the joint acceleration. Detailed formulations of all other constraints are referred to Arefeen & Xiang (2020, 2021), Xiang & Arefeen (2020), and Xiang et al. (2009).

Results

The nonlinear optimization problem of collaborative lifting was solved using an SQP algorithm in SNOPT. $\mathbf{P} = [\mathbf{P}_{human}, \mathbf{P}_{robot}, \mathbf{P}_{current}, \mathbf{P}_{box}] = \mathbf{0}$, $\mathbf{f}_{c1} = \mathbf{f}_{c2} = 10$ were used as the initial guesses for the optimization. The current initial guesses generate the minimal optimal objective function value after evaluating various initial guesses for the gradient-based optimization. There was a total of 229 design variables and 907 nonlinear constraints. Here, a 70W brushless DC motor (EC 45-Flat, Maxon Motors) with a gearbox ratio of 1: 79.45 was used to provide a maximum of 10 Nm output torque of the exoskeleton (Nguyen et al., 2020). The optimal solution was obtained in 136.11 seconds on a laptop with an Intel® Core™ i7 2.11 GHz CPU and 16 GB RAM. The input data related to the collaborative box-lifting task are also given in Table 1. The optimal human-robot collaborative lifting motion was presented in Figure 2. Grasping forces and exoskeleton torque were presented in Figures 3 and 4, respectively.

Table 1. Task parameters for the collaborative box lifting

Parameters	
Box weight (kg)	10
Box width (m)	0.30
Box height (m)	0.1
Box depth (m)	0.35
Initial and final human feet contact position (m)	0.375
Initial hand and end-effector position (m)	0.1
Initial and final robot base contact position (m)	0.675
Vertical final hand and end-effoctor position (m)	0.6
Horizontal final hand and end-effector position (m)	0.3
Standing distance, *L* (m)	1.3
T (s)	0.5

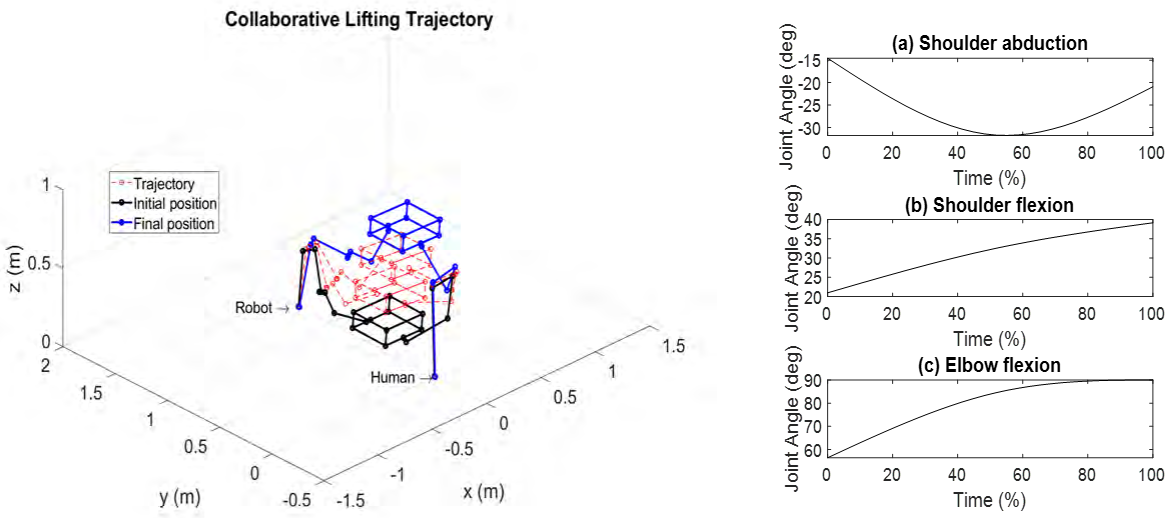

(a) (b)

Figure 2. (a) Snapshot of the human-robot arm collaborative lifting motion for a 10 kg box and (b) Human arm joint angle profiles

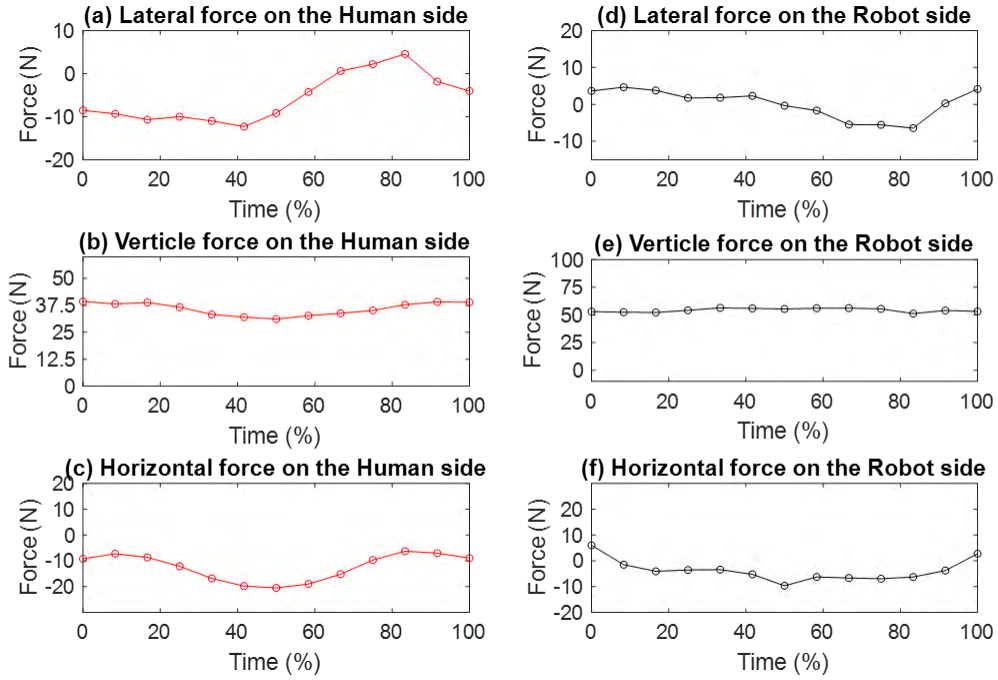

Figure 3. Box grasping forces for human-robot lifting

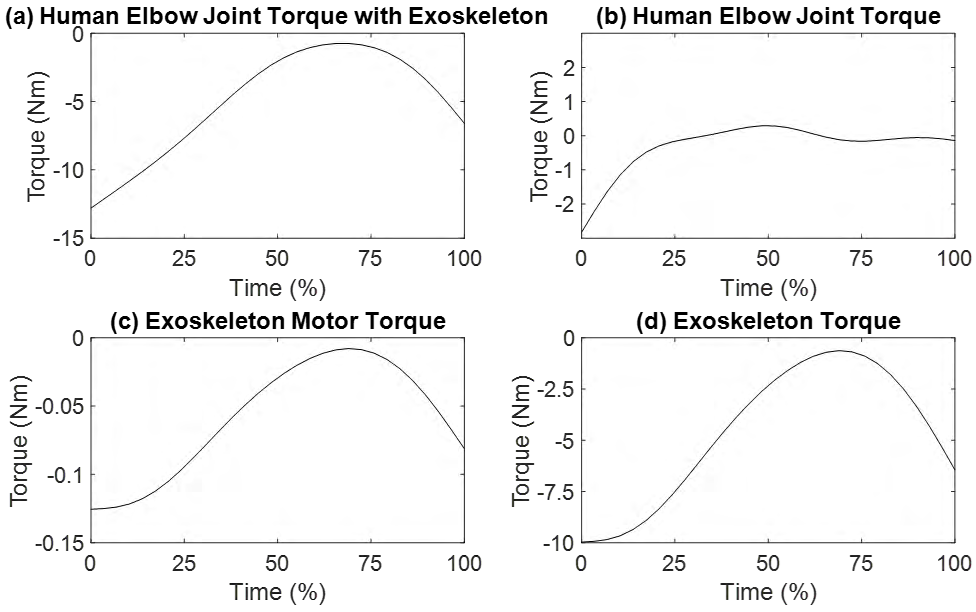

Figure 4. (a) Human elbow joint torque with an exoskeleton, (b) human elbow joint torque, (c) exoskeleton motor torque, and (d) exoskeleton output torque with a gearbox.

Discussion and Conclusions

The simulated human-robot arm lifting motion trajectory is depicted in Figure 2 (a). It is seen that the initial and final box locations are not symmetric because of the given final box location. The proposed optimization can predict a natural collaborative lifting motion. The joint angle profiles of the human arm's shoulder and elbow flexion have similar trends in the positive direction, as shown in Figure 2 (b). To maintain the box balanced, lateral and horizontal grasping forces are equal in magnitude but opposed in direction, as shown in Figure 3. In addition, the weight of the box is about equal to the total of the vertical grasping forces.

In this study, we optimized the output torque of the powered exoskeleton at the human elbow joint. The comparison of human elbow joint torque with exoskeleton assistance, human elbow torque without exoskeleton assistance, exoskeleton motor torque, and exoskeleton output torque is shown in Figure 4. It is noted that initially, the exoskeleton has maximum output torque in a negative direction. Both magnitudes of exoskeleton torque and human elbow joint torque during the lifting have decreased and then increased negatively. The exoskeleton aids the human elbow joint during the collaborative lifting process. As a result, these optimal results help to prevent human elbow joint injuries and mitigate joint fatigue during collaborative lifting.

Finally, this paper presents an optimization-based dynamic collaborative lifting motion prediction of a 13-DOF 3D human arm model with a 1-DOF exoskeleton and a 10-DOF 3D robotic arm. The simulation findings are reasonable. The collaborative lifting problem was formulated as an NLP optimization problem and efficiently solved using a gradient-based optimizer SNOPT. The results show that the proposed optimization formulation can achieve the exoskeleton's optimal control and lifting motion for the human-robot collaborative lifting task. In the future, we will validate the simulation results and apply the powered exoskeletons at multiple human joints for a lifting task.

Acknowledgments

This research was partially supported by NSF projects (CBET 1849279 and 2014281).

References

Agarwal, P., Kuo, P.H., Neptune, R. R., & Deshpande, A. D. (2013). A novel framework for virtual prototyping of rehabilitation exoskeletons. In *2013 IEEE 13th International Conference on Rehabilitation Robotics (ICORR)* (pp. 1-6), Seattle, WA, USA. 24-26 June 2013.

Arefeen, A., Quarnstrom, J., Syed, S. P. Q., Bai, H., & Xiang, Y. (2022a). Human-robot collaborative lifting motion prediction and experimental validation. *International Journal of Intelligent Robotics and Applications.* (under review).

Arefeen, A., Quarnstrom, J., Syed, S. P. Q., Bai, H., & Xiang, Y. (2022b). Human grasping force prediction, measurement, and validation for human-robot lifting. In *2022 International Design Engineering Technical Conferences and Computers and Information in Engineering Conference*, St. Louis, Missouri, August 14 – 17, 2022. (accepted).

Arefeen, A., & Xiang, Y. (2020). Two-dimensional team lifting prediction with different box weights. *Proceedings of the ASME 2020 International Design Engineering Technical Conferences and Computers and Information in Engineering Conference. Volume 9: 40th Computers and Information in Engineering Conference (CIE).* Virtual, Online. August 17–19, 2020. V009T09A004. ASME.

Arefeen, A., & Xiang, Y. (2021). Design human-robot collaborative lifting task using optimization. *Proceedings of the ASME 2021 International Design Engineering Technical Conferences and Computers and Information in Engineering Conference. Volume 2: 41st Computers and Information in Engineering Conference (CIE).* Virtual, Online. August 17–19, 2021. V002T02A010. ASME.

Bai, S., & Rasmussen, J. (2011). Modelling of physical human-robot interaction for exoskeleton designs. The Proceedings of Multibody Dynamics 2011, ECCOMAS Thematic Conference.

Cheng, H., Obergefell, L., & Rizer, A. (1994). Generator of body (GEBOD) manual. Armstrong Laboratory, Air Force Material Command.

Gill, P. E., Murray, W., & Saunders, M. A. (2005). SNOPT: An SQP algorithm for large-scale constrained optimization. *SIAM review, 47*(1), 99-131.

Manns, P., Sreenivasa, M., Millard, M., & Mombaur, K. (2017). Motion optimization and parameter identification for a human and lower back exoskeleton model. *IEEE Robotics and Automation Letters, 2*(3), 1564-1570.

Nguyen, V. Q., LaPre, A. K., Price, M. A., Umberger, B. R., & Sup IV, F. C. (2020). Inclusion of actuator dynamics in simulations of assisted human movement. *International Journal for Numerical Methods in Biomedical Engineering, 36*(5), e3334.

Wei, W., Zha, S., Xia, Y., Gu, J., & Lin, X. (2020). A hip active assisted exoskeleton that assists the semi-squat lifting. *Applied Sciences, 10*(7), 2424.

Xiang, Y., & Arefeen, A. (2020). Two-dimensional team lifting prediction with floating-base box dynamics and grasping force coupling. *Multibody System Dynamics, 50*(2), 211-231.

Xiang, Y., Arora, J. S., Rahmatalla, S., & Abdel-Malek, K. (2009). Optimization-based dynamic human walking prediction: One step formulation. *International Journal for Numerical Methods in Engineering, 79*(6), 667-695.

Zhang, T., & Huang, H. (2018). A lower-back robotic exoskeleton: Industrial handling augmentation used to provide spinal support. *IEEE Robotics & Automation Magazine, 25*(2), 95-106.

Zhou, L., Bai, S., Andersen, M. S., & Rasmussen, J. (2015). Modeling and design of a spring-loaded, cable-driven, wearable exoskeleton for the upper extremity. *Modeling, Identification and Control (Online), 36*(3), 167-177.

Prediction of Walking Kinematics and Muscle Activities under Idealized Lower Limb Exoskeleton Assistances

Neethan Ratnakumar[1], Vinay Devulapalli[2], Niranjan Deepak[3] and Xianlian Zhou[1*]
[1]Department of Biomedical Engineering, New Jersey Institute of Technology, NJ, USA
[2]South Brunswick High School, NJ, USA
[3]Middlesex County Academy for Science, Mathematics, and Engineering Technology, NJ, USA
*Corresponding author, alexzhou@njit.edu

Abstract

This study examines the biomechanical effects of idealized multi-joint exoskeleton assistances on hip, knee, and ankle joints. We conducted predictive simulations of walking without assistance and with seven different assistance cases including assistance to each joint, assistance to any two joints, and assistance to all three joints. A 2D musculoskeletal model with 10 degrees of freedom and 18 muscles was used and the OpenSim Moco optimal control solver was employed for all predictive simulations, which aimed to minimize the weighted sum of several objectives including metabolic cost, muscle activation, joint coordinate acceleration, motion tracking, and whole-body center of mass (COM) acceleration. The results showed that all assistance cases changed the joint kinematics of the walking motion to different degrees and for most cases the exoskeleton assistance reduced muscle effort substantially. By comparing with the unassisted case, we found that the two cases with assistance to all three joints and to the hip-ankle joints both provided more than 50% reduction in metabolic cost of transport (COT), followed by assistance to hip-knee and knee-ankle joints with less than 40% reduction. As for the single joint assistance cases, assistance to the hip joint appeared to be the most effective with around 34% reduction in COT, followed by the assistance to the ankle joint with around 22% reduction, whereas the assistance to the knee joint was much less effective (with less than 10%).

Keywords: Exoskeleton, Musculoskeletal Model, Optimization.

Introduction

Given the importance of walking in the daily activities of human life, researchers in the field of assistive robotics have dedicated substantial effort to develop wearable devices known as exoskeletons to assist human for the applications of human performance augmentation or rehabilitation. As straightforward as it might seem to most of us, walking is a very skillful activity and requires the interplay and coordination of

several motor control circuitries in the human brain, spinal reflexes, sensory feedback and muscle activations (Nielsen, 2003). Injecting assistance to such a complex process for the benefit of the wearer is a particularly challenging task. Regardless of several decades of exoskeleton research it was only in 2013 that an exoskeleton was able to achieve metabolic cost savings in walking (i.e., the exoskeleton being able to lower energy expenditure in comparison to the no device baseline). As of 2020 around twelve exoskeletons had recorded net metabolic savings ranging from 3.3 to 19.8% in walking (Sawicki et al., 2020). This holdup can be attributed to the limitations in the intuition based experimental methods with control parameter tuning that were used in the past. In recent years, systematic methods like the human-in-the-loop (HIL) optimization method have enabled faster exploration of optimum assistance parameters and have achieved high metabolic energy savings (Bryan et al., 2021; Ding et al., 2018; Kim et al., 2019; Zhang et al., 2017).

In contrast to the experimental methods, physics-based simulations have the potential of exploring assistive device control parameters more thoroughly with no risk to the subjects. Additionally, all related kinematic, kinetic and muscle mechanics details are readily available at the end of the simulation for analysis. Several studies have used this kind of an approach to study the effects of assistive devices on humans during walking (Grabke et al., 2019) or running (Zhou & Chen, 2020). A human walking with idealized assistive devices while carrying loads was simulated using the CMC (Computed Muscle Control) algorithm available within OpenSim (Dembia et al., 2017). Another simulation utilizing CMC revealed that idealized hip actuators have significantly greater benefit on energy cost saving in the elderly population compared to idealized ankle actuators (Cseke et al., 2022). The CMC method tracks experimental kinematic data with minimal variation in kinematics and cannot handle global objectives that depend on the entirety of the motion (Dembia, 2020).

On the other hand, optimization with the direct single shooting method has been used by some researchers (Geijtenbeek, 2019; Ong et al., 2019; Song & Geyer, 2015; Veerkamp et al., 2021) to overcome some of the limitations inherent to CMC. In our previous work, we employed a single shooting based method to find optimized hip assistance profiles, together with reflex based neural control, during walking (Ratnakumar & Zhou, 2021). Nonetheless, the single shooting method requires numerical integration of the dynamic equations to generate the motion trajectory and hence is computationally expensive (Dorn et al., 2015). In addition to single shooting, direct collocation, a direct optimal control method that relies on gradient-based optimization has been used for musculoskeletal motion tracking and prediction (Falisse et al., 2022; Febrer-Nafría et al., 2022; Nguyen et al., 2019; Park et al., 2022). The introduction of the open-source toolkit, OpenSim Moco (Dembia et al., 2020), has made direct collocation more accessible to the

musculoskeletal biomechanics community. In direct collocation, the controls and states are parameterized and the need for explicit integration is eliminated.

In this study, a direct collocation-based optimization method was adapted to co-optimize idealized exoskeleton hip, knee and ankle joint assistance torques in conjunction with the gait and muscle control parameters. The optimization objective includes several terms such as metabolic cost, muscular effort, center of mass acceleration, and tracking of a reference walking motion. Using the tracking term in the objective function and optimizing the gait allows the kinematics to deviate from the tracking data, which enables motion adaptation to exoskeleton assistances. The optimization method was used to solve a case of walking without assistance and seven cases of walking with bi-directional hip, knee, and ankle assistances, for which we compared the changes in kinematics, metabolic cost, and muscle activation.

Methods

The musculoskeletal model used in this study represents an adult with a mass of 62 kg and an approximate height of 1.7 m, which represents a global anthropometric average for mass (Walpole et al., 2012) and a normal mid-range body mass index of 21.5. The model shown in Figure 1 is a modified version of 'gait10dof18musc.osim' available within OpenSim Moco. It is a 2D model and has 10 degrees of freedom (DOFs) (lumbar, bilateral hips, knees, and ankles, and 3 global DOFs) and 9 major muscles per leg: gluteus maximus (GMAX), iliopsoas (IL), hamstrings (HAMS), rectus femoris (RF), vasti (VAS), biceps femoris short head (BFSH), gastrocnemius (GAS), tibialis anterior (TA) and soleus (SOL). This model utilizes the smooth and differentiable DeGrooteFregly muscle model (De Groote et al., 2016), which is suited for gradient-based optimization methods. The lumbar joint was modeled as a pin joint and a coordinate actuator is added to the joint as no muscles span this joint. A modified version of the Hunt Crossley contact model (Serrancolí et al., 2019) was utilized to model smooth contact forces between the ground and the spheres placed at the heels and at the fronts of the feet.

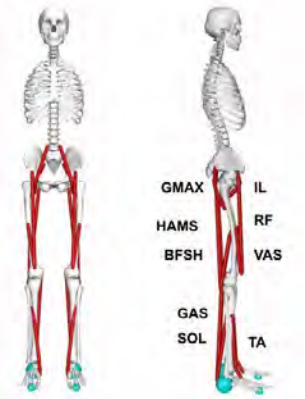

Figure 1. The musculoskeletal model.

Walking without assistance (NoExo) and walking with seven different combinations of bi-directional single- and multi- joint torques were optimized with the OpenSim Moco framework. The term "bi-directional torque" means that the torque can vary in both flexion and extension directions. The following joint assistance cases were realized by adding ideal actuators with bounds between -100 Nm to 100 Nm to the model: HIP – only hip joints are assisted; KNE – only knee joints are assisted; ANK – only ankle joints are assisted; HIP+KNE – hips and knees are assisted; HIP+ANK – hips and ankles are assisted; KNE+ANK – knees and ankles are assisted; ALL – all hips, knees and ankles are assisted.

Optimization of walking with and without assistances was formulated as optimal control problems within Moco. The optimization variables include controls and states (i.e., muscle controls or excitations, joint coordinate angles, and assistance torques as coordinate actuation). The constraints include equations of motion, kinematic constraints (such as symmetry and periodicity), state and control upper and lower bounds, boundary constraints and time limits, etc. A reference walking motion data, originally obtained from predictive simulations representing walking at a speed of 1.32 m/s (Falisse et al., 2019), was used as tracking data and as the initial guess for the NoExo case as well as for the assistance cases except for ALL and HIP+KNE cases, for which the kinematics deviated from the reference motion the most and thus the predicted results from other cases were used instead.

The objective or cost function employed in this study is defined as follows:

$$Total\ Cost\ (J_T) = \int_0^{t_f} \left(w_1 J_{MER} + w_2 J_{COM} + w_3 J_{Joint} + w_4 J_{Control} + w_5 J_{Track}\right) dt \quad (1)$$

The sum of normalized muscle metabolic energy rates (i.e. COT), J_{MER}, is calculated with a smooth approximation of the 2016 Uchida metabolic model (Uchida et al., 2016). The whole-body COM acceleration goal, $J_{COM} = w_x a_x^2 + w_y a_y^2 + w_z a_z^2$ with the weights $[w_x, w_y, w_z] = [30.0\ 2.0\ 0.0]$, penalizes excessive acceleration of the body which helps with reducing the vertical ground reaction during initial contact. The joint acceleration term, $J_{Joint} = \sum_i \ddot{\theta}_i^2$ with θ_i denoting the i-th joint angle, encourages minimal jerk in the lower limb joints. The control term, $J_{Control} = \sum_i w_i\, x_i^2$ with x_i denoting the control signals, includes only the muscle effort by setting the weight w_i for the exoskeleton assistance torques and the lumbar coordinate actuation to zero and all muscle weights to one.

The weights for each cost function term used for the simulations are: $w_1 = 1, w_2 = 0.01, w_3 = 2.5e^{-4}$, $w_4 = 10$ & $w_5 = 10$. The number of mesh intervals was set to 40 and convergence tolerance at $1.0e^{-4}$. All optimizations were run on a personal computer with an Intel Core i7-8550U processor, containing a total of 8 cores, at 1.8 GHz. The simulation time per case varied between 30 minutes and a few hours.

Results

Figure 2 shows the kinematics and vertical GRF for all simulated cases. Experimental human gait data (joint angles and ground reaction forces) at free walking speed reported by Schwartz et.al. (Schwartz et al., 2008) is used for comparison. The hip angles show the closest fit to the experimental data whereas the ankle angles have the largest deviation from the experimental data. The knee angle deviations are higher in the stance phase with relatively small flexion, and the swing phase also exhibits a lower flexion angle compared to the experimental value.

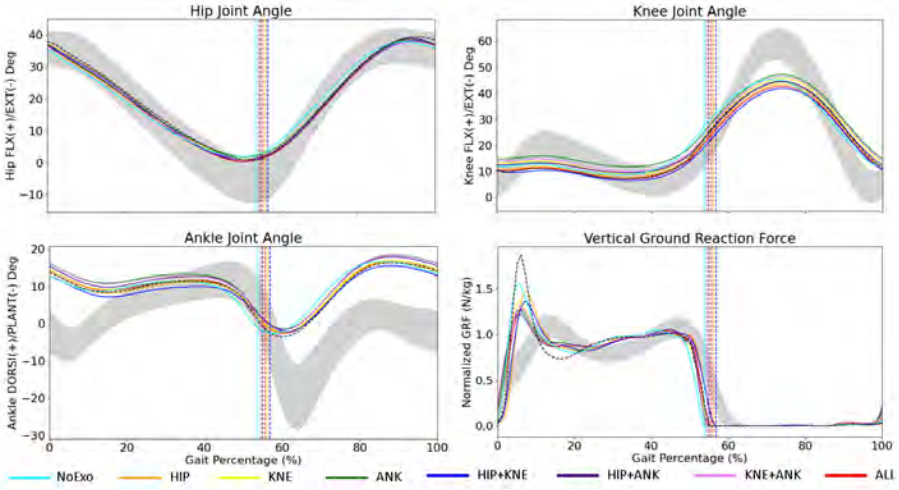

Figure 2. Kinematic and vertical GRF variations for all cases. The vertical lines indicate the stance-swing transition times. The black dash lines are the reference motion data (Falisse et al., 2019) for tracking. The reference data for GRF was not used in the optimization but is included here for comparison. The experimental free speed kinematic/GRF Mean+/-SD data from (Schwartz et al., 2008) is plotted as the gray shaded area.

Muscle activations from the simulations are plotted in Figure 3 and compared with electromyography (EMG) data from Knutson et.al. (Knutson, 1995). As it can be seen from the figure, most of the muscles have similar activation timing or patterns as the experimental data with the exception of the RF muscle. We noticed that there are inconsistencies in reported RF EMG measurements in literature. For example, the RF EMG data from Rajagopal et al. (Rajagopal et al., 2016) has quite different timing and pattern and is closer to our prediction. The VAS muscle exhibits some additional activation during the stance-swing transition in the simulations while the experimental data from Knutson et.al. does not display this behavior. Nonetheless, the data from Rajagopal et al. does show VAS activation during the transition. Our optimization predicted very low activation for the BFSH muscle similar to the study by Falisse et al. (Falisse et al., 2019) and the reasons for this remain to be investigated.

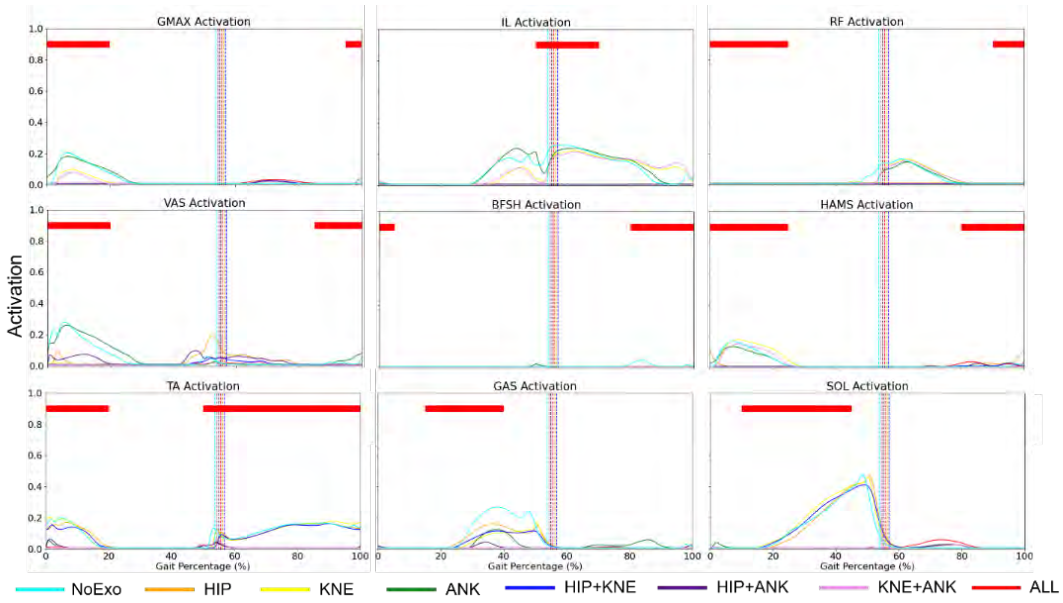

Figure 3. Predicted muscle activations compared to experimental data from (Knutson, 1995). The red horizontal bars indicate when a muscle is active during walking based on (Knutson, 1995).

The changes in COT, defined as the normalized metabolic energy cost by the distance traveled and subject weight, is presented in Figure 4. The baseline NoExo case has a COT of 3.56 J/kg/m which is slightly higher than typical experimental readings that are around 3.35 ± 0.25 J/kg/m (Miller, 2014). The HIP assistance case has the highest reduction in COT amongst the single joint cases with 34% (COT drops to 2.36 J/kg/m), followed by the ANK case with 22% reduction. The KNE assistance case by itself only reduces the COT by 8%. But adding knee assistance to the ankle for the KNE+ANK case seems to be relatively effective (the COT reduction of KNE+ANK is higher than the summation of the ANK case and the KNE case). Adding knee assistance to the HIP+ANK case for the ALL case seems to help very little (an additional 1.5% reduction only).

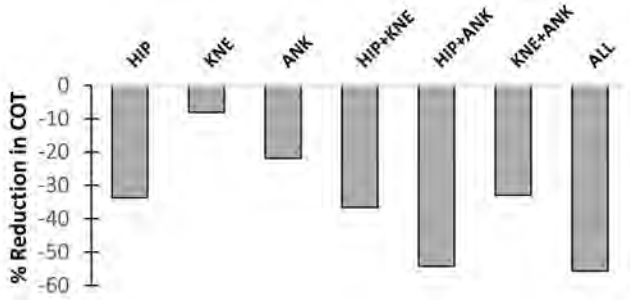

Figure 4. COT reductions in comparison with the NoExo case.

Discussion and Conclusions

This paper presents a direct collocation-based optimization approach to co-optimize idealized exoskeleton assistances with gait (joint motions) and muscle control for walking prediction. Predicted joint coordinate motions and muscle activations of a full gait cycle are compared for all cases including the case without exoskeleton and seven cases of single- or multi- joint assistance. Clearly, we can observe the changes to the gait due to the assistances. The predicted joint motions are close to the reference motion we chose but deviate from the experimental data. Since the reference motion was also predicted with optimization from a 2D model (Falisse et al., 2019), the deviation is explained by Falisse et al. as a result of model choices instead of local optima. Extending the model from 2D to 3D (Falisse et al., 2019) or adding toe degrees of freedom to the foot (Falisse et al., 2022) likely will improve the prediction outcomes. Since in our prediction method, tracking is a part of the objective function, we expect better joint motion prediction if real experimental data is used as the reference motion, which is a planned next step of this study. In terms of the predicted GRFs, we found that the use of a whole-body COM acceleration objective term has a substantial impact on reducing the first peak in the vertical GRF, which is closer to the experimental data. We also noticed slight dragging of the feet (very small GRF during the swing phase) in several cases as shown in Figure 2. This issue may be resolved if we use real experimental data as indicated above. Otherwise, adding an additional term to the objective function to penalize foot dragging during the swing phase can also be considered in the future work.

By comparing with the case without assistance, we observed that most assistance cases reduced the muscle activations and as a result the COT substantially. For single joint assistance, the hip assistance is the most effective in reducing COT, followed by the ankle assistance, whereas the knee assistance is the least effective with only 8% reduction in COT. These results are coherent with the current understanding of the positive work performed by the hip or ankle is much greater than the knee in the total energy expenditure of walking (Sawicki et al., 2009). For the two-joint assistance cases, the HIP+ANK assistance is the most effective, with the reduction in COT being over 50% and very close to the ALL case. Our findings in COT reduction with single- or multi- joint assistances are similar in trend to the results by Bianco et al. (Bianco et al., 2022). However, in their study, the gait kinematics was not co-optimized with the assistances and the unassisted and assisted simulations used the same walking kinematics. In addition, only uni-directional joint assistance was considered in each of their assisted simulations whereas our study considered bi-directional assistance for all cases.

In summary, we believe our modeling study has a great value in exoskeleton actuation design and optimization. Experimental methods such as the HIL optimization (Zhang et al., 2017) are becoming

more popular but they still require extensive subject testing and oftentimes the number of control parameters that can be optimized are limited. Our study provides insights on the effects and limits of single- or multi- joint assistance and can help engineers and scientists in prioritizing assistance to certain joints and in providing assistance with optimal timing and assistance profiles.

References

Bianco, N. A., Franks, P. W., Hicks, J. L., & Delp, S. L. (2022). Coupled exoskeleton assistance simplifies control and maintains metabolic benefits: A simulation study. *PLoS ONE*, *17*(1), e0261318-e0261318. https://doi.org/10.1371/journal.pone.0261318

Bryan, G. M., Franks, P., Song, S., Reyes, R., O'Donovan, M., Gregorczyk, K., & Collins, S. (2021). Optimized Hip-Knee-Ankle Exoskeleton Assistance Reduces the Metabolic Cost of Walking With Worn Loads. *Journal of NeuroEngineering and Rehabilitation volume*, *18*(161). https://doi.org/doi.org/10.1186/s12984-021-00955-8

Cseke, B., Uchida, T., & Doumit, M. (2022). Simulating Ideal Assistive Strategies to Reduce the Metabolic Cost of Walking in the Elderly. *IEEE Transactions on Biomedical Engineering*.

De Groote, F., Kinney, A. L., Rao, A. V., & Fregly, B. J. (2016). Evaluation of Direct Collocation Optimal Control Problem Formulations for Solving the Muscle Redundancy Problem. *Annals of Biomedical Engineering*, *44*(10), 2922-2936. https://doi.org/10.1007/s10439-016-1591-9

Dembia, C. L. (2020). *Simulating Assistive Technology: Insights, Tools, and Open Science, PhD thesis* Stanford University].

Dembia, C. L., Bianco, N. A., Falisse, A., Hicks, J. L., & Delp, S. L. (2020). OpenSim Moco: Musculoskeletal optimal control. *PLOS Computational Biology*, *16*.

Dembia, C. L., Silder, A., Uchida, T. K., Hicks, J. L., & Delp, S. L. (2017). Simulating ideal assistive devices to reduce the metabolic cost of walking with heavy loads. *PLoS ONE*, *12*(7), e0180320.

Ding, Y., Kim, M., Kuindersma, S., & Walsh, C. J. (2018). Human-in-the-loop optimization of hip assistance with a soft exosuit during walking. *Science Robotics*, *3*(15), eaar5438. https://doi.org/10.1126/scirobotics.aar5438

Dorn, T. W., Wang, J. M., Hicks, J. L., & Delp, S. L. (2015). Predictive simulation generates human adaptations during loaded and inclined walking. *PLoS ONE*, *10*(4), e0121407. https://doi.org/10.1371/journal.pone.0121407

Falisse, A., Afschrift, M., & De Groote, F. (2022). Modeling toes contributes to realistic stance knee mechanics in three-dimensional predictive simulations of walking. *PLoS ONE*, *17*(1), e0256311. https://doi.org/10.1371/journal.pone.0256311

Falisse, A., Serrancolí, G., Dembia, C. L., Gillis, J., & De Groote, F. (2019). Algorithmic differentiation improves the computational efficiency of OpenSim-based trajectory optimization of human movement. *PLoS ONE*, *14*(10), e0217730. https://doi.org/10.1371/journal.pone.0217730

Febrer-Nafría, M., Fregly, B. J., & Font-Llagunes, J. M. (2022). Evaluation of Optimal Control Approaches for Predicting Active Knee-Ankle-Foot-Orthosis Motion for Individuals With Spinal Cord Injury [Original Research]. *Frontiers in Neurorobotics*, *15*. https://doi.org/10.3389/fnbot.2021.748148

Geijtenbeek, T. (2019). SCONE: Open Source Software for Predictive Simulation of Biological Motion. *Journal of Open Source Software*, *4*(38), 1421.

Grabke, E. P., Masani, K., & Andrysek, J. (2019). Lower limb assistive device design optimization using musculoskeletal modeling: a review. *Journal of Medical Devices*, *13*(4).

Kim, M., Liu, C., Kim, J., Lee, S., Meguid, A., Walsh, C. J., & Kuindersma, S. (2019, 20-24 May 2019). Bayesian Optimization of Soft Exosuits Using a Metabolic Estimator Stopping Process. 2019 International Conference on Robotics and Automation (ICRA),

Knutson, L. S., GL. (1995). EMG: Use and interpretation in gait. In *Gait analysis theory and application* (pp. 307-325). St. Louis: Mosby.

Miller, R. H. (2014). A comparison of muscle energy models for simulating human walking in three dimensions. *Journal of Biomechanics*, *47*(6), 1373-1381.

Nguyen, V. Q., Umberger, B. R., & Sup, F. C. (2019, 24-28 June 2019). Predictive Simulation of Human Walking Augmented by a Powered Ankle Exoskeleton. 2019 IEEE 16th International Conference on Rehabilitation Robotics (ICORR),

Nielsen, J. B. (2003). How we Walk: Central Control of Muscle Activity during Human Walking. *The Neuroscientist*, *9*(3), 195-204. https://doi.org/10.1177/1073858403009003012

Ong, C. F., Geijtenbeek, T., Hicks, J. L., & Delp, S. L. (2019). Predicting gait adaptations due to ankle plantarflexor muscle weakness and contracture using physics-based musculoskeletal simulations. *PLOS Computational Biology*, *15*(10), e1006993. https://doi.org/10.1371/journal.pcbi.1006993

Park, S., Caldwell, G. E., & Umberger, B. R. (2022). A direct collocation framework for optimal control simulation of pedaling using OpenSim. *PLoS ONE*, *17*(2), e0264346. https://doi.org/10.1371/journal.pone.0264346

Rajagopal, A., Dembia, C. L., DeMers, M. S., Delp, D. D., Hicks, J. L., & Delp, S. L. (2016). Full-body musculoskeletal model for muscle-driven simulation of human gait. *IEEE Transactions on Biomedical Engineering*, *63*(10), 2068-2079.

Ratnakumar, N., & Zhou, X. (2021). Optimized Torque Assistance During Walking With an Idealized Hip Exoskeleton. International Design Engineering Technical Conferences and Computers and Information in Engineering Conference,

Sawicki, G. S., Beck, O. N., Kang, I., & Young, A. J. (2020). The exoskeleton expansion: improving walking and running economy. *Journal of neuroengineering and rehabilitation*, *17*(1), 25. https://doi.org/10.1186/s12984-020-00663-9

Sawicki, G. S., Lewis, C. L., & Ferris, D. P. (2009). It pays to have a spring in your step. *Exercise and sport sciences reviews*, *37*(3), 130-138. https://doi.org/10.1097/JES.0b013e31819c2df6

Schwartz, M. H., Rozumalski, A., & Trost, J. P. (2008). The effect of walking speed on the gait of typically developing children. *J Biomech*, *41*(8), 1639-1650. https://doi.org/10.1016/j.jbiomech.2008.03.015

Serrancolí, G., Falisse, A., Dembia, C., Vantilt, J., Tanghe, K., Lefeber, D., Jonkers, I., Schutter, J. D., & Groote, F. D. (2019). Subject-Exoskeleton Contact Model Calibration Leads to Accurate Interaction Force Predictions. *IEEE Transactions on Neural Systems and Rehabilitation Engineering*, *27*(8), 1597-1605. https://doi.org/10.1109/TNSRE.2019.2924536

Song, S., & Geyer, H. (2015). A neural circuitry that emphasizes spinal feedback generates diverse behaviours of human locomotion. *The Journal of Physiology*, *593*(16), 3493-3511.

Uchida, T. K., Seth, A., Pouya, S., Dembia, C. L., Hicks, J. L., & Delp, S. L. (2016). Simulating ideal assistive devices to reduce the metabolic cost of running. *PLoS ONE*, *11*(9), e0163417.

Veerkamp, K., Waterval, N. F. J., Geijtenbeek, T., Carty, C. P., Lloyd, D. G., Harlaar, J., & van der Krogt, M. M. (2021). Evaluating cost function criteria in predicting healthy gait. *Journal of Biomechanics*, *123*, 110530. https://doi.org/https://doi.org/10.1016/j.jbiomech.2021.110530

Walpole, S. C., Prieto-Merino, D., Edwards, P., Cleland, J., Stevens, G., & Roberts, I. (2012). The weight of nations: an estimation of adult human biomass. *BMC Public Health*, *12*(1), 439. https://doi.org/10.1186/1471-2458-12-439

Zhang, J., Fiers, P., Witte, K. A., Jackson, R. W., Poggensee, K. L., Atkeson, C. G., & Collins, S. H. (2017). Human-in-the-loop optimization of exoskeleton assistance during walking. *Science*, *356*(6344), 1280-1284. https://doi.org/10.1126/science.aal5054

Zhou, X., & Chen, X. (2020). Design and Evaluation of Torque Compensation Controllers for a Lower Extremity Exoskeleton. *Journal of Biomechanical Engineering*, *143*(1). https://doi.org/10.1115/1.4048572

Experimental assessment of effectiveness of arm-supporting exoskeleton for overhead work

Parisa Torkinejad Ziarati, Ting Xia, Simon Kudernatsch, and Donald Peterson
Northern Illinois University, United States

Abstract

It is well known that overhead work is associated with musculoskeletal disorders in the upper extremities. Arm-supporting exoskeletons (ArmExos) help to reduce mechanical load to the shoulder joint and subsequently risk of injury in the area. The ArmExos are adopted rapidly by industries such as car and airplane manufacturers, although there lack studies examining the effectiveness of the ArmExos in these industry settings as the associated overhead tasks often involve use of power hand tools. To simulate overhead tasks with use of power hand tools, an electromagnetic shaker was hung from the ceiling and produced a random vibration spectrum modified from the ISO 10819. In this posture the ArmExos exerted the highest torque to the upper arm when it was flexed 90 degrees. As comparison, the shaker was also placed in front of the body, in which the ArmExos produced minimum torque to the upper arm when it was hanging down along the body. Vibration transmissibility along the arm and the spine was monitored using accelerometers. Activity of the shoulder muscles was obtained using surface electromyography. The grip force was assessed in the shaker handle while the push force was assessed using a force plate placed under subject's feet. Live feedback was shown on a computer monitor for the subjects to maintain an average grip force at 30 N and an average push force at 50 N. The data demonstrated that wearing ArmExos didn't alter vibration transmissibility along the body. Wearing ArmExos led to lower shoulder muscle activities. The agonist muscle activities in the overhead posture were higher when compared to the front-of-body posture. Antagonist muscle activities tended to increase with vibration turned on. The existence of vibration significantly increased the peak grip force and push force, indicating a higher mechanical load to the shoulder. These findings suggest that the impact of ArmExo use in overhead tasks involving power tools is complex. Shoulder joint load analysis using advanced musculoskeletal models is recommended to understand the effectiveness of ArmExos in such industry settings.

Keywords: exoskeleton, work posture, vibration, muscle activity.

Introduction

Musculoskeletal disorders (MSDs) are painful disorders of muscles, tendons, joints, and nerves commonly occurring in the neck, shoulder, arm, and back regions. According to the 2019 US Bureau of Labor Statistics survey of nonfatal occupational injuries and illness, a total of 272,780 MSD cases were reported in private industry in 2018. Among them, 86,410 cases were injuries in the upper extremities, including sprains, rotator cuff tears, arthritis, tendinitis, and bursitis. It is noteworthy that one half of the upper extremity MSD cases occurred at the shoulder joint, suggesting that this joint is the weakest part in the upper extremities. The upper extremity MSDs are more disabling as indicated by a median of 20 days away from work compared to a median of 12 days away from work for all MSDs. One particular physical exposure contributing to upper extremity MSDs is overhead work in which workers need to raise one or both arms above their shoulders for a substantial time of their work schedule. This in part explains a high prevalence of upper extremity MSDs in industrial sectors such as that often involve overhead tasks. Overhead work is particularly detrimental to the shoulder joint due to several biomechanical disadvantages, including exertion away from the optimal working range of shoulder muscles, a faster fatigue rate, and reduced ability to maintain joint stability. Safety measures such as decreasing the load, modifying the arm working posture, raising body position, and limiting exposure time have been recommended to reduce the risk associated with overhead work.

In recent decades, occupational exoskeletons have received great attention for their potential to improve efficiency, increase productivity, and reduce injuries (Kim et al., 2018). According to a recent systematic literature review of the effectiveness of workplace interventions (Van Eerd et al., 2016), arm support is the only intervention shown to be moderately effective in reducing the upper extremity MSDs, while most other interventions, such as workstation adjustment, work redesign to minimize shoulder load, ergonomic training, and attendance at an occupational health and safety workshop, appear to be ineffective. The early adopters of arm-supporting exoskeletons (ArmExos) include manufacturing industries. It is noteworthy that in these industries, hand-operated power tools are often used when wearing Exos (Kamping-Carder, 2019). For example, Boeing has about 100 passive ArmExos across five site locations in the US, with 100% of the users working with vibratory tools. Toyota Motor North America has acquired Exos for 500 workers across six vehicle plants in North America, with most using vibratory tools. Ottobock, a major exoskeleton developer and manufacturer, reported that it has placed their products in over 1,000 plants worldwide, where about 80% of the plants are for manufacturing with 100% of those environments requiring the use of hand tools.

Because the ArmExos can decrease the physical load experienced by the users, particularly during overhead work, the rate of implementation into the workplace continues to exceed the research results needed to demonstrate short-term and long-term effectiveness (De Looze et al., 2016). Additionally, there

is a lack of guidelines available for developers to design effective Exos or for users to select the proper Exos for specific work environment (Lowe et al., 2019). Therefore, the purpose of this research was to collect preliminary data that can be used to investigate the effectiveness of ArmExo in dealing with the combined effects of overhead posture and power hand tools. The preliminary study outcomes involved vibration transmissibility (VT) along the arm and the upper body, electromyography (EMG) activities from muscles surrounding the shoulder joint, and coupling forces (i.e., grip force and push force) between the users and the tool handle. These data will be fed into DHM in future studies to examine the comprehensive effects of ArmExo in overhead work with use of power hand tools.

Methods

Subjects

For this preliminary study, two right-handed, healthy male participants were recruited with age between 18 and 60, hand size between 7 and 10 (ISO 10819, 2013), and no history of major musculoskeletal injury or surgery. The participants underwent informed consent process, and their signatures were obtained. The study was carried out at the main campus of Northern Illinois University, DeKalb, IL with the IRB approval number HS20-0219.

Experimental Procedures

A full-factorial, nested design using within-subject comparisons was employed to investigate 1) VT along the arm and the spine, 2) shoulder muscle EMG, and 3) coupling forces when the subjects were exposed to simulated tool vibrations. The three main factors in this nested design are: posture condition as level 1 (overhead – OH and front-of-body – FOB), Exo condition as level 2 (vest-type Exo, strap-type Exo, and not wearing Exo); and vibration condition as level 3 (vibration turned on and turned off), or a total of 12 testing conditions. Each condition was repeated 3 times or a total of 36 recordings for each subject. In the present study, muscle activities were collected using a surface EMG system. A maximum voluntary contraction (MVC) procedure was necessary to normalize the EMG data for between-subject comparisons and within-subject comparisons of multiple study visits. The MVC test was done before the main tests.

Posture conditions

An overhead posture and a front-of-body posture were examined in the present study. For the overhead posture, both the elbow and shoulder joints were flexed 90° in the sagittal plane (Figure 1.a). The front-of-body posture was defined in the ISO 10819 (2013), in which the forearm was flexed 90° and the upper arm hangs down in a natural position (Figure 1.b). A scissor lift (Presto Lifts Inc, Norton, MA) was used

to adjust subject standing height such that the arm posture is standardized across all subjects and all testing conditions.

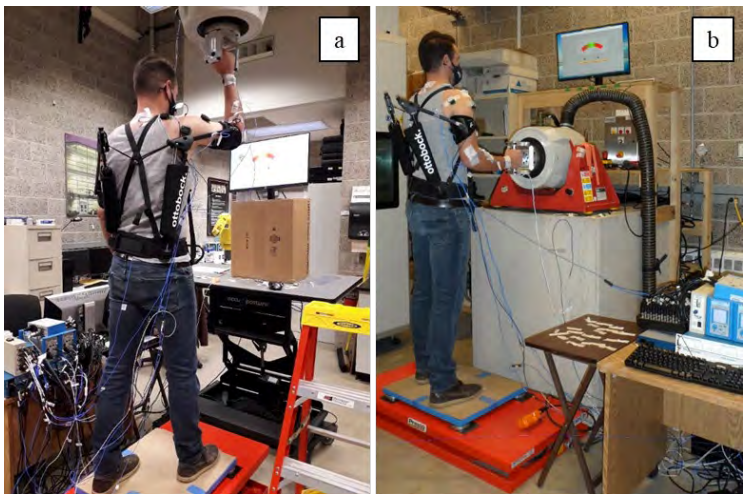

Figure 1. Illustration of the overhead posture (a) and the front-of-body posture (b).

Exoskeleton conditions

Two commercially available Arm Exos were used in the present study, including 1) a vest-type Exo – EksoVest, Model V-1.0-0574, Ekso Bionics, Richmond, CA (Figure 2.b) and a strap-type Exo – Paexo Shoulder, Model 6ES100=2, Ottobock, Duderstadt, Germany (Figure 2. c). A condition of not wearing ArmExo was also tested to serve as control (Figure 2.a).

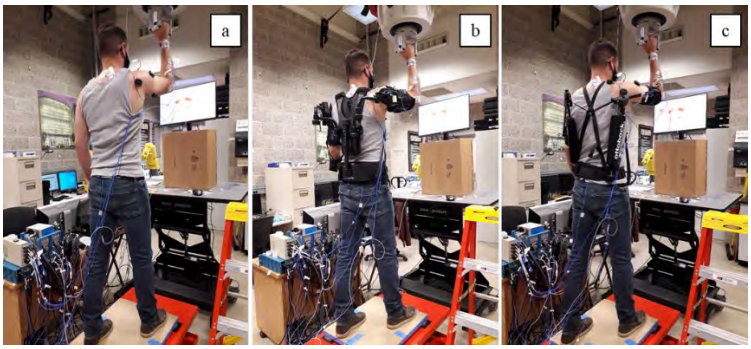

Figure 2. Illustration of not wearing exoskeleton (a), wearing a vest-type exoskeleton (b), and wearing a strap-type exoskeleton (c).

Vibration conditions

The power tool vibration was simulated using an electromagnetic shaker (LDS V651 shaker, Brüel & Kjær, Nærum, Denmark). A vibration control system (VR8500, Vibration Research, Jenison, MI) was used to drive the shaker. The vibration spectrum was adapted from the random vibration spectrum defined in the ISO 10819 (2013) with the lower limit extended from 25 Hz to 2 Hz while the upper end remaining at 1600 Hz. Data analysis demonstrated that the shaker could drive random vibration with a lower limit of approximately 7 Hz, which was used in data analysis.

Test sequence

The nested design was chosen to minimize fatigue and streamline the testing procedures. Because the time needed for the overhead shaker setup takes about 4 to 5 hours and 1 to 2 hours for the front-of-body setup, two study visits were required to accommodate the two posture conditions. Additionally, the two vibration conditions were examined with the no vibration condition tested first immediately followed by the vibration turned on. There was a one-minute separation between the two vibration conditions as it takes the shaker approximately 1 minute to achieve the designated waveform and amplitude. The subjects were allowed to have a 3-minute break before the next testing trial to prevent muscle fatigue. The time to change ArmExo was about 5 minutes, thus no extra rest was needed between the exoskeleton conditions. The Exo conditions were permutated using a Latin Squares – Williams design.

Outcome measures

Vibration transmissibility

To understand VT along the arm and the spine, vibration was assessed using triaxial accelerometer placed at the wrist (between radial and ulnar styloid process), elbow (lateral epicondyle), shoulder (acromion), and upper back (C7), middle back (T10), and lower back (L3). One additional triaxial accelerometer was placed at the right arm-link of the ArmExos. The VT was calculated between the acceleration at different body locations and the acceleration at the shaker handle. Since the vibration response of the human body is frequency dependent, VT was treated in the frequency domain using power spectral density (PSD). The overall VT was calculated as the area under the curve of PSD between 7.3 Hz and 500 Hz. Note that the PSD value is the root-mean-square (RMS) amplitude squared. The VT calculated this way is the squared value of VT calculated using RMS amplitude.

Electromyography

A 16-channel wireless surface EMG system (Trigno, Delsys Inc., Natick, MA) was used to obtain activities of nine muscle surrounding the shoulder. These muscles included anterior, medial, and posterior deltoids, upper trapezius, latissimus dorsi, pectoralis major; serratus anterior, biceps brachii, and triceps brachii. Prior to surface EMG sensor attachment, the skin over the target muscles was shaved if necessary and cleaned using alcohol pads twice to attenuate impedance. The EMG signals were output as analog signals for recording.

Couple forces

To standardize testing within- and between-subjects, the coupling forces (i.e., grip force and push force) were tightly controlled based on the coupling forces specified in the ISO 10819 (2013). The grip force assessment was conducted with subjects held onto the shaker handle instrumented with two uniaxial force transducers (Kistler model 9212, Kistler amplifier type 5018, Kistler Instrument Corp., Novi, MI). The push force assessment was conducted using a Kistler force plate (model 9260AA, amplifier type 5233A, Kistler Instrument Corp., Novi, MI) was placed under the subject's feet. A computer monitor was placed in front of the subjects to provide live feedback to control the grip force and push force levels at 30 N ±5 N and 50 N ±8 N, respectively (ISO 10819, 2013)

Acceleration, EMG, and force signals were recorded using a custom-written LabVIEW program (Version 17, National Instrument, Austin, TX) and with two 32-channel analog-to-digital converters (NI USB-6363 and NI–9205, National Instrument, Austin, TX). The sampling frequency was set at 5000 Hz. The sampling duration was 12 seconds for each testing condition. A custom-written MATLAB program was used to calculate all outcome values. The average of 3 trials was used to conduct descriptive analysis.

Results

Figure 3 shows the VT along the body as compared to the shaker handle when split according to exoskeleton conditions. The overall trend of the VT was not affected. The same observation was made when splitting data according to the posture conditions.

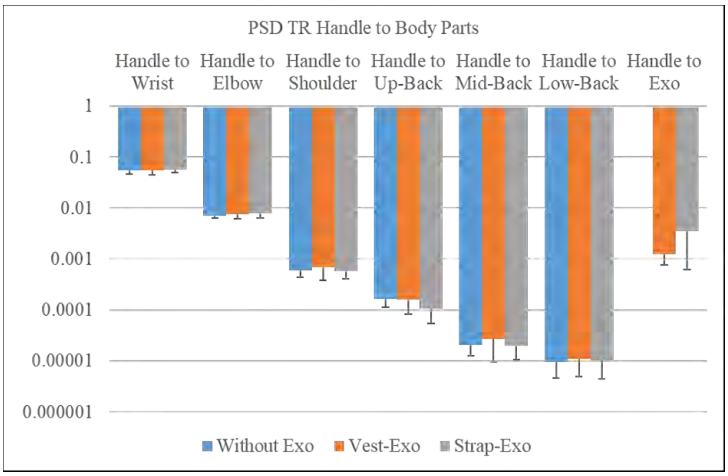

Figure 3. Exoskeleton effect on transmissibility.

Figure 4 shows normalized EMG data under three Exo conditions, respectively. Most muscles examined exhibited lower activities when wearing ArmExos. The agonist muscle activities in the overhead posture were higher when compared to the front-of-body posture. Antagonist muscle activities tended to increase with vibration turned on.

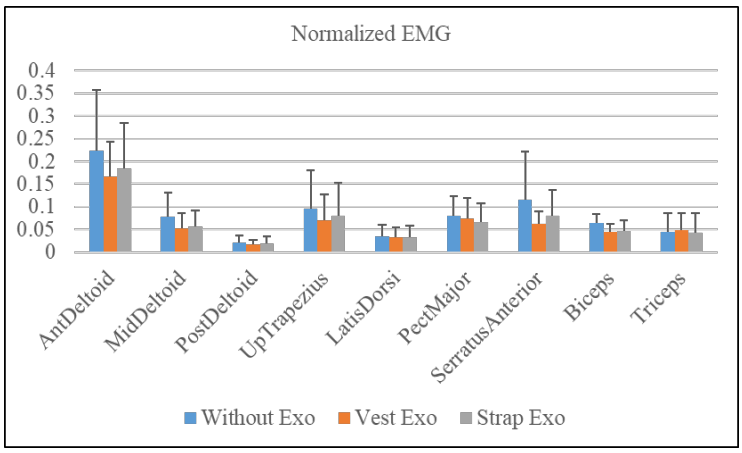

Figure 4. Exoskeleton effect on shoulder muscle activities.

In the present study, the coupling forces were controlled (e.g., same average values). However, the variations of the coupling forces as represented by the standard deviation (SD) of the data demonstrated the peak-to-peak response. Figure 5.a shows that the exoskeleton effect on peak-to-peak coupling force was minimum. As expected, the existence of vibration increased the peak push force significantly, indicating a higher peak mechanical load to the body (Figure 5.b).

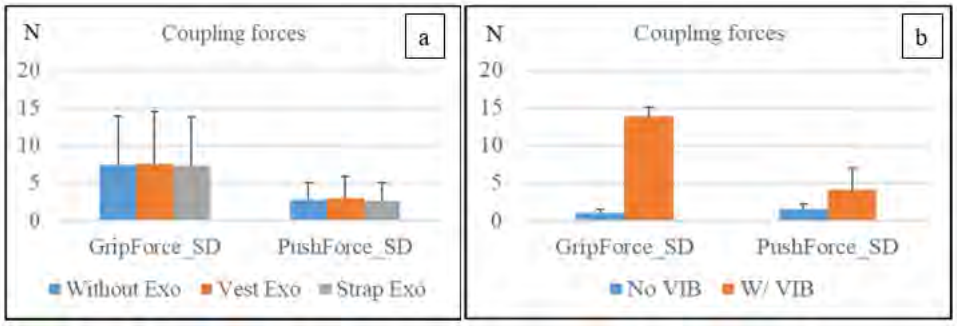

Figure 5. Exoskeleton effect (a), and vibration effect (b) on peak-to-peak coupling forces.

Discussion and Conclusions

The primary aim of this thesis research was to collect preliminary data to assess the combined effects of overhead posture and use of power hand tools on effectiveness of ArmExos. The first observation made on in the present study is the amplitude of VT decreased drastically along the arm and the spine based on the distance of the body parts from the shaker handle. The trend of VT response with respect to distance from the shaker handle was also reported previously. Xu et al. (2017) reported peak response at the frequency of 7 Hz and 12 Hz for the upper arm, 7 Hz and 9 Hz for the shoulder, 6 Hz and 7 Hz for neck and back in the front-of-body vibration. Except the neck, these values are similar to the front-of-body posture in the present study. The overhead vibration posture examined in the present study showed that there was a significant shift in peak VT frequency at the shoulder when compared to the front-of-body posture. The related health effect remains to be investigated. Regarding the exoskeleton effect, there is a large body of literature examining performance of ArmExos in overhead tasks. However, few studies examined the overhead tasks with power hand tools simultaneously. This was the primary reason to conduct the present study. The major finding of the present study was that wearing Exo had minimal effects on VT except at the wrist joint where the peak VT value in the frequency domain decreased significantly with ArmExos.

In present study, the biggest increase in muscle activity was observed in the anterior deltoid and the upper trapezius when compared to the front-of-body posture. These results are consistent with literature findings. Rohmert et al. (1989) examined arm and shoulder muscle activity in overhead vibration and found that the upper trapezius muscle had significant increase in activity in the overhead posture. Kim et al. (2018) examined overhead drilling and showed muscle activities for anterior deltoid, middle deltoid, and descending trapezius were greater in the overhead tasks comparing with the shoulder height task. In the present study, there was a decrease in activity in most shoulder muscles with ArmExos, consistent with the literature (Kim et al., 2018). However, existence of vibration was not found to affect muscle

activity much with only a slight increase in some muscles.

Regarding the coupling forces, the peak-to-peak coupling forces as calculated as SD over the 12 seconds of recordings showed that overhead posture with vibration turned on resulted in a higher push force detected at the subject feet. These findings indicate that there was an increase in mechanical load in the body under the overhead condition and under the vibration turned on condition. There is no literature specifically looks at the peak-to-peak coupling force.

In summary, posture and exoskeleton conditions had little effect on VT along the arm and the spine. The shoulder muscle activity was more significant in the overhead posture, especially for the anterior deltoid and upper trapezius. The effects of Exo and vibration conditions on muscle activities showed promising results as expected, though shouldn't be over interpreted. There was a moderately higher peak push force for the overhead posture. There were a significantly higher peak grip force and a moderately higher peak push force with vibration turned on. These results suggest that power tool use in the overhead posture may increase mechanical load in the body. Future studies with a larger sample size are needed to validate the findings of the present study.

Acknowledgments

The present study was in part supported by Northern Illinois University Great Journey's scholarship.

References

De Looze, M. P., Bosch, T., Krause, F., Stadler, K. S., & O'Sullivan, L. W. (2016). Exoskeletons for industrial application and their potential effects on physical workload. *Ergonomics*, *59*(5), 671-681.

Kamping-Carder, L. (2019). Industrial Exoskeletons Give Workers a Lift. In *The Wall Street Journal*. [online]. Available: https://www.wsj.com/articles/industrial-exoskeletons-give-workers-a-lift-11547730001

Kim, S., Nussbaum, M. A., Esfahani, M. I. M., Alemi, M. M., Alabdulkarim, S., & Rashedi, E. (2018). Assessing the influence of a passive, upper extremity exoskeletal vest for tasks requiring arm elevation: Part I – "Expected" effects on discomfort, shoulder muscle activity, and work task performance. *Applied ergonomics, 70*, 315-322.

Lowe, B. D., Billotte, W. G., & Peterson, D. R. (2019). ASTM F48 formation and standards for industrial exoskeletons and exosuits. *IISE transactions on occupational ergonomics and human factors*, *7*(3-4), 230-236

Rohmert, W., Wos, H., Norlander, S., & Helbig, R. (1989). Effects of vibration on arm and shoulder muscles in three body postures. *European journal of applied physiology and occupational physiology, 59*(4), 243-248.

Van Eerd, D., Munhall, C., Irvin, E., Rempel, D., Brewer, S., Van Der Beek, A. J., Dennerlein, J.T., Tullar, J., Skivington, K., Pinion, C. & Amick, B. (2016). Effectiveness of workplace interventions in the prevention of upper extremity musculoskeletal disorders and symptoms: an update of the evidence. *Occupational and Environmental Medicine*, *73*(1), 62-70.

Xu, X. S., Dong, R. G., Welcome, D. E., Warren, C., McDowell, T. W., & Wu, J. Z. (2017). Vibrations transmitted from human hands to upper arm, shoulder, back, neck, and head. *International journal of industrial ergonomics*, *62*, 1-12.

Definition of spinal joint coordination laws for repositioning a digital human model based on MRI observations in four different postures

Shabahang Shayegan and Xuguang Wang
Université Gustave Eiffel, France

Keywords: Spinal coordination law, Non-standard anatomical postures, Digital human model repositioning.

Introduction

Thanks to recent studies about the relationship between joint center locations, external body shape and landmarks positions, we can build a personalized kinematic human model in standing posture. It is though challenging to position it into a seated posture. This is particularly true for positioning pelvis and spine due to the high number of degrees of freedom (DOF) involved and very low number of anatomical landmarks available for palpation/motion capture. This is an under-determined problem. A priori knowledge is needed to find anatomically correct solutions. One way is to reduce the DOFs of spine model by either not allowing all intervertebral joint rotate freely or introducing relationships between them. (Alemi et al. 2021) reduced spinal DOFs from 51 to 5 by defining kinematic constraints and showed that a 5DOF-simplified model could produce smooth spine motions. Monnier et al., (2007) used the relationships between spinal joint angles, called spinal coordination laws, to prevent unrealistic postures in motion reconstruction process. However, evidence based statistical models are missing. The objective of this paper is to investigate the variation of spinal joint angles when changing posture and to identify spinal coordination laws.

Methods

In this research, a previously collected data by Beillas et al., (2009) from MRI observations of three females and six males in four postures (standing, seated, supine and 45° forward-flexion), were used. In their study, positional MRI and custom designed adjustable fixtures were used to define and impose the four postures. We defined a spinal model with 17 spherical joints, from S1L5 to T1C7, and we personalized the segment lengths for each participant. Since postural changes between the four studied positions were mainly in the sagittal plane, only flexion-extension was allowed for each joint. All joints were aligned when joint angles were zeros. Then, the intervertebral joint angles were obtained by minimizing the distance between the joint positions of the subject-specific kinematic models and those from MRI image. One factor ANOVA was used to analyze the effect of posture on joint angles. We also defined two overall spinal parameters to

characterize the global spinal posture: 1) distance between T1C7 and S1L5 (trunk_d) for trunk compression, 2) angle between L5S1-midHip and S1L5-C7T1 (trunk_a) for trunk flexion. Statistical relationships between overall spinal parameters and joint angles were analyzed.

Results

Figure 1 shows the reconstructed spines corresponding to the four postures for one male participant (M01). Significant differences between four postures were observed only for S1L5 (F=9.19, p=0.0002), L5L4 (F=7.28, p=0.0007), L4L3 (F=2.95, p= 0.0475), and T7T6 (F=3.13, p=0.0391) joint angles (Table 1). Taking standing posture as reference, joint angle changes were calculated for forward-flexion, seated and supine postures. Regression equations of joint angle changes for S1L5, L5L4, L4L3 and T7T6 were obtained (Table 2).

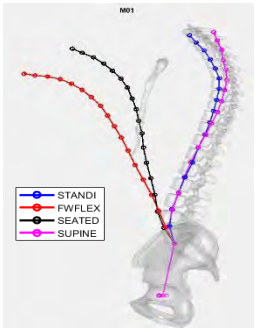

Figure 1. Reconstructed spinal models for four postures for a male participant (M01)

Table 1. Means (± standard deviations) of spine joint angles for the four postures and the global spinal postural parameters trunk_a (flexion-extension) and trunk_d (compression). Angles are in degrees, positive for flexion and negative for extension. *FWFLEX=forward-flexion, SEATED=seated, STANDI=standing, SUPINE= supine

Posture	S1L5	L5L4	L4L3	T7T6	Trunk_d(mm)	Trunk_a
FWFLEX	35.21 ± 8.33	- 11.74 ± 7.38	-3.70 ± 5.18	7.62±7.11	445.81±19.73	37.51±12.52
SEATED	34.37 ± 5.86	-10.84 ± 3.71	-8.07 ±4.29	7.65±4.84	450.98± 15.32	29.62±5.40
STANDI	24.82 ± 7.58	-19.98 ± 3.59	-10.46 ±5.12	9.92±4.78	440.30±15.66	10.80±5.61
SUPINE	21.10 ± 5.57	-18.42 ± 4.96	-7.90 ± 5.00	2.03±5.72	453.82±20.08	5.15±7.06

Table 2 Regression equations of joint angle changes. D_Trunk_d (%) is the variation of trunk_d normalized by its value in standing posture, and D_Trunk_a is the change of trunk_a with respect to the standing posture.

Joint	Constant	D_Trunk_d (%)	D_Trunk_a	Adjusted R^2 (%)	MSE
S1L5	3.09	1.12	0.36	68.84	22.67
L5L4	0.41	1.32	0.28	45.87	20.12
L4L3	1.96	0	0.14	25.33	15.24
T7T6	7.54	0	0.25	20.29	60.22

Discussion and Conclusions

Only three lumbar joints (S1L5, L5L4, L4L3) and one thoracic joint (T6T7) were found to contribute to spinal posture changes, suggesting a kinematic model with these four joints would be enough to describe spinal curvature. This highlights the importance of lower lumbar joints in spine postural changes especially for flexion-extension. Kuai et al., (2018) showed that S1L5, L5L4, L4L3 joints contributed to total spinal motion more than other lumbar joints. Alemi et al. (2021) found that, comparing to thoracic joints, lumbar joints contribute more to overall spine flexion-extension. In this study, evidence-based spine coordination laws have been obtained. Results will be applied to reconstruct seated postures using a whole body model. High R-squared value for the variation of S1L5 and L4L5 angles imply that the two global spinal postural

parameters could be enough to predict these variables using linear regressions. However low R-squared value for L4L3 and T7T6 suggest that other predictors might be needed to characterize the global spinal posture.

References

Alemi, M. M., Burkhart, K. A., Lynch, A. C., Allaire, B. T., Mousavi, S. J., Zhang, C., Bouxsein, M. L., & Anderson, D. E. (2021). The Influence of Kinematic Constraints on Model Performance During Inverse Kinematics Analysis of the Thoracolumbar Spine. *Frontiers in Bioengineering and Biotechnology*, *9*(688041). https://doi.org/10.3389/fbioe.2021.688041

Beillas, Ph., Lafon, Y., & Smith, F. W. (2009). The effects of posture and subject-to-subject variations on the position, shape and volume of abdominal and thoracic organs. *Stapp Car Crash Journal*, *53*, 127–154. https://doi.org/10.4271/2009-22-0005

Kuai, S., Guan, X., Zhou, W., Zhang, R., Ji, R., Liao, Z., Guo, D., Liu, W., & Wang, D. (2018). Continuous lumbar spine rhythms during level walking, stair climbing and trunk flexion in people with and without lumbar disc herniation. *Gait & Posture*, *63*, 296–301. https://doi.org/10.1016/j.gaitpost.2018.05.006

Monnier, G., Beurier, G., & Wang, X. (2007). Coordination of Spine Degrees of Freedom during a Motion Reconstruction Process. *SAE Technical Paper*, *116*, 835–841. https://doi.org/10.4271/2007-01-2454

Forward and Backward Reaching Inverse Kinematics (FABRIK) Solver for DHM: A Pilot Study

Maurice Lamb[1], Seunghun Lee[2], Erik Billing[1], Dan Högberg[1], and James Yang[2]

[1] *University of Skövde, Sweden*

[2] *Texas Tech University, United States*

Abstract

Posture/motion prediction is the basis of the human motion simulations that make up the core of many digital human modeling (DHM) tools and methods. With the goal of producing realistic postures and motions, a common element of posture/motion prediction methods involves applying some set of constraints to biomechanical models of humans on the positions and orientations of specified body parts. While many formulations of biomechanical constraints may produce valid predictions, they must overcome the challenges posed by the highly redundant nature of human biomechanical systems. DHM researchers and developers typically focus on optimization formulations to facilitate the identification and selection of valid solutions. While these approaches produce optimal behavior according to some, e.g., ergonomic, optimization criteria, these solutions require considerable computational power and appear vastly different from how humans produce motion. In this paper, we take a different approach and consider the Forward and Backward Reaching Inverse Kinematics (FABRIK) solver developed in the context of computer graphics for rigged character animation. This approach identifies postures quickly and efficiently, often requiring a fraction of the computation time involved in optimization-based methods. Critically, the FABRIK solver identifies posture predictions based on a lightweight heuristic approach. Specifically, the solver works in joint position space and identifies solutions according to a minimal joint displacement principle. We apply the FABRIK solver to a 7-degree of freedom human arm model during a reaching task from an initial to an end target location, fixing the shoulder position and providing the end effector (index fingertip) position and orientation from each frame of the motion capture data. In this preliminary study, predicted postures are compared to experimental data from a single human subject. Overall the predicted postures were very near the recorded data, with an average RMSE of 1.67°. Although more validation is necessary, we believe that the FABRIK solver has great potential for producing realistic human posture/motion in real-time, with applications in the area of DHM.

Keywords: Inverse Kinematics, Posture Prediction, IK validation, FABRIK

Introduction

Predicting human posture is one of the core functions of many digital human modeling (DHM) tools. However, because human biomechanical systems consist of many highly redundant degrees of freedom posture prediction is a particularly difficult challenge (Aristidou et al., 2018; D'Souza et al., 2001; Yang et al., 2004). Further, to make DHM tools easy and efficient to use, many tools provide control over manikin posture in the form of control points, typically located on end effectors (EE). While this simplifies control, it also means that the DHM tool must solve an inverse kinematics (IK) problem in which it must identify and select a plausible human posture given a possibly infinite set of posture solutions. Most modern approaches to IK posture prediction take inspiration from robotics where highly precise and optimized solutions are the focus (Aristidou et al., 2018; De Magistris et al., 2013; D'Souza et al., 2001; Yang et al., 2004). IK solvers in robotics are often guaranteed to find a plausible solution in finite time if there is one, but they can be slow and sometimes difficult to understand to end users. In this paper we introduce and explore one candidate IK solver developed in the context of computer graphics and recently extended to robotics. The Forward and Backward Reaching Inverse Kinematics (FABRIK) solver has been deployed in multiple computer game engines and 3D design contexts as a real-time posture prediction method (Aristidou et al., 2016; Aristidou & Lasenby, 2011). To our knowledge, the FABRIK solver has not been validated in a DHM context. Initial indications using human skeleton models for games animations are that it can produce plausible human postures (Aristidou et al., 2016). However, accurate predictions typically require appropriate biomechanical constraints and consistent coordinate conventions. The aim of this paper is to introduce the FABRIK solver to the DHM community, provide a pilot demonstration of its feasibility, and discuss some of the challenges in moving the solver from computer graphics to DHM contexts.

Optimization-Based IK Solutions

A posture, for the current purposes, is defined by a biomechanical model (joints and spatial relations between them) and the states of the joints (specified in local angles). Often DHM tools are used to predict and evaluate postures given a particular task. If the user knows all the joint angles, then the posture can be specified using forward kinematics methods to apply the joint angles to each joint moving from a root joint out towards the EEs. While forward kinematic methods can be useful in some instances, it is rare for users to know all the joint angles needed to specify a posture used to accomplish a specific task. In the typical case, only the position and orientation of a few control points, typically EEs, can be known or reasonably anticipated and the DHM tool needs to predict a feasible posture that can meet those constraints. Given the expected EE states, some form of IK method can be applied to estimate a good solution or set of solutions. One method for solving IK problems, e.g., the possibility for infinite valid solutions, in DHM software is to identify a set of constraints on the biomechanical system that can be

optimized (Howard et al., 2012; Yang et al., 2004, 2011; Yang & Ozsoy, 2020). Taking this approach, the set of solutions can be limited to those that meet the optimization criteria and search/selection criteria can be used to identify an optimal or nearly optimal solution. Once a solution is identified it can be used to specify the joint configuration of a multi-joint system where the EEs are positioned and oriented according to the specified goal. Optimization methods are highly effective and can produce results for arbitrarily complicated joint systems as well as balance multiple optimization objectives and constraints using multi-objective optimization methods. A challenge for optimization-based methods is that they can be computationally expensive and must be front loaded theoretically, that is they cannot identify a solution without first specifying which biomechanical constraints to optimize and then defining what is optimal. For many DHM applications, it is tricky to formulate optimization criteria that produce results similar to real human motion. While optimization may be ultimately indispensable, alternative approaches to identifying IK solutions may facilitate the formation of a cluster of tools which can quickly and accurately converge on a posture prediction with minimal theoretical front-loading. To this end, the FABRIK solver may provide a fast and minimally theory laden approach to identifying plausible IK solutions.

FABRIK

While the FABRIK solver was introduced to provide a fast and lightweight IK solver for computer graphics applications, it has been implemented in many domains for both pre-recorded and real-time solvers for human and non-human animations (Aristidou & Lasenby, 2011, Aristidou et al., 2016; Lansley et al., 2016). Recently, FABRIK has been extended for application in robotics for both fixed position and mobile multi-joint robots (M. Santos et al., 2021; P. C. Santos et al., 2020; Tao et al., 2021; Tenneti & Sarkar, 2019).

FABRIK is a heuristic IK solver meaning that it identifies a valid posture by applying a limited set of rules to transform an initial posture into a final posture where the EE(s) is in the specified final posture (See Figure 1 for algorithm sketch). An advantage of this approach is that very little information beyond the structure of the kinematic chain is needed, i.e., segment length, relative joint position, joint type, and joint range limits. This means that a solution can be identified quickly and with minimal theory leadenness. While FABRIK is correspondingly not guaranteed to provide a feasible or plausible solution, current applications of the solver in design and game development contexts suggest that it can provide good solutions in the vast majority of human motion prediction problems (Aristidou et al., 2016; Aristidou & Lasenby, 2011; M. Santos et al., 2021; Tao et al., 2021).

The FABRIK solver works in joint position space and is applied hierarchically to each joint and iteratively until a solution is identified. At its core the FABRIK solver involves moving each joint the shortest distance possible given the expected re-positioning of the previous joint in the kinematic chain and while adhering to the biomechanical constraints of the system (e.g., segment lengths and joint limits). A 2D application of the FABRIK solver is illustrated in FIGURE 1. A single iteration of the FABRIK solver starts at the EE and is applied to each joint in the kinematic chain moving towards a root joint. In the first step, the EE is repositioned and aligned to the new EE target (Figure 1A-C). Each joint moving from EE to root is then repositioned along the shortest line that can be drawn between the new position of the joint above and the current joint position while preserving bone length (Figure 1D). Joint limits are applied locally while repositioning joints to ensure that they are not violated in the predicted posture. Once the root node is reached the process is repeated in the reverse direction along the chain (Figure 1E). Assuming the root node is fixed, it is repositioned to its initial position and the process continues back to the EE. This process can be iterated until either the EE is within a specified tolerance of the goal, or a specified number of iterations has been completed. Several modifications and variations of the FABRIK solver have been developed that allow for multi-chain/branching systems, non-fixed root nodes, whole system repositioning, handling unsolvable targets, and obstacles (Aristidou et al., 2016; P. C. Santos et al., 2020; Tao et al., 2021). In the current project we used only the original algorithm along with a hinge constraint applied to the elbow as discussed in Aristidou and Lasenby (2011).

One aim of this project is investigating the extent to which the FABRIK solver can identify a plausible solution given minimal information about the system. As such, the shoulder and wrist joints in the 7 DOF arm model used below are unconstrained 3 DOF joints and the elbow is a 1 DOF hinge joint with a range of motion of 0-120°. An unconstrained version of the FABRIK solver treats all joints as unconstrained ball joints. The elbow joint requires introducing constraints to limit to a hinge joint and allows for a discussion of applying joint constraints in FABRIK. A 1 DOF hinge constraint can be implemented in the FABRIK solver by a method which limits the possible hinge joint positions to a plane partial defined by a line connecting the joint before and the joint after the hinge joint in the kinematic chain (Aristidou & Lasenby, 2011; M. Santos et al., 2021). The discussions of hinge joints in these papers center on general computer avatar or non-humanoid robots respectively, and do not consider how existing human biomechanical limits might affect the results. Notably while the primary plane axis is defined according to the line segment that intersects the wrist and shoulder joints for a human arm, the selection of a secondary and corresponding orthogonal axis must be specified. Given only the primary plane axis there are infinitely many planes to project the joint onto and the selection of plane can have a significant impact on predicted elbow position and orientation as well as the orientation of the other joints. For the study below

we chose the secondary axis based on the fixed geometric relationships between the most recently predicted joint and the elbow. In this case, we could use the second axis of the wrist (joint 6 in Table 1) and the first axis of the shoulder (joint 1) respectively. The plane normal was then defined as the cross product of the selected secondary and the primary axes. This plane definition could be verified by testing a small set of samples and ensuring that the predicted rotational axis of the elbow was parallel to the second rotational axis of the shoulder (joint 2) as specified by the arm model in defined by Figure 2 and Table 1 and observed in the recorded data. Biomechanically this is the result of the fact that the rotational axis of the elbow is rigidly coupled to the shoulder joint. We acknowledge that the human shoulder is a relatively complicated joint and that the current model simplifies this joint greatly. However, even without a more representative shoulder joint, the initial testing of the hinge joint constraint allowed for plausible predictions.

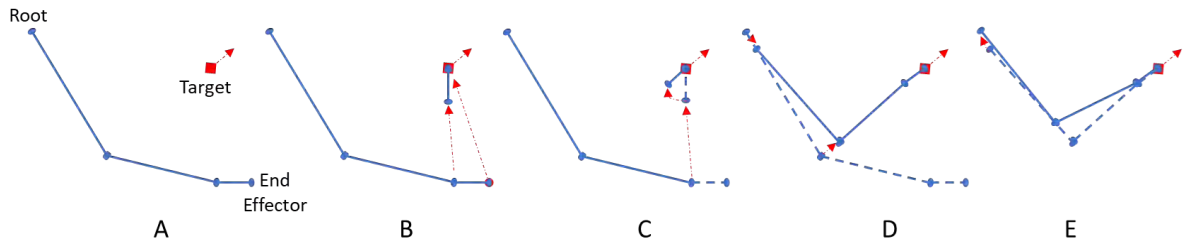

Figure 1. One iteration of the FABRIK solver. The target location and orientation are specified (A) along with an initial arm posture. EE is moved to the target and the other end of segment is moved along a line specified by its initial position and the new target position preserving bone segment length (B). The segment is aligned with the target orientation respecting local rotational constraints (C). Then the process repeated for each joint to the root (D). Since the root is likely moved by the final step, it is returned to its initial position and the process is repeated in reverse to the EE (E). This entire process is repeated until the EE is within the set tolerance or iteration limits.

Methods

In order to determine the initial feasibility of a FABRIK based DHM solution we collected motion capture data for a simple single arm reaching task from a single human actor. The aim of this pilot study is to apply FABRIK to a relatively simple 7 DOF arm model to see how well it can predict the actual arm postures during the reaching motions.

Motion Capture

The data was collected for 19 directed reaching motions performed by a single participant at Texas Tech University Human-Centric Design Research Lab. 7 Eagle-4 camera system (Motion Analysis Corporation, CA) were utilized in this experiment, and each of them has 40megapixel resolution with 500 frames per second. For one arm motion capture, 9 retroreflective markers were attached to the participant's right shoulder and arm. Each reaching motion consisted of sitting in a neutral position and then reaching to a predefined target position in front of the participant. Each reach to target from the initial posture is treated as a single task instance, starting with an initial neutral posture, and moving to an extended final posture. A total of 6 reach targets were used, with each reach cycle repeated 3 times. For data processing, Cortex (Motion Analysis Corporation, CA) was used to smooth the labeled marker movements at 60 Hz.

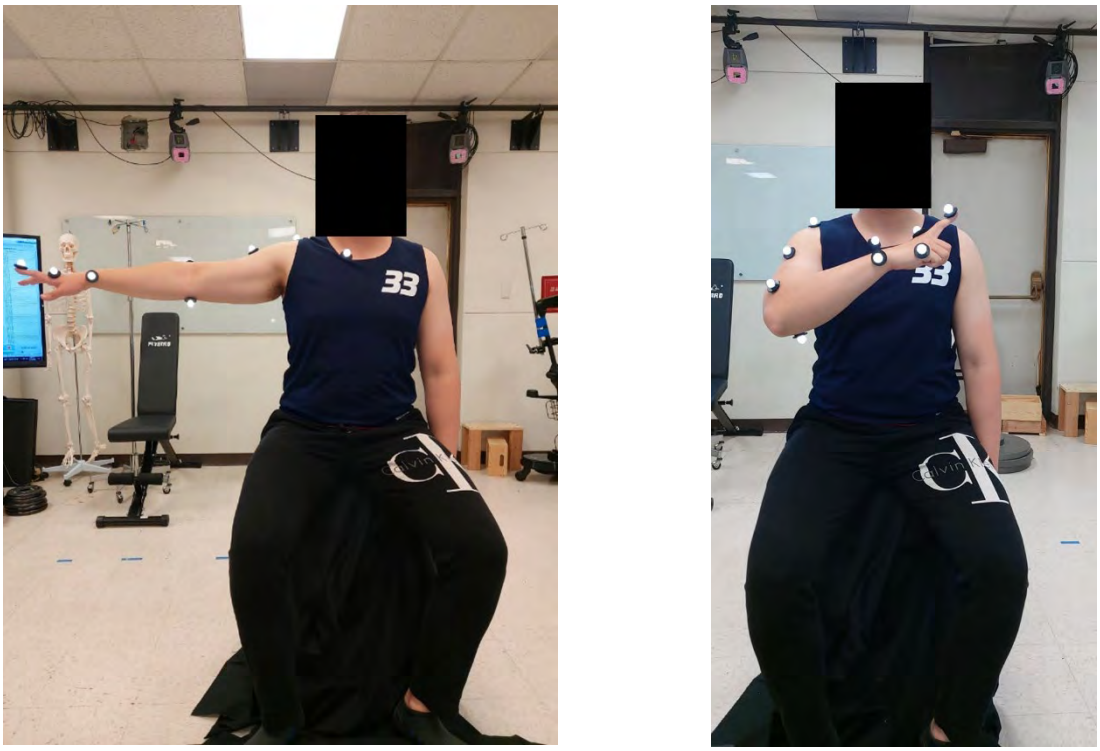

(A) (B)

Figure 2. Marker protocol: neutral pose (A) and reaching to a predefined target (B) observed from the front view

Figure 2 shows the marker locations. The markers were placed on the participant's sternum, back, and arm to track each relevant joint center (shoulder, elbow, and wrist) and the index fingertip. The marker

data was converted to the joint angles using Visual 3D (C-Motion, MD), and a 7 DOF arm model (Figure 3) was defined with Deviant-Hartenberg (DH) parameters (See Table 1).

Simulations using the FABRIK method were carried out in Matlab 2021b. The shoulder was treated as the root node and fixed to the origin of the simulation space. The EE positions and orientations were extracted from the experimental data as the control signal for the simulated arm. All simulations were initialized using the configuration of the arm at the beginning of a simulated task instance, setting the arm joints to match the initial recorded joint configuration. After initialization FABRIK was used to solve the next recorded arm configuration based on the EE's configuration in the next recorded frame. For each subsequent step of the simulation the FABRIK solver used the previous simulated arm configuration as the initial arm configuration. Based on initial testing, the FABRIK solver was run until the predicted arm configuration placed the simulated EE <1mm of the target position or the FABRIK solver ran 500 iterations. The final simulated arm configuration was stored as 7 angles matching the conventions in Table 1 for each simulated frame. Timing and iteration counts were also stored, though because computational efficiency was not explicitly considered in the development of the test software, timing is not indicative of best-case performance.

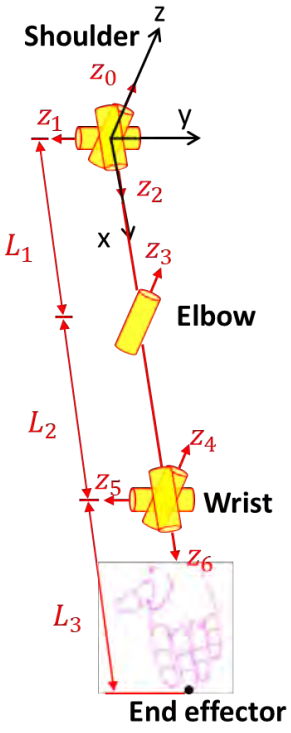

Table 1

DH-Parameters for arm model

Joint (i)	θ_i (rad)	d_i (cm)	α_i (rad)	a_i (cm)
1	$0 + q_1$	0	$\pi/2$	0
2	$\pi/2 + q_2$	0	$\pi/2$	0
3	$\pi/2 + q_3$	L_1	$\pi/2$	0
4	$\pi/2 + q_4$	0	0	L_2
5	$0 + q_5$	0	$\pi/2$	0
6	$\pi/2 + q_6$	0	$\pi/2$	0
7	$0 + q_7$	L_3	0	0

Figure 3. Arm Model (See Table 1).

After simulations were completed, the experimental and simulated arm configurations at each frame were compared for each task instance. Comparisons were quantified by calculating root mean square error (RMSE) for each joint angle (θ_n) that specified the arm configuration,

$$err(\theta_n) = \sqrt{\sum_{i=2}^{len}\left(\theta_i^{en} - \theta_i^{sn}\right)^2} \quad (1)$$

where $\theta_i^{en}$is the experimental angle on the n^{th} joint on the i^{th} frame and θ_i^{sn} is the corresponding simulated angle during that frame. Each task consisted of len number of frames. The first frame is excluded from the calculation of θ_n because it is taken from the recorded data.

Results

The FABRIK solver was able to identify a solution for every target in the experimental data. The provided solutions placed the EE within an average of 0.007 mm of the target position with a max distance to EE goal of 0.013 cm. RMSE for each joint was calculated between predicted and recorded joint angles for each trial and the average and standard deviation RMSE across trials for each joint DOF is presented in Table 2. Across all joints the average RMSE was 1.67°. While the code used for the current study was not optimized for speed, on average the FABRIK solver converged on a solution at each frame in 0.03 seconds and with an average number of 24 iterations.

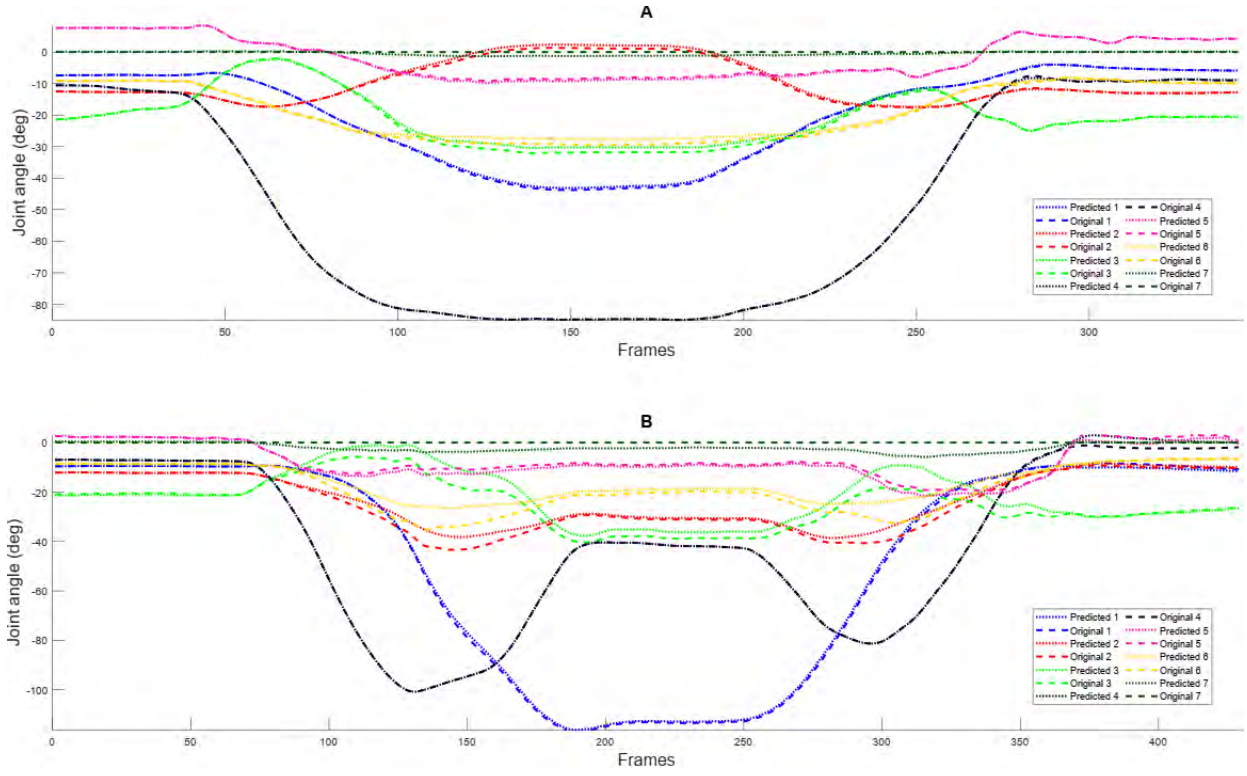

Figure 4. Joint angle plots for 2 trials. Dashed lines are the data from the motion-capture and dotted lines are the predictions. When run through the forward kinematics model, the top plot, A, was visually indistinguishable from the original, the bottom plot, B, showed some visible separation in the elbow joint around frame 275.

The predicted values were run through a forward kinematic solver and visualized as animations in Matlab for visual inspection. Overall the predicted postures were very near the recorded solutions with only a few trials where there was clear seperation between the predicted and recorded postures. Two representtive plots of the predicted and recorded joint angles are presented in Figure 4 to illustrate the predictions for a case with no easily visible seperation (Figure 4A) and a case with a clear moment of seperation (Figure 4B).

Table 2
RMSE between predicted and experimental joint angles[ab]

Joint 1	Joint 2	Joint 3	Joint 4	Joint 5	Joint 6	Joint 7
0.99 (2.13)	1.38 (1.73)	2.42 (3.46)	0.33 (0.33)	2.00 (4.65)	2.20 (2.99)	2.34 (4.51)

a. mean (standard deviation) b. all values in degrees.

Discussion and Conclusions

In this pilot study, the FABRIK solver was able to provide plausible predictions of the recorded human arm postures across the entire motion path. While this is only an initial exploration of the feasibility of the FABRIK solver for DHM purposes, we believe it is a compelling indication of its possible application. Implementations of FABRIK in modern game engines can converge on a solution for a full humanoid kinematic chain within 4 iterations and continuously provide real-time solutions at 90 Hz or faster. However, while these implementations of the FABRIK solver have proven effective in entertainment contexts, further work needs to be done to validate and optimize the FABRIK solver for DHM applications to ensure fidelity to real-world postures and motions. For the FABRIK solver to provide results consistently and to be a useful tool, the underlying kinematic chain and biomechanical assumptions for joint ranges and limits must be appropriately implemented. Further, it is unclear how far the FABRIK solver may diverge from plausible or valid solutions in more complicated DHM use cases. Systems and checks to ensure plausibility and validity for DHM applications need to be explored. The speed and flexibility of FABRIK also opens for potentially very powerful solutions when combined with traditional optimization based approaches. Once the initial validity of a lightweight version of FABRIK is

determined, we believe that additional insights from optimization methods and approaches may synergistically benefit both and contribute to new insights into human postures and behavior prediction. FABRIK provides static IK solutions which may be valid for DHM when correctly implemented. The minimal theory-ladenness, fast convergence to a solution, and relative simplicity makes it an ideal candidate for testing motion planning and control insights from cognitive science research in DHM tools.

References

Aristidou, A., Chrysanthou, Y., & Lasenby, J. (2016). Extending FABRIK with model constraints. *Computer Animation and Virtual Worlds*, *27*(1), 35–57. https://doi.org/10.1002/cav.1630

Aristidou, A., & Lasenby, J. (2011). FABRIK: A fast, iterative solver for the Inverse Kinematics problem. *Graphical Models*, *73*(5), 243–260. https://doi.org/10.1016/j.gmod.2011.05.003

Aristidou, A., Lasenby, J., Chrysanthou, Y., & Shamir, A. (2018). Inverse Kinematics Techniques in Computer Graphics: A Survey. *Computer Graphics Forum*, *37*(6), 35–58. https://doi.org/10.1111/cgf.13310

De Magistris, G., Micaelli, A., Evrard, P., Andriot, C., Savin, J., Gaudez, C., & Marsot, J. (2013). Dynamic control of DHM for ergonomic assessments. *International Journal of Industrial Ergonomics*, *43*(2), 170–180. https://doi.org/10.1016/j.ergon.2013.01.003

D'Souza, A., Vijayakumar, S., & Schaal, S. (2001). Learning inverse kinematics. *Proceedings 2001 IEEE/RSJ International Conference on Intelligent Robots and Systems. Expanding the Societal Role of Robotics in the the Next Millennium (Cat. No.01CH37180)*, *1*, 298–303 vol.1. https://doi.org/10.1109/IROS.2001.973374

Howard, B., Cloutier, A., & Yang, J. J. (2012). Physics-based seated posture prediction for pregnant women and validation considering ground and seat pan contacts. *Journal of Biomechanical Engineering*, *134*(7). https://doi.org/10.1115/1.4007006

Lansley, A., Vamplew, P., Smith, P., & Foale, C. (2016). Caliko: An Inverse Kinematics Software Library Implementation of the FABRIK Algorithm. *Journal of Open Research Software*, *4*(1), e36. https://doi.org/10.5334/jors.116

Santos, M., Molina, L., Carvalho, E. A. N., Freire, E. O., Carvalho, J. G. N., & Santos, P. (2021). FABRIK-R: An Extension Developed Based on FABRIK for Robotics Manipulators. *IEEE Access*, *9*, 53423–53435. https://doi.org/10.1109/ACCESS.2021.3070693

Santos, P. C., Freire, R. C. S., Carvalho, E. A. N., Molina, L., & Freire, E. O. (2020). M-FABRIK: A New Inverse Kinematics Approach to Mobile Manipulator Robots Based on FABRIK. *IEEE Access*, *8*, 208836–208849. https://doi.org/10.1109/ACCESS.2020.3038424

Tao, S., Tao, H., & Yumeng, Y. (2021). Extending FABRIK with Obstacle Avoidance for Solving the Inverse Kinematics Problem. *Journal of Robotics*, *2021*, 1–10. https://doi.org/10.1155/2021/5568702

Tenneti, R. A., & Sarkar, A. (2019). Implementation of modified FABRIK for robot manipulators. *Proceedings of the Advances in Robotics 2019*, 1–6. https://doi.org/10.1145/3352593.3352605

Yang, J., Marler, R. T., Kim, H., Arora, J. S., & Abdel-Malek, K. (2004). Multi-objective optimization for upper body posture prediction. *Collection of Technical Papers - 10th AIAA/ISSMO Multidisciplinary Analysis and Optimization Conference*, 2288–2305. https://scholars.ttu.edu/en/publications/multi-objective-optimization-for-upper-body-posture-prediction

Yang, J., Marler, T., & Rahmatalla, S. (2011). Multi-objective optimization-based method for kinematic posture prediction: Development and validation. *Robotica*, *29*(2), 245–253. https://doi.org/10.1017/S026357471000010X

Yang, J., & Ozsoy, B. (2020). Three dimensional unassisted sit-to-stand prediction for virtual healthy young and elderly individuals. *Multibody System Dynamics*, *49*(1), 33–52. https://doi.org/10.1007/s11044-019-09699-9

Balance Stability Characteristics of Human Walking with Preferred, Fast, and Slow Speeds

William Peng and Joo H. Kim
New York University, United States

Abstract

This work presents a model-based method of evaluating and quantifying stability characteristics of human walking in the sagittal plane. The stability criteria used for this analysis are boundaries in the state space of the center of mass (COM), which represent the maximum capability of a human to maintain balance in single support (SS) and double support (DS) phases or to make a desired step without falling. Complete models of the system dynamics, biomechanical characteristics, its contact interaction with the ground, and gait parameters, are considered. Experimental human COM trajectories during walking are analyzed against computed stability boundaries to quantify the nature of human gait across walking speeds. Stability comparisons with other robotic platforms, an exoskeleton and a humanoid robot, are also provided.

Keywords: Balance Stability, Center-of-Mass State Space, Walking

Introduction

The definitions of stability states considered here (Peng et al., 2022) are with respect to a specific contact configuration (SS or DS balanced) or transition (steppable), where a balanced state is a state from which a given biped can maneuver such that its (SS or DS) contact can be indefinitely maintained and a steppable state is one from which a desired step is achievable before any undesired contact occurs (Figure 1).

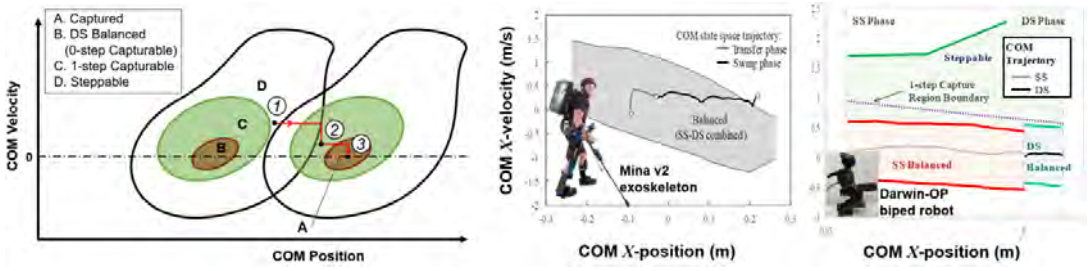

Figure 1. Schematics of general stability regions (left) and with mostly balanced walking trajectories of Mina v2 exoskeleton (Mummolo et al., 2018) (center) and DARwIn-OP robot (Peng et al., 2022) (right)

Methods

The stability boundaries are computed as the solutions to a series of constrained optimization problems subject to dynamics, system-specific (e.g., joint (Norkin & White, 2009) and torque (Anderson et al., 2007) limits), and region-specific (for consistency with the corresponding state definition) constraints evaluated at COM states along the given walking trajectory. Two healthy subjects of similar mass and height were recruited and provided informed consent for the walking experiments. The COM trajectories were obtained at 85% (slow), 100% (preferred), and 115% (fast) of their self-selected preferred walking speeds.

Results

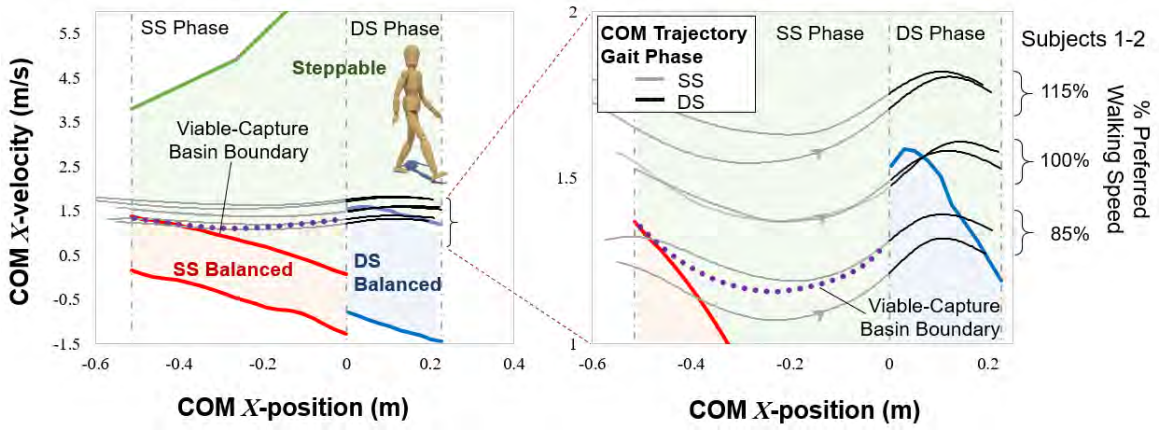

Figure 2. Experimental walking COM trajectories for two subjects. The human stability regions are shown for one subject, along with the viable-capture basin boundary for 1-step capturability (Peng & Kim, 2020).

Discussion and Conclusions

The results show that normal human walking at preferred, fast, and slow speeds is mostly unbalanced, with the exception of slow walking during the DS phase (Figure 2). For accurate comparison, each COM trajectory should be compared to the stability region corresponding to that COM trajectory. In this work, stability regions are only shown for the preferred walking speed of one human subject, due to the spatial similarity of the COM trajectories across walking speeds. For extremely slow speeds, the walking will be highly balanced, similar to that of robotic gait (Figure 1), as opposed to during extremely high speeds, when the walking will be highly unbalanced. This framework can be used for the analysis of gait impairment and the associated rehabilitation and for the design and control of powered lower-limb exoskeletons.

References

Anderson, D. E., Madigan, M. L., & Nussbaum, M. A. (2007). Maximum voluntary joint torque as a function of joint angle and angular velocity:

Model development and application to the lower limb. *Journal of Biomechanics*, *40*(14), 3105–3113.
Mummolo, C., Peng, W. Z., Agarwal, S., Griffin, R., Neuhaus, P. D., & Kim, J. H. (2018). Stability of Mina V2 for robot-assisted balance and locomotion. *Frontiers in Neurorobotics*, *12*(62), 1–16.
Norkin, C. C., & White, D. J. (2009). *Measurement of joint motion a guide to goniometry* (4th ed.). F. A. Davis Company.
Peng, W. Z., & Kim, J. H. (2020). Normalized Criteria and Comparative Analysis of Legged Stability. *Proceedings of the 8th IEEE International Conference on Biomedical Robotics and Biomechatronics (BioRob)*, 803–808. .
Peng, W. Z., Mummolo, C., Song, H., & Kim, J. H. (2022). Whole-body balance stability regions for multi-level momentum and stepping strategies. *Mechanism and Machine Theory*, *174*, 104880.

Evaluation of personalized Human Body Buttock-Thigh Finite Element Models in terms of soft tissue deformation for seat comfort assessment

Goutham Sridhar [1,2], Leo Savonnet [1,2], Yoann Lafon [3], Xuguang Wang [2]

(1) SAFRAN SEATS, France (2) Laboratoire de Biomécanique et Mécanique des Chocs (LBMC), Université Gustave Eiffel (3) Université Claude Bernard Lyon 1

Introduction

Finite Element Models (FEM) of the human body (HBM) are used to analyze static seating discomfort mainly in terms of interface pressure distribution on the seat surface (*Savonnet et al. 2018*). However, most of the HBMs are not validated under actual seating conditions due to the difficulty in measuring internal body loads such as soft tissue deformation, intervertebral disc pressures, etc. The rare HBM related studies claiming validation have only analyzed the interface pressure distribution. Recent experiments conducted with and without foam for different seat pan inclinations (Fig 1b) using Open MRI indicate that soft tissue deformation below the Ischial Tuberosity (IT) is affected by both contact pressure and shear and thus could be an objective indicator in seat discomfort assessment (*Wang et al. 2021*). The aim of this present study is to report a preliminary evaluation of FE-HBMs against these subject-specific experimental data in terms of interface pressure and soft tissue deformation.

Methods

FE Model

Mesh. Among four participants (P) in the experimental study, two subject-geometry-specific FEMs were developed for two volunteers, P1 and P2 in *Wang et al. (2021)*. Fat, muscles, skin and bones were manually segmented using 3D Slicer in the MRI acquisition defined for four test conditions, one called ‘unloaded’ and three seated. An automatic tetrahedral mesh with a characteristic length of 5 mm was used for soft tissues (fat and homogeneous muscles) (Fig 1a), while shell layers of 2 mm made of linear triangle elements were used for the boundary of the bones and the skin. A surface-to-surface Type 25 contact with a friction coefficient of 0.4 was used to model the interaction between the skin and the seat. Three seating configurations were reproduced in agreement with experiments: horizontal flat seat pan (Shear), flat seat pan with an inclination of 7° (Reference), and a foam layer added to the reference seat (Foam) (Fig 1b).

Material properties. The pelvis and femur bones were considered as rigid bodies without relative rotation. Hyperelastic materials were distinctly defined per soft tissue type (Ogden material model, law 62

with parameters from *Al Dirini et al. (2016))*. The skin was modelled with a linear elastic material law (Young's modulus of 0.15 MPa and Poisson ratio of 0.49, as recommended by *Verver et al. (2004)*. The geometry and material law for the seat are extracted from *Wang et al. (2021))*

(a) (b) (c)

Figure 1: (a) Mesh of the subject-specific geometric seating model, with the skin, fat and muscle layers made visible; (b) 3 Experimental seating conditions in *Wang et al (2021)*, from left to right: Shear (SC), Reference (RC) and Foam (FC) conditions; (b) ROIs for tissue volume measurement.

Boundary conditions. For each subject, the pelvis and femur positions of the FE model relative to the numerical seat surface were extracted from experimental data identified as the reference posture. The six degrees of freedom of the bones were fixed. The two components of the seat pan reaction force measured experimentally were applied on the seat, free to translate along the force direction. The seat was initially translated to be in contact with the body surface. A quasi-static simulation with an explicit time integration scheme was run using the Altair RADIOSS FE-solver, with dynamic relaxation to avoid artificial vibration.

Post-processing and indicator for seat discomfort. The standard outputs for the FEMs' evaluation against experiments were used: the seat pressure distribution criterion (SPD%) was computed as defined by Ahmadian et al. (2002), and surface contact elements with pressure greater than zero were identified for contact area calculations. For precise focus below the Ischial Tuberosity (IT), cylindrical region of interests (ROIs) with three different diameters (10, 20 and 50 mm) were defined under the IT with their longitudinal axis perpendicular to the seat surface, as illustrated in Figure 1c. The Tissue Volume reduction % (R) was calculated as the variation of soft tissue volumes in the three ROIs and the tissue thicknesses in the ROIs were compared, from both experiments and simulations, as defined by *Wang et al. (2021)*.

Results

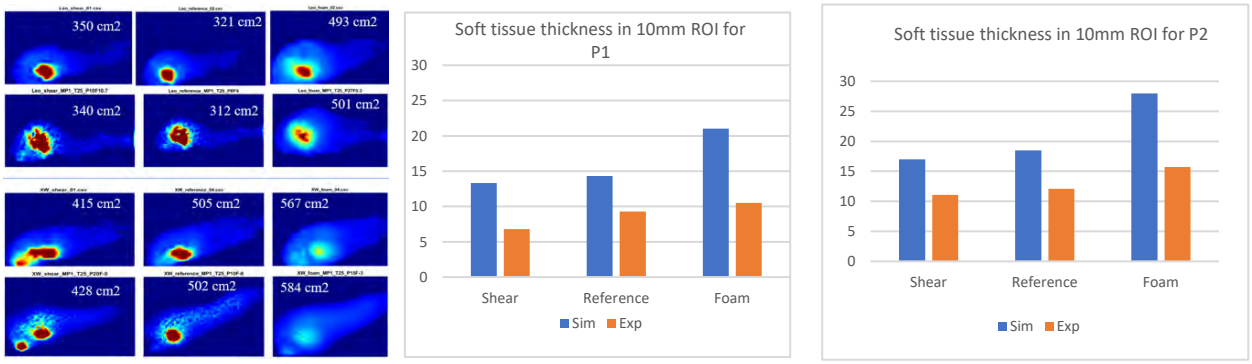

(a) (b) (c)

Figure 2: (a) Comparison of seat pan contact pressure distribution with corresponding contact areas of one limb in (left to right) Shear, Reference and Foam conditions for P1 (first two rows) and P2 (third and fourth rows) between experiment (Top) and simulation (Bottom). (b) Comparison of mean bulk tissue thickness (in mm) inside the 10mm ROI for P1, (c) for P2.

First, the pressure distribution from the IT to the thigh is effectively captured (Fig. 2a) in terms of contact surface area for the three different conditions, and SPD% criterion (prediction vs. experiments: 83.5 vs. 68.8, 83.9 vs. 68.0 and 27.9 vs. 33.3 for P1 and 52.4 vs 58, 51.4 vs 57.1 and 17.0 vs 6.26 for P2 in SC, RC and FC respectively). SPD% indicates that pressure is most uniformly distributed in the Foam condition, followed by the Reference. As for the tissue volume reduction (R in %) comparison, R from predictions in all cases is lower than the experimental values; In the 50 mm ROI, the volume reduction error (in %) was 20.5%, 23.7%, 40.3% and 26.2%, 26.9% and 41.9% respectively for P1 and P2 in SC, RC and FC. Whereas, in the 20mm ROI, it was 17.7%, 7.5% and 32.1% for P1 and 15.9%, 14.3% and 33.3% for P2 in SC, RC and FC respectively. Finally, in the 10 mm ROI, it was 18.0%, 10.9% and 32.4% for P1 and 12.3%, 13.4%, 28.3% for P2 in the SC, RC and FC respectively. As the ROI is more focused below the IT, the error in tissue volume reduction and correspondingly the tissue thickness seems to be more. Nevertheless, the predicted tissue thickness trend for P1 & P2 (Fig 2b&c) echo global experimental observations related to soft tissue deformation; the SC led to the highest deformation followed by RC and FC, thus indicating lesser tissue displacement under the IT for shear reduced conditions, especially with added seat cushion foam.

Conclusion

Two Subject specific finite element models of the human body buttock-thigh, personalized only regarding the bones and soft tissue spatial distribution and the external forces, seems to reproduce both the pressure distribution on the seat and the deformation of soft tissue under the IT for the three seating configurations in a discriminating manner. These encouraging results will be strengthened by extending the simulation to other subjects reported in *Wang et al. (2021).*

References

Ahmadian M, Seigler T.M., Alternative Test Methods for Long Term Dynamic Effects of Vehicle Seats, SAE 2002-01-3082

Al-Dirini, R.M.A., Reed, M.P., Hu, J. et al. Development and Validation of a High Anatomical Fidelity FE Model for the Buttock and Thigh of a Seated Individual. Ann Biomed Eng 44, 2805–2816 (2016). https://doi.org/10.1007/s10439-016-1560-3

Léo Savonnet, Xuguang Wang & Sonia Duprey (2018) Finite element models of the thigh-buttock complex for assessing static sitting discomfort and pressure sore risk: a literature review, 21:4, 379-388, DOI: 10.1080/10255842.2018.1466117

M.M. Verver , J. van Hoof , C.W.J. Oomens , J.S.H.M. Wismans & F.P.T. Baaijens (2004) A Finite Element Model of the Human Buttocks for Prediction of Seat Pressure Distributions, 7:4, 193-203, DOI: 10.1080/10255840410001727832

Xuguang Wang, Léo Savonnet, Loïc Capbern & Sonia Duprey (2021): A Case Study on the Effects of Foam and Seat Pan Inclination on the Deformation of Seated Buttocks Using MRI, IISE Transactions on Occupational Ergonomics and Human Factors, DOI: 10.1080/24725838.2021.1984340

Developing a Full Body Finite Element Model and Its Preliminary Validation for Seating Comfort

Shenghui Liu[1,2], Philippe Beillas[2,3], Li Ding[1], and Xuguang Wang[2,3]

[1] *Beihang University, China*

[2] *Université Gustave Eiffel-LBMC, France*

[3] *Université Claude Bernard Lyon 1, France*

Abstract

Human body finite element (FE) models can be used for seating comfort assessment by providing biomechanical related parameters such as internal loads and soft-tissue deformations. However, most of the published models were only validated under a condition far from a real seating situation. Their ability to be repositioned may also be limited. In recent years, an open-source PIPER software package has been developed to help personalize and position Human Body Models (HBMs) for crash simulation. We have morphed the PIPER Child model into an adult FE model. In this paper, we present how the initially morphed adult FE model was adapted for assessing seating comfort and validated for different seating conditions. Experimental data was collected using a reconfigurable experimental seat and pressure mats. Four seat configurations were defined with the seat pan angle (SPA) from 0° to 15° (5° in steps) and seat pan to seat backrest angle (SP2BA) kept to 100°. Simulated results in terms of seat contact area (ContactA), peak pressure (PeakP), mean pressure (MeanP), and pressure profiles showed good agreement with experimental observations. The full-body FE model developed and validated in this work will be used as a reference for further development of scalable and positionable models using the PIPER software framework. The model will be open source to facilitate reuse and further improvements.

Keywords: Seating dis/comfort, Full-body finite element model, Open-source, Validation

Introduction

People spend more and more time in a seating posture for transportation, office work, or leisure (Le and Marras, 2016). Improving seating comfort is not only a sale argument for seat manufacturers (Grujicic et al., 2009) but also important for consumers and healthcare-related fields (Oomens et al., 2015). Sustained loads on the soft tissue of the buttocks may cause seating discomfort or even physiological problems (Elsner & Gefen, 2008), especially for drivers and wheel-chair users (Cheng et al., 2018). However, soft tissue deformations and internal loading in terms of strain, and stress, which are generally considered relevant for seating discomfort assessment, cannot be all directly measured in vivo (De Looze et al., 2003).

With the development of computational capability, more and more researches have been devoted to build Finite Element (FE) HBM for assessing seating discomfort (Du et al., 2013; Levy et al., 2014). However, most of these models were not validated under real seating conditions including several postures, thus limiting their application to real world. For example, Al-Dirini et al. (2016) validated the model using only a rigid seat pan without a soft cushion. Huang et al. (2015) and Du et al. (2013) validated their models with a real seat under only one seat configuration. However, more seating conditions are needed for validating their sensitivity to seat parameter changes for seat comfort assessment.

In recent years, an open-source software package has been developed to personalize and position HBMs for crash simulation (available at www-piper-project.org). We also recently described the ongoing development of a full body adult FE model, morphed from the PIPER Child model (Liu et al., 2020). In this paper, we present how the initially morphed model was further adapted for assessing seating comfort at first, and then the preliminary validation results using the experimental data collected from a reconfigurable seat.

Model development

Developing a full-body finite element model is a time-consuming and complex process. Therefore, an open-source model, the PIPER Child model for impact simulation, was morphed into an adult-sized model. The baseline model corresponds to a 6 years old child, 1146 mm in stature. It includes 353 parts (deformable skull, brain, abdomen muscles, internal organs, neck, neck muscles, and pelvis, etc.) for a total of 531000 elements. The model was validated under multiple conditions for traffic injury assessment such as side-impact, and regional part validation including head, femur, neck, etc.(Beillas et al., 2016).

Brief description of the initial morphing

As presented in (Liu et al., 2020), we morphed the PIPER child model into an adult male. The morphing target was a male aged 40 years, 1740 mm in stature and 77.6 kg in weight. The morphing was based on different types of data collected on the same person. The spine and pelvis were obtained from the 3D reconstructions of the target subject who participated in a MRI study corresponding to a seated position with seat pan to backrest angle of 100° (Beillas et al., 2009). The same seating condition was reproduced for scanning the external body shape with a handheld laser scanner. After building the geometrical targets, the model was morphed by kriging interpolation using the PIPER software. The geometric errors and the elements quality were checked, and the model was used as the basis for further work.

Model adaptation

Numerous changes were carried out on the morphed model to adapt it to the comfort application. The main objectives were to (1) symmetrize it (2) reduce its computational cost (3) refine the mesh in regions of interest for seating comfort (4) adapt its material properties, which were initially selected for high-speed impact.

The work was initiated by symmetrizing the model with respect to the sagittal plane. The PIPER child model geometry and mesh are mostly symmetric. The exceptions are (1) the internal organs, which are not expected to be symmetric and will not be symmetrized, and (2) the mesh of some vertebrae and of the sternoclavicular ligaments, which will be symmetrized. Furthermore, the target geometry was directly derived from experimental data and hence, the geometry of the morphed model is not symmetric.

The vertebral meshes from the 12th thoracic vertebra (T12) to the 5th lumbar vertebra (L5) were first symmetrized within the PIPER child model (including intervertebral discs). For this, one side of the vertebral mesh was kept. This half side was used to generate solid elements before symmetrizing it (Figure 1 a and b). The sternoclavicular ligaments were also symmetrized by keeping one of the two sides.

Then, as the morphed model uses the same numbering scheme as the child model, the mesh symmetry of the child model were used to symmetrize the morphed model. First, the pairs of nodes that are symmetric with respect to the midsagittal plane and nodes laying on the midsagittal plane were identified in the child model. This allowed computing symmetric positions of these nodes on the morphed model by averaging (e.g. skeletal symmetry). However, this cannot be directly applied to the model as this approach would not transform the non-symmetric structures (e.g. internal organs). Hence, the symmetrized nodes were used as control points to transform the model using the Kriging in PIPER.

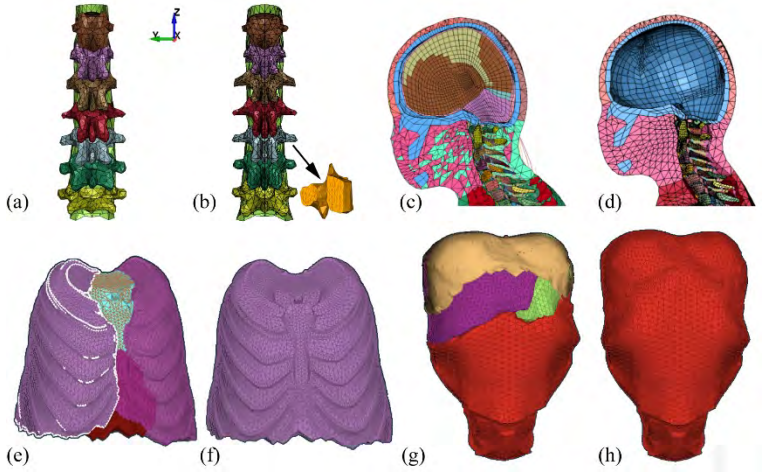

Figure 1 Comparison of some body structures before and after adaptation: lumbar vertebrae and intervertebral disc before and after symmetrisation (a,b), brain and neck muscles before and after simplifications (c,d), chest before and after simplification (e,f), abodomen before and after simplification (g,h)

The computational cost was then addressed. Some anatomical components which are marginally relevant for seating comfort were deleted, including the brain (initially modeled using hexahedral elements) and neck muscles (Figure 1 c and d). The mass of the brain was compensated for by increasing the skull density. The internal organs were also simplified into two incompressible controlled volumes described by their envelope (similar to airbags): one for the chest (Figure 1 e and f), and one for the abdomen organs (Figure 1 g and h). The mass of the organs was evenly distributed onto the nodes of the envelopes. The properties of the bones were changed to rigid (one rigid body per bone).

The buttock region was then refined as the simulation of the body and seat interaction in the region of the buttocks and thighs is of importance for seating comfort assessment. As shown in Figure 2a, the coccyx of the initial child model appears shorter than the one of adults, likely due to the presence of growth cartilage in that region (as the coccyx is not fully ossified at 6 years old, it could not be segmented on the CT scan). As the coccyx is an important anatomical structure that is susceptible to be involved in pressure ulcer (Farshbaf et al., 2013), the coccyx was modified based on adult data. As the pelvic skeleton derived from the MRI was in a low resolution, a pelvic segmentation from an adult CT-scan that is a publicly available (subject LTE605 available on www.piper-project.org) was scaled and aligned onto the pelvis model (Figure 2b) and used as a reference to adjust for the structure of the coccyx (Figure 2c).

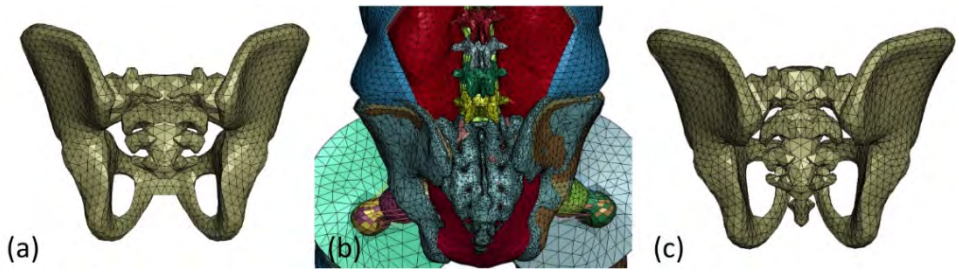

Figure 2 Replacement of the initial child coccyx by an adult one: the initially morphed pelvis based on the PIPER Child model (a), aligning an adult pelvis onto the model (b) and modified pelvis with an adult coccyx (c).

Then, as depicted in Figure 3, the mesh of the soft tissue underneath the ischial tuberosity (IT) was locally refined. This area is important for seating comfort assessments since it is the place with the highest pressure and a high risk of pressure ulcers (Tang et al., 2010) with a compressive strain of more than 50% (Elsner & Gefen, 2008; Sonenblum et al., 2013).

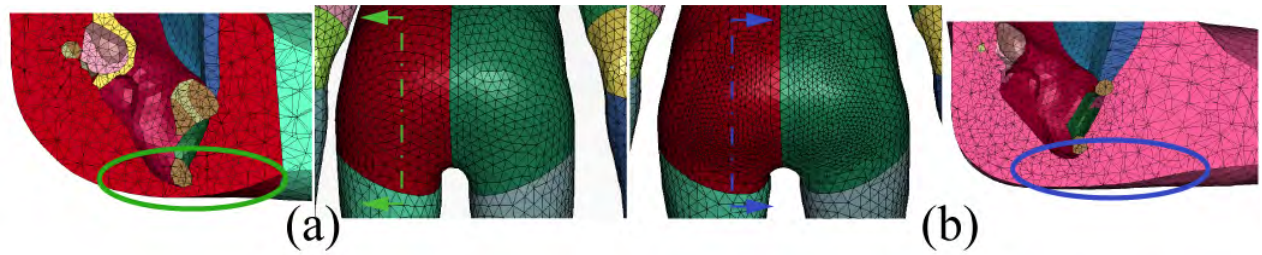

Figure 3 Local refinement of the soft tissue mesh under the ITs (a) mesh of the child model(b) refinement of the local mesh of buttocks with the adult model.

The geometry of the buttocks was obtained by the subject in a kneeling posture using a laser scan. It was not the same as the pre-sitting posture. The thickness of tissue was modified referring to the pre-loading seated MRI data from a study by (Wang et al., 2021). The shape of the buttocks before and after modification are shown in Figure 4. The soft tissue-ischium initial distance was set to 40mm.

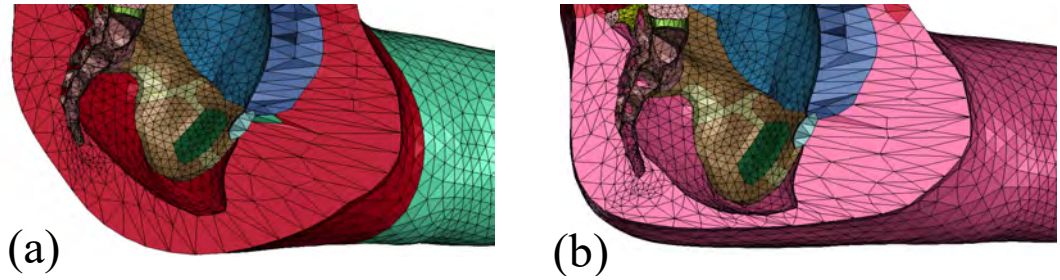

Figure 4 Buttocks shape. (a) the initial model using the kneeling posture obtained buttocks geometry. (b) pre-shaped after adaptation

The soft tissue material model and properties were changed from a simplified rubber to low modulus Neo Hookean model as in the work of Janak (2020) on obese modeling. The mass distribution of the model was checked and aligned with those by Huang et al. (2015) through adjusting the density of soft tissue and bone. The mass proportions are now 7.41%, 16.15%, 51.53%, 4.38% for the head, the lower limbs (thigh, calf, and foot), the torso, and the upper limbs (upper arm, forearm, and hands), respectively. Finally, some small penetrations and negative volume elements were fixed manually.

Model validation

Experimental data collection

To validate the model, an experiment was carried out with a reconfigurable experimental seat (Beurier et al., 2017). The participant was the person whose external scans and internal skeleton information were used as targets for the model development (Liu et al., 2020). Two wooden flat rectangular plates covered by a

foam of 50 mm thick were used for the seat pan (620 by 565 mm) and the seat backrest (550 by 550 mm). To measure the contact pressure, two sensor mats (XSENSOR, X3 PRO V6, Canada) were attached to the foam. Four configurations were tested varying the seat pan angle (SPA) from 0° (horizontal) to 15° in a step of 5°, while the seat pan to backrest angle (SP2BA) was fixed at 100° (Figure 5) corresponding to the seating configuration used in the MRI study by Beillas et al (2009). For each configuration, the participant was allowed to adjust the seat pan length and the foot support height to be seated comfortably. The subject was instructed to half flex his knees and the popliteal to the frontal seat edge was about 40mm.

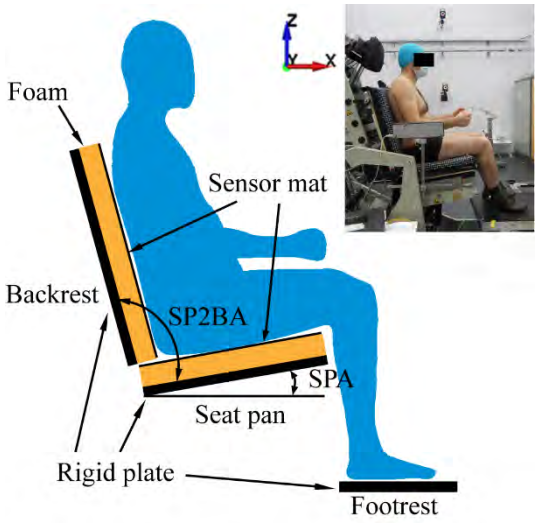

Figure 5. Experimental seat.

FE Simulation

The four experimental seating conditions were simulated with the developed adult model using LS-DYNA R11 MPP solver using 64 cores of a cluster. The time step was 2µs. Relaxation was used to help stabilize the contact force. The results (pressure, forces, etc.) were gathered at 400ms of simulation time, which took about 6 hours of elapsed time on the machines used for each simulation.

FE model prepositioning and boundary conditions

The bottom of the seat pan and backrest were fixed. The FE model was pre-positioned so that the back, buttocks and thighs were as close as possible to the seat without getting into contact. The feet were put on the footrest, which was simulated as a massless rigid body. To better control the distribution of the contact forces on the backrest, seat pan and footrest, the actual contact force on the footrest measured experimentally was imposed. For this, the footrest was oriented so that its normal direction was the same as the contact force measured experimentally. It was allowed to move only in this direction.

Automatic surface to surface contact was defined for the backrest and seat pan with a coefficient of friction (COF) of 0.1 (covered with the sensor map), while a COF of 0.4 was used for the footrest contact (Derler et al., 2008). To reduce computational time and maintain posture, we constrained some bones into one rigid body so that no relative movements were allowed between them: the skull and cervical spine, the calf and foot (left and right), the upper limb bones including the humerus, radius, ulna, hand (right and left bones). A gravity loading environment was applied.

To obtain the property of the foams on the seat pan and backrest, strain-stress curves were obtained through compression tests with a sample size of 8×8×5 cm using an Instron material testing machine. The curves are provided in the appendix.

Data analyses

Pressure and contact forces were compared between simulations and experiments. Pressure-related parameters include contact area (ContactA), mean pressure (MeanP), peak pressure (PeakP), and frontal and lateral pressure profiles (summation of pressure in rows and columns).

Results

Simulated and measured pressure distributions and profiles on the seat pan and backrest are compared in Figure 6 for the four test configurations. FE simulations were able to approach the corresponding measured pressure distributions (Figure 6a), with some discrepancies on the thighs and between the ITs. Some left/right asymmetry was visible in the experimental data, while the FE model responded symmetrically as expected. The differences were more pronounced for the backrest (Figure 6b), with some contacts near the pelvis which were not visible in the experiment. Predicted pressure profiles (Figure 6c) were close to the experimental data.

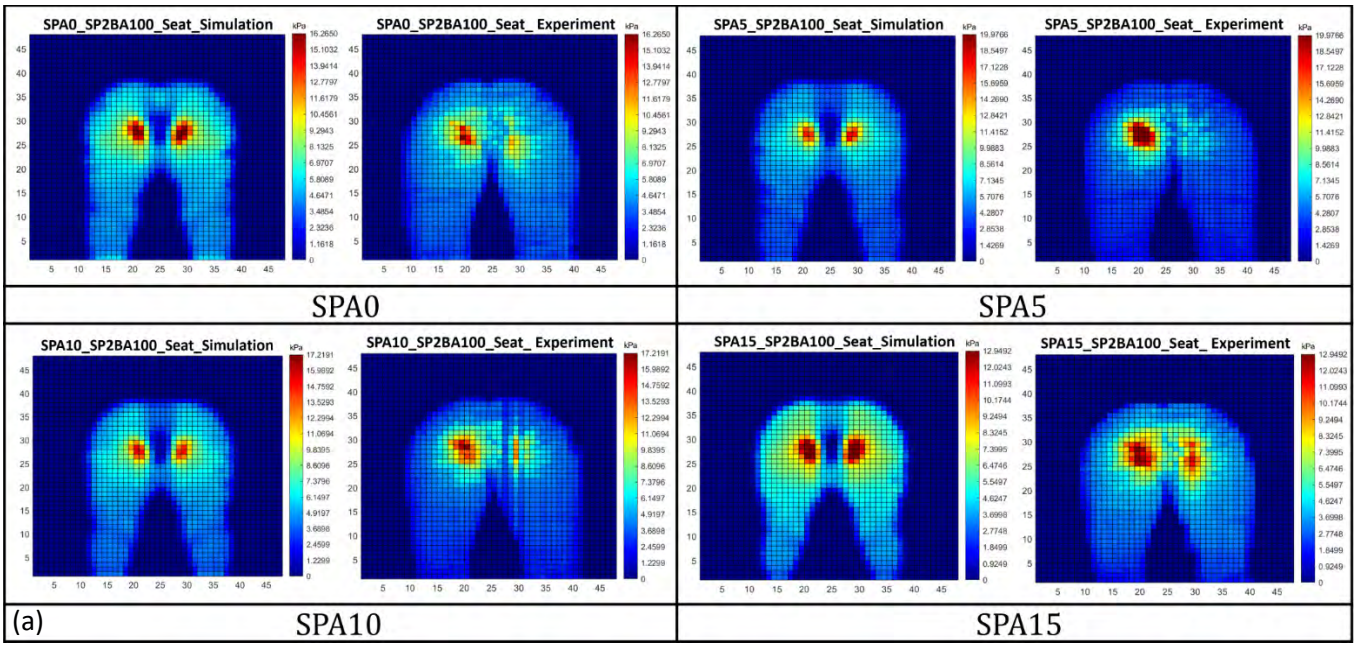
SPA0_SP2BA100_Seat_Simulation
SPA0_SP2BA100_Seat_ Experiment
SPA5_SP2BA100_Seat_Simulation
SPA5_SP2BA100_Seat_ Experiment
SPA0
SPA5
SPA10_SP2BA100_Seat_Simulation
SPA10_SP2BA100_Seat_ Experiment
SPA15_SP2BA100_Seat_Simulation
SPA15_SP2BA100_Seat_ Experiment
(a)
SPA10
SPA15

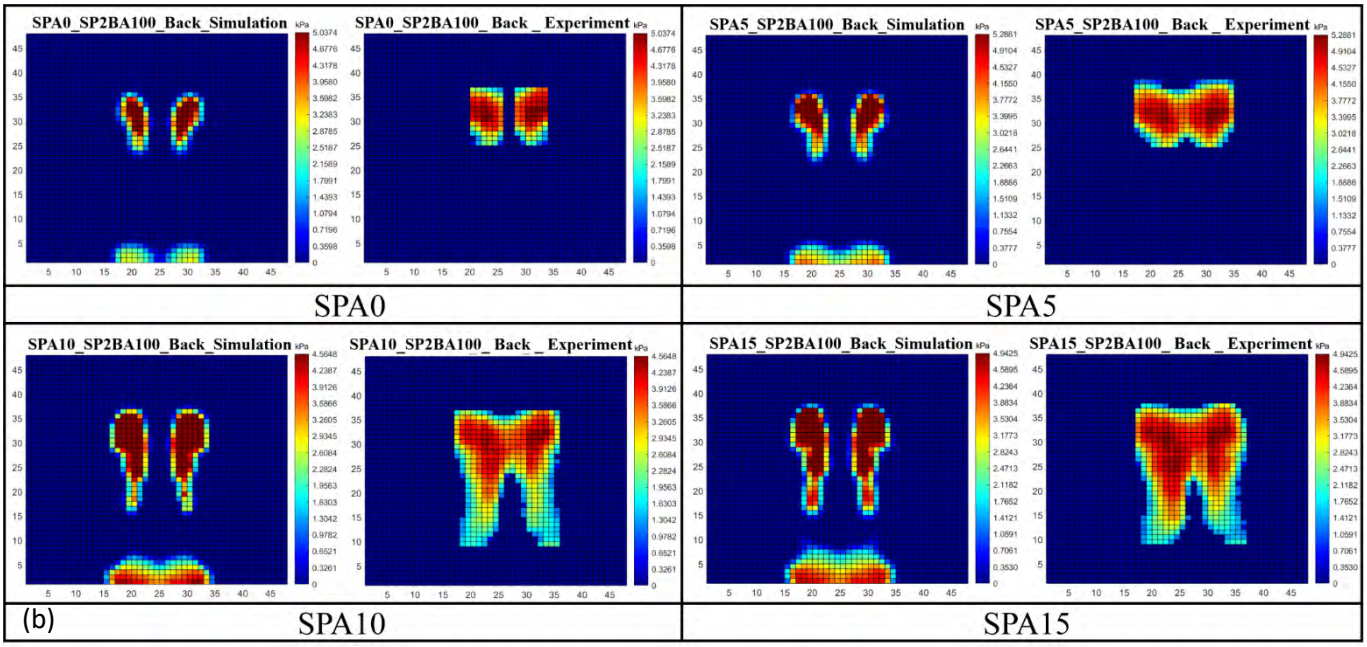
SPA0_SP2BA100_Back_Simulation
SPA0_SP2BA100_Back _ Experiment
SPA5_SP2BA100_Back_Simulation
SPA5_SP2BA100_Back _ Experiment
SPA0
SPA5
SPA10_SP2BA100_Back_Simulation
SPA10_SP2BA100_Back _ Experiment
SPA15_SP2BA100_Back_Simulation
SPA15_SP2BA100_Back _ Experiment
(b)
SPA10
SPA15

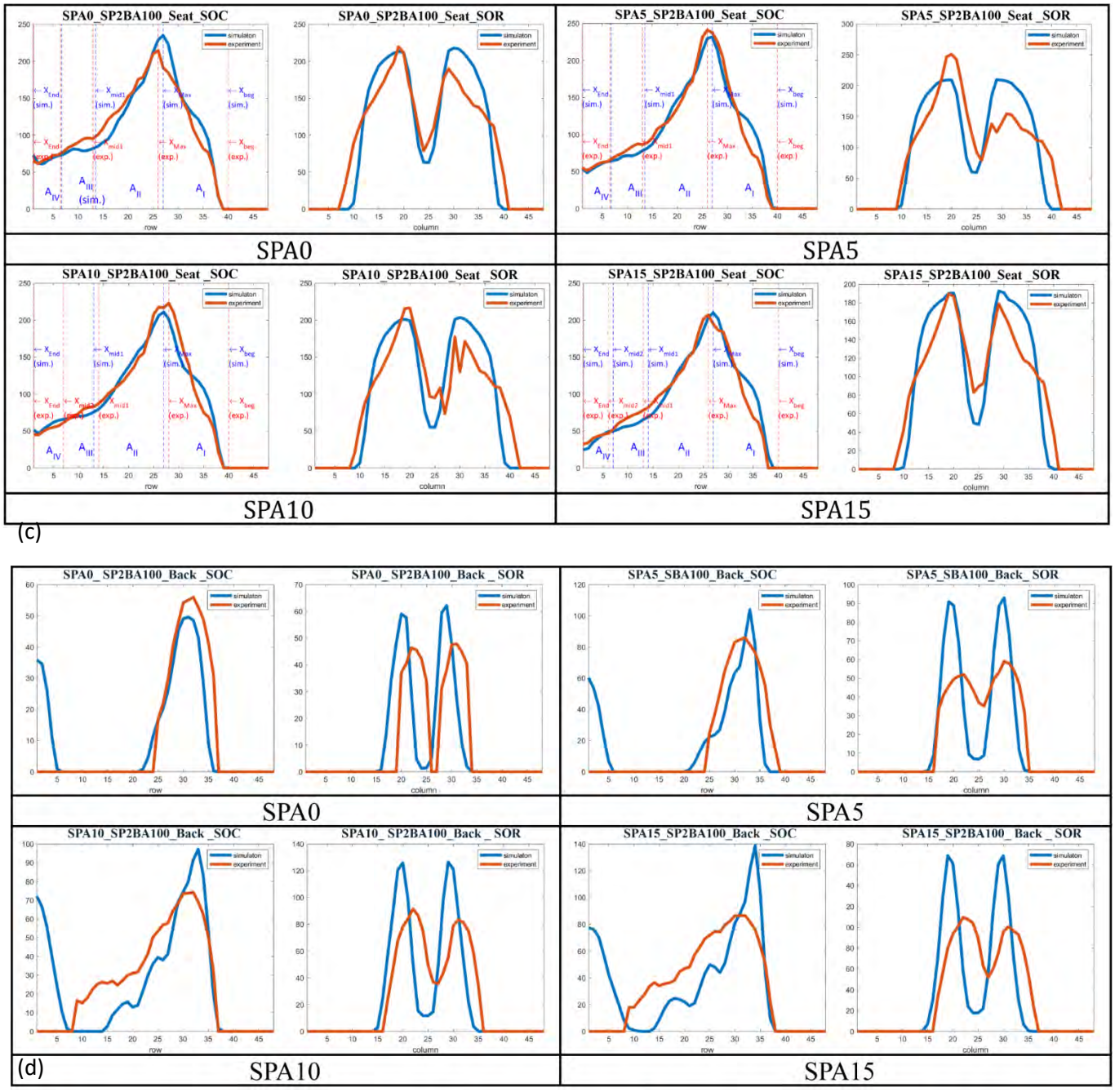

Figure 6. Comparison of simulated pressure distribution and profiles with experimental data for the four seat pan angles (SPA: 0°, 5°, 10° and 15°). (a) pressure on the seat pan, (b) pressure on the backrest, (c) lateral (SOC) and frontal (SOR) pressure profiles on the seat pan, (d) lateral (SOC) and frontal (SOR) pressure profiles on the backrest.

The contact area (ContactA); peak pressure (PeakP), mean pressure (MeanP), and shear (SF_SP) and normal (NF_SP) forces on the seat pan are summarized in Table 1. Compared to experimental data, the simulation had an average error of -3.2%, 3.8%, and 8.1% respectively for contact area, peak pressure, and mean pressure. Concerning contact force on the seat pan, simulated shear and normal forces showed the

same trend as experimental observations when increasing the seat pan angle. However, a high error in percentage was observed for shear force (up to 37.1%).

Table 1 Simulated (S) and experimental (E) values of contact area (ContactA), peak (PeakP), and mean pressures (MeanP), and contact forces: seat pan shear force (SF_SP), and normal force (NF_SP), as well as the errors (%) of simulation relative to experiment.

SPA	ContactA (mm^2)		PeakP (kPa)			MeanP (kPa)			SF_SP (N)			NF_SP (N)		
(°)	(S)	Error	(S)	(E)	Error	(S)	(E)	Error	(S)	(E)	Error	(S)	(E)	Error
0	162257.7	-4.0	16.8	16.3	3.4	4.6	4.3	8.7	58.7	59.2	-0.5	-709.0	-697.0	-12.0
5	161128.7	-2.6	17.4	20.0	-12.9	4.5	4.3	6.4	56.1	28	28.1	-689.5	-694.3	4.8
10	159031.9	-4.8	15.2	15.1	0.8	4.4	4.0	8.5	37.7	0.6	37.1	-661.6	-652.8	-8.8
15	153225.5	-3.7	15.4	12.4	23.9	4.2	3.9	8.7	31.8	-4.2	36.0	-607.9	-597.4	-10.5
Mean	158911.0	-3.2	16.2	15.9	3.8	4.6	4.1	8.1	46.1	20.9	25.2	-667.0	-660.4	-6.6
SD	3480.6	0.8	0.9	2.7	13.2	0.1	0.2	1.0	11.55	25.3	15.2	38.0	40.4	6.7

Discussion and Conclusions

Compared to experimental observations, simulated pressure distribution showed good agreement. Although the model did not simulate muscle forces, the targeted postures correspond to a relaxed state in which the muscle forces were expected to be small. The passive stiffness of the model and the choice of initial conditions hence played a role in the response. For example, there could be no contact near the pelvis on the backrest if the pelvis was positioned further away from the backrest. Overall, the choice of passive properties and boundary conditions appeared reasonable for the relaxed seating with an SP2BA of about 100°. They may need to be adjusted for postures that would further differ from the validation conditions (e.g. more reclined seating).

According to Figure 6, the simulated backrest pressure distribution and profiles had some differences compared to the experiment, especially in the lower back area and near the location of the scapulae. In simulations, the lower back was in contact with the backrest, while this was not the case for the experiment. This could be because the final loaded spine curvature was used at the preloading and the body may move under gravity: In addition, the initially scanned back shape is certainly not the same as the one that the subject adopted.

For the seat pan, the simulated contact areas (ContactA) were slightly smaller than the experimental results while the mean pressures (MeanP) were higher. As we can see from Figure 6, the middle area of between the two buttocks showed no contact in the simulation, quite different from experimental observations. Soft tissues were modeled a homogeneous material assuming an initial no strain / no stress state. More detailed

modeling of this area may be useful, including muscles and fat tissues. Most importantly, their initial strain states should be considered, as the body shape prior to loading is not known.

In this preliminary validation, only four configurations were tested with a fixed seat pan to backrest angle of 100°. Therefore, more seat configurations are needed to test the effect of seat parameters. Since the compression of the soft tissue under the ischial tuberosities is an important factor to evaluate seating comfort, the model will be further validated with soft tissue compressive deformations and observed using an open MRI (Wang et al., 2021).

In a summary, a personalized model for seating comfort has been developed and its predictions in terms of force and contact pressure distribution were checked against experimental data in four seat conditions. The models showed a reasonable agreement and further work will be conducted to expand upon the validation with more seating conditions and the analysis of local tissue deformation. The FE model will be published under an open source license to facilitate its reuse and improvement.

Acknowledgments

One of authors was funded by the China Scholarship Council [grant number 202006020192].

References

Al-Dirini, R. M. A., Reed, M. P., Hu, J., & Thewlis, D. (2016). Development and Validation of a High Anatomical Fidelity FE Model for the Buttock and Thigh of a Seated Individual. *Annals of Biomedical Engineering*, *44*(9), 2805–2816. https://doi.org/10.1007/s10439-016-1560-3

Beillas, P., Giordano, C., Alvarez, V. S., Li, X., Ying, X., Kirscht, S., & Kleiven, S. (2016). Development and Performance of the PIPER Scalable Child Human Body Models. *14th International Conference Protection of Children in Cars. Dec 8-9, 2016, Munich, Germany*, 1–19.

Beillas, P., Lafon, Y., & Smith, F. W. (2009). The effects of posture and subject-to-subject variations on the position, shape and volume of abdominal and thoracic organs. *Stapp Car Crash Journal*, *53*(November), 127–154.

Beurier, G., Cardoso, M., & Wang, X. (2017). A new multi-adjustable experimental seat for investigating biomechanical factors of sitting discomfort (No. 2017-01-1393). SAE Technical Paper.

Cheng, Z., Smith, J. A., Pellettiere, J. A., & Fleming, S. M. (2007). Considerations and experiences in developing an fe buttock model for seating comfort analysis (No. 2007-01-2458). SAE Technical

Paper.

De Looze, M. P., KUIJT-EVERS, L. F. M., & VAN DIEËN, J. (2003). Sitting comfort and discomfort and the relationships with objective measures. *Ergonomics*, *46*(10), 985–997. https://doi.org/10.1080/0014013031000121977

Derler, S., Kausch, F., & Huber, R. (2008). Analysis of factors influencing the friction coefficients of shoe sole materials. Safety Science, 46(5), 822–832. https://doi.org/10.1016/j.ssci.2007.01.010

Janák, T. (2020). Personalization of human body models to simulate obese occupants in automotive safety .(pp.140) ,Université Claude Bernard - LYON 1, Lyon , France.

Du, X., Ren, J., Sang, C., & Li, L. (2013). Simulation of the interaction between driver and seat. *Chinese Journal of Mechanical Engineering*, *26*(6), 1234–1242. https://doi.org/10.3901/cjme.2013.06.1234

Elsner, J. J., & Gefen, A. (2008). Is obesity a risk factor for deep tissue injury in patients with spinal cord injury? *Journal of Biomechanics*, *41*(16), 3322–3331. https://doi.org/10.1016/j.jbiomech.2008.09.036

Farshbaf, M., Yousefi, R., Pouyan, M. B., Ostadabbas, S., Nourani, M., & Pompeo, M. (2013). Detecting high-risk regions for pressure ulcer risk assessment. In 2013 IEEE International Conference on Bioinformatics and Biomedicine (pp. 255-260). IEEE.

Grujicic, M., Pandurangan, B., Arakere, G., Bell, W. C., He, T., & Xie, X. (2009). Seat-cushion and soft-tissue material modeling and a finite element investigation of the seating comfort for passenger-vehicle occupants. *Materials and Design*, *30*(10), 4273–4285. https://doi.org/10.1016/j.matdes.2009.04.028

Huang, S., Zhang, Z., Xu, Z., & He, Y. (2015). Modeling of human model for static pressure distribution prediction. International Journal of Industrial Ergonomics, 50, 186-195.. https://doi.org/10.1016/j.ergon.2015.09.017

Le, P., & Marras, W. S. (2016). Evaluating the low back biomechanics of three different office workstations: Seated, standing, and perching. *Applied Ergonomics*, *56*, 170–178. https://doi.org/10.1016/j.apergo.2016.04.001

Levy, A., Kopplin, K., & Gefen, A. (2014). An air-cell-based cushion for pressure ulcer protection remarkably reduces tissue stresses in the seated buttocks with respect to foams : Finite element studies. *Journal of Tissue Viability*, *23*(1), 13–23. https://doi.org/10.1016/j.jtv.2013.12.005

Liu, S., Beillas, P., Ding, L., & Wang, X. (2020). Morphing an existing open source human body model into a personalized model for seating discomfort investigation. SAE Int, 2020, 01-0874

Oomens, C. W. J., Bader, D. L., Loerakker, S., & Baaijens, F. (2015). Pressure Induced Deep Tissue Injury Explained. *Annals of Biomedical Engineering*, *43*(2), 297–305. https://doi.org/10.1007/s10439-014-1202-6

Bader, D. L., Bouten, C., Colin, D., & Oomens, C. W. (Eds.). (2005). Pressure ulcer research: current and future perspectives., pp.150-155.

Sonenblum, S. E., Sprigle, S. H., Cathcart, J. M. K., & Winder, R. J. (2013). 3-dimensional buttocks response to sitting: A case report. *Journal of Tissue Viability*, *22*(1), 12–18. https://doi.org/10.1016/j.jtv.2012.11.001

Tang, C. Y., Chan, W., & Tsui, C. P. (2010). Finite Element Analysis of Contact Pressures between Seat Cushion and Human Buttock-Thigh Tissue. *Engineering*, *02*(09), 720–726. https://doi.org/10.4236/eng.2010.29093

Wang, X., Savonnet, L., & Duprey, S. (2021). A Preliminary Study on the Effects of Foam and Seat Pan Inclination on the Deformation of the Seated Buttocks Using MRI. In Congress of the International Ergonomics Association (pp. 434-438). Springer, Cham.

Yadav, S. K., Huang, C., Mo, F., Li, J., Chen, J., & Xiao, Z. (2021). Analysis of seat cushion comfort by employing a finite element buttock model as a supplement to pressure measurement. *International Journal of Industrial Ergonomics*, *86*(May 2020), 103211. https://doi.org/10.1016/j.ergon.2021.103211

Appendix

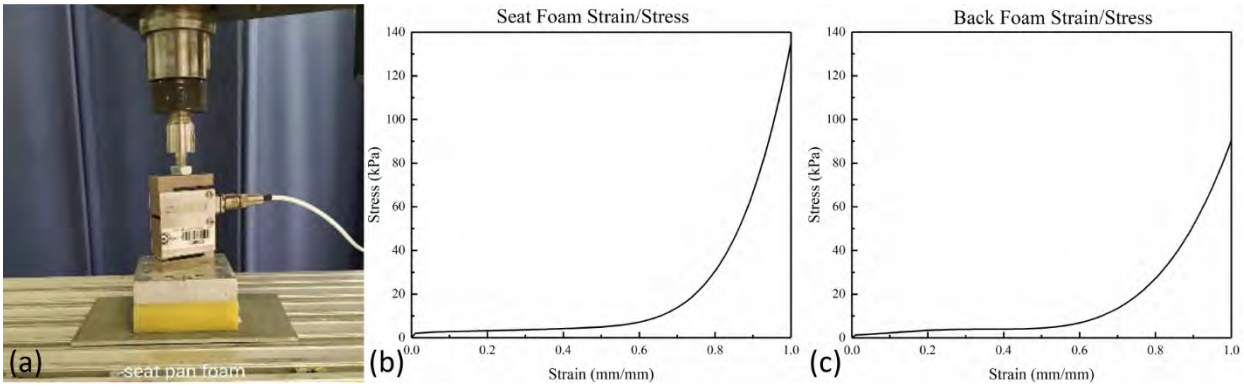

Seat pan and backrest foam strain-stress curves

Moving deforming mesh modeling of human organ systems

Hamidreza Mortazavy Beni[a,*], Hamed Mortazavi[a], Gunther Paul[b,*], Mohammad Saidul Islam[c]

[a] Department of Biomedical Engineering, Arsanjan Branch, Islamic Azad University, Arsanjan, Iran.

[b] Australian Institute of Tropical Health and Medicine, James Cook University, Mackay, QLD 4741.

[c] School of Mechanical and Mechatronic Engineering, University of Technology Sydney (UTS), 15 Broadway, Ultimo, NSW-2007, Australia.

Abstract

Dynamic modeling of body organs has become an elementary part of modern digital human modeling (DHM), where advanced biomedical models incorporate biomechanical behavior of tissues down to the cell level. While the biomechanical response of organs to impact and trauma has traditionally been considered an important aspect in developing safety related models such as for vehicle crash simulation, organ behavior is now also reflected in models used for medical purposes, such as the simulation of breathing or cardiovascular circulation. All human body cells have in vivo nonlinear viscoelastic properties. Moreover, body tissue is composed of cells wrapped in an extracellular matrix (ECM). Body tissue in vivo nonlinear viscoelastic properties depend on its function in an organ system, which directly affects the tissue viscoelasticity modulus. For advanced perfusion or fluid passage simulation, we propose to represent the nonlinear viscoelastic behavior of the body tissue in a solid boundary condition using the moving deforming mesh (MDM) method. The MDM method considers the viscoelastic perfusion wall during transient fluid flow responding to the pressure pulse from the human organ systems as the lung or heart. Also, changing the volume fraction of the ECM constituents due to aging or diseases like cancer leads to changes in the viscous modulus (loss modulus) and elastic modulus (storage modulus) of organ tissue. Therefore, the MDM method can produce a reliable result that corresponds to reality by considering the precise viscoelastic properties of the fluid passage wall. In this study, we use the MDM method to examine two organ geometries from the respiratory and cardiovascular systems. Although the simulation effort using this method is more time-consuming, the simulation outcomes are expected to be in better accordance with the real organs when compared to simulation results using the computational fluid dynamic (CFD) method, where perfusion wall behavior is considered to be rigid. In this regard, accurate computational

* Corresponding author.
E-mail address: gunther.paul@jcu.edu.au (Gunther Paul).
E-mail address: HRM.Beni@iau.ac.ir & HRM.Beni@gmail.com (Hamidreza Mortazavy Beni).

modeling leads to pre-visualizing in surgical planning to define the best favorable reformative techniques to determine the most probable patient condition consequences.

Keywords Respiratory, Cardiovascular, In silico modeling, Viscoelasticity, Cancer.

Introduction

Throughout modern medical history, study of the functions of human body organs has always been a focus of research. In modern societies however ethical restrictions impose significant limitations on the study of organs to be examined in vivo, whereas most organ functions cannot be accessed in vitro. Mathematical modeling methods based on the use of powerful computers and software inform the modern and state-of-the-art way of in vitro simulation to avoid any experimental restrictions. In the human body, functions of the respiratory system and the circulatory system are closely related. Humans in average breathe about 6 liters of air per minute, which coincides with the volume of blood the heart pumps each minute. In this paper, selected functions of these two important organs of the body are modelled and investigated using the moving deforming mesh (MDM) method, with a restriction to the upper respiratory system and the circulatory system in the aorta.

Respiratory System

The nose, nasal cavity, and sinuses form the intricate geometry of the upper respiratory tract. The nose performs important physiological functions, including thermal management (heat, humidity), air filtration, and odor inhalation. The nose also separates breathable air from pollution and toxic particles that may enter its tract. More advanced aspects of toxicology, particle dispersion, the effect of drugs, filtration of airborne particles from the respiratory air, and planning for surgery have been discussed after the study of dynamic characteristics of airflow in the nasal passages. In the CFD method though, a rigid airway wall is assumed which contradicts the actual viscoelastic behavior of the airway. Therefore, this study aims to expand our understanding how airflow behaves in the upper respiratory system by using the moving deforming mesh (MDM) method which considers a viscoelastic behavior of the airway.

Circulatory System

Accumulation of fatty deposits in blood vessels causes narrowing of arteries and impaired blood flow. This condition, called atherosclerosis, causes many problems in the circulatory system. One of the vessels in which the onset of this disease is critical is the aortic arch, which eventually leads to the risk of rupture of the vessel wall by creating an aneurysm. Most previous numerical studies on atherosclerosis are based on the CFD method, in which the arterial wall is assumed to be rigid [1].

Tissue behavior however is viscoelastic, and the rate of change in duct diameter in systole and diastole is high. In this study, the behavior of the aortic arch is examined using the MDM method.

Methods

Geometry of models

The models are based on CT scan images which represent a wide range of different tissues. By adjusting a grey value threshold, the desired organ is extracted. Under expert supervision, the boundary between fluid and wall is determined and considered in the CT image segmentation. The borders are connected to create a continuous and smooth surface and species volume. This study is based on computerized radiography of the head, neck, and chest of a 70-year-old smoker with a height of 170 cm, weighing 75 kg with a tumor in the upper respiratory tract in the larynx [2]. Fig. 1a shows the respiratory system studied in this study. The model includes the nasal cavity, nasopharynx, oropharynx, larynx, and trachea. Fig. 1b shows the aortic system studied in this study. This model includes the aortic arch with the descending aorta (DA) , Left Common Carotid artery (LCC), Left Subclavian artery (LS), Brachiocephalic Trunk (BT), and the Ascending Aorta (AA).

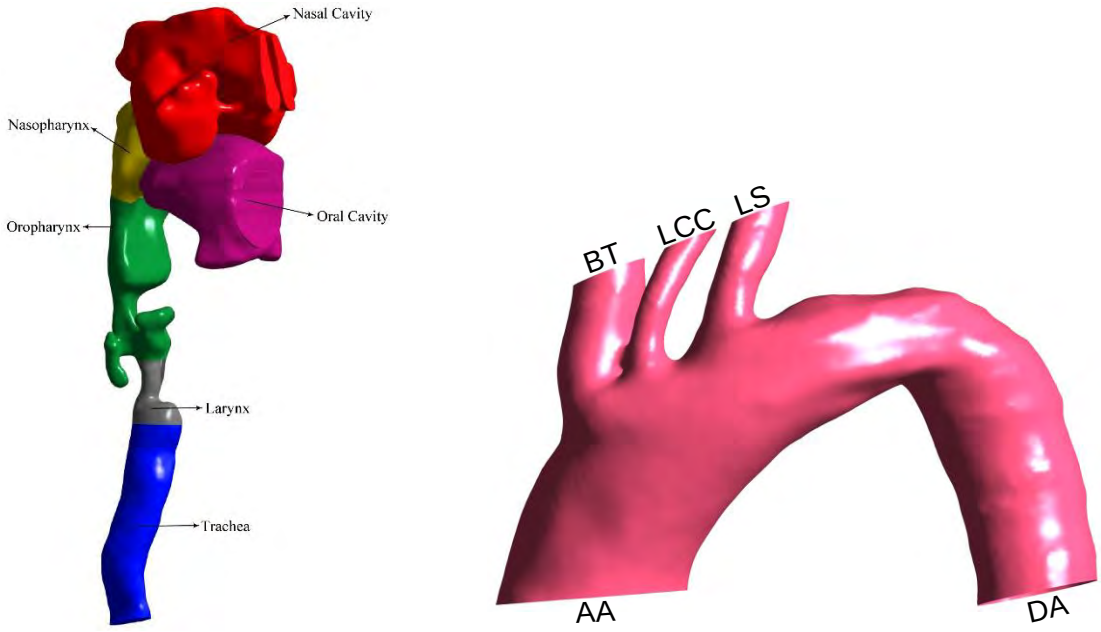

(a) **(b)**

Figure 1. The geometry of the upper respiratory system and the aortic arch in the present study. (**a**) Upper respiratory system. (**b**) Aortic arch.

In a fluid domain, solving nonlinear equations of continuity and momentum is necessary. In these equations, velocity and pressure are coupled. Also, due to the pulsed flow in the respiratory system and blood circulation, the analysis of changes at the interface between the fluid passage and the solid wall is dynamically transient. Governing equations were presented in previous studies and are not mentioned again for the sake of brevity [3, 4].

Respiratory system

Due to the low air velocity, incompressible and laminar flow is considered at resting status. The physical properties of air are selected at 37 °C. Other physical properties such as Young's modulus of 100.64 kPa and the Poisson's ratio of 0.33 have been selected for solid walls based on a previous study [5].

Circulatory system

In this case, blood is considered an incompressible and turbulent fluid. An important characteristic of turbulent flow is that it is not silent. The heart sounds heard with a stethoscope are caused mostly by turbulent flow. Turbulent flow occurs at the opening and closing of heart valves. Thus the flow is turbulent during part of the systole. The physical properties of blood at 37 °C are considered. According to the previous study, physical properties such as Young's modulus of 0.88 MPa and the Poisson's ratio of 0.17 have been selected for solid walls [6].

Boundary Conditions

Creating any physical or computational model of flow requires recognizing and defining the boundaries of the fluid passage. In practice, the boundaries of the biomechanical fluid passage and the flow rate of the fluid change with time. Also, the geometric structure of the fluid passage alone has a great influence on the dynamics of the fluid inside it. In the present work, modeling was done in the individual's resting condition. Two basic boundary conditions are used at the boundary of fluid and solid domains. Firstly, there is a non-slip condition along the wall, where the values of the fluid velocity components are zero. Secondly, the MDM boundary condition between fluid and solid is assumed. The output results of the simulation are studied after several cycles of repeated fluid flow in a transient condition to ensure that the responses are stable.

Respiratory system

The exhale airflow rate is applied for normal inhalation at rest. Therefore, the amplitude of 6 l/min is set at the inlet of the trachea. Inhalation and exhalation are performed in a 4 seconds period. Then the inlet velocity equation is defined by the relation of:

$$V = 6\sin\frac{\pi}{2}t \tag{1}$$

The pressure conditions at the nostrils outlet are set to 101,325 Pa (1 atm). In this model, a closed mouth is assumed. For the solid domain, the fixed support boundary condition is applied for the model inputs in the trachea and the model outputs in the nose. Additionally, after the transient flow conditions have stabilized, cigarette smoke particles with a diameter of 1 μm and a density of 1200 $^{kg}/_{m^3}$ are injected into the model to observe the pattern of particle deposition during exhalation.

Circulatory system

The cardiac cycle includes systole and diastole and lasts for about 0.8 seconds per period. In the current model, the boundary conditions are adjusted for the inlets and outlets of the aorta in accordance with Fig. 2 [7]. These conditions are applied in the simulation with the help of a user-defined function (UDF) definition. For the solid domain, the fixed support boundary condition is applied for model input in AA and model outputs in BT, LCC, LS, and DA. In addition, after the transient flow conditions stabilize, fat particles with a diameter of one micron and a density of 900 $^{kg}/_{m^3}$ are injected into the model to observe the pattern of particle deposition in the aortic wall.

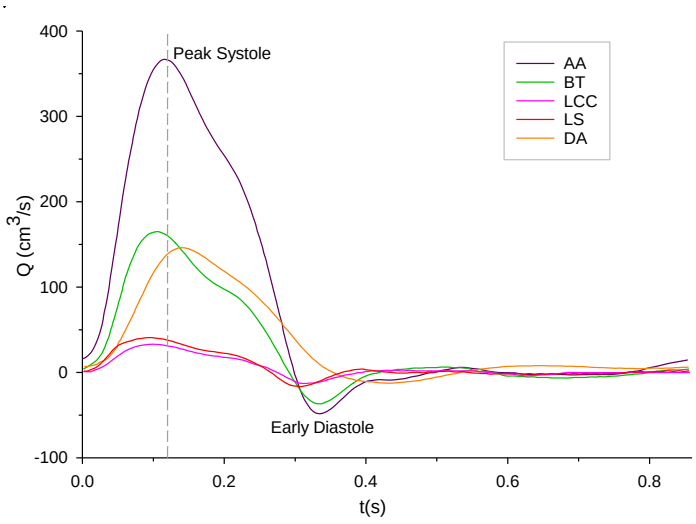

Figure 2. Boundary condition definition in the inlet and outlets of the aortic arch.

Numerical Solution

Fluid and solid fields are divided into computational elements to solve the governing equations. The very fine mesh for the solid domain is selected, and different mesh numbers for the fluid domain are considered to ensure the accuracy of the results of the produced mesh. The fluid grid generation is

chosen so finely that the difference between the results obtained during the previous cycle can be ignored. The mesh created in this model contains tetrahedral elements for the respiratory and aortic systems, 3,502,459 and 1,312,338 respectively, after examining a grid independency analysis. Nonlinear analysis is necessary for large deformations. As a solver for the Lagrangian formulation of the solid model and the Arbitrary Lagrangian-Eulerian (ALE) formulation of the fluid model Ansys 2021 R1 software (ANSYS, Inc., Canonsburg, PA, USA) is used. The $k-\varepsilon$ turbulence model is used to solve the turbulent flow in the aorta. The number of iterations and the convergence criterion for both solid and fluid models are 100 and 0.001 in a 0.001 s time step, respectively. Eliminating the effect of initial conditions in periodic nonlinear problems is important. Five consecutive cycles are repeated to achieve a stable cycle, and the results presented are related to the fifth cycle.

Results

While the MDM method provides simulated analytic results for the two studies of the vital organs, a comparison between fluid velocity profiles in experiment and simulation is required to validate the modeling. Ball et al. [8] have used hot-wire anemometry to obtain experimental analytic results on the respiratory system, producing similar results to this study. Tse et al. [9] have reported time-averaged wall shear stress (WSS) results for six different human models of aortic geometry in a different CFD study, with less than 5% deviation to results of this study.

Respiratory System

Fig. 3a and Fig. 3b show the exhalation streamline and velocity vector pattern for the respiratory model at peak exhalation at 6 l/min, respectively. At the site of the larynx, with airway stenosis due to the presence of a tumor, a maximum velocity of 2.6 m/s is observed. Airflow recirculation in the oropharyngeal region is considerable. Fig. 3c shows the pressure contour in exhalation for the respiratory model. The trachea bears the most pressure, and its value is uniformly equal to 3.5 Pa along the trachea. Fig. 3d shows the WSS contour in exhalation. The larynx and oropharynx tolerate most WSS at 0.36 Pa. Fig. 3e and Fig. 3f show the stress and strain at the time of exhalation, respectively. The highest stress and strain are observed in the trachea, at 23 Pa and 2.3×10^{-4}, respectively. Fig. 3g shows the displacement contour during exhalation. The oropharyngeal region tolerates most displacement, equating to 0.005 mm. Fig. 3h shows the deposition contour in exhalation. The larynx and oropharynx are the most affected areas. The percentage of total deposition in the model is 8.3%.

Circulatory System

Fig. 3a and Fig. 3b show the streamline and velocity vector pattern in the aortic arch model at systolic peak, respectively. The highest blood velocity in the aortic arch is 1.7 m/s. Also, the maximum

pressure is equal to 11.7 kPa. Fig. 4c shows the aortic model's Y^+ contour at the peak systole. The maximum Y^+ reaches 7.4. This indicates that a high quality grid was generated and that the right solution method was chosen for the turbulent aortic blood flow. Fig. 4d shows the WSS contour at peak systole. The highest WSS is located at the entrance, the branches root and the abdominal aorta; its value reaches 55.9 Pa. Fig. 4e and Fig. 4f show the stress and strain

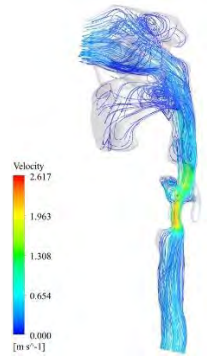

(a)

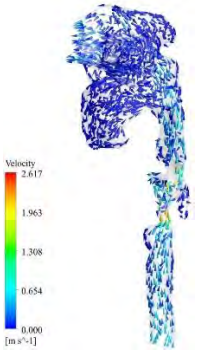

(b)

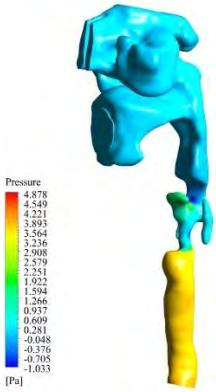

(c)

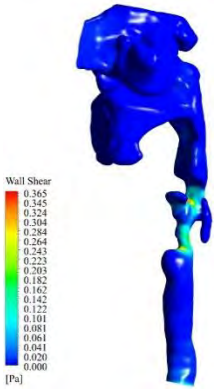

(d)

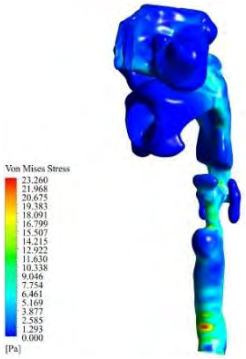

(e)

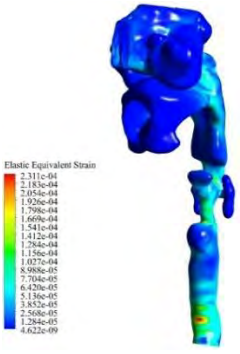

(f)

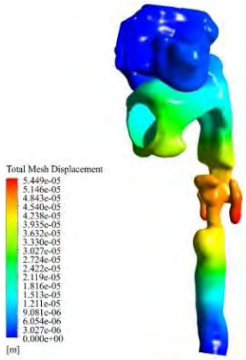

(g)

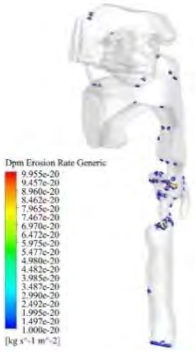

(h)

Figure 3. The contour of streamlines, velocity vector, pressure, WSS, stress, strain, deformation, and deposition pattern in the upper airway for a rest condition of peak exhalation at 6 l/min. (**a**) Streamlines. (**b**) Velocity vector. (**c**) Pressure. (**d**) WSS. (**e**) Von Mises stress. (**f**) Elastic equivalent strain. (**g**) Total mesh displacement. (**h**) Deposition pattern.

at peak systole, respectively. The highest stress and strain are observed at the supra-aortic branches. Fig. 4g shows the displacement contour at peak systole. The maximum displacement is found in the descending aorta zone reaching 0.08 mm. Fig. 4h shows the deposition contour at peak systole. Most deposition occurs at the ascending aorta and the location of the branches root and the descending aorta. The percentage of total deposition in the model is 8.2%. Notably, 84.8% of fat particles escape to the abdominal aorta.

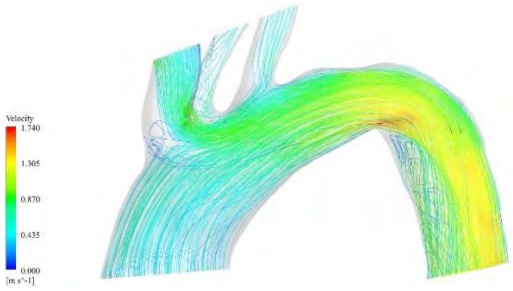

(a)

(b)

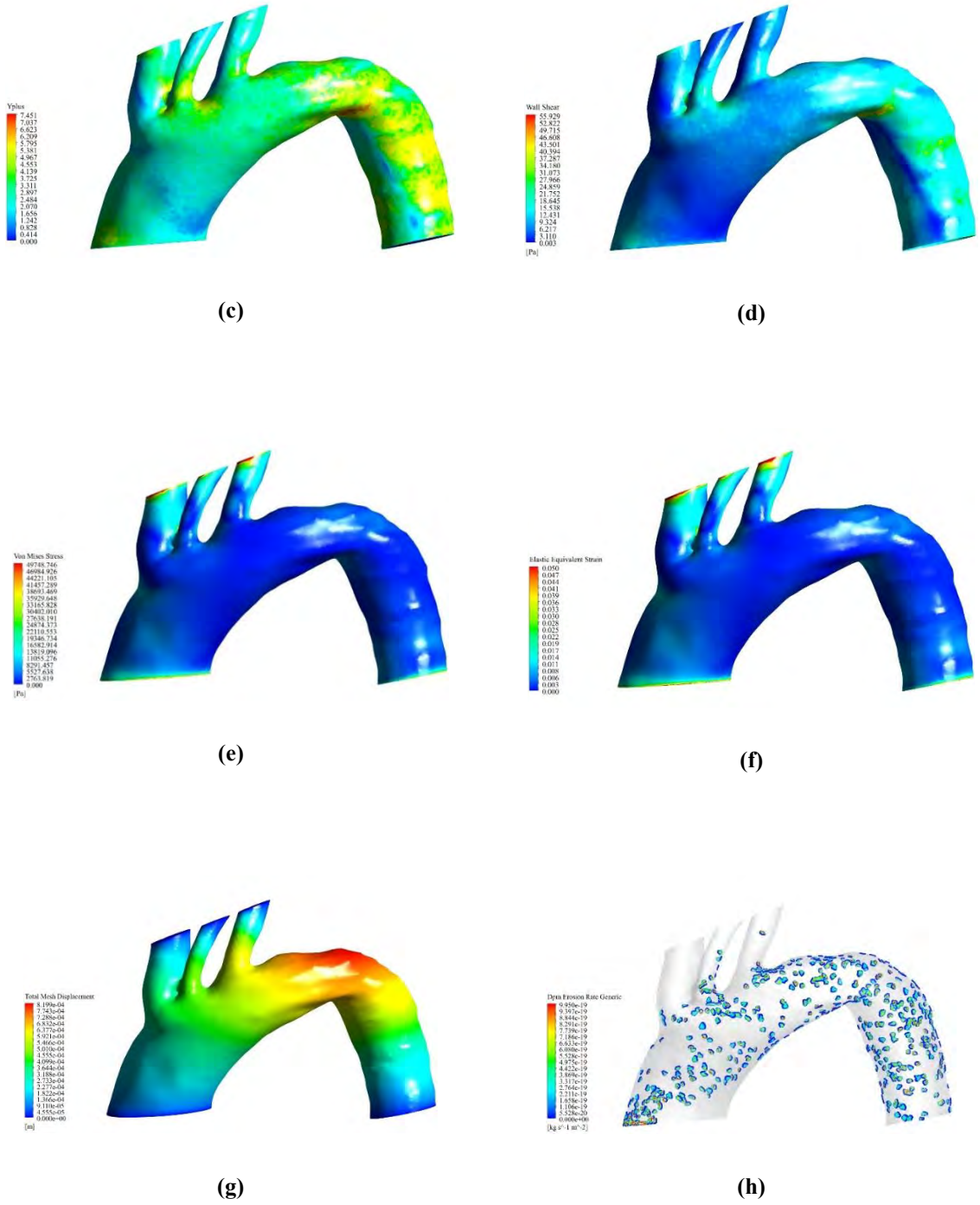

Figure 4. The contour of streamlines, pressure, Y^+, WSS, stress, strain, deformation, and deposition pattern in the aortic arch for a rest condition of systolic peak. (**a**) Streamlines. (**b**) Pressure. (**c**) Y^+ variation in the geometry domain. (**d**) WSS. (**e**) Von Mises stress. (**f**) Elastic equivalent strain. (**g**) Total mesh displacement. (**h**) Deposition pattern.

Discussion and Conclusion

With the help of accurate numerical methods, the conditions are provided for examination of the human body in a way that in vitro results can accurately predict in vivo processes in the body [10, 11]. The present study simulated two essential and related body organs, namely the circulatory system and the respiratory system, using the MDM method at rest condition. In the upper airway, the larynx and oropharynx tolerate most WSS. On the other hand, those are the most affected areas by cigarette smoke particles. In the circulatory system, the abdominal aorta is a high-risk zone for fat particles to settle. Indeed most fat particles accumulate in the abdominal aorta, which may be due to the lower speed of blood flow and longer path in the abdominal aorta. Also noteworthy in both the respiratory and the aorta models is that in places of geometry with the maximum WSS, particle deposition is highest. In other words, the deposition pattern of particles is directly related to the WSS index.

Digital human modeling of fluid flow can be essential in understanding and treating disease. It is necessary to conduct further studies on pulmonary blood flow and hemodynamic behavior of patient blood flow to reduce the risk of invasive vascular surgery. The present study used CT images to determine boundary conditions of the aortic and respiratory systems. Models showed that the junctions of bifurcation have a higher risk of particle deposition. The values of instantaneous hemodynamic parameters in the rigid wall state are far from the elastic wall state. Using viscolelastic wall modeling improved results vs. CFD-based rigid wall models. An important result of the current model-based simulation is that particle deposition was highest in both the respiratory and aorta models in places where WSS was highest. WSS is an index that cannot be obtained in vivo. In contrast, the in-vitro method based on precise numerical models can accurately calculate the changes of this parameter in the whole model. We propose that future studies model the whole respiratory system, including the upper and lower airways. Similarly, the circulatory system should be whole modeled, including the carotid arteries and the abdominal aorta. Studies using such expanded organ models will help to understand complex health conditions and diseases more precisely.

References

1. Mortazavy Beni, H., Mortazavi, H., and Islam. (2021). Biomedical and biophysical limits to mathematical modeling of pulmonary system mechanics: a scoping review on aerosol and drug delivery. Biomech Model Mechanobiol, 21, 79–87.

2. Mortazavy Beni, H., Mortazavi, H., Tashvighi, E., & Islam, M. S. (2022). Investigation of the Upper Respiratory Tract of a Male Smoker with Laryngeal Cancer by Inhaling Air Associated with Various Physical Activity Levels. Atmosphere, 13(5), 717.

3. Mortazavi, H., Mortazavy Beni, H., Aghaei, F., Sajadian, H. (2020). SARS-CoV-2 droplet deposition path and its effects on the human upperairway in the oral inhalation. Computer Methods and Programs in Biomedicine, 200(5448), 105843.

4. Mortazavy Beni, H., Mortazavi, H., Aghaei, F., Kamalipour, S. (2021). Experimental tracking and numerical mapping of novel coronavirus micro-droplet deposition through nasal inhalation in the human respiratory system. Biomech Model Mechanobiol., 20(3), 1087-1100.

5. Mortazavy Beni, H., Hassani, K., Khorramymehr, S. (2019). Study of the sneezing effects on the real human upper airway using fluid–structure interaction method. J Braz Soc Mech Sci Eng., 41(4), 181.

6. Cameron, J. R., Skofronick, J. G., and MGrant, R. (1992). Medical Physics: Physics of the body. Medical Physics Publishing Corporation.

7. Alimohammadi, M., Agu, O., Balabani, S., Díaz-Zuccarini, V. (2014). Development of a patient-specific simulation tool to analyse aortic dissections: assessment of mixed patient-specific flow and pressure boundary conditions. Med Eng Phys, 36(3), 275–84.

8. Ball, C. G., Uddin, M., Pollard, A. (2008). High resolution turbulence modelling of airflow in an idealized human extra-thoracic airway. Comput. Fluids, 37, 943–964.

9. Tse, K. M., Chang, R., Lee, H. P., Lim, S. P., Venkatesh, S. K., and Ho, P. (2013). A computational fluid dynamics study on geometrical influence of the aorta on haemodynamics. European journal of cardio-thoracic surgery: Official journal of the European Association for Cardio-thoracic Surgery, 43(4), 829–838.

10. Alaodolehei, B., Jafarian, K., Sheikhani, A., Mortazavy Beni, H. (2020). Performance Enhancement of an Achalasia Automatic Detection System Using Ensemble Empirical Mode Decomposition Denoising Method. J. Med. Biol. Eng., 40, 179–188.

11. Mortazavy Beni, H., Mortazavi, H. (2022). Mathematical modeling of the solar regenerative heat exchanger under turbulent oscillating flow: Applications of renewable and sustainable energy and artificial heart. Results Eng., 13, 100321.

Understanding Buttock Deformation in a Seated Posture

Russell Marshall[1], Michael Harry[1] and Michael Fray[1]

[1]School of Design and the Creative Arts, Loughborough Universty, Ashby Road, Loughborough, Leicershire, United Kingdom, LE11 3TU
Corresponding author: r.marshall@lboro.ac.uk

Abstract

This paper presents PhD research conducted at Loughborough University in the UK, into flesh deformation of the buttocks in a seated posture. Due to a lack of detailed understanding of how the soft tissues of humans behave when in contact with a seat surface, this research aims to explore the deformation behaviour of these tissues across the sitting task. In particular the research aims to understand the relationships between the three main degrees of freedom: compression (C), anterior-posterior spread (AP), and lateral-medial spread (LM). The paper presents the analysis of C, LM and AP deformation behaviour from a study of 42 participants. Data were collected using motion capture markers attached to tight fitting clothing across one buttock of each participant via the Codamotion system. A rigid platform was used to act as a 'seat'. Participants were suspended via a hoist such that they could adopt a seated posture just short of the seat surface. Data were then captured through the sitting process from first contact to fully deformed. The resulting coordinate changes throughout this process were captured and analysed. In addition to buttock deformation data, a range of anthropometric data were captured from each participant to explore correlations between anthropometric measures and deformation behaviour to inform any later modelling activity. Findings identify clear deformation behaviour types for AP and LM spread and that participants can display predominant deformation behaviour in one axis. Typically, AP spread is greater than LM spread, and the maximum deformations occur in the lower regions of the buttocks closer to the seat surface. The development of useful models of deformation behaviour is ongoing.

Keywords: anthropometry, buttock deformation, seat design, DHM.

Introduction

The 'seated operator' is a well-known condition of human interaction with products, workplaces and environments (Li & Haslegrave, 1999). Humans adopt seated postures for a variety of tasks, and this poses particular challenges for practitioners looking to optimize the relationship between the human and their environment. As such, anthropometric databases (Dreyfuss, 1967; Gordon et al., 2014; Peebles &

Norris, 1998; Pheasant & Haslegrave, 2006) and digital human modelling systems: AnyBody, JACK, IPS-IMMA, RAMSIS, SAMMIE, Santos, amongst others, all have the capability of representing humans in a range of postures, including sitting. This provides data and tools to model and evaluate the seated human and their interactions with the world around them (Scataglini & Paul, 2019).

Seating, and the interaction with the seated human, are common areas of research (Dempster, 1955; Estrada & Vea, 2018; Quigley et al., 2001). This is partly driven by the prevalence of the seated human in everyday situations, with the majority of transport taking place with seated passengers, and many working, study, and leisure activities engaged in whilst seated. Furthermore, it is commonly understood that prolonged sitting, and / or sitting without appropriate support and / or in a 'poor' posture can lead to musculoskeletal issues (Daneshmandi et al., 2017; Picavet et al., 2016; Robb & Mansfield, 2007).

Whilst extensive research has been conducted into seating and the seated human the understanding of human-seat interactions remains a challenge, in particular soft tissue deformation experienced in the thigh-buttock region. Previous researchers have explored various methods across finite element modelling (Savonnet et al., 2018), medical imaging (Sonenblum et al., 2018), and interface pressure measurement (Oomens et al., 2003). Whilst progress in understanding has been made, variability in approaches and in the populations being studied make it difficult to draw generalisable conclusions or for broad and applicable models to be developed (Hiemstra-van Mastrigt et al., 2016).

This paper presents PhD research at Loughborough University in the UK exploring the soft tissue deformation process during sitting. The aim is to develop a model that quantifies how the human buttocks deform when contact is made with a surface. The approach taken has been to evaluate the deformation observed externally at the skin layer across the buttock and to use this to explore deformation during different stages of sitting. Ultimately models of deformation behaviour will be correlated with a range of anthropometric characteristics to provide models of deformation behaviour to inform practitioners seeking to design for this interaction.

Methods

The full description of the data collection process is documented in Harry et al., (2020), a summary is provided here. A total of 42 participants (34M-8F) were recruited from the student population. Whilst mostly a convenience sample, efforts were made to obtain a range of anthropometric variability (e.g. BMI 18.9-29.7; % Fat 4.1-38.8; hip girth 880-1250mm, waist breadth 814-1017mm; sitting height 814-1017mm). Standard ethical processes were followed. To limit variability due to external factors participants were asked to adhere to a pre-trial protocol limiting food and drink consumption, exercise etc.

A total of 31 body dimensions were collected from participants including body composition measures as well as general demographic information as shown in Table 1. Measurements were taken three times and averaged. Equipment included: digital scales (Mettler Toledo kcc150), body composition monitor (Tanita), stadiometer, anthropometer, skinfold calliper (Holtain Ltd), and measuring tape. Measurements were selected to be a combination of measures directly relevant to the buttock / thigh region (e.g. gluteal crease, hip girth), those that indicate body composition (e.g. BMI, mass, waist depth) and those that would allow categorisation against standard anthropometric data used in more general human modelling applications (e.g. stature, sitting height).

Table 1. Anthropometric data collected

General	age, mass, stature
Body Composition	% fat, fat mass, muscle mass, bone mass, BMI, physique rating
Skinfolds	pectoral, midaxillary, biceps, triceps, suprailiac, abdominal, subscapular, mid-thigh, suprapatella, medial calf, posterior-suprailiac, lumbo-sacral and gluteal crease
Girths, circumferences and others	waist girth, waist depth, waist breadth, hip girth, hip depth, hip breadth, bi-acromial breadth, buttock-knee length, knee height, sitting height, shoulder height (sitting), arm length and hand length

Data collection focused on the use of the Codamotion motion capture system that utilises infrared markers that are tracked through 3-dimensional space by tripod mounted sensor arrays. Participants all wore tight fitting leggings to which the markers were attached. The Greater Trochanter (GT) was chosen as a consistent landmark and identified by palpation and marked with a sticker or chalk pen. Using a reference template, markers were affixed horizontally from the GT around the circumference of the right buttock in 15˚ increments (labelled GT: GTmain (0), GT15, GT30, GT45, GT60, GT75). A second row of markers (GTX: main,15,30,45,60,75) were also positioned 40mm directly below the GT line as shown on the right in Figure 1. Markers were also placed on other body locations including the acromion, C7, sacrum and lateral condyle, to serve as reference locations.

To replicate a seat surface, a rigid platform was used, 700mm square in three conditions: horizontal, and two angled conditions where the rear of the seat was inclined down at 5˚ and 10˚. Note that only results from condition 1, flat seat, are presented here. Participants were suspended by a ceiling hoist via chest strap and braced against a padded knee rest to minimise sway as shown on the left in Figure 1. Participants were raised and then lowered until just at the point of contact (first contact) and held for 5-10 seconds. They were then lowered until their full weight was borne by the seat surface (fully deformed). The process was repeated 2-3 times for each participant and 3-dimensional data were sampled at 100Hz to ensure accurate readings throughout the process.

Figure 1. The experimental setup

Results

Data were captured using the Codamotion ODIN software, and then analysed using a combination of IBM SPSS, Microsoft Excel and MATLAB. Analysis focused on three core deformations: Compression (z axis), Anterior-Posterior (AP – y axis) and Lateral-Medial (LM – x axis). Throughout the analysis data were checked for consistency, missing values and outliers. A hybrid approach was taken to identifying representative deformation values. Where two good data points were available for a given marker they were averaged, where data were missing from one or more trial results were excluded.

Compression, AP Spread and LM Spread

Using MATLAB, the z-axis data for the GTmain marker was plotted per trial for all participants, as shown in Figure 2. A start and end point within 'First contact' and 'Fully Deformed' were manually identified to define a compression time domain that was then used as the frame of reference for all other markers across Compression, AP and LM spreads. As can be seen from Figure 2 the 'flat' regions defining first contact and fully deformed consist of small variations in the z value. Thus, the compression value was defined as the numerical difference between the average value taken from the first contact region and the average value taken from the fully deformed region.

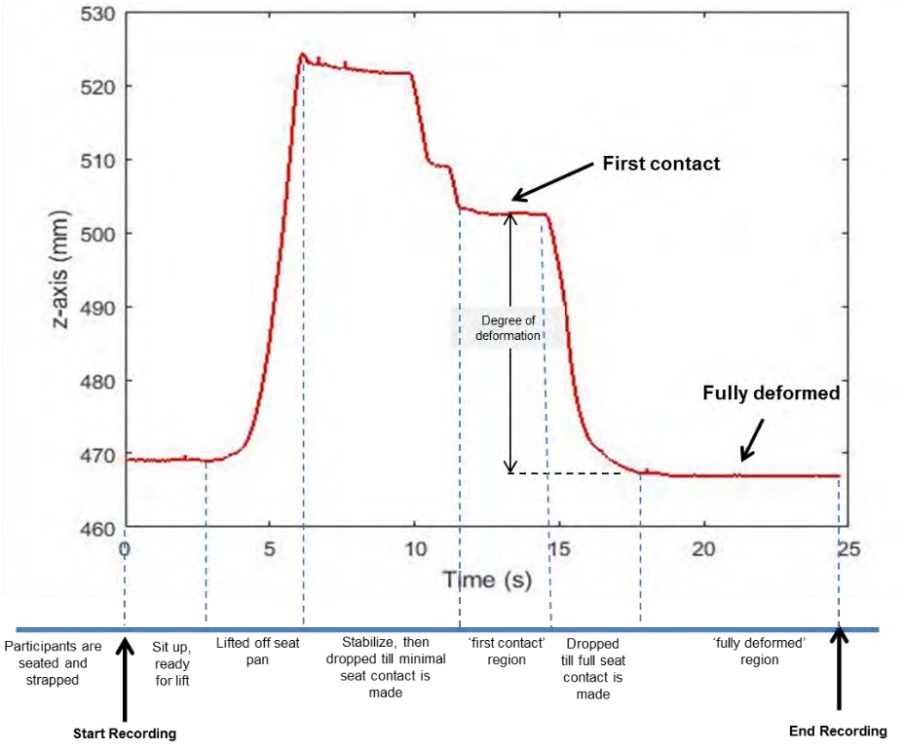

Figure 2. Exemplar results for one participant showing compression (z-axis) for GTmain

Tables 2, 3 and 4. Present the mean and standard deviations for Compression (z-axis), AP Spread (y-axis) and LM Spread (x-axis) respectively across all participants and all markers.

Table 2. / Figure 3. GT and GTX Compression values

Markers	**Mean (S.D)**		
	Trial 1	**Trial 2**	**Overall**
GTmain	33.45 (8.06)	33.75 (8.08)	33.60 (7.57)
GT15	36.48 (8.05)	37.34 (9.51)	36.91 (8.45)
GT30	41.21 (9.71)	42.19 (10.33)	41.70 (9.54)
GT45	43.37 (10.81)	44.50 (11.33)	43.96 (10.77)
GT60	43.96 (9.51)	45.87 (12.10)	44.98 (10.02)
GT75	43.19 (10.11)	44.20 (11.50)	43.70 (10.37)
GTXmain	32.23 (6.74)	33.02 (8.57)	32.81 (7.29)
GTX15	37.27 (7.22)	37.72 (9.27)	37.95 (6.98)
GTX30	41.24 (9.13)	41.60 (10.11)	41.38 (9.21)
GTX45	43.64 (9.25)	43.98 (10.37)	44.72 (8.94)
GTX60	44.36 (11.81)	46.83 (12.36)	46.01 (11.44)
GTX75	45.98 (10.33)	47.90 (11.76)	47.40 (11.12)

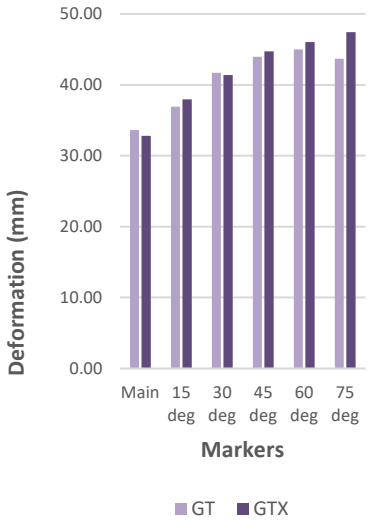

Table 3. / Figure 5. GT and GTX AP spread values

Markers	Mean (S.D)		
	Trial 1	**Trial 2**	**Overall**
GTmain	9.23 (5.48)	9.23 (6.23)	9.23 (5.59)
GT15	11.33 (5.24)	11.10 (6.14)	11.22 (5.39)
GT30	11.31 (5.27)	11.47 (6.34)	11.39 (5.54)
GT45	9.86 (6.75)	9.68 (7.58)	9.79 (6.82)
GT60	10.02 (12.35)	8.58 (8.49)	9.44 (8.74)
GT75	8.44 (8.36)	8.88 (11.80)	8.90 (9.92)
GTXmain	15.18 (15.80)	11.20 (7.31)	13.22 (9.44)
GTX15	13.94 (8.65)	11.92 (9.59)	13.35 (7.43)
GTX30	20.67 (17.54)	22.61 (20.47)	20.63 (17.95)
GTX45	25.65 (21.18)	28.13 (21.05)	25.69 (18.78)
GTX60	26.95 (24.52)	31.31 (27.01)	25.31 (21.68)
GTX75	33.83 (26.74)	35.56 (27.68)	31.19 (25.03)

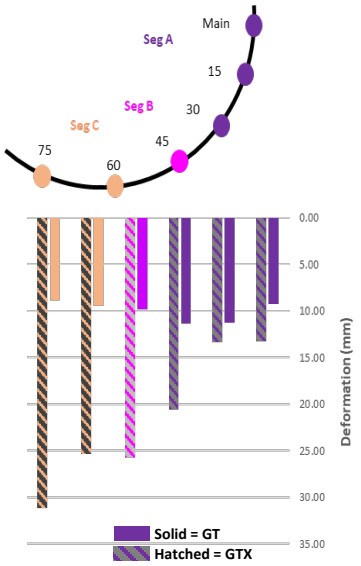

Table 4. / Figure 6. GT and GTX LM spread values

Markers	Mean (S.D)		
	Trial 1	**Trial 2**	**Overall**
GTmain	3.64 (4.11)	3.70 (4.78)	3.67 (4.32)
GT15	4.56 (5.15)	4.63 (5.38)	4.59 (5.17)
GT30	1.71 (3.73)	2.05 (4.36)	1.88 (3.90)
GT45	-0.15 (4.15)	-0.07 (4.45)	0.02 (3.97)
GT60	-2.78 (5.10)	-2.29 (4.72)	-2.37 (4.61)
GT75	-3.30 (3.76)	-3.85 (5.33)	-3.43 (3.67)
GTXmain	11.08 (5.33)	11.07 (5.21)	11.13 (5.03)
GTX15	11.20 (6.95)	10.72 (7.03)	11.02 (6.72)
GTX30	8.68 (8.73)	9.21 (9.79)	8.77 (8.96)
GTX45	9.34 (9.88)	11.62 (11.03)	10.59 (10.10)
GTX60	6.32 (8.67)	6.46 (8.84)	5.72 (8.00)
GTX75	3.18 (8.78)	5.50 (8.87)	4.05 (7.52)

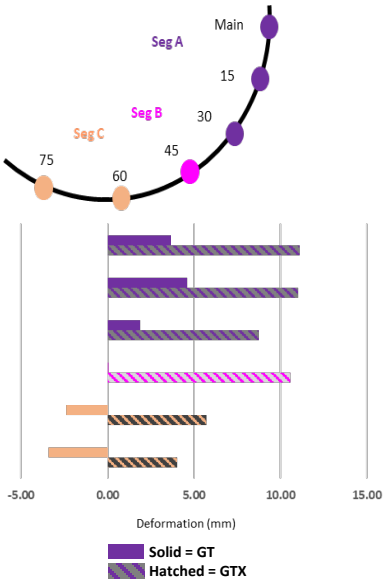

In addition to statistical treatment of the deformation for each marker across the three deformation types a range of tests were performed exploring correlation within a deformation type between markers and across deformation types. Furthermore, correlations were explored to identify any relationships between deformation types and anthropometric variables. As the analysis is ongoing at this time, and for the purposes of brevity, further results will be disseminated in future publications.

Discussion

As can be seen from the results compression is the greatest magnitude of deformation for a seated human. The data highlight compression varies between 33mm and 47mm for this sample. In comparison AP deformation or front-to-back 'spread' varies between 8mm and 35mm and for LM or side-to-side spread between 0mm and -4mm and +12mm. There are various interesting observations. Firstly compression is very consistent with a steady increase from GTmain to GT75 and broadly similar levels of compression across GT and GTX suggesting deformation is relatively linear. However, for AP and LM spread deformation behaviour is much more varied. It is interesting to note that typically participants spread more to the rear than they do to the sides. Unlike compression the spread is also more pronounced closer to the seat surface (GTX) than level with the Greater Trochanter (GT). LM spread also reveals deformation behaviour that is otherwise hidden by the mean values presented here. Not all deformation observed is in the positive direction (Posterior, and Lateral). At the GT level GTmain to GT30 all spread laterally, however, GT60 and GT75 spread medially. Such behaviour is observable not only across participants but also across markers for a single participant. Due to the averaging of these results deformation for an individual can be much more variable. This highlights that the tissues of the buttocks are not only prone to spreading outwards, but also folding, in the sitting process.

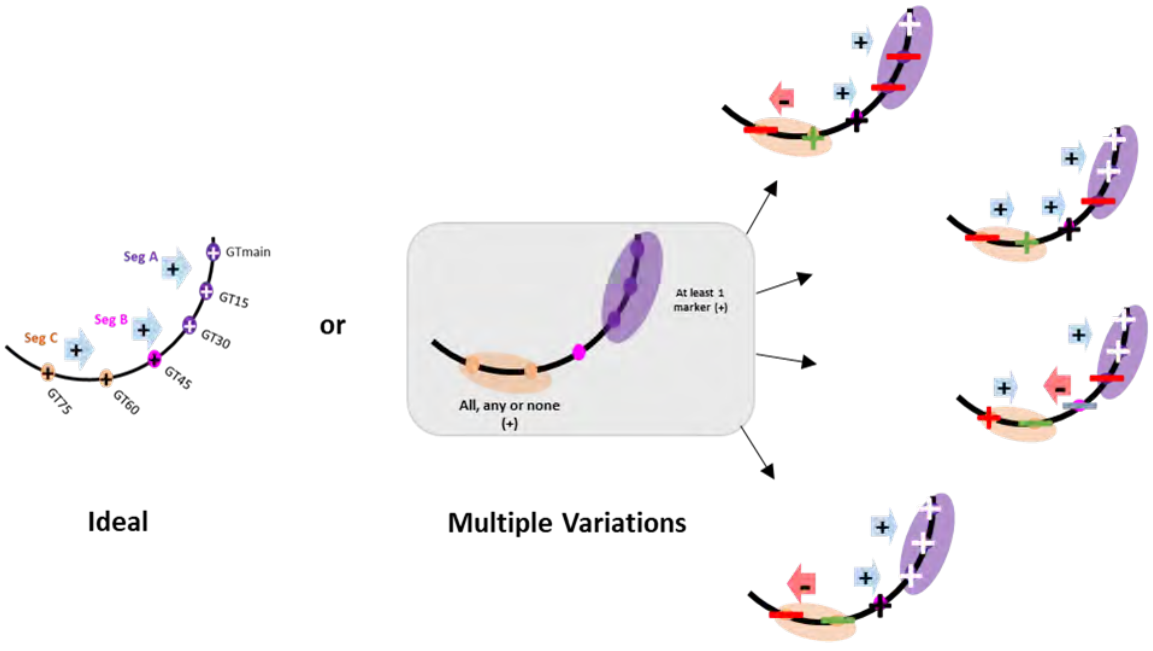

Figure 7. Exemplar LM spread types with the ideal spread shown in the left and multiple variations shown on the right.

As introduced earlier, one of the aims of this research is to quantify deformation but to also provide models for practitioners. Models are being explored investigating spread magnitude and behaviour. To assist in this process, behaviour across the buttock is examined both at the marker level and in grouped marker segments, where Segment A consists of markers to the side of the buttocks including GT(X)main to GT(X)30 and Segment C is the rear segment consisting of GT(X)60 to GT(X)75. These are separated by Segment B consisting of GT(X) 45 only. An example is shown in Figure 7. that presents an ideal Lateral spread and also many variations of Lateral spread. The intention is to explore the prevalence of spread types and provide common spread type models. These will also be combined with spread strength.

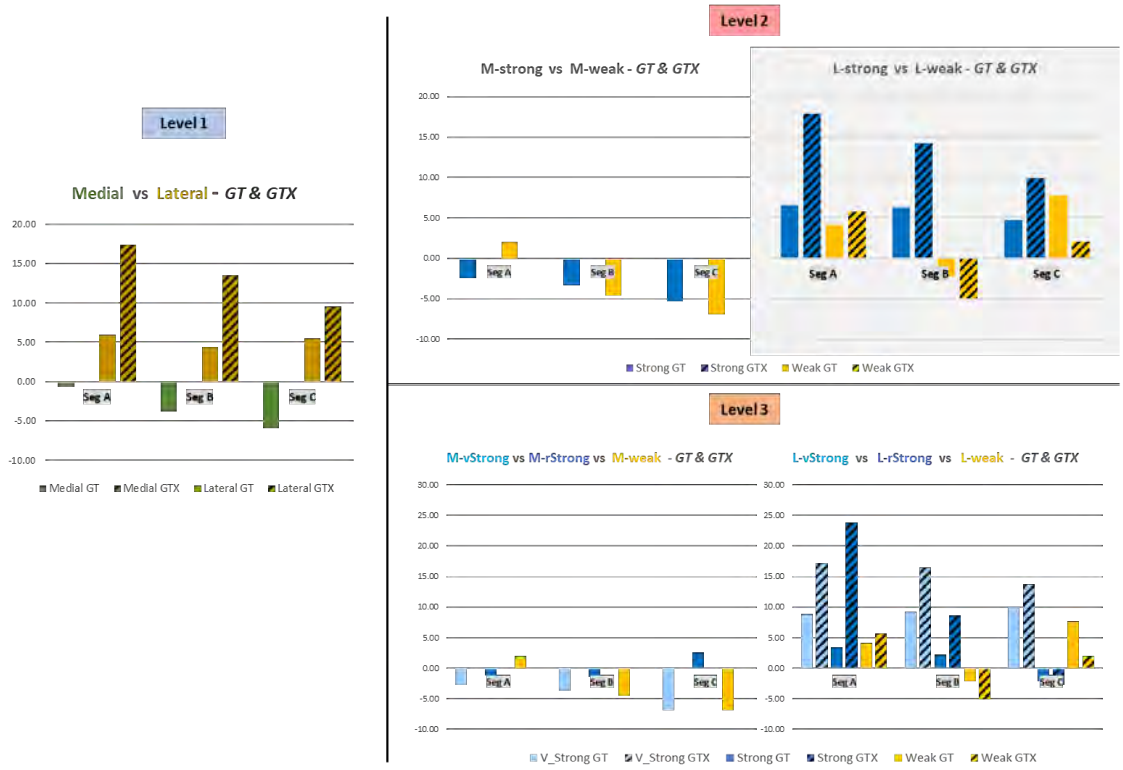

Figure 8. Exemplar LM spread strength levels

Figure 8. shows how spread varies in magnitude for each segment for both GT and GTX, across three levels of spread strength analysis ranging from Level 1 that only considers cases where participants are considered to be only Lateral or Medial spreaders, Level 2 where participants can be Strong or Weak Lateral or Medial spreaders, and Level 3 where a participant can be a very-strong, strong, or weak Lateral or Medial spreader. It is considered likely that useful spread pattern models are likely to pertain to the strongest categories of spread behaviour to inform the extremes, in a similar manner to how anthropometric models tend to rely on percentile extremes or boundary cases. However, a mapping of the full range of deformation behaviour is still useful to explore all the possible variability.

It is important to acknowledge the limitations of this research, whilst a good range of anthropometric variability is represented the sample size is ultimately limited, the data were collected with an assumption of symmetry, and the data do contain some occlusions that highlight the complexity of trying to map behaviour of human tissue that effectively becomes hidden by the very act being studied.

Conclusions

Research into buttock deformation during sitting has been presented. From a sample of 42 participants data have been collected using a motion capture system that tracks key points on the surface of the buttocks in 3-dimensions. These data provide an insight into Compression, Anterior-Posterior Spread and Lateral-Medial spread. Analysis has begun to develop models that represent the most common and most extreme spread behaviours to inform practitioners looking to understand the implications of this spread behaviour on, for example, seat design, clothing or Personal Protective Equipment. Only a sample of the research and the data have been presented here due to practical constraints. The full analysis will explore many more variables including the inclined seat surfaces, a non-rigid seat and also the correlations between deformation behaviour and anthropometric measures. Here the aim is to be able to provide predictor models such that a human with a particular BMI and waist measurement, for example, is likely to be a given type of 'spreader'.

References

Daneshmandi, H., Choobineh, A., Ghaem, H., & Karimi, M. (2017). Adverse Effects of Prolonged Sitting Behavior on the General Health of Office Workers. *Journal of Lifestyle Medicine*, *7*(2), 69. https://doi.org/10.15280/JLM.2017.7.2.69

Dempster, W. T. (1955). *Space Requirements of the Seated Operator: Geometrical, Kinematic and Mechanical Aspects of the Body with Special Reference to the Limbs*. Wright Air Development Center, Wright Patterson Air Force Base.

Dreyfuss, H. (1967). *The Measure of Man, Human Factors in Design* (2nd Editio). Whitney Library of Design.

Estrada, J. E., & Vea, L. A. (2018). Modelling and Simulation of Spine in Sitting Posture in a Computer-Related Workplace Cite this paper International Journal of Computer Science and Mobile Computing Modelling and Simulation of Spine in Sitting Posture in a Computer-Related Workplace. *International Journal of Computer Science and Mobile Computing*, *7*(11), 121–135.

Gordon, C., Blackwell, C. L., Bradtmiller, B., Parham, J. L., Barrientos, P., Paquette, S. P., Corner, B. D., Carson, J. M., Venezia, J. C., Rockwell, B. M., Mucher, M., & Kristensen, S. (2014). *2012 Anthropometric Survey of U.S. Army Personnel: Methods and Summary Statistics*. U.S. Army Natick Soldier Research, Development and Engineering Center Natick. http://www.dtic.mil/dtic/tr/fulltext/u2/a611869.pdf

Harry, M., Marshall, R., & Fray, M. (2020). Quantification of buttock deformation on a rigid seat. In *Advances in Intelligent Systems and Computing* (Vol. 975). https://doi.org/10.1007/978-3-030-20216-3_44

Hiemstra-van Mastrigt, S., Groenesteijn, L., Vink, P., & Kuijt-Evers, L. F. M. (2016). Predicting passenger seat comfort and discomfort on the basis of human, context and seat characteristics: a literature review. *Ergonomics*, *0139*(May 2017), 1–23. https://doi.org/10.1080/00140139.2016.1233356

Li, G., & Haslegrave, C. M. (1999). Seated work postures for manual, visual and combined tasks. *Ergonomics*, *42*(8), 1060–1086. https://doi.org/10.1080/001401399185144

Oomens, C. W. J., Bressers, O. F. J. T., Bosboom, E. M. H., Bouten, C. V. C., & Bader, D. L. (2003). Can Loaded Interface Characteristics Influence Strain Distributions in Muscle Adjacent to Bony Prominences? *Computer Methods in Biomechanics and Biomedical Engineering*, *6*(3), 171–180. https://doi.org/10.1080/1025584031000121034

Peebles, L., & Norris, B. (1998). *Adultdata. The handbook of adult anthropometry and strength measurements – data for design safety.* Department of Trade and Industry.

Pheasant, S., & Haslegrave, C. M. (2006). *Bodyspace : Anthropometry, Ergonomics, and the Design of Work* (Second Edi). Taylor & Francis. https://www.crcpress.com/Bodyspace-Anthropometry-Ergonomics-and-the-Design-of-Work-Third-Edition/Pheasant-Haslegrave/p/book/9780415285209

Picavet, H. S. J., Pas, L. W., Van Oostrom, S. H., Van Der Ploeg, H. P., Verschuren, W. M. M., & Proper, K. I. (2016). The Relation between Occupational Sitting and Mental, Cardiometabolic, and Musculoskeletal Health over a Period of 15 Years – The Doetinchem Cohort Study. *PLOS ONE*, *11*(1), e0146639. https://doi.org/10.1371/JOURNAL.PONE.0146639

Quigley, C., Southall, D., Freer, M., Moody, A., & Porter, M. (2001). *Anthropometric study to update minimum aircraft seating standards*. Joint Aviation Authorities. https://repository.lboro.ac.uk/articles/report/Anthropometric_study_to_update_minimum_aircraft_seating_standards/9353039

Robb, M. J. M., & Mansfield, N. J. (2007). Self-reported musculoskeletal problems amongst professional truck drivers. *Http://Dx.Doi.Org/10.1080/00140130701220341*, *50*(6), 814–827. https://doi.org/10.1080/00140130701220341

Savonnet, L., Wang, X., & Duprey, S. (2018). Computer Methods in Biomechanics and Biomedical Engineering Finite element models of the thigh-buttock complex for assessing static sitting discomfort and pressure sore risk: a literature review Finite element models of the thigh-buttock complex for assessing static sitting discomfort and pressure sore risk: a literature review. *Computer Methods in BiomeChaniCs and BiomediCal Engineering*, *21*(4), 379–388. https://doi.org/10.1080/10255842.2018.1466117

Scataglini, S., & Paul, G. (2019). *DHM and Posturography*. Academic Press.

Sonenblum, S. E., Ma, J., Sprigle, S. H., Hetzel, T. R., & McKay Cathcart, J. (2018). Measuring the impact of cushion design on buttocks tissue deformation: An MRI approach. *Journal of Tissue Viability*, *27*(3), 162–172. https://doi.org/10.1016/J.JTV.2018.04.001

Optimization of nucleus pulposus removal rate in the intervertebral disc during artificial nucleus replacement using lumbar finite element model simulation

Yeeun Kang, Jaemin Kim, and Junghwa Hong
Korea University, South Korea

Abstract

A herniated intervertebral disc (HIVD) is a disease caused by the prolapse of the nucleus pulposus of the intervertebral disc due to aging and repeated damage. To treat this, artificial nucleus replacement (ANR) is used to restore the height and flexibility of the reduced intervertebral disc by replacing a portion of the aged nucleus pulposus with an artificial one. However, few studies provide quantitative criteria for partial nucleus pulposus removal. Therefore, through finite element model (FEM) simulation of the lumbar spine (L4-L5), we obtained the optimal location and rate of nucleus pulposus removal and analyzed the movement of the model after ANR in this study. We modeled the FEM in which 60%, 80%, 87%, and 93% of the total nucleus pulposus were replaced by the artificial nucleus pulposus in each of the four directions (left, right, anterior, posterior). Then, a z-axis load of 400N was applied to the model to obtain an axial compression displacement, and a y-axis moment of -6 Nm~+6 Nm was applied to the model to analyze a flexion-extension range of motion (ROM). As a result, regardless of the location of the remaining nucleus pulposus, the compression displacement of the 80% and 87% nucleus pulposus removed model was restored to about 98% of that of the intact model. In addition, the ROM of the 87% nucleus pulposus removed model was restored in 96% of that of the intact model. It is expected that the data obtained through this study can be utilized in digital twin research to predict the prognosis of ANR and to improve surgical techniques.

Keywords: Finite element model simulation, Artificial nucleus replacement, Herniated intervertebral disc

Introduction

A herniated intervertebral disc (HIVD), in which the nucleus pulposus of the intervertebral disc prolapses, causes back pain, and radiating pain. To treat HIVD, total discectomy surgery is generally used. However, after the surgery, excessive movement of the adjacent segment decreases the normal range of motion (ROM), resulting recurrence of the disease.[1-3] To compensate for this shortcoming, artificial nucleus replacement (ANR) has been proposed, in which a part of the nucleus pulposus is removed and then an artificial nucleus pulposus is inserted. Clinical studies of ANR are still lacking, and there are few studies on intervertebral finite element analysis on spine movement after surgery.[4] The purpose of this study is to

investigate the optimal location and rate of nucleus pulposus removal through FEM simulation and to analyze the axial compression displacement and flexion-extension ROM of the lumbar spine after ANR.

Methods

The intact FEM of the fourth and fifth lumbar spine consists of the cortical bone, annulus fibrous, endplate, and nucleus pulposus. The ANR FEMs are designed in the form of removing 60%, 80%, 87%, and 93% of the total nucleus pulposus in the left, right, anterior, and posterior directions. The removed part was filled with a fluid cavity with a density of 1000 kg/m^3. To obtain the axial compression displacement, we applied a z-axis load of 400 N to the center of the model which is perpendicular to the transverse plane.[5,6] And, to analyze the flexion-extension ROM, we applied a moment of -6 Nm ~ +6 Nm along the y-axis to the model.

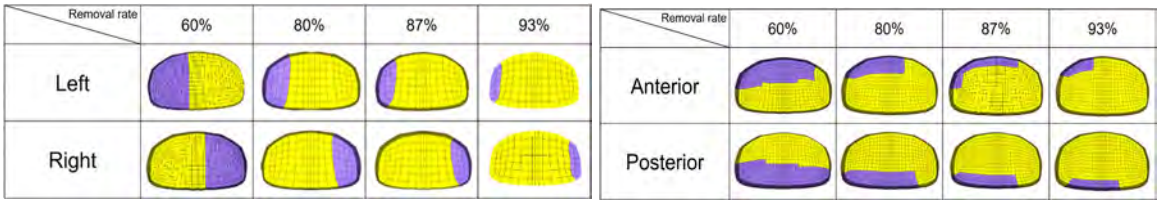

Figure 1. ANR FEMs with 60%, 80%, 87% and 93% nucleus removal. (Purple: original, Yellow: removed)

Results

The graphs below are the axial compression displacement graphs of the model when a 400 N load was applied. To verify that ANR is better than just removing the nucleus (partial discectomy), we compared all ANR data with partial discectomy data. Regardless of the location of the remaining nucleus pulposus, the displacement of the 80% and 87% nucleus pulposus removed model was restored to about 98% of that of the intact model. In addition, when the -6 Nm ~ +6 Nm moment was applied, the flexion-extension ROM of the 87% nucleus removed model in the posterior direction was restored in 96% of that of the intact model while that of partial discectomy was restored in 93% in the same conditions.

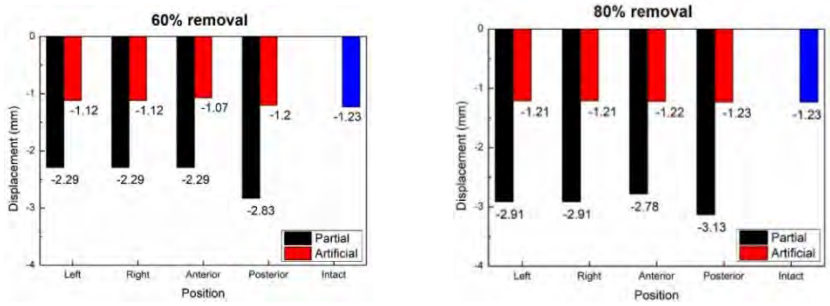

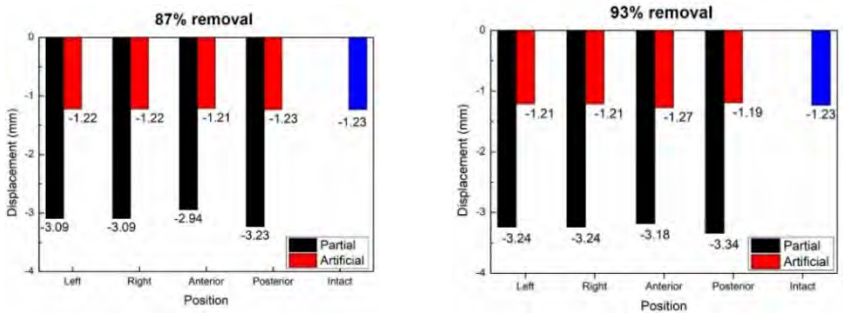

Figure 2. Axial compression displacement when applied 400 N to the model.

Discussion and Conclusions

Overall, ANR is more useful because the compression displacement and flexion-extension ROM of ANR are smaller than partial discectomy data. Moreover, compared to partial discectomy, ANR showed 5% more enhancement in flexion ROM and 2% in extension ROM. Combining the above results, the optimal ANR method is to replace 87% of the nucleus pulposus while remaining the original nucleus pulposus in the posterior direction. These results can be used in digital twin research to improve ANR surgical techniques.

Acknowledgments

This research was supported by the BK21 FOUR (Fostering Outstanding Universities for Research) funded by the Ministry of Education (MOE, Korea) and the National Research Foundation of Korea (NRF).

References

[1] Aota, Y., Kumano, K., & Hirabayashi, S. (1995). Postfusion instability at the adjacent segments after rigid pedicle screw fixation for degenerative lumbar spinal disorders. Journal of spinal disorders, 8(6), 464-473. [2] Harris, R. I., & Wiley, J. J. (1963). Acquired spondylolysis as a sequel to spine fusion. JBJS, 45(6), 1159-1170. [3] Lee, C. K. (1988). Accelerated degeneration of the segment adjacent to a lumbar fusion. Spine, 13(3), 375-377. [4] Strange, D. G., Fisher, S. T., Boughton, P. C., Kishen, T. J., & Diwan, A. D. (2010). Restoration of compressive loading properties of lumbar discs with a nucleus implant—a finite element analysis study. The Spine Journal, 10(7), 602-609. [5] Nachemson, A. (1966). The load on lumbar disks in different positions of the body. Clinical Orthopaedics and Related Research (1976-2007), 45, 107-122. [6] Cripton, P. A., Bruehlmann, S. B., Orr, T. E., Oxland, T. R., & Nolte, L. P. (2000). In vitro axial preload application during spine flexibility testing: towards reduced apparatus-related artefacts. Journal of biomechanics, 33(12), 1559-1568.

Automatic generation of partially homogenized FEM human body models based on 3D body scan data

Yordan Kyosev, Tino Kühn, and Ann-Malin Schmidt
TU Dresden, ITM, Germany

Keywords: human model, automatic generation, FEM, 3D scan, high speed (4D) scan

Introduction

The design of any functional clothing requires elastic human body models. The detailed FEM models as for instance THUMS (Total Human Model for Safety) (Toyota THUMS Webpage) for car crash simulations are unnecessary accurate, computational intensive and not practicable for clothing and other product development processes. For correct simulation of the mechanical interaction a full-scale FEM Models of the humans with enough suitable accuracy and complexity, but at efficient computation and often in specific poses are required. This works presents the development steps and current state of an algorithm for automatic solid FEM mesh generator for human bodies, based on high speed 3D (4D) scan data.

Methods

The data from the 3D scanner is used for two purposes: a) for detection of the main sizes of the bones of the human body and b) the surface mesh is used as a basis for the building of the inner solid layers of the skin, inner soft structures and the bones.

The high speed 3D scanning (4D scanning) hardware obtains all data points within milliseconds. This allows accurate reconstruction of the body geometry at different poses, and does not contain the errors from the human body during its motion and breath as the classical and slower 3D scanning process. The multiple frames allow reconstruction of the deformations of the body during the motion (Figure 1). After the triangulation of the raw data points and closing the geometry to watertight mesh (Figure 1b), one closed mesh for the body at each pose is available. The workflow, described in Figure 2 is applied for the construction of the FEM mesh from the scan data. After filling the closed boundary of the body surface with solid elements, different level of accuracy can be applied. The bone geometry has to be scaled to the size of the human and after that based on their position, the suitable material properties are applied on the solid elements in this region. The procedure is implemented currently in its initial simplified form within

gmsh Software and python script, where the bones are considered only in some parts of the body (legs) and are approximated as cylinders.

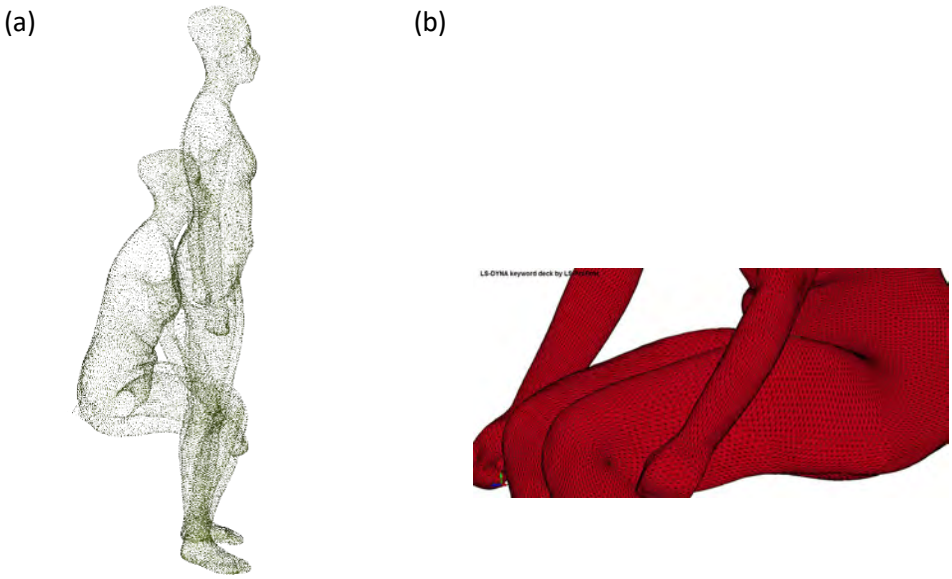

Figure 1. Scanned human geometries a) raw points of a human at two different positions after high speed 3D body scanning with MOVE4D b) triangulated mesh of the body at one position

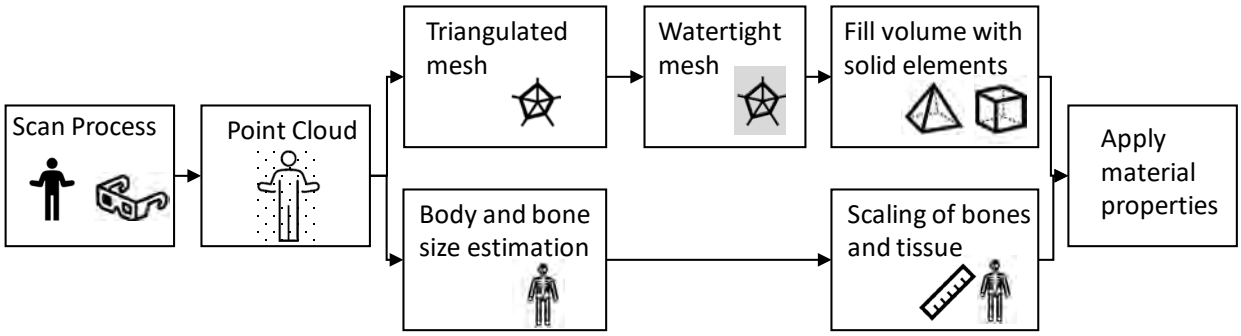

Figure 2. Workflow for the homogenized FEM mesh generation

References

https://www.toyota.co.jp/thums/

Y. Kyosev and Doudou Zhang, "Algorithmic Issues During the FEM Mesh Preparation of Human Models Based on 3D body Scans", Proc. of 3DBODY.TECH 2020 - 11th Int. Conf. and Exh. on 3D Body Scanning and Processing Technologies, Online/Virtual, 17-18 Nov. 2020, #48, https://doi.org/10.15221/20.48.

Simulation of hip joint location for occupant packaging design

Estela Perez Luque, Erik Brolin, Maurice Lamb, and Dan Högberg
University of Skövde, Sweden

Abstract

DHM tools have been widely used to analyze and improve vehicle occupant packaging and interior design in the automotive industry. However, these tools still present some limitations for this application. Accurately characterizing seated posture is crucial for ergonomic and safety evaluations. Current human posture and motion predictions in DHM tools are not accurate enough for the precise nature of vehicle interior design, typically requiring manual adjustments from DHM users to get more accurate driving and passenger simulations. Manual adjustment processes can be time-consuming, tedious, and subjective, easily causing non-repeatable simulation results. These limitations create the need to validate the simulation results with real-world studies, which increases the cost and time in the vehicle development process. Working with multiple Swedish automotive companies, we have begun to identify and specify the limitations of DHM tools relating to driver and passenger posture predictions given predefined vehicle geometry points/coordinates and specific human body parts relationships. Two general issues frame the core limitations. First, human kinematic models used in DHM tools are based on biomechanics models that do not provide definitions of these models in relation to vehicle geometries. Second, vehicle designers follow standards and regulations to obtain key human reference points in seated occupant locations. However, these reference points can fail to capture the range of human variability. This paper describes the relationship between a seated reference point and a biomechanical hip joint for driving simulations. The lack of standardized connection between occupant packaging guidelines and the biomechanical knowledge of humans creates a limitation for ergonomics designers and DHM users. We assess previous studies addressing hip joint estimation from different fields to establish the key aspects that might affect the relationship between standard vehicle geometry points and the hip joint. Then we suggest a procedure for standardizing points in human models within DHM tools. A better understanding of this problem may contribute to achieving closer to reality driving posture simulations and facilitating communication of ergonomics requirements to the design team within the product development process.

Keywords: hip joint, H-point, seated reference point, simulation, digital human modelling

Introduction

Occupant packaging primarily aims to accommodate an intended range of drivers and passengers within the vehicle. However, this primary aim also constitutes one of the significant challenges, accommodating a maximal group of target users. Ideally, a vehicle will be designed to meet occupant needs while considering human diversity (Gkikas, 2016). Digital human modelling (DHM) tools have been widely used to analyze and improve vehicle occupant packaging and interior design in the automotive industry. However, these tools still present some limitations for this application. Current human posture and motion predictions in DHM tools are not accurate enough for the precise nature of vehicle interior design, hence typically requiring manual adjustments from DHM users to get more accurate driving and passenger simulations (Bhise, 2016; Brolin et al., 2020). Manual adjustment processes can be time-consuming, tedious, and subjective, easily causing non-repeatable simulation results. These limitations create the need to validate the simulation results with real-world studies, which increases the cost and time involved in the vehicle development process (Lämkull & Zdrodowski, 2020).

Working with multiple Swedish automotive companies, we have begun to identify and specify the limitations of DHM tools relating to driver and passenger posture predictions given predefined vehicle geometry points/coordinates and specific human body parts relationships. Two general issues frame the core limitations. First, human kinematic models used in DHM tools are based on biomechanics models that do not provide definitions of these models in relation to vehicle geometries. Second, vehicle designers follow standards and regulations to obtain key human reference points in seated occupant locations. However, these reference points can fail to capture the range of human variability. DHM tools aim to represent digital human models (manikins) within detailed CAD environments for analyzing and evaluating human interactions. Moreover, a lack of clear connections between occupant packaging guidelines and human biomechanical knowledge creates a limitation for ergonomics designers using DHM tools as they are not necessarily experts on all the nuances in both the guidelines and biomechanics. Perez Luque et al. (2022) reported that one of the main issues in vehicle development is the lack of accurate and reliable driving task simulation predictions. The lack of understanding and standardized procedures to make the manikin adopt the initial driving posture realistically means that ergonomics designers rely on their perception or expertise for quantifying driver seated positions and the consequential occupant packaging analyses.

This paper describes the relationship (or lack of it) between seated reference point in seat geometries and the hip joint for driving simulations, and presents an approach to sit manikins in a virtual environment considering geometric reference points and human body shape.

Problem description

Understanding and quantifying the initial seated posture is crucial for ergonomic and safety evaluations because the design and development of other ergonomic requirements such as seated posture comfort, operating controls, and interior and exterior visibility depend on it. Moreover, it is imperative to consider a diverse population with different body types and preferences to ensure a good fit for end-users (Gkikas, 2016). Successful vehicle interior design requires involvement insights from various fields, including biomechanics, ergonomics, engineering, and design. However, there is a lack of standardized methodologies connecting the different fields.

Ergonomics designers in automotive companies follow standards and legislation within occupant packaging and vehicle design. Standards, such as SAE and ISO, provide recommended tools and practices for defining key reference points, which specify the relative positions of the occupants with vehicle components. One of the essential reference points is the H-point (sometimes called the hip point). The H-point describes a theoretical intersection of a reference occupant's torso and thigh lines (Gkikas, 2016). This means that the H-point simulates but does not precisely represent the human mid-hip joint location and its variability across people. The location of the H-point relative to a physical seat is commonly determined using the H-point machine (HPM-II) (Figure 1), which will be called HPM in this paper, and which can be physical or digital (Reed et al., 1999; Yang et al., 2014; ISO 20176, 2020). Vehicle manufacturers define a vehicle design-specific H-point, the seated reference point (SgRP), as a fundamental reference point for determining seating location for occupant packaging and vehicle dimensions (Bhise, 2016). The SgRP enables correlation between physical and virtual environments, and provides a consistent method for comparing vehicles. While fixed seats have only one H-point position (the H-point and SgRP is the same point), adjustable seats have more than one H-point location. All these H-point locations are mapped and described in the seat movement envelope, hence representing an area rather than a point. The representation of the H-point in the virtual environment can be used as a reference point to position manikins since it does not say how they sit, but rather where they sit. However, using such standards does not ensure the consideration of human diversity and variability sufficiently.

An alternative to starting with design standards is to investigate human body angles in driving situations to determine expected human driving postures. Over the years, many authors have followed this approach from the biomechanical and ergonomic design fields, mainly focusing on values of subjective comfort,

human structure and functions in driving situations (Schmidt et al., 2014). However, the results of these works are typically not specified in terms of actual vehicle reference points, making it difficult or impossible to apply the results in current design contexts without significant effort. Moreover, authors often consider and observe variability in posture among different factors, including gender, anthropometric measurements, age, symmetry, seat design, vehicle model, and driving venue (Reed et al., 2002; Schmidt et al., 2014; Park et al., 2016a). While these studies focus on human driving posture and body joint angles, they rarely define the relation of those angles to the driver seat geometries, limiting their current influence on DHM tools and design processes in general.

Figure 1. Physical HPM-II model (ISO 20176, 2020)

Park et al. (2016) have developed a data-based prediction model for passengers considering body dimensions, age, and gender from humans with reference to vehicle layout measurements. This model follows a "cascade" approach, in which the most relevant variables are predicted first, followed by less important variables. One component of this model is a regression model, which predicts the mid-hip location to the H-points of the automotive seat. The main limitations of this study include the fixed position of the backrest angle, the use of a non-naturalistic laboratory setting and the limitation to participants in the USA. Reed et al. (2019) expanded this model for pelvis position and rotation in the automotive seat by including data from highly reclined postures in automotive seats. They concluded that the spine and pelvis posture changes as the torso reclines in an automotive seat.

While existing human posture studies have been used to develop data-driven and optimization methods, some additional considerations complicate predicting hip joint locations related to vehicle geometries. The appearance of the manikins in DHM tools can lead to different and/or inaccurate predictions when it is tied to collision volumes determining the boundaries of the manikin relative to the seat geometry (Lämkull et al., 2007; Lämkull & Zdrodowski, 2020). Thus, even with possibly accurate predictions of where the mid-

hip should be placed, ergonomics designers may modify the manikin's position and posture until the manikin body shape looks appropriately aligned to the automotive seat and realistically represents a human-vehicle interaction. Brolin et al. (2020) introduced DHM functionality which uses the mid-hip to H-point relationship from Park et al. (2016) together with constraints and adjustment ranges of vehicle components to statistically predict seated driving postures. Even though the results were promising, initial comparisons of such predictions with data from user tests showed some differences, which indicates that further research is needed.

In this paper, we compare the regression models from Park et al. (2016) with an approach to seat manikins in driving environments using more realistic human body meshes with a wide range of body mass index (BMI).

Approaches for initial seated driving posture

Several DHM tools are currently used for occupant packaging and automotive design like Ramsis, Santos, Jack Siemens, and IPS IMMA. While these tools are based on different modelling and prediction methods for defining the seated driving posture, they all mostly follow the same procedure for adopting the initial seated driving posture. A *DHM standard procedure*, identified in discussions with companies, consists of the following steps: First, DHM users make the manikin or manikin family assume the driving posture, which is generally defined by the DHM software following specifying angles according to a particular study. Second, constraints are set to fulfil basic requirements and get an initial seated driving posture consistent across manikins and simulations. These constraints or requirements are typically defined in the feet (e.g. heels should take up support, right foot on the accelerator pedal), grip points on the steering wheel, eye or mid-eye vector to define the head direction, and top of the head to ensure the manikin stays within a particular space. Finally, manual adjustments are often made. Typically, the mid-hip, torso or the automotive seat position are manually adjusted and constrained to get postures visibly fitting the seat geometry, following the ergonomics designer criteria. Notably, this DHM procedure has a limitation of not having any clear and direct relationship relating the mid-hip point and the H-point and the adjustment range of the seat. So, even if the manikin has "optimal angles", we would not know how or where to place it in the automotive seat.

As an attempt to fill this gap, in this paper, an approach is presented as an alternative to the previous ones to be able to sit manikins realistically and consistently while considering the standards and legal requirements for occupant packaging, a wide range of BMI, and the mid-hip and H-points relationship in driving environments. This approach was compared to the *Statistical Prediction* approach proposed by Park et al. (2016), which showed some issues for particular cases as mentioned in the literature.

Method

Figure 2 summarises the main steps of the *Body Shape Alignment*, the proposed approach in this paper. The first step consists of loading a virtual template of the HPM in the digital environment and positioning it in the vehicle direction. Next, the H-point of the HPM template should be aligned to the SgRP of the driver seat as well as the HPM template surfaces to the driver seat surfaces. Once the HPM template is correctly aligned to the seat, the manikin should be aligned to the HPM template surfaces. As the last step, the coordinates of the SgRP, H-point and mid-hip point could be extracted from DHM software to analyze the relationship or offset between these different variables further.

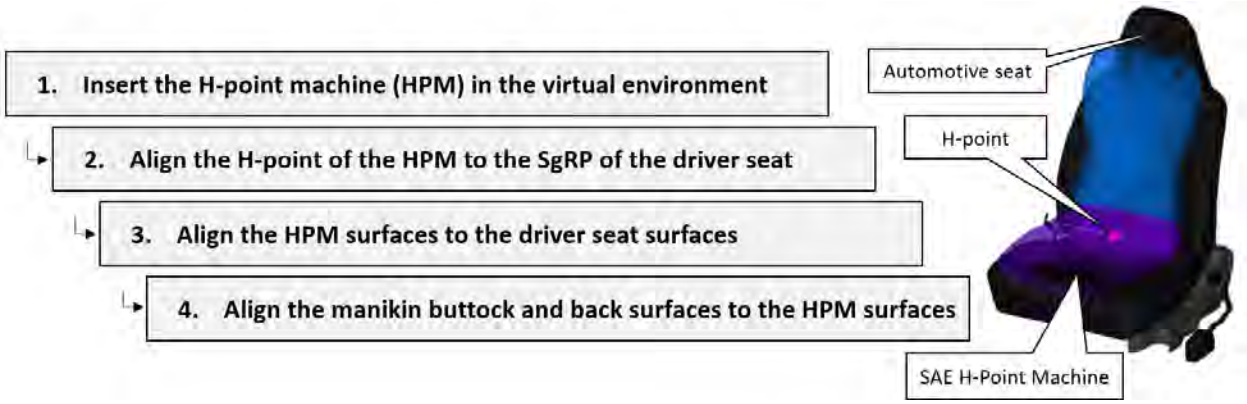

Figure 2. Body Shape Alignment approach.

Comparison procedure

The Statistical Prediction and Body Shape Alignment approaches were used to sit manikins in virtual driving environments using a wide range of BMI human body meshes. The automotive vehicle model was a Volkswagen Beetle from the training repository of Siemens Jack (Siemens, 2017). The human body meshes were obtained from the BioHuman website (*UMTRI BioHuman*, 2022) which provides 3D manikin meshes based on statistical analyses of high-resolution laser scans. The human body meshes were used for the comparison of seated driving approaches due to their closer to reality appearance. A manikin family of 7 females and 7 males was considered in the simulations. The anthropometric measurements of the manikin family were generated from two three-dimensional boundary ellipsoids, with a confidence level of 90% (Brolin et al., 2012). One ellipsoid for each sex, based on stature, body weight, and sitting height. The anthropometric data was taken from the CAESAR data set (Robinette et al., 2002). In addition to an average manikin case for each sex, six manikin cases were defined at the ends of the three axes of each of the two

ellipsoids. US population was selected on the BioHuman website to generate the meshes since the regressions models of the Statistical Prediction from Park et al. (2016) are done considering the US population. 40 years was the defined age for all the manikins. Table 1 describes the anthropometric measurements of the manikin family. It should be noted that the generated test manikins span a more extensive range of BMI values compared to the sample from Park et al. (2016), which might affect the results. However, the measurement combinations of the generated test manikins are realistic and could be found within the CAESAR data set, which motivates the use of these more extreme test manikins.

Table 1. Anthropometric measurements of the manikin family cases.

Manikins	Body weight (kg)	Stature (mm)	Sitting height (mm)	BMI (kg/m^2)	Manikins	Body weight (kg)	Stature (mm)	Sitting height (mm)	BMI (kg/m^2)
Case F1	65	1639	865	24	**Case M1**	83	1775	926	26
Case F2	95	1814	949	29	**Case M2**	124	1974	1018	32
Case F3	50	1475	785	23	**Case M3**	61	1604	836	24
Case F4	47	1678	893	17	**Case M4**	62	1818	959	19
Case F5	115	1600	837	45	**Case M5**	122	1734	892	40
Case F6	64	1695	838	22	**Case M6**	82	1834	899	24
Case F7	66	1584	891	26	**Case M7**	85	1719	953	29

Results

Figure 3 shows the human mid-hip to the H-point of the automotive seat locations using the Statistical Prediction and Body Shape Alignment approaches. Figure 4 shows the initial driving posture of the human body meshes by using the Statistical Prediction and the Body Shape Alignment. It can be seen how the meshes in the former are more spread on the x-axis compared to the second approach (Figure 4).

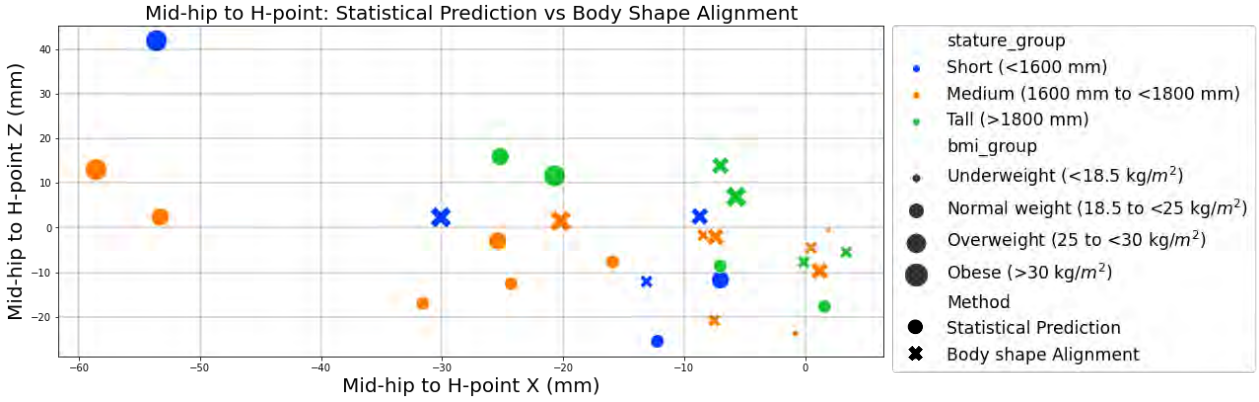

Figure 3. Mid-hip to H-point: Statistical Prediction vs Body Shape Alignment.

The most evident differences in the mid-hip to the H-point location were observed concerning the BMI. Figures 3 and 4 show how manikins with higher BMI move forward in the x-axis with the Statistical

Prediction approach. This might not be seen as a problem at first. However, the gap between the manikin with higher BMI and the seat is significantly evident when observing the human body meshes in such a position. That would lead to manual adjustments, making the statistical prediction not accurate. On the other hand, it can be seen how the spread in the x and z-axis is not as wide with the Body Shape Alignment as with the Statistical Prediction.

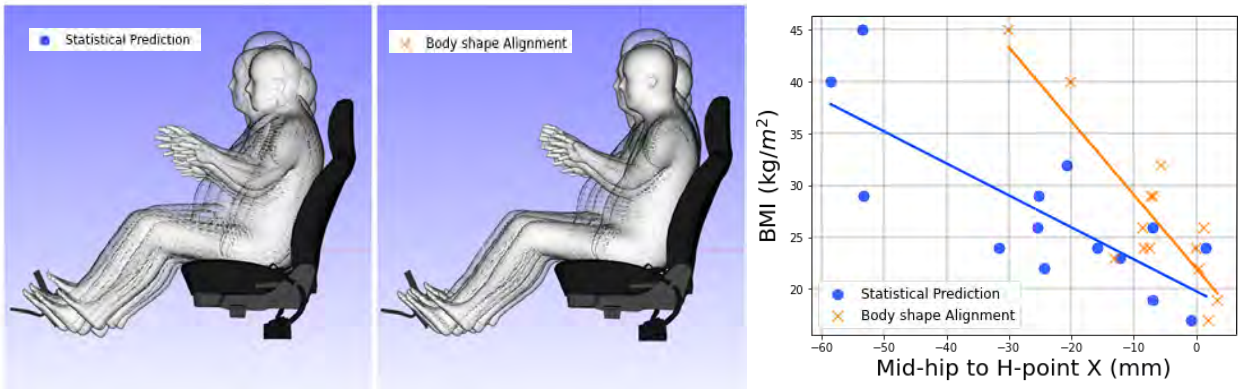

Figure 4. Initial seated driving posture: Statistical Prediction (left) and Body Shape Alignment (right).

Discussion and Conclusion

The presented Body Shape Alignment is an procedure for seated driving posture. Although the results show that obtaining the initial seated driving posture is possible, it needs further development. In its current state, it predicts the mid-hip to the H-point location of the automotive seat in a standardised way considering standards and legal requirements and human body shape variability. However, this initial procedure might involve subjectivity in the alignments. This can be fixed by further defining appropriate constraints between the automotive seat, HPM, and the manikins or body shapes meshes in the virtual environment. In this way, if you move the seat, the H-point's location and the mid-hip point's prediction will also move. The human body meshes used in the comparison were calculated with sex, stature, BMI, SH/S, and age from the BioHuman framework. However, people with the exact anthropometric measurements could also have different body shapes. Fit people could have BMI rates of overweight people due to the larger muscle mass. That is not reflected in the presented study. In addition, changing the body joint angles of the meshes was not possible since it is defined in the 3D mesh generation from the BioHuman framework. Going further, the use of the body shape alignment approach for getting a proper initial driving posture relies on, and therefore requires, accurate human body meshes within DHM software. The accuracy of the body shape alignment approach could be further advanced by implementing models regarding seat foam and human buttock deformation (Wang et al., 2021). The mid-hip location prediction on the human body shapes could

also be further advanced, e.g. by considering the study from Brynskog et al. (2021), in which detailed pelvis geometry is predicted with overall anthropometric variables. While the presented approach seems to have consistent results across different anthropometries, more research is needed to know, for example, if this approach applies to non-US populations and other types of vehicles.

Figure 4 shows that the more considerable differences between mid-hip to H-location with different approaches come as the BMI increases. One reason could be the limited representation of people with higher BMI values in the developed regression models compared to the manikin family used in this study. In addition, measurement errors could occur since the mid-hip is a problematic and challenging point to identify. At the same time, the differences could have been due to the estimations of the mid-hip point in the human body meshes used in this study. While previous studies have found mid-hip locations typically forward of the H-point (Reed et al., 2002; Park et al., 2016a, 2016b), it can be seen in this study that various mid-hip locations are slightly rearward of seat H-point, as shown in Reed et al. (2019). Delving deeper into these mid-hip to H-point differences, we should consider the postural diversity within a population. Then, what can be viewed as a postural variety and an error? What can be considered an accurate initial driving posture? The Statistical Prediction approach includes root mean square error (RMSE) that could be used to represent human diversity. However, while statistical predictions can be beneficial, we should also consider that such values are determined for the specific conditions and population of that study and might be limited to use in other conditions, vehicle types, and different populations. The driving posture was different in the past and will be different in the future, especially considering the introduction of autonomous vehicles and new concepts of transportation (Yang et al., 2019). Simulation and evaluation of different sitting postures and non-driving related activities are becoming critical for developing future vehicles in regards to ergonomics and safety. When modelling human-product interactions, the main challenge comes with the need to be able to predict any possible interaction (in existing and future vehicles) accurately and realistically. Further research is required to identify and define suitable interaction models for engineering design covering a universal valid approach.

Acknowledgements

This work has been made possible with the support from the Knowledge Foundation in Sweden in the project ADOPTIVE- Automated Design and Optimisation of Vehicle Ergonomics, and SAFER - Vehicle and Traffic Safety Centre at Chalmers, Sweden, and by the participating organizations. This support is gratefully acknowledged. The authors would also like to acknowledge the resource of online body shape models provided by UMTRI/BioHuman research group at the University of Michigan.

References

Bhise, V. D. (2016). Ergonomics in the Automotive Design Process. CRC Press. https://doi.org/10.1201/b11237

Brolin, E., Högberg, D., & Hanson, L. (2012). Description of boundary case methodology for anthropometric diversity consideration. International Journal of Human Factors Modelling and Simulation. https://www.inderscienceonline.com/doi/10.1504/IJHFMS.2012.051097

Brolin, E., Högberg, D., & Nurbo, P. (2020). Statistical Posture Prediction of Vehicle Occupants in Digital Human Modelling Tools. HCI. https://doi.org/10.1007/978-3-030-49904-4_1

Brynskog, E., Iraeus, J., Reed, M. P., & Davidsson, J. (2021). Predicting pelvis geometry using a morphometric model with overall anthropometric variables. Journal of Biomechanics, 126, 110633. https://doi.org/10.1016/j.jbiomech.2021.110633

Gkikas, N. (Ed.). (2016). Automotive Ergonomics: Driver-Vehicle Interaction (1st edition). CRC Press.

ISO 20176. (2020). Road vehicles – H-point machine (HPM-II) – Specifications and procedure for H-point determination.

Lämkull, D., Hanson, L., & Örtengren, R. (2007). The influence of virtual human model appearance on visual ergonomics posture evaluation. Applied Ergonomics, 38(6), 713–722. https://doi.org/10.1016/j.apergo.2006.12.007

Lämkull, D., & Zdrodowski, M. (2020). The Need for Faster and More Consistent Digital Human Modeling Software Tools. IOS Press, 12. https://doi.org/10.3233/ATDE200037

Park, J., Ebert, S. M., Reed, M. P., & Hallman, J. J. (2016a). A statistical model including age to predict passenger postures in the rear seats of automobiles. Ergonomics, 59(6), 796–805. https://doi.org/10.1080/00140139.2015.1088076

Park, J., Ebert, S. M., Reed, M. P., & Hallman, J. J. (2016b). Statistical Models for Predicting Automobile Driving Postures for Men and Women Including Effects of Age. Human Factors: The Journal of the Human Factors and Ergonomics Society, 58(2), 261–278. https://doi.org/10.1177/0018720815610249

Perez Luque, E., Brolin, E., Högberg, D., & Lamb, M. (2022). Challenges for the Consideration of Ergonomics in Product Development in the Swedish Automotive Industry – An Interview Study. Proceedings of the Design Society, 2, 2165–2174. https://doi.org/10.1017/pds.2022.219

Reed, M. P., Ebert, S. M., & Jones, M. L. H. (2019). Posture and belt fit in reclined passenger seats. Traffic Injury Prevention, 20(sup1), S38–S42. https://doi.org/10.1080/15389588.2019.1630733

Reed, M. P., Manary, M. A., Flannagan, C. A. C., & Schneider, L. W. (2002). A Statistical Method for Predicting Automobile Driving Posture. Human Factors: The Journal of the Human Factors and Ergonomics Society, 44(4), 557–568. https://doi.org/10.1518/0018720024496917

Reed, M., Roe, R., & Schneider, L. (1999). 999-01-0963 Design and Development of the ASPECT Manikin. https://doi.org/10.4271/1999-01-0963

Robinette, KM., Blackwell, S., Daanen, H., Boehmer, M., Fleming, S., Brill, T., Hoeferlin, D., & Burnsides, D. (2002). Civilian American and European surface anthropometry resource (CAESAR). Air Force Research Laboratory, Wright-Patterson AFB, OH, and Society of Automotive Engineers International, Warrendale, PA., 70.

Schmidt, S., Amereller, M., Franz, M., Kaiser, R., & Schwirtz, A. (2014). A literature review on optimum and preferred joint angles in automotive sitting posture. Applied Ergonomics, 45(2), 247–260. https://doi.org/10.1016/j.apergo.2013.04.009

Siemens. (2017). Jack version 9.0, California, USA: Siemens Product Lifecycle Management Software Inc. https://www.plm.automation.siemens.com/store/en-us/index.html

UMTRI BioHuman: 3D Human Shapes. (2022). http://humanshape.org

Wang, X., Savonnet, L., Capbern, L., & Duprey, S. (2021). A Case Study on the Effects of Foam and Seat Pan Inclination on the Deformation of Seated Buttocks Using MRI. IISE Transactions on Occupational Ergonomics and Human Factors, 9(1), 23–32. https://doi.org/10.1080/24725838.2021.1984340

Yang, J., Lee, I., Choi, H., & Sah, S. (2014). Development of aspect dummy considering seat dimension factor. Journal of Mechanical Science and Technology, 28(7), 2489–2492. https://doi.org/10.1007/s12206-014-0606-4

Yang, Y., Klinkner, J. N., & Bengler, K. (2019). How Will the Driver Sit in an Automated Vehicle? – The Qualitative and Quantitative Descriptions of Non-Driving Postures (NDPs) When Non-Driving-

Related-Tasks (NDRTs) Are Conducted. In S. Bagnara, R. Tartaglia, S. Albolino, T. Alexander, & Y. Fujita (Eds.), Proceedings of the 20th Congress of the International Ergonomics Association (IEA 2018) (pp. 409–420). Springer International Publishing. https://doi.org/10.1007/978-3-319-96074-6_44

Using Santos Pro™ trade-off analysis to inform the rear chassis design of a novel electric scooter

Steven Fischer, Justin Davidson, and Sanjay Veerasammy

University of Waterloo, Canada

Abstract

The need for nimble, eco-friendly transportation solutions in metropolitan areas continues to rise. To meet this need companies have begun to design and manufacture small profile, high payload, electric scooters. Yet, balancing the claim space requirements for payload, mechanical systems, and the battery pack while also maintaining effective occupant packaging considerations is a challenge. The claim space required for a battery that can sustain a sufficient driving range (>150km) directly influences the shape and size of the rear chassis. However, the size and shape of the rear chassis also influences the potential for an occupant's heel and calf to catch under the rear chassis when raising or lowering a foot for balance during common vehicle maneuvers.

The aim of this analysis was to identify possible collision points between the heel or calf of a 50th and 95th percentile male stature occupant and the rear chassis when lowering a foot towards the ground when the scooter was in upright and tilted by 30° positions (turning).

Santos Pro™ (SantosHuman Inc., Coralville, IA) was used to model the required occupant behaviors. The Zone Differentiation tool then generated a range of motion volume map for the calf and heel assuming a seated occupant posture. The volume map was overlaid on the geometry to assist the engineering team in visualizing possible collision points for each avatar. The engineering team was able to revise the geometry for the rear chassis to reduce overlaps with the heel and calf volume map, while also maintaining minimum claim space needs for the battery pack. The improved rear chassis design was then imported into the Santos Pro™ software to visualize and verify the reduction of potential collision locations.

Santos Pro™ provided a time-efficient design-on-the-fly method to understand the potential severity of, and to correct, a heel and calf clearance concern within early-stage CAE. By evaluating the clearance concern proactively, the problem was quantified and solved within days, prior to costly physical prototyping and human testing.

Keywords: scooter, upstream design, CAE, virtual prototyping.

Identifying the best objective function weightings to predict comfortable motorcycle riding postures.

Justin Davidson and Steven Fischer
University of Waterloo, Canada

Abstract

Appropriate motorcycle design is essential to mitigate the discomfort and fatigue that a rider may experience. This can be achieved by combining computer-aided engineering and digital human modeling to investigate interactions between motorcycles and riders prior to developing physical prototypes. When predicting riding postures for novel designs, it is useful to use optimization-based predictive models. However, to effectively use optimization, it is important to know what objective function(s) and associated weightings are necessary to predict realistic riding behaviors.

The purpose of this analysis was to identify the objective function weightings that best predict preferred riding postures.

A scoping review was conducted to identify preferred riding postures based on experimental data. Santos Pro™ was used in manual manipulation mode to recreate a preferred (gold standard) riding posture. Posture prediction mode was then used to predict riding postures using various objective functions which can be applied and weighted in Santos Pro™. However, it is unclear which weightings would predict the closest posture to the gold standard. Therefore, a response surface methodology was used to compute joint angle errors between the gold standard and predicted postures. The predicted postures used combinations of three minimization objective functions: (1) discomfort, (2) joint displacement, and (3) maximum joint torque, at varying weights (0-100%). Both 50th and 95th percentile males and females were analyzed. Error results were fit with a multivariate model, which was minimized to estimate the objective function weights that resulted in the lowest error between the gold standard and predicted postures.

When averaging the best objective function weighting results across all avatars, the estimated best objective function weighting combination was 100%, 24%, and 0% for discomfort, joint displacement, and maximum joint torque objective functions, respectively. These results indicate that the best way to model comfortable riding postures is to weight the minimize discomfort objective highly. The response surface method was able to provide an empirical means to identify the best objective function weights. By

determining the best weighting combinations needed to model rider postures, end-users can quickly evaluate the influence of a structural design change within a virtual environment.

Keywords: motorcycle, posture prediction, CAD, objective function weighting

Analysis of the influence of non-driving related activities on seat parameters and sitting postures

Manuel Kipp[1]

[1]Technical University of Munich, TUM School of Engineering and Design, Chair of Ergonomics, Garching, Boltzmannstraße 15, 85748, Germany

Keywords: Non-Driving Related Tasks and Activities, Autonomous Vehicles, Seat Parameter, Digital Human Modeling

Abstract

Changing mobility scenarios are leading to innovative vehicle concepts. The absence of the driver has opened up a wide range of modified interiors and seating configurations for highly automated vehicles, which are the focus of research.

With the ongoing automatization in the car industry, new questions arise about human factors. From SAE level 3, conditional driving automation allows the driver to disengage from the driving task without the need for supervision. With an increasing degree of automation, the active vehicle driver is transformed into a passive vehicle passenger. This gives the driver the possibility to deal with non-driving related activities and tasks (NDRA, NDRT) whenever the automation is active. The question of what people are likely to do during an automated ride has mostly been addressed via online surveys or by analyzing other means of transportation like train and bus. Various studies examining train or bus journeys using different methods such as (online) surveys or observation of passengers in different means of transport show a wide variety of activities such as listening to music, looking at the surroundings, relaxing, talking on the phone, reading or working, and the use of electronic devices such as laptops, tablets and smartphones [1-2]. Other studies additionally examined seating parameters such as seat and recline angle [3-8].

However, knowing about desired activities allows researchers and developers to design future car interior including seat and seating position, internal HMI, air-conditioning and the automated driving functions according to user needs. Highly automated and autonomous vehicles enable different seating postures. Space in front of the seat allows the passenger more range for movement and postures [4]. Moreover, several studies contribute to the space managements of interior design in the future and show significant effects of NDRTs on driving postures concerning the seat positions and backrest angles [3,8].

The vehicle interiors are always designed to suffice the ergonomic requirements and enhance passenger comfort. The shift of focus from the primary task of driving to using the travel time for various NDRTs was the basis for this research. This research considers the transitional change in automotive development in transfer of vehicle control completely to the car and it evaluates its impact on the seat parameter regarding NDRTs. Change in occupant orientation and activities undertaken during the travel in a fully autonomous vehicle will affect the conventional movement space considerations in the vehicles. The occupant orientation, positions and tasks performed while travelling have an influence on the interior volume and layout. Thus, the possibility of new seat constellations will influence the spatial considerations.

The following research analyses the influences of NDRTs on seat parameters, which seat and backrest settings need to be adjusted for each activity. Furthermore, it is discussed, what main groups of NDRT for each seat setting can be classified. With the help of RAMSIS^{TM} different seating postures for each activity are simulated.

References

[1] Hecht, T., Darlagiannis, E., & Bengler, K [Klaus] (2020). Non-driving Related Activities in Automated Driving – An Online Survey Investigating User Needs. In T. Z. Ahram, W. Karwowski, S. Pickl, & R. Taiar (Eds.).

[2] Pfleging, B., Rang, M., & Broy, N. (2016). Investigating user needs for non-driving-related activities during automated driving. In Proceedings of the 15th International Conference on Mobile and Ubiquitous Multimedia - MUM '16 (pp. 91–99). ACM Press. https://doi.org/10.1145/3012709.3012735Jorlöv, S., Bohmann, K., Larsson, A. (2017). Seating Positions and Activities in Highly Automated Cars – A Qualitative Study of Future Automated Driving Scenarios

[3] Fleischer, Martin; Wendel, Nikko: Desirable Backrest Angles in Automated Cars. In: Communications in Computer and Information Science. Springer International Publishing, 2021

[4] Fleischer, Martin; Li, Rongqian: Spatial Needs for Non-driving Related Activities. In: Wright, Barber et al. (Hrsg.): Advances in Simulation and Digital Human Modeling. Springer International Publishing, 2021

[5] Parida, S., Mallavarapu, S., Abanteriba, S., Franz, M., & Gruener, W. (2019). Seating Postures for Autonomous Driving Secondary Activities. In Y.-W. Chen, A. Zimmermann, R. J. Howlett, & L. C. Jain (Eds.), Smart innovation, systems, and technologies: Vol. 145, Innovation in medicine and healthcare systems, and multimedia: Proceedings of KES-InMed-19 and KES-IIMSS-19 conferences / editors Yen-Wei Chen, Alfred Zimmermann, Robert J. Howlett and Lakhmi C. Jain (pp. 423–434). Springer Nature : Springer.

[6] Parida, S., Mallavarapu, S., Franz, M., & Abanteriba, S. (2019). A Literature Review of Seating and Body Angles for Non-driving Secondary Activities in Autonomous Driving Vehicles. In N. A. Stanton (Ed.), Advances in intelligent systems and computing, 2194-5357: volume 786, Advances in human aspects of transportation [electronic resource]: Proceedings of the AHFE 2018 International Conference

on Human Factors in Transportation, July 21-25, 2018, Loews Sapphire Falls Resort at Universal Studios, Orlando, Florida, USA / Neville Stanton, editor (pp. 398–409). Springer.

[7] Jorlöv, S., Bohmann, K., Larsson, A. (2017). Seating Positions and Activities in Highly Automated Cars – A Qualitative Study of Future Automated Driving Scenarios

[8] Yang, Y., Klinkner, J. N., & Bengler, K [Klaus]. (2019). How Will the Driver Sit in an Automated Vehicle? – The Qualitative and Quantitative Descriptions of Non-Driving Postures (NDPs) When Non-Driving-Related-Tasks (NDRTs) Are Conducted. In S. Bagnara, R. Tartaglia, S. Albolino, T. Alexander, & Y. Fujita (Eds.)

Evaluation of Upper Body Postural Assessment of Forklift Driving using a Single Depth Camera

Veeresh ELANGO [a,b,1], Simona PETRAVIC [b] and Lars HANSON [a,b]

[a] *University of Skövde, School of Engineering Science, 541 28 Skövde, Sweden*

[b] *Scania CV, Södertälje, Sweden*

Abstract

Observational postural assessment methods which are commonly used in industry are time consuming and have issues of inter- and intra-rater reliability. Computer vision (CV) based methods have been proposed, but they have mainly been tested inside lab environments. This study aims to develop and evaluate an upper body postural assessment system in a real industry environment using a single depth camera and OpenPose for the task of forklift driving. The results were compared with XSens, an Inertial Measurement Unit (IMU) based system. Data from three forklift drivers performing seven indoor and outdoor tasks were recorded with a depth camera and XSens sensors. The data were then analyzed with OpenPose with additional custom processing. The angles calculated by the computer vision system showed small errors compared to the XSens system and generally followed the trend of the XSens system joint angle values. However, the results after applying ergonomic thresholds were vastly different and the two systems rarely agreed. These findings suggest that the CV system needs further study to improve the robustness on self-occlusion and angle calculations. Also, XSens needs further study to assess its consistency and reliability in industrial environments.

Keywords: upper body postural assessment, forklift driving, depth camera, OpenPose.

Introduction

Occupational ergonomics is a discipline which attempts to adapt the job to the worker with the goal of promoting worker health, safety, comfort, and productivity (Frederick et al., 1984). The promotion and maintenance of good occupational ergonomics reduces the risk of chronic injuries and illnesses, and consequently decreases the cost incurred by lost productivity, sick leave, and medical care (Kok et al., 2020). Forklift driving in industry is one of the work tasks linked to increased risk of upper body problems (Flodin et al., 2018; Viruet et al., 2008). The risk factors are commonly identified and managed using observational methods based on direct on-site observation or watching recorded videos of workers performing their usual tasks. Examples of such methods for postural assessment are RULA (McAtamney

& Nigel Corlett, 1993), REBA (Hignett & McAtamney, 2000), and RAMP (Lind et al., 2014). Apart from requiring a time-consuming manual analysis, the major disadvantage of observational ergonomic assessments is that they are heavily subjective which leads to considerable intra- and inter-rater variability (Burdorf et al., 1992; Fagarasanu & Kumar, 2002).

Industry 4.0 has led to the incorporation of motion capture (MoCap) solutions in industrial applications for improving processes and productivity, with a focus on workers' health and safety (Menolotto et al., 2020). In line with that, low-cost MoCap systems based on computer vision (CV) have been researched to solve the aforementioned posture assessment problems. One such MoCap solution is OpenPose, a real-time multi-person 2D pose estimation system, which has been used for postural assessments with both 2D (Lin et al., 2022) and 3D approaches (Kim et al., 2021). These studies have shown that OpenPose has acceptable accuracy for posture assessment with joint angle errors of 8.0° and 8.4° respectively.

Previous studies on CV solutions for postural assessments were mainly constrained to lab simulations. Factors such as spatial constraints, limited field of view, (self-)occlusions, and external interference (light conditions, vibrations) could deteriorate the performance of the aforementioned solutions (Menolotto et al., 2020), and these factors are often present in industry environments such as forklift driving. To the best of the authors' knowledge, no studies have been performed to evaluate postural assessment in forklift driving in industry using a CV system.

Therefore, the aim of this paper is to develop and evaluate an upper body postural assessment system for forklift driving in a real industry environment using a single depth camera and OpenPose.

Methods

Computer Vision System Setup

A single depth camera (Intel RealSense D455) was rotated vertically and positioned in front of the driver at an angle of 45° above their head, to obtain the best view on the operator's upper body posture, as shown in Figure 1. Forklift driving has low possibility of external occlusions between the driver and camera. To calculate all angles needed for upper body posture analysis including neck and trunk twist, 3D representation of the posture is required. Calibration of multiple cameras is complex and time-consuming, and the setup requires space which is limited inside a forklift. Hence, a single depth camera was selected for the study.

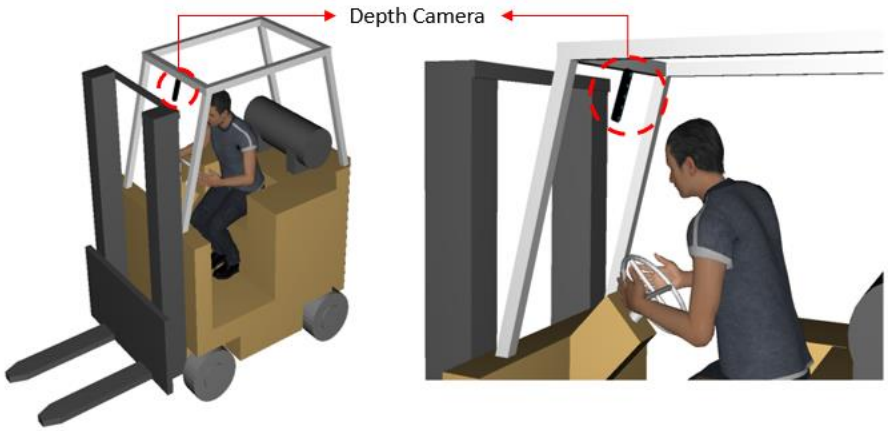

Figure 1. Depth camera placement inside forklift.

To capture data from the depth camera, a Python script was developed which records RGB images and depth maps at the rate of 15 frames per second with resolution of 640 x 360 (width x height) pixels. The depth maps were aligned with the RGB images using methods in the Pyrealsense2 library, an opensource library developed and released by the camera manufacturer. The depth data may contain some missing values where data is not available. This may happen because of occlusions between the two depth sensors or between the depth and color stream which do not see exactly the same image, under- or over-exposure, objects being too close to the camera (less than the minimum depth range), etc. In order to correct missing depth data in the resulting depth images, a hole filling filter was applied which uses the value from the neighboring pixel closest to the sensor. Python 3.8 environment was used to execute the code.

Inertial Measurement Unit (IMU) System Setup

XSens MTw Awinda, an IMU-based MoCap system, was chosen as the reference system for this study because it has shown acceptable performance for ergonomic analysis (Kim et al., 2020). 11 inertial sensors were used to record joint angles from the upper part of the body as shown in Figure 2. XSens MVN Analyze Pro 2021.2 software was used for calibration and data collection.

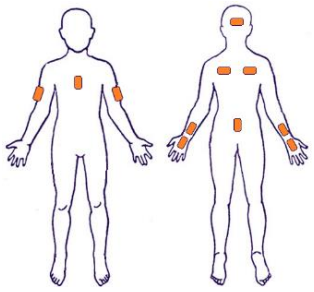

Figure 2. Placement of XSens sensors on the upper part of the body.

Participants

One female and two male forklift operators participated in the study. Their average age was 30 ± 11, their average height was 171 ± 4 cm, and they have been working as a forklift operator for 4 ± 1 years on average. The participants took part in the study voluntarily and they gave consent for processing and using the recorded photos and videos for research purposes. The forklifts used by the participants in the experiments were Linde E30, E25, and E20.

Ergonomic Assessment Method

The ergonomic assessment thresholds selected for this study were the upper body joint angle thresholds from RAMP II (Lind et al., 2019). This method considers the duration of the postures such that the longer the duration, the higher the risk for the operator. The resolution of the method is at the level of seconds.

Experimental Procedure

The forklift operator wore an XSens T-shirt and Velcro straps on the upper part of the body where 11 inertial measurement units were attached in accordance with the manufacturer's instructions (Figure 2). The XSens calibration for initializing the setup was performed using the XSens MVN software set up in vehicle mode. The data was recorded at a frequency of 60 Hz. Calibration was repeated until the estimated quality was 'good'.

Like the XSens system, the CV system needed to be calibrated to obtain the baseline position of the forklift driver. Thus, the participant was asked to sit inside the forklift and remain static in their usual sitting posture with hands placed on the thighs and looking straight ahead for 30 seconds. The laptops connected to both the systems and the XSens Awinda's recording and docking station were placed inside the forklift for the duration of the task performed.

Dataset

The three forklift drivers performed seven different forklift driving tasks within the logistics area of the automotive industry, both in indoor and outdoor conditions. In total, 65.17 minutes of data were processed. The XSens and CV system data were split into seven parts corresponding to each task.

Data Processing

The CV system dataset consisted of RGB images and their corresponding depth maps. Both were rotated to counteract the rotated position of the camera, and then the RGB images were processed with OpenPose

to obtain the 2D keypoints of eyes, nose, ears, shoulders, neck, elbow, wrists, hips, knees and feet of the driver. The resulting 2D keypoints and the corresponding depth values from the depth maps were deprojected into the camera coordinate system using the intrinsic camera parameters to obtain 3D keypoints.

For the calibration of the CV system, the coordinates of the hips and the offset values for three joint angles (head flexion and extension, trunk flexion and extension, and trunk lateral bending) were calculated from the 3D keypoints. The offset values were set as the average of all angle values calculated from 15 frames selected from the collected calibration data. The reason for this is that these joint angles, by definition, are non-zero in the baseline position. Regarding the hips, they are prone to occlusions due to arm movement while steering the vehicle but remain mostly static during driving. Hence, the hip coordinates were calculated at the beginning and fixed throughout the task.

After calibration, the joint angles were calculated similar to other publications (Kim et al., 2021; Van Crombrugge et al., 2022) for the remaining frames using the fixed hip coordinates, followed by the application of the previously calculated offset values. The joint angle values from XSens were exported from the MVN Analyze Pro software. The XSens C1 Head Flexion/Extension angle was also offset to counterbalance the non-zero angle in the baseline position. The joint angles and the corresponding XSens angles for comparison are defined in Table 1.

Table 1. Joint angle equations, were $v\_(i,j)$ is a vector pointing from joint i to joint j, $vertical$ is a line pointing up (opposite of the y-axis), and $proj(v\_(i,j),n)$ is an orthogonal projection of vector m on n.

Joint Angle	Equation	XSens Angle
Head lateral bending	$angle(proj(v\_(left\ eye, right\ eye), v\_(neck, left\ eye) \times v\_(neck,\ right\ eye)),$ $proj(v\_(left\ shoulder, right\ shoulder), v\_(neck, left\ eye) \times v\_(neck,\ right\ eye)))$	C1 Head Lateral Bending
Head flexion/ extension	$angle(v\_(midhip, neck), v\_(neck, nose)) - offset$	C1 Head Flexion/ Extension + 10°
Head twist	$90° - angle(proj(v\_(neck, nose), xz - plane),$ $proj(v\_(left\ shoulder, right\ shoulder), xz - plane))$	C1 Head Axial Rotation
Trunk lateral bending	$angle(proj(v\_(midhip, neck), xy - plane), vertical) - offset$	Vertical_T8 Lateral Bending
Trunk flexion/ extension	$angle(v\_(midhip, neck), vertical) - offset$	Vertical_T8 Flexion/ Extension

Trunk twist	$angle(proj(v\_(left\ shoulder, right\ shoulder), xz-plane), proj(v\_(left\ hip, right\ hip), xz-plane))$	Vertical_T8 Axial Bending

The 2D keypoints of the shoulders were prone to self-occlusions by the head while performing twisting or bending motions. A self-occlusion correction script was created to assess if the head occluding a shoulder based on the depth of the shoulders, nose, and ears. The occlusion was corrected with the depth of the other (non-occluded) shoulder. In addition, most of the time the head was occluding the neck keypoint because of the perspective from the top, hence it was calculated as the midpoint of the shoulders. The outliers which were further than 3 standard deviations from the median of each angle were removed and Gaussian smoothing with variance of 2 was applied on the resulting joint angles. The XSens data was down sampled to 15 samples per second using Fourier method and synchronized with the CV data by manual inspection.

The CV system results may contain missing values. This can happen because the CV system could not detect some of the keypoints needed for angle calculation or because the depth camera could not estimate the depth at some of the required joint locations. These missing value frames (MVF) were removed, and they were not used for further comparison.

To apply RAMP for upper body ergonomic assessment, the average of each joint angle was calculated for every 15 frames on both CV and XSens data. Then, the RAMP thresholds were applied to generate binary data for each joint angle which states if the average angle, in that second is above or below the threshold. To evaluate the performance after applying RAMP thresholds, the precision, recall and specificity (Hossin & Sulaiman, 2015) were calculated as mentioned in Table 2.

Table 2. Evaluation Metrics

Evaluation Metric	Formula
Precision	$TP/(TP+FP)$
Recall	$TP/(TP+FN)$
Specificity	$TN/(TN+FP)$

Note: TP-True Positive, FP-False Positive, TN-True Negative

Results

The root mean square error (RMSE) was chosen to assess the closeness of the joint angles between XSens and the CV system and it was calculated for every frame per task. The distribution of RMSE of each joint angle across tasks is shown in Figure 3. The overall mean of RMSE of all joint angles was 7.1 ± 3.2 °.

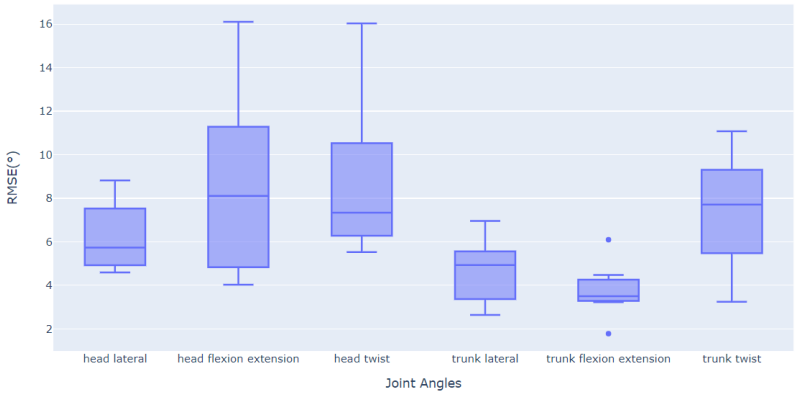

Figure 3. Distribution of RMSE (°) of joint angles between XSens and CV results across tasks.

In addition, for every joint angle, the ratio of MVF and total frames of the task was calculated and averaged across tasks as shown in Table 3.

Table 3. Frames with missing values as a percentage of the total number of frames.

Joint Angle	Mean (%)	Standard Deviation (%)
Head lateral	13.27	11.48
Head flexion/extension	3.55	2.49
Head twist	5.06	3.61
Trunk lateral	0.72	1.08
Trunk flexion/extension	0.72	1.08
Trunk twist	2.40	1.52

Table 4. Comparison of CV and XSens system after applying RAMP thresholds.

Joint Angle	Precision	Recall	Specificity	Mean Absolute Difference (°) of FN CV and Threshold	FN Count (secs)
Head lateral	0.00	0.00	0.99	8.6 ± 1.2	674
Head flexion	0.00	0.00	0.92	18.0 ± 2.5	3
Head extension	0.50	0.24	1.00	5.3 ± 3.9	38
Head twist	0.27	0.75	0.96	7.1 ± 5.9	20
Trunk lateral - moderate	0.39	0.70	0.85	3.6 ± 2.8	139
Trunk lateral - considerable		0.00	1.00	14.2 ± 0.8	2
Trunk flexion - moderate	0.82	0.61	1.00	6.6 ± 3.5	30
Trunk flexion - considerable			1.00		0
Trunk extension		0.00	1.00	7.5 ± 7.5	24
Trunk twist			1.00		0

The postures where the angle is greater than the RAMP thresholds are considered bad postures. The seconds where the XSens found bad postures and the CV system missed are false negatives (FN). These FN seconds were investigated to understand how close the CV system angles are to the threshold as shown in Table 4.

Discussion and Conclusions

The CV system was robust to dynamic light conditions and the mean RMSE of all joint angles across different tasks is in line with earlier studies (Kim et al., 2021; Lin et al., 2022). Figure 3 shows that in comparison with other joint angles, the head flexion/extension angle had higher variance across tasks. The angle difference in two tasks suddenly increased after a period of time, which might be caused by a change of hip position. Also, on isolated occasions the head flexion angle difference was unusually high, which needs further inspection as it is inconsistent with the general behavior. Furthermore, the head twist formula estimates higher twist angles when the nose is moving along with other motions, which causes overestimation in specific cases. In similar terms, the back twist is estimated from the shoulders which are prone to more variations due to arm movements compared to the XSens sensors placed directly on the back. The results in Table 3 show that the angle with most MVF is head lateral bending. This can be attributed to at least one of the eyes often going out of the camera view when performing head twist or flexion.

From the binary data generated after applying the RAMP thresholds summarized in Table 4, it can be seen that the system can identify many bad postures for head twist and trunk lateral – moderate, but it also falsely classifies many postures as bad due to overestimation and aforementioned issues. Identification of bad postures is more precise in trunk flexion – moderate, but many bad postures were also missed. This is due to self-occlusion of the shoulders which directly affects the neck keypoint and results in underestimation of the angle after correcting the occlusions. Head flexion and extension are affected in a similar way. In the case of head lateral bending, the system performs poorly as the calculated angles are overall very small compared to XSens. Trunk lateral – considerable, suffered from underestimation due to the operator going out of the camera field of view, where the CV system predicted the neck and shoulder keypoints closer to the center of the image and resulted in classification as moderate instead of considerable lateral bending. For trunk extension, apart from one task, the RMSE between the systems was low, indicating that the CV values were close to XSens, but just under the threshold. No bad postures were identified by both systems in the cases of trunk flexion - considerable and twist.

Table 4 also shows that in most of the FN seconds the difference between the CV system and the respective RAMP angle threshold was close to the average error of the system. This indicates that the CV system would find more of the bad postures identified by XSens if the thresholds applied to the CV data are adjusted using methods like receiver operating characteristic (ROC) curve (Metz, 1978). However, a suitable balance between the precision and recall has to be found along with ergonomists. This behavior can be expected not only when using RAMP, but also any other ergonomic method that applies hard angle thresholds.

Also, issues with the XSens data were identified which brings up the question of its validity in certain moments. For example, calibration needed several attempts to achieve good quality similar to (Zelck et al., 2022). Even then, visual inspection showed issues where the XSens representation of the body did not correspond to the operator's static pose. This also existed in the recordings where certain postures recorded by XSens were incorrect which was identified by visual inspection. Lastly, sudden changes in angle and glitches were discovered with no apparent motion performed by the operator that can be seen in the video. However, these problems were not noticed during simulations in the lab. The reason might be magnetic disturbances in the industry environment, vibrations, or motions that caused the sensors to move from their original position.

Based on the findings discussed above, this study was unable to confirm the applicability of the proposed CV system directly for RAMP ergonomic assessment in industry, even though previous studies from lab environments suggested otherwise (Kim et al., 2021; Lin et al., 2022; Massiris Fernández et al., 2020). Even though the CV system closely followed the trend of the XSens angles, the performance of the CV system after applying RAMP thresholds resulted in vastly different outcomes because of self-occlusion, camera perspective and field of view, angle calculation methods and the hard angle thresholds. However, there were inconsistencies with the XSens system which may have affected the overall results.

Future work should investigate the reliability of XSens data in order to determine the limitations of the CV system. The digital human modeling (DHM) technique could be used to model the data from both the systems for comparison which might reduce the noise and maintain appropriate postures. In addition, further research should be done into alternative camera positions, handling of self-occlusions and utilization of more cameras within the surrounding environment. Lastly, threshold adjustments can be made in consultation with ergonomists, considering that the calculated angles overall closely match XSens. The findings of this study suggest that obtaining results through CV methods may be more repeatable, faster and efficient compared to manual assessment of occupational ergonomics. This can

catalyze the identification and reduction of injuries and illnesses as well as promote worker's safety and comfort.

Acknowledgments

This research was funded by Scania CV AB. Thanks for the support from Juan Luis Jiménez Sánchez, Martin Sandberg, Malin Baresso and all the forklift drivers who participated in this study.

References

Burdorf, A., Derksen, J., Naaktgeboren, B., & van Riel, M. (1992). Measurement of trunk bending during work by direct observation and continuous measurement. *Applied Ergonomics*, *23*(4), 263–267. https://doi.org/10.1016/0003-6870(92)90154-n

Fagarasanu, M., & Kumar, S. (2002). Measurement instruments and data collection: A consideration of constructs and biases in ergonomics research. *International Journal of Industrial Ergonomics*, *30*(6), 355–369. https://doi.org/10.1016/S0169-8141(02)00101-4

Flodin, U., Rolander, B., Löfgren, H., Krapi, B., Nyqvist, F., & Wåhlin, C. (2018). Risk factors for neck pain among forklift truck operators: A retrospective cohort study. *BMC Musculoskeletal Disorders*, *19*(1), 44. https://doi.org/10.1186/s12891-018-1956-3

Frederick, L., Habes, D., & Schloemer, J. (1984). An Introduction to the Principles of Occupational Ergonomics. *Occupational Health Nursing*, *32*(12), 643–645. https://doi.org/10.1177/216507998403201206

Hignett, S., & McAtamney, L. (2000). Rapid Entire Body Assessment (REBA). *Applied Ergonomics*, *31*(2), 201–205. https://doi.org/10.1016/S0003-6870(99)00039-3

Hossin, M., & Sulaiman, M. N. (2015). A Review On Evaluation Metrics For Data Classification Evaluations. *International Journal of Data Mining & Knowledge Management Process*, *5*(2), 1–11.

Kim, W., Huang, C., Yun, D., Saakes, D., & Xiong, S. (2020). Comparison of Joint Angle Measurements from Three Types of Motion Capture Systems for Ergonomic Postural Assessment. In W. Karwowski, R. S. Goonetilleke, S. Xiong, R. H. M. Goossens, & A. Murata (Eds.), *Advances in Physical, Social & Occupational Ergonomics* (pp. 3–11). Springer International Publishing. https://doi.org/10.1007/978-3-030-51549-2_1

Kim, W., Sung, J., Saakes, D., Huang, C., & Xiong, S. (2021). Ergonomic postural assessment using a new open-source human pose estimation technology (OpenPose). *International Journal of Industrial Ergonomics*, *84*, 103164. https://doi.org/10.1016/j.ergon.2021.103164

Kok, J., Vroonhof, P., & Snijders, J. (2020). *Work-related musculoskeletal disorders: Prevalence, costs and demographics in the EU*. European Agency for Safety and Health at Work. https://data.europa.eu/doi/10.2802/66947

Lin, P.-C., Chen, Y.-J., Chen, W.-S., & Lee, Y.-J. (2022). Automatic real-time occupational posture evaluation and select corresponding ergonomic assessments. *Scientific Reports*, *12*(1), 2139. https://doi.org/10.1038/s41598-022-05812-9

Lind, C., Forsman, M., & Rose, L. (2019). Development and evaluation of RAMP II - a practitioner's tool for assessing musculoskeletal disorder risk factors in industrial manual handling. *Ergonomics*, *63*, 1–35. https://doi.org/10.1080/00140139.2019.1710576

Lind, C., Rose, L., Franzon, H., & Nord-Nilsson, L. (2014). *RAMP: risk management assessment tool for manual handling proactively*. 4.

Massiris Fernández, M., Fernández, J. Á., Bajo, J. M., & Delrieux, C. A. (2020). Ergonomic risk assessment based on computer vision and machine learning. *Computers & Industrial Engineering*, *149*, 106816. https://doi.org/10.1016/j.cie.2020.106816

McAtamney, L., & Nigel Corlett, E. (1993). RULA: A survey method for the investigation of work-related upper limb disorders. *Applied Ergonomics*, *24*(2), 91–99. https://doi.org/10.1016/0003-6870(93)90080-S

Menolotto, M., Komaris, D.-S., Tedesco, S., O'Flynn, B., & Walsh, M. (2020). Motion Capture Technology in Industrial Applications: A Systematic Review. *Sensors*, *20*(19), 5687. https://doi.org/10.3390/s20195687

Metz, C. E. (1978). Basic principles of ROC analysis. *Seminars in Nuclear Medicine*, *8*(4), 283–298. https://doi.org/10.1016/S0001-2998(78)80014-2

Van Crombrugge, I., Sels, S., Ribbens, B., Steenackers, G., Penne, R., & Vanlanduit, S. (2022). Accuracy Assessment of Joint Angles Estimated from 2D and 3D Camera Measurements. *Sensors*, *22*(5), 1729. https://doi.org/10.3390/s22051729

Viruet, H. B., Genaidy, A., Shell, R., Salem, S., & Karwowski, W. (2008). Effect of forklift operation on lower back pain: An evidence-based approach. *Human Factors and Ergonomics in Manufacturing & Service Industries*, *18*(2), 125–151. https://doi.org/10.1002/hfm.20105

Zelck, S., Verwulgen, S., Denteneer, L., Vanden Bossche, H., & Scataglini, S. (2022). Combining a Wearable IMU Mocap System with REBA and RULA for Ergonomic Assessment of Container Lashing Teams. In N. L. Black, W. P. Neumann, & I. Noy (Eds.), *Proceedings of the 21st Congress of the International Ergonomics Association (IEA 2021)* (pp. 462–465). Springer International Publishing. https://doi.org/10.1007/978-3-030-74614-8_59

Improving the efficiency of virtual-reality-based ergonomics assessments with digital human models in multi-agent collaborative virtual environments

Francisco Garcia Rivera, Maurice Lamb, and Melanie Waddell
University of Skövde, Sweden

Abstract

Often new digital tools are introduced alongside existing tools and workflows to augment and fill gaps in current processes. Virtual and augmented reality (XR) tools are currently being deployed in this way within design processes, allowing for interactive visualization in virtual environments including the use of DHM tools. Currently, the focus is on how to implement XR as a stand-alone tool for single user scenarios. However, in collaborative design contexts, screen-based and XR tools can be used together to leverage the benefits of each technology maximizing the potential of multi-user design processes. XR allows for an immersive exploration of designed objects in 3D space, while screen-based tools allow for easier notetaking and integration of additional non-3D software and meeting tools. Ensuring that these technologies are integrated in a mutually beneficial manner requires a framework for determining the best combination of technologies and interfaces for diverse design teams. This paper presents a framework for performing collaborative design reviews in a digital environment that can be accessed using both XR and 2D screen devices simultaneously. It enables asymmetric collaboration to provide each design team member with the technology that best fits their workflow and requirements.

Keywords: Collaborative design, Asymmetric collaboration, Extended Reality

Introduction

Developing a product is a complicated process that often requires collaboration from various stakeholders to succeed (Redante et al., 2019). Often, stakeholders in large organizations collaborate with globally dispersed teams in the product design process. Moreover, recent events, such as the Covid-19 pandemic and awareness of climate change, have further boosted interest in reducing the air travel for in-person meetings (Becken & Hughey, 2022). As a result, there is increasing demand for tools that can effectively mediate remote collaboration in all stages of the design process.

Design reviews are one stage of the design process that can often require collaboration among multiple stakeholders and have traditionally depended on in-person meetings and videoconferencing tools. In design reviews, several stakeholders come together to consider and critique a current design before production plans are finalized. The design review process is an essential control point for any design project to transit

from one stage to another and can include not only assessing the physical properties of designed artefact but also ergonomics and human factors through the use of DHM tools (Huang, 2002). Often, the designers and production managers performing these reviews are not geographically co-located, and remote collaboration tools can improve workflows when travel is not possible or not prefered (Tea et al., 2021). For many companies, videoconferencing apps and their corresponding screen-sharing capabilities constitute state-of-the-art for this kind of remote collaboration. Extended reality (XR) tools have recently been incorporated into collaboration workflow (Cooper et al., 2021). However, they are typically integrated alongside existing videoconferencing workflows and treated as another screen to be shared with online collaborators (Chen, 2021). While this approach is functional, it limits and misses many key benefits that XR can introduce into a design process. While a more integrated XR solution is needed to access these benefits, it is also important to consider that not everyone will benefit from using XR technologies in a collaborative design process (Burova, Mäkelä, et al., 2022). As a result, we anticipate that future collaborative design processes will involve a mixture of technologies resulting in various asymmetries between collaborators. Because this kind of intentional mixing of technical systems is new in the context of collaborative design, more frameworks are needed for organizing technologies, users, and user roles (Reski et al., 2022). In turn, such a framework can support determining user needs and assessing implementations for multiuser asymmetric (i.e., collaboration using different devices).

This paper presents an initial framework for asymmetric XR collaboration and applies it to a simple collaborative design review in a digital environment using both XR and 2d screen devices simultaneously. The central idea of this framework is to enable asymmetric collaboration to provide each design team member with the technology that best fits their workflow and requirements. We ran a small pilot study to validate the framework using an existing workflow at the Chinese-Swedish company CEVT.

Method

While some tools for multiuser XR and asymmetric design exist (Burova, Palma, et al., 2022), there is little guidance regarding how these tools might be best used for design teams. Discussions with CEVT gave us insights into their current workflow and needs, and we developed a prototype software accordingly. After that, we evaluated the software in a controlled environment to check the viability of the proposed framework. This process is illustrated in Figure 1.

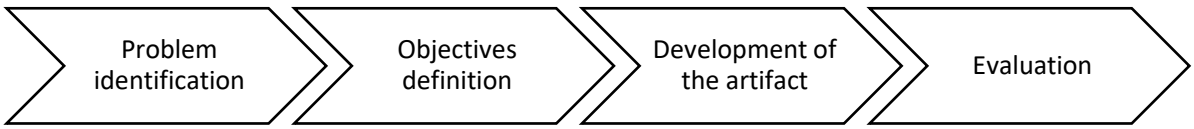

Figure 1. Development process

Problem specification and initial prototype

Some companies, including CEVT, have started including XR in their design review processes to support assessment of ergonomics and assembly feasibility within DHM tools. The expectation is that the use of digital tools and XR technology will allow for more efficient multi-user remote collaboration. However, current XR applications in DHM have limited multiuser interfaces, minimal screen sharing options, limited interaction options and underdeveloped workflows from CAD to XR tools.

CEVT currently implements XR-based design reviews by having one person in XR share their screen over a videoconferencing app with different stakeholders (see Figure 2). These stakeholders (the audience) watch as the person in XR (the VR navigator) assembles the product component by component. After each component is assembled, the VR navigator places a DHM manikin in an expected position and pose for that assembly step. Once the appropriate stakeholders have evaluated an assembly step and identified issues and risks for the current component, they move on to the new component.

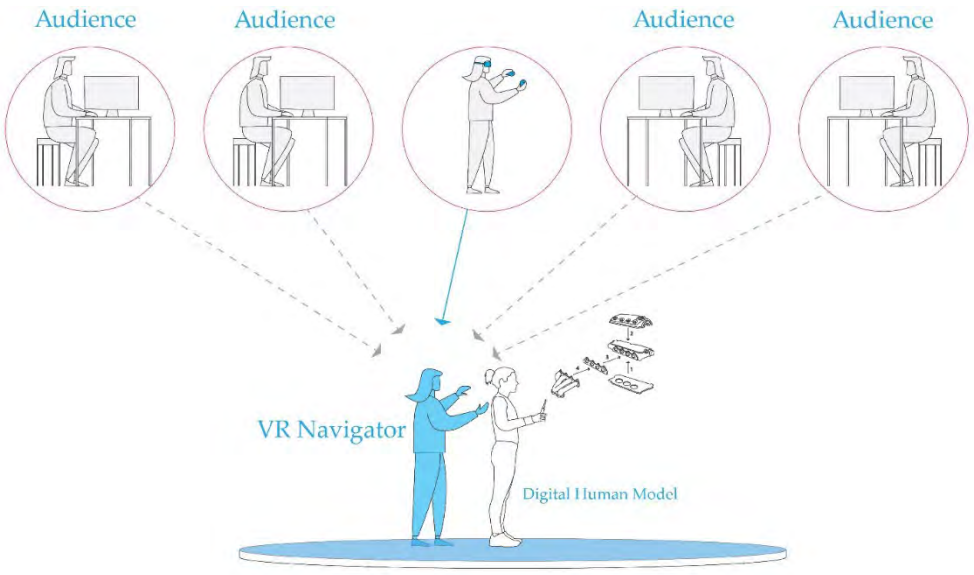

Figure 2. Illustration of current design review approach.

Having only one person able to navigate the environment (the VR navigator) and limiting the audience's view to the VR navigator's perspective are significant limitations in this workflow. The audience includes operators, manufacturing engineers, mechanical engineers, and ergonomists, among others. Not everyone needs the same kind of information or interaction capabilities, and their needs may not match the aims and

focus of the VR navigator. As an initial division of roles, we identified that some users needed more direct engagement with the 3D environment and that others needed to split their attention among other software tools that are not and may not be integrated into the 3D environment. As such, for some users XR tools are likely be beneficial but for others, the tools may be a hindrance, requiring frequent changes between the XR device and a 2D screen. In both cases, the ability to freely navigate the 3D scene appeared potentially valuable meaning that it may not be beneficial to limit free movement to only the XR users. Thus, it may be helpful if XR users can navigate the digital environment by using controllers or their bodies and screen-based users can use a keyboard and mouse to navigate the digital environment. Taking these insights, we developed a prototype multiuser asymmetric design review environment, as illustrated in Figure 3.

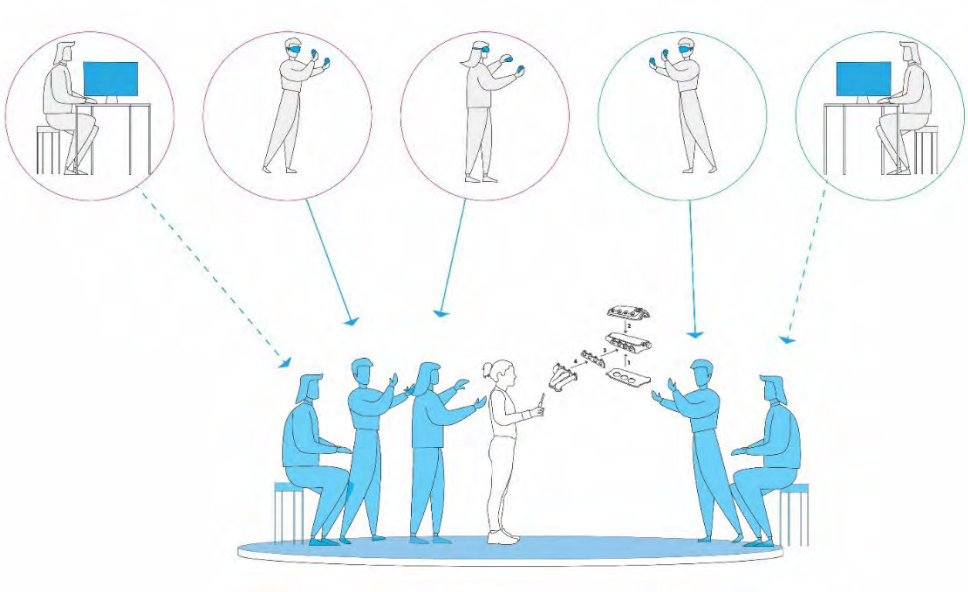

Figure 3. Illustration of software prototype roles and interfaces

As an initial solution, we developed a shared digital environment that the users can connect to either using a PC with a traditional monitor or an XR device (Figure 4). All users can navigate the environment, have avatar representations, and communicate using voice. The avatars allowed users to see one anothers location in the environment but were not intended to be a detailed representation of the users body state. Only users who access the digital environment using XR equipment can grab and move objects. Object models based on 3D CAD designs could be imported into the environment and simple interactions (grab and move) could be specified for the objects as needed. A digital human manikin is included in the environment which can be manipulated by moving the black spheres (visible in figure 4) attached to its hands and head allowing for visualization of static poses in an assembly process. In the current implementation, all the objects and

manikin movements are visible to all the users connected to the digital environment, though visibility could be limited based on user role or even clearence status within the company.

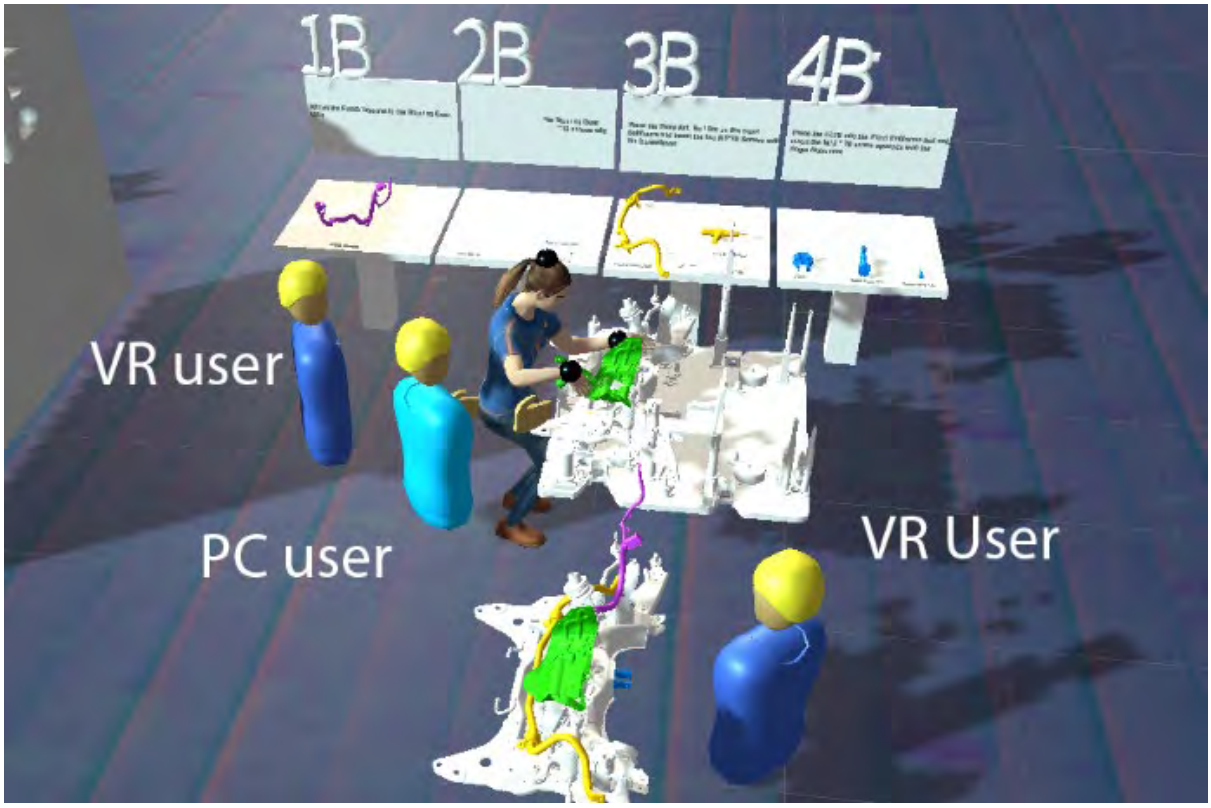

Figure 4. Digital environment with 2 XR users and one PC user

Material used in the development

We developed the prototype using Unity 2020.3 (Unity technologies, San Francisco, California). The software was built to run on either a Windows PC with a monitor or on the Oculus Quest 2, though the program could run on other XR platforms if needed. Users movements, object interactions and verbal conversations, were synchronized using Photon, a cloud service for multiplayer games (Exit Games, Hamburg, Germany). The manikin mesh was built in makehuman (*Make Human Community*, 2022), and its motions were driven by the FABRIK solver (Aristidou & Lasenby, 2011) in the Unity plugin FINALIK (*RootMotion*, 2022)

Evaluation

A pilot study was developed to test the design review tool and validate this framework implementation. The objective of this evaluation was to determine if collaboration in XR could be more effective when all

users can navigate the digital environment. In addition, we evaluated the user experience to identify the impact of free navigation and asymmetric tools.

Fifteen healthy subjects split into three groups were used as test subjects for the pilot study. All participants are current or recently graduated students at the University of Skövde. Ten participants are in the age range of 18-25 years, three participants are between 26-30 and one participant each is in the age range of 31-35 and 36-40. They were asked to perform five assembly tasks with the current approach used by CEVT (see Figure 4 condition A) and with the proposed for the prototype (see Figure 4 condition B). In condition A, there was an VR navigator, an observer and an assessor. The VR navigator assembled the components following instructions presented in the scene and posed the manikin. The observer and the assessor helped identify issues in the assembly process but were only able to see the scene from the VR navigators point of view. In condition B, the VR navigator's tasks remained the same. However, the assessor was in XR, and the observer used a PC with a 2D screen. The assessor and observer were allowed to navigate the digital environment and select viewing positions independently, but they could not interact with the assembly components or manikin.

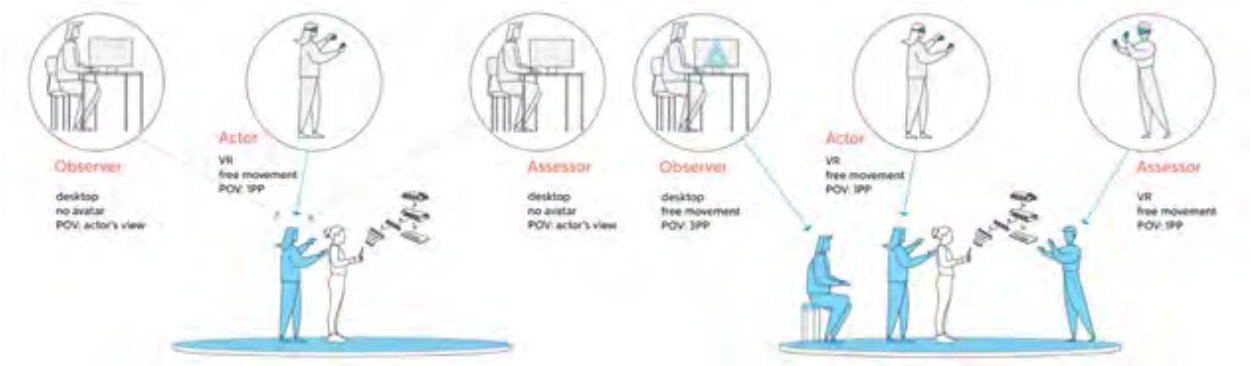

Figure 5. Illustration of condition A (right) and condition B (left)

Condition order was counterbalanced such that three groups started with condition A and two groups started with condition B. There were three issues planted in the sample assembly task: the posture of the manikin, an unfeasible sequence of assembly operations, and one required tool for the assembly not fit in the spot where it had to be used. Participants were instructed to note any issues they saw in the assembly process. We hypothesized that the participants would be more likely to find these issues when all of them could independently navigate the digital environment (Condition B). After the study, the participants completed a questionnaire (see Table 1) evaluating their experience comparing the two conditions (Schrepp et al.,

2017). The first four items evaluate pragmatic features of the system and the second four categories evaluate hedonic features.

Results

In condition A, the participants correctly identified issues 12 times and missed or mis-identified issues 11 times. In condition B, the participants correctly identified the issues 19 times and missed or misidentified issues 11 times. Figure 5 shows the data for the identified issues by the participants divided by correctly identified, missed, and misidentified. Correct identifications involve identifying a planted issue while misidentification involves indicating an issue exists that was not planted. In the case of misidentification, it is possible that an issue did exist, but later assessment suggests this was not the case. When an issues was planted but not identified it was counted as being missed. Note that in situations where one issue was planted and the participant reported a different issue the response was counted as both a miss and a misidentification. Results from the questionare are summarized in Figure 7.

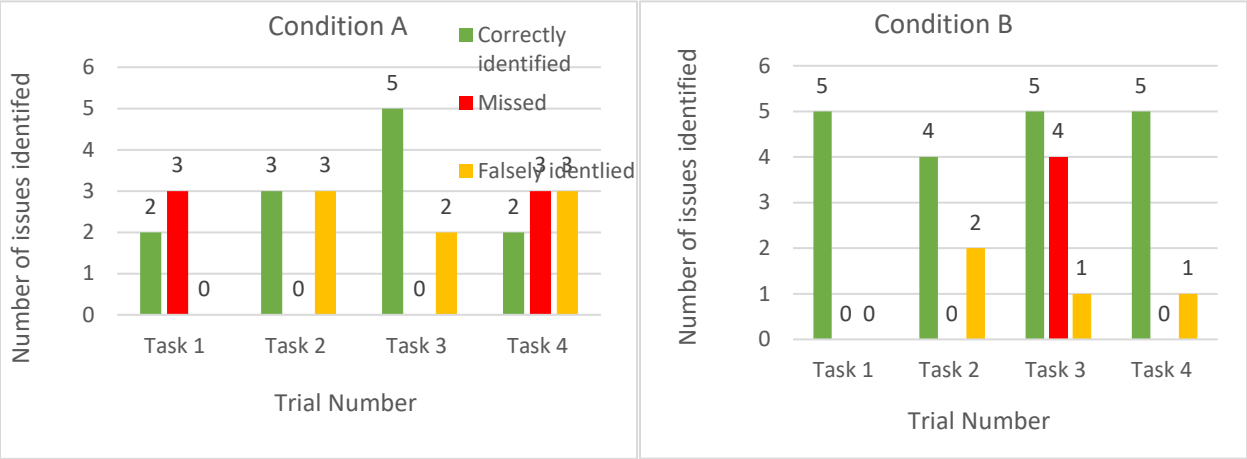

Figure 6. Identification of issues by the participants.

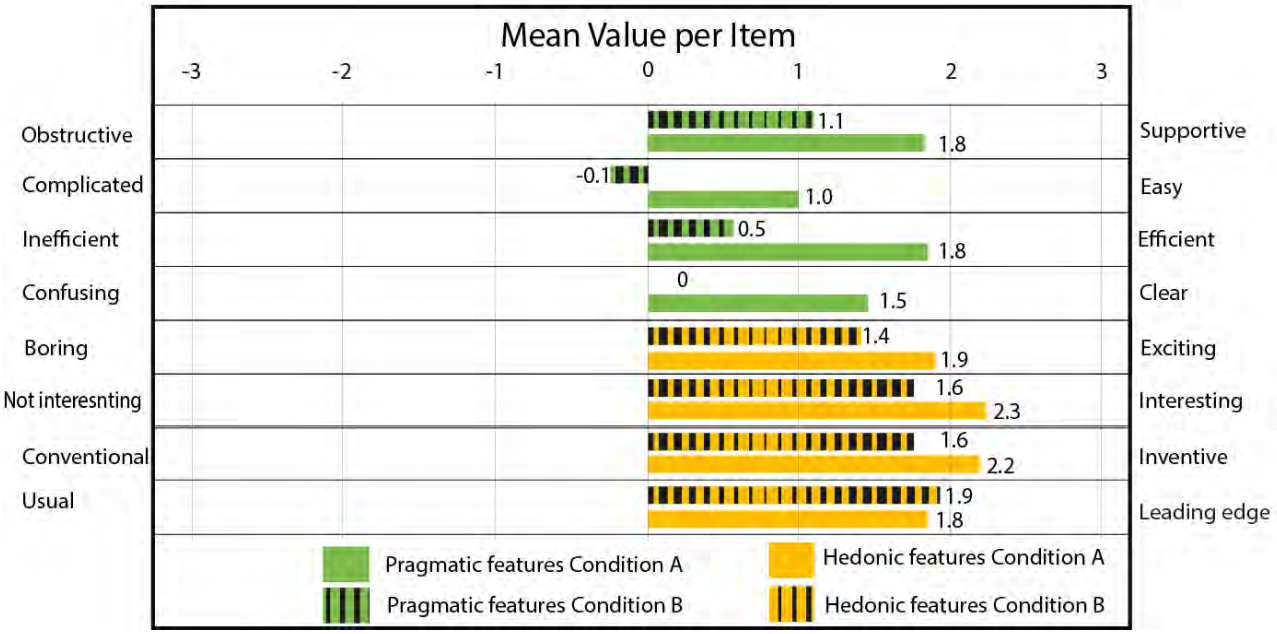

Figure 7. Mean values for the short user experience questionnaire conditions A and B

Discussion and Conclusions

In this pilot study, participants found the planted issues more easily when they could independently navigate the digital environment. In general the results show a consistent trend towards condition B in terms of correctly identifying planted issues. Note, in condition B task 3 the large number of missed issues is likely due to an error that resulted in there being 2 planted issues, so the spike may be due to the fact that users did not expect 2 errors in that case.

The user experience questionnaire also seems to indicate that the participants found condition B to be more practical and enjoyable. Given the size of the study and the limited scope of investigation, it is not clear if the enjoyment is related to the ability to navigate independently or the more streamlined inclusion of XR in condition B.

While the pilot and corresponding assessment is limited, the results are at least positive and indicative more work that needs to be done. Specifically, future work will need to investigate if there is any particular benefit due to XR integration or if the ability to navigate independently is sufficient for improving issue identification and creating an enjoyable process.

Collaboration and meetings using videoconferencing apps have become the norm. While design collaboration using screensharing and videoconferencing apps provides a functional solution that works

now, more work is needed to enable effective collaboration within DHM and CAD tools. Specifically, consideration of how different roles in a design process might benefit or be harmed from hardware and software constraints. Future XR design tools should consider not just multi-user XR collaboration but also how asymmetric collaboration can be incorporated. In this paper we have demonstrated an initial conceptualization of how asymetric tools can be enabled for remote collaboration.

Future work will focus on integrating more forms of XR while also making a more thorough and clear investigation of the benefits and potential challenges of using aysmetric XR systems in design processes.

Acknowledgements

This work has been made possible with the support from the Knowledge Foundation supported research environment INFINIT at the University of Skövde, in the project Synergy Virtual Ergonomics (SVE), Recruitment and Strategic Knowledge Reinforcement initiative and with support from VINNOVA. This support is gratefully acknowledged.

References

Aristidou, A., & Lasenby, J. (2011). FABRIK: A fast, iterative solver for the Inverse Kinematics problem. *Graphical Models*, *73*(5), 243–260. https://doi.org/10.1016/j.gmod.2011.05.003

Becken, S., & Hughey, K. F. (2022). Impacts of changes to business travel practices in response to the COVID-19 lockdown in New Zealand. *Journal of Sustainable Tourism*, *30*(1), 108–127. https://doi.org/10.1080/09669582.2021.1894160

Burova, A., Mäkelä, J., Heinonen, H., Palma, P. B., Hakulinen, J., Opas, V., Siltanen, S., Raisamo, R., & Turunen, M. (2022). Asynchronous industrial collaboration: How virtual reality and virtual tools aid the process of maintenance method development and documentation creation. *Computers in Industry*, *140*, 103663. https://doi.org/10.1016/j.compind.2022.103663

Burova, A., Palma, P. B., Truong, P., Mäkelä, J., Heinonen, H., Hakulinen, J., Ronkainen, K., Raisamo, R., Turunen, M., & Siltanen, S. (2022). Distributed Asymmetric Virtual Reality in Industrial Context: Enhancing the Collaboration of Geographically Dispersed Teams in the Pipeline of

Maintenance Method Development and Technical Documentation Creation. *Applied Sciences*, *12*(8), 3728. https://doi.org/10.3390/app12083728

Chen, M. F. Y. (2021). Co-immersive-Creation: A Hybrid Approach for Using Virtual Reality and Telepresence Systems in Co-design Research. *Communications in Computer and Information Science*, *1420*, 217–224. https://doi.org/10.1007/978-3-030-78642-7_29

Cooper, N., Kelsey, S., Emond, B., Lapointe, J.-F., Astles, S., & Trudel, C. (2021, August 2). *Evaluating VR practices to support collaborative cabin design process using a human factor approach*. https://doi.org/10.2514/6.2021-2774

Huang, G. Q. (2002). Web-based support for collaborative product design review. *Computers in Industry*, *48*(1), 71–88. https://doi.org/10.1016/S0166-3615(02)00011-8

Make Human Community. (2022). http://www.makehumancommunity.org/

Redante, R. C., de Medeiros, J. F., Vidor, G., Cruz, C. M. L., & Ribeiro, J. L. D. (2019). Creative approaches and green product development: Using design thinking to promote stakeholders' engagement. *Sustainable Production and Consumption*, *19*, 247–256. https://doi.org/10.1016/j.spc.2019.04.006

Reski, N., Alissandrakis, A., & Kerren, A. (2022). An Empirical Evaluation of Asymmetric Synchronous Collaboration Combining Immersive and Non-Immersive Interfaces Within the Context of Immersive Analytics. *Frontiers in Virtual Reality*, *2*, 743445. https://doi.org/10.3389/frvir.2021.743445

RootMotion. (2022). http://root-motion.com/

Schrepp, M., Hinderks, A., & Thomaschewski, J. (2017). *Design and Evaluation of a Short Version of the User Experience Questionnaire (UEQ-S)*. https://doi.org/10.9781/ijimai.2017.09.001

Tea, S., Panuwatwanich, K., Ruthankoon, R., & Kaewmoracharoen, M. (2021). Multiuser immersive virtual reality application for real-time remote collaboration to enhance design review process in the social distancing era. *Journal of Engineering, Design and Technology*, *20*(1), 281–298. https://doi.org/10.1108/JEDT-12-2020-0500

Reinforcement Learning with Digital Human Models of Varying Visual Characteristics

Nitesh Bhatia [a], Ciara M. Pike-Burke [b], Eduardo M. Normando [c], and Omar K. Matar [a]

[a] Department of Chemical Engineering, Imperial College London, Exhibition Road, South Kensington, London, SW7 2AZ, UK

[b] Department of Mathematics, Imperial College London, Exhibition Road, South Kensington, London, SW7 2AZ, UK

[c] Department of Surgery & Cancer, Imperial College London, Exhibition Road, South Kensington, London, SW7 2AZ, UK

Abstract

Digital Human Modelling (DHM) is rapidly emerging as one of the most cost-effective tools for generating computer-based virtual human-in-the-loop simulations. These help better understand individual and crowd behaviour under complex situations. For tasks such as target search and wayfinding, the eye is the primary channel for processing perceptual information and decision making. Existing experimental human studies in the literature have highlighted the relationship between the field of vision, visual acuity, accommodation, and its effect on visual search performance. This paper presents a methodology for the simulation of visual behaviour in target search and a wayfinding task by employing DHM as a reinforcement learning agent with functional vision characteristics. We used Unity 3D game engine to build the DHM and virtual workspace, Unity ML-Agents package to realise its connection with TensorFlow, and the Proximal Policy Optimization (PPO) algorithm to train DHM in finding a target through intensive reinforcement learning (RL). For the functional vision system, we have considered three human-inspired vision personas: (i) 'good vision', (ii) 'poor vision' type 1 (low acuity like), and (iii) 'poor vision' type 2 (high myopia like). We have compared the emergent behaviour of DHM for each of the three personas and RL training performance. The results conclude that simulating reinforcement learning agents with varying vision characteristics can evaluate their impact on visual task performance.

Keywords: human simulation, functional vision, cognitive model, visual search, wayfinding

Introduction

Moving away from the traditional ergonomics design process and using digital human modelling (DHM) for virtual simulations of human interaction and behaviour in a workspace has helped the

designers significantly (Zhu et al., 2019). DHM technology offers human factors and ergonomics specialists the promise of an efficient means to simulate a large variety of ergonomics issues early in designing products and manufacturing workstations. This advanced technology assesses human factors issues in a virtual digital prototype of a workplace with a digital human model. Most products and manufacturing work settings are specified and designed using sophisticated Computer-Aided Design (CAD) systems. By integrating a computer-rendered avatar (or humanoid) and the CAD-rendered graphics of a prospective workspace, one can simulate issues regarding who can fit, reach, see and manipulate (Chaffin, 2005; Chaffin et al., 2001).

A standard DHM framework consists of a 3D human avatar often representing a population and a virtual workplace environment comprising tools and machines where tasks can be automated (Jung et al., 2009). As an advantage, a computer-based simulation approach can generate multiple failure scenarios without causing any harm to the existing system (Irshad et al., 2018). The implementation of DHM reduces and often eliminates the requirement of dummy models, cardboard manikins, 2D drawings, and even actual human trials in expensive physical mock-ups (Chang & Wang, 2007). This technology has reduced the design time, cycle time, and cost of designing new products, improved quality, production, and operation, and lowered maintenance costs (Duffy, 2016). Being a relatively new area of research and development, current DHM applications are mostly dominant towards whole body posture and bio-mechanical analysis used for simulations of material handling tasks primarily dominated in the areas of automotive production, assembly-line simulations and vehicle safety (Berger et al., 2004; Colombo & Cugini, 2004).

Vision is one of the fundamental attributes a person needs to access and use everyday products, walk around the world, and perform tasks requiring close integration of visual feedback and cognitive decision-making (Findlay, 1998; Ryu et al., 2013). Failure to take account of this reduced functional capability in the design process results in users facing challenging environments or becoming excluded from product use and jobs that demand high visual inputs (Wahl, 2013; White et al., 2015). With the rise in the human population, it has become essential to consider visual system characteristics as the primary necessity for a sustainable vision friendly system. In the current world, many people are affected by low vision and several visual impairments such as myopia, hypermetropia, cataract and complete blindness. The challenge today is to develop human behavioural analytics frameworks aimed at designing vision-friendly products and services that serve the marketplace today while ensuring the development of its production does not negatively impact future generations.

The present state-of-the-art DHM technology provides valuable but minimal information for the simulation of vision-centric tasks. It is impossible to design and simulate tasks and evaluate human performance, which depends highly on the operator's visual capabilities. For modelling and simulation of vision-dependent cognitive tasks, although there have been a few advanced vision simulation

frameworks (Bhatia et al., 2016), the present DHM tools are mostly limited to qualitative visualisation techniques such as symmetric visual fields and line-of-sight based visibility analysis. For instance, in (Chaffin et al., 2001), Siemens Jack has been used to evaluate vehicle dashboard visibility and driver's visual field using the uniform Field of Vision (FoV) cones. In (Reed et al., 2005), similar FoV cones were used to assess the direct exterior vision of a postal delivery vehicle driver. Comparable uniform FoV-based vision analysis tools are available in DHM frameworks such as Delmia Human, Humancad/SAMMIE and RAMSIS.

For the tasks such as target search and wayfinding, the eye is the primary channel for processing perceptual information and decision making. We believe that since the support for comparative assessment of any system for human vision is very narrow in DHM, although it is vital, the industry uptake is minimal. The fundamental mechanisms underlying human sensory and perceptual systems that are effective in obtaining predictive information from multiple information sources, estimating and anticipating critical system states, and resolving ill-posed optimisation problems on subconscious levels of cognitive control are neither well understood nor modelled. Therefore, in addition to a pragmatic approach, there is a need for a scientific method to augment human perception, cognition and motor functions in DHM-based simulation frameworks.

In recent times, deep reinforcement learning (RL) has been successfully applied to various games, robotics, recommendation systems and many training platforms and simulation environments (Afsar et al., 2021; Rajeswaran et al., 2020; Wu & Gao, 2017). However, applying deep RL to the visual navigation of DHM with realistic environments is challenging. This paper presents an RL-based DHM framework for simulating observable behaviour in target search and wayfinding tasks by employing DHM as a RL agent. For the simulation of natural human visual characteristics, by varying the field of vision, acuity and accommodation, we have modelled three personas to train RL models. Using these trained models, we have shown the variation in the behaviour of DHM while locating targets in a wayfinding task for each case. The modelling methodology is discussed in the next section, followed by the results, discussion, and conclusion.

Methods

Overview

To model this DHM framework, we have used the Unity game engine and ML-agents, its reinforcement learning framework. Figure 1 represents a hierarchical abstraction of our framework. It comprises a unity application having a DHM in a virtual workspace. The DHM model consists of the following three modules. The framework modules are explained in detail in the later sections.

1. A low-level module that includes motion synthesis. It takes four discrete actions (A_t) as input and directly controls the movement (forward, backward, right, left) and animation of DHM.
2. A high-level decision-making module which controls task planning. Based on the visual input states (s_t) and deep reinforcement learning policy (π_t), it generates a series of inferential actions (A_t) for the low-level module that direct DHM to move toward the target.
3. A functional vision module consists of a set of four cameras for sensing the virtual workspace objects. The images captured by this module are passed on as visual input states (s_t) to the high-level decision-making module. Since this module is attached to the DHM body (head), the visual input varies according to the DHM movement. By modifying the camera properties such as FoV, resolution, and near and far clip planes, we have modelled three vision personas to simulate 'good' and 'poor' vision.

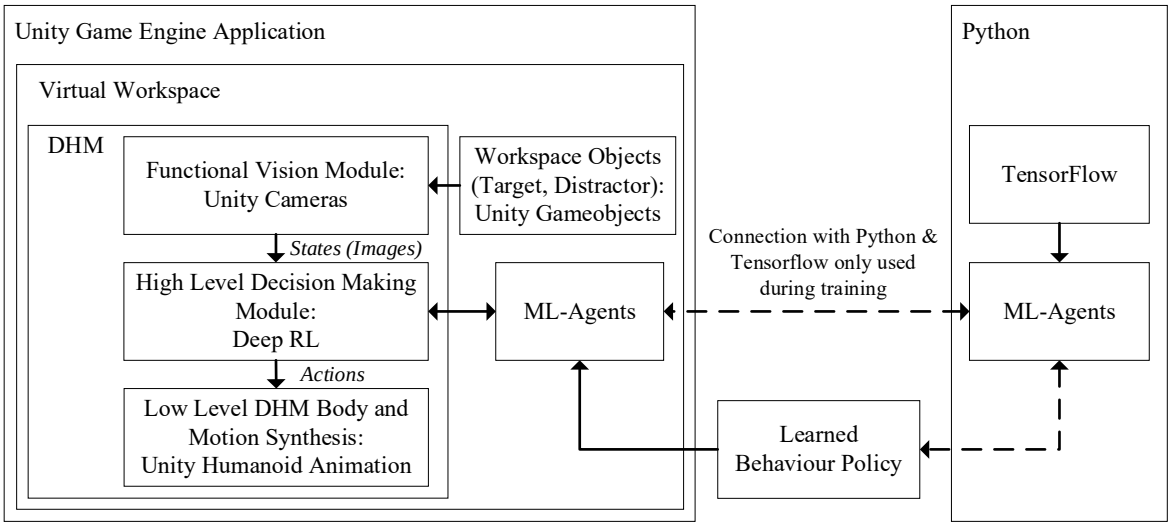

Figure 1 DHM Framework and the links between each module. Please note that the connection with Python environment is only used during reinforcement learning training.

We have evaluated this framework in a virtual workspace that consists of a target and a distractor. The reinforcement learning task of target search is modelled as a Markov decision process (MDP). At the beginning of each trial, the DHM starts from state s0 sampled uniformly from the set of all possible initial states Start: $s_0 \sim U(\text{Start})$. At discrete time steps t = 0, 1, 2, . . . the DHM executes actions A_t according to some policy π_t. As a result of each action, the DHM moves to the next state s_{t+1}. The experience which the DHM has collected in a single trial is defined as the following sequence of states (s_t), actions (a_t) and a reward (r): $\zeta = s_0, a_1, s_1, a_2, \ldots r$. A trial ends when the DHM satisfies one of the three following conditions:

1. DHM reaches the target. A positive reward of r=1.0 is offered (Figure 6a).
2. DHM reaches a distractor. A negative reward r=-0.1 is offered (Figure 6b).
3. A predefined maximum number of time steps, which is 5000 in the current setup, has elapsed.

Modelling a Digital Human with Functional Vision

A percentile-based model is the most common method of creating a human model in DHM software (Jung et al., 2009). It is possible to generate a 3D DHM model by querying an anthropometric database having several predefined percentiles such as 5th, 50th, and 95th) according to several personas such as gender, age group, and specific physical measurements such as stature and weight (Serre et al., 2006). For creating a custom 3D DHM model, we utilised the DINED platform that provides such data by querying the CAESAR population database with personas (DINED, 2022). A static 3D human model can be downloaded using the DINED mannequin portal (Molenbroek, 1999). We have requested the 50th percentile 3D male body model for this work. The static human model is converted to a rigged and animated model for the Unity game engine using Adobe Mixamo (Adobe, 2022). Using Unity's scripting system, we have programmed the DHM model to perform four actions: walking forward and backwards, and turning left or right (See, Table 1).

	Persona 1	
	Value	Percentile
Stature	1818 mm	50
Age	39 years	52

(a) Persona 1 values for 50thPercentile Male Human

(b) 3D Mannequin generated by Dined

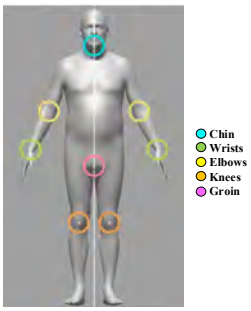

(c) Rigged Human Model for Unity with Mixamo

Figure 2. DINED 3D Mannequin for the creation of DHM

Functional vision is an individual's ability to perceive visual information in a variety of tasks primarily based on its field of vision (FoV), eyesight (acuity), and near and far vision (focus and accommodation) (Colenbrander, 2005, 2010). Visual perception can be divided into two stages for information processing. The first stage involves image formation on the retina, where information is quantified by sampling over retinal cells. The second stage involves assessing if the quantified information makes any sense, or in other words, a piece of clear information is processed further by a higher cognitive process for recognition and decision making (Bülthoff et al., 1998; Fairclough et al., 2005; Gibson, 2014). We have followed a similar two-step approach for modelling a human like perception and decision making in DHM.

To construct a functional vision model for DHM, we created a simplified model of how the human visual system works. In most humans, the FoV expands approximately 190° with the two eyes, out of which about 120° make up binocular vision (Coull et al., 2000; Rash et al., 2009). We have uniformly

divided the FoV into central, left, and right FoV regions. The model consists of four cameras positioned at DHM eye level, each covering a part of the FoV, as shown in Figure 3. Unity provides configurable cameras having features such as FoV, viewport distance, and resolution. All the cameras have a fixed FoV of 40º, thereby simulating a central FoV equivalent to 40º along with an additional 40º range for left and right FoV. Visual acuity refers to a human ability to see small details and distinguish shapes and the details of objects at a given distance (Kniestedt & Stamper, 2003). By setting the resolution of cameras from low to high, it is possible to simulate a visual system with low and high ranges of acuity. For high acuity, the camera resolution is selected as 100x100 pixel density, whereas a low acuity is set to a density of 25x25 pixels. In our model, two cameras cover near and far central FoV, whereas the remaining two are rotated at a fixed angle to cover left and right peripheral FoV. By changing the viewport distances, we have modified the visibility ranges of these cameras, effectively giving us a simulation of near and far vision in humans. As shown in Figure 3d, by varying the eleven modelling parameters for each of the four cameras, we created three personas to simulate different types of visual characteristics. They are as follows:

1. **'Good Vision':** This is modelled as a natural vision in humans. We have selected high acuity for near and far central FoV and low acuity for peripheral FoV. The focusing range is kept equivalent to the longer edge of workplace dimensions. As shown in Figure 3c, the objects appear detailed in central but fuzzy in peripheral FoV from all distances.
2. **'Poor Vision' - Type 1:** This is modelled as low acuity natural vision. We have selected low acuity for all the FoV regions. The focusing range is kept like a 'good vision' persona. As shown in Figure 3c, the objects appear fuzzy in both central and peripheral FoV from all distances.
3. **'Poor Vision' - Type 2:** It is modelled like a high myopia vision in humans. The near and far cameras for the central vision are configured with high and low acuity. The peripheral vision cameras are configured with low acuity and half the focusing range of the 'good vision' persona. As a result, objects seen from far appear fuzzy and only appear in the far central FoV. In contrast, objects within near distance appear detailed in central but remain fuzzy in peripheral FoV (Figure 3c).

Using this vision model for DHM, it is possible to functionally evaluate a workspace to establish what parts are easy or difficult to see in terms of visibility and clarity, for different personas. For example, as shown in Figure 5, the two letters in a workspace seen by a DHM with a 'good vision' persona may appear differentiable; however, with 'poor vision' personas, they may appear indistinguishable.

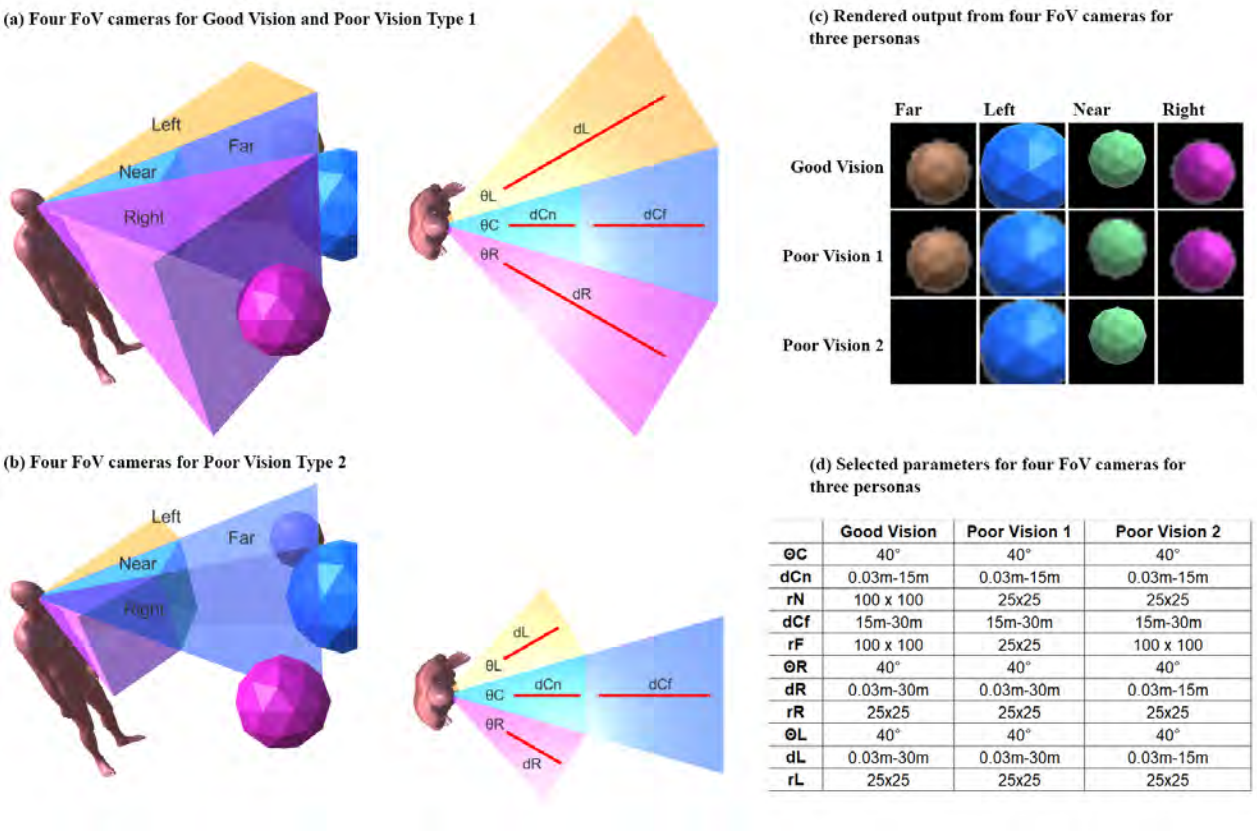

	Good Vision	Poor Vision 1	Poor Vision 2
ΘC	40°	40°	40°
dCn	0.03m-15m	0.03m-15m	0.03m-15m
rN	100 x 100	25x25	25x25
dCf	15m-30m	15m-30m	15m-30m
rF	100 x 100	25x25	100 x 100
ΘR	40°	40°	40°
dR	0.03m-30m	0.03m-30m	0.03m-15m
rR	25x25	25x25	25x25
ΘL	40°	40°	40°
dL	0.03m-30m	0.03m-30m	0.03m-15m
rL	25x25	25x25	25x25

Figure 3. Visualisation of Functional Vision Module

Design of Virtual Workspace and the Reinforcement Learning Task

To illustrate the proposed method, we modelled a virtual workspace having a target and a distractor. Figure 4 shows the design of the virtual workspace. The workspace having dimensions of 30m × 20m × 15m consists of a rectangular room enclosed by walls. The target consists of a Landolt C with a gap on the right side and the distractor being a mirror-inverted target, i.e., a Landolt C with an opening on the left side. At the beginning of the task, the DHM starts at a random position and orientated within the region marked by red rectangles. The target and distractor appear interchangeably on one of the walls of the areas marked by green rectangles at the beginning of the task. The task aims at training the DHM to identify and walk toward the target.

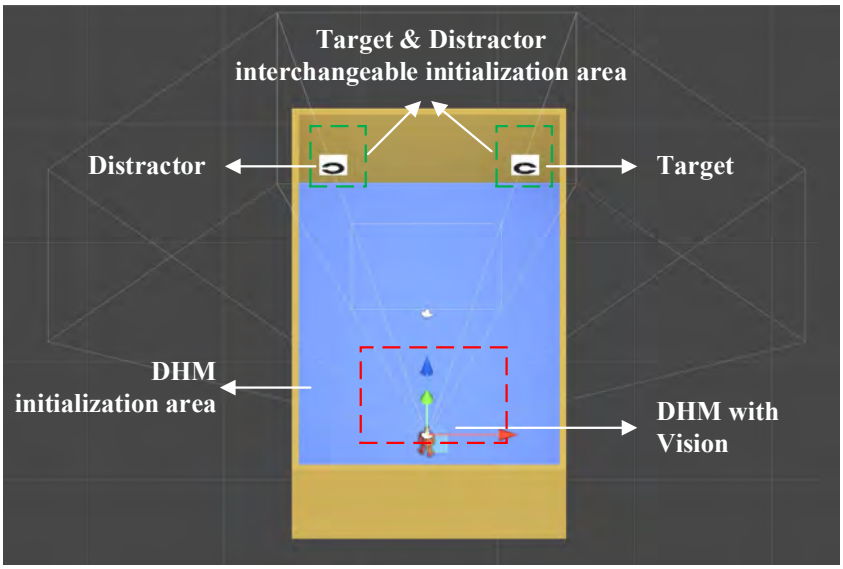

Figure 4. Virtual Workspace Setup

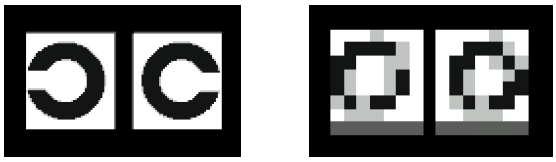

(a) High Acuity (100x100) (b) Low Acuity (25x25)

Figure 5. Visualisation of letters as seen by a DHM's vision system with high and low acuity

We have used Unity's open-source ML-Agents framework to model the decision-making system (Juliani et al., 2018). ML-Agents provides two reinforcement learning algorithms out of the box—first, Proximal Policy Optimization (PPO) and second, Soft Actor-Critic (SAC). We chose PPO over SAC due to its simplicity: it is a general-purpose algorithm that works in discrete action space and uses on-policy learning. The value function is learnt from observations made by current policy exploring the environment (Nandy & Biswas, 2018; Schulman et al., 2017). In our approach, the PPO uses a visual encoder of type simple, having two layers of 128 hidden units in a neural network to approximate the ideal decision-making policy. This policy maps the observations from the four cameras of DHM's vision system (which are defined as the state in our problem) to an action. During the training phase, these actions are primarily exploratory findings that help learn the best policy for each vision system type. The RL training process of the DHM includes the following components:

1. Observations: The DHM collects the observation input data for each location using the vision system. These are encoded as the state in our reinforcement learning system.
2. Action: The possible actions the agent can take are given in Table 1.
3. Policy: The policy maps the state to the action and indicates which action the agent should take from a given state.

4. Trial: A trial ends when the agent finds the target or a distractor as shown in Figure 6.
5. Rewards: Policy rewards for the DHM as shown in Table 2.
6. Reset: Resets and reinitialises the DHM after each trial.

Actions by RL-Model	Actions by DHM
0	No Action
1	Move Forward by 1 metre
2	Move Backward by 1 metre
3	Turn Left by 3 degrees
4	Turn Right by 3 degrees

Table 1. Mapping of Actions generated by RL models with the action taken by DHM

State	Reward
Target found	1.0
Distractor found	-0.1

Table 2. Rewards offered at the end of the trial

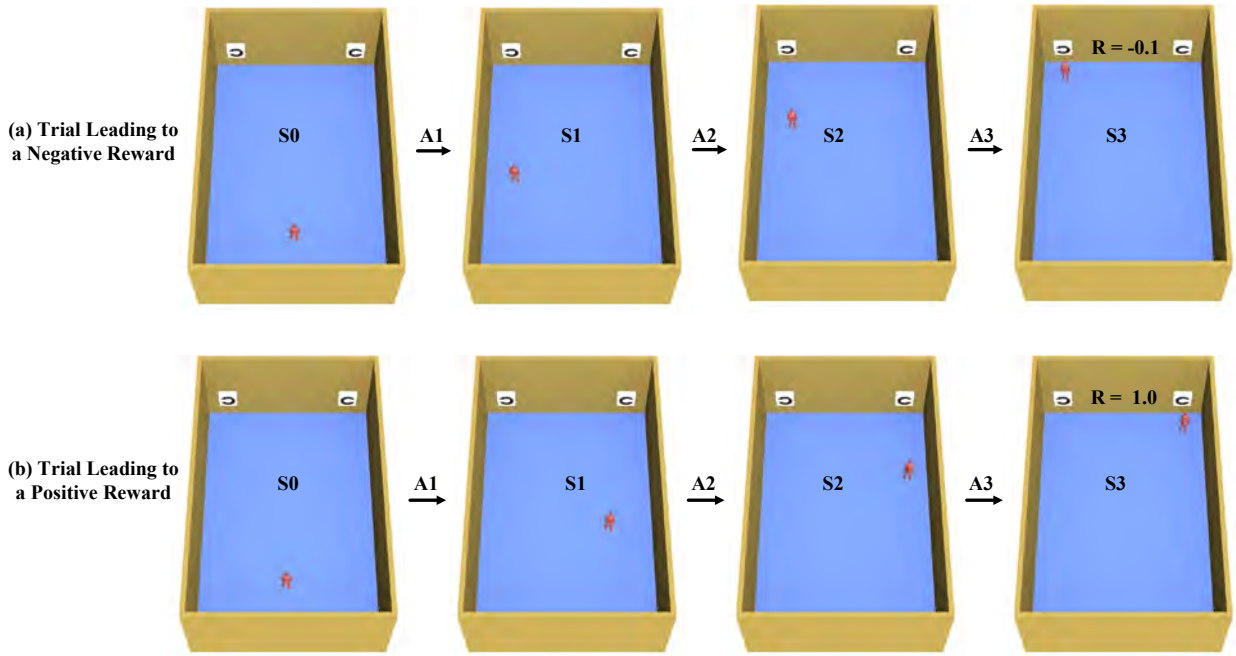

Figure 6. Visualisation of states and actions leading to positive and negative reward

At the time of learning, the goal of the DHM is to maximise the cumulative reward. It proves beneficial to train the neural network to predict whether a given state leads to a positive reward or not since it helps the network to build useful features to recognise potentially fruitful states. Using the ML-Agents interface for TensorFlow, we trained the neural network models for each of the three vision personas. We utilised eight parallel Unity instances during the training until the trained models exceeded a cumulative reward of 0.95, eventually making them 95% accurate. Since the implementation of RL training work is based on TensorFlow, the learned policy is only a TensorFlow model file. After the training, the TensorFlow policy learned for each persona was converted to an open neural network exchange (ONNX) file which is supported natively by Unity. In the behaviour simulation phase, we switched the DHM's decision-making inference type to the predictions by the ONNX neural network model generated from the training phase.

Results

We discuss the results in two categories. First, we discuss the variations in DHM's behaviour using the learned policies for the three personas in a natural world context. Second, we compare the results obtained with RL training for the three personas.

DHM Behaviour Simulations using trained RL Models

Using the trained model for each of the three personas, we obtained the results from 1000 task trails as discussed in this section. Figure 7 visualises a top-down workspace where a heatmap indicates the area explored by the DHM for each of the three personas. Hot spots (Red to Orange) show the regions most visited by the DHM. We consider them as decision-making zones. In the case of the 'good vision' persona, since the target can be easily identified, decision-making for path planning takes place during the early phase, as indicated by the hot region in the DHM's initialisation zone. It is also evident from a clear V-shaped path trajectory (Figure 7a). The trajectory of the 'poor vision' type 1 persona is similar to normal vision. However, the deeper green regions in Figure 7b indicate a relatively slow motion due to more number of actions. In the case of a 'poor vision' type 2 persona, the primary decision-making involves moving forward until a target or distractor is found within the visible range. As extended hot zones and branching in Figure 7c indicate, the secondary decision-making phase involves identifying the target and moving towards it.

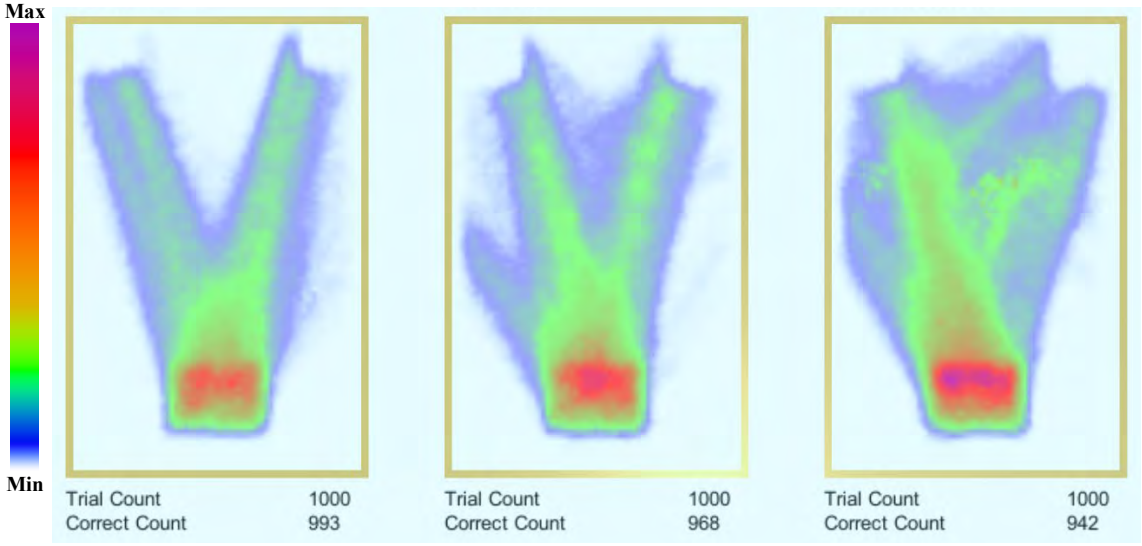

Figure 7. Heatmap visualisation of DHM's movement for three vision personas

For each trial, we logged all the actions of the DHM to reach the target and the trial completion time. 'Actions per Trial' consists of five actions from Table 1 and the total number of DHM actions for each trial. Figure 8 shows a plot of 'Actions per Trial' for each of the three personas. 'Good vision' persona had the lowest total number of actions per trial whereas 'poor vision' type 2 persona had nearly twice the total number of actions per trial. Turning right, left or backwards for reorienting shows the behaviour of workspace exploration, which shows an increasing trend from 'good vision' to 'poor vision' type 1 and 2 personas. There is also an increase in moving backward action in 'poor vision' type

2 persona compared with 'poor vision' type 1 persona which indicates backtracking the states or a decision sequence.

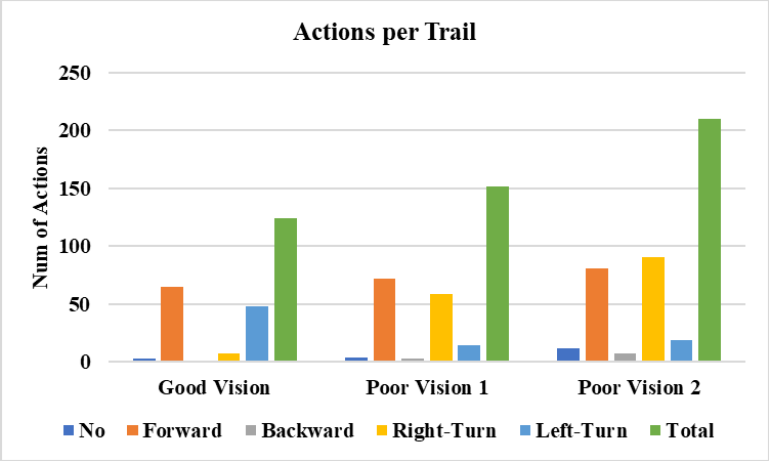

Figure 8. Comparison of actions per trial for the three vision personas

'Mean trial duration' is defined as the average time taken by the DHM to complete a task. Figure 9 shows the 'Mean trial duration' for each of the three personas. Based on the data from 1000 trials, DHMs with 'poor vision' type 1 and 2 personas took an average of 10.03 sec and 12.68 sec to complete the task, which is more than twice that with 'good vision' persona (5.1 sec).

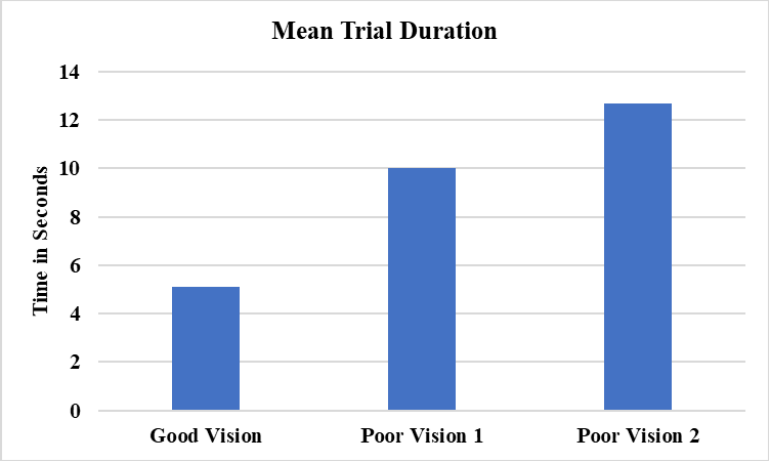

Figure 9. Comparison of mean task duration for the three vision personas

RL Training Time

In this section, we compare the model training time taken by three personas for the target finding task. We trained each persona on a Windows PC having a 16-core CPU (AMD 5950X) and a CUDA-capable GPU (NVIDIA RTX 3090). On the software side, we used Unity version 2020.3 supporting ML-Agents version 19, which uses a GPU for model training. To speed up training, we created 16 duplicates of the DHM workplace, which all contribute to training the same model in parallel. Figure 10 compares the

training time for the three personas. The DHM with a 'good vision' persona was the fastest in learning the task and took nearly 1.2 hours to surpass a mean cumulative reward of 0.9. In contrast, DHMs with 'poor vision' personas were slower and required up to 6 hours of training. The training time for each of the three personas may not represent the time taken for actual human learning. The purpose is to demonstrate that a reinforcement learning task model can be trained using a consumer-grade GPU within a reasonable time.

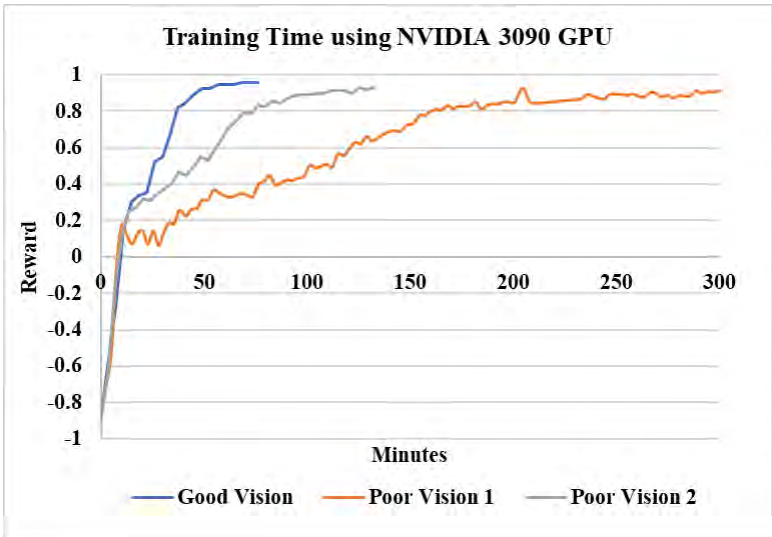

Figure 10. RL Training Time for the three vision personas

Discussion and Conclusions

In this paper, we have employed DHM with three types of visual personas as a reinforcement learning agent for the simulation of visual behaviour. By varying the field of vision, acuity, near and far distance for each visual persona, we can mimic variations in DHM behaviour for good and poor vision. In this framework, we used Unity to build the DHM and virtual workspace, ML-Agents to realise the connection between TensorFlow and Agents, and the PPO algorithm to train DHM in finding a target through intensive reinforcement learning. Compared with the traditional state or step-based task simulation methods used by DHM tools like Jack or Delmia, Vision and RL-based behaviour simulations can automate task planning and generate variations for population or vision personas. Since the presented approach allows us to concentrate more on high level decision-making and functional vision modules and utilise virtual human and workspace with any DHM module, we also plan to explore integrations of a trained behaviour policy with existing DHM tools such as Jack. We have shown that the DHM has learned the skills of searching for the target after the training. However, the variation in behaviour for each of the three personas can be distinctly observed in the results. While the target search task is simple, it is a good test bed for assessing modelling choices' impact on DHM's behaviour. Fundamentally it provides a more understandable context in natural vision settings. Humans with low

vision sometimes take longer to learn about their surroundings and associated tasks, which many research articles have covered (Consortium, 2019; Ray et al., 2008; Starke et al., 2020). Moreover, discussed in the results, the motion heatmap shown in Figure 7 resembles a more exhaustive wayfinding study and model reported by (Gath-Morad et al., 2021). We also found an increase in the mean trial duration for 'poor vision' personas compared with 'good vision' persona (Figure 9). In a wayfinding study by (Freedman et al., 2019), the authors compared the trial time with normal and low-vision human subjects and found a similar trend. Cognitive modelling is a long goal of the DHM community (Billing et al., 2019; Bubb, 2007). The main research challenge currently lies in developing an appropriate representation of the varied human behaviour and combining cognitive and anthropometric models. We believe that the performance of our DHM framework can be matched and brought closer to natural human behaviour through a similar study by introducing human-in-the-loop deep reinforcement learning (Wu et al., 2021). In the future, we plan to enhance this framework by incorporating data from virtual reality-based human-in-the-loop user studies.

Acknowledgments

Funding through Imperial College London Pedagogy Transformation Programme and the EPSRC PREMIERE Programme Grant (EP/T000414/1) is gratefully acknowledged.

References

Adobe. (2022). *Adobe Mixamo*. Retrieved 18/8/2022 from https://www.mixamo.com/

Afsar, M. M., Crump, T., & Far, B. (2021). Reinforcement learning based recommender systems: A survey. *arXiv preprint arXiv:2101.06286*.

Berger, U., Lepratti, R., & Otte, H. (2004). Application of digital human modelling concepts for automotive production. In *Proceedings of TMCE 2004* (pp. 365-373).

Bhatia, N., Sen, D., & Pathak, A. V. (2016). A functional vision based human simulation framework for complex social system design. *International Journal of Design Sciences & Technology*, *22*(1).

Billing, E., Hanson, L., Lamb, M., & Högberg, D. (2019). Digital human modelling in action. SweCog 2019, the 15th SweCog conference, Umeå, Sweden, November 7-8, 2019,

Bubb, H. (2007). Future applications of DHM in ergonomic design. International Conference on Digital Human Modeling,

Bülthoff, I., Bülthoff, H., & Sinha, P. (1998). Top-down influences on stereoscopic depth-perception. *Nature Neuroscience*, *1*(3), 254-257. https://doi.org/10.1038/699

Chaffin, D. B. (2005). Improving digital human modelling for proactive ergonomics in design. *Ergonomics*, *48*(5), 478--491.

Chaffin, D. B., Nelson, C., & et al. (2001). *Digital human modeling for vehicle and workplace design*.

Chang, S. W., & Wang, M. J. J. (2007). Digital human modeling and workplace evaluation: Using an automobile assembly task as an example. *Human Factors and Ergonomics in Manufacturing & Service Industries*, *17*(5), 445-455.

Colenbrander, A. (2005). Visual functions and functional vision. International Congress Series,

Colenbrander, A. (2010). Assessment of functional vision and its rehabilitation. *Acta ophthalmologica*, *88*(2), 163-173.

Colombo, G., & Cugini, U. (2004). Virtual manikins and prototypes to evaluate ergonomics safety. In *Proceedings of TMCE 2004* (pp. 375-382).

Consortium, W. W. W. (2019). Accessibility requirements for people with low vision. In.

Coull, J., Weir, P. L., Tremblay, L., Weeks, D. J., & Elliott, D. (2000). Monocular and binocular vision in the control of goal-directed movement. *Journal of Motor Behavior*, *32*(4), 347-360.

DINED. (2022). *DINED Anthropometry in design.* https://dined.io.tudelft.nl/en/mannequin/tool

Duffy, V. G. (2016). *Handbook of digital human modeling: research for applied ergonomics and human factors engineering.* CRC press.

Fairclough, S. H., Venables, L., & Tattersall, A. (2005). The influence of task demand and learning on the psychophysiological response. *International Journal of Psychophysiology*, *56*(2), 171--184.

Findlay, J. (1998). Active vision: Visual activity in everyday life. *Current Biology*, *8*(18), R640-R642.

Freedman, A., Achtemeier, J., Baek, Y., & Legge, G. E. (2019). Gaze behavior during navigation with reduced acuity. *Experimental eye research*, *183*, 20-28.

Gath-Morad, M., Thrash, T., Schicker, J., Hölscher, C., Helbing, D., & Aguilar Melgar, L. E. (2021). Visibility matters during wayfinding in the vertical. *Scientific reports*, *11*(1), 1-15.

Gibson, J. J. (2014). *The ecological approach to visual perception: classic edition*. Psychology press.

Irshad, L., Ahmed, S., Demirel, O., & Tumer, I. Y. (2018). Identification of human errors during early design stage functional failure analysis. International Design Engineering Technical Conferences and Computers and Information in Engineering Conference,

Juliani, A., Berges, V.-P., Teng, E., Cohen, A., Harper, J., Elion, C., Goy, C., Gao, Y., Henry, H., & Mattar, M. (2018). Unity: A general platform for intelligent agents. *arXiv preprint arXiv:1809.02627*.

Jung, K., Kwon, O., & You, H. (2009). Development of a digital human model generation method for ergonomic design in virtual environment. *International Journal of Industrial Ergonomics*, *39*(5), 744-748.

Kniestedt, C., & Stamper, R. L. (2003). Visual acuity and its measurement. *Ophthalmology Clinics of North America*, *16*(2), 155-170, v.

Nandy, A., & Biswas, M. (2018). Unity ml-agents. In *Neural Networks in Unity* (pp. 27-67). Springer.

Rajeswaran, A., Mordatch, I., & Kumar, V. (2020). A game theoretic framework for model based reinforcement learning. International conference on machine learning,

Rash, C. E., Russo, M. B., Letowski, T. R., & Schmeisser, E. T. (2009). *Helmet-mounted displays: Sensation, perception and cognition issues.*

Ray, C. T., Horvat, M., Croce, R., Mason, R. C., & Wolf, S. L. (2008). The impact of vision loss on postural stability and balance strategies in individuals with profound vision loss. *Gait & posture*, *28*(1), 58-61.

Reed, M. P., Satchell, K., & Nichols, A. (2005). *Application of digital human modeling to the design of a postal delivery vehicle.*

Ryu, D., Abernethy, B., Mann, D. L., Poolton, J. M., & Gorman, A. D. (2013). The role of central and peripheral vision in expert decision making. *Perception*, *42*(6), 591-607.

Schulman, J., Wolski, F., Dhariwal, P., Radford, A., & Klimov, O. (2017). Proximal policy optimization algorithms. *arXiv preprint arXiv:1707.06347*.

Serre, T., Brunet, C., Bruyere, K., Verriest, J., Mitton, D., Bertrand, S., & Skalli, W. (2006). HUMOS (Human Model for Safety) Geometry: from one specimen to the 5th and 95th percentile. 2006 Digital Human Modeling for Design and Engineering Conference,

Starke, S. D., Golubova, E., Crossland, M. D., & Wolffsohn, J. S. (2020). Everyday visual demands of people with low vision: A mixed methods real-life recording study. *Journal of Vision*, *20*(9), 3. https://doi.org/10.1167/jov.20.9.3

Wahl, H.-W. (2013). The psychological challenge of late-life vision impairment: Concepts, findings, and practical implications. *Journal of ophthalmology*, *2013*.

White, U. E., Black, A. A., Wood, J. M., & Delbaere, K. (2015). Fear of falling in vision impairment. *Optometry and vision science*, *92*(6), 730-735.

Wu, J., Huang, Z., Huang, C., Hu, Z., Hang, P., Xing, Y., & Lv, C. (2021). Human-in-the-loop deep reinforcement learning with application to autonomous driving. *arXiv preprint arXiv:2104.07246.*

Wu, W., & Gao, L. (2017). Posture self-stabilizer of a biped robot based on training platform and reinforcement learning. *Robotics and Autonomous Systems*, *98*, 42-55.

Zhu, W., Fan, X., & Zhang, Y. (2019). Applications and research trends of digital human models in the manufacturing industry. *Virtual reality & intelligent hardware*, *1*(6), 558-579.

Human Digital Twin with Applications

Zhiqing Cheng

Innovision, LLC, Dayton, Ohio, USA

ABSTRACT

The concept formation of Human Digital Twin (HDT), including basic considerations, construct of HDT, and the features of HDT is presented in this paper. The steps and methods for HDT construction are described, which include template human model creation, human model unification, individualization, data links with data driven models, and integration. Two projects where HDT are used for practical problems are introduced.

1. INTRODUCTION

A 'Digital Twin' is a virtual representation or digital form of a physical object or process in the real world. The digital twin technology has been widely implemented by industry in recent years (Grieves 2021). As the real world is centered around the human, the digital representation or virtual self of the human should be at the center of the digital world. This basic consideration motivated the concept and technology of the Human Digital Twin (HDT) developed at Innovision since 2017 (Cheng 2019). The HDT developed by Innovision is based on individualized human models combined with personal data containers linked to sensors. The data can be processed using analytics to provide an integrated, dynamic representation of one's personal physical and physiological states. Combined with physics solvers, a HDT can be used to perform physics-based analysis, simulation, and prediction of physical and physiological performance of an individual (Cheng et al., 2020).

This paper presents the development of HDT technology, including concept formation, construction, potential applications, current limitations, and prospects. As practical examples of HDT applications, two funded projects are introduced, where patient digital twin is used to improve the compliance of Physiotherapy Scoliosis Specific Exercises (PSSEs) and pilot digital twin is used to mitigate the acute neck injury and chronic neck pain of military pilots, respectively.

2. HDT CONCEPT FORMATION

2.1 Basic Considerations

1) Traditional human models have two major limitations: (a) Each describes a single aspect or small set of human features/characteristics; and (b) They typically describe the average properties of a human. Often, one model is used to represent a group or population. Humans, however, embody a complicated system with distinct characteristics ranging from physical, biological, and physiological features to cognitive and behavioral traits. Though a complete digital representation of human is still far from reality, a unified representation of multiple features of human with a high level of details and fidelity is possible due to rapid advancement of digital human modeling and computer technology in recent years. Conventionally, human body shape (with anthropometry), musculoskeletal characteristics, and anatomy are described separately by three independent models with different data representations. However, human features/characteristics are inter-dependent. It is advantageous that they be described in a unified way, if possible, so that the unification can more accurately describe a human. Particularly, human body shape, musculoskeletal characteristics, and anatomy all embody human physical features and lend themselves to the unified modeling.
2) Humans share common gender-specific anatomy and gross physical attributes. Therefore, we can create a unified model structure and data structure and standard models (templates) that can be used for all

humans. Humans' differences make each of us unique and differentiated from others in anthropometry, race, ethnicity, biomechanical, metabolic, and physiologic attributes. This motivates the creation of individualized human models.

3) Creating a digital human model for an individual requires a large amount of work as more individual details are included. To keep the effort tractable and affordable, one can use standard models as templates and then create individualized (instance) models from the template models via fitting, morphing, and scaling based on the personal data. In this fashion, the individualized models will provide a representation of the person, with the level of details and medical fidelity that is sufficient for the intended applications.
4) In special applications as joint replacement and augmented reality assisted surgery, the regional models of particular parts of body or tissue groups can be created from the actual data of that person (e.g., Magnetic Resonance Imaging (MRI) data, and X-ray Computed Tomography (CT) data, etc.) so that a higher level of anatomical details and medical fidelity is attained.
5) Some human physical and biological features are not suitable to be represented by a static model and their states need to be updated frequently. Therefore, we use data containers to store and manage these data and data-driven models to describe these features and states.
6) As an approximate representation of a real human, HDT is far from a complete digital replica of human. As digital human modeling technology advances, more models of human physical and psychological characteristics (e.g., cognitive, behavioral, and bio-physics models) will become technically feasible. The structure of our HDT is open, allowing these human models to be integrated in the future.

2.2 Construct of HDT

As shown in Figure 1, HDT comprises individualized and unified human models combined with personal data containers with data analytics. We incorporate and integrate three different models:

1) 3D Human body shape model with anthropometry, which provides a complete 3D surface mesh description of human body shape along with anthropometric measurements.
2) Full body musculoskeletal model, which includes skeletal geometry, rigid linkage with multiple degrees of freedom to define joint kinematics, and Hill-type models of muscles and tendons. This provides a non-invasive means to study human kinematics and movement.
3) Full body finite element model, which uses solid finite element meshes to describe the complete anatomical structure of the human body in terms of tissue groups.

Other models, such as a human behavior model, lifestyle model, and cognitive model will be explored and evaluated in the future. They will be integrated into the unified framework when they become technically mature. These models, each of which describes specific human aspects, are integrated into a framework having unified model and data structures. This framework facilitates the sharing of common data and functional information exchange among model elements. These elements remain the same for every individual. The state-of-the-art standard models are used as the templates for the individualized models.

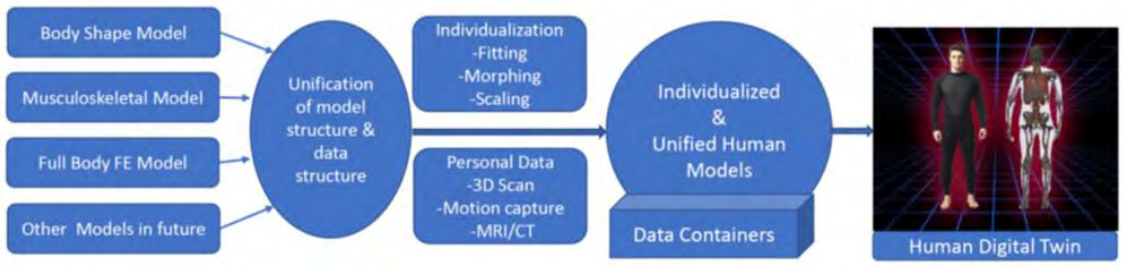

Figure 1. An overview of Human Digital Twin.

An individualized model is created from the template models via morphing and fitting that is appropriate for the individual. The personal data to be used includes the 3D body scan, motion capture data, MRI data, and X-ray data, each of which provides different levels of details of body.

Data containers are linked to wearable sensors, ambient environmental conditions, and other data sources. Data containers are used to store and manage the personal data of physical, physiological, and cognitive status, health data, activity tracking data, and medical treatment data. These data can be used to establish predictive alerts and guide people to healthier lifestyles (Bruynseels et al., 2018). Moreover, data-driven models (e.g., empirical regression models and deep neural network models) can be created from these data (Brunton and Kutz, 2019).

2.3 Features of HDT

The unique feature of HDT can be summarized as follows.

1) **Physics or first principle based:** HDT is created based on the physics and/or first principles of anthropometrics, biomechanics, physiology, biology, behavioral and cognitive sciences. Integrated with physics solvers, HDT can be used to analyze and simulate personal physical and physiological responses and status.
2) **Individualized**: HDT contains individualized human models, which are created based on the personal data, thus providing fair description of the unique features/characteristics of an individual.
3) **Unified**: Different types of human model are integrated into a unified framework with unified model structure and data structure. The unification leads to more effective and coherent representation of various features/characteristics of human and promotes synergetic utilization of different models.
4) **Quick generation:** The state-of-the-art standard models are used as the template models. The individualized models are then created from the template models by means of fitting, morphing, scaling, and other methods based on the personal data. As such, one can quickly build individualized models with tractable efforts and at the same time provide sound approximate representation of an individual.
5) **Dynamic**: Data containers are linked to wearable sensors or other data sources, so that the parameters, features, and states of HDT will be updated at different time scales which are appropriate for respective human features/characteristics.
6) **Progressive**: HDT has an open structure, allowing for new human models to be integrated when they are technically feasible.
7) **Flexible**: The level of details and bio-fidelity of the models is flexible, depending on the intended uses and data availability. Whereas the base models are intended to meet basic requirements for common applications, the refined and enhanced models can meet more stringent requirements for special applications.
8) **Affordable:** The individualized models are created from the templates via individualization. As such, the effort to build individual models becomes tractable and affordable. This is crucial to a variety of applications where cost matters.

3. HDT CONSTRUCTION

The process for HDT construction includes template model creation, model unification, and individualization. The methods used in these steps are described as follows.

3.1 Template Model Creation

Various methods have been developed for creating static and dynamic human shape models (Cheng and Robinette, 2009), including deriving 3D body shape models from 2D imagery via deep learning (Dibra et al, 2017). We use the parameterized human shape model developed (Figure 2(a)) as the template for human shape modeling. This template model, which can be gender-specific, is fit to the 3D body scan of an individual to generate a body shape model. Point-to-point surface registration methods, such as coherent point drift (Myronenko and Song, 2009), can be used to fit the template model to the target scan surface via non-rigid registration. By this approach, point-to-point correspondence will be established between the template model and an individual model and among all individual models.

(a) Shape model

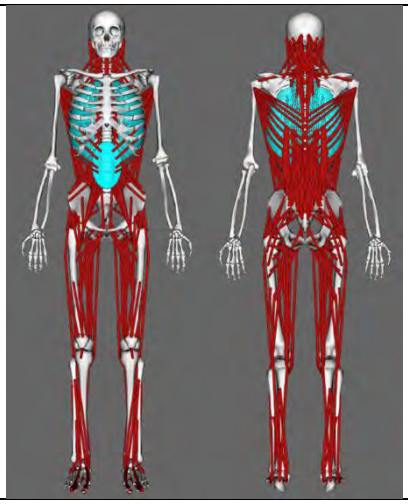

(b) Musculoskeletal model

(c) Full body FE model

Figure 2. Template models for creating individual models.

Full body musculoskeletal models are of great interest due to their ability to provide a more accurate representation of human motion. Under Dynamic Avatars with Complete Articulated Anatomy (DACAA) (Cheng et al., 2020), a small business innovative research Phase I and Phase II program sponsored by the Defense Health Agency, a full body musculoskeletal model (Figure 2(b)) was developed by combining previously validated OpenSim (Delp et al., 2007) (https://simtk.org) models, including the full body lumber spine model (Raabe and Chaudhari, 2016), the musculoskeletal model for spinal injuries (Cazzola et al., 2017), and the upper extremity model (Saul et al., 2015). We can use this model as the template for all individual musculoskeletal models.

Full body finite element models have advanced significantly for the past decade as an important tool for assessing protection for humans exposed to dynamic events. In DACAA, we have developed a framework to convert an Individual Avatar with Complete Anatomy (IAVCA) developed by Zientara and Hoyt (2017) at the US Army Research Institute of Environmental Medicine (USARIEM) to a fully functional full body finite element model, as shown in Figure 2(c). We can use this model as the template model for all individual full body finite element models.

3.2 Human Model Unification

Human body shape, musculoskeletal system, and internal anatomical structures represent different human physical features. Yet, these are inter-related features. The unification of different types of models used to represent these features leads to a more coherent representation of various aspects of human features and characteristics. The unification promotes (a) sharing of common data; (b) exchanging/transferring information between different models; (c) synchronizing the status of different models; and (d) working together to provide more capabilities for analysis and prediction.

Contributing factors supporting model unification include: (a) Surface (skin) landmarks can be used to determine joint centers for the musculoskeletal model and bony structural features; (b) The inertial properties of body segments can be approximately determined using full body finite element model based on the body shape model; (c) An injury to or a surgery on the body can affect the body shape, anatomical structure, and musculoskeletal simultaneously; and (d) The musculoskeletal model can be used to predict a person's motion, while the full body finite element model can be used to predict the stress in a body region per frame (in an animation). The predictions from both models can then be input for a physiology engine

to predict one's physiological states and vital signs (e.g., metabolic energy consumption, heart rate, breath rate, etc.).

3.3 Individualization

Human digital twin is a virtual rendition of an individual with all human characteristics. This requires all the technical means available for individualization. Individual model can be created one for one based on personal data, but a significant effort is required to build a model from scratch. Given potential applications of HDTs, if a large number of HDTs are created, the modeling effort may become intractable. To ensure the feasibility of creating HDTs, one can create the models for an individual via individualization which generates instance (individual) models from the template models by fitting, morphing, and scaling, as shown in Figure 3.

- Fitting: To create an individualized shape model, we fit a template shape model to the 3D full body scan or full body X-ray scan data of the person. This work can be done using a non-rigid registration method.
- Morphing: In DACAA program, a method was developed for morphing a parametric finite element model to a surface (shape) model. The process begins with statistical models of human geometry (skeleton and external body surface) that describe morphological variations within the population as functions of human parameters (age, sex, stature, and/or body mass index). Mesh morphing methods are used to rapidly morph a baseline human model into other geometries while maintaining high geometry accuracy and good mesh quality. Given a target age, sex, stature, and body mass index, the statistical human geometry models developed previously predict thousands of points that define the body posture, the size and shape of the external body surface, and ribcage and lower extremity bone geometries. The skeleton and external body shape geometries are integrated together based on the landmarks and joint locations shared in both models. Once the target geometries are developed, the baseline model is morphed to match the target geometries using a technique based on radial basis functions, as shown in Figure 4.
- Scaling: To create an individualized musculoskeletal model from its template, we will use the full body finite element model of this person to determine his joint centers and calculate linkage lengths and segment inertial properties. These parameters will be then used in OpenSim to calculate scaling factors for scaling the template model to the individual model.

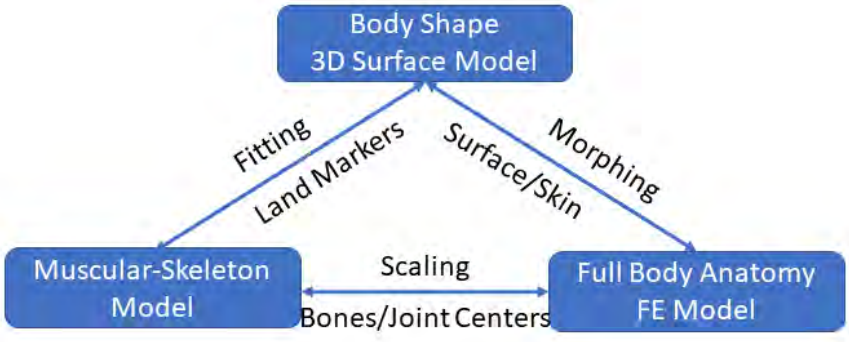

Figure 3. Unification and individualization of human models.

The individualized models created from the templates provide an acceptable approximation to the ground truth, having a level of details and medical fidelity that meet the requirements of many applications. This approach is the primary method that we will use to create HDTs. Alternatively, to attain a higher level of details and fidelity, full body finite element model can be created from MRI or X-ray data directly, which requires specialized efforts that may exceed practical safety and financial limits. The MRI scans of the

whole body are extremely rare due to motion artifacts from internal organs. MRI of large portions of anatomy are extremely expensive. The X-ray CT scans are rarely performed for ethical reasons unless there is a critical health risk that warrants the very high X-ray dose received. A full body musculoskeletal model can be created from motion capture data by registering virtual markers on the template model in OpenSim with the markers placed on the body.

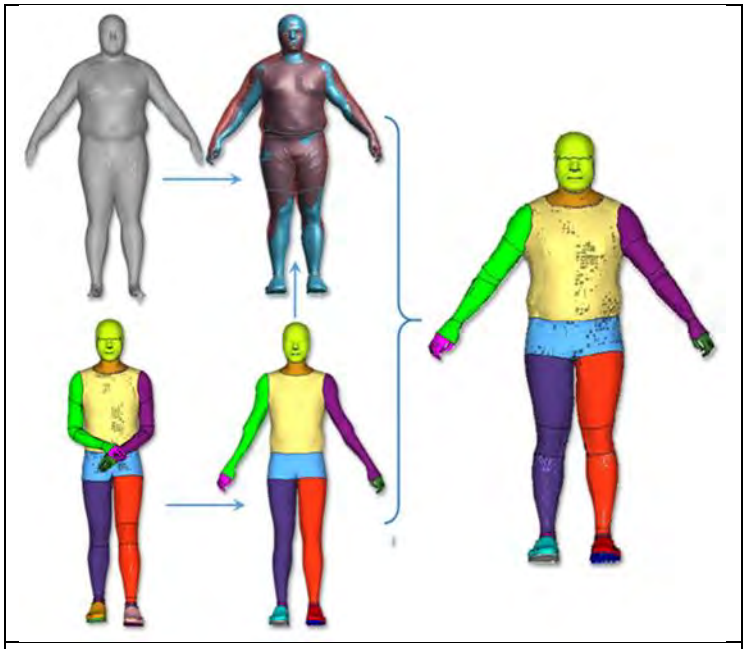

Figure 4. Morphing an FE model to a target body surface.

3.4 Data Containers with Data Driven Models

Data containers with data driven models are used for HDT to describe the human characteristics of physical components not fully parameterized or modeled. A conceptual design of HDT data containers is shown in Figure 5. Data analytics and machine learning can be applied to these data to create data driven models, which range from basic linear regression models to sophisticated DNN models (Brunton and Kutz, 2019).

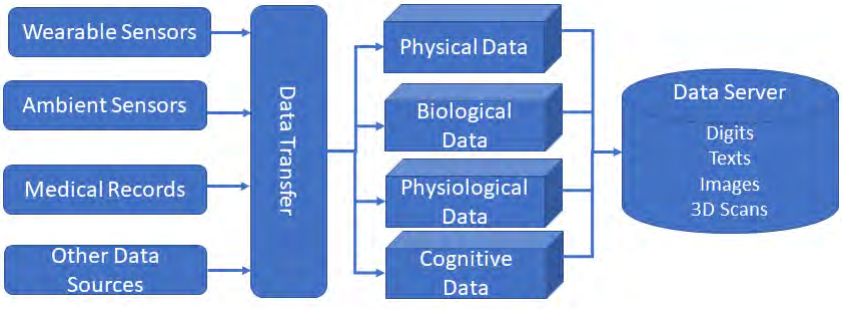

Figure 5. Data Containers for HDT.

4. APPLICATIONS

HDT has wide applications in human-centered products, services, and performance, such as digital health or telehealth, human-machine interface, fit and accommodation, physical therapy, and physical training. Two funded projects are briefly described as follows.

4.1 Patient Digital Twin for Scoliosis Physiotherapy

This is a small business innovative research (SBIR) Phase I sponsored by National Science Foundation. In this project, the patient digital twin as a digital or virtual copy of an individual patient is created from body scan and X-ray images. It allows the diagnosis of scoliosis and the assessment of spine deformity to be performed in 3D space, thus improving the completeness of assessment and the design of PSSEs. By graphically displaying muscles involved in a PSSE and the effects of muscle activation and stretching, a physiotherapist can clearly explain the cause-effect of a specific PSSE on the spine deformity. The prescribed PSSEs are represented by 3D games by animating the patient digital twin with motion captured during clinic practice. Then, with a home-based performance capture device, the actual poses and motion of a patient during home exercise can be monitored, evaluated, and instructed to adjust with 3D games as reference.

(a) Body scan	(b) X-rays	(c) Skeletal model	(d) PDT

Figure 6. Human digital twin for a scoliosis patient.

Scoliosis PDT, as shown in Figure 6, is created through individualization process which includes multiple steps as follows.

1) Shape model creation. In clinic or at home, the patient's body shape can be captured by Kinect and then the body shape model can be readily created from depth images. After a shape is derived from 3D point clouds, it will be parameterized by projecting the model in an eigen space composed by principal components of human body shape.
2) MS model creation. Usually, a Scoliosis patient will not do a body CT scan, instead, X-ray images are often taken. Therefore, in the current stage we will focus on utilizing X-ray images to create an instance MS model from its template via the following procedures.
   - Scaling: we will first scale the musculoskeletal model based on the subject's height and weight. Then, the body segment lengths will be adjusted according to the skeleton model provided by Kinect. This will be done using OpenSim which runs on the central server.
   - Skeleton morphing: we have developed a method for skeleton morphing, which includes four steps: (a) Registration: to register x-Ray images (back and side views) which are usually taken for a patient to the body shape model in the coronal plane and sagittal plane, respectively; (b) Spine reconstruction: to reconstruct spine column from c1 to L5 in 3D space based on the registered and calibrated X-ray images; (c) Match: to match each vertebrate from MS template model with the counter one from the reconstructed patient spine by adjusting vertebrate disk position and orientation; and (d) Morphing: to morph other bone structure of the template MS model accordingly assuming that the connection between a bone (e.g., rib) and its attached vertebrate is rigidly.
   - Muscle morphing: The muscle groups of the MS template model will be adjusted in length, orientation, and attachment accordingly based on the skeleton structure of the patient. As such, the

MS model for a patient can be quickly derived from the template MS model to match his/her actual height, weight, and spine curvature. This model provides a sound approximate modeling of the muscular skeleton and can be used to define/demonstrate a pose, to replicate a motion, and to compute scoliosis curves (Cobb angles), thoracic kyphosis (T4-T12 Cobb angle) and lumbar lordosis (L1-L4 Cobb angle) for an individual patient.

3) Integration. The shape model and the MS model will be integrated to become a full body model by associating the body surface vertices with its underlying bone structure. As such, realistic body deformation can be attained when the entire body is articulated. The integrated model constitutes the main part of patient digital twin. In addition, we use data containers to hold other physical and physiological data, pose data, motion capture data, and other medical information.

4.2 Pilot Digital Twin (PDT)

This is a SBIR Phase I sponsored by the United States Air Force. As shown in Figure 7, Pilot Digital Twin, as a virtual copy or digital representation of an individual pilot, is composed by physics-based human models, data-driven models, and data containers linked to wearable sensors, cockpit environments, and other data source. It provides integrated, holistic, and dynamic representation of physical/ physiological attributes of an individual pilot and tracks a pilot's physical and physiological performance and health status. It can be used for (a) Personalized design and fitting of pilot gears and equipment; (b) Adaptive cockpit accommodation; (c) Personalized physical fitness training and mission performance training; (d) Acute and chronic injury mitigation; and (e) Physiological status monitoring and prediction.

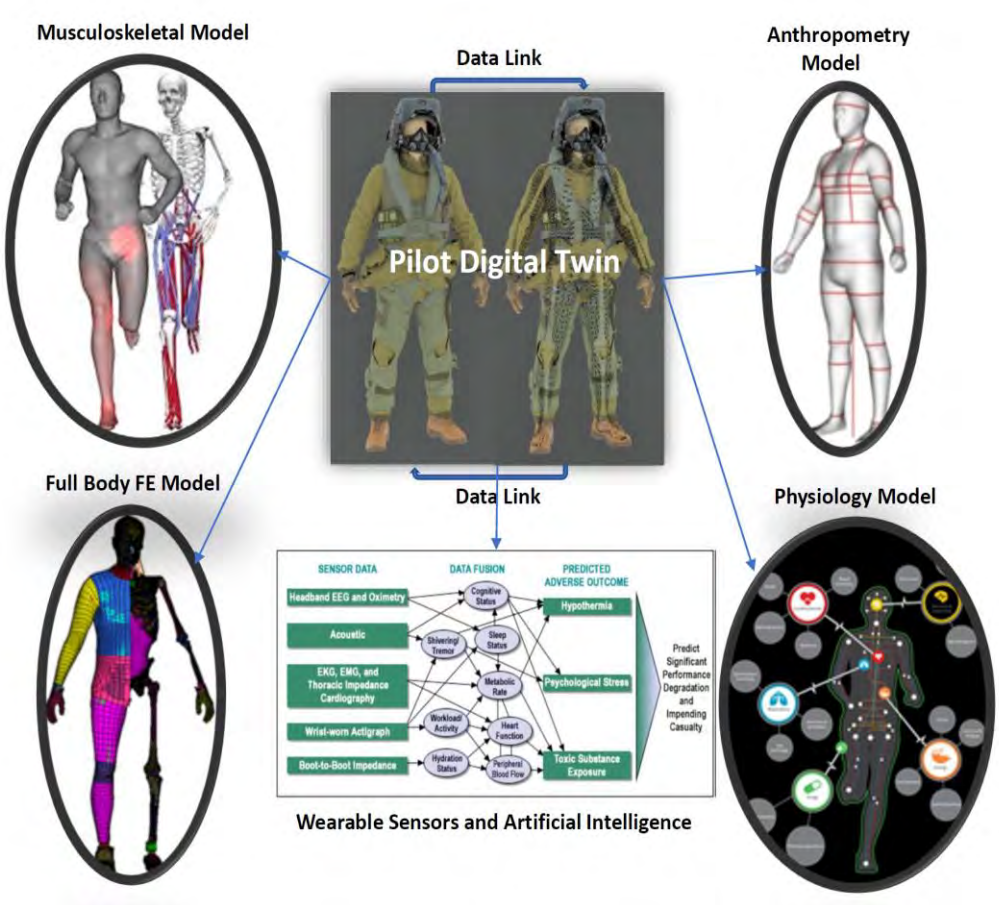

Figure 7. Pilot Digital Twin (PDT)

5. DISCUSSION

Digital twins have become an enabling technology implemented by industry in recent years (Grieves 2021). We introduced the development of the HDT technology that could be used for various applications. The human body is a complicated biological system. Any digital representation or virtual copy of human body is an approximate representation with the limited level of details and bio-fidelity. The same is true for the HDT presented in this paper. For the HDT introduced in this paper, we use physics-based digital human models (unified and individualized) and data containers with data analytics. Based on the data collected by a HDT, various data-driven models can be derived, ranging from the simplest regression models to the most advanced deep neural network models. While many human characteristics can be effectively and rigorously represented by physics-based digital models (e.g., anthropometric and biomechanical features), others (e.g., cognitive and behavior attributes) can be more easily described by data-driven models. Moreover, human characteristics can be described by a hybrid model that integrates a physics-based model with a data-driven model (Brunton and Kutz, 2019).

A data link can be established between a HDT (HDT) and its biological counterpart to synchronize their dynamic states in real-time. This clearly differentiates a HDT from a traditional human model or an individualized avatar which is manipulated by user commands. The future states predicted by use of the digital twin's multisystem data can be fed back to human via the data link. If the digital twin is considered as a body, data stream is the 'blood' of the body. In practice, the physics-based models of the HDT need to be updated periodically according to substantial body changes induced by injury, physical training, or other causes. The data-driven models of the HDT can be updated more frequently, or in real-time, based on the data stream from wearable sensors/other sources. If a HDT were to accompany its biological twin for a significantly lengthy period, it would need to reflect changes during growing and aging processes.

The development of the HDT technology will be a progressive process from its current rudimentary form to a full scale, accurately-modeled digital twin in the future, incorporating state-of-the-art technologies that improve its level of details and bio-fidelity. Regarding the HDT described in this paper, extensive efforts are still required to complete development and to fulfill its designated functions. From general HDTs which are for average people, digital twins can be created for a specific group of people with common environments, needs, requirements, or purposes, such as patients (e.g., scoliosis patients or those with chronic back pains), Warfighters (e.g., pilots), athletes (e.g., football players), astronauts, fire fighters, first responders, etc.

As the HDT contains personal data, the information security and privacy protection become important issues. During HDT design and development, various measures can be adopted for information security and privacy protection. During HDT utilization, strict procedures need to be implemented for the data access. Policies may need to be established at high levels for HDT management.

6. CONCLUSIONS

The concept of human digital twin along with an approach to construction was presented. By using individualized, unified physics-based models, HDT can effectively describe human physical and physiological characteristics. By using data containers linked to data streams, HDT can reveal personal status and performance in a timely fashion. By using data driven models, HDT can represent human cognitive, behavioral, and other performances. Integrated with physics solvers, HDT can be used to analyze and predict human physical and physiological status under force, acceleration, and other extreme conditions. Integrated with wearable sensors and ambient sensors, HDT can be used to enhance and expand human performance monitoring and assessment. There are various potential uses of HDT in the integrated digital environments or metaverse. HDTs can work with advanced digital technologies including big data, data analytics, deep learning, and artificial intelligence to protect, enable, and empower individual human.

REFERENCES

Bruynseels K, Santoni de Sio F and van den Hoven J (2018). Digital Twins in Health Care: Ethical Implications of an Emerging Engineering Paradigm. Front. Genet. 9:31. doi: 10.3389/fgene.2018.00031.

Brunton, Steven L. and Kutz, J. Nathan (2019). *Data-Dirven Science and Engineering, Machine Learning, Dynamical systems, and Control*. Cambridge University Press, ISBN 978-1-108-42209-3.

Cazzola, D., Holsgrove, T., Preatoni, E., Gill, H., and Trewartha, G. (2017). Cervical spine injuries: A whole-body musculoskeletal model for the analysis of spinal loading. *PLoS ONE*, 12(1), e0169329.

Cheng, Zhiqing (2019). Warfighter Digital Twin. *Defense TechConnect Innovation Summit & Showcase*, Oct. 8-10, 2019, National Harbor, MD.

Cheng, Z. and Robinette, K. (2009). Static and Dynamic Human Shape Modelin—A Review of the Literature and State of the Art. *Technical Report*, *Air Force Research Laboratory, AFRL-RH-WP-TR-2010-0023*.

Cheng, Z., Hu, J., Yang, J., Sanford, D., Hoyt, R.W., Zientara, G.P. (2020). Individualized Avatars with Complete Anatomy: Repositioning of Superficial Anatomy. *USARIEM Technical Report* T20-06.

Delp, S., Anderson, F., Arnold, A., Loan, P., Habib, A., John, C., Guendelman,E., and Thelen, D. (2007). OpenSim: Open-source software to create and analyze dynamic simulations of movement. *IEEE Trans Biomed. Eng.*, Vol. 54, No. 11, 1940-1950.

Department of Defense (2018). Digital Engineering Strategy. Office of the Deputy Assistant Secretary of Defense for Systems Engineering, Washington, D.C.

Dibra, E., Jain, H., Oztireli, C., Ziegler, R., and Gross, M. (2017). Human shape from silhouettes using generative hks descriptors and cross-modal neural networks. *CVPR*, Honolulu, HI, USA.

Friedl, K. E. (2018). Military applications of soldier physiological monitoring. *Journal of Science and Medicine in sport*. 21:1147-1153.

Grieves, M. (2021). Digital Twin Today: Advancements and Opportunities. A presentation at *Digital Twin Summit*, ASME.

Kim, J. and Roberts, D. (2015). A joint-space numerical model of metabolic energy expenditure for human multibody dynamic system, International Journal for Numerical Methods in Biomedical Engineering, 31(9): e02721.

Myronenko, A. and Song, X. (2009). Point Set Registration: Coherent Point Drift. *arXiv:0905.2635v1 [cs.CV]*.

Looney D., Santee, W., Hansen, E., Bonventre, P., Chalmers, C., and Potter, A. (2019). Estimating Energy Expenditure during Level, Uphill, and Downhill Walking. *Medical & Science in sports & Exercise*, 51(9):1954–1960.

Raabe, M. and Chaudhari, A. (2016). An Investigation of Jogging Biomechanics Using the Full-Body Lumbar Spine Model: Model Development and Validation. *J. of Biomechanics*, vol. 49, no. 7, 1238-1243.

Saul, K., Hu, X., Goehler, C., Daly, M., Vidt, M., Velisar, A., and Murray, W. (2015). Benchmarking of dynamic simulation predictions in two software platforms using an upper limb musculoskeletal model. *Computer Methods in Biomechanics and Biomedical Engineering*. 18:1445-58.

Zientara, GP and Hoyt, RW (2017). Individualised Avatars with Complete Anatomy Constructed from the ANSUR II 3-D Anthropometric Database. *Int. J. Digital Human*, Vol. 1, No. 4, pp 389-411.

Modeling Ability to Perform Common Soldier Tasks Based on the Army Combat Fitness Test Deadlift

Laura A. Frey-Law, Rajan Bhatt, Russell Schneider, Guillermo Laguna Mosqueda, Marco Tena Salais, Landon Evans, and Karim Abdel-Malek

Virtual Soldier Research Team, Iowa Technology Institute, The University of Iowa

Introduction

The US Army has developed a battery of physical fitness test events to measure soldier readiness to engage with and overmatch the enemy in close combat. The original Army Physical Fitness Test (APFT) only assessed three events: a two-mile run, push-ups, and sit-ups. To better represent the myriad of physical tasks soldiers are exposed to and expected to complete, a new Army Combat Fitness Test (ACFT) was developed (US Army, 2018). The ACFT comprises six physical exercise tasks: (a) three-repetition maximum deadlift; (b) standing power throw; (c) hand-release push-ups; (d) a combination sprint, drag, and carry task; (e) leg tuck (or plank); and (f) two-mile run. The Army performed several investigations comparing task performance of the ACFT to a simulated battle drills and common soldier tasks (CSTs) obstacle course, where completion time was the primary outcome measure. However, the Army was not able to compare more detailed aspects between CSTs and the new ACFT, such as biomechanical analyses based on digital human modeling.

CSTs and battle drills represent the wide range of tasks that may be expected as part of any soldier's day, ranging from sedentary, desk-based work to vigorous tasks such as marching in full gear or having to extract and transport soldiers in battle. The goal of the ACFT was to assess multiple physical domains, including strength, power, endurance, oxygen consumption, and energy expenditure, to represent the more physical components of CSTs to ensure they would be capable of completing these tasks as well as reduce the risk of injury.

The work presented here is part of a bigger project in which the Iowa Technology Institute's Virtual Soldier Research (VSR) lab simulated and analyzed the ACFT test events and several moderate- to high-demand CSTs. The aim of this paper is to compare the strength requirements at several major joints based on advanced inverse dynamics and digital human modeling between one of the ACFT tasks, the deadlift, and several more demanding CSTs (Abdel-Malek, 2008; Xiang, 2010). We focused on two primary questions:

1) Is the ACFT predictive of CSTs?
2) Are the minimum ACFT event standards sufficiently rigorous to meet standard CST requirements?

Methods

Six Army Reserve Officer Training Cadets (ROTC) students (3F, 3M) were recruited to complete a series of ACFT and CSTs with motion capture over three visits. However, 1 female did not complete the study, thus only 5 subjects' data are considered for these analyses. All participants provided written informed consent, as approved by the Institutional Review Board (IRB). ROTC students were recruited in order to ensure some level of familiarization with Army testing and maneuvers (see below for more detail). The motion capture data was then transferred to the Iowa Technology Institute Santos simulation engine and processed using the advanced inverse dynamics algorithms developed by the research team at VSR. Using the Santos® and Sophia® DHMs, joint torque profiles (i.e., estimated workloads) were modeled. Peak torques were extracted for each task for the knee, hip, truck, shoulder, and elbow. Values were compared across tasks.

Motion Capture

Motion capture (Thewlis, Bishop, Daniell, & Paul, 2013) of all tasks were performed using OptiTrack, with the Motive software. Study participants wore a black bodysuit with fifty-five 9 mm infrared markers attached with velocro following a customized markerset protocol (Rahmatalla, 2011) that our team had previously developed to work with the proprietary Santos program (see Figure 1). For all ACFT events, the body suits were worn over clothing that closely resembled the standard Army Physical Fitness Uniform (APFU): t-shirt, shorts, socks, and running shoes. This allowed the participant to have a full range of motion while conducting the data capture. The motion capture suit is a combination Spandex and Velcro suit that allowed the motion capture team to attach sensors on the body at prescribed locations. The suit included a top, pants, and covers that go over the shoes that allow the sensors to be placed on the feet. During the ACFT portion of the study, the participants also wore a cap of the same material that allowed sensors to be placed on the head. To ensure proper labeling of the markers, the participants were instructed to start and end in T-pose with their arms extended to the side and palms facing downward. This position allowed for all the markers to be visible to the Motive program as well as allowing the motion capture team to properly label the markers while processing the data.

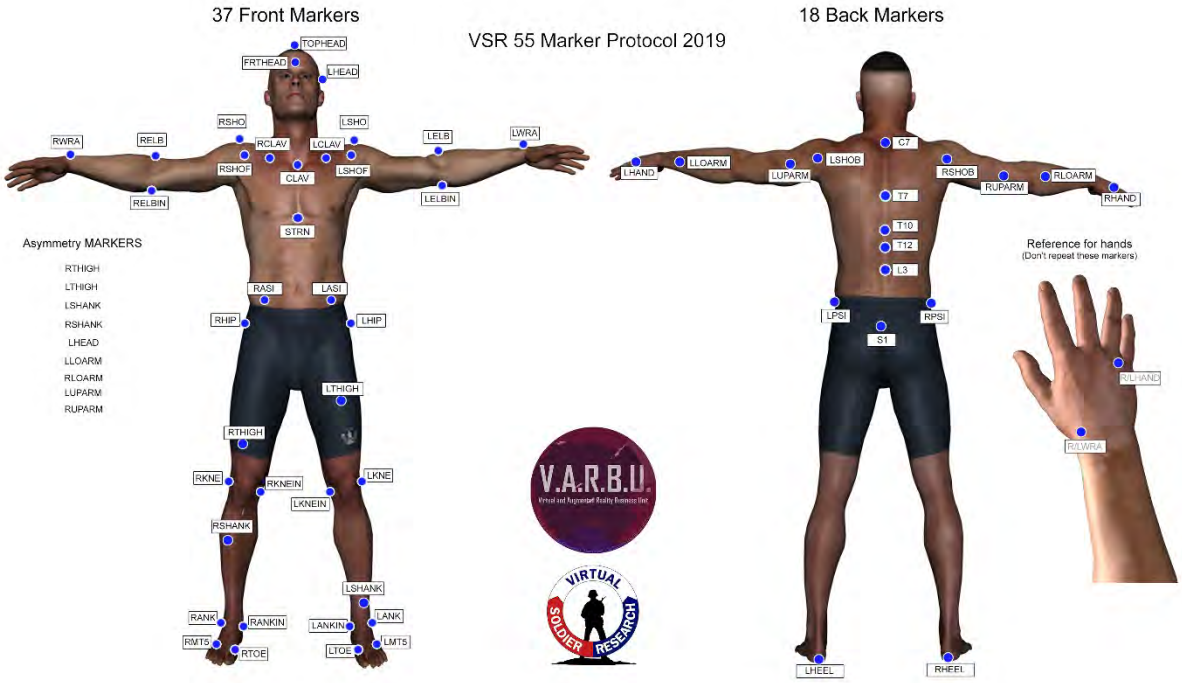

Figure 1. Markerset protocol developed for use with Santos proprietary software for motion capture analysis with OptoTrack.

Twelve OptiTrack Flex 13 cameras were used to capture and track the markers via infrared light during the ACFT and CST tasks. Figure 2 shows the layout of the cameras in the laboratory space. In addition to motion capture, video recordings of the tasks were made to document the movements for later reference as needed. For the larger study, a few of the tasks were collected in an alternate venue, a racquetball court, due to height limitations in the laboratory; however, for this report, none of these tasks were needed.

During the CSTs portions of the data capture phase, participants were sometimes required to wear additional items as used by regular Army soldiers, either as “fighting load” or “sustainment load.” The fighting load consists of body armor or armor plate carrier with pouches, the Army Combat Helmet (ACH). which replaces the beanie worn during the ACFT portion, and an inert rubber dummy M-4 rifle. The motion capture team utilized a plate carrier instead of the Army Improved Outer Tactical Vest (IOTV) due to the analysis of the plate carrier being more widely used and issued to Army soldiers as a replacement for the IOTV. As prescribed in Army Technical Manual 10-8465-236-10, the plate carrier consisted of the plate carrier itself with front, back, and side plates. The external pouches were added to the plate carrier to simulate the average weight that a soldier would carry into a battle. The pouches

included the following: (a) two 3-slot M4 magazine pouches, (b) pouch with two DUMMY grenades, (c) 3-liter hydration pack on back, (d) Individual First Aid Kit (IFAK), and (e) radio pouch.

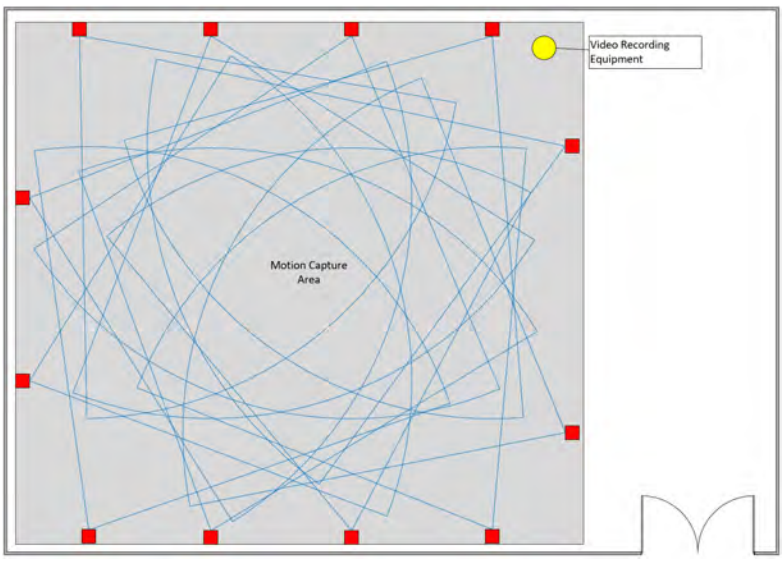

Figure 2. Layout for collecting motion capture data of the deadlift and several CSTs. The cameras are represented by red squares. The orientation of the cameras is shown as blue arcs converging in a central area of the motion capture area. The yellow circle represents the location of video recording equipment used to record the tasks being completed for reference.

Three sizes of body armor were available to accommodate different body types, but all weighed approximately 17.3 kg (38 lbs). The helmet weighed 1.4 kg (3 lbs) and the dummy rifle was 2.5 kg (5.6 lbs). The fighting load configuration is shown in Figure 3. The “sustainment load” consists of all fighting load gear with the addition of a 23 kg (45.9 lbs) rucksack (see Figure 4). Thus, the total added weight of gear under the sustainment load was approximately 42.3 kg (93 lbs).

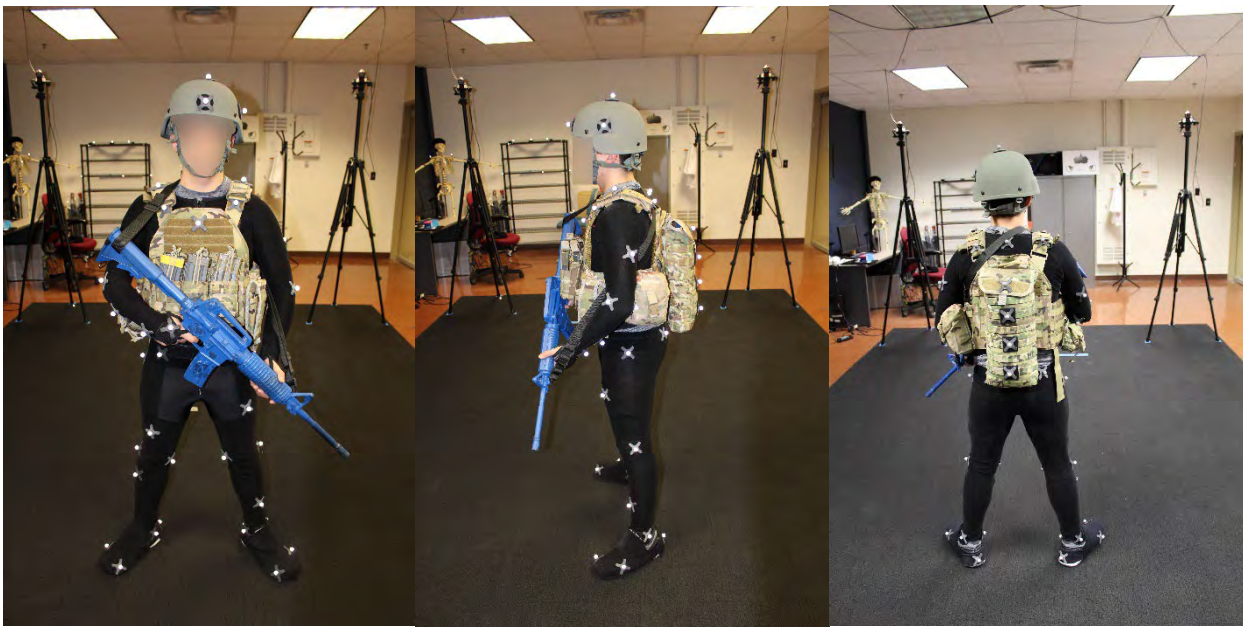

Figure 3. Participant with "fighting load" configuration during motion capture sessions for select CSTs, wearing the "small" vest.

Figure 4. Participant with "sustainment load" configuration during motion capture sessions for select CSTs.

Deadlift

The hexagon deadlift bar with weight plates ranging from 4.5 – 20.5 kg (10 – 45 lbs) was provided by Rogue fitness. While the ACFT standard is to perform a three-repetition maximum for deadlift, for the purposes of human subjects' safety and approvals, a maximum of 31.8 kg (70 lbs) was used. The minimum weight requirement for passing the deadlift portion of the ACFT is 63.6 kg (140 lbs) across men and women at the time of this study; thus, during the DHM simulation phase of this study, the applied weight was assessed as 63.6 kg when estimating joint torques.

The deadlift was performed by the participant standing in the middle of the motion capture area in a T-pose. A hexagonal deadlift bar was placed in front of the participant with the required amount of weight. When instructed, the participant lowered their arms and stepped into the hexagonal bar with their feet shoulder-width apart. They bent at the waist, hips, and knees and grasped the bar. After grasping the bar, the participant raised and lowered the bar three times, then stepped either backward or forwards out of the hexagonal bar and returned to the T-pose. The participant was instructed to not drop or bounce the bar on the ground, but to lower it in a controlled manner as they returned the weights to the ground (see Figure 5).

Figure 5. Example of the deadlift ACFT task as performed for motion capture purposes.

Common Soldier Tasks

Multiple CSTs were assessed as part of the larger study. For the purposes of these analyses, only a subset will be discussed: casualty extraction (horizontal and vertical extraction), high crawl, being in a fighting position, prone position with sustainment load, lift and carry sustainment load, marching with sustainment load, climb through 42" window or over 52" wall (see Figure 6A), jump over 18" obstacle, jump from 50" height, stack sandbags, and hand-to-hand grapple. To accomplish these tasks, several additional pieces of equipment were purchased, borrowed, or built, such as a fabric sled with pull straps and a SKED

litter from the National Guard, for different types of casualty extraction, and vertical wall obstacles of various heights as needed.

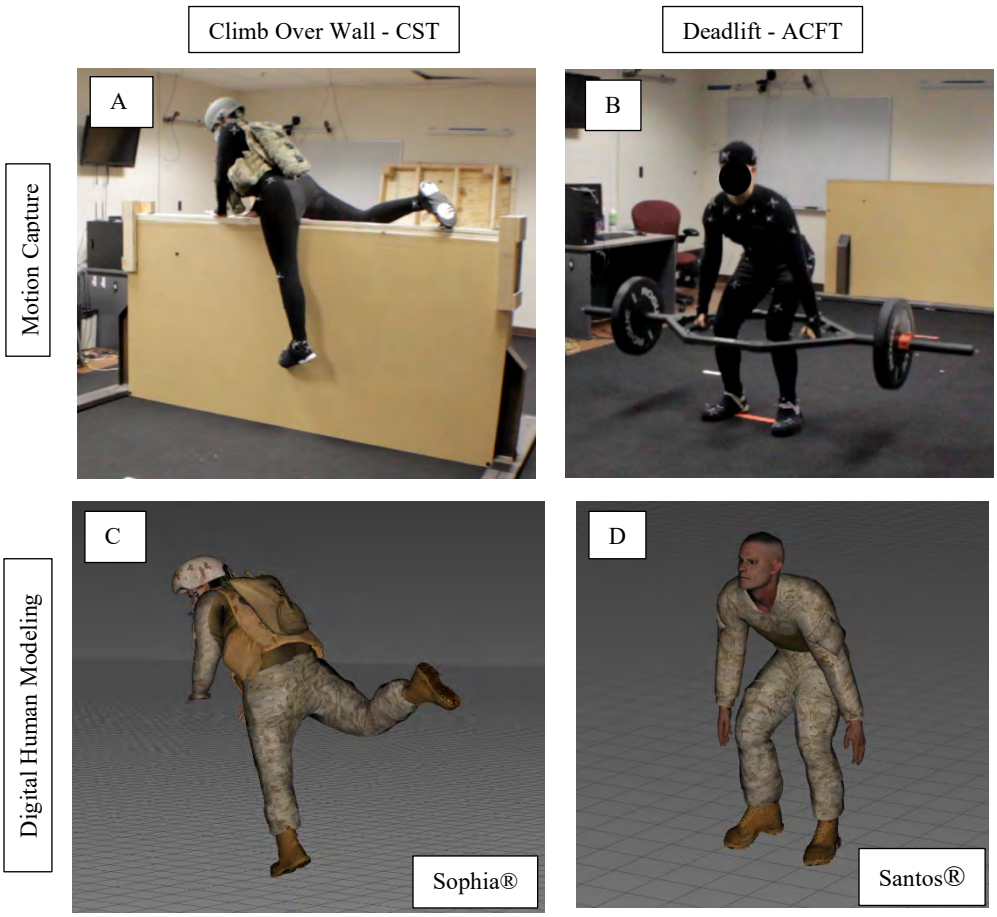

Figure 6. Two examples of transforming data from motion capture (A, B) to perform the workload analysis with digital human modeling (C, D).

Analyses

The motion analysis and digital human modeling was performed for the deadlift and multiple simulated CSTs for five major joints of the body: trunk (low-back extension and abdominal flexion), hip flexion/extension, knee flexion/extension, shoulder flexion/extension, and elbow flexion/extension. The ratio of the peak torque required to complete the CSTs relative to the torque required to complete the deadlift provides estimates of how challenging soldier tasks are relative to the strength needed to perform the deadlift at each joint, where 100% indicates equal levels of muscle strength is required for both. Ratios less than 100% indicate that the soldier tasks are less strenuous than the corresponding ACFT deadlift, and ratios over 100% indicate the CSTs require more strength than the corresponding deadlift (at

the passing 60-point level, assuming 63.6 kg (140 lbs) lift). Means of peak torques and of ratios across all five subjects were performed using SPSS statistical software (IBM) to summarize findings. Lastly, values for men and women were considered separately to evaluate for apparent sex differences.

Results

Examples of single-subject ratios between the strength required to perform several CSTs and the deadlift are provided in Tables 1 and 2. Note in these two individuals, who represent a male and a female subject, respectively, that clear patterns are present. The deadlift requires more strength than does marching with a sustainment load or jumping over an 18" wall but is easier than performing a casualty extraction. While the movement strategies used by different subjects may differ, due to anthropometric differences, these overall patterns were notably consistent.

Table 1. Ratio of peak torques required to complete a series of CSTs relative to the Deadlift at passing level (male subject, 1.78m tall, 71.7 kg).

Deadlift (male):

Color Code:		
CST/ACFT	$0 < x \leq 0.7$	ACFT requires more torque than CST
	$0.7 < x \leq 1.3$	ACFT requires similar torque as CST
	$1.3 < x$	ACFT requires less torque than CST

CSTs compared against Deadlift for Participant 4 (Male, 1.78 m, 71.67 Kg)

Joint	Casualty Drag	Vertical Casualty Extraction	High Crawl	Marching Sustainment Load	Prone Sustainment Load	18" Wall Jump	42" Window	50" Wall Jump
Lower Back								
Right Shoulder								
Left Shoulder								
Right Elbow								
Left Elbow								
Right Hip								
Left Hip								
Right Knee								
Left Knee								

Table 2. Ratio of peak torques required to complete a series of CSTs relative to the deadlift at passing level (female subject, 1.59m tall, 55.3 kg).

Deadlift (female):

CST/ACFT	Color Code:	
0 < x ≤ 0.7		ACFT requires more torque than CST
0.7< x ≤1.3		ACFT requires similar torque as CST
1.3 < x		ACFT requires less torque than CST

CSTs compared against Deadlift for Participant 6 (Female, 1.59 m, 55.3 Kg)

Joint	Casualty Drag	Vertical Casualty Extraction	High Crawl	Marching Sustainment Load	Prone Sustainment Load	18" Wall Jump	42" Window	50" Wall Jump
Lower Back								
Right Shoulder								
Left Shoulder								
Right Elbow								
Left Elbow								
Right Hip								
Left Hip								
Right Knee								
Left Knee								

When evaluating the averages across the five participants, the muscle force requirements for the deadlift often represent similar workloads associated with several of the more strenuous CSTs, yet are less than the tasks involving extracting casualties. See Figure 7 for the heat map of the ACFT deadlift versus eight of the CSTs assessed as an average of all subjects, for muscle groups most involved in the deadlift.

Figure 7. Heat map of the CST/ACFT ratio between muscle torque requirements, where >100% indicates the CST requires more joint torque than the deadlift at 60-pt level (140# - 3 rep max). Note: red = CST > ACFT strength needed; yellow = CST < ACFT strength needed; orange = approx. equal strength needed for CST and ACFT.

Similarly, Figure 8 highlights tasks which exceed the requirements of the passing deadlift level, involving most commonly the knee, but also the trunk and shoulder. However, the absolute torques needed to complete the ACFT deadlift and select CSTs (casualty extraction and stacking sandbags) are quite similar overall (Figure 9).

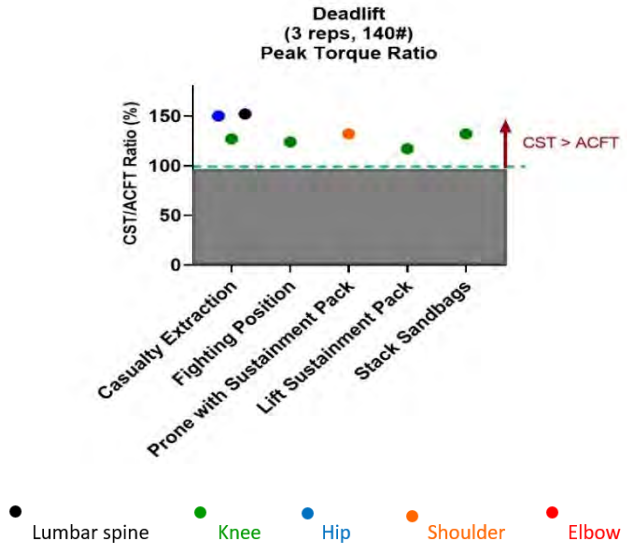

Figure 8. Force requirements for CSTs that exceed the ACFT deadlift (60-pt level), based on the ratios of the CST /ACFT peak torques (%). The colors indicate different joints.

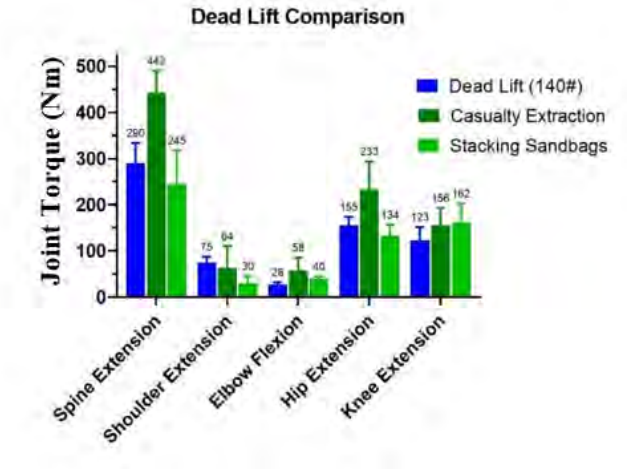

Figure 9. Mean (SD) torque requirements needed to complete ACFT deadlift in blue and two comparable CSTs (in green), considering the key joints involved.

When comparing the biomechanical strength requirements for the deadlift as well as CSTs (see Figure 10), minimal differences between the men and women were observed. Task requirements are not based on strength per se, but on body weight and height, movement speed, acceleration, and any additional external loads that must be lifted, moved, or carried. Further, some tasks can be performed in different manners, yet achieve the same goal, such as when lifting a load, one can place more load on the spine or the knees

depending on the lifting strategy used. Accordingly, in general there is as much variation within, as there is between, men and women in terms of the joint torque requirements needed to accomplish CSTs as well as the ACFT deadlift.

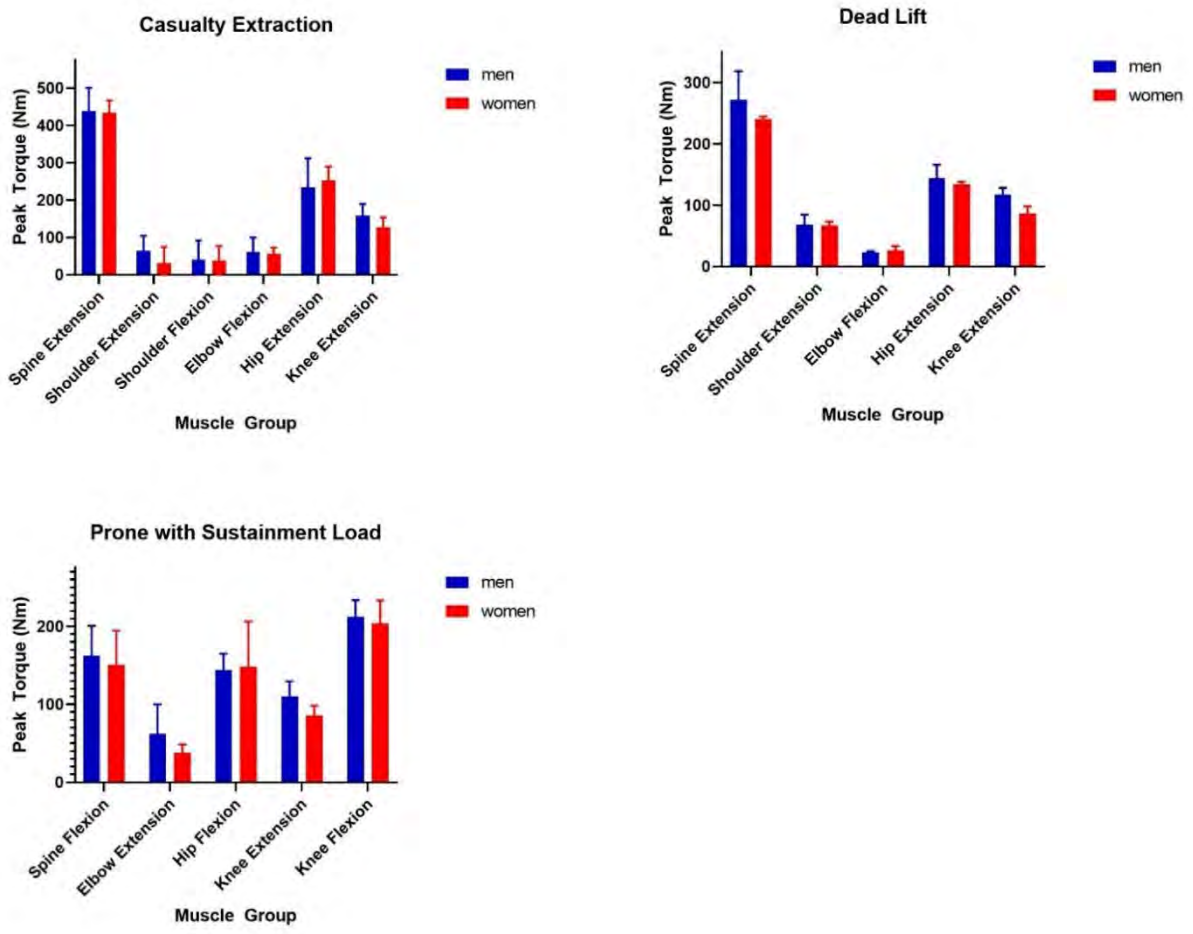

Figure 10. Mean (SD) torque requirements needed to complete 2 CSTs and the ACFT deadlift for the male (blue bars) and female (red bars) study participants. Note that there were no significant differences observed.

Discussion

The primary aim of this paper was to evaluate the biomechanical workloads associated with the ACFT deadlift and compare it to several simulated CSTs. Our modeling with Santos and Sophia DHMs demonstrates that the deadlift requirements at the passing level of 63.6 kg provides largely a good match for several major muscle groups and is even less strenuous than tasks involving casualty extraction and transfers. Accordingly, the deadlift, one of six ACFT tasks, provides a means to assess muscular strength

that is relevant to the expected strenuous workloads for a soldier. That is, the peak muscle strength requirements to complete one of the casualty extractions, for example, required from 127 – 152% of the peak strength required for key muscles involved in completing three repetitions of the deadlift using 63.6 kg.

While prior efforts to validate the ACFT showed correlations with completion times of a battery of CSTs, this adds additional information targeting strength and task workloads. The use of DHMs in conjunction with motion capture methodology enabled us to make these analyses possible, as direct measures of task workload are not readily measurable otherwise. This application of DHM provides insights into which common soldier tasks most closely match the deadlift, the most strength-intensive of the ACFT tasks. This approach maps strength requirements needed to perform the various common soldier tasks at several major muscle groups to the strength needed to complete the deadlift. For a strength-dominant ACFT task, this analysis approach is very appropriate. Further, this mapping of strength requirements as a comparator to determine capability or potentially strength cut-points could be applied to other work-intensive environments.

The ACFT was developed to incorporate multiple physical fitness domains, such as muscle strength, endurance, aerobic capacity, power, speed, etc. The use of DHMs as described here to model peak torque requirements is particularly of use for assessing muscle strength domains of fitness. Other planned and ongoing analyses include assessing the development of muscle fatigue over time with repeated tasks, such as the hand-release push-ups, or the infleunce of performing multiple tasks serially while applying the revised three comparment controller (3CC-r) model of muscle fatigue (Xia & Frey-Law, 2015) (Looft, Herkert, & Frey-Law, 2018) (Looft, Herkert, & Frey-Law, 2018). The use of DHMs in combination with other models may provide similarly useful metrics for comparison when considering other domains of human performance.

These analyses involved both men and women and found that the strategies employed were largely similar. At the time of this study, the Army had defined cut-points for passing that were age- and sex-neutral. Our analyses supported that the loads required were indeed also largely gender-neutral. However, the relative requirements in terms of percent of peak capability indeed differed between men and women. That is peak strength is typically lower in women than men by approximately 40% based on normative data (Frey-Law, et al., 2012) (Hussain & Frey-Law, 2016). It is analyses such as these that may help provide the necessary data to help guide decision-making for the use of gender-specific vs gender-neutral physical performance metrics.

Limitations

Interpretation of this study must consider the following limitations. First, this current evaluation focuses on the strength domain when making comparisons between the deadlift and CSTs. While this may be ideal for the deadlift, it may not be as relevant to the other ACFTs, which may represent other fitness domains moreso than the deadlift. Second, due to the intensive nature of this data collection and analysis process, sample sizes for these types of biomechanical studies are typically small. However, the motion data collected from this cohort can be used to examine these tasks with digital human models of varying anthropometry. Third, technical aspects of modeling the large range of motion of the shoulder in 3-D space make the shoulder torque estimates prone to error, as flexion and extension planes can collapse with abduction and adduction planes, as well as issues of gimbal lock; thus, shoulder torques are at higher risk of error than the remaining joints assessed. This study also assumes that a change in parameters such as anthropometry and deadlift load would not change the manner in which a motion is performed. Lastly, traditional inverse dynamics analyses require force plates to assess normal reaction forces at the feet; however, the dynamic and varied contact sites inherent with several CSTs makes the use of force plates virtually impossible. Thus, estimates were made using assumptions of normal force distributions at multiple body sites as appropriate. Ongoing and future evaluations will continue to investigate additional physical domains, including metabolic requirements, muscle power, and endurance/fatigue, when extending these analyses to the other ACFT tasks.

Summary

In summary, despite the known limitations, this preliminary report found that the 60-point minimum performance requirements for the ACFT deadlift are typically a reasonable match to several expected soldier tasks. However, while the three-repetition maximum deadlift requirement to lift 63.6 kg (140 lbs) may seem high to some, it was not always sufficient to ensure that soldiers can execute the absolute workload demands of several CSTs, such as casualty extraction for either men or women. Finally, the overall workloads of the CSTs evaluated were similar between men and women, from a physical perspective, i.e., peak torques at several major joints (knee, hip, lower back, elbow, shoulder), suggesting men and women perform CSTs and the ACFT deadlift events in largely similar ways despite differences in typical strength and anthropometry.

References

Frey-Law, L., Laake, A., Avin, K., Heitsman, J., Marler, T., & Abdel-Malek, K. (2012). Knee and elbow 3D strength surfaces: peak torque-angle-velocity relationships. *Jounral of Applied Biomechanics, 28*(6), 726-737.

Hussain, S., & Frey-Law, L. (2016). 3D strength surfaces for ankle plantar- and dorsi-flexion in healthy adults: an isometric and isokinetic dynamometry study. *Jounral of Foot and Ankle Research, 9*(43), 1-10.

Karim Abdel-Malek, J. S.-L. (2008). Santos: A digital human in the making. *50th Annual Meeting of the Human Factors and Ergonomics Society.* San Francisco, CA.

Looft, J., Herkert, N., & Frey-Law, L. (2018). Modification of a Three-Compartment Muscle Fatigue Model to Predict Peak Torque Decline During Intermittent Tasks. *Journal of Biomechanics, 77*, 16-25.

Salam Rahmatalla, Y. X. (2011). A validation framework for predictive human models. *International Journal of Human Factors Modelling and Simulation*, 67-84.

Thewlis, D., Bishop, C., Daniell, N., & Paul, G. (2013). Next generation low-cost motion capture systems can provide comparable. *Paul, 29*(1), 112-117.

US Army. (2018, 08 18). *FIELD TESTING MANUAL.* Retrieved from Army Combat Fitness Test: https://www.army.mil/e2/downloads/rv7/acft/acft_field_testing_manual_final.pdf

Xia, T., & Frey-Law, L. (2015). Wrist joint torque-angle-velocity performance capacity envelope evaluation and modelling. *International Journal of Human Factors Modelling and Simulation, 5*(1), 33-52.

Yujiang Xiang, H.-J. C.-M. (2010). Predictive dynamics: an optimization-based novel approach for human motion simulation. *Structural and Multidisciplinary Optimization*, 465-479.

Identifying benefits of using an instruction language for virtual simulation of manual assembly and logistics

Peter Mårdberg[1], Johan S. Carlson[1], and Dan Högberg[2]

[1] *Fraunhofer-Chalmers Centre, Sweden*

[2] *University of Skövde, Sweden*

Abstract

A digital human modelling (DHM) software is a valuable tool in virtual manufacturing since it supports proactive consideration of ergonomics when designing new workstations by facilitating simulation of manual assembly work and by providing ergonomic assessments of different design proposals. Despite the advantage, there are still a lot of assembly tasks that are not simulated and assessed proactively. One reason is that it is time consuming for the user, even for simple tasks, to create and set up the assembly simulations.

Increasing the automation level of DHM software has the potential to both increase the number of assembly task simulated as well as enabling ergonomics to proactively be included in other manufacturing and product design related decisions.

However, an increased automation level requires a manikin that automatically can compute collision free and ergonomically sound motions based on some sort of instruction language that supports the DHM software user to communicate to the manikin of what tasks the manikin is to perform. The instructions are, during simulation, interpreted by a simulation framework as path planning instances for the manikin, which results in motions that accomplishes the tasks.

In this work, we explore the possibility to use the DHM software IMMA's instruction language to further increase the automation level and to identify gaps between the current functionality and the functional requirements for a more automated simulation framework. More specifically, we investigate the requirements for simulations where: 1) Manikins perform collaborative tasks, such as when two manikins jointly handle an object, and where predicted motions are collision-free and ergonomically sound, and the forces needed to handle the object are distributed between both manikins; 2) Robots and manikins collaborate when performing tasks. The simulation of such interaction needs to consider collisions, weight of carried objects, ergonomics of the manikin, as well as other automation equipment used in the

assembly station; and 3) Manikins interact with moving objects, e.g. during assembly of a part on a moving assembly line, or grasping a part that is moved by a collaborative robot.

Keywords: Digital human modelling, Virtual assembly, Simulation, Instruction language

Improved Modeling Approach for the Usage of Mixed Linear Effects Models in Empirical Digital Human Models

Martin Fleischer, Technical University of Munich, TUM School of Engineering and Design, Chair of Ergonomics, martin.fleischer@tum.de

Abstract

When designing the interior of automated cars, it is necessary to take the non-driving related tasks and the take-over maneuver into account. These take-overs are critical moments since the driver needs to take back control of the vehicle as fast as possible. To facilitate this, interior designers need to design the cabin with enough space to carry out this movement. This paper presents a revised modelling approach using mixed linear effects models to predict the grasping movement of the hand during take-over scenarios. A study with 52 participants doing grasping movements was carried out to model the data obtained via motion capture. The participants were instructed to carry out movements from predefined grasping elements mounted in front of them. The trajectory of the hand was recorded using a marker-based motion capturing system. It is observed that the trajectories can be assumed as a two-dimensional phenomenon, since they seem to lie on one plane. Thus, the trajectories were modeled as a 1+2-dimensional problem. A one-dimensional model for the plane and a second two-dimensional model for the trajectory. The model of grasping trajectory described in this paper was modeled using 4th degree polynomials. In older approaches, the trajectory was modeled in four different models for each constant of the polynomial. In this paper a new modeling approach is used to merge the polynomial into one model. This increased the R^2_m and R^2_c drastically and led to three major discoveries on the nature of human grasping movements: Task factors, such as grasping handle and handle position, play the major role in the grasping trajectory. Body height plays a role in the modelling of hand trajectories. Gender, age, and dominant hand show only negligible influence on the trajectory. Other individual human factors not evaluated in this study do not seem to heavily influence the hand movement.

Keywords: Mixed Linear Effects Models, Automated Driving, Take-Over, Grasping.

Introduction

Automated driving seeks to revolutionize the way people travel by car. With increasing automation levels, the driver becomes a passenger and is able to carry out non-driving related activities. When the automation reaches its limit, the driver needs to again take-over the driving task again. Non-driving related activities

and the take-over are new scenarios for tools used in the design of the cars (Albers et al., 2021). Digital human models are no exception to this. Current models used for vehicle design focus on ingress/egress (Björkenstam et al., 2020; Lu et al., 2013; Reed et al., 2010; Robert et al., 2013) , sight (Marshall et al., 2020; Remlinger & Bengler, 2016) or the driving task (Bubb et al., 2006; Bubb et al., 2021; Reed et al., 2006). To predict the take-over, a method is needed for predicting directed grasping movements. There are different approaches to simulate such a motion. Fritzsche et al. (2011) and Brauns (2017) use a set of motion captured movements that are manipulated according to the user defined tasks. Obentheuer (2020) uses biomechanical simulation with optimized muscle activity control to generate a forward kinematic. Faraway (2001), Faraway (2003) and Faraway and Choe (2009) use regression models on the trajectory of the hand. The later models need to be expanded by an inverse kinematic model of the rest of the body. Compared to the biomechanical models, the regression models require less computational power for the user of the model and less skilled operators of the model. Biomechanical models on the other hand are easier to be generalized, while regression models often fail to find universal truths.

When looking at the human grasping movement it can be observed that the trajectory moves through the room on a two-dimensional plane (Arlt, 1999; Cherednichenko, 2007). This understanding can be used to split the three-dimensional problem into a one-dimensional and a two-dimensional problem. Since start and end point of the simulation are already known, it is only necessary to find one additional point to define the plane (Fleischer et al., 2021). The trajectory can be modeled as a two-dimensional polynomial on this plane. In this paper only the trajectory model is described and compared to an older approach described by Fleischer et al. (2020).

Fleischer et al. (2020) modeled the same data set used in this paper to predict grasping trajectories. Four separated mixed linear effect models were used to predict the four coefficients ($C_{1\text{-}4}$; $C_0 = 0$). But the determination coefficients indicate a poor goodness-of-fit (Ferguson, 2009). R^2_m never surpasses .1 and R^2_m is below .333 for all four models. Three major insights are described:

“

1. *Task factors (handle type and handle position) play the major role for the grasping trajectory.*
2. *Body height plays a role in the modelling of hand trajectories. Gender, age, and dominant hand only show negligible influence on the trajectory.*
3. *Other individual human factors not evaluated in this study seem to heavily influence the hand movement.*

“ - Fleischer et al., 2021, p. 184

Methods (Fleischer et al., 2021)

A participant study with 52 participants was carried out in a laboratory setting to model the grasping trajectories of take over movements. The subjects were asked to perform 24 grasping movements and the data were recorded using VICON Nexus (four MX T10S and four MX10 cameras, 100 Hz recording frequency, 12mm reflective markers, VICON Nexus 1.85). Four different grasping elements (see Figure 1) were presented on two orthogonal wooden boards: One-finger contact handle, three-finger contact handle, a ball, and a cylinder.

Figure 1. Grasping handles from left to right: One-finger contact, three-finger contact, ball, cylinder.

The four handles were mounted on the horizontal board, while two additional cylinder handles were fastened to the vertical board. As shown in Figure 2 the four handles were positioned either directly under the vertical cylinders or laterally offset to the right. The position of the handles on the horizontal plane was shifted halfway through the trails.

Figure 2. Experimental setup with the one-finger contact handle and the cylinder handle directly under the vertical cylinders and the ball and the three-finger contact offset to the right.

Before the measurements, the participants had time to train the movements to perform the tasks routinely. The participants were instructed to grasp the handles on the horizontal plane and to carry out a grasping movement to the handle on the vertical board. Four handles in two positions each with three repeated measures resulted in 24 recorded grasping trajectories for each participant. Two participants were excluded from the sample due to measurement complications.

Table 1. Individual data of the collective

N = 50	
Average body height	174.5 cm [SD = 8.1 cm]
Average age	26.8 [SD = 10.7]
Right hand dominant	90 %
Male gender	62 %

The recorded trajectory data is transformed into two-dimensional data with the following approach: For each trajectory a best fitting plane is determined using principal component analysis. The trajectory is then projected onto this plane resulting in data points with two coordinates x and y. X is the distance travelled and y is the elevation above the direct connection of start and end point. This data were written in the dataframe "df" and used for the modeling. The model is fitted using the R-package "lme4" (Bates et al., 2020) using a polynomial of the 4th degree:

*mdl <- lmer(y.coordinates ~ poly(x.coordinates, 4, raw = TRUE) * gender + poly(x.coordinates, 4, raw = TRUE) * height + poly(x.coordinates, 4, raw = TRUE) * grasping_handle + poly(x.coordinates, 4, raw = TRUE) * grasping_position + poly(x.coordinates, 4, raw = TRUE) * age + poly(x.coordinates, 4, raw = TRUE) * dominant_hand + (1 | name) , data = df)*

Gender, body height, the type of grasping handle, the position of the handles, the age and the dominant hand are modeled as fixed effects. The participant is modeled as a random intercept to account for factors not measured.

Results

The Q-Q-plot (Figure 3) shows a heavily tailed distribution in the upper quantiles. The scaled residuals (Figure 4) show a linear homoscedastic behavior. The x-axis is clearly visible on the lower left of the data points.

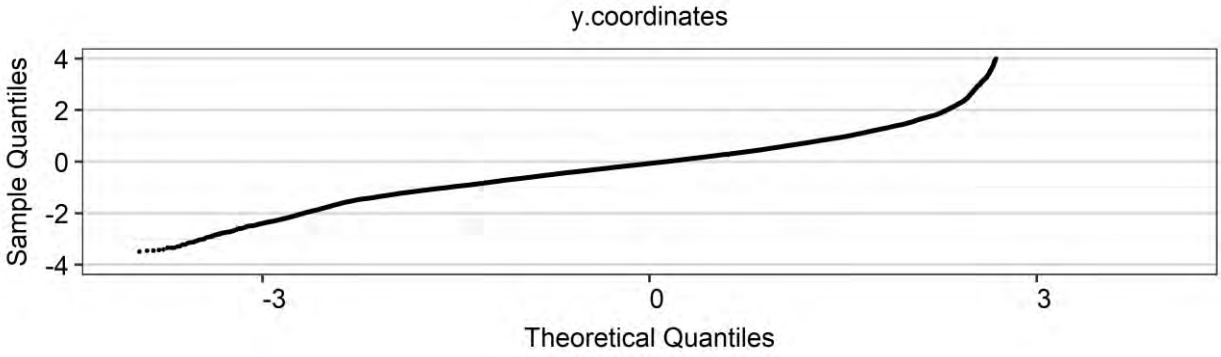

Figure 3. Q-Q Plot of the model

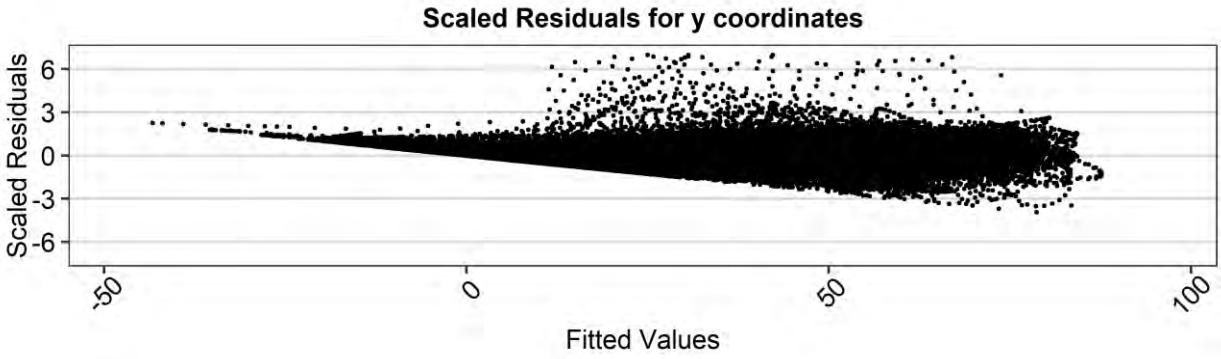

Figure 4. Scaled residuals of the model

The determination coefficients are $R^2_m = .5$ and $R^2_c = .56$. The significant main effects of the model are the grasping element ($p < .001$) and the position of the grasping element ($p < .001$).

Discussion and Conclusions

Compared to Fleischer et al. (2020) the key insights needed to be revised:

1. Task factors (handle type and handle position) play the major role for the grasping trajectory.
2. None of individualistic factors recorded has a significant effect on the trajectory.
3. Other individual human factors not evaluated in this study do not influence the hand movement.

Insight 1 stays the same, since these are the significant main effects. Compared to the older models the body height is no longer a relevant factor. The other individualistic factors remain insignificant. Insight 3 is the biggest change on the nature of grasping trajectories. The two determination coefficients are close to each other, thus the random effect does not influence the model as much as in Fleischer et al. (2020). Also the R^2 greater than .5 can be interpreted as moderate to strong effect sizes (Ferguson, 2009) and have improved

greatly compared to the modeling method of Fleischer et al. (2020). This can be attributed to two aspects. With the improved modeling method each data point can be used for the fitting, while the older method reduced every trajectory to the polynomial coefficients. Also, the four coefficients are now modeled in the same fitting process. This accounts for correlation of the coefficients between each other.

Mixed linear effects models need to fulfil the assumption of linear homoscedasticity. The scaled residuals show a good fit for this criterion, but due to the trajectories only having positive y-values the x-axis is clearly visible on the lower left of the plot. The data are not normally distributed, but according to Gelman and Hill (2007) this criterion is obsolete by today's standards.

The modeling approach seems promising due to the high determination coefficient. Especially compared to biomechanical digital human models, the computational effort and user expertise needed is greatly reduced. Although the applicability of empirical models is less general. In the model presented here, balance is irrelevant, as the persons sit during the movement. It is to be researched to which extend the grasping model can be transferred to different scenarios.

Acknowledgments

This study was conducted in the context of the project INSAA funded by the Bundesministerium für Bildung und Forschung of Federal Republic of Germany.

References

Albers, D., Radlmayr, J., Grabbe, N., Hergeth, S., Naujoks, F., Forster, Y., Keinath, A., & Bengler, K. (2021). Human-Machine Interfaces for Automated Driving: Development of an Experimental Design for Evaluating Usability. In N. L. Black, W. P. Neumann, & I. Noy (Eds.), *Springer eBook Collection: Vol. 221. Proceedings of the 21st Congress of the International Ergonomics Association (IEA 2021): Volume III: Sector Based Ergonomics* (1st ed., Vol. 221, pp. 541–551). Springer International Publishing; Imprint Springer. https://doi.org/10.1007/978-3-030-74608-7_66

Arlt, F. (1999). *Untersuchung zielgerichteter Bewegungen zur Simulation mit einem CAD-Menschmodell*. Herbert Utz Verlag.

Bates, D., Maechler, M., Bolker, B., Walker, S, Christensen, R. H. B., Singmann, H., Dai, B., Scheipl, F., Grothendieck, G., Green, P., & Fox, J. (2020). *lme4* (Version 1.1-23) [Computer software]. https://cran.r-project.org/web/packages/lme4/index.html

Björkenstam, S., Mårdberg, P., Roller, M., & Carlson J. S. (2020). Digital Human Motion Planning of Operation Sequences Using Optimal Control of Hybrid Systems. In L. Hanson, D. Högberg, & E. Brolin (Eds.), *Advances in Transdisciplinary Engineering: Vol. 11. DHM2020: Proceedings of the 6th International Digital Human Modeling Symposium.* IOS Press.

Brauns, S. (2017). *Web-basierte Referenzarchitektur für virtuelle Techniken: Mit Anwendungsbeispielen aus der Industrie*. *Essentials Ser*. Springer Fachmedien Wiesbaden. https://doi.org/10.1007/978-3-658-17249-7

Bubb, H., Engstler, F., Fritzsche, F., Mergl, C., Sabbah, O., Schaefer, P., & Zacher, I. (2006). The development of RAMSIS in past and future as an example for the cooperation between industry and university. *International Journal of Human Factors Modelling and Simulation*, *1*(1), Article 11686, 140. https://doi.org/10.1504/IJHFMS.2006.011686

Bubb, H., Vollrath, M., Reinprecht, K., Mayer, E., & Körber, M. (2021). The Human Being as a Driver. In H. Bubb, K. Bengler, R. E. Grünen, & M. Vollrath (Eds.), *Automotive ergonomics* (pp. 63–159). Springer. https://doi.org/10.1007/978-3-658-33941-8_3

Cherednichenko, A. (2007). *Funktionales Modell der Einstiegsbewegung in einen PKW* [Dissertation]. Technische Universität München, München.

Faraway, J. J. (2001). *Modeling Hand Trajectories During Reaching Motions* [Technical Report # 383 Department of Statistics University of Michigan]. Department of Statistics, University of Michigan. https://people.bath.ac.uk/jjf23/papers/trajectory.pdf

Faraway, J. J. (2003). Regression modeling of motion with endpoint constraints. *The Journal of Visualization and Computer Animation*, *14*(1), 31–41. https://doi.org/10.1002/vis.303

Faraway, J. J., & Choe, S. B. (2009). Modelling orientation trajectories. *Statistical Modelling: An International Journal*, *9*(1), 51–68. https://doi.org/10.1177/1471082X0800900104

Ferguson, C. J. (2009). An effect size primer: A guide for clinicians and researchers. *Professional Psychology: Research and Practice*, *40*(5), 532–538. https://doi.org/10.1037/a0015808

Fleischer, M., Elbauer, J., & Bengler, K. (2021). Modeling the Orientation of Take-Over Trajectories Using Mixed Linear Effects Models. In N. L. Black, W. P. Neumann, & I. Noy (Eds.), *Springer eBook Collection: Vol. 221. Proceedings of the 21st Congress of the International Ergonomics Association (IEA 2021): Volume III: Sector Based Ergonomics* (1st ed., Vol. 221, pp. 633–638).

Springer International Publishing; Imprint Springer. https://doi.org/10.1007/978-3-030-74608-7_77

Fleischer, M., Hetzenecker, A., & Bengler, K. (2020). Modelling Take-Over Hand Trajectories Using Linear Mixed Effects Models. In L. Hanson, D. Högberg, & E. Brolin (Eds.), *Advances in Transdisciplinary Engineering: Vol. 11. DHM2020: Proceedings of the 6th International Digital Human Modeling Symposium* (pp. 178–186). IOS Press. http://ebooks.iospress.nl/publication/55300

Fritzsche, L., Jendrusch, R., Leidholdt, W., Bauer, S., Jäckel, T., & Pirger, A. (2011). Introducing ema (Editor for Manual Work Activities) – A New Tool for Enhancing Accuracy and Efficiency of Human Simulations in Digital Production Planning. In V. G. Duffy (Ed.), *Lecture Notes in Computer Science / Information Systems and Applications, incl. Internet/Web, and HCI: Vol. 6777. Digital human modeling: Third international conference, ICDHM 2011, held as part of HCI International 2011, Orlando, FL, USA, July 9-14, 2011 ; proceedings* (Vol. 6777, pp. 272–281). Springer. https://doi.org/10.1007/978-3-642-21799-9_31

Gelman, A., & Hill, J. (2007). *Data analysis using regression and multilevel/hierarchical models*. *Analytical methods for social research*. Cambridge University Press.

Lu, J.-M., Tada, M., Endo, Y., & Mochimaru, M. (2013). Ingress/egress motion strategies of the elderly people for the rear seat of minivans with sliding doors. In *2nd International Digital Human Modelling Symposium,* Ann Harbor.

Marshall R., Summerskill, S., Paterson A., & Eland A. (2020). The Use of Digital Human Modelling for the Definition and Contextualisation of a Direct Vision Standard for Trucks. In L. Hanson, D. Högberg, & E. Brolin (Eds.), *Advances in Transdisciplinary Engineering: Vol. 11. DHM2020: Proceedings of the 6th International Digital Human Modeling Symposium* (pp. 99–107). IOS Press.

Obentheuer, M. (2020). *Transfer of Human Motion Primitives for Digital Human Model Control in the Scope of Ergonomic Assessment*. Technische Universität Kaiserslautern.

Reed, M. P., Ebert, S., & Hoffman, S. (2010). Modeling Foot Trajectories for Heavy Truck Ingress Simulation. In G. Salvendy (Ed.), *Advances in Human Factors and Ergonomics Series. Advances in human digital modeling* (Vol. 56, pp. 19–27). CRC Press. https://doi.org/10.1201/EBK1439835111-4

Reed, M. P., Faraway, J., Chaffin, D. B., & Martin, B. J. (2006). The HUMOSIM Ergonomics Framework: A New Approach to Digital Human Simulation for Ergonomic Analysis. In *SAE Technical Paper Series, SAE Technical Paper Series.* SAE International400 Commonwealth Drive, Warrendale, PA, United States. https://doi.org/10.4271/2006-01-2365

Remlinger, W., & Bengler, K. (2016). RAMSIS kognitiv als Instrument zur Analyse und Auslegung von Sichtbedingungen. In A. C. Bullinger-Hoffmann & J. Mühlstedt (Eds.), *Homo Sapiens Digitalis - Virtuelle Ergonomie und digitale Menschmodelle* (Vol. 66, pp. 297–302). Springer Berlin Heidelberg. https://doi.org/10.1007/978-3-662-50459-8_13

Robert, T., Causse, J., Denninger, L., & Wang, X. (2013). A 3-D dynamics analysis of driver's Ingress-Egress Motion. In *2nd International Digital Human Modelling Symposium,* Ann Harbor.

Multi-factorial modelling of comfort in an aircraft cabin considering thermal, noise and vibration metrics

Neil Mansfield, Geetika Aggarwal, Frederique Vanheusden, Steve Faulkner

Department of Engineering, Nottingham Trent University, UK. Neil.mansfield@ntu.ac.uk.

Abstract

Comfort in aircraft cabins is influenced by many ergonomic and physical environment factors. For reasons of sustainability, the fleet of future regional passenger aircraft are expected to have an increased proportion that are propeller powered. Current turboprop regional aircraft have a reputation for being noisy and exposing passengers to vibration. Laboratory studies have simulated the aircraft cabin including noise, vibration and thermal stressors and sought subjective responses from volunteers. These data were used to build multi-factorial models of comfort in an aircraft cabin. Two modelling approaches were used: second order polynomial curve fitting allowed for prediction of subjective ratings from measurements of noise and vibration at discrete temperatures. A multi-factorial model including noise, vibration, and thermal parameters was developed using a linear regression machine-learning approach. This model allows for the prediction of subjective responses within a range of noise, vibration, and temperature levels that are experienced in aircraft.

Keywords: Discomfort, noise, vibration, thermal, aircraft.

Introduction

Air travel is a contributor to carbon emissions and therefore climate change. For regional transportation, turboprop aircraft (i.e. those with a propeller) are more efficient than equivalent jets (Babikian, Lukachko, & Waitz, 2002). Turboprops typically carry less than 100 passengers and include series from De Havilland (formerly Bombardier, Dash 8), Embraer EMB, and ATR42/72. Many future propulsion systems for ultra-low carbon aviation include propeller power units. A barrier to wider acceptance of turboprops has been the perception that they are uncomfortable due to the tonal nature of the noise and vibration. This has been highlighted with the 2022 announcement of a more comfortable ATR model with reduced noise and vibration, including a redesigned propeller (ATR, 2022)

Individual space, the thermal environment, hygiene, noise and vibration are concerns for aircraft passengers (Bouwens, Hiemstra-van Mastrigt, & Vink, 2018; Mansfield, West, Vanheusden, & Faulkner, 2021). To target future aircraft development, manufacturers need a tool by which technological innovation can be prioritized. Improved passenger comfort will lead to improved passenger acceptance and product reputation.

This paper presents the development of a model of the human response to noise, vibration and thermal stimuli. The model allows for the prediction of the response to noise, the response to vibration, the response to the thermal environment and the overall discomfort. It also predicts which of the modalities will be most important in terms of human response.

Methods

Experimental data collection

Data was obtained from a study conducted in an environmental chamber. The details of the study are published elsewhere. 20 volunteers were exposed to combinations of samples of noise and vibration whilst seated in an aircraft seat in an environmental chamber (Figure 1). The vibration was a reproduction of turboprop vibration generated using the 'VibPlate' vibration plate and had magnitudes between 0.75 to 3.0 m/s² r.m.s. (unweighted) at the seat. Noise was a reproduction of turboprop noise and reproduced using loudspeakers at levels between 78 and 90 dB(A). The air temperature ranged between 20 and 32 °C. All combinations of noise, vibration and thermal environment were tested. After each sample volunteers were required to rate the noise and the vibration on 11 point (0 to 10) Likert scales, and thermal comfort on the ISO 7730 'PMV' thermal comfort scale (-3 to 3) (International Organization for Standardization, 2005). They were also required to rate their overall discomfort using a modified Borg CR-100 scale (Sammonds, Fray, & Mansfield, 2017). The study was approved by the NTU Ethical Advisory Committee.

Figure 1. Image of experimental facility used for human data collection.

Table 1. Environmental conditions tested in the study.

Noise (dB(A))	**Vibration (m/s² r.m.s.)***	**Temp (ºC)**
78	0.75	20
82	1.50	24
86	2.25	28
90	3.00	32

*vibration are reported as band-limited unweighted, 0.63-100 Hz.

Data analysis and modelling approach

Data were analyzed using data visualization tools in MATLAB, curve fitting tools in MATLAB, and statistical analysis in SPSS.

Polynomial digital models

Individual models were generated for each of the four temperatures tested, and to predict noise, vibration, thermal, and overall ratings. These models were designed to indicate the expected response of the participants for any combination of noise and vibration within the range of experimental conditions tested. Second order polynomial models were used in MATLAB (Poly22)

Expressions were generated in the form:

$$f(x,y) = p00 + p10x + p01y + p20x^2 + p11xy + p02y^2$$

Where x represents the noise level, and y represents the magnitude of the vibration. The x and y variables are transformed using the mean of 84 and standard deviation 4.479 for noise, and 1.875 and 0.8398 for vibration. Coefficients *p* represent the first and second order polynomial coefficients (Table 2).

Table 2. Descriptors for polynomial coefficients

Coefficient	Description
p00	Constant value
p10	Linear coefficient (noise)
p20	Second order coefficient (noise)
p01	Linear coefficient (vibration)
p02	Second order coefficient (vibration)
p11	Coefficient of interaction between noise and vibration

Models were generated on the full data set of responses from participants (i.e. 20 responses for each combination of noise, vibration and temperature representing the 20 participants).

Machine learning digital models

The k-fold cross-validation machine learning (KFML) technique was used to generate an overall multifactorial model including noise, vibration, and thermal stressors. Data were randomly allocated to one of 5 test sets, each comprising 256 (20%) test conditions. Five training sets comprised the 1024 (80%) non-allocated data points. Multiple linear regression for each training set was conducted in SPSS, to generate model coefficients for that set. The overall model was generated by taking the mean coefficients across the 5 tests.

Models were generated in the form:

$$f(x, y, z) = q000 + q100x + q010y + q001z$$

where x represents the noise level, y represents the magnitude of vibration and z represents the temperature. Variables were not transformed. Coefficients are described in Table 3.

Table 3. Descriptors for multiple linear coefficients

Coefficient	Description
q000	Constant value
q100	Linear coefficient (noise)
q010	Linear coefficient (vibration)
q001	Linear coefficient (temperature)

Results

Summary experimental data

In summary, discomfort due to noise increased with noise level but not with vibration or temperature; discomfort due to vibration increased with vibration but not with noise level or temperature, showing no cross-modal interaction (i.e. no masking or synergistic effect). Overall discomfort increased with noise and vibration showing and additive effect (Figure 2). Overall discomfort also increased as the temperature increased.

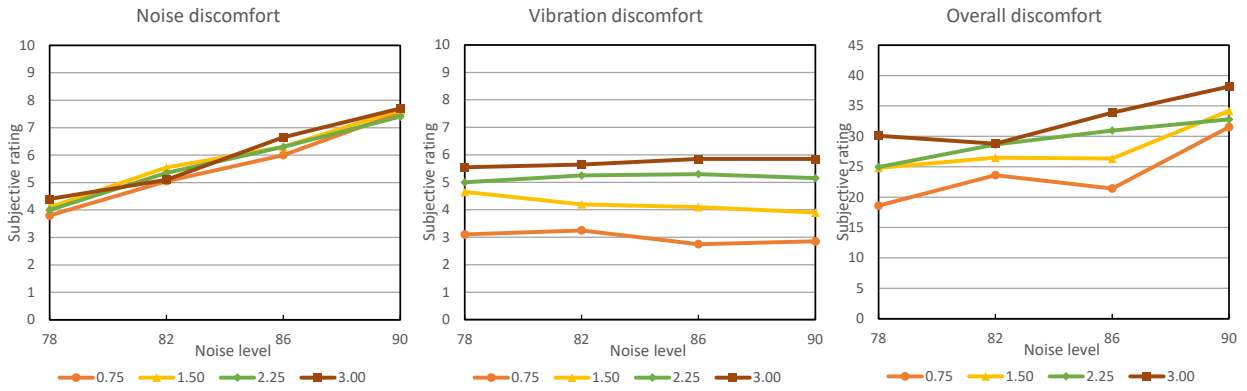

Figure 2. Mean data from laboratory study at 24 deg C showing subjective ratings of noise (*left*), vibration (*centre*) and overall discomfort (*right*) with changes in noise and vibration.

Polynomial digital models

Polynomial digital models of the human were created for noise discomfort, vibration discomfort, and overall discomfort. Models were fitted to individual data points, whereas RMS error (%RMSE) was calculated to the mean data.

For noise and vibration discomfort, RMS errors were less than 4% in all cases (Table 4). Models followed patterns as expected in the data, showing increases in discomfort with noise and vibration (Figure 2). Data in Figure 3 are for 20 degrees C, similar trends were obtained for other temperatures.

Table 4. Polynomial parameters for models of noise and vibration discomfort at four different temperatures.

Temp deg C	**Model type**	**p00**	**p10**	**p01**	**p20**	**p11**	**p02**	**%RMSE**
20	Noise	5.797	1.284	0.046	-0.106	0.037	0.043	2.45
	Vibration	4.342	-0.071	1.020	-0.027	-0.066	-0.231	3.27
24	Noise	5.814	1.293	0.106	0.024	-0.031	-0.031	3.01
	Vibration	4.759	-0.056	1.027	-0.024	0.124	-0.212	3.64
28	Noise	5.659	1.291	0.050	0.063	-0.119	-0.047	2.55
	Vibration	5.006	0.000	1.047	-0.110	0.044	-0.204	3.94
32	Noise	5.387	1.341	0.073	0.157	-0.088	-0.063	2.32
	Vibration	4.944	0.029	1.093	-0.051	0.068	-0.216	2.72

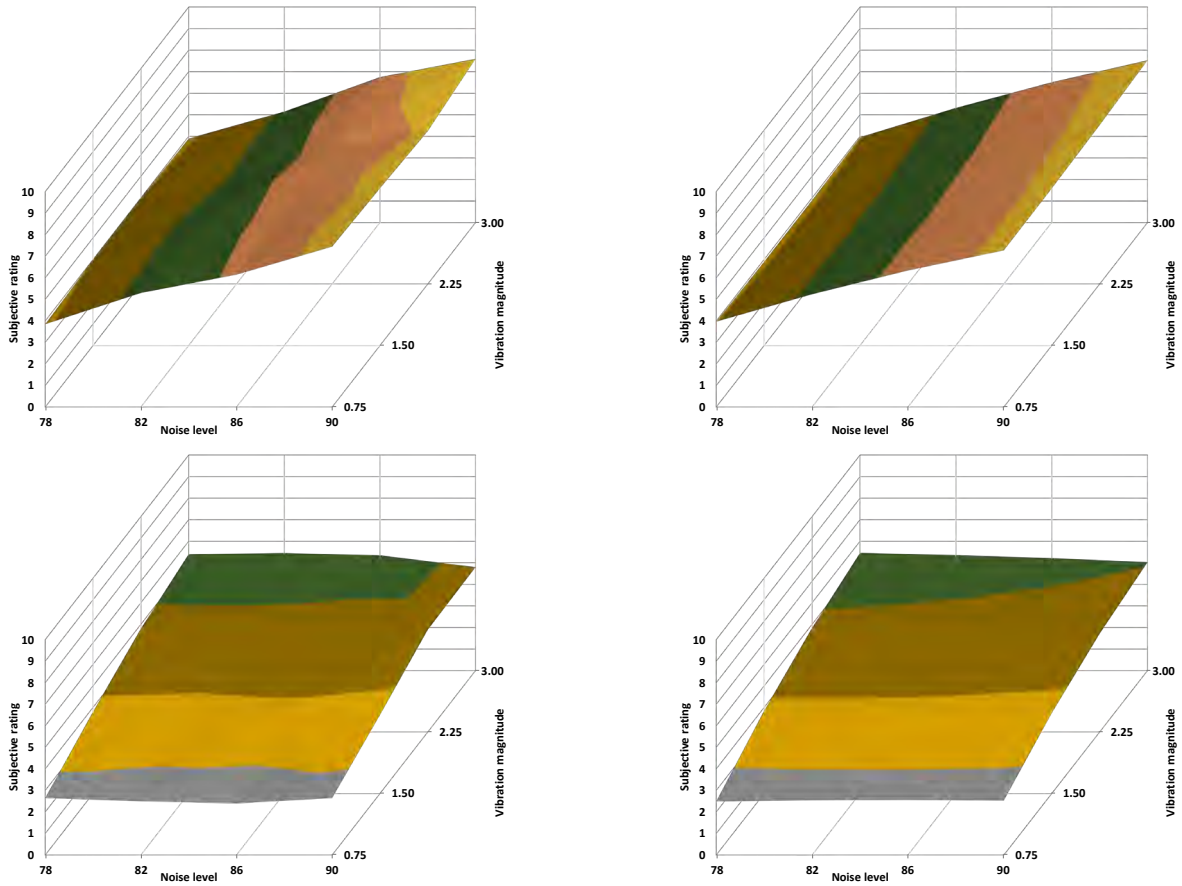

Figure 3. Mean data from laboratory study (left column) and polynomial model output (right column). Example data are shown for 20 degree C, *noise* discomfort (top row) and *vibration* discomfort (bottom row).

Overall discomfort was measured using a different scale to individual modality discomfort. Model parameters (Table 5) were therefore not directly comparable to those in Table 4. Results showed that the overall discomfort was a function of the temperature, the noise and the vibration (Figure 4).

Table 5. Polynomial parameters for models of overall discomfort at four different temperatures.

Model type	**Temp deg C**	**p00**	**p10**	**p01**	**p20**	**p11**	**p02**	**%RMSE**
Overall	20	25.460	3.744	2.381	0.499	-0.879	-0.250	4.68
Overall	24	27.530	3.358	3.158	1.174	-0.293	-0.242	6.30
Overall	28	31.430	3.090	3.051	0.496	-0.718	-0.025	4.47
Overall	32	38.320	3.518	2.977	0.312	-0.257	-0.382	2.15

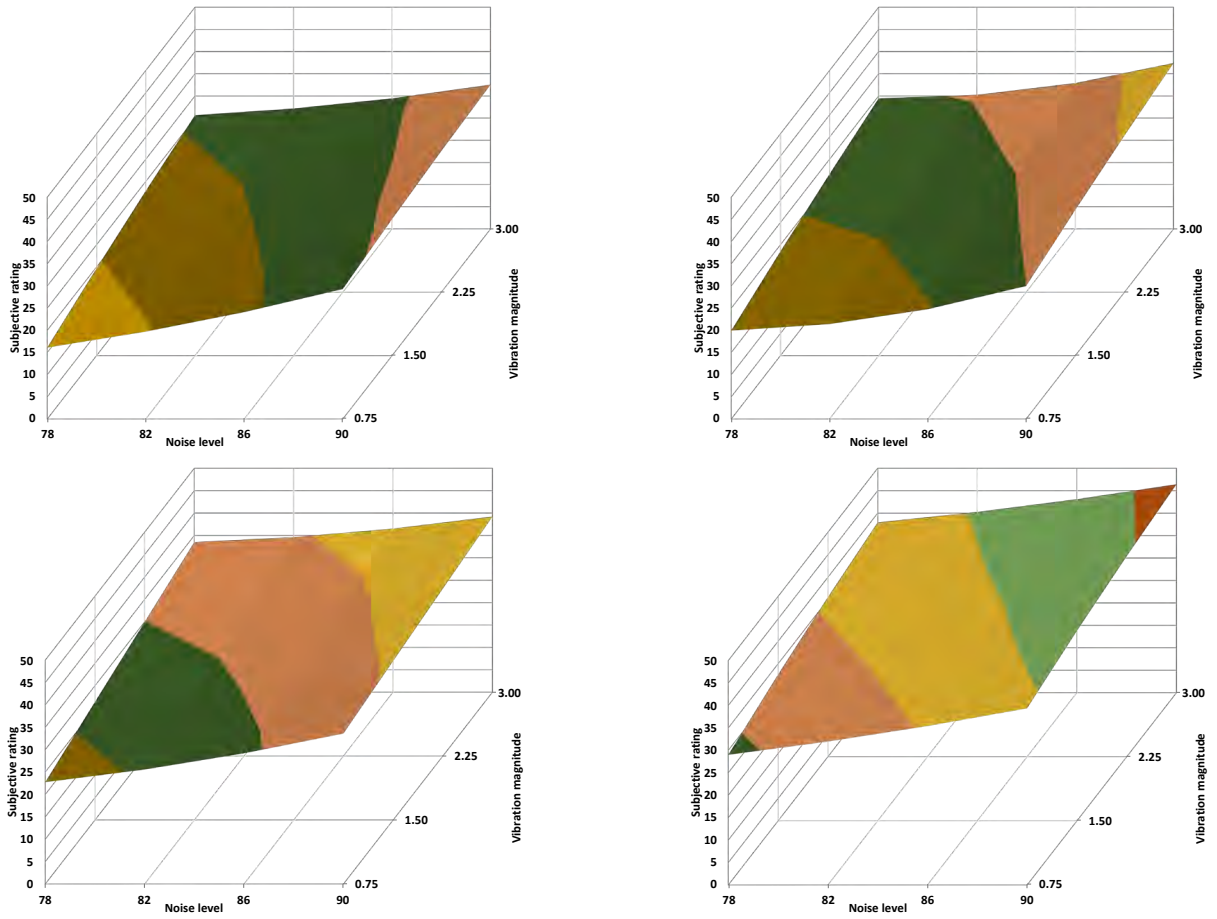

Figure 4. Polynomial model output for human model of *overall* discomfort at four different temperatures. Top row 20 and 24 deg C, bottom row 28 and 32 dec C.

Multiple linear regression machine-learning digital models

Five linear regression machine-learning (LRML) models were developed on 80% of the full data set and tested on 20% of the data. Model parameters are shown in Table 6. The RMS errors in comparison to mean data were 6.44 to 6.99%, with mean model error of 6.40% across all combinations of temperature, noise, and vibration.

Table 6. Linear regression machine-learning model parameters for overall discomfort.

Model	**q000**	**q100**	**q010**	**q001**
k-fold LRML 01	-61.98	0.69	3.18	1.10
k-fold LRML 02	-73.31	0.84	3.41	1.04
k-fold LRML 03	-58.70	0.66	3.43	1.06

k-fold LRML 04	-73.86	0.86	3.83	1.00
k-fold LRML 05	-64.02	0.77	3.36	0.93
k-fold LRML MEAN	**-66.37**	**0.77**	**3.44**	**1.03**

Discussion and conclusions

Digital models of the response of the human to aircraft environments have been shown to successfully fit to experimental data. For models that are designed to represent noise discomfort and vibration discomfort the polynomial model parameters were dominated by those addressing the modality of interest, indicating little cross-modal interaction. Future development of the models could remove those parameters that have little influence on the predicted values. All parameters were important for the overall discomfort model. The polynomial model was not comprehensive and needed parameters redefining for each temperature.

A linearized general model was developed using a machine learning algorithm. This method allowed for the prediction of the overall discomfort on the basis of 4 model parameters. Testing the model on mean data from 20 participants showed an RMS error of 6.4%.

The source data for the development of the model was obtained within a pre-determined range of temperatures, noise and vibration. Simulated cabin temperatures were designed to be in a comfortable range. Application of the model outside of the range may not be valid. For example, the predicted discomfort reduces in the model if the temperature reduces. However, if the temperature falls below 20 degrees, participants could feel discomfort due to cold.

Acknowledgments

This study was supported by EU CleanSky ComfDemo project — H2020-CS2-CFP08-2018-01.

References

ATR. (2022, May 18). *ATR paves way for next generation of its best-selling aircraft.* Retrieved from atr-aircraft.com: https://www.atr-aircraft.com/presspost/atr-paves-way-for-next-generation-of-its-best-selling-aircraft/

Babikian, R., Lukachko, S. P., & Waitz, I. A. (2002). The historical fuel efficiency characteristics of regional aircraft from technological, operational, and cost perspectives. *Journal of Air Transport Management*, 389-400.

Bouwens, J., Hiemstra-van Mastrigt, S., & Vink, P. (2018). Ranking of human senses in relation to different in-flight activities contributing to the comfort experience of airplane passengers. *International Journal of Aviation, Aeronautics, and Aerospace, 5*(2), 1-15. doi:10.15394/ijaaa.2018.1228

International Organization for Standardization. (2005). *ISO 7730 Ergonomics of the thermal environment.* Geneva: International Organization for Standardization.

Mansfield, N. J., West, A., Vanheusden, F., & Faulkner, S. (2021). Comfort in the Regional Aircraft Cabin: Passenger Priorities. *Congress of the International Ergonomics Association* (pp. 143-149). Vancouver: Springer.

Sammonds, G. M., Fray, M., & Mansfield, N. J. (2017). Effect of long term driving on driver discomfort and its relationship with seat fidgets and movements (SFMs). *Applied Ergonomics*, 119-127. doi:10.1016/j.apergo.2016.05.009

The study of endolymph flow and hair cell control analysis simulation model through electromagnetic fields

Hyeyeong Song, Soonmoon Jung, and Junghwa Hong
Korea University, South Korea

Abstract

When rotational acceleration occurs in the body, the endolymph moves with velocity owing to rotational inertia, and the cupula is tilted by the force generated by the endolymph. When the cupula is tilted, hair cells are also tilted to create a sense of rotation. At the same time, a rotational signal is transmitted, and if the signal does not match the field of sight, various symptoms such as dizziness, nausea, and headache appear. To resolve the discrepancy between the rotational signal and the sight caused by the tilt of hair cells such as motion sickness, in this study, we developed a vestibular finite element (FE) simulation model to control the angle of hair cells in the cupula. The simulation model consisted of a straight (linear) model and a model identical to the actual shape (curved) model. A fluid velocity of around 0.2 Hz, which is associated with motion sickness, was applied to the model to bend the cupula. [1] A magnetic field was applied by positioning the coil along the three axes based on the cupula and a current is passed to generate a Lorentz force. By increasing or decreasing the current, the displacement moved by the cupula according to the magnetic field was measured. As a result, in both models, the displacement of the cupula tends to decrease when the current is increased.

Introduction

Motion sickness is a symptom of not being able to resolve the imbalance between vision and rotation felt by the vestibular system and causes discomfort or dizziness.[2] And symptoms of motion sickness can be alleviated by reducing the degree of hair cell deflection by causing the flow of the endolymph to act in the opposite direction. Since the endolymph is an ionic liquid, it can change the flow direction of the endolymph by the Lorentz force derived from the strength of the electromagnetic field and the electrode direction.[3] The purpose of this study is to develop a finite element (FE) simulation model of the vestibular system and analyze the endolymph flow pressure, velocity, and hair cell pressure and angle applied by an electromagnetic field through FE simulation to control the angle of hair cells in the cupula.

Methods

A model of the semicircular canal was created to implement the vestibular system. The simulation model consisted of a straight (linear) model and a model identical to the actual shape (curved) model. In the center of this model, cupula is inserted, and endolymph is filled to allow ion liquid to flow in one direction. At this time, the displacement of the cupula slope that occurs was the main focus of this study. The solenoid coil is located on the cupula side at the center of ampulla (Fig.1 (a)-b, (b)-d, e, f, g) and surrounds the ampulla and the utricle. The rotational speed and radius of the solenoid coil were adjusted based on the calculation value of the enamel coil with a diameter of 0.4 mm, and the strength of the internal magnetic field was changed by changing the current from 0 to 15 A. After that, the displacement that the cupula moves with the magnetic field was measured by increasing or decreasing the current.

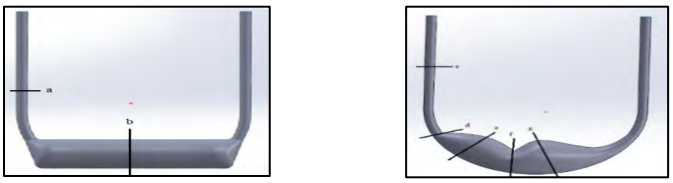

(a) (b)

Figure 1. Linear Semicircular Canal (a) Experiment Optimization Linear Model, (b) Experiment Optimization Curved Model.

Results

In both models, the maximum displacement moved by the cupula decreased when the current increased. As the current increases, the falling pattern has the shape of a decreasing first-order graph. Overall, there was a difference in amplitude in the graph, and the shape was maintained. In the linear model, when the original and 15A currents flowed, the difference was 1.41%. In the case of the curved model, when the original and 15A currents were applied, the difference was 1.719%. When the linear model is compared with the 15A simulation, the reduced displacement of the cupula is 0.02259mm and that of the curved model is 0.0281mm. Both values have an error of 19.69%. The factors that can have an error are the fluid vortex flowing in the above-mentioned curved model and the increase in the flow velocity owing to the rotational moment. Although there is a difference in values, the decrease in cupula displacement according to the increase in current is identical.

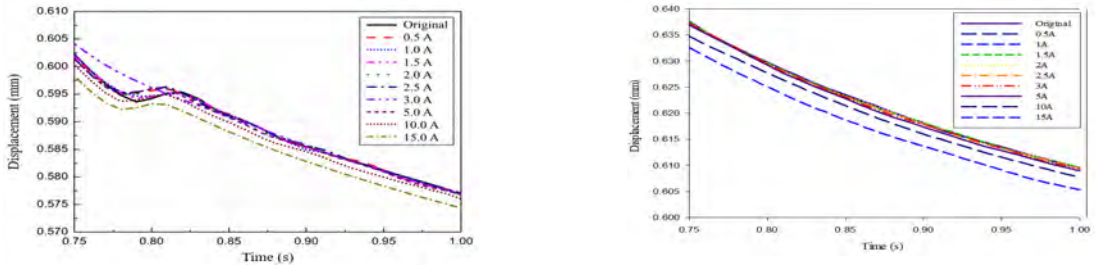

(a) (b)

Figure 2. (a) Linear Model and (b) Curved Model Cupula Displacement due to Magnetic Field Change

Discussion and Conclusions

When the intensity of the magnetic field in the Z-axis direction was increased with an electric current, the inclination angle of the cupula was reduced. The reason for this is gravity and vortex and has the same tendency that the Z axis-oriented magnetic field and increased magnetic field strength most affect the reduction in the displacement. These results can potentially be used for the treatment of vestibular system diseases, such as a non-invasive mechanical motion sickness relief device.

Acknowledgments

This research was supported by the BK21 FOUR (Fostering Outstanding Universities for Research) funded by the Ministry of Education (MOE, Korea) and National Research Foundation of Korea (NRF).

References

[1] Winther, F. Ø., Rasmussen, K., Tvete, O., Halvorsen, U., & Haugsdal, B. (1999). Static magnetic field and the inner ear: A functional study of hearing and vestibular function in man after exposure to a static magnetic field. Scandinavian audiology, 28(1), 57-59. [2] Brainard, A., & Gresham, C. (2014). Prevention and treatment of motion sickness. American family physician, 90(1), 41-46. [3] Ward, B. K., Roberts, D. C., Della Santina, C. C., Carey, J. P., & Zee, D. S. (2015). Vestibular stimulation by magnetic fields. Annals of the New York Academy of Sciences, 1343(1), 69-79.

Methods for Including Human Variability in System Performance Models

Randall J. Hodkin Jr. & Dr. Michael E. Miller
Air Force Institute of Technology, Department of Systems Engineering and Management

Abstract

To understand system performance, it is rational to consider all system components, including the humans involved in the control or maintenance of the system. Previous research has included human performance by modeling human tasks as events within Discrete Event Simulation (DES) models. These models typically represent the variability of task performance times and error rates by calculating the mean and variance across multiple individuals. Such approaches assume independence of task performance measures between individuals, but evidence exists which indicates that task performance measures are correlated between individuals. The current research seeks to understand methods to account for performance variability within DES models. A taxonomy of potential methods to address variability in DES models is developed and discussed. Among the findings derived through development of this taxonomy is the need to differentiate models of performance envelopes from models of average system performance and alternatives for modeling the human when predicting each class of performance.

Keywords: Discrete Event Simulation, Variability, Performance Envelopes, Mean Performance

Introduction

In its 2016 report on modeling, Sandia National Laboratories concluded that Model Based Systems Engineering (MBSE) provides significant advantage to project performance (Carroll & Malins, 2016). However, to obtain useful information from a simulation, modelers must adopt an approach appropriate for the specific engineering problem and capture sufficient system details to address the problem. Since humans interact with most systems, it is often important to include representations of human attributes or behaviors within system models when attempting to estimate system performance. In fact, one study by Baines et al in 2004 found that simulation results including Human Performance Models (HPM) could vary by as much as 35% when compared to results where human factors were not considered (Baines, Mason, Siebers, & Ladbrook, 2004).

Discrete Event Simulation (DES) environments, such as the Improved Performance Research Integration Tool (IMPRINT), have been used to predict human and system performance (Mitchell, 2000). These models typically require the modeler to decompose mission segments into a network of interdependent,

discrete human activities or tasks and system activities. Generally, each human task and system activity is modeled as a discrete event having a time distribution and a probability of successful task completion. While several studies have illustrated that DES models can accurately predict mean times for mission completion, the models often underestimate variability in mission completion times (Kim, Miller, Rusnock, & Elshaw, 2018; Goodman, Miller, Rusnock, & Bindewald, 2017). A potential reason for this deficiency is the practice of collapsing task times across multiple individuals to obtain a mean while also assuming that each task is independent of the time required to complete other tasks.

In anthropometrics, it has long been recognized that some human measures are related to others with varying degrees of correlation. Initially, systems considering physical measures were designed to accommodate individuals with average anthropometric dimensions, assuming this strategy would produce systems that adequately accommodate most individuals. However, in 1952 Daniels showed that human anthropometric measures could have varying degrees of correlation with each other (Daniels, 1952). Specifically, Daniels demonstrated that from 4,000 pilots, not even one was within 30 percent of the mean in every one of ten physical dimensions, indicating that there was no "average" pilot. Since this study, anthropometric modeling has primarily shifted to defining a range or envelope of dimensions that accommodate a desired range of humans. Several statistical modeling methods that account for correlated measures were developed to define this envelope of human dimensions (Brolin, 2016; Kuo, Wang, & Lu, 2020; Hsiao, 2013; Kim & Whang, 1997; Jung, Choi, Lee, You, & Kwon, 2021; Zehner, Meindl, & Hudson, 1989).

Similarly, human performance varies across numerous dimensions, with some humans performing certain tasks consistently faster or more accurately than others. The effect is that, as with anthropometric dimensions, an individual's performance measures of similar tasks can be correlated. Additionally, comparably skilled people may experience correlation in task performance across individuals. Therefore, task performance is subject to correlation both within and across individuals. Since present human modeling is limited in these situations, this research explores methods for including task performance correlation and variability in DES models. Specifically, the current research undertakes a literature review to develop a taxonomy of approaches for quantifying or including human variability in DES models.

Background

DES as a human modeling approach simulates time-dependent real-world processes as events, updating system parameters during the events and approximating the system as fixed between events (Mathworks, 2021). It is particularly well suited for problems in the HPM domain since human interaction with a system can be characterized by procedures and broken down into task networks (Laughery, 1999). Each

task in the network represents a time-dependent discrete event where human performance parameters are calculated. There are many methods for calculating system parameters during a discrete event and updates can either be programmed as deterministic or stochastic (Alion Science and Technology, 2018). Since every human has unique physical and cognitive limitations which can fluctuate over time depending on environmental and individual stressors, human performance is subject to between-subject and within-subject variation that typically requires stochastic DES methods (Belyavin & Fowles-Winkler, 2003).

A common source of uncertainty in human modeling is the variability of performance between individuals, which is often captured in DES as probably distributions that are developed from theory or more commonly determined using empirical data (Batarseh, 2010). To model with stochastics, an engineer must develop a probability distribution and parameters through analysis of empirical data (Greasley, 2016). Unfortunately, it is common to assume variable independence when developing distributions since this assumption simplifies analysis and modeling (Kruskal, 1988). In fact, some of these simplifications are inherent in DES software and can contribute to a modeler assuming independence. To better understand how independence can be assumed so easily it is important to understand the process for applying DES to HPM.

Modeling Human Performance Using DES

There are many ways different ways to conceptualize the steps in creating a simulation model. However, these models often include the five phases described by Allen (Allen, 2011). The first three phases outline model development while the final two phases are dedicated to model application. These five phases include:

Phase 1: Define (who, what, when, how)
Phase 2: Input Analysis (data collection and fitting distributions)
Phase 3: Simulation/Calculation (create/validate prediction models)
Phase 4: Output Analysis (alternative comparisons)
Phase 5: Decision Support (charts, tables, reports)

The primary model components that must be defined during phase one are the tasks required to complete the procedure being modeled, events that change the state of the system, entities that perform or participate in tasks, and state variables that define what is happening within a system at a given point in time (Banks, 1998). Task network modeling is an approach to understand what is to be modeled in DES where individual performance decomposed into a sequence of tasks. This process requires that a modeler possess knowledge about the system. If system knowledge is limited, then a task analysis may be required to appropriately scope the model and define model components (Rusnock, 2021). Simulation entities must be further defined by attributes that characterize how they interact with tasks and events must also be

further defined to include proper sequence that maintains the systems physical cause-and-effect constraints (Banks, 1998). The amount of task decomposition and the overall model scope depends on the engineering problem posed (Laughery, 1999). Phase one of WSC model development is complete when all the components are defined at a level sufficient to support the modeling scope.

Transitioning to phase two, data is collected to quantify the time distributions, logic, and other relationships. This data is then analyzed to define the time distributions. For human modeling, this usually includes gathering data for multiple individuals, plotting the data to characterize the distribution of the data, and fitting probability distributions to the data. This last step often includes the use of analysis tools such as Q-Q plots and tests, such as the Kolmogorov-Smirnoff (K-S) test, to determine the best distribution, as well as calculating the parameters for the probability distribution.

To complete the process of developing a DES HPM, phase three includes creation of the tangible model. The process is comprised of creating the task network, entities, state variables, and entering the task probability parameters or any other parametric relationships. For human modeling in tools such as the IMPRINT this can also include setting up performance shaping parameters (PSF) to adjust human performance for changes in human, system, or environmental states. Additionally, IMPRINT permits one to estimate the workload for each task as well as how it influences simulation performance, and the tool must be properly configured to provide these values where needed. Finally, once the model is fully created and all the appropriate details are entered, the last step in this process is to validate the HPM.

When working through the three phases of the WSC development process, an engineer is determining all the information that will be used to approximate human behaviors. It is important that all the input parameters be meaningfully derived from theory, or more likely, determined from empirical data. For this reason, input analysis is prone to mistakes that can affect the accuracy of predictions and care should be taken when performing analysis to determine input parameters. Incorrectly assuming independence, lack of knowledge about dependencies, missing data, and measurement error all increase model uncertainty and reduce the accuracy of predictions if not appropriately considered (Batarseh, 2010).

DES and The Assumption of Independence

Unfortunately, it is common practice to assume variable independence when developing probability distributions (Kruskal, 1988). Although event independence is not necessarily inherent in DES, this common assumption in simulations stems from four influences. First, DES assumes discrete events that are each isolated in time and defined by probability distributions which assume independent and identically distributed data (Biller & Gunes, 2010; Corlu, Akcay, & Xie, 2020). Second, there is often

insufficient data to characterize dependencies between tasks (Batarseh, 2010; Corlu, Akcay, & Xie, 2020). Third, the assumption of independence simplifies model construction by reducing the work required to determine input parameters (Kruskal, 1988; Romeu, 2006). Finally, while many input processes may exhibit dependence, DES software has not been updated to include an inherent method to handle variable dependency and it can only be implemented through difficult coding or iterative simulations (Corlu, Akcay, & Xie, 2020). Thus, new methods to manage dependencies can be difficult to understand and implement in existing software (Biller & Ghosh, Multivariate Input Processes, 2006).

It is important to point out that variability in HPM differs from many other domains. Human modeling seeks to understand the performance of a system given distinct interactions with multiple individuals. Many people will perform tasks within a system multiple times under different physical and mental conditions, and therefore HPM often needs to capture both within-subject and between-subject variability. However, it is common that both within-subject and between-subject variability is modeled using a single distribution. But, since each human participates in multiple tasks, an individual's specific abilities or state often influence not only their performance on the current task but also affect their performance in other tasks in a similar manner.

Therefore, human task performance is not truly independent and the amount of dependence between ability or state and performance is not static but can also vary based on the type of task performed. In fact, research has been performed to decompose tasks into a taxonomy of relatively independent sensory, cognitive, psychomotor, or physical tasks where performance is highly correlated (Fleishman, 1967; Furnham, von Stumm, Makedrayogam, & Chamorro-Premuzic, 2009). Thus, an individual who generally performs well at psychomotor tasks compared to his or her peers will frequently perform well at similar tasks in relation to their peers. The implication is that a DES model of performance across tasks will be correlated based on an individual's ability and state. Since task times are generally summed for all events, the total time will depend on correlations that should be included in the simulation. Thus, it is clear the traditional approach of combining data to find a distribution for each task will produce a model which has the highest likelihood of predicting the average task time but will reduce predictions of the system variability. Therefore, it is important to account for the correlations between an individual's skill and performance as we discuss methods that can adjust HPM to better predict variability.

Methods

A series of literature searches was conducted to develop a taxonomy for modeling population variability in HPM DES. The goal of initial searches was to better understand the steps used to develop a DES model, which steps might be modified to increase the accuracy of variability predictions, and to

understand the factors that contributed to the need for modified steps. A final literature search was performed, applying the knowledge from previous searches, to determine approaches that could be used to better represent population variability in HPM DES models. From this final literature review, a taxonomy was then constructed to represent DES modeling approaches which provide more accurate predictions of human variability. The taxonomy also provides a quick visual reference to a range of tools, of varying prediction accuracy and rigor to implement, that can be employed at a modeler's discretion based on project needs.

All literature reviews conducted were structured to provide academic publications about DES and variability between the start of heavy commercial DES use in 1970 and the current date. Literature searches were completed using Google Scholar, EBSCO Discovery Services, and Academic Search Ultimate. Reviews followed the steps of examining abstracts, determining significance, and full review of important papers. Other relevant papers were also identified through a review of references from papers discovered during the literature search process. Some of the papers discovered through reference review were outside the search period but were still relevant and therefore cited as references for this paper.

Searches were conducted using key words, including DES in combination with terms to include human modeling, human performance, modeling people, independence assumption, input modeling, variability, uncertainty, and modeling techniques. The final literature search focused on DES, human variability, within-subject, between-subject, and modeling variability. Searches for these key words directly returned publications cited in this paper or returned papers that led to others through a reference review.

Results

Evidence has shown that the casual assumption of independence and limited capabilities available in many existing DES software are not adequate for accurately predicting population variability (Batarseh, 2010; Jung, Choi, Lee, You, & Kwon, 2021). As systems become increasingly complex the interactions humans have with them are also becoming more intricate. Hardware and interfaces are being tailored to accommodate individual differences in capabilities by balancing workload between humans and non-human agents so overload can be avoided. The result is that the demand for accurate human variability predictions is increasing and new approaches for modeling variability are necessary to meet the need.

The articles reviewed during this research tended to fall into one of two categories that described methods for either quantifying or reducing uncertainty, or variability, in a model. As shown in Figure 1, the first classification is based on whether a method actively attempts to reduce model uncertainty or whether it seeks to quantify the amount of uncertainty expected in model results.

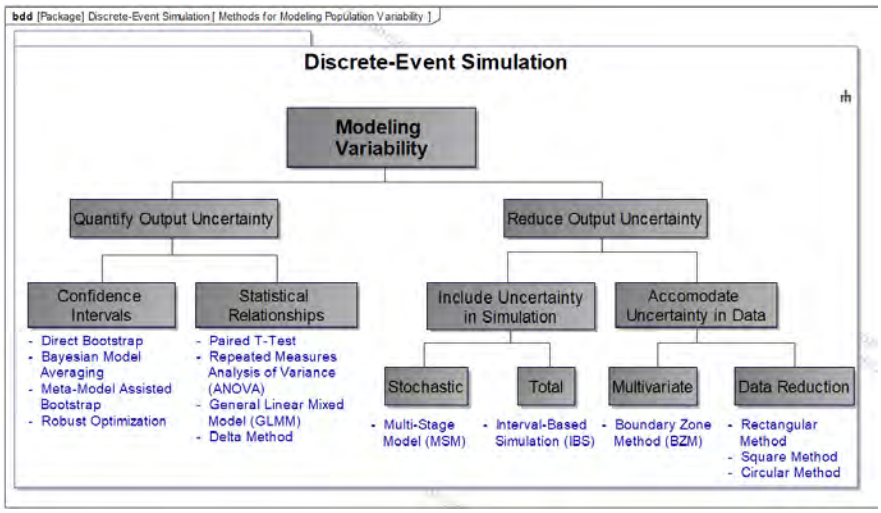

Figure 1. Taxonomy of Methods for Modeling Population Variability in DES

While methods for quantifying uncertainty have been around since the 1970's or earlier, approaches to reduce output uncertainty only started to emerge in the early 2000's with articles like the one published by Belyavin et al in 2003. This paper the discussion of ways to reduce uncertainty by introducing additional variability to models.

The two broad approaches of quantifying or reducing output uncertainty are quite different in specific technique and results but achieve the same overall goal of understanding variability in DES models. quantification methods return DES model outputs and report their associated confidence interval (CI) while reduction methods return outputs that have typically been adjusted to fall within a certain CI. From a practical standpoint, this means that methods for quantify uncertainty are good for risk assessment and decision support while uncertainty reduction methods are a better choice for engineering design where results will feed other analyses. As the approaches to quantifying output uncertainty are relatively well understood, it is useful to focus on methods to reduce output uncertainty.

The taxon for reducing output uncertainty is further decomposed into two categories. The first permits uncertainty to be included in a simulation directly while the second seeks to understand uncertainty due to between-subject differences. The next level of taxon further divides these techniques into four distinct categories with each technique providing a method for modeling and understanding data using simulation loops or iterative simulation to model within-subject and between-subject variability. However, only the multi-stage model (MSM) and Interval Based Simulation (IBS) methods for representing total uncertainty have currently been discussed in literature as a potential methods specific to DES.

Methods in the stochastic taxon apply multi-stage stochastic models to predict performance. For example, Belyavin et al suggested a multi-stage stochastic model where operator state is predicted and used to

influence the normal DES model, thereby introducing additional variability through an extra modeling stage (Belyavin & Fowles-Winkler, 2003). Similarly, IBS introduces imprecise probabilities via iterative simulation to represent total uncertainty (reducible & epistemic) and better capture system variability.

Methods like MSM or IBS that introduce uncertainty terms to a model still relate to prediction of the total variability about the mean, but another approach is to attempt to understand the envelope of performance. Techniques that accommodate uncertainty have previously been applied in the anthropometric domain and permit one to understand representative individuals whose performance encompass a defined envelope of performance. The task performance of these representative individuals can then be modeled using appropriate probability distributions, and their performance distributions iteratively modeled within a DES. Through this approach, one can understand the boundary of performance across a population of individuals without modeling the effect of each individual within a population.

Discussion and Conclusions

Overall, this research did not identify any current methods in DES literature which address the lack of dependence in task performance across individuals. Belyavin's MSM approach suggests methods to improve within-subjects variability and approaches such as IBS might be used to address this issue, but its implementation would require substantial modification of existing DES tools to provide a practical approach. However, one can envision a combination of MSM and anthropometric tools like BZM to select representative humans for simulations where an inner loop simulates the performance of an individual and an outer loop simulates individual differences to capture a better estimate of variability.

As part of this research, it appears some classes of HPM may benefit from performance envelopes rather than average system performance. As with anthropometrics, there are classes of HPM for which the goal may be to accommodate a range of performance rather than predict the average result. Methods like BZM that were originally designed for multivariate anthropometric accommodation can be leveraged to achieve this result. BZM and similar approaches may not only help with variability predictions but might also open the door to new DES approaches that can predict human task performance envelopes.

Overall, HPM tools like DES have been updated with new interfaces and some features like PSF and workload calculations, but it may be time to consider more drastic changes to improve prediction accuracy. Methods like IBS and BZM documented in this research offer ways that DES can be modernized to allow consideration of human performance envelopes when the situation dictates.

References

Alion Science and Technology. (2018). *IMPRINT Pro User Guide.* Louisville, CO: Alion Science and Technology, HSI DIvision.

Allen, T. (2011). *Introduction to Discrete Event Simulation and Agent-based Modeling.* London: Springer-Verlag.

Baines, T., Mason, S., Siebers, P., & Ladbrook, J. (2004). Humans: the missing link in manufacturing. *Simulation Modelling Practice and Theory*, 515-526.

Banks, J. (1998). *HANDBOOK OF SIMULATION Principles, Methodology, Advances, Applications, and Practice.* New York: John Wiley and Sons, INC.

Batarseh, O. (2010). *An Interval Based Approach to Model Input Uncertainty in Discrete-Event Simulation.* Orlando: University of Central Florida.

Belyavin, A., & Fowles-Winkler, A. (2003). Subject Variability and the Effect of Stress in Discrete-Event Simulation. *Proceedings 15th European Simulation Symposium.*

Biller, B., & Ghosh, S. (2006). Multivariate Input Processes. *Elsevier Handbook in OR & MS, Vol 13*, 123-153.

Biller, B., & Gunes, C. (2010). Introduction to Simulation Input Modeling. *2010 Winter Simulation Conference*, (pp. 49-58).

Brolin, E. (2016). *Consideration of Anthropometric Diversity - Methods for Virtual Product and Production Development.*

Carroll, E. R., & Malins, R. J. (2016). *Systematic Literature Review: How is ModelBased Systems Engineering Justified?* Albuquerque, NM: Sandia National Laboratories.

Colombi, J., Miller, M., Bohren, J., & Howard, J. (2014). Conceptual Design Using Executable Architectures for a Manned Mission to Mars. *IEEE Systems Journal 2014*, 1-18.

Colombi, J., Miller, M., Schneider, M., McGrogan, J., Long, D., & Plaga, J. (2011). Model Based Systems Enegineering with Department of Defence Architectural Framework. *Systems Engineering 2011:4(3)*, 305-326.

Corlu, C., Akcay, A., & Xie, W. (2020). Stochastic simulation under input uncertainty: A Review. *Elsevier Operations Research Perspectives*, 1-16.

Daniels, G. (1952). *The Average Man?* Dayton: Wright-Patterson Air Force Base.

Fleishman, E. (1967). Development of a Behavior Taxonomy for Describing Human Tasks: A Correlational-Experiment Approach. *Journal of Applied Psychology*, 1-10.

Furnham, A., von Stumm, S., Makedrayogam, A., & Chamorro-Premuzic, T. (2009). A Taxonomy of Self-Estimated Human Performance. *Journal of Individual Differences*, 188-193.

Goodman, T., Miller, M., Rusnock, C., & Bindewald, J. (2017). Effects of Agent Timing on the Human-Agent Team. *Cognitive Systems Research 2017:46*, 40-51.

Greasley, A. (2016). Methods of Modelling People using Discrete-event Simulation. *6th International Conference on Simulation and Modeling Methodologies, Technologies and Applications* (pp. 312-317). SCITEPRESS – Science and Technology Publications.

Hsiao, H. (2013). Anthropometric Procedures for Protective Equipment Sizing and Design. *Human Factors 2013:55(1)*, 6-35.

Jung, K., Choi, Y., Lee, B., You, H., & Kwon, O. (2021). A Boundary Zone Method for the Generation of Multivariate Representative Humanoids. *MDPI Applied Sciences*.

Kim, J., & Whang, M. (1997). Technical Note: Development of a set of Korean Manikins. *Apllied Ergonomics 1997:28*, 407-410.

Kim, S., Miller, M., Rusnock, C., & Elshaw, J. (2018). Spatialized audio improves call sign recognition during multi-aircraft. *Elsevier Applied Ergonomics*, 51-58.

Kruskal, W. (1988). Miracles and Statistics: The Casual Assumption of Independence. *Journal of the American Statistical Association*, 929-940.

Kuo, C., Wang, M., & Lu, J. (2020). Developing Sizing Systems using 3D Scanning Head Anthropometric Data. *Measurement Journal of the International Measurement Confederation*.

Laughery, R. (1999). Using Discrete-Event Simulation to Model Human Performance in Complex Systems. *Winter Simulation Conference*, (pp. 815-820).

Madni, A., & Madni, C. (2018). Architectural Framework for Exploring Adaptive Human-Machine Teaming Options in Simulated Dynamic Environments. *Systems 2018:6(4)*, 44.

Mathworks. (2021, December 8). *Understanding Discrete Event Simulation*. Retrieved from Mathworks: https://www.mathworks.com/videos/understanding-discrete-event-simulation-part-1-what-is-discrete-event-simulation--1494873178760.html

McManus, H., Richards, M., Ross, A., & Hastings, D. (2007). A Framework for Incorporating "ilities" in Tradespace Studies. *A Collection of Technical Papers: AIAA Space 2007 Conference* (pp. 941-954). AIAA.

Mitchell, D. (2000). *Mental Workload and ARL Workload Modeling Tools.* ARL.

Romeu, J. (2006). Teaching Engineering Statistics to Practicing Engineers. *7th International Conference on Teaching Statistics* (pp. 1-6). Salvador, Bahia, Brazil: ICOTS-7.

Rusnock, C. (2021). Human Systems Modeling: Task Analysis. Dayton, OH, USA.

Watson, M., Rusnock, C., Miller, M., & Colombi, J. (2017). Informing System Design Using Human Performance Modeling. *Systems Engineering 2017:20(2)*, 173-187.

Zehner, G., Meindl, R., & Hudson, J. (1989). *A Multivariate Anthropometric Method for Crew Station Design.* DTIC.

Santos the Virtual Soldier Predicts Human Behavior

Karim Abdel-Malek, Rajan Bhatt, Chris Murphy, and Marco Tena Salais
The University of Iowa, United States

Abstract

Human modeling and simulation environments have become sophisticated, providing capabilities for posturing the digital avatar, conducting dynamic tasks, assessing human performance, and obtaining scientific analysis. Physics-based analysis of human motion has also enabled capabilities for predicting the dynamics of the motion whereby the avatar is able to respond to external effects such as load conditions or the physical environment. However, the behavior of the avatar is typically the same. Indeed, the same input to the system yields the same output. This work is concerned with obtaining more realistic and different behaviors for the human while conducting a task in a physics-based environment.

While the Santos[1] digital human modeling (DHM) system has been successfully used in the analysis and prediction of human motion, the resulting behavior of a specific soldier is the same. An (avatar) individual doing a task will do the same task exactly the same way if the simulation is executed again. In reality, however, a soldier may adopt a different strategy to accomplish the same task.

This paper discusses the development of a rigorous scientific method using human performance functions as the driving force to induce different behavior.

The Santos platform uses 215 degrees of freedom to model a human. The research and development of this platform over the past 15 years has made significant strides in the development of *predictive dynamics*[2] as a methodology for predicting behavior and is physics-based. Rather than solving the highly complex and coupled algebraic-differential equations of motion governing the human's behavior, predictive dynamics uses optimization to solve for the behavior.

---

[1] Abdel-Malek, Karim, et al. "Santos: An integrated human modeling and simulation platform." *DHM and Posturography*. Academic Press, 2019. 63-77.

[2] Abdel-Malek, Karim, and Jasbir Singh Arora. *Human Motion Simulation: Predictive Dynamics*. Academic Press, 2013.

In this paper we use a new methodology that employs seed scenarios before executing predictive dynamics, thus allowing the system to provide variations in task execution. A tall person will execute a task differently than a short person, if height is an influencing factor.

The results of predictive dynamics are autonomous prediction of the motion while subject to the laws of motion (we use Lagrange's equations of motion). These results are not pre-recorded but rather a prediction of what a human can do. Depending on the task at hand, the soldier in the DHM environment will accomplish the task unaided by human analysis but subject to physics, biomechanics, physiology, and the constraints of the environment.

This paper will present the methodology for predictive behavior to affect various strategies. Results of this work will be presented.

Keywords: soldier, human performance, predicting behavior, physics-based

Introduction

The problem of the dynamic prediction of human motion is the subject of significant research this time because it is difficult to replicate human behavior in a digital format. This work aims to provide one methodology for such prediction using years of research into the modeling and simulation of human motion with the addition of a system for a computer to also select a strategy for an initial seed motion.

Dynamic motion prediction is a challenging problem because the equations of motion (EOM) are nonlinear and cannot be solved in a closed form. Robust nonlinear programming algorithms (NLP) have been developed and applied to solve the motion prediction problem. Inverse dynamics is usually adopted in the optimization formulation so that integration of the equations of motion is avoided. Sensitivity of the nonlinear dynamics equations with respect to the state variables is needed in the optimization process to solve the problem efficiently and accurately. Sohl and Bobrow (2001) developed a sensitivity algorithm of recursive Newton-Euler equations for branched or tree-topology systems. http://www.engineeringvillage2.org/controller/servlet/Controller?CID=quickSearchCitationFormat&searchWord1={Redhe,+M.}&section1=AU&database=1&startYear=1884&endYear=2005&yearselect=yearrangeKim *et al.* (1999) presented a class of Newton-type algorithms to analytically compute both the first and second derivatives of the dynamics equations with respect to arbitrary joint variables. Xiang *et al.* (2009a) carried out sensitivity analyses for dynamic motion prediction of a mechanical system by using the recursive Lagrangian formulation.

Recently, dynamic motion planning of digital humans has been solved using optimization, which requires sensitivity analysis of dynamics equations. Forward dynamics can be used to solve equations of motion in modeling human motion (Roussel et al., 1998; Chevallereau et al., 1998; Anderson & Pandy, 2001a). Anderson and Pandy (2001b) presented a model with 23 degrees of freedom (DOF) and 54 muscles for normal symmetric walking on level ground. The objective function was metabolic energy per unit distance, and the design variables were the muscle actuations. Equations of motion of the bio-system were integrated at each iteration in the optimization process. The parallel computation techniques were used to evaluate gradients by finite differences. The initial walking postures obtained from experiments were imposed as constraints in the formulation so that accurate kinetics data were recovered from the simulation. However, this approach suffers from high computation cost and availability of the motion capture data.

To circumvent these difficulties, alternative formulations may be used for the optimization problem, in which both forces and joint state variables are treated as unknowns. Equations of motion are either evaluated using inverse dynamics or simply imposed as equality constraints (Kim *et al*. 2008, Wang *et al*. 2007). Lo *et al*. (2002) presented a framework for human motion prediction incorporating inverse recursive Newton-Euler equations with analytical gradients. Saidouni and Bessonet (2003) used optimization to solve for cyclic, symmetric gait motion of a 9-DOF model that moves in the sagittal plane; the control points for the B-spline curves along with the time durations for the gait stages were optimized to minimize the actuating torque energy. Xiang *et al*. (2009b) presented the dynamic human walking prediction by using a 55-DOF skeleton digital human model. The joint angle profiles were treated as design variables, and the dynamic effort was minimized to generate the optimal symmetric walking motion. The simulation results matched well with the joint profiles, joint torques, and ground reaction forces obtained from experiments.

Optimization-based motion prediction has been widely used in biomechanics to synthesize control strategies, analyze muscle forces, predict optimal motion, and so on. However, the performance measure and necessary constraints are critical issues for predictive dynamics to simulate human motion. Marler et al. (2008) overviewed the computational approaches in digital human modeling. Schiehlen (1997) gave a review of multibody system dynamics in which optimal design of a mechanical system was discussed, especially the multicriteria optimization approach. Leboeuf et al. (2006) compared two performance criteria: the minimum effort cost and the minimum energy cost for predicting human handstand motion. It was concluded that the former tended to generate more natural motion and the latter gave a smoother motion. Vukobratović *et al*. (2007) derived a general model to simulate human and humanoid motions. The human was treated as a free spatial system, and particular tasks were considered as different contact

problems between the human model and various objects. Bottasso et al. (2006) proposed a computational procedure for inferring the cost functions that underlie the experimentally observed human strategies. Although many performance measures have been studied for human motion prediction, there is limited work on constructing constraints for a bio-system for the optimization formulation.

The Method

The figure below shows the basic methodology behind predicting human behavior using predictive dynamics but incorporating seed scenarios. Seed scenarios allow for the consideration of variation in task execution among people.

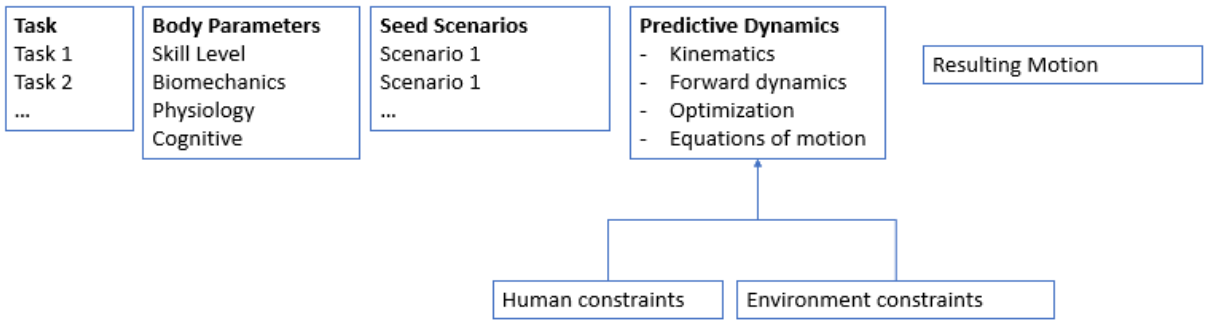

Figure 1. Methodology for predicting human behavior using predictive dynamics and incorporating seed scenarios

Below we define each element in this methodology.

A Task

A task in this context is defined as an action that is needed to be accomplished. Several tasks can be queued to accomplish an entire motion scenario. A task, for example, could be defined as jump from a high platform to the ground. Another task could be to push a lever with a specific force.

Body Parameters

There are several characteristics that define this set of parameters, including but not limited to skill level (level of training) and the biomechanics of the person (body height, weight, distribution, dimensions, anthropometry, etc.). The physiology of the human is also included in terms of strength, fatigue levels, metabolics, etc.

Seed Scenarios

We have adopted this methodology to include the acquisition of a number of scenarios that are executed by humans as a seed scenario for the predictive dynamics. This is where the variation between one person and another comes into play. A tall person will execute a task differently than a short person.

Acquiring motions requires the actual physical execution of a task by someone. The figure below shows the actual execution of a task (deadlift) while motion tracked.

Figure 2. Execution of a deadlift task while motion tracked

The number of seed scenarios to record is determined by observing the execution of the task. It is not scientific. In some cases, females execute the task differently than males. Tall people execute differently than short people, if the task required is affected by height.

For the tasks that we observed, on average, we had to record two to four seed scenarios.

Predictive Dynamics

The predictive dynamics approach was successfully applied to simulate digital human walking (Xiang et al. 2009b) and stair climbing (Bhatt et. al. 2008) tasks and was then further developed. The problem statement for the prediction of motion for dynamics tasks can be stated as "Given task-based parameters, human anthropometry, segment inertial properties, physical joint motion and actuation limits, and desired time for completion of task, generate visually appealing and dynamically consistent task simulations that minimize human performance." Such a description of the problem statement lends itself to an optimization formulation.

Joint angle profiles, $\mathbf{q(t)}$, are approximated as linear combinations of cubic B-spline basis functions. Thus, the control points representing the B-splines are the design variables for the optimization problem. Corresponding joint angle, joint velocity, and joint acceleration values are calculated at each iteration from these control point values.

The dynamic effort, which is defined as the time integral of squares of joint torques, is chosen as the objective function to be minimized for the general human motion prediction as in Equation (1).

$$J = \int_0^T \boldsymbol{\tau}^{\mathrm{T}} \boldsymbol{\tau} dt \quad (1)$$

The general constraints are categorized into physical constraints and task-based constraints. Physical constraints include the joint angle limits, joint torque limits, and equations of motion to impose law of physics as depicted in the following equations:

$$\mathbf{q}^L \leq \mathbf{q}(t) \leq \mathbf{q}^U \quad (2)$$

$$\boldsymbol{\tau}^L \leq \boldsymbol{\tau}(t) \leq \boldsymbol{\tau}^U \quad (3)$$

$$\boldsymbol{\tau} - f(\mathbf{q}, \mathbf{t}) = \mathbf{0} \quad (4)$$

The common task-based constraints being used to generate predictions for all tasks include ground penetration, dynamic stability, and self/collision avoidance. These constraints have been discussed in detail for dynamic walking prediction (Xiang et al. 2009b). The EOMs are calculated using recursive Lagrangian dynamics, and the analytical gradients are provided to the optimization solver. The dynamic stability of the digital human model is calculated from these equations of motion. The predicted motions are verified using determinants obtained from motion capture experiments. Well-accepted determinants based on literature are used if available. If the determinants are not available, new determinants are selected such that they characterize the motion being predicted. The formulation also showed high fidelity in predicting joint torques and ground reaction forces.

This paper presents the recent advances of predictive dynamics to simulate human motion including box lifting, running, throwing, and sideways walking. In addition, the new approach of segment-based collision avoidance and its applications in predictive dynamics is also addressed. It is noted that many dynamic tasks share same objective functions and constraints in the optimization formulation. Therefore, only those task-based constraints that feature the characteristics of each task are emphasized in the following section.

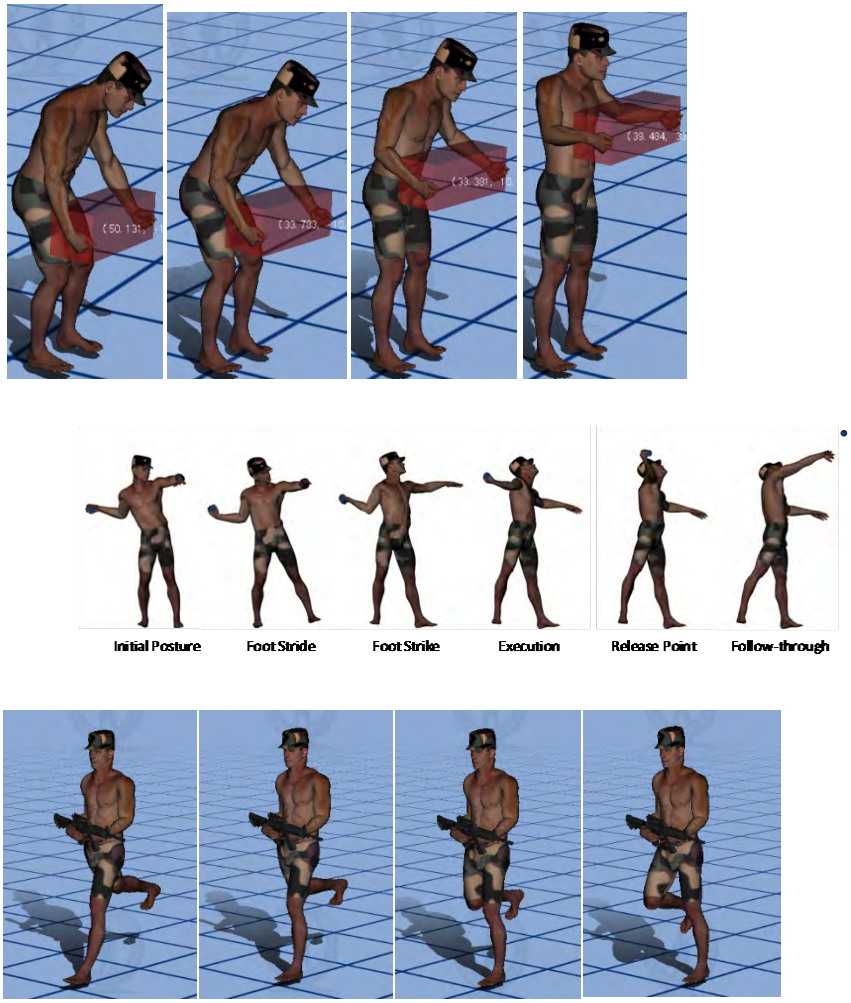

Figure 3. Santos executing the tasks of box-lifting, throwing, and walking while carrying

Constraints

The feasible set of solutions for the problem is an important issue for predictive dynamics. An infeasible set will result in a null solution space for the system. This situation should always be avoided while formulating a predictive dynamics problem. For a bio-system, feasibility of all the constraints can be tested by solving the predictive dynamics problem with a constant objective function as follows:

$$\begin{aligned} \min_{\mathbf{q},\boldsymbol{\tau}} \quad & J(\mathbf{q}, \boldsymbol{\tau}, \mathbf{t}) \equiv c \\ s.t.: \quad & \boldsymbol{\tau}\text{-}\boldsymbol{f}(\mathbf{q}, \mathbf{t}) = \mathbf{0} \\ & \mathbf{g}(\Upsilon) \le \mathbf{0} \\ & \mathbf{q}^L \le \mathbf{q} \le \mathbf{q}^U \\ & \boldsymbol{\tau}^L \le \boldsymbol{\tau} \le \boldsymbol{\tau}^U \end{aligned} \quad (6)$$

where c is a constant.

The solution of Equation (6) implies that the output set $(\mathbf{q}^f, \boldsymbol{\tau}^f)$ satisfies all linear and nonlinear constraints but does not optimize any performance measure for the biosystem. This is a feasible solution of the predictive dynamics problem. There are two purposes for obtaining a feasible solution for the system: one is to test the feasibility of all the constraints, and the other is to get a solution that might be used as a good initial guess for the predictive dynamics with a physical performance measure.

Minimal set of constraints

It is obvious that the more information about the biosystem that is available, the more accurate the predictive dynamics solution is. As an extreme case, all the displacement and force histories can be available in the time domain $\Omega \cup \Gamma$. However, in most cases, only minimal information about the biosystem is available, so predictive dynamics seeks the minimal constraint set $\mathbf{g}(\Upsilon_{minimal})$ and an appropriate performance measure to simulate the applied force and response histories for the biosystem, as follows:

$$\begin{aligned} \min_{\mathbf{q},\boldsymbol{\tau}} \quad & J(\mathbf{q}, \boldsymbol{\tau}, \mathbf{t}) \\ s.t.: \quad & \boldsymbol{\tau}\text{-}\boldsymbol{f}(\mathbf{q}, \mathbf{t}) = \mathbf{0} \\ & \mathbf{g}(\Upsilon_{minimal}) \le \mathbf{0} \\ & \mathbf{q}^L \le \mathbf{q} \le \mathbf{q}^U \\ & \boldsymbol{\tau}^L \le \boldsymbol{\tau} \le \boldsymbol{\tau}^U \end{aligned} \quad (7)$$

The minimal constraint set depends on the complexity of the biosystem and the motion to be simulated. For a simple motion, boundary conditions alone might be enough to reveal the entire motion; in this case, the minimal constraint set includes only boundary conditions. In contrast, for a complex motion, some state responses between the boundaries need to be known to simulate the real motion. Therefore, these state responses have to be included in the minimal constraint set.

Resulting Motion

We have experimented with this methodology using a number of prescribed tasks. Examples include climbing over a box, lifting a box, and several others.

The presentation at DHM will share some of these results as videos.

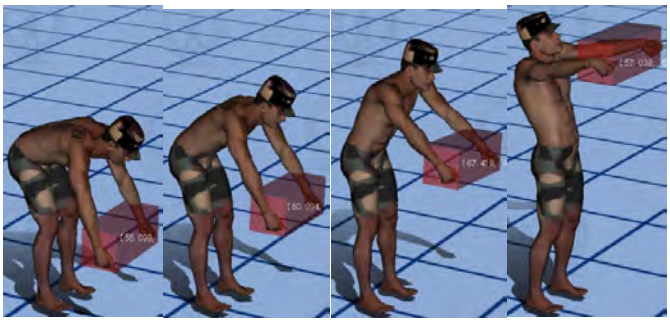

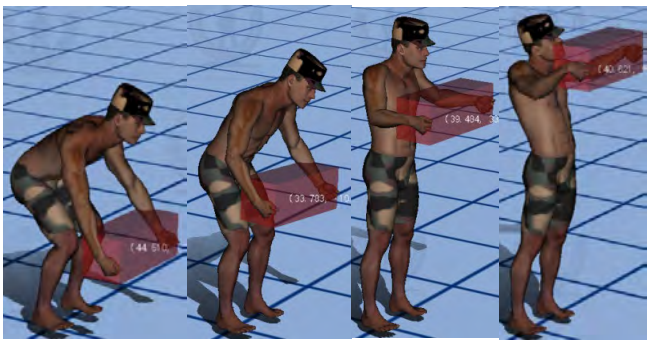

Figure 4: Two instances of Santos executing a box-lifting task

While this methodology shown merit for the prediction of behavior and for accounting for the variation in task execution among people, this is only a start, and significantly more work is needed.

References

Anderson, F.C., and Pandy, M.G. Static and dynamic optimization solutions for gait are practically equivalent. *Journal of Biomechanics*, v 34, 2001 a, p 153-161.

Anderson, F.C., and Pandy, M.G. Dynamic optimization of human walking. *Journal of Biomechanical Engineering*, v 123(5), 2001 b, p. 381-390.

Bhatt, R., Xiang, Y., Kim, J., Mathai, A., Penmatsa, R., Chung, H-J., Kwon, H-J., Patrick, A., Rahmatalla, S., Marler, T., Beck, S., Yang, J., Arora, J. S., Abdel-Malek, K., & Obusek, J.P. (2008, June). Dynamic optimization of human stair-climbing motion. Paper presented at the SAE Digital Human Modeling Conference, Pittsburgh, PA.

Bottasso, C. L., Prilutsky, B.I., Croce, A., Imberti, E., and Sartirana, S. A numerical procedure for inferring from experimental data the optimization cost functions using a multibody model of the neuro-musculoskeletal system. *Multibody System Dynamics*, v 16, 2006, p. 123-154.

Chevallereau, C., Formal'sky, A., and Perrin, B. Low energy cost reference trajectories for a biped robot, *Proceedings of IEEE International Conference on Robotics and Automation*, Leuven, Belgium, v 2, 1998, p. 1398-1404.

Kim, H.J., Wang, Q., Rahmatalla, S., Swan, C.C., Arora, J.S., Abdel-Malek, K., and Assouline, J.G., Dynamic motion planning of 3D human locomotion using gradient-based optimization. *International Journal of Biomechanical Engineering*, 2008; 130(3):031002.

Kim, J.G., Baek, J.H., and Park, F.C. Newton-type algorithms for robot motion optimization. *Proceedings of IEEE/RSJ International Conference on Intelligent Robots and Systems,* v 3, 1999, p. 1842-1847.

Leboeuf, F., Bessonnet, G., Seguin, P., and Lacouture, P. Energetic versus sthenic optimality criteria for gymnastic movement synthesis. *Multibody System Dynamics*, v 16, 2006, p. 213-236.

Lo, J., Huang, G., and Metaxas, D. Human motion planning based on recursive dynamics and optimal control techniques. *Multibody Sys. Dyn*, v 8(4), 2002, p. 433-458.

Marler, T., Arora, J., Beck, S., Lu, J., Mathai, A., Patrick, A., and Swan, C. Computational approaches in DHM, in *Handbook of Digital Human Modeling for Human Factors and Ergonomics*, Vincent G. Duffy, Ed., 2008.

Roussel, L., Canudas-de-Wit, C., and Goswami, A. Generation of energy optimal complete gait cycles for biped robots, *Proceedings of IEEE International Conference on Robotics and Automation*, Leuven, Belgium, v 3, 1998, p. 2036-2041.

Schiehlen, W. Multibody system dynamics: roots and perspectives. *Multibody System Dynamics*, v 1, 1997, p. 149-188.

Saidouni, T., and Bessonnet, G. Generating globally optimized sagittal gait cycles of a biped robot. *Robotica*, v 21(2), 2003, p 199-210.

Sohl, G.A., and Bobrow, J.E. A recursive multibody dynamics and sensitivity algorithm for branched kinematic chains. *ASME J. Dyn. Syst., Meas., Control*, v123, 2001, p. 391-399.

Vukobratović, M., Potkonjak, V., Babković, K., and Borovac, B. Simulation model of general human and humanoid motion, *Multibody System Dynamics*, v 17, 2007, p. 71-96.

Wang, Q., Xiang, Y., Arora, J.S., and Abdel-Malek, K. Alternative formulations for optimization-based human gait planning, *48th AIAA/ASME/ASCE/AHS/ASC Structures, Structural Dynamics and Materials Conference*, Honolulu, Hawaii, Apr. 23 – 26, 2007.

Xiang, Y., Arora, J.S., and Abdel-Malek, K. Optimization-based motion prediction of mechanical systems: sensitivity analysis. *Structural and multidisciplinary optimization*, v 37(6), 2009a, p. 595-608.

Xiang, Y., Arora, J.S., Rahmatalla, S., and Abdel-Malek, K. Optimization-based dynamic human walking prediction: one step formulation. *International Journal for Numerical Methods in Engineering*, 2009b (in press, DOI: 10.1002/nme.2575).

ME-BVH: Memory Efficient Bounding Volume Hierarchies

Evan Shellshear, Yi Li, and Johan S. Carlson
The Geometry and Motion Planning Department
Fraunhofer Chalmers Centre
SE-412 88 Gothenburg, Sweden
E-mail address of the corresponding author: evan.shellshear@fcc.chalmers.se

Abstract

Collision detection and distance computation algorithms often form the bottlenecks of many digital human modelling simulations in industrial processes. When designing vehicle assembly lines or cobot assembly cells it is essential to be able to accurately simulate collision free interactions both for efficient and safe operations. Hence, any attempt to improve such algorithms can have a broad and significant impact. Most of the focus is typically on speeding up the queries, however, with models becoming larger as scenarios become more realistic and simulations include more elements such as musculoskeletal models and 3D human body modelling, other parts of the proximity query performance are becoming important such as the management of memory. In this paper, we demonstrate a new technique called ME-BVH (Memory Efficient Bounding Volume Hierarchies) to improve memory usage for proximity queries with bounding volume hierarchies. The approach utilizes a simple and effective way of grouping primitives together at the leaf level and building the bounding volume hierarchy top down to the grouped primitive leaves. The paper then shows ways of efficiently carrying out primitive and bounding volume queries to offset the greater number of potential queries. In addition, the modifications taken are simple enough to be easily applied to most bounding volume hierarchies. By using these approaches, we demonstrate on a number of real-life assembly scenarios with millions of primitives that, compared to existing approaches, our proposed method is able to save up to half of the memory used and can reduce the build times at little cost to the query performance. In addition, the methods developed here are compatible with all BVH types and queries used in ergonomic simulations, unlike many other approaches. The developed algorithms present advantages for proximity queries for deformable meshes used in digital human modelling by reducing the time it takes to build a bounding volume hierarchy which often must be rebuilt or updated many times during simulations due to mesh deformations.

Keywords: Bounding Volume Hierarchies, Collision Detection, Proximity Queries, Automated Assembly, Simulation

Introduction

Collision queries (CQ) and distance queries (DQ), proximity queries, are key processes used in many applications (Shellshear & Bohlin, 2014) (Eriksson & Shellshear, 2014). The field of proximity queries is a well-researched area of study and there exist many effective algorithms for proximity queries in a variety of scenarios. However, given these queries are a key bottleneck in many areas, such as motion planning for virtual manikin assembly (Li, Delfs, Mårdberg, Bohlin, & Carlson, 2018), any improvements to the algorithms underpinning these techniques can benefit many industries beyond digital human modelling and reveal new approaches to solving well-known problems.

In this paper, we analyze algorithmic improvements to traditional Bounding Volume Hierarchies (BVHs) to quickly perform both collision queries and distance queries between a moving rigid body and static obstacles in digital human modelling scenarios such as vehicle assembly. The focus of our algorithmic improvements is on removing bounding volumes around primitives (triangles, lines, or points (Tafuri, Shellshear, Bohlin, & Carlson, 2012)) and then adapting the build and query phases to correctly handle the missing bounding volumes. By doing so, we are able to theoretically remove up to half of all bounding volumes required in a BVH, leading to faster build times and less memory requirements. To ensure the proximity queries are not impaired, we develop specific BV-primitive distance queries, where BV stands for a Bounding Volume.

Related Work

The foundational technology which we use to solve the problem of interest is the well-known Bounding Volume Hierarchy solution (Hubbard, 1993), with Rectangular Swept Spheres (RSSs) (Larsen, Gottschalk, Lin, & Manocha, 2000) as our chosen bounding volumes. RSSs are constructed by taking the Minkowski sum of some core primitive shape and a sphere. To create the set of bounding volumes that can be defined by RSSs one can have a point, line, or rectangle as the core primitive (resulting in a sphere, lozenge, or RSS), the first two cases being considered as degenerate rectangles (i.e., with one or two side lengths equal to zero). By enclosing an entire triangle mesh in an RSS one is then able to build a BVH top-down using well-known algorithms. The superiority of computing proximity queries with RSSs over other types of bounding volumes has been demonstrated in papers such as (Larsen, Gottschalk, Lin, & Manocha, 2000), (Lauterbach, Mo, & Manocha, 2010), and (Pan, Chitta, & Manocha, 2012).

However, as shown in (Terdiman, 2001), although RSS BVHs produce the best performance for distance queries, they also consume the greatest amount of memory by a factor of four over BVHs built on simpler

shapes such as spheres. Hence, for large scenes with millions of triangles, any optimization of RSS BVHs which doesn't sacrifice (or minimally impacts) performance is a welcome advance.

Since the creation of BVHs, there have been numerous attempts at finding ways to reduce the memory footprint via quantization (Terdiman, 2001), simplifying the representation of shapes (Zachmann, 1995), levels of detail (Yoon, Salomon, Lin, & Manocha, 2004), lazy building approaches (Krishnan, Pattekar, Lin, & Manocha, 1997) and many more. Although many of these methods produce some advantages, they are either not general enough to apply to all types of BVHs, not applicable to the intended applications here (exact calculations with fast query times) or are only relevant for collision queries and not distance queries. In the case of lazy build strategies (i.e., incrementally updating especially for deformable meshes), these can result in the update phases causing proximity queries to be up to 10x slower (Shellshear, Bitar, & Assarsson, 2013).

There is a known approach that is not only applicable to all BVHs and query types but also significantly reduces memory usage by removing unnecessary BVHs and does not result in slowing down the proximity queries by orders of magnitude. This approach either increases the number of primitive shapes (e.g., triangles) in each leaf or simply removes BVs around primitives, to a similar effect.

In the first case of increasing the number of primitive shapes in a leaf, this has been carried out and applied in many scenarios that use BVHs (Dammertz, Hanika, & Keller, 2008) (Ericson, 2004). The results, however, typically require using low-level SIMD (single instruction multiple data streams) instructions such as SSE (streaming SIMD extensions) or AVX (advanced vector extensions) (Shellshear & Ytterlid, Fast distance queries for triangles, lines, and points using SSE instructions, 2014) to speed up the slowdowns caused by unnecessary primitive tests.

In this paper we avoid this approach due to the additional complexity of coding SIMD or AVX instructions and also due to the fact that compilers are typically able to carry out SIMD and AVX optimizations better than manually coded instructions (Shellshear & Ytterlid, Fast distance queries for triangles, lines, and points using SSE instructions, 2014). Hence, existing approaches that are compiled in a modern compiler will likely be benefiting from this already.

Although increasing the number of primitive shapes in a leaf may lead to individual primitives without a specific BV surrounding them, it is not the same as the second approach mentioned above (i.e., removing BVs around primitives). The second approach leads to just having to test a single primitive when a leaf is reached, hence preserving the benefit of traditional BVHs. However, it requires developing BV-primitive collision and distance queries to be able to work which are not always a part of many BVH packages.

This paper focuses on the second approach of simply removing the BV around the final primitive to potentially reduce the memory footprint by up to fifty percent. Surprisingly there are very few papers which have addressed this and the one relevant paper (Terdiman, 2001), ended up carrying out a comparison which does not lead to any obvious conclusions (due to comparing two different types of BVHs) and also does not test the improvements for distance queries which can have fundamentally different performance profiles.

The ME-BVH Algorithm

In this section we introduce the ME-BVH (Memory Efficient Bounding Volume Hierarchies) algorithm via discussing the changes to traditional BVHs. When building a BVH for a triangle mesh, the typical process is top-down, whereby a BV is built around the entire triangle mesh, which is then split recursively into smaller disjoint subsets around which new BVs are built until the algorithm reaches a single triangle around which a final BV is built, and the process stops.

If we begin with a triangle mesh with N triangles, this leads to $2N - 1$ BVs. When dealing with millions of triangles, this then requires memory to store twice as many BVs as triangles and for certain types of BVs (such as RSSs), the storage required per BV is greater than the storage requirements per triangle. If we remove unnecessary BVs from the BVH leaves, we immediately avoid building N BVs. Additionally, by not having to build these BVs, the construction phase would be faster. However, doing so requires changes to existing query routines to handle the leaf cases which no longer have BVs around them, which typically means creating a BV-triangle collision or distance routine. As mentioned in (Terdiman, 2001), such BV-triangle routines exist for simple shapes like Box-triangle, however, in our case of an RSS BVH we were required to implement a new routine.

Algorithm 1: The traditional BVH build process

```
1 RecurseBuild (T)
  Input: T a non-empty set of triangles
  Output: BVH
2 Build a BV around triangle(s) T
3 if |T| > 1 then
4 |   Split triangles into two sets T_1 and T_2
5 |   RecurseBuild(T_1), RecurseBuild(T_2)
6 else
7 |   return
```

Build Phase in ME-BVH

In many current top-down BVH construction algorithms, at each stage, criteria are used to determine whether a further split is required and when a single triangle is reached the criteria return false (e.g., the traditional BVH build process detailed in Algorithm 1. In our case the simple adaptation was to change the criteria to false as soon as we reached two or less triangles (i.e., in line 3 in Algorithm 1, we changed the condition to $|T| > 2$).

Query Routine in ME-BVH

Compared to standard BVHs, the ME-BVH contains leaves without BVs. Consequently, the standard traversal routine has to be updated in order to handle the following four cases: the usual RSS-RSS traversal, the RSS-triangle traversal, the triangle-RSS traversal and the usual triangle-triangle test.

The first part of the traversal where distances or collisions are computed between RSSs can use existing approaches (Larsen, Gottschalk, Lin, & Manocha, 2000). For the RSS-triangle and triangle-RSS cases we had to come up with a new algorithm. The main part of this was to create a new RSS-triangle distance query as well as logic during the query traversal for the ability to handle when a BV was to be tested against a leaf.

Due to the way the build phase is carried out, the algorithm now needs to handle "leaves" which may have two triangles in them. If we reach a leaf with two triangles, we traverse one triangle against the other BVH first, then traverse the second triangle. This effectively achieves the goal of having a single triangle tested against another hierarchy unlike approaches which simply have multiple triangles in a leaf with a BV around them. In the case that we reach two leaves with multiple triangles, we test all pairs of triangles against each other (either two or four pairs).

The creation of an RSS-triangle distance query was straightforward and used the same approach for the Triangle-Triangle distance query in the PQP package (Larsen, Gottschalk, Lin, & Manocha, 2000). This algorithm works by first finding the minimum distance between each pair of triangle edges (9 total combinations), then it examines the off-edge vertices and checks if either are within the slab between the two planes defined by the line connecting the closest points on the current triangle edges being tested. In the triangle case, there is only one off vertex to check for each triangle, however, with an RSS, we need to test both off-edge vertices, see Figure 1, which demonstrates the scenario where we need to test if the off-edge vertices A, D and G lie in the slab defined by the lines L_1 and L_2.

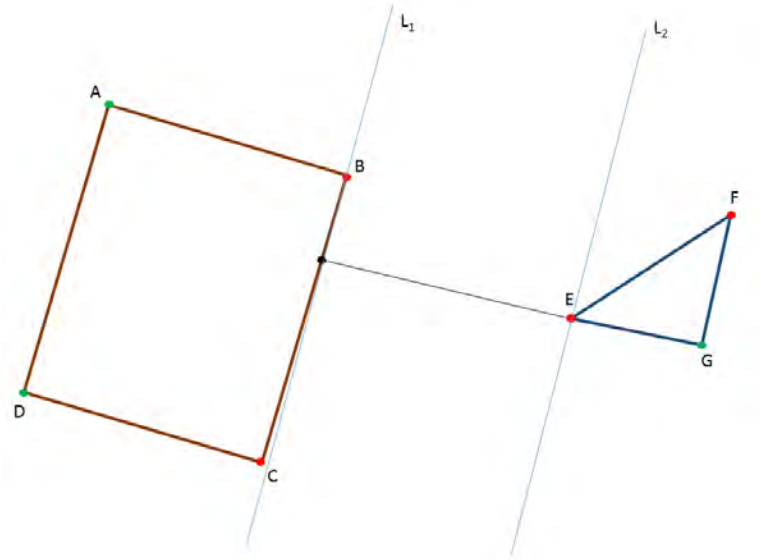

Figure 1. Testing off-edge vertices A and D and G between a rectangle and a triangle when testing edges BC and EF.

If the minimum distance is not found due to vertices being contained in the slab between the closest points on a given edge-edge test, then we need to check four other cases:

1. one of the closest points is a vertex of one triangle and the other closest point is on the face of the other RSS (or vice versa).
2. the triangle and RSS intersect.
3. an edge of one triangle is parallel to the face of the other RSS or vice versa.
4. one or both triangles and/or RSS are degenerate.

The adaptations were straightforward to the existing Triangle-Triangle distance query in the PQP package (Larsen, Gottschalk, Lin, & Manocha, 2000) and led to good performance. We also tested a simpler version of the above RSS-Triangle routine by splitting a rectangle into two triangles and then simply using two Triangle-Triangle distance routines to compute the shortest distance, however, this turned out to be much slower than the above more tailored version, even with optimizations to avoid one of the Triangle-Triangle routines in obvious situations.

Results

To test the performance of the ME-BVH, we developed a number of experiments based on real life, virtual manikin assembly scenarios with millions of triangles. We not only tested collision and distance query timings but also tested the effect of the ME-BVH on the performance of IPS Path Planner (Li,

Shellshear, Bohlin, & Carlson, 2020). This planner is widely by industry to plan collision-free disassembly paths and it relies on the underlying collision and distance computation module (IPS CDC) instead of the PQP package (Larsen, Gottschalk, Lin, & Manocha, 2000) to perform collision queries and distance queries. Both IPS Path Planner and IPS CDC have been presented in a number of papers (Li, Shellshear, Bohlin, & Carlson, 2020) (Spensieri, Carlson, Bohlin, Kressin, & Shi, 2016) (Forsberg, Mårdberg, Roll, Rilby, & Carlson, 2018) and we refer the reader to those papers for more details.

Currently, IPS CDC uses the traditional approach to construct BVHs. To demonstrate the effectiveness of our algorithm (i.e., the ME-BVH), we implemented it on top of IPS CDC in lieu of the traditional approach. The source code was written in C++ and compiled in Microsoft Visual Studio Professional 2019 (Version 16.7.7) on Windows 10 Pro 64 bit. The computer that we used contained an Intel® Core™ i7-7700K CPU @ 4.20 GHz (4 cores, 8 threads), a NVIDIA GeForce GTX 970 (4 GB) GPU, and 32 GB RAM.

To compare the memory required by BVHs constructed with the traditional approach and the ME-BVH, we collected five different test cases (TC) from the manufacturing industries:

1. TC Air Filter Assembly, the models are proprietary, so we are unable to show an image. This test case involves a virtual manikin having to move an air filter assembly out of a motorcycle frame where the initial assembled state of the frame and air filter assembly are very close to each other so that the movements are very constrained. The total number of triangles in this test case is more than 1.5 million.
2. TC Cylinder Head, as above the models are also proprietary so we are unable to show an image. This test case involves moving the cylinder head cover of an engine block from the top of the engine block in the frame of the motorbike to a location outside of the frame. Again, in the final assembled state there are many parts of both the rigid and static geometry which are very close to each other and almost being in collision. The total number of triangles in this test case is more than 650,000.
3. TC CEM (central electronic module) Box, see Figure 2 and Table 1 for details.
4. TC Large Environment, see Figure 3 and Table 1 for details.
5. TC Tunnel Console, see Figure 4 and Table 1 for details.

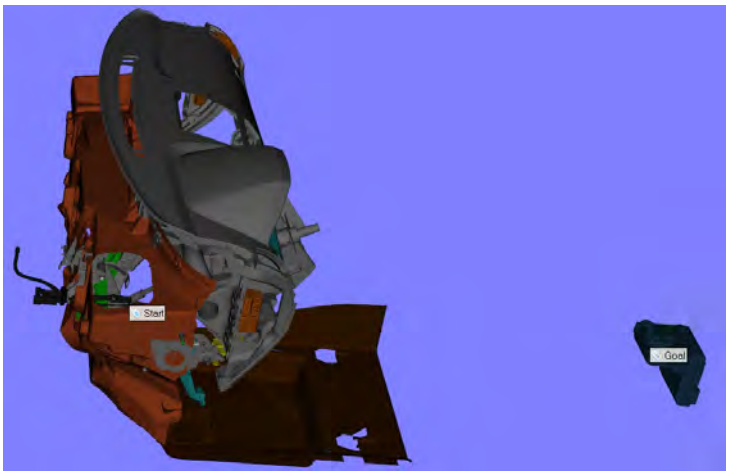

Figure 2. TC CEM Box: The CEM (central electronic module) box on the right side of the figure is the rigid body, whereas the parts of the dashboard on the left is considered to obstacles. Labels *Start* and *Goal* mark the rigid body's positions when it is assembled and disassembled, respectively.

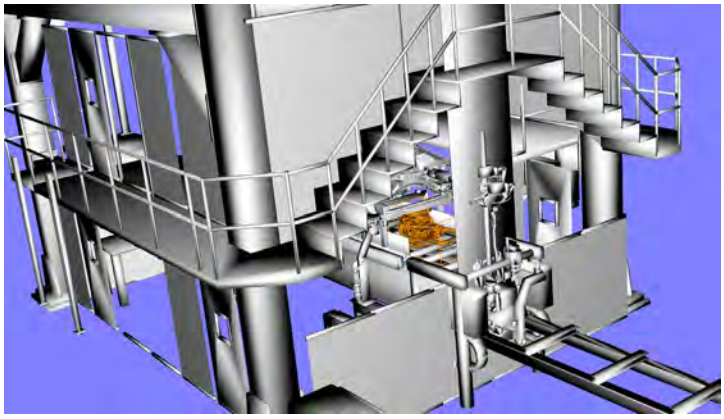

Figure 3. TC Large Environment: The spot-welding machine (highlighted in brown) is the rigid body, whereas the structures around it are considered to be the obstacles.

We evaluate the performance of IPS Path Planner using IPC CDC with the ME-BVH by using it to solve the following three test cases that are the more challenging ones (for path planners) among the test cases listed in Table 1: TC Air Filter Assembly, TC Cylinder Head, and TC Tunnel Console. In each test case, parts to be disassembled are grouped into a single rigid body and the goal of IPS Path Planner is to compute a collision-free disassembly path for the rigid body as fast as possible. For comparison, we also solved these path planning problems using IPS CDC with the traditional approach to construct BVHs. In addition, given the focus is on the performance of the BVH we didn't add human dynamic or simulation elements to the computations.

Table 1. The number of vertices and triangles in all 3D triangular meshes used by the test cases. Models with superscript † represent the triangular meshes of the rigid bodies, whereas models with superscript ‡ represent the triangular meshes of the obstacles. Bolded numbers are for the ME-BVH.

3D Models	No. of Vertices	No. of Triangles	No. of BVs	Memory (kb)	Build Time (msec)
TC Air Filter Assembly†	797,076	1,253,476	2,506,951 vs **1,525,577**	190,507 vs **125,337**	8,272 vs **7,900**
TC Air Filter Aassembly‡	290,433	415,378	830,755 vs **500,159**	63,438 vs **41,484**	2,195 vs **2,056**
TC Cylinder Head†	264,495	246,584	493,167 vs **305,365**	38,738 vs **26,267**	1,375 vs **1,266**
TC Cylinder Head‡	423,742	413,742	827,483 vs **512,659**	64,764 vs **43,858**	2,218 vs **2,094**
TC CEM Box†	23,691	32,615	65,229 vs **39,817**	4,991 vs **3,308**	209 vs **193**
TC CEM Box‡	312,349	456,782	913,563 vs **568,917**	69,679 vs **46,806**	3,134 vs **2,896**
TC Large Environment†	64,184	127,265	254,529 vs **156,349**	19,145 vs **12,626**	771 vs **753**
TC Large Environment‡	1,161,904	1,742,755	3,485,509 vs **2,104,553**	265,498 vs **173,794**	14,706 vs **14,135**
TC Tunnel Console†	65,997	73,469	146,937 vs **90,269**	11,391 vs **7,628**	421 vs **375**
TC Tunnel Console‡	288,484	300,567	601,133 vs **374,789**	46,821 vs **31,791**	1,688 vs **1,578**

Table 2. The average numbers of Collision Queries (CQ) and Distance Queries (DQ) that IPS CDC is able to perform per second with BVHs built by the traditional approach and the ME-BVH, respectively. Averaged over 100 runs.

Test Cases	Traditional BVH		ME-BVH	
	CQ	DQ	CQ	DQ
CEM Box	14,103	2,259	12,177	949
Large Environment	57,009	2,201	55,454	1,184
Tunnel Console	7,891	4,754	6,376	1,519

Before running the path planning problems, we tested the number of possible distance queries and collision queries that ME-BVH could carry out each second compared to the default algorithm in a number of different configurations arising during the path planning exercise. These results are presented in Table 2.

After solving the three path planning problems (i.e., TC Air Filter Assembly, TC Cylinder Head, and TC Tunnel Console) with IPS Path Planner using IPS CDC with the ME-BVH algorithm, the experimental running times and the speedups (compared to IPS Path Planner using IPS CDC with the traditional approach to construct BVHs) are listed in Table 3.

(a) start position (b) goal position

Figure 4. TC Tunnel Console: The tunnel console (in green) in start and goal configurations.

Table 3. The experimental running times (in seconds) of IPS Path Planner using IPS CDC with the traditional approach to construct BVHs and IPS CDC with the ME-BVH. The speedups (compared with the traditional approach to construct BVHs) are listed in the parentheses.

Test Cases	Traditional BVH	ME-BVH
Air Filter Assembly	16 (1.00)	20 (0.80)
Cylinder Head	136 (1.00)	149 (0.91)
Tunnel Console	33 (1.00)	33 (1.00)

The results in this section demonstrated on the five case studies that ME-BVH reduced memory consumption by an average 33% and ME-BVH reduced build time by an average 6%. These benefits are gained for less than a 10% average reduction in collision query performance and up to 66% reduction in distance query performance. It should be noted that the BVH build phase in IPS CDC is highly parallelized with each branch being built with a separate thread and so if a user is unable to use a parallel build strategy, we expect even larger improvements to the build times for non-threaded scenarios.

Although the ME-BVH led to slower distance queries, overall, the ME-BVH algorithm did not lead to significantly slower planning times, which is the key benchmark. This is due to several heuristics in the IPS CDC path planner which depend on the pairs of nodes in the BVH hierarchies tested against each other during the proximity queries and so the path planning timings don't always correspond 1-1 with distance query performance.

Discussion and Conclusions

In this paper, we have presented a new technique called ME-BVH with the main aim to substantially reduce memory requirements by not building unnecessary BVs. Overall, we see the approach achieving

its desired goals of memory reduction and build time reduction at little or no cost to path planning execution times.

Digital human modelling typically requires modelling deformable meshes due to the movements carried out by virtual manikins during assembly activities. The ME-BVH has advantages for deformable meshes. A common approach to accelerating distance and collision queries for deformable meshes is to rebuild BVHs at specific points in time. A key advantage of the ME-BVH is that it has half as many BVs in the BVH and hence faster rebuild times as seen above. Building a whole BVH takes 10,000 to 100,000 times longer than a distance query or collision query which is why BVH designs for deformable meshes balance BVH query performance with rebuild time (Shellshear, Bitar, & Assarsson, 2013).

If we save 6% on the build time, as the results here demonstrate, then for BVH algorithms for deformable meshes like in (Shellshear, Bitar, & Assarsson, 2013), the benefit of faster build times will outweigh the slightly slower distance and collision queries. (Shellshear, Bitar, & Assarsson, 2013) showed that even a smarter build phase which intelligently balances the need to rebuild with query performance, still means the build phase makes the distance queries ten times slower on average (collision queries would take an even larger performance hit than that). So, a 6% improvement in the build phase would offset a 60% slowdown of the average collision query or distance query time. This implies using the ME-BVH in these contexts saves us memory without any penalty to the average distance query performance and faster collision queries on average.

Further avenues for investigation would be to test balancing the BVH before building to ensure more nodes have two leaves as children instead of the typical one third, although challenges exist due to worse performance in hierarchies which are forced to be balanced (Held, Klosowski, & Mitchell, 1995). Further research could also look at the performance of ME-BVH with other bounding volume types instead of RSSs.

Acknowledgments

This work is part of the Sustainable Production Initiative and the Production Area of Advance at the Chalmers University of Technology. We would like to acknowledge the generosity of Volvo Cars in providing the models that were used for the experiments in this work.

References

Dammertz, H., Hanika, J., & Keller, A. (2008). Shallow bounding volume hierarchies for fast SIMD ray tracing of incoherent rays. In *Computer Graphics Forum* (pp. 1225-1233). Wiley.

Ericson, C. (2004). *Real-time collision detection.* CRC Press.

Eriksson, D., & Shellshear, E. (2014). Approximate distance queries for path-planning in massive point clouds. *Proceedings of the 11th International Conference on Informatics in Control, Automation and Robotics (ICINCO)*, (pp. 20-28).

Forsberg, T., Mårdberg, P., Roll, R., Rilby, E., & Carlson, J. S. (2018). Demonstration of simulation software industrial path solutions IPS. *Proceedings of the 2018 Winter Simulation Conference*, (pp. 4259-4259).

Held, M., Klosowski, J. T., & Mitchell, J. S. (1995). *Speed comparison of generalized bounding box hierarchies.* Department of Applied Math, SUNY Stony Brook.

Hubbard, P. M. (1993). Interactive collision detection. *Proceedings of 1993 IEEE Research Properties in Virtual Reality Symposium*, (pp. 24-31).

Krishnan, S., Pattekar, A., Lin, M. C., & Manocha, D. (1997). Spherical Shell: A Higher Order Bounding Volume for Fast Proximity Queries. *Proceedings of Third International Workshop on Algorithmic Foundations of Robotics.*

Larsen, E., Gottschalk, S., Lin, M. C., & Manocha, D. (2000). Fast distance queries with rectangular swept sphere volumes. *Proceedings of 2000 IEEE International Conference on Robotics and Automation*, (pp. 3719-3726).

Lauterbach, C., Mo, Q., & Manocha, D. (2010). gProximity: hierarchical GPU-based operations for collision and distance queries. *Proceedings of 2010 Computer Graphics Forum*, (pp. 419-428).

Li, Y., Delfs, N., Mårdberg, P., Bohlin, R., & Carlson, J. S. (2018). On motion planning for narrow-clearance assemblies using virtual manikins. *Procedia CIRP*, (pp. 790-795).

Li, Y., Shellshear, E., Bohlin, R., & Carlson, J. S. (2020). Construction of Bounding Volume Hierarchies for Triangle Meshes with Mixed Face Sizes. *Proceedings of 2020 IEEE International Conference on Robotics and Automation*, (pp. 9191-9195).

Pan, J., Chitta, S., & Manocha, D. (2012). FCL: A General Purpose Library for Collision and Proximity Queries. *Proceedings of 2012 IEEE Int. Conference on Robotics and Automation.*

Shellshear, E., & Bohlin, R. (2014). A heuristic framework for path planning the largest volume object from a start to goal configuration. *Proceedings of of the 11th International Conference on Informatics in Control, Automation and Robotics (ICINCO)*, (pp. 264-271).

Shellshear, E., & Ytterlid, R. (2014). Fast distance queries for triangles, lines, and points using SSE instructions. *Journal of Computer Graphics Techniques*.

Shellshear, E., Bitar, F., & Assarsson, U. (2013). PDQ: Parallel Distance Queries for deformable meshes. *Graphical Models*, 69-78.

Spensieri, D., Carlson, J. S., Bohlin, R., Kressin, J., & Shi, J. (2016). Optimal robot placement for tasks execution. *Procedia CIRP*, (pp. 395-400).

Tafuri, S., Shellshear, E., Bohlin, R., & Carlson, J. S. (2012). Automatic collision free path planning in hybrid triangle and point models: a case study. *Proceedings of the 2012 Winter Simulation Conference (WSC)*, (pp. 1-11).

Terdiman, P. (2001). *Memory-optimized bounding-volume hierarchies*. Retrieved from www.codercorner.com/Opcode.pdf

Yoon, S.-E., Salomon, B., Lin, M. C., & Manocha, D. (2004). Fast collision detection between massive models using dynamic simplification. *Proceedings of the 2004 Eurographics/ACM SIGGRAPH symposium on geometry processing*, (pp. 136-146).

Zachmann, G. (1995). The BoxTree: Exact and fast collision detection of arbitrary polyhedra. *First Workshop on Simulation and Interaction in Virtual Environments (SIVE 95).*

Developing a response surface methodology to determine the best objective function weightings for predicting probable postures

Justin Davidson[1], Joshua Cashaback[2], and Steven Fischer[1]

[1] *University of Waterloo, Canada*

[2] *University of Delaware, United States*

Abstract

The ability to predict human postures when simulating interactions with different workspaces and objects is valuable for effective proactive ergonomic evaluation. Using previously collected human motions to predict postures appears to be one effective method; however, when modeling more unique postures, optimization approaches may be useful. Optimization-based predictive modeling is rooted in optimal control theory principles, which are built on the assumption that humans adopt movement strategies that minimize or maximize some underlying performance criteria (e.g., minimize joint torques).

Santos Pro™ is an optimization-based digital human model that uses multiple objective functions to predict postures. However, it is unclear which objective functions and associated weightings are ideal for predicting probable human postures.

The purpose of this research was to develop a response surface methodology approach to optimize objective function weighting to predict realistic floor-to-shoulder lifts. Three minimization objective functions were evaluated to demonstrate this quantitative method: (1) discomfort, (2) total joint torque, and (3) maximum joint torque.

Ten participants completed box lifting from floor to shoulder while their motion was tracked using motion capture. Postures for the initiation (origin) and end (destination) of the lift were extracted and mapped onto anthropometrically matched avatars. Separately, avatar lifting postures were also predicted using the built-in multi-objective optimization. The avatar's hands and feet were constrained to match a human participant's hand and foot location. The remaining degrees of freedom on the avatar were predicted using the various objective functions and their associated weightings. Three objective functions were weighted systematically at 10% weighting increments to predict 1,331 postures from the various weighting combinations. Joint angle errors were calculated between the motion capture data and each predicted posture. The resultant error surface (error as a function of objective function weighting) was then fit with a multivariate function and subsequently minimized to estimate the objective function weighting combination that best predicted the true participant postures.

Discomfort alone tended to best predict lift origin and destination postures. Thus, minimizing discomfort may be an important objective for predicting un-fatigued lifting. The response surface methodology provides a quantifiable method to estimate the best objective function weighting to predict task-focused human behaviors.

Keywords: response surface methodology, posture prediction, objective function weightings